SCIENTIFIC SOCIETY
OF MECHANICAL ENGINEERS

SECTION OF TECHNICAL SCIENCES,
HUNGARIAN ACADEMY OF SCIENCES

PROCEEDINGS OF THE SEVENTH CONFERENCE ON FLUID MACHINERY

Volume 1

AKADÉMIAI KIADÓ, BUDAPEST 1983

Conferences on fluid machinery have been arranged regularly by the Section of Technical Sciences of the Hungarian Academy of Sciences and the Hungarian Scientific Society of Mechanical Engineers.

These two volumes contain the texts of 108 lectures delivered at the seventh Conference held in Budapest in the autumn of 1983. The authors are recognized as eminent scientists in their respective fields. They represent 21 countries of four continents. The papers deal with topics related to design, testing, and operation of fluid machinery, presented as follows: Ideal and real flow through passages, boundary layers, flows around bodies, flow through cascades; Two-phase flow, mixing; Cavitation, erosion, noise, surge; Positive displacement pumps; Water turbines; Axial fans, compressors; Centrifugal fans, pumps, compressors; Seals; Branching networks and distribution systems; Turbocompressors; Nozzles, jet pumps; Flow measurements, orifice flows; Fluid couplings; Stresses in rotors.

Beyond the discussion of these topics, the papers also forecast the further development of this important field.

ISBN 963 05 3462 2 vols 1–2

ISBN 963 05 3463 0 vol. 1

PROCEEDINGS
OF THE SEVENTH CONFERENCE
ON FLUID MACHINERY

SCIENTIFIC SOCIETY
OF MECHANICAL ENGINEERS

SECTION OF TECHNICAL SCIENCES,
HUNGARIAN ACADEMY OF SCIENCES

PROCEEDINGS OF THE SEVENTH CONFERENCE ON FLUID MACHINERY

Volume 1

AKADÉMIAI KIADÓ, BUDAPEST 1983

Editors:

L. Kisbocskói and Á. Szabó

ORGANIZING COMMITTEE
OF THE SEVENTH CONFERENCE
ON FLUID MACHINERY

Chairman:

Professor Dr h. c. Dr J. J. Varga

Vice-Chairman:

L. Kisbocskói

Secretary:

Á. Szabó

Members:

Prof. Dr T. Czibere, Dr Á. Fáy, Dr Cs. Fáy, Prof. Dr O. Fűzy, Mrs. E. Hajós, Dr Z. Hankó, Prof. Dr M. Kozák, Dr L. Mátay, Prof. Dr A. Nyíri, Prof. Dr L. Pápai, D. Pattantyús-Á., L. Pázmány, Mrs. É. Pesti, Dr Gy. Sebestyén, Dr Sz. Szabó, Prof. Dr T. Szentmártony, Dr D. Szüle, Prof. Dr Z. Terplán, E. Trenka, Dr Z. Vajna, Dr A. Verba, Miss M. Wagner

ISBN 963 05 3462 2 Vols 1—2
ISBN 963 05 3463 0 Vol. 1

Printed in Hungary

CONTENTS TO VOLUME 1

P R E F A C E

The Section of the Technical Sciences of the Hungarian Academy of Sciences and the Scientific Society of Mechanical Engineers have herewith pleasure of presenting the Proceedings of the Seventh Conference on Fluid Machinery.

The Organizing Committee is proud of the renowned authors and greets amid them quite a number of regular participants. Their constant and faithful help was a support in gaining a world-wide good reputation of our meetings. We ask them to receive our best thanks.

Our new authors are welcome, too. Their complimentary contributions to our work exerts an inspiring influence on it.

Since our contributors are excellent specialists in their own areas of science we hope that our Proceedings will provide a valuable and indispensable contribution to research in this field.

As the authors are prominent authorities on their professional line the Organizing Committee does not consider itself entitled to alter the texts submitted even if the contents of the papers do not coincide with its own opinion on some details. The authors had to prove the correctness of their ideas and theses in front of the conference publicity. Publication of the manuscripts in photostat underlines this responsibility, too.

We hope that both research workers and practicing engineers will avail themselves of perusing and studying the material of these volumes.

And at the same time it is our duty to renew our heartfelt thanks to the authors for their assistance to have made the Conference successful by submitting the papers now published here.

Varga

Prof. J. J. Varga
Dr.Techn., Dr.Econ., Dr.Sc., Dr.h.c.
Chairman of the Organizing Committee

SWIRLING FLOW IN RADIAL INWARD PASSAGE

S. Akaike and T. Toyokura

SUMMARY

This paper presents experimental results on the swirling inward flows in the passage between two parallel disks where the inlet flow is uniform, and in the inward flow section of interstage return channel. The velocity distribution in the passage is measured in ditail and the property of end wall boundary layer is also discussed. The distribution of peripheral velocity component in the passage is fairly uniform, but that of radial velocity component depends strongly on the secondary flow developed in the boundary layer. When the mean flow angle is less than or nearly equal to 7°, the reverse flow occurs in the middle region in the passage and the fluid flows mainly along the end walls.

1. INTRODUCTION

The swirling inward flow is experienced in the return channel of multi-stage centrifugal turbomachinery or in the stationary radial inward passage of a water turbine and so on. The flow separation of the boundary layer along the end wall in the passage does not occurs because of the accelerating flow, but the secondary flow appears in the boundary layer due to the effect of centrifugal force acting on a fluid particle in the direction normal to a stream line and the velocity profile in the boundary layer is skewed as shown in Fig.1. Since the fluid particle at the middle plane in the passage moves toward the wall region by the secondary flow, the distribution of radial velocity component is affected remarkably when the peripheral velocity is much greater than the radial velocity component. In fact, the existence of the reverse flow was reported in the flow downstream of the guide vanes of a reversible pump-turbine for small guide vanes openings (1).

There were a number of studies on the swirling flow in the radial outward passage such as a vaneless diffuser, and the authors have shown the experimental results on the flow in the interstage return bend of centrifugal turbomachinery in a previous paper (2). With respect to the swirling flow in the radial inward passage, the flow on the vortex chamber was studied (3),(4), but the details of the flow behaviour are not made clear up to date.

This study is intended to make clear the behaviour of the swirling flow in a

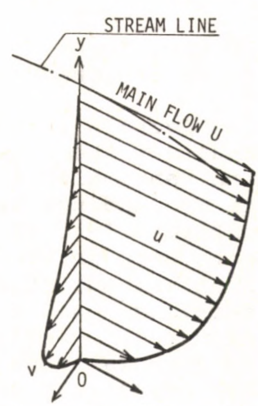

Fig.1 Skewed boundary layer

radial inward passage. Experiments are carried out on the flows in the passage composed of two parallel disks where the inlet flow is uniform, and in the inward flow section after the model interstage return bend. The velocity distribution in the passage is measured in detail and the property of end wall boundary layer is also discussed.

2. EXPERIMENTAL EQUIPMENTS AND PROCEDURE

2.1 Experiment on Flow Between Two Parallel Disks

Figure 2 shows a skeleton view of the test section using an air as working fluid, which is drawn by a blower installed at the end of a long straight duct (about 4m). A swirl component of inlet flow is given by 40 guide vanes set at the inlet of passage.

Velocity distributions were measured by using three-holes yaw probe at the inlet datum radius r_0 =280mm and radii r=260, 240, 220, 200mm (r/r_0 =0.929, 0.857, 0.786. 0.714).As the width b of the passage is 20mm and 37mm, the ratio b/r_0 is 0.071 and 0.132, respectively. Experiments were made for the mean flow angle $\bar{\alpha}_0$=3°~30° measured from the peripheral direction at the inlet radius r_0. The Reynolds number $Re=(\bar{c}_0 \cdot 2b)/\nu$ based on the mean absolute velocity $\bar{c}_0$ at r_0 and b is about 0.6×10^5. Here, ν is the kinetic viscosity.

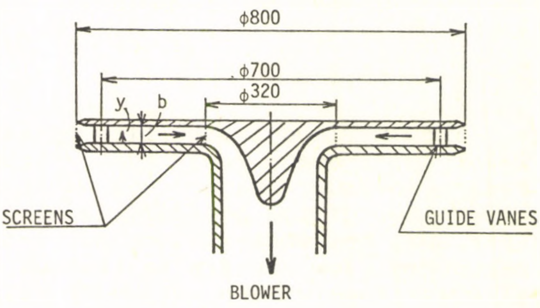

Fig.2 Sectional view of model passage (unit, mm)

2.2 Experiment on Flow in Return Channel

Figure 3 shows the model passage of the interstage return bend, which was shown in the proceedings of the last conference(2). Flow measurements were carried out at the inlet and outlet of the bend (sections A and B, r_0=270mm), and at radii r=232mm and 193mm in the radially parallel passage downstream of the bend. The width b of passage is 22.5mm and kept constant. Experiments were made for the mean flow angle at the inlet

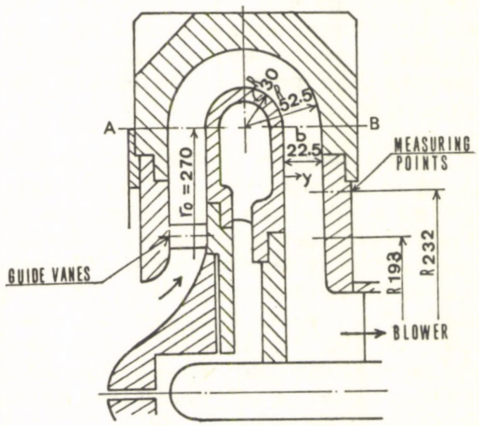

Fig.3 Sectional view of model interstage return bend (unit, mm)

of the bend (section A) $\overline{\alpha}_A$ =16°~30°. The Reynolds number $Re=(\overline{c}_A \cdot 2b)/\nu$ ($\overline{c}_A$: mean absolute velocity at A) is also 0.6×10^5.

3. EXPERIMENTAL RESULTS AND DISCUSSION

3.1 Flow Between Two Parallel Disks

Flow in Passage.- At first, the flow symmetry in the passage is verified by measuring the velocity distribution and the static pressure at 4 sections divided by 90° pitch on a circumference at r/r_0 =0.857. The following results are obtained from the measurement on a meridian section.

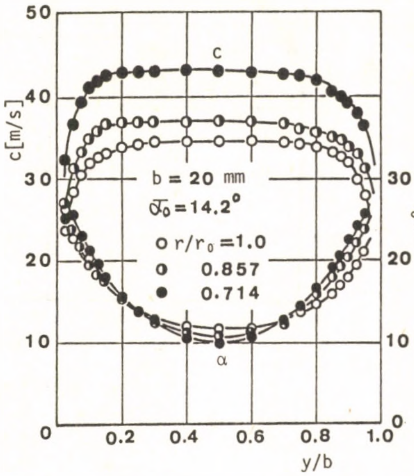

Fig.4 Flow in passage

Figure 4 shows the flow pattern in the passage for b=20mm as an example. In the figure, c is absolute velocity, α is flow angle and y is the distance measured from the lower end wall. At the inlet radius r/r_0=1.0, the wakes of the guide vanes disappear and a symmetrical velocity distribution in the direction to the width is obtained. At r/r_0=0.714 near the suction nozzle, the main flow has a tendency to move a little toward the lower end wall. The flow angle near the end wall is much greater than that of the middle region. This phenomenon is caused by the secondary flow developed in the boundary layer.

Property of Skewed Boundary Layer.-The velocity distribution in the boundary layer is divided into two distributions of u and v, which give the velocity components in the main flow direction and in the vertical direction to it, as shown in Fig.1. As an example, the distributions of u/U and v/v_{max} at r/r_0=0.857 are shown in Fig.5, where U and v_{max} give the maximum absolute velocity and the maximum value of v at the measuring section.

As the fluid particle at the main flow is transported toward the wall region by the secondary flow, u/U is uniform in wide region, i.e., $y/(b/2) \gtrsim 0.5$. The outer edges of u- and v-distributions, which give the boundary layer thickness determined by u and v, are usually treated to be the same, but it should be noted that the cross flow component v is observed in the middle section of the passage.

If the thickness of the boundary layer for v is given by a half width of the passage, the distribution of v/v_{max} is approximated as the following well-known distribution.

$$\frac{v}{v_{max}}=1.69\left(\frac{2y}{b}\right)^{\frac{1}{7}}\left[1-\left(\frac{2y}{b}\right)\right]^2 \qquad ----(1)$$

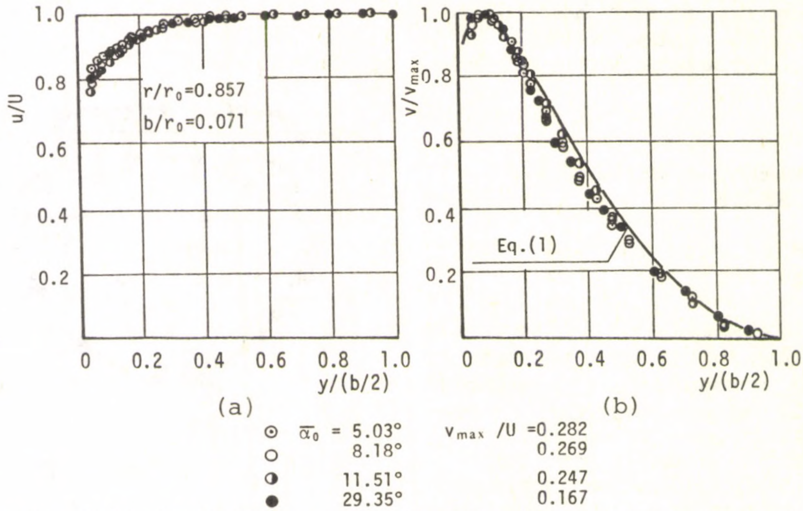

Fig.5 Distributions of u/U and v/v_{max} in boundary layer

As given in the figure, the maximum value v_{max}/U is considerably large for the samll flow angle.

For the distribution of u/U, displacement thickness δ^*, momentum thickness θ and shape factor H are derived from the following equations.

$$\delta^* = \int_0^{b/2}\left(1-\frac{u}{U}\right) dy \qquad ---(2)$$

$$\theta = \int_0^{b/2}\left(\frac{u}{U}\right)\left(1-\frac{u}{U}\right) dy \qquad ---(3)$$

$$H = \delta^*/\theta \qquad ---(4)$$

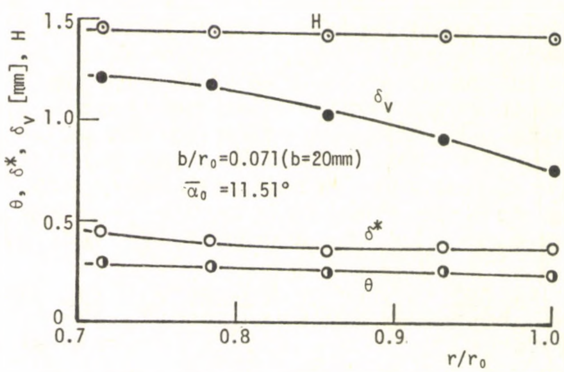

Fig.6 Variation of boundary layer parameters with radius

For the distribution of v/U, the skewness δ_v of the layer is introduced.

$$\delta v = \int_0^{b/2}\left(\frac{v}{U}\right) dy \qquad ---(5)$$

Figure 6 shows the typical variation of those boundary layer parameters with the radius. δ^*, θ and H are almost constant and $H \doteqdot 1.45$. Those parameters are also independent on the flow angle and the width of passage within the limit of this experiment. On the other hand, δ_v increases with decreasing the radius. This results from that the radius of curvature of a stream line becomes small according as the radius decreases and the centrifugal force acting on a fluid particle increases. The effect of the mean flow angle on the secondary flow will be shown later.

Distributions of Peripheral and Radial Velocities.-Practically, it is important to know the distributions of peripheral and radial velocity components. Figure 7 shows the peripheral velocity distribution c_u/c_{umax}. Here, δ is the distance from the end wall where c becomes the maximum value $c_{u_{max}}$ and its value is about $0.5\cdot(b/2)$. The distribution of c_u/c_{umax} at $r/r_0=0.857$ is approximated by 1/11-th-power law independently of the flow angles and the widths of passage. Similar results are obtained at other radii.

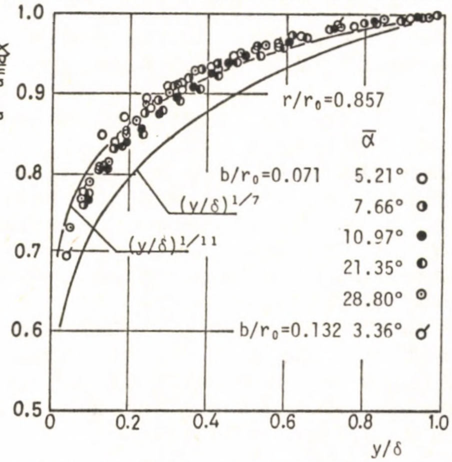

Fig.7 Peripheral velocity distributions

Figures 8 and 9 show the dimensionless radial velocity distributions $c_r/\bar{c}_r$, where $\bar{c}_r$ is the mean value of c_r at the measuring section. The variation of $c_r/\bar{c}_r$-distributions with the radius is given in Fig.8. $c_r/\bar{c}_r$ near the wall surface increases with decreasing the radius. The distribution of $c_r/\bar{c}_r$ is influenced considerably by the flow angle as shown in Fig.9. The reverse flow of c_r occurs when the mean flow angle $\bar{\alpha}_0$ is considerably small (marks ◑, o, ơ). On the other hand, the nearly constant distribution of $c_r/\bar{c}_r$ is obtained for

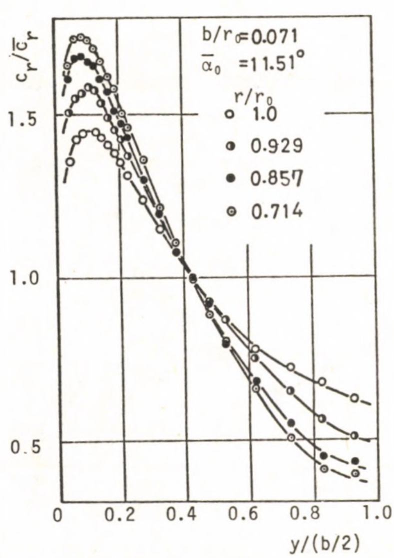

Fig.8 Variation of $c_r/\bar{c}_r$ with radius

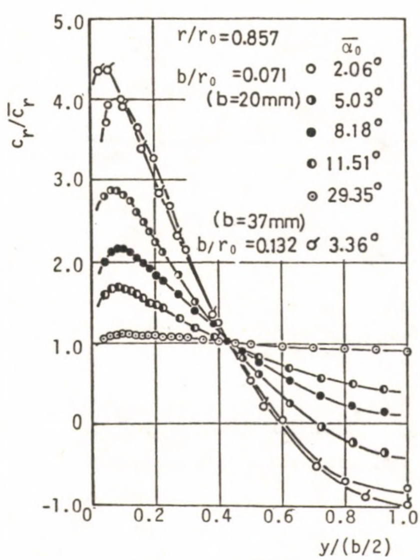

Fig.9 Variation of $c_r/\bar{c}_r$ with flow angle

the moderate flow angle. In the latter cases, the secondary flow seems rather effective to rectify the flow. It is noticeable that the dimensionless distance from the end wall $y/(b/2)$ where c_r becomes the mean value $c_r/\bar{c}_r=1.0$ is constantly about 0.43 for the various flow conditions within the limit of this experiment.

3.2 Flow Downstream of U-Turn Bend

As the flow in the U-turn bend has already been reported(2), the flow pattern in the radial inward passage of the same channel is mainly discussed here.

Figure 10 shows an example of the distributions of dimensionless peripheral and radial velocity components $c_u/\bar{c}_u$ and $c_r/\bar{c}_r$ when the mean flow angle $\bar{\alpha}_A$ at the inlet of the U-turn bend is 16.6°. $\bar{c}_u$ and $\bar{c}_r$ are the mean values at the measuring section and y is the distance measured from the inner wall. A symmetrical $c_u/\bar{c}_u$-distribution is obtained at the outlet of the bend (section B) disregarding the velocity profile at the inlet. The distribution of $c_r/\bar{c}_r$ at the outlet takes a little large value near the outer wall, when the velocity profile at the inlet section (A) has a distorted distribution as shown in Fig.10. c_r along the inner wall is accelerated in the radial passage downstream of the bend and a nearly symmetrical distribution can be obtained at r=193mm.

The typical variation of the boundary layer parameters H and δ_v in the passage is given in Fig.11. The shape factor H≑ 1.5 nearly equal to the experimental result mentioned above is obtained for all measurements. As for the distribution of v of

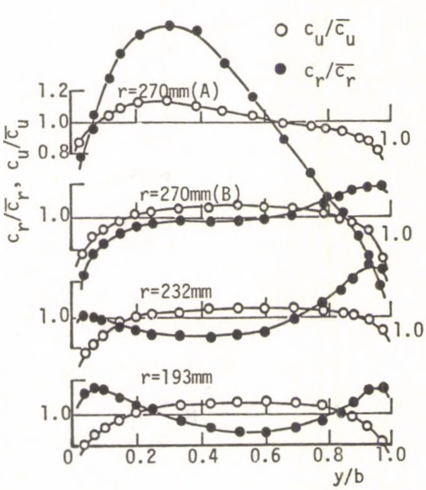

Fig.10 $c_u/\bar{c}_u$- and $c_r/\bar{c}_r$-distributions in return channel ($\bar{\alpha}_A$=16.6°)

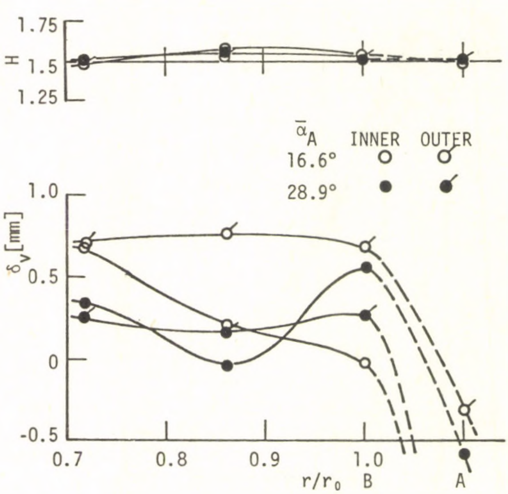

Fig.11 Variation of boundary layer parameters H and δ_v in return channel

$\bar{\alpha}_A$=16.6°, δ_v on the outer wall side is greater than the inner wall side at the outlet of the bend (section B, r/r_0=1.0). In the radial passage, δ_v on the inner wall side increases with decreasing the radius and takes the same value as the outer wall side at r/r_0=0.714 (r=193mm). When the swirling component is samll and δ_v is large at the outlet of the bend, it seems that δ_v decreases in the passage and then reaches the equilibrium as seen from the variation of δ_v on the inner wall side of $\bar{\alpha}_A$=28.9°. In all cases, the variation of δ_v on the outer wall side with the radius is less than the inner wall side.

It is suggested that such an unsymmetrical distribution of radial velocity component of the swirling flow as shown in this study may be improved in a comparatively short passage. Similar to the flow between the two parallel disks, however, c_r near the both walls has a tendency to become faster than that at the middle region in the passage owing to the secondary flow.

3.3 Relation Between Mean Flow Angle and Secondary Flow

The flow pattern in the radial inward passage is considerably affected by the secondary flow. The radial velocity distribution depends mainly on the flow angle, but is not affected by the radial position so much as seen from the comparison of Figs. 8 and 9.

Figure 12 shows the relation between the mean flow angle $\bar{\alpha}$ and the skewness parameter δ_v in the boundary layer. The notations P and R in the figure represent the results from the experiments on the two parallel disks and the return channel, and G is the result from the flow downstream of the guide vanes of reversible pump-turbine(1). Some scattering of the measured points is observed, but there is no remarkable difference between them. It seems that δ_v increases in inverse proportion to $\bar{\alpha}$. It is practically important to know the critical flow angle at which the reverse flow occurs.

Figure 13 shows the minimum flow angle α_{min} at the middle plane in the passage and the deviation of flow angle $\Delta\alpha$ defined by

$$\Delta\alpha = \alpha_{max} - \alpha_{min} \quad ----(6)$$

where α_{max} is the maximum flow angle in the passage. α_{min} decreases almost linearly with the mean flow angle. The critical mean flow angle $\bar{\alpha}_{cr}$ and the maximum flow angle $\alpha_{max.cr}$ in the passage, at which the reverse flow occurs, are shown in Fig.14 for the flow between the two parallel disks. It shows that $\bar{\alpha}_{cr}$ increases a little according to the decrease of the radius. $\bar{\alpha}_{cr}$ is about 6° at r/r_0=1.0 and becomes about 7.5° at r/r_0=0.714. For the flow angle smaller than the critical flow angle, the fluid in the passage flows only along the end walls and the deviation of the flow angle $\Delta\alpha$ is larger than 15°.

The deviation $\Delta\alpha$ becomes large at $\bar{\alpha}\lesssim$15° (see Fig.13) and the flow in the passage is distorted considerably, even if there is no reverse flow. It is also evident from Fig.15. The figure shows the deviation (c_{rmax}-c_{rc}) of the maximum radial velocity

c_{rmax} in the passage section from c_{rc} at the middle plane. The deviation tends to become large at $\bar{\alpha} \lesssim 15°$ and $(c_{rmax} - c_{rc})$ becomes larger than 3 times of the mean radial velocity $\bar{c}_r$, when the reverse flow occurs. On the contrary, the deviation is scarcely recognized at $\bar{\alpha} \gtrsim 15°$ and a fairly uniform distribution of c_r is obtained.

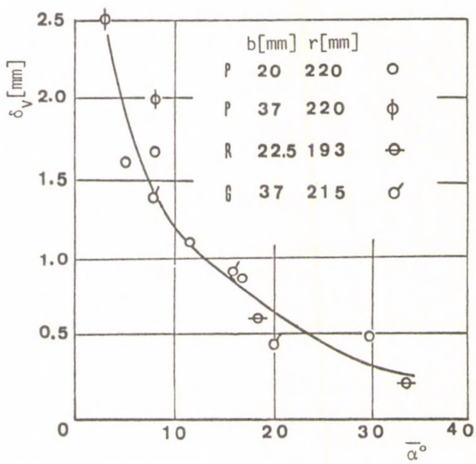

Fig.12 Relation between mean flow angle $\bar{\alpha}$ and skewness parameter δ_V

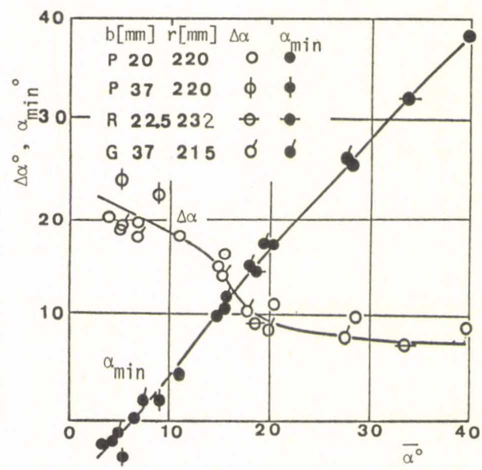

Fig.13 Distributions of minimum flow angle and deviation angle in passage

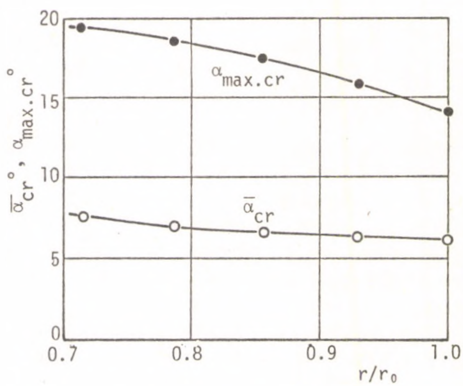

Fig.14 Variation of critical flow angle $\bar{\alpha}_{cr}$ and maximum flow angle $\alpha_{max.cr}$ with radius for flow between two parallel disks

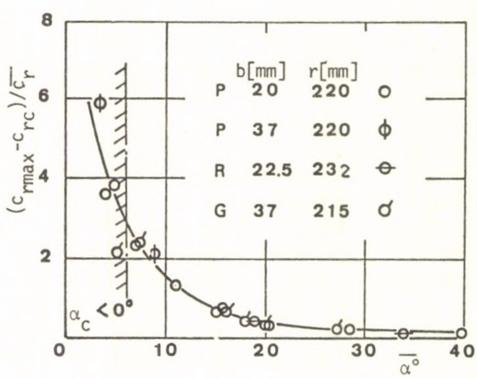

Fig.15 Deviation of radial velocity component

4. CONCLUSIONS

Experiments were carried out on the swirling inward flows in the passage between two parallel disks and in the radial passage of interstage return channel. The flow is affected remarkably by the secondary flow developed in the end wall boundary layer. The distribution of peripheral velocity component c_u is fairly uniform, but that of the radial velocity component c_r is classified by the mean flow angle $\bar{\alpha}$ as follows.

(1) When the mean flow angle is less than or nearly equal to 7°, the reverse flow occurs in the middle region in the passage and the fluid flows only along the end walls.

(2) At $7° \lesssim \bar{\alpha} \lesssim 15°$, there is no reverse flow but the distribution of c_r is affected conspicuously.

(3) At $\bar{\alpha} \gtrsim 15°$, a fairly uniform distribution is obtained. In this case, the secondary flow seems rather effective to rectify the flow.

REFERENCES

(1) T. Toyokura, S. Akaike and T. Kanemoto, "Study on Turbine Flow Through Guide Vanes and Stay Vanes for a Reversible Pump-Turbine", Proceedings of 10th IAHR Symposium, Tokyo, Vol.1, (1980), p.353.

(2) S. Akaike and T. Toyokura, "Flow in Interstage Return Bend of Centrifugal Turbomachinery", Proceedings of 6th Conference on Fluid Machinery, Vol.1, (1979), p.11.

(3) D. N. Wormley, "An Analytical Model for the Incomplessible Flow in Short Vortex Chambers", Trans.ASME, Journal of Basic Engineering, Vol.91, No. 2(1969), P.264.

(4) C. C. K. Kwok, N. D. Thinh and S. Lin, "An Investigation of Confined Vortex Flow Phenomena", Trans.ASME, Journal of Basic Engineering, Vol.94, No.3(1972), p.689.

Shiro AKAIKE
Professor, Ikutoku Technical University, Atsugi, Kanagawa, JAPAN.

Tomitaro TOYOKURA
Professor, Faculty of Engineering, Yokohama National University, Yokohama, JAPAN.

PERFORMANCE OF MULTIPLE-DISK SHEAR PUMP PROVIDED WITH RADIAL BLADES AT OUTLET

BY

Ahmed Ayyad
Assiut University, Assiut, Egypt

SUMMARY

Performance maps and characteristics of both multiple-disk shear pumps and radial blades centrifugal pumps, have been individually investigated [1], [2] . The shear-force pump utilizes properties of real fluids for pumping action. Very stable pump operation results, without fluid separation. The conventional pumps use lift forces to accelerate the pumped fluid. Shear pump has stable characteristics, low efficiency and cavitation-free. Radial pump has high head , high efficiency, bad cavitation characteristics. An unconventional type of pumps employing a rotor composed of disks at the inner part of the passage and provided with radial vanes at the outlet part, is described in this paper. Experimental tests are carried out on this water pump. The new pump has the advantages of high head, high efficiency, and stable operation. Radial-shear ratio λ which is the ratio between radial height part to the shear height part, and its effect on the performance of the pump has been studied.

INTRODUCTION

In conventional pump, momentum exchange between the fluid and rotor is affected by providing blades to deflect and constrain the flow in the rotor. The resulting lift forces accelerate the pump fluid. These forces are the result of a purely potential flow , namely, the free-vortex circulation around a moving lifting surface [3]. At high angle of attack, disturbances of the potential flow character are most imminent and flow separation occurs leading to operational instablities. Moreover, due to existance of high pressure on one side of the blade and low pressure on the other side, cavitation inherently occurs in radial vaned pumps. The shear-force pump utilizes the viscous properties of real fluids for pumping action. Shear forces depend on the velocity difference between fluid and shear surface. There is no danger of separation and the forces increase steadily with increasing velocity difference between the fluid and the shear surface [4] . Very stable operation should result. The idea is to design a new unconventional pump having the advantages of both shear-force pump and the radial vaned pump. It consists of inner portion operating as shear-force pump and the outer portion which operates as radial vaned pump. Design, results, discussion , and conclusions are reported here.

TEST RIG

Figure 1 shows schematic diagram of the test rig used in this work. It had been established previously in the hydraulic laboratory of the Faculty of Engineering Assiut University for testing the unconventional pumps. The pump was driven by a variable speed electric motor cradled to form a dynamometer for measuring torque. Water at approximately 20 C was the pumped fluid. Delivery and suction pressures were measured at the delivery and suction flanges respectively by using U-tube

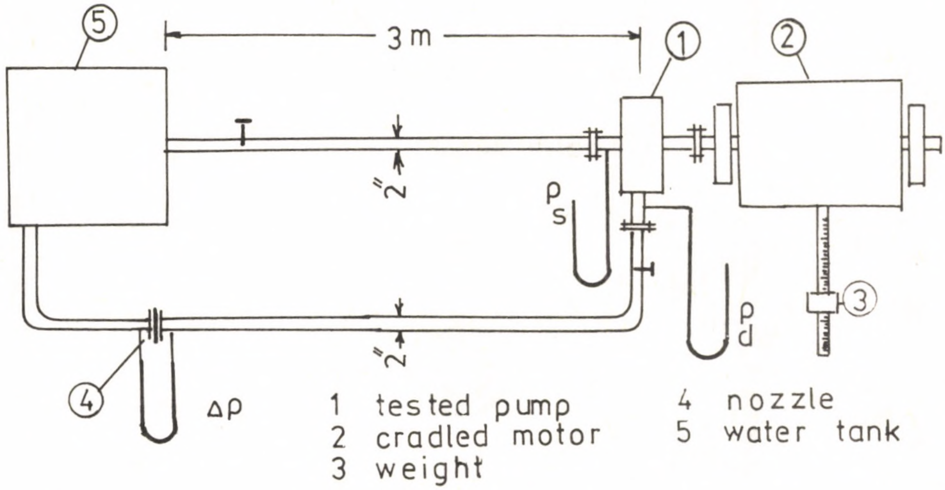

Fig. 1 Schematic diagram of the test rig

manometers. A calibrated standard (A.S.M.E.) nozzle is used for measuring pump flow rate.

TESTED ROTORS

Five rotors have been tested, each has 120 mm outer diameter, 36 mm inner diameter and constant width of 32 mm and classified as:-

1- Double shrouded 6-blades radial rotor.
2- Multiple-disk rotor, composed of 8 disks, each 1 mm thick, and with 3 mm disk spacing.
3- Shear-radial rotor having 8 disks , 3mm spacing to a height of 12 mm followed by 6-radial blades of 30 mm height.
4- Shear-radial rotor having 8 disks, 3 mm spacing to a height of 22 mm followed by 6-radial blades of 20 mm height.
5- Shear-radial rotor having 8 disks, 3 mm spacing to a height of 32 mm followed by 6-radial blades of 10 mm height.

The radial-shear ratio which is defined as the ratio be-

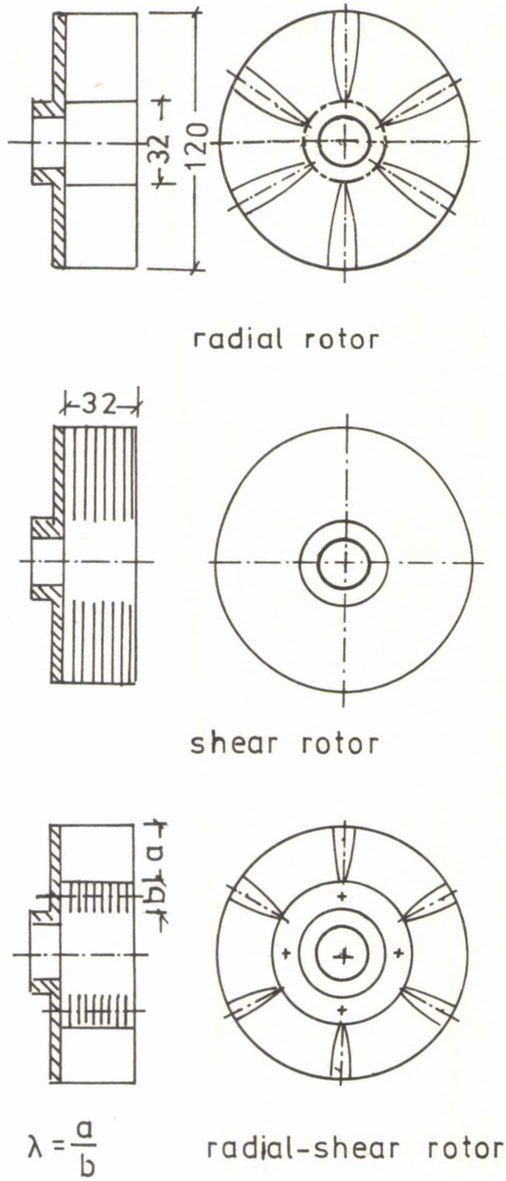

Fig. 2 Pump tested rotors

tween the radial height part and the shear height part, for these rotors are 0.31 , 0.92, and 2.5 respectively. The disks were held together, spaced , and stiffened by four throughbolts. The radial blades were also mounted to the main rotor flange by a suitable number of throughbolts as shown in Fig. 2.

RESULTS AND ANALYSIS

The experimental results of the five rotors are presented for three rotor speeds of 1500 rpm, 2000 rpm, and 2500 rpm. Total pump head and efficiency were plotted against the volume flow rate. Performance of the five rotors are presented together to facilitate the comparison. Head-discharge and efficiency discharge curves for the five rotors at a speed of 1500 rpm are shown in Figs. 3 and 4. The radial rotor gives a maximum efficiency 36 percent at the corresponding volume flow rate of 2.6 liters per second and head of 5.8 meters. Shear-force pump gives maximum efficiency of 16.5 percent at a volume flow rate of 2.3 liters per second and a corresponding head of 2.4 meters. As it is shown, the radial rotor has an unstable head-discharge curve. This is due to the high angle of attack, disturbance of potential flow character and the separation of flow which reduces the lift action [3] . Shear rotor has stable characteristics and no separation occurs. Forces increase steadily with increasing velocity difference between the fluid and shear surfaces. The shear-radial rotors having stable characteristics. They have higher efficiencies and higher heads than the pure shear rotor. For example, for the case of radial-shear ratio of 2.5, the maximum efficiency obtained is 25% at a volume flow rate of 2.25 liters per second and a head of 4.6 meters. However, a further decrease in the shear part causes a

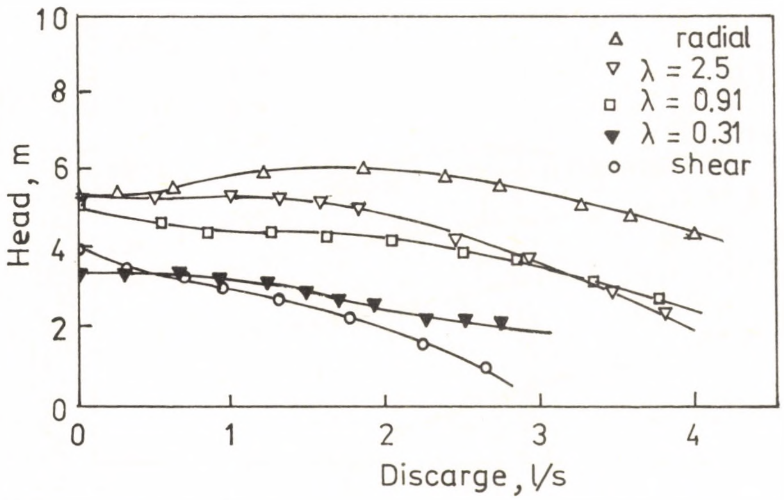

Fig.3 Head-discharge curves for the tested rotors at 1500 rpm.

decrease in the pump efficiency.

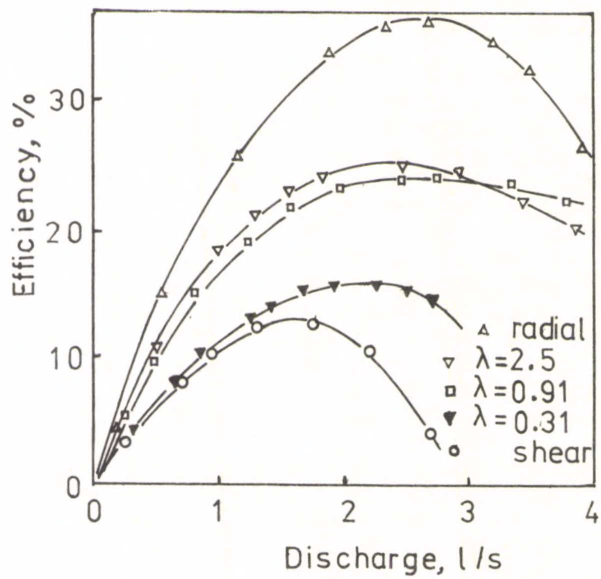

Fig. 4 Efficieny-discharge curves for the tested rotors at 1500 rpm.

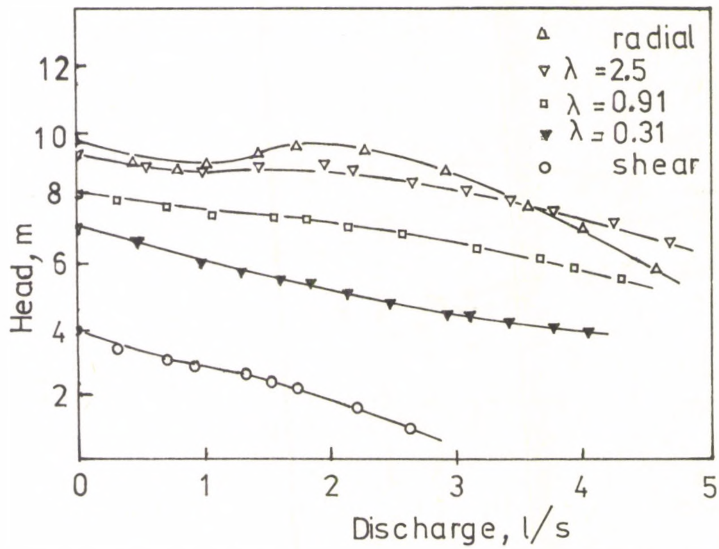

Fig. 5 Head-discharge curves for the tested rotors at 2000 rpm.

The characteristics of the tested rotors at a speed of 2000 rpm, shown in Figs. 5 and 6 , give the same sequence as the characteristics were obtained at the speed of 1500 rpm. For all radial-shear ratios, the maximum efficiency and the corresponding head and discharge, are higher than its value at 1500 rpm.

Shear-force pumps usually operate at high speeds [4], thus Figs.7 and 8 for maximum available speed of 2500 rpm are excepected to give an approximate tendency of the characteristics of the pump at higher speeds. The shear-radial pump at the speed of 2500 rpm gives a maximum efficiency , high head corresponding to a high flow rate. For example shear pump shows a maximum efficiency of 16.5 percent, while radial pump gives a maximum efficiency of 36 percent. The rotor of radial-shear ratio of 0.91 is the more stable and having higher efficiency, head, and capacity. The results of the performance tests of the shear-radial pump are given in table 1.

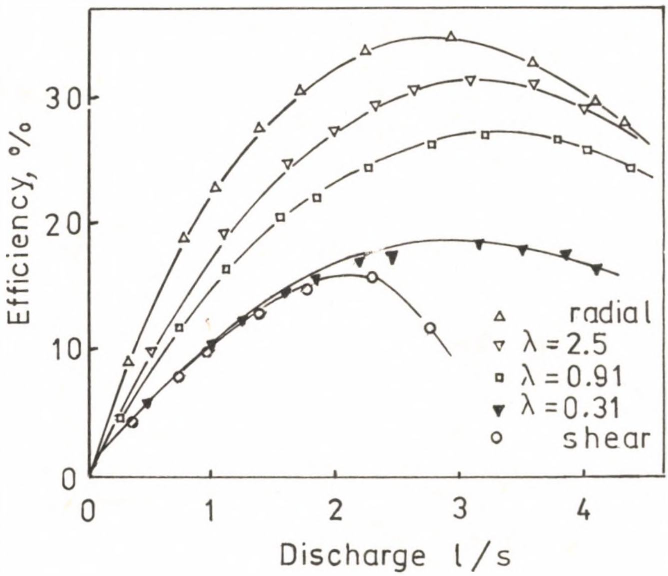

Fig. 6 Efficiency-discharge curves for the rotors at 2000 rpm.

The resultant conclusion of the tests are shown in Fig.9. Increasing the radial-shear ratio, will increase the maximum efficiency and the total pump head. Pump capacity increases with increasing the radial-shear ratio up to the value of 1.3 for the case of speed of 2500 rpm and then decreases again. The net hydraulic power given by the pump, for example at 2500 rpm is maximum at radial-shear ratio of approximately 1.65 and at a reasonable maximum efficiency of about 23 percent.

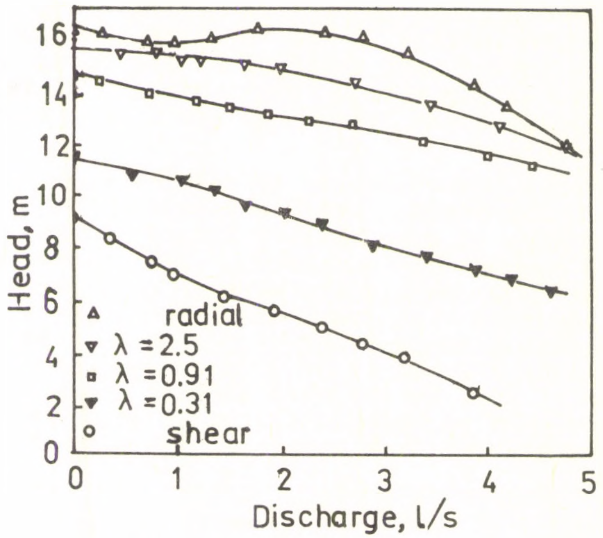

Fig. 7 Head-discharge curves for the tested rotor at 2500 rpm.

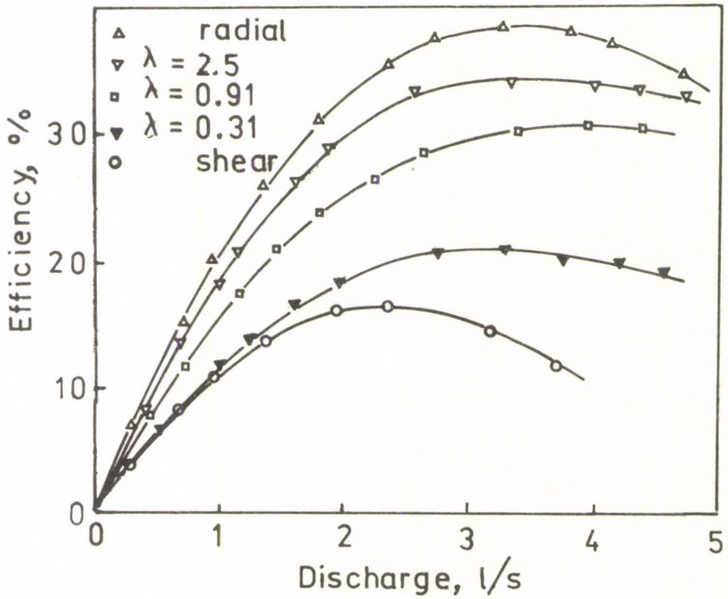

Fig. 8 Efficiency-discharge curves for the tested rotor at 2500 rpm.

Table 1 Optimum characteristics of shear-radial pump

rotor speed rpm.	radial-shear ratio	discharge, l/s	head, m	maximum efficiency %
1500	0.31	2.10	2.4	16.0
	0.91	2.75	3.7	24.5
	2.50	2.25	4.6	25.0
2000	0.31	2.70	5.1	19.0
	0.91	3.25	6.8	27.5
	2.50	3.00	8.4	31.5
2500	0.31	3.00	8.2	21.0
	0.91	4.00	10.8	30.5
	2.50	3.50	11.8	34.5

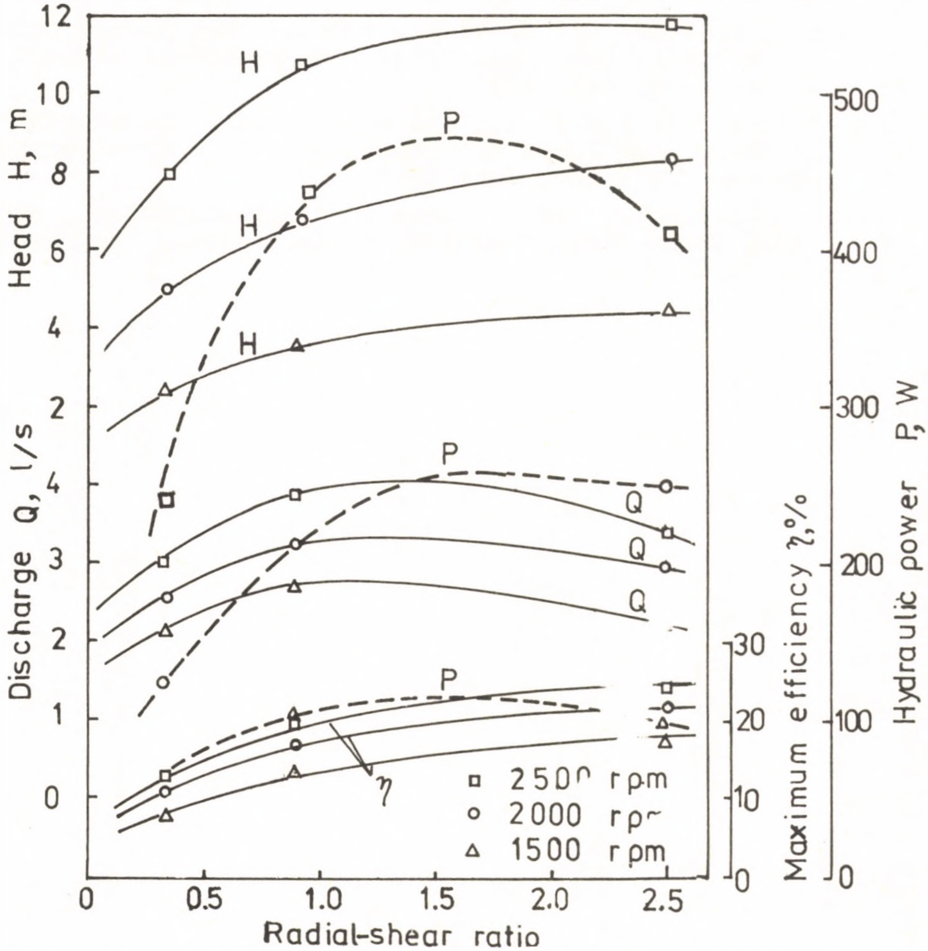

Fig. 9 Maximum efficiency, discharge, head, and maximum hydraulic power against radial-shear ratio at different rotor speeds.

CONCLUSION

From the above results, the combination between shear and radial pumps gives an interest results, stable characteristics, high efficiency, and no danger of separation. So, it is recommended that, to improve the characteristics of a shear pump, it must be provided with radial blades at outlet. Also to improve the stability of a radial pump, it must provided with a shear part at inlet.

REFERENCES

1- Abo-Ismail, " Unconventional pump" , M.Sc Thesis, Assiut University, 1971.

2- M.E. Crawford and W. Rice , " Calculated Design Data for the Multiple-Disk Pump Using Incompressible Fluid." Trans. of the ASME, July 1974.

3- W.Rice," An Analytical and Experimental Investigation of Multiple Disk Pumps and Compressors.", Journal of Engineering for Power, July 1963.

4- S.H. Hasinger, and L.G. Kehrt, " Investigation of a Shear Force Pump. " Journal of Engineering for Power , July 1963.

RECIRCULATION AT PUMP INLET

K.Balakrishnan and S.Soundranayagam

1. Introduction

Flow reversal often takes place at the tip region of axial pumps when the flow is reduced below a certain level with a resultant flow configuration as in Fig.1. Recirculation occurs with the reverse flow reacting well ahead of the impeller. The fluid in the recirculation eddy passes several times through the blade region acquiring a high total pressure and also partaking in the angular momentum of the impeller. This angular momentum moving ahead of the impeller with the recirculating flow provides the mechanism for inducing a prerotation of the inlet flow. Flow reversal at the tip sometimes referred to as return flow is well recognised [1] and attempts have been made to ascribe and calculate a flow loss connected with the phenomenon [2].

Fig.1. Schematic representation of recirculation at inlet.

Recent work on the stalling of axial impellers has thrown new light on the details of inlet recirculation [3] . The results discussed here were obtained from aerodynamic tests on an axial impeller of 381 mm diameter and a hub to tip diameter ratio of 0.5 running at 2880 rpm. There were fifteen blades of constant chord in the test impeller with a space to chord ratio at the tip of approximately 1.6. The design blade setting or stagger measured from the axial direction was 81.5°

(stagger A). The impeller was also tested at other tip blade settings of 69.5°(stagger B) and 58.5°(stagger C). Measurements were made with 3 hole cylindrical yaw-pitot combination probes of 5 mm stem diameter as well as hot wire probes and rapid response miniature pressure transducers. The overall frequency response of the rapid response instrumentation including the recording apparatus was of the order of 10 KHz.

2. Experimental Results and Discussion

The head flow characteristics of the impeller at the three blade settings are shown in Fig.2. At the high stagger setting A, a continuously increasing head flow characteristic was obtained. Below a certain flow rate there was a gradual increase in the noise level as the flow was reduced right up to the minimum flow rate, the noise being attributed to increased blade wakes and turbulence. An elementary view of the quasi 2-dimensional flow through an impeller would suggest that there would be no droop of the characteristic as flow is decreased if the rate of increase of blade loss after "stall" is smaller than the rate of increase of head with throttling [1]. The greater effect of blade overlap in high stagger configuration tends to limit the transverse extent of separation regions in a way not unlike what happens in a vaned diffuser thus limiting the magnitude of the losses. This combined with the greater slope of the ideal head flow characteristic at high stagger gives a continuously rising experimental characteristic. The head flow characteristic for stagger B is different from stagger A in that a clearly marked kink occurs at ϕ=0.233. There was a small but clearly discernible dip as the flow was throttled below this with a subsequent rise in the characteristic. Careful exploration of the region of the kink showed no signs of hysteresis, the experimental points for opening and closing the throttle lying on the same curve over the entire characteristic. Further decrease of the setting angle to stagger C caused the machine characteristic to have a well defined hysteresis loop.

On closing the throttle the head flow characteristic exhibited a discontinuous jump from A to B at about ϕ=0.38 with progress along the left hand side of the characteristic with further throttling. With opening of the throttle the stalled branch of the characteristic was retraced upto B and then along BC when it suddenly jumped to D. Further closing of the throttle took the characteristic back to A forming a clearly defined hysteresis loop while further opening of the throttle caused the unstalled portion of the characteristic to be retraced.

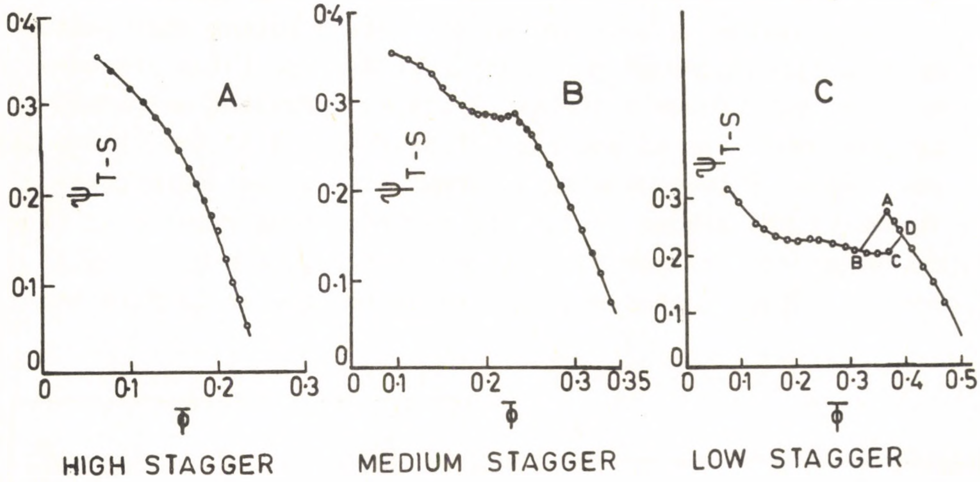

Fig.2. Impeller characteristics.

At the lowest blade setting (stagger C) the sudden dip in the head flow characteristic at stall was accompanied by the formation of discrete stall cells that extended over a part of the annulus circumferentially. The cells extended from hub to tip forming full span stall though it is also possible for the stall to extend over only part of the blade span. The cells propagate relative to the impeller so that in the absolute frame of reference they rotate at a fraction of the impeller speed which in this case was about 0.58 of the impeller speed. The flow is unsteady and not axisymmetric with the blades being subjected to a periodic varying load as the stall cell sweeps past them. Even if the NPSH is high enough to completely suppress cavitation the blades would be subject to the periodic varying loads. At the higher staggers A and B the onset of inlet recirculation was not accompanied by the formation of discrete stall cells rotating at a fraction of the impeller speed.

Velocity traverses made with the combination yaw-pitot probe showed upstream flow reversal and recirculation at all the staggers tested once the flow was reduced below a certain limit. The total pressure in the reversal region also rises to a high value as the flow in the recirculating eddy passed several times through the blade region. The total pressure does not rise above a certain limit as turbulent entrainment carries away some of the high pressure fluid in the recirculating eddy. This causes an abnormal rise in pressure downstream of the blades in the tip region. Some results of flow traverses for stagger B are shown in Figs.3,4 and 5. Fig.3 shows a slight increase in the relative flow angle β_2 in the

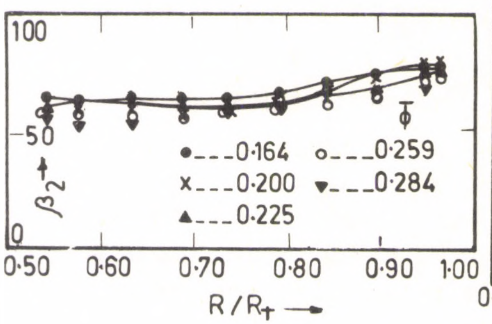

Fig.3. Radial variation of β_2. Stagger-B.

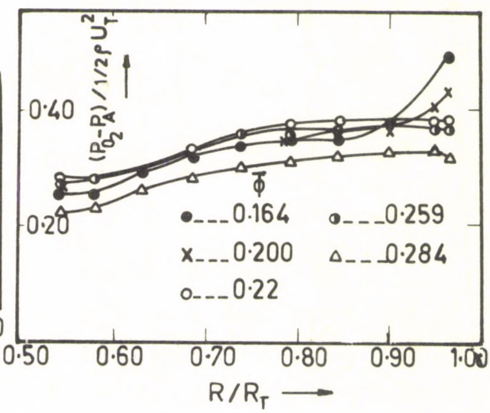

Fig.4. Radial variation of downstream total pressure. Stagger-B.

outer span region at ϕ=0.225 indicating that the dip in the characteristic is related to blade stall. Measurements at the higher stagger A showed no such increase in β_2 when recirculation started. The increase in total pressure at the tip for ϕ=0.20, Fig.4, due to upstream flow reversal will be noticed. This reversal is also seen in the upstream distributions of axial velocity corresponding to ϕ=0.192, Fig.5. At ϕ=0.217 flow reversal is not seen in Fig.5 though blade stall has set in at the tip as the recirculation eddy has not grown enough in size to reach the upstream traverse station. The increases in total pressure are purely local and confined to the tip region and contribute to the measured rise in the head flow characteristic.

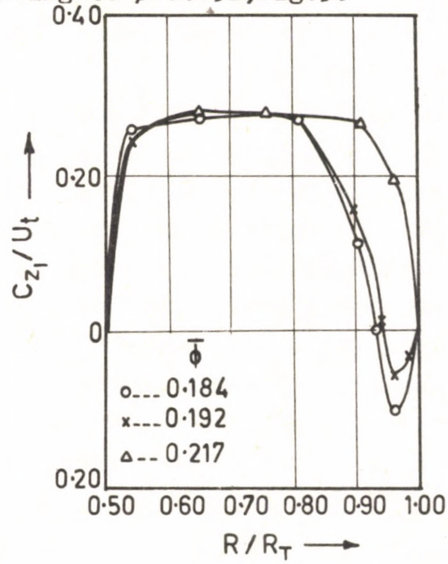

Fig.5. Radial variation of upstream axial velocity. Stagger-B.

An examination of the instantaneous velocity traces downstream of the impeller obtained using hot wire probes showed that for staggers A and B the onset on recirculation was accompanied by an enlargement of the blade wakes confirming the existence of blade stall. As the flow is decreased, individual blades stall with a partial mixing and grouping of the wakes. The clustering of the wakes was a transient feature and there was no evidence of any cluster tending to form an organised stall cell pattern propagating at constant angular velocity around the annulus as was found for stagger C. This was verified also in an FFT system wherein hot-wire traces obtained simultaneously from two downstream probes separated circumferentially at the same axial location were analysed and checked for common prominent frequencies. The FFT analysis indicated strong peaks at the blade passing frequency in the recirculation regime indicating the existence of large blade wakes. There was also a spread of minor peaks right up to the blade passing frequency but dying down very rapidly beyond that. At flow rates above that at which recirculation is present the blade wakes were hardly noticeable in the hot wire traces downstream confirming that the enlarged wakes noticed in the recirculation region were due to blade stall. A conclusion that can be drawn is that at the higher staggers recirculation is associated with the occurrence of blade stall though there is no drastic effect on the rising head flow characteristic. Also no organised stall cell structure is present that rotates relative to the impeller subjecting the blades to a periodic variation of blade force. However at the lower stagger recirculation is associated with an organised structure of propagating stall cells with a catastrophic drop in the head flow characteristic.

Some properties of the stall cells measured in the impeller with the lowest stagger (stagger C) are shown in the following figures. Fig.6 shows ensemble averaged variation of the axial velocity within the stall cells immediately downstream of the impeller at two radial locations. The circumferential sweep is indicative of the circumferential extent of the stall cell. Near the tip the cell extensive occupying almost two thirds of the annulus. It reaches right down to the root of the blade but has become much smaller in extent. The magnitude of the velocity changes in the cell together with associated changes in incidence is indicative of the magnitude of the force changes experienced by the blade.

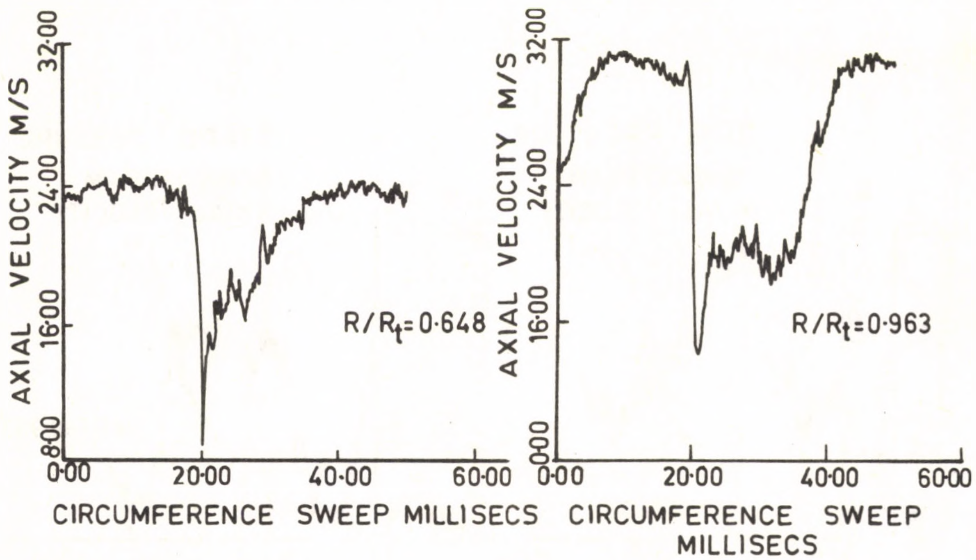

Fig.6. Variation of axial velocity across the stall cell.
Flow coeff.=0·284. Stagger-C.

The total and static pressure changes in the cell at two radial locations downstream are shown in Fig.7. The dotted line superimposed on the pressure variations in this and the following figures is an axial velocity trace taken at one fixed radial position downstream and gives some indication of the cell positions. It will be noticed that the pressure variation near the tip is markedly different from that near the root. Near the root there is a static pressure decrement in the wake as is the case over most of the span. At the tip there is an increase of total pressure in the recirculation eddy upstream as discussed earlier. The fluid in the upstream eddy would have acquired a tangential momentum in the same direction as impeller rotation due to its having passed several times through the blade region. The upstream recirculating eddy forms a part of the tip region of the stall cell. Within this region upstream the high total pressure fluid is moving tangentially relative to cell towards its leading edge. This is because the recirculating fluid will have a tangential velocity

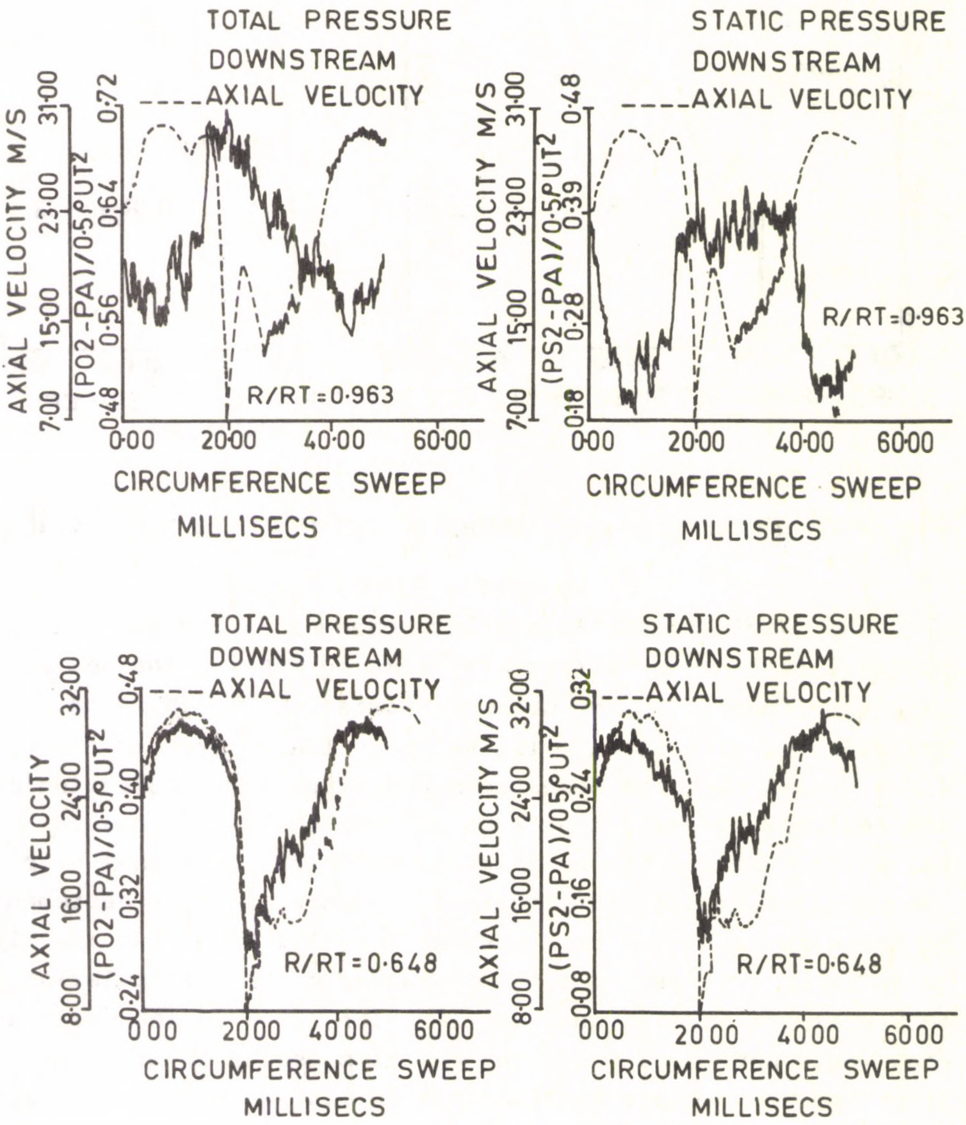

Fig. 7. Variation of downstream pressures.
Stagger-C, Flow coeff.=0·284.

nearly the same as the impeller while the cell propagates towards at only a fraction of the impeller speed. The high total pressure fluid then is pushed towards the cell leading edge and from there is entrained to pass downstream causing a concentration of high total pressure at the cell leading edge downstream. This is clearly seen in the total pressure trace in the tip region of Fig.7. The static pressure variation across the cell at the tip is fairly flat but higher than outside the cell.

The variation of total pressure upstream in the tip region of the cell is shown in Fig.8 which again shows higher total pressure near the leading edge. It also is a confirmation that the recirculation region upstream is not axisymmetric. The wall static pressure measured downstream shows the characteristic peak at the cell leading edge associated with the high total pressure there. Comparison with Fig.7 shows that the pressure variations at the wall are not representative of conditions lower down within the annulus.

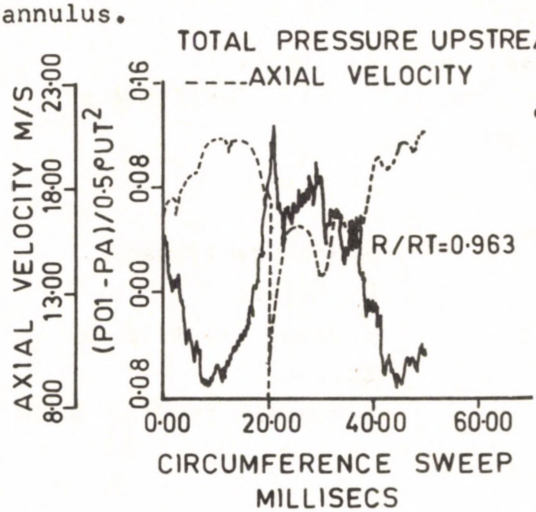

Fig.8. Variation of upstream pressures
Stagger-C Flow coeff.=0·225.

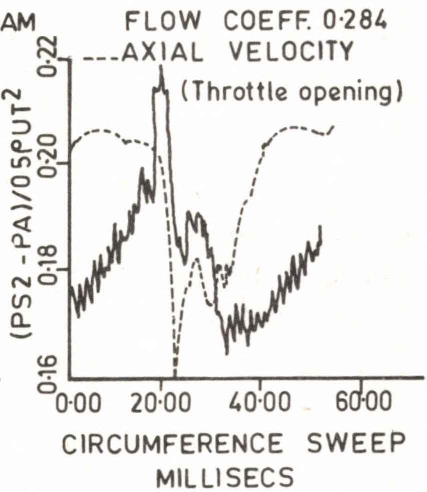

Stagger-C
Fig.9. Wall static pressure downstream.

Nomenclature

C_z	axial velocity
p_o	total pressure
p_s	static pressure
U_t	tip speed
β	relative flow angle
ϕ	flow coefficient C_z/U_t
ψ_{T-S}	total to static flow coefficient $\dfrac{p_{s2} - p_{o1}}{\rho U_t^2}$

Subscripts

1	inlet
2	outlet

References

[1] Stepanoff Centrifugal and Axial flow pumps, Wiley 1964

[2] Radhakrishna H.C. Return flow on the suction side of an axial flow impeller. IAHR symposium. Stockholm 1970

[3] Balakrishnan K. Stall in Axial Impellers Ph.D.thesis. Indian Institute of Science 1982.

K.Balakrishnan
Research Scholar
Indian Institute of Science
Bangalore 560012 India

S.Soundranayagam
Professor
Indian Institute of Science
Bangalore 560012 India

HORIZONTAL WATER TURBINE RADIAL BEARINGS

J. Bednář

SUMMARY

Analysed are the problems in the account of small water turbines radial guide bearings horizontal construction main of all of straight flow turbines. Here preference is given to the application of guide bearing water lubricated.

Problems of water lubricated bearings having rubber made linning are dealt with based upon results of experimental authentication and comparison classical hydrodynamic with hybrid bearing which hydrostatic principle is utilized to form suitable and convenient start stop conditions of the machine.

1. INTRODUCTION

Contemporary tendency of invest non-pretentious realization to the small water power stations is of outstanding contribution and use of power gained from water flow so that is being found and solved lack of resources and problems of them i.e. fuel-power balance. One of most convenient judgement of that trend is exploitation of water stations and schemes for water economy to install machinery generating electric power. In spite of possible installed output of these power station is relatively small but their aim is continuous performance of machinery /excluded topics are short lasting periods of extraordinary hydrologic conditions of flow/ and assumption of economic exploitation of power potential to water economic schemes.

The choice of the most suitable solution of machinery from technical and economical point of view leads in many cases and calls for application of straight flow turbines either horizontal or slant construction. Of applied alternatives to the straight flow turbines from economical reasons more and more and greater portion is considered toward S-turbine design of which is depicted and seen from fig. 1.

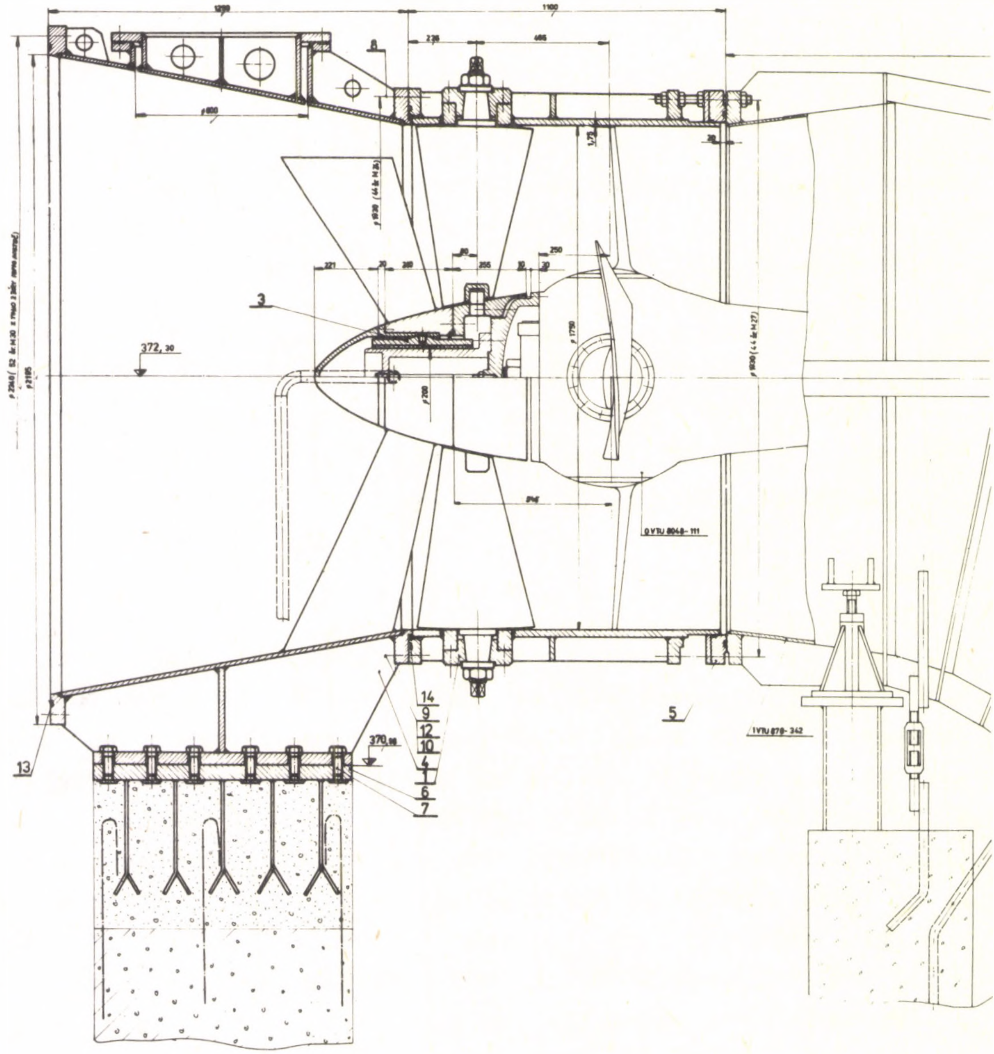

Fig. 1

With regard to ecology demands here completly is eliminated possibility of oil leakage or grease. The runner wheel blades rest in self lubricated bushes so that the hub itself is of no oil fill. Possible oil leakage from servomotor faced are apart of the turbine. Radial bearing, however, is introduced to be one of most pretentious constructions nodes.

2. APPLICATION OF BEARINGS WITH RUBBER MADE LINING

To clear up problem and to eliminate fully dangerous oil escape or lubrication grease off bearing here comes into being in fact even single possibility being the use of water for purposes of lubrication and cooling medium of bearing. From point of view of realization possible is to apply special antifriction bearings self lubricated bushes or bearings with rubber made lining. Just of them bearings with rubber made lining introduce classical clear up supported by long lasting experience in series of analogic applications.

Well known manufacturers of water turbines apply bearings with rubber made lining for vertical machines. One of most pretentious applications is the bearing of Bratsk Power Station rate of which is 256 MW, diameter of the main shaft 1 520 mm. Even well known also are the applications for horizontal units [1] .

Here admitted are also not to speak about reference problems solution and design of bearing and start and stop of in connection with imprint of solid trunion into flexible rubber lining. From point of view of that problem and inconvenient performance parameters /unambiguous orientation of load forces high portion of specific pressure, low measure of circumferential velocity/ introduced here is the judgement and solution of guide bearing difficult to solve tribological problem.

3. PROBLEMS OF THEORETICAL SOLUTION OF ELASTOHYDRODYNAMIC BEARINGS

Bearings of rubber lining are considered to be elastohydrodynamic bearings here necessary is to joint hydrodynamic theory of lubrication with the one of elasticity and strength of distorted lining. Initial equation remains the Reynolds reference for pressure fields of slide bearing. Attention must be paid to specific problems of bearings having flexible lining residing in the course of pressure in supporting gap being not determined by geometry of the gap but vice versa the form of the gap is the function of pressure separation in bearing zone of bearing. Pressure distribution is thus determinative measure of bearing.

Real performance mode of bearings having rubber lining for horizontal construction corresponds the make of resultant excentricity of trunion sum defined of radial play of bearing and apparent imprint of trunion into lining. Over relatively long period application of rubber lined bearings theoretical acconnt of referred to above problems were not till now published. Initiation of application remain and are analyses to experimental outcomes of clear up involved for various construction of bearing [1, 2, 3].

4. HYBRID TYPE GUIDE BEARING RUBBER LINED

Bearings of rubber lining might be loaded up to specific pressure of p = /4,2+5,6/ MPa under condition that load is deduced as soon as necessary circumferential velocity is gained to trunion needed for generation of hydrodynamic effect 1 . This assumptiom would not be met for horizontal water turbines bearings. Mass of rotor being first of all runner wheel which place is close vicinity of bearing to define initial load for start.

The necessity to exclude possibility for trunion to touch rubber lining when starting requires the forming of supporting gap and its pressure field even in zero speed of the unit. The simpliest way to solve is application of hydrostatic principle.

Supposed we substitute slots of lubrication of classical hydrodynamic bearings for pockets with separated supply of forced water attained is macroimprint of trunion into flexible lining closed volume in which fully enforced is pressure of lubrication medium. In sufficient pressure of medium formed will be the supporting gap flowing by lubrication medium separating the trunion from lining. Thus come into being necessitable conditions to start. The unit running pressure of lubrication medium would be lowered to attain the measure customary for hydrodynamic bearing. For the unit run out there is no need to rise pressure of lubricant.

5. EXPERIMENTAL AUTHENTICATION

For reference comparison of guide bearing properties rubber lined of hydrodynamic and hybrid type experimental authentication has been carried out of both possibilities of concrete application with following parameters:

bearing shell diameter $D = 290$ mm
bearing shell length $l = 500$ mm
circumferential speed $u = 2{,}278\ m.s^{-1}$
specific pressure $p = 0{,}31$ MPa

Treatment of both bearings possibilities fig. 2.

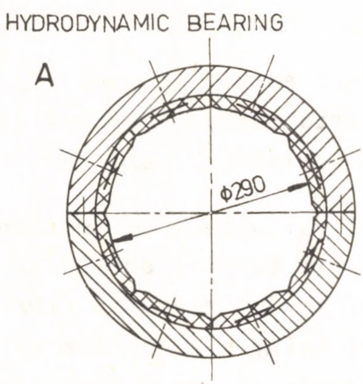

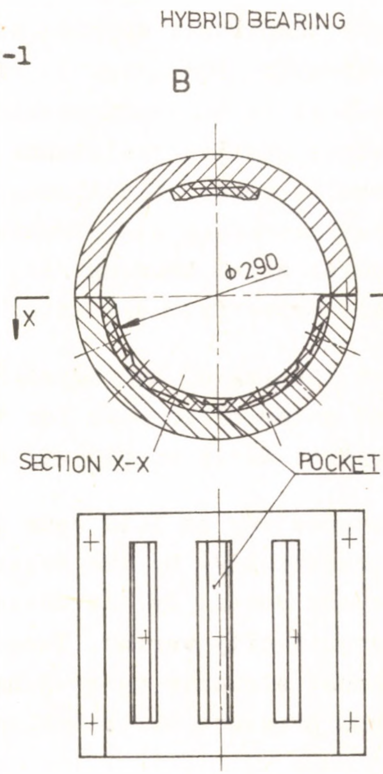

Fig. 2

Hybrid bearing is made partial three pockets and skip pad in upper half of bearing. For both constructions same bearings have been withheld to indicate play δ = 1,075 mm.

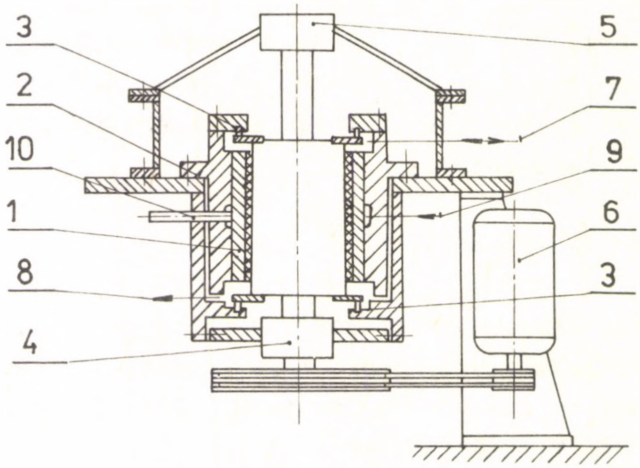

Fig. 3

To authenticate applied has been versatile stand schematic illustration from fig. 3. Proper authenticated bearing /1/ was fatened in the body resting on slide surface /2/ possible to reduce passive resistance in radial movement of the body. Hydraulic space of authenticated bearing had been closed by mechanical seals /3/. Trunion fastened at radial bearing /4/ and radial axial bearing /5/. Trunion rotation is maintained over belt drive from el. motor /6/.

For testing of hydrodynamic bearing water supply is used /7/ and water bleed /8/. For testing of hybrid bearing applied is central water supply /9/ and for bleed outlets /7/ and /8/.

Inverse way of load came into being and variations of trunion excentricity. By the movement of body with bearing shell /1/ toward radial by the means of couple of thrust elements /10/ excentricity varied. Tensometer pick up being the portion of thrust elements metered had been components of force that came from pressure distribution in bearing gap.

6. DISCUSSION OF RESULTS OF EXPERIMENTAL AUTHENTICATION

Applied type of test stand, thrust elements and search units and the manner of measurement of trunion excentricity made it possible to define objective dependence of outcome elastohydrodynamic force of tested bearing upon excentricity. Such dependence is for both types of bearing fig. 4 depicted while the curve "A" is found out dependence of hydrodynamic and the curve "B" of hybrid bearing.

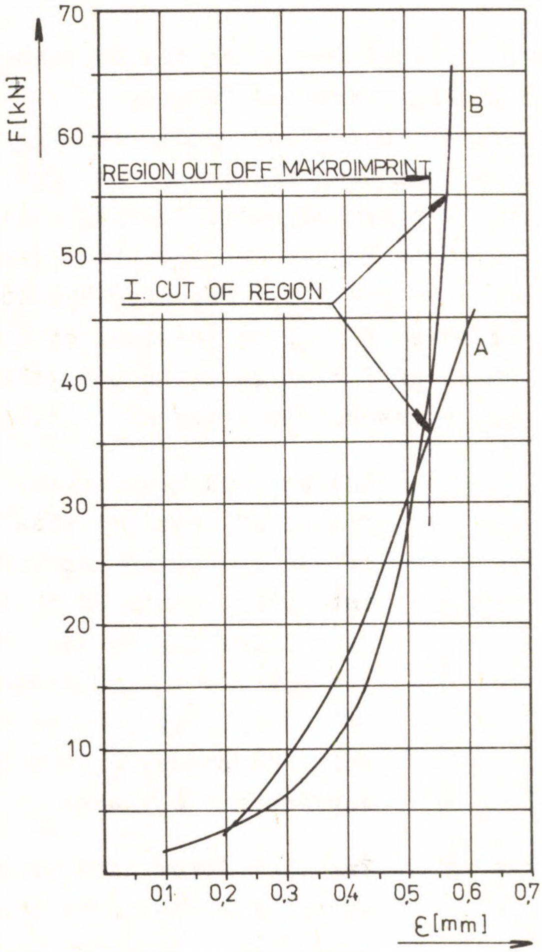

Fig. 4

In addition ascertained has been relative dependence of friction force of trunion upon trunion excentricity depicted for both types of bearing from fig.5. It is the outcome of testing in pressure of lubricant p = 0,04 MPa which was initial pressure for testing of hydrodynamic bearing and for comparison tests of both types.

For assesment of dependence of elastohydrodynamic force upon excentricity defined had been couple of cut-off fields.

First of them is defined from load force in which the macroimprint of trunion into rubber lining makes it possible to form liquid film to start. For hydrodynamic bearing available geometry this region has been defined by the force of F = 35 kN to which the pressure in slide surface p = 0,241 MPa corresponds, in pressure of lubricant p = 0,04 MPa. For hybrid bearing used geometry and equal value of lubricant pressure first cut-off zone is defined by the load F = 55 kN and here again specific pressure corresponds in slide surface p = 0,397 MPa. Outstanding difference is modified to the reality that for the case of greater macroimprint the trunion remains in connection with lubricant that fills the pocket while the pocket geometry together with distortion form conditions to let increase liquid film to start.

Second cut-off region is force defined for which the macroimprint of trunion into rubber lining prevented forming of liquid film to start. With regard to test stand conception to be criterium for that field applied has been maximum moment for starting of stand electromotor. For hydrodynamic bearing this sphere has been defined by the force F ≐ 46 kN specific pressure of corresponds in the slide area p ≐ 0,317 MPa. For hybrid bearing second cut-off zone is moved for given pressure of lubricant p = 0,04 MPa to the value of F ≐ 65 kN being possible of arbitrar feed depending upon pressure variation of lubricant.

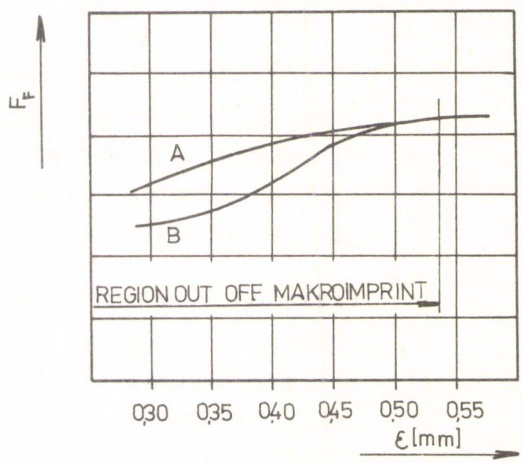

Fig. 5

The applied bearing has proved at pressure rise of feeding water supplied into the pockets of the hybrid bearing up to p = 0,4 MPa the full operation ability even at the specific pressure in slide surface p = 0,5 MPa.

Friction force dependence of trunion upon excentricity fig. 5 depicted indicates in the field of large values of excentricity equal course for both types of bearing. Outstanding difference of friction force in the zone of small values of excentricity is consequence of forming of continuous liquid film of larger thickness in hybrid bearing slide zone.

7. CONCLUSIONS

Comparing measurement answers of both possibilities to guide bearing indicating rubber lining loaded unambiguously affecting by radial force consequence of which are following conclusions:

a/ Hydrodynamic bearing is possible to perform steadily when loaded slide surface by specific pressure of p = 0,32 MPa while start is possible only in the case load being less than p = = 0,25 MPa.

b/ Hybrid bearing is fully aby to perform /start, sustained performance/ conditioned the pressure of lubricant is specific pressure equivalent of slide surface. Steady performance of no start is, however, possible to attain under outstanding lower pressure of lubricant than specific pressure defined for slide surface.

In spite of answer toward experimental authentication relate to certain applied geometry of bearing, lubrication slots and pockets indicate explicit answer for the sake to use water lubricated guide bearing with rubber lining for horizontal units and large measures of radial load.

REFERENCES

1. DAVYDOV, A.P.: "Rezinovyje pošipniky v mašinostrojenii", Mašinostrojenie, Leningrad, 1972
2. PIEPER, H.: "Untersuchungen an wassergeschmierten weichgummigleitlagern", Hannover, Der Technischen Universitaet, 1968

3. NEISCHEL, J. - BRICHTA, J. - VYSLOUŽIL, J.: "Pryžová ložiska mazaná vodou a hydrosměsí", Strojírenství, 1982, No. 10, pg. 556 ÷ 572

4. BEDNÁŘ, J.: "Ověření funkčních vlastností hydrostatického a hydrodynamického ložiska s pryžovou výstelkou", Research report ČKD Blansko 4 VTU 9961-636

5. BAGLIN, K.P. - ARCHAND, J.F.: "An analytic solution of the elastohydrodynamic lubrication of material of low elastic modulus", Elastohydrodynamic Lubrication - 2nd Symposium, 1972

SYMBOLS

F -elastohydrodynamic force, thrust force
F_F -friction force
p -slide surface specific pressure
P -performance
ε -excentricity
δ -bearing play

BEDNÁŘ, Josef, Eng., BSc.,
Scientist of water turbines design bureau
ČKD Blansko
Blansko, Czechoslovakia

EXAMINATION OF FORCED GAS OSCILLATIONS BY THE AID OF COMPUTER

F.Bencze - A.Hoffmann - F.Szlivka

SUMMARY

The aim of our examinations by the aid of computer was to gain experience on the extent of errors due to different neglections, caused in the oscillation pattern in the course of setting up the mathematical model.

The unsteady flow pattern developing in a pipe, produced by means of excitation, has been considered as onedimensional in the course of our examinations, while the change of state has been regarded as isentropic. The possibility of the abrupt changes of the state of characteristics has been excluded. After these presumptions, the equation of motion, the law of continuity and of the isentropic change of state have been established.

In our model a piston was moving with determined frequency at one end of a pipe of finite length L, while the other end of the pipe was open, connected with the atmosphere.

In the course of the calculations we compared the computed results of the wave equation of acoustics and of gas dynamics with the boundary condition that in each state atmospheric pressure prevails at the open pipe-end. During our further investigations we used the more accurate boundary condition determined by means of the energy equation for the solution of the wave equation of gas dynamics at the open pipe-end. The results obtained in this manner were compared with our previous calculations, too.

To write down the wave equation of acoustics, we started from the simplified form of the equation of motion and of the law of continuity, i.e.:

$$\frac{\partial c}{\partial t} + \frac{1}{\rho_o}\frac{\partial p}{\partial x} = o \qquad /1/$$

$$\frac{\partial c}{\partial x} + \frac{1}{\varrho_o a_o} \frac{\partial p}{\partial t} = o, \qquad /1/$$

where c flow velocity; p pressure; t time; z length, measured along the pipe-axis; ϱ_o density; a_o speed of sound, for atmospheric state.

The equation system /1/ has been solved by the aid of the Bernoulli-Fourier method [1] , [2] , considering the following initial and boundary conditions:

$$c\,(x,o) = o, \qquad p\,(x,o) = p_o,$$
$$c_d(L,t) = R\omega \sin\omega t, \quad p\,(L,t,) = p_o, \qquad /2/$$

where R radius of link drive, producing excitation, ω circular frequency.

The form of the solution, rendered non-dimensional:

$$W = \frac{R\,\omega}{a_o}\left\{\frac{\sin[\Omega\,(T-X) - N_1\varepsilon]\,\sin[(N_1+1)\varepsilon]}{\sin\varepsilon} - \right.$$
$$\left. - \frac{\sin[\Omega\,(T+x) - (N_4+1)\varepsilon]\,\sin N_4\varepsilon}{\sin\varepsilon}\right\}, \qquad /3/$$

$$P = 1 + \frac{\varrho_o a_o R\,\omega}{p_o}\left\{\frac{\sin[\Omega(T-X) - N_1\varepsilon]\,\sin[(N_1+1)\varepsilon]}{\sin\varepsilon} + \right.$$
$$\left. + \frac{\sin[\Omega(T+X) - (N_4+1)\varepsilon]\,\sin N_4\varepsilon}{\sin\varepsilon}\right\}, \qquad /4/$$

where

$$\varepsilon = \Omega - \frac{\pi}{2},$$
$$N_1 = \mathrm{ENT}\left[\frac{T-X}{2}\right], \qquad N_4 = \mathrm{ENT}\left[\frac{T+X}{2}\right],$$

and we are stipulating that $\varepsilon \neq k\,\pi$, where k represents an integer, furthermore

$$W = \frac{c}{a_o}, \; P = \frac{p}{p_o}, \; \Omega = \frac{\omega L}{a_o}, \; T = \frac{a_o t}{L}, \; X = \frac{x}{L}.$$

The wave equation of gas dynamics uses the basic relations without neglections, although it is more expedient to modify the equation system in such a manner that the dependent variables in it should be the velocity $c = c(x,t)$ and the speed of sound $a = a(x,t)$. Hence

$$a \frac{\partial c}{\partial x} + \frac{2}{\varkappa-1} c \frac{\partial a}{\partial x} + \frac{2}{\varkappa-1} \frac{\partial a}{\partial t} = 0$$

/5/

$$\frac{\partial c}{\partial t} + c \frac{\partial c}{\partial x} + \frac{2}{\varkappa-1} a \frac{\partial a}{\partial x} = 0$$

The quasi-linear partial differential equation system is hyperbolic, to the numerical solution of which the method of characteristics [3] has been applied.

At the physical plane [X, T,] along the projection of the characteristic curve with a given tangent, the correlations of the independent variables can be written in the non-dimensional form, in the well-known manner, as

$$\left(\frac{DX}{DT}\right)_1 = W + A \Rightarrow \frac{\varkappa-1}{2} W + A = \alpha \;, \qquad /6/$$

$$\left(\frac{DX}{DT}\right)_2 = W - A \Rightarrow -\frac{\varkappa-1}{2} W + A = \beta \;, \qquad /7/$$

where α and β are the Riemann-constants and $A = \frac{a}{a_o}$.

The isentropic change of state has been used in each case to determine pressure, namely:

$$P = A^{\frac{2\varkappa}{\varkappa-1}} \qquad /8/$$

The boundary condition is obtained, on the one hand by means of the non-dimensional piston velocity

$$W_d = \frac{c_d}{a_o}$$

in form of the relationship between the Riemann-variables,

$$\alpha = \beta + 2\, W_d \qquad /9/$$

and on the other hand, at the open pipe-end during the inlet, the expediently made non-dimensional form of the energy equation yields the relation:

$$\beta = \frac{3-\varkappa}{\varkappa+1}\,\alpha + 2\sqrt{\frac{\varkappa-1}{\varkappa+1}}\left[1 - \frac{2\beta^2}{\varkappa+1}\right]^{\frac{1}{2}} , \qquad /1o/$$

while during the outlet, from the atmospheric value of pressure:

$$\beta = 2 - \alpha \qquad /11/$$

will be obtained.

Some variations of our calculations have been carried out approximatively by using relation /11/ for the open pipe-end, in the case of inlet and outlet as well.

The results of our calculations were shown in diagrams. In the figures the pressure P was illustrated as a function of the time T for the pipe length L = 5 m, the speed of sound a_o = 347,8 m/s and the radius of the link drive R = o,oll m.

In Fig. 1., 2. and 3. the pressure ratios were demonstrated in the case of ω = 313 m/s for the solution of the wave equation of acoustics and gas dynamics, resp. at various boundary conditions.

According to Fig. 1. where we have considered pressure as P_L = 1 at the open pipe-end, the solution of the wave equation of acoustics has shown an error of about lo %, related to that one of gas dynamics. According to Fig. 2. the solutions of the wave equation of gas dynamics considering the boundary conditions /1o/ and /11/, as well as P_L = 1 are

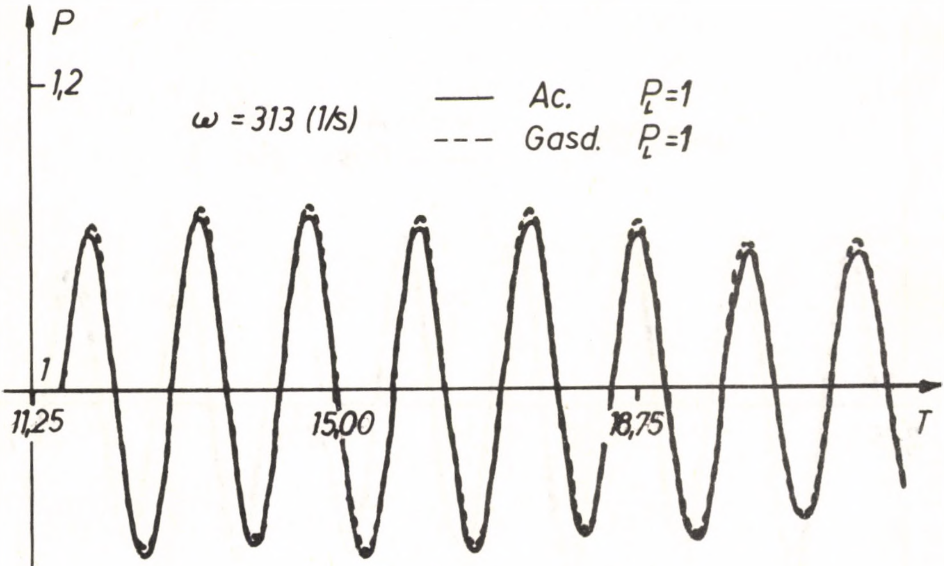
P
1,2
ω = 313 (1/s)
Ac. P_L=1
Gasd. P_L=1
1
11,25
15,00
18,75
T

Fig. 1.

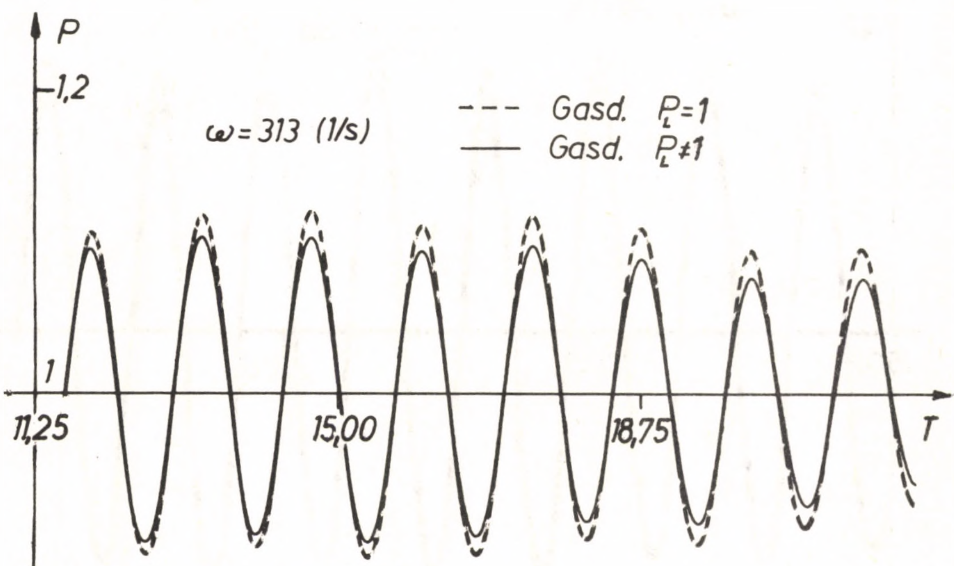
P
1,2
ω = 313 (1/s)
Gasd. P_L=1
Gasd. P_L≠1
1
11,25
15,00
18,75
T

Fig. 2.

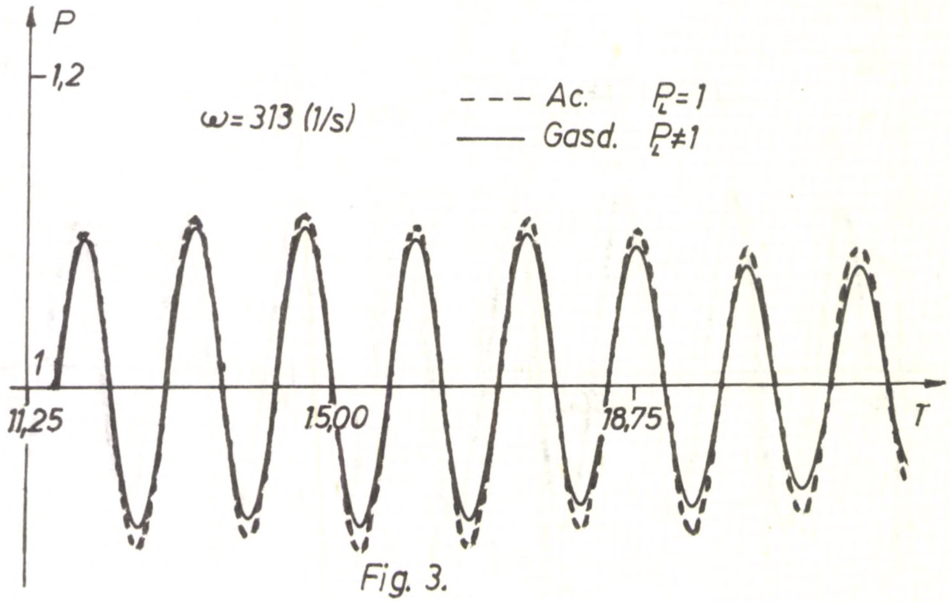
P
1,2
ω=313 (1/s)
Ac. P_L=1
Gasd. P_L≠1
1
11,25
15,00
18,75
T

Fig. 3.

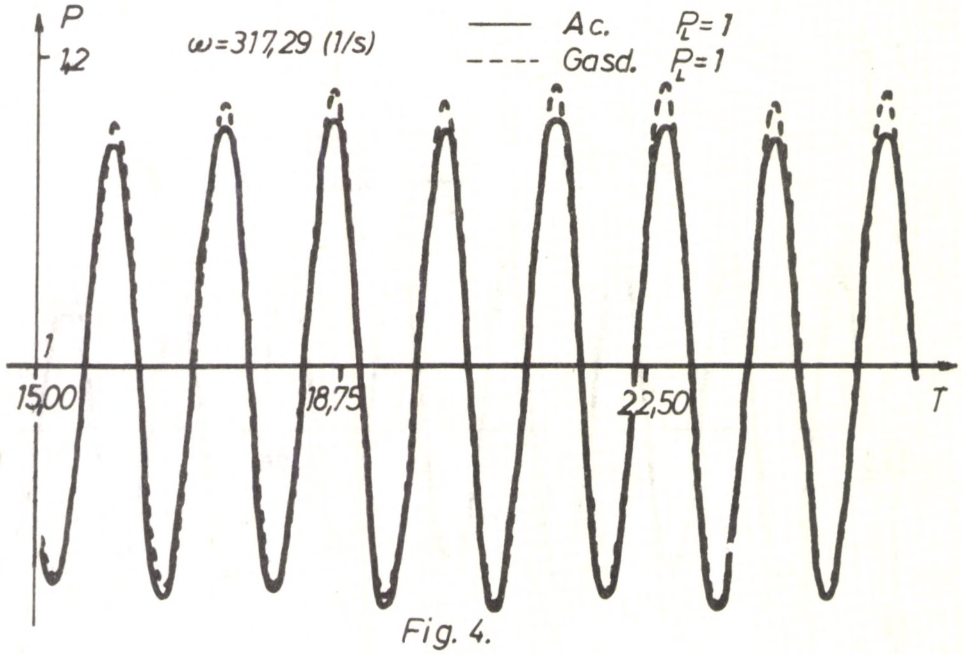
P
1,2
ω=317,29 (1/s)
Ac. P_L=1
Gasd. P_L=1
1
15,00
18,75
22,50
T

Fig. 4.

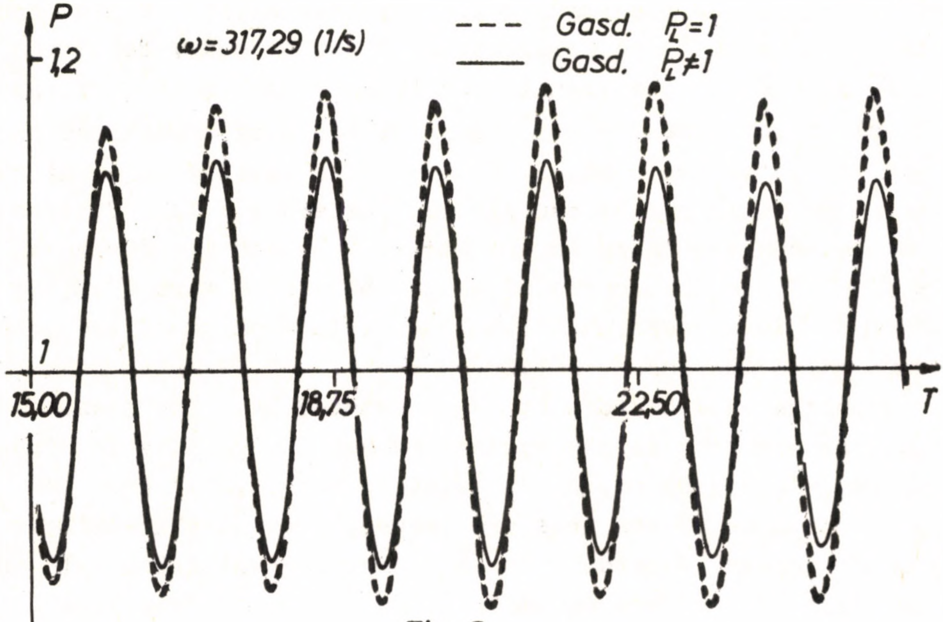
P
1,2
ω=317,29 (1/s)
Gasd. P_L=1
Gasd. P_L≠1
1
15,00
18,75
22,50
T

Fig. 5.

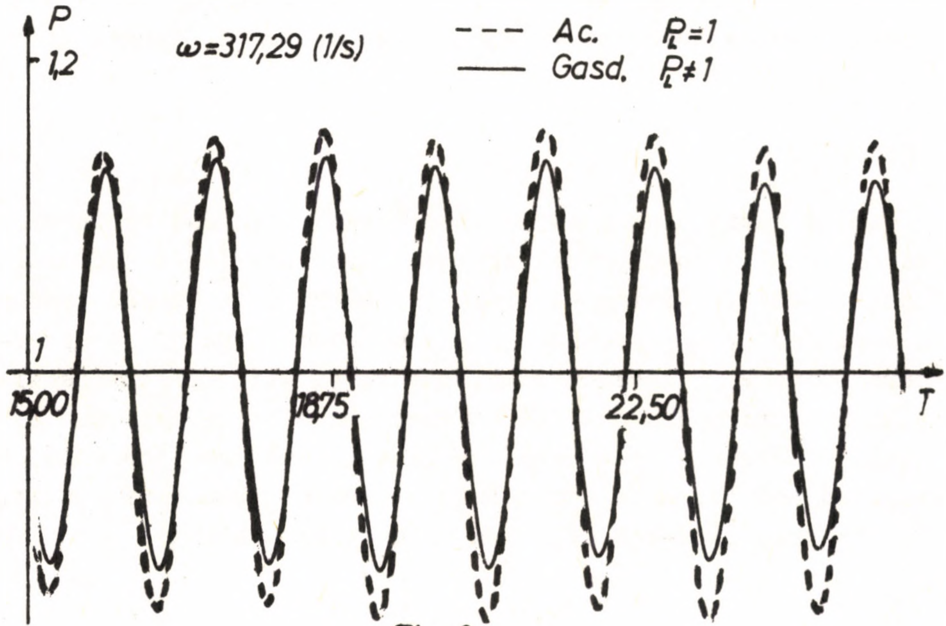
P
1,2
ω=317,29 (1/s)
Ac. P_L=1
Gasd. P_L≠1
1
15,00
18,75
22,50
T

Fig. 6.

compared with one another, showing an error of 26 %. Fig. 3. illustrates the results obtained by application of the acoustic model with the consideration of the boundary condition /2/, as well as the results obtained by application of the model of gas dynamics utilizing the boundary conditions /1o/ and /11/; the error was 22 %, here. The maximum value of the pressure ratio in the oscillation pattern was 1.1. Similar comparisons are shown in the Fig. 4., 5. and 6., for ω = = 317 1/s, in the course of which the errors were 17 %, 43 % and 33 % in succession, while the maximum value of the pressure ratio increased to 1.15.

From the examinations it can be stated that the pressure patterns forming in the system are equal regarding the frequency, depending on the calculation method, but from the point of view of the pressure values, considerable differences appear, according to the preceding valuations. If the solution of the wave equation of gas dynamics, applying the boundary conditions /1o/ and /11/ is regarded as most accurate it can be stated that the more accurate system of boundary conditions affects the result of computation in a higher degree than the linearization of the differential equation.

CONCLUSION

On the basis of our summarized experiences and by further development of our preceding investigations [4] concerned, we came to the following conclusion: in the case of the system determined by the problem if the maximum value of the pressure ratio P_{max} exceeds 1.o5, the calculation of the oscillation pattern can only be carried out with an acceptable limit of error if the wave equation of gas dynamics will be applied and the more accurately determined boundary condition of the open pipe-end is taken into consideration.

REFERENCES

[1] Hoffmann,A. - Fényes,T.: Rechenverfahren zur Untersuchung von Wellenerscheinungen in Rohrleitungen.
Periodica Polytechnica Mech.Eng. 26/1, 1982. Budapest.

[2] Szlivka,F.: Konvergenzbeschleunigungsverfahren bei der Lösung des partiellen Differentialgleichungssystems von Gasschwingungen. Periodica Polytechnica Mech.Eng.(in print), Budapest.

[3] Jenny,E.: Berechnung und Modellversuche über Druckwellen mit grossen Amplituden in Auspuff-Leitungen.
Dissertation ETH Zürich, 1949.

[4] Bencze,F. - Hoffmann,A. - Szlivka,F.: Untersuchung der Wellenerscheinung in Rohrleitungen.
ZAMM 63 1983. Berlin.

Dr. Ferenc BENCZE - Dr. Andor HOFFMANN - Dr. Ferenc SZLIVKA

Department of Fluid Mechanics
Technical University of Budapest
H-1111 Budapest
Bertalan Lajos u. 4-6.
Hungary

DETERMINATION OF THE EIGENFREQUENCY OF AXIAL FANS

K. Bordás

The eigenfrewuency of four differently shaped hollow wing blades have been calculated by the two dimensional transfer matrix method, using the similarity princuple. The results are given by diagrams which can be used for the determination of the eigenfrequancy without any special knowledge.

1. Introduction

The blades investigated are presumed to satisfy the following conditions:

- The fan consists of a few large-size helical hollow blades fixed on the hub.
- The centres of the cross sections form a line perpendiculary to the axis. /centre line/
- The blades are specially shaped in order to maintain the efficiency.

There is no general method available for the optimum stressing of the blades.

2. Difference equations of the bending vibrations

The cordinate system used for the geometrical description of the fan is shown in Fig. 1. Before stressing the blade the centres are on the z axis z which is parallel to the axis of rotation. The ξ,η,z system is defined by the principal axis of the inertia; the angle between the principal axis concerning to the cross section and the x,y plane is denoted by γ.

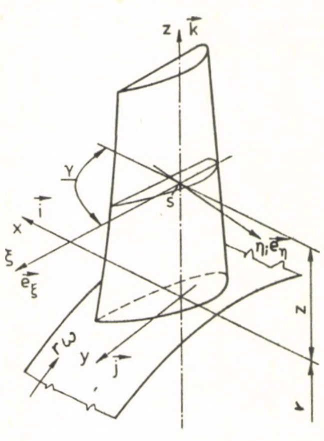

Fig. 1. cordinate system

When the blade is rotaring the component forces of the centrifugal and inertia forces in the direction of the principal inertia axis have to be calculated for a deformed blade.

Taking into account all the conditions given above we get following equations for the equilibrium of the external and internal forces:

$$\frac{\partial^2}{\partial z^2}\left(I_\eta E \frac{\partial^2 \xi}{\partial z^2}\right) - \frac{\partial}{\partial z}\left(F_z \frac{\partial \xi}{\partial z}\right) + \varrho A \frac{\partial^2 \xi}{\partial t^2} = 0$$

$$\frac{\partial^2}{\partial z^2}\left(I_\xi E \frac{\partial^2 \eta}{\partial z^2}\right) - \frac{\partial}{\partial z}\left(F_z \frac{\partial \eta}{\partial z}\right) - \varrho A \omega^2 \eta + \varrho A \frac{\partial^2 \eta}{\partial t^2} = 0 \qquad /1/.$$

$$\frac{\partial F_z}{\partial z} + \varrho A \left(r + z\omega^2\right) = 0$$

The assymetry of the blade, the variation of the direction of the principal inertia axis along the blade and the different cross sections cause great difficulties in the solution of Eq. /1/.

3. The two dimensional transfer matrix method

Dividing the blade into n pieces and contracting the mass of the single pieces to a point at the upper end of them we get a system of flexible and massless sections. The i-th section can be described by the translation and rotation of the cross sectional centre and by bending and shearing forces occuring in the cross section. These parameters are given with a single state-vector:

$$\underline{z}_i^T = \left[x, y, \varphi_x, \varphi_y, M_x, M_y, V_x, V_y\right]_i^T , \qquad i = 1,2, \dots n.$$

The relationsship between the component:

$$\varphi_x = y' , \quad \varphi_y = x' , \quad M = - IE\varphi' , \quad V = - M' \qquad /2/.$$

Neglecting the mass of the ℓ_i blade section Eq. /1/ will be reduced and the state vectors will meet at the common end of two sections:

$$\frac{\partial^4 x}{\partial z^4} = 0 , \quad \frac{\partial^4 y}{\partial z^4} = 0 \qquad \underline{z}_i(0,t) = \underline{z}_{i-1}(\ell_{i-1},t) \qquad /3/.$$

Using these relations the matrix equations concerning with the blending vibrations can be derived for a blade section of the length ℓ_i and then for the wholen blade:

$$\underline{z}_i = \underline{\underline{P}}_i \cdot \underline{\underline{T}}_i^T \cdot \underline{\underline{S}}_i \cdot \underline{\underline{T}}_i \cdot \underline{z}_{i-1} \,, \quad \underline{z}_n = \prod_{i=1}^{n} \underline{\underline{P}}_i \cdot \underline{\underline{T}}_i^T \cdot \underline{\underline{S}}_i \cdot \underline{\underline{T}}_i \cdot \underline{z}_{i-1}$$

$$i = 1,2, \dots n \qquad /4/.$$

Here $\underline{\underline{T}}_i$ is the transfer matrix, $\underline{\underline{S}}_i$ is the stiffness matrix and $\underline{\underline{P}}_i$ is the mass-point matrix. /The indes is zero for the blade root and n for the outside end./

$$\underline{\underline{S}}_i = \begin{bmatrix} 1 & 0 & 0 & \ell & 0 & 3k_y\ell & 0 & k_y\ell^2 \\ 0 & 1 & \ell & 0 & -3k_x\ell & 0 & k_x\ell^2 & 0 \\ 0 & 0 & 1 & 0 & -6k_x & 0 & 0 & 3k_x\ell \\ 0 & 0 & 0 & 1 & 0 & -6k_y & 3k_y l & 0 \\ 0 & 0 & 0 & 0 & 1 & 0 & 0 & -\ell \\ 0 & 0 & 0 & 0 & 0 & 1 & -\ell & 0 \\ 0 & 0 & 0 & 0 & 0 & 0 & 1 & 0 \\ 0 & 0 & 0 & 0 & 0 & 0 & 0 & 1 \end{bmatrix}_i \qquad k_x = \left.\frac{\ell}{6I_xE}\right|_i \qquad k_y = \left.\frac{\ell}{6I_yE}\right|_i \qquad /5/.$$

$$\underline{\underline{T}}_i = \begin{bmatrix} \cos\gamma & \sin\gamma & 0 & 0 & 0 & 0 & 0 & 0 \\ -\sin\gamma & \cos\gamma & 0 & 0 & 0 & 0 & 0 & 0 \\ 0 & 0 & \cos\gamma & \sin\gamma & 0 & 0 & 0 & 0 \\ 0 & 0 & -\sin\gamma & \cos\gamma & 0 & 0 & 0 & 0 \\ 0 & 0 & 0 & 0 & \cos\gamma & \sin\gamma & 0 & 0 \\ 0 & 0 & 0 & 0 & -\sin\gamma & \cos\gamma & 0 & 0 \\ 0 & 0 & 0 & 0 & 0 & 0 & \cos\gamma & \sin\gamma \\ 0 & 0 & 0 & 0 & 0 & 0 & -\sin\gamma & \cos\gamma \end{bmatrix}_i \qquad /6/.$$

$$\underline{\underline{P}}_i = \begin{bmatrix} 1 & 0 & 0 & 0 & 0 & 0 & 0 & 0 \\ 0 & 1 & 0 & 0 & 0 & 0 & 0 & 0 \\ 0 & 0 & 1 & 0 & 0 & 0 & 0 & 0 \\ 0 & 0 & 0 & 1 & 0 & 0 & 0 & 0 \\ 0 & p_{52} & p_{53} & 0 & 1 & 0 & 0 & 0 \\ 0 & 0 & 0 & p_{64} & 0 & 1 & 0 & 0 \\ p_{71} & 0 & 0 & 0 & 0 & 0 & 1 & 0 \\ 0 & p_{82} & 0 & 0 & 0 & 0 & 0 & 0 \end{bmatrix}_i \qquad \begin{aligned} p_{52} &= \ell_i \cdot m_i \cdot \omega^2 \,, \\ p_{53} &= -\ell_i (r + z \cdot m_i)\omega^2 \,, \\ p_{64} &= p_{53} \,, \\ p_{71} &= m_i \cdot \alpha^2 \,, \\ p_{82} &= m_i(\alpha^2 - \omega^2) \,, \\ n &= 1,2 \dots n \,. \qquad /7/. \end{aligned}$$

The argument is the α eigenfrequency that can be calculated with consideration to the boundary conditions:

$$x_o = y_o = \varphi_{xo} = \varphi_{yo} = M_{xn} = M_{yn} = V_{xn} = V_{yn} = 0 \ . \qquad /8/.$$

The critical speed of rotation is determined by the eigenfrequency:

$$n_{cr} = \frac{1}{N} \frac{\alpha_{cr}}{2\pi}$$

where N is the number of the guide vanes installed in front of the impeller.

4. <u>The dynamical similarity of the blade vibrations</u>

The dynamical similarity means more than the similarity in space and time; the ratio of the main forces has to be invariant as well.

In the case considered the main forces are the elastic and the inertia forces:

$$\frac{\partial}{\partial z}\left(I_x E \frac{\partial^2 y}{\partial z^2}\right) \quad \text{and} \quad dm \frac{\partial^2 y}{\partial t^2} \ . \qquad /10/.$$

The similarity in time provided by allowing free vibrations only /harmonic funktions of time/; the similarity in space requires uniform profile and curvature.

The scale of the elastic force:

$$\rho_{FE} = \frac{1}{\rho_L} \rho_I \rho_E \frac{\rho_L}{\rho_L^2} = \rho_L^2 \rho_E \ , \quad \text{since} \quad \rho_I = \rho_L^4 \qquad /11/.$$

The scale of the inertia forces:

$$\rho_{FI} = \frac{dm\, \alpha^2 y|1}{dm\, \alpha^2 y|2} = \rho_m \rho^2 \rho_L = \rho_\varsigma \rho_f^2 \rho_L^4 \qquad \rho_m = \rho_L^3 \quad \rho_\alpha = \rho_f \qquad /12/.$$

Using /11/ and /12/ we get the scale for the dynamical similarity:

$$\rho_{dyn} = \frac{\rho_{FE}}{\rho_{FI}} = \frac{\rho_E}{\rho_\varsigma \rho_L^2 \rho_f^2} \ , \quad \text{when} \quad \rho_{dyn} = \rho_\varsigma = \rho_E = 1 \ , \qquad /13/.$$

then: $\rho_L \rho_f = \frac{\ell_1}{\ell_0} \frac{f_1}{f_0} = 1$, and so $f_1 = f_0 \frac{\ell_0}{\ell_1}$. /14/.

Eq. /14/ enables us to determine the eigenfrquency of a blade with the length of ℓ_1 from the f_0 and ℓ_0 data of a known blade.

5. Eigenfrequency digrams

As the number of parameters is great, a reduction -- if possible -- is reasonable. In the case of a fan with slow we have to take into consideration neither the effect of the centrifugal force nor the twisting effect. The similarity principle results in further reduction.

The diagrams shows in Fig. 2-5 heve been derived according to the principles outlined above. The data are valid for a blade with a length of 500 mm and a torsion 15°. The torsion and the variation of the chord length are constant along the blade.

6. Summary

The method outlined above /the two dimensional transfer matrix method/ is suitable for the determination of the eigenfrequency of wing blades appled in axial fans and the accuracy is satisfactory. The correlation between the calculated and measured values is rather good. Using the diagrams /2-5/ and the dinamical similarity the method is rapid enaugh.

The working speed has to be far enaugh from the eigenfrequency determined.

K. Bordás, Dept. of Mechanical Enginneering
University of Chemical Engineering, Veszprém/Hungary
H-8200 Veszprém, Schönherz Z. u. 10-12.

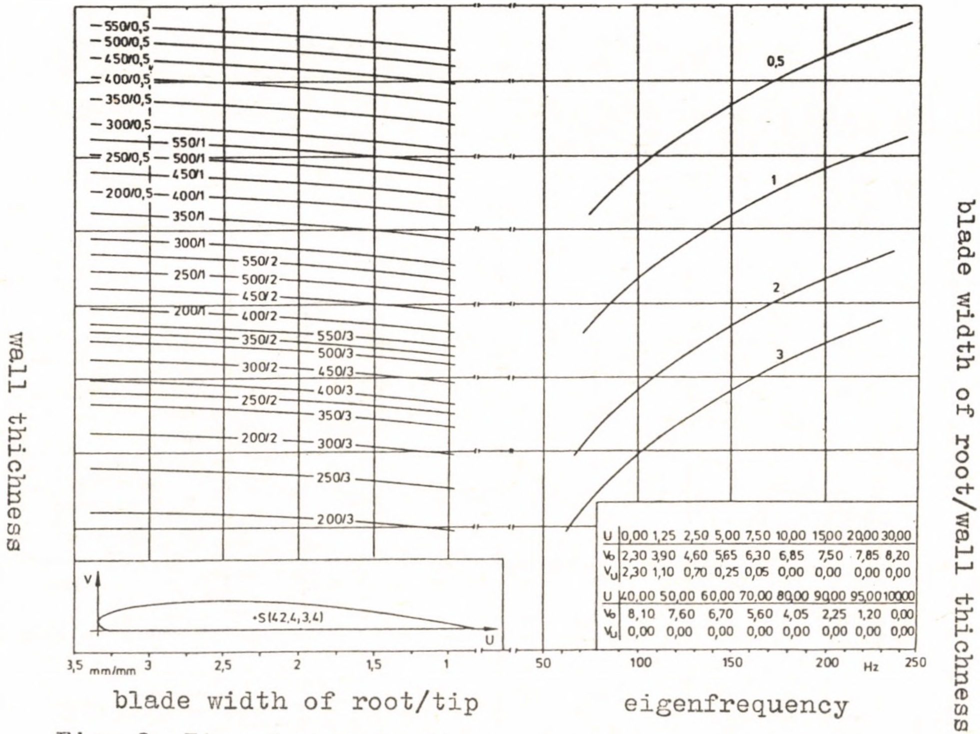

Fig. 2. Eigenfrequency diagram; profile Gö 564

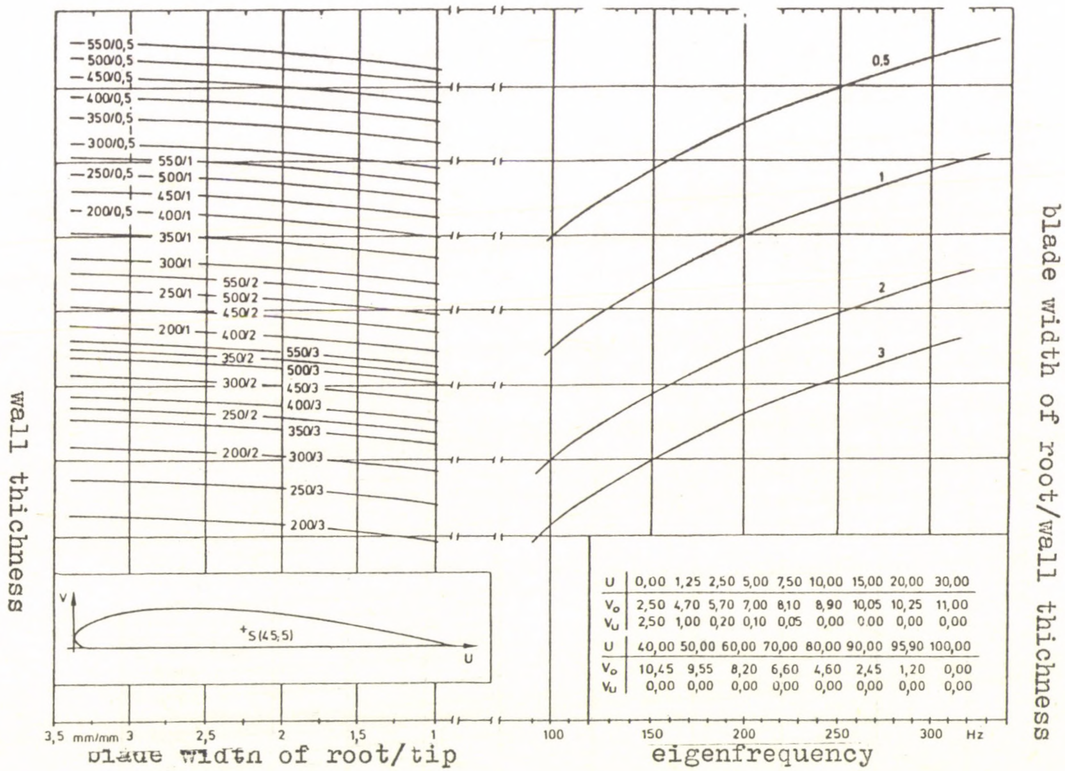

U	0,00	1,25	2,50	5,00	7,50	10,00	15,00	20,00	30,00
V_o	2,50	4,70	5,70	7,00	8,10	8,90	10,05	10,25	11,00
V_u	2,50	1,00	0,20	0,10	0,05	0,00	0,00	0,00	0,00

U	40,00	50,00	60,00	70,00	80,00	90,00	95,90	100,00
V_o	10,45	9,55	8,20	6,60	4,60	2,45	1,20	0,00
V_u	0,00	0,00	0,00	0,00	0,00	0,00	0,00	0,00

Fig. 3. Eigenfrequency diagram; profile G" 436

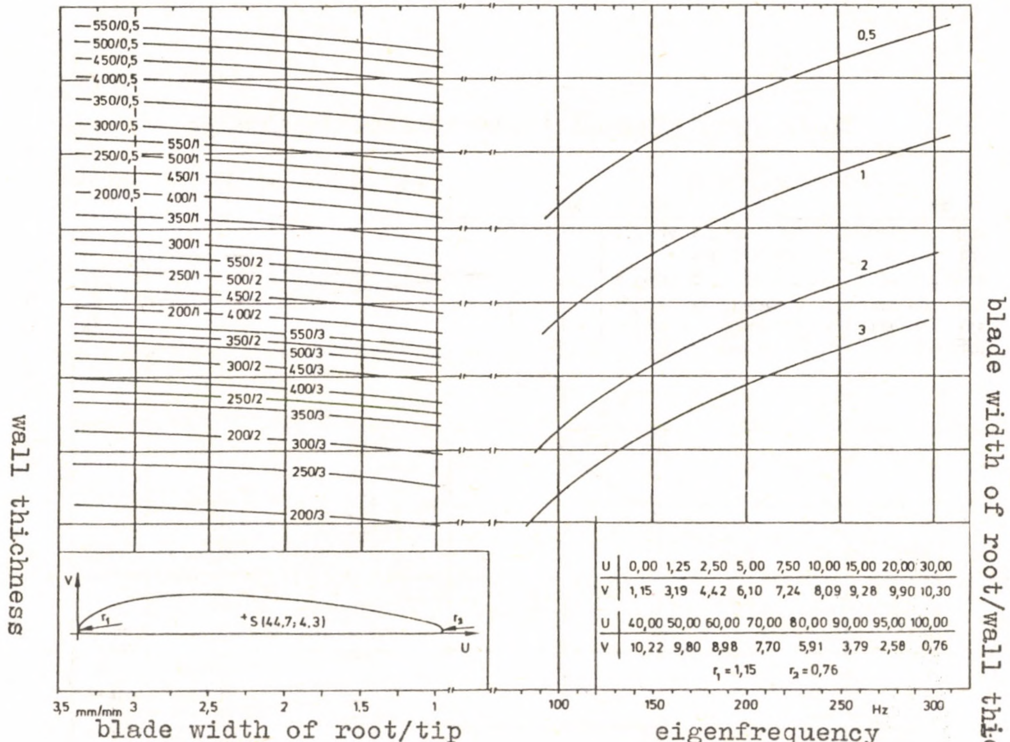

Fig. 4. Eigenfrequency diagram; profile RAF 6 E

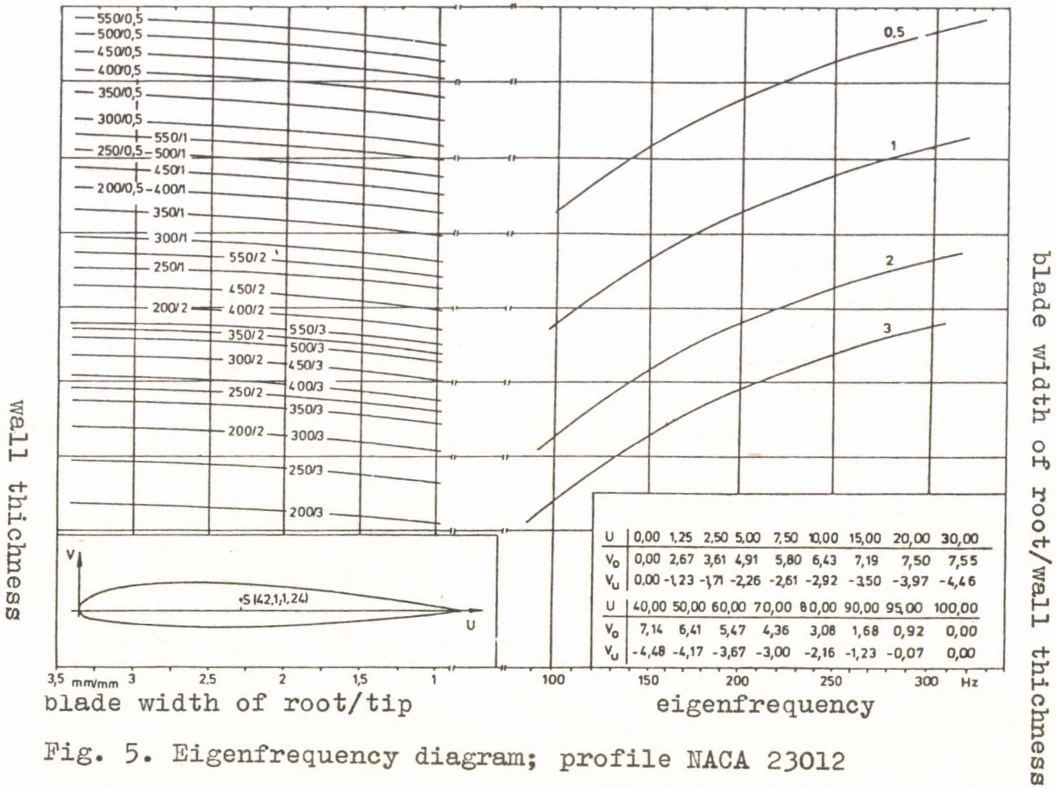

U	0,00	1,25	2,50	5,00	7,50	10,00	15,00	20,00	30,00
V_o	0,00	2,67	3,61	4,91	5,80	6,43	7,19	7,50	7,55
V_u	0,00	-1,23	-1,71	-2,26	-2,61	-2,92	-3,50	-3,97	-4,46

U	40,00	50,00	60,00	70,00	80,00	90,00	95,00	100,00
V_o	7,14	6,41	5,47	4,36	3,08	1,68	0,92	0,00
V_u	-4,48	-4,17	-3,67	-3,00	-2,16	-1,23	-0,07	0,00

Fig. 5. Eigenfrequency diagram; profile NACA 23012

AN IMPROVED SLIPFACTOR FORMULA

V. Bothmann, J. Reffstrup

ABSTRACT

A new slipfactor formula as an improvement of Stodola's formula is presented. The slipfactor definition is discussed and considerations leading to the improvement are mentioned. The results of comparing the new formula to other known methods and to testresults from the literature are illustrated.

INTRODUCTION

As an improvement of Stodola's formula a new slipfactor formula will be presented. The new formula has been incorporated in the course notes (1) and it has been used successfully by pump manufacturers. Hence it is believed that the formula might be of interest to a wider range of possible users.

Most of the known slipfactor formulas only contain the blade angle and the number of blades and some of them also the radius ratio as parameters. Thus it is possible, as known, in a very simple but approaching manner to determine the dimensionless head-capacity-line for the enthalpy to be induced into a radial rotor. As the slipfactor represents nothing but this head-capacity-line, the slipfactor will in this paper be defined as the ordinate of this line and not - as often - as the quotient of the tangential components of the real absolute exit velocity and the theoretical one, which follows the blade. With the latter the original definition of the slipfactor the nominator as well as the denominator of the quotient depend on the abscissa, the volume flow rate. This means a unnecessary hiding of the linearity of the relation.

In the literature related to the matter the potential theoretical solution of Busemann (2) is often used as basis for a comparison of the quality of a slipfactor formulation.

Busemann's slipfactor cannot be obtained from a simple formula, but from diagrams, tables or with the aid of a computer program. In this paper Busemann's solution is obtained numerically by means of an ALGOL-program. These numerical values will be used as a basis of comparison together with measured slipfactor values from the literature. Moreover a comparison will be made with other slipfactor formulas known from literature and practice.

THE SLIPFACTOR DEFINITION

Figure 1 shows the correlation between the outlet angle BB of the rotor blade, the theoretical blade work PB and the real work P, which is reduced owing to the finite number of blades. PB and P are shown as functions of the volume flow

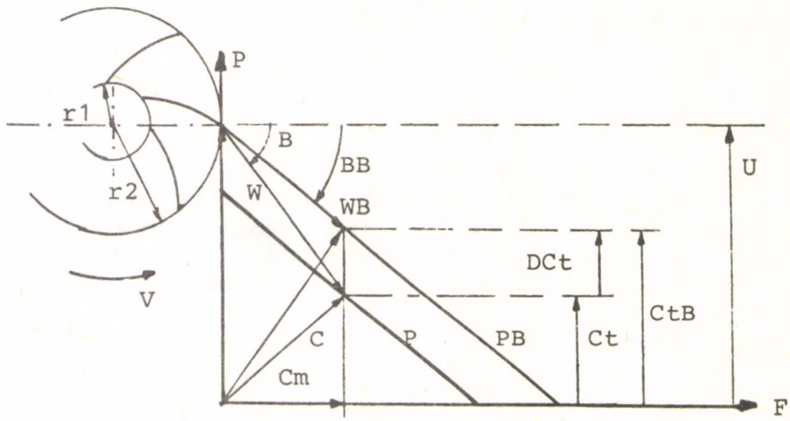

Figure 1: Slipfactor definition

F. All the quantities are represented dimensionless or so to say with the periferal velocity U = 1 as the unit of measure. The figure shows clearly how the two lines PB(F) = CtB/U and P(F) = Ct/U are correlated to the velocity triangles depending on the volume flow F. Both are straight lines.

As the blade angle BB is constant, PB is the geometric locus of the vector tip of the theoretical relative velocity WB as a function of F. The line of the real blade work P, here defined as the slipfactor, lies a distance of DCt = CtB - Ct below the theoretical blade work PB.

In most of the known slipfactor formulas this quantity representing the tangential velocity slip is constant or almost constant that means independent of the volume flow F. Therefore the two lines PB and P are parallel or nearly parallel. The exact theory of Busemann confirms this fact except for extremely high radius ratios r1/r2, in which case the PB-line is somewhat steeper than the P-line.

STODOLA'S FORMULA AND ITS IMPROVEMENT

Stodola's formula (3) in the present definition of the slipfactor is written in the following way:

$$P(STOD) = 1 + F \tan(BB) - (pi/z) \cos(BB)$$

An interpretation of this formula as given in different textbooks (4) will be reviewed here, since this interpretation has been part of the inspiration to the improvement of Stodola's formula, the subject of this paper.

The parallel displacement that means the slip

$$DCt/U = DWt/U = (pi/z) \cdot \cos(BB) \quad \text{(see figure 1)}$$

can be interpreted by means of the relative eddy existing between two blades. As shown in figure 2 the relative eddy is approximated by a circle having a common tangent with each of the two blades. The circle's radius is approximately given by a geometrical consideration:

rr = (r2) (pi/z) cos(BB)

While the impeller is rotating with the angular velocity V the relative eddy will not be rotating in the absolute coor-

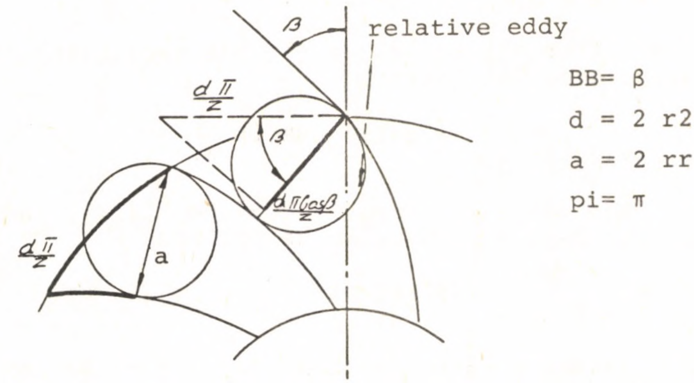

Figure 2: The relative eddy

dinate system.

The slip is explained as the relative velocity at the periphery of the eddy. With r2*V = U the slip is written as follows:

DWt = DCt = (pi/z) cos(BB) U

As shown in (5), the circles, with radii calculated with the above mentioned formula for rr, differ considerably from

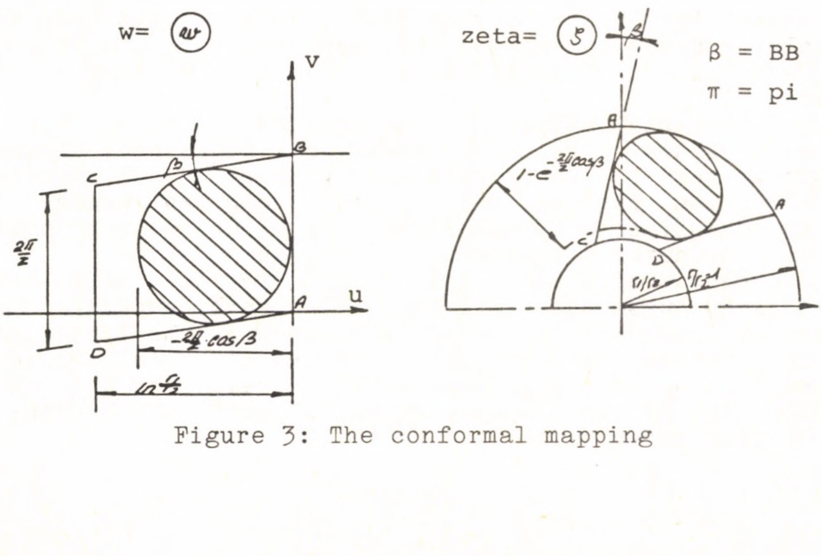

Figure 3: The conformal mapping

the desired circles, that touch both blades. This happens especially with small blade angles and low numbers of blades. To meet this requirement the circle between the rotor blades has been replaced by a conformal mapping of a circle from a straight cascade into a rotor with logarithmic blades (figure 3). The mapping function is the following (5):

$$\text{zeta} = e^{iw} \qquad \text{with } w = u + iv$$

In this way a better approximation for the equivalent radius of the relative eddy is obtained:

$$rr = (r2)/2 \; (1 - e^{-(2pi/z)\cos(BB)})$$

Consequentely the improved formula for the slip, the displacement of the P-line is written as follows:

$$DCt/U = 1/2 \; (1 - e^{-(2pi/z)\cos(BB)})$$

Finally the improved formula for the slipfactor becomes:

$$P(IMPR) = 1 + F\tan(BB) - 1/2 \; (1 - e^{-(2pi/z)\cos(BB)})$$

With high numbers of blades this formula converges to Stodola's original formula. When the perifery of the conformal mapped circle touches the blade inlet circle with radius r1, the following expression is valid as seen in figure 3 in the limit case:

$$r1/r2 = Rl = e^{-(2pi/z)\cos(BB)}$$

This means, that if the number of blades z becomes less than the value corresponding to this expression, the relative eddy will expand inwards beyond the annular area of the blades.

Some of the usual slipfactor methods as Busemann's contain the radius ratio r1/r2 as a parameter. Busemann's diagrams are often seen in the literature with r1/r2 as abscissa. These diagrams show a clear limit between two areas. One area with constant slipfactor and the other one with considerably increasing dependance on the radius ratio.

The above-mentioned limit relation Rl for the radius ratio plotted into Busemann's diagrams will clearly separate these two areas. This formula indeed is a practical tool to calculate the critical radius ratio. Beyond the limit value Rl the overlapping of the blades for given values of the number of blades and of the bladeangle gives poor results with all approximated formulas.

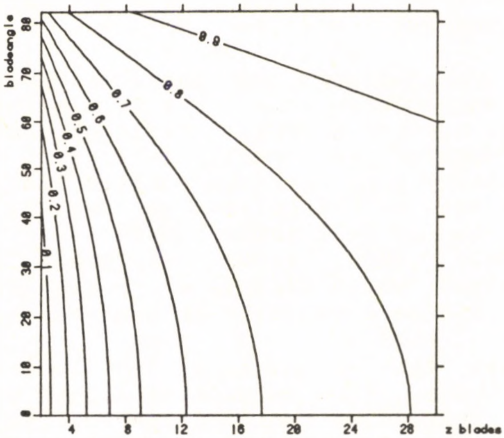

Figure 4: Limit radius ratio curves

Figure 4 shows curves with constant limit radius ratio Rl. The slipfactor will be independent of the radius ratio, if the number of blades with given bladeangle is chosen ahead of the curve corresponding to the given radius ratio. To design new rotors this diagram might be helpful.

SYSTEMATIC OF COMPARISON

As the values of measured slipfactors taken from the literature correspond to volume flows with different F-values, the comparison is made at zero volume flow with correspondingly extrapolated values. That is, to compare a slipfactor Px measured at Fx to a slipfactor formula Pa, the value of Pa at F = 0 is compared to the value cut off on the ordinate at F = 0 by a line parallel to Pa through Px.

When comparing two methods (formulas) Pa(F) and Pb(F) correspondingly Pa(0) and Pb(0) are compared.

RESULTS OF COMPARISON

A considerable number of 3-dimensional figures have been plotted in order to study and compare the different slipfactor methods. Of these the most instructive ones are shown in figures 5 to 7 . The peaks appearing in the 3-dimensional surfaces correspond to the 65 measured splipfactor values taken from the literature and documented in (5) . These values are inserted instead of the local surface value. The unit of measure in the perpendicular direction corresponds in all these figures to the slipfactor unit CtB/U = 1.

The compared methods not yet mentioned correspond to the following equations:

Pfleiderer (6)

P(PFLE) = (1 + F tan(BB)) / (1 + Pf) with

Pf = 1.2 (1 + cos(BB)) / z / (1 - (R R))

Eck (7)

P(ECK1) = (1 + F tan(BB)) / (1 + Ec) with
Ec = pi cos(BB) / z / (1 - (R R))

In figure 5 the 3-dimensional surfaces show the deviation of the different methods from Busemann's method (BUSE). The comparison is made at a radius ratio of zero since simple slipfactor formulations usually fail with insufficiently overlapping blades. The surfaces contain lines with constant number of blades z and lines showing constant deviation levels in distances of 0.02 units between -0.1 and +0.3. The improved formula (IMPR) shows only small deviations from Busemann's method, while Stodola's formula (STOD) shows considerable deviations especially in the area corresponding to small numbers of blades.

Figure 6 shows the deviations of the testresults from the respective methods. The calculated values are obtained on the basis of the radius ratios given in the literature for each of the testresults. Again the new formula shows a nice result having the best distribution of positive and negative deviations over the area compared to the other methods.

In the figure 7 the surfaces show the slipfactor itself calculated by the different formulas again as a function of the number of blades and the bladeangle at radius ratio R = 0. The peaks interrupting the surfaces are the testresults somewhat corrected for the different given radius ratios. These figures give a good impression of the different methods' absolute variation with the number of blades and the bladeangle.

LIST OF SYMBOLS

C	absolute velocity
Ct	" , tangential component
CtB	" , " , B: flow follows blade
Cm	" , meridional component
U	periferal velocity
W	relative velocity
WB	relative velocity, B: flow follows blade direction
Wt	" , tangential component
BB	bladeangle ; angles between the relative velocity and
B	rel. flowangle; the radiusvector, positive, when Wt and ; U have the same direction.
PB	Ctb/U bladework, dimensionless, B: flow follows blade
P	Ct/U bladework = slipfactor, dimensionless
F	Cm/U volume flow, dimensionless
R	r1/r2 radius ratio : 1 = bladeinlet, 2 = bladeoutlet
Rl	limit radius ratio for blade overlapping range
rr	radius of the relative eddy
V	angular velocity
z	number of blades
pi	= 3.141592 e = 2.71828 -

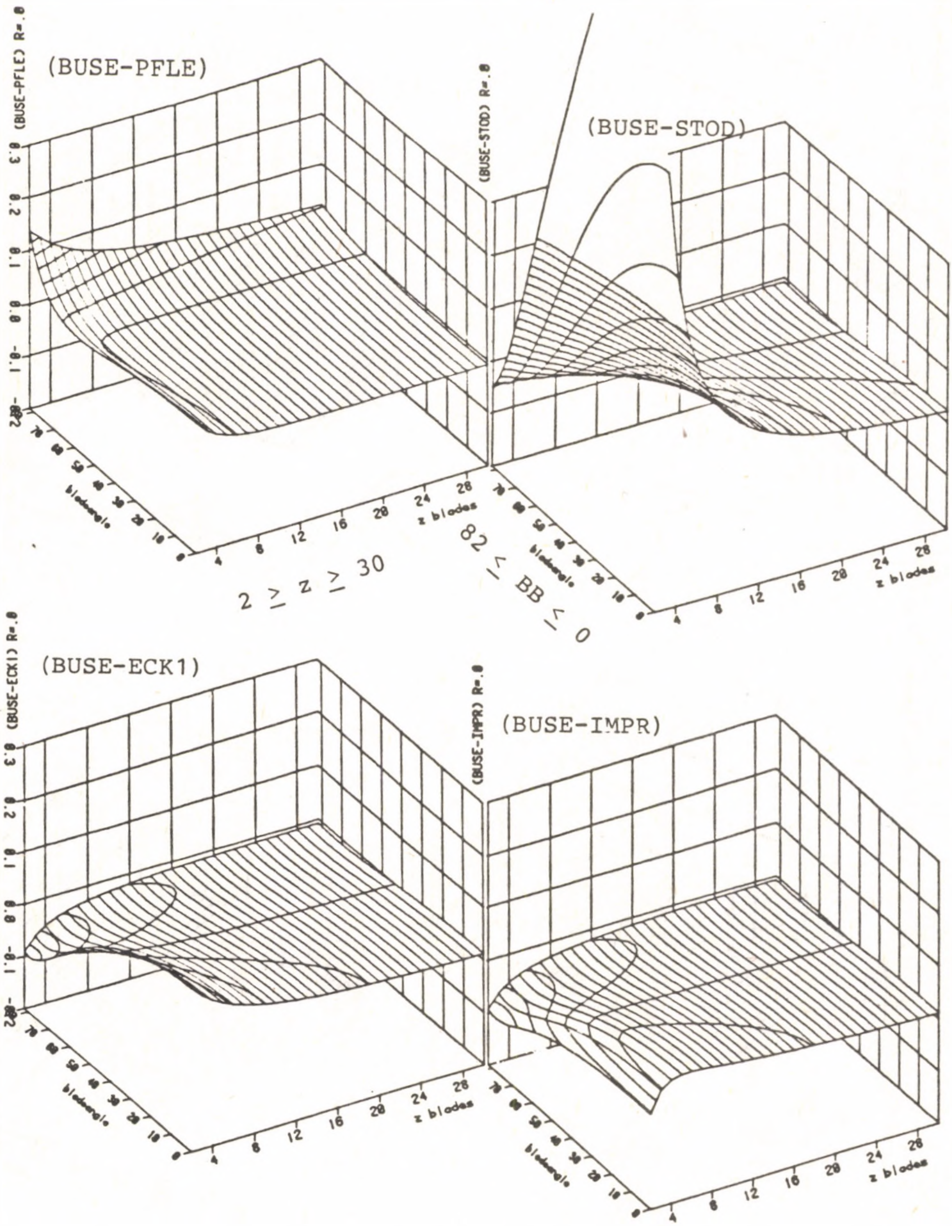

Figure 5: Other methods' deviation from Busemann's method

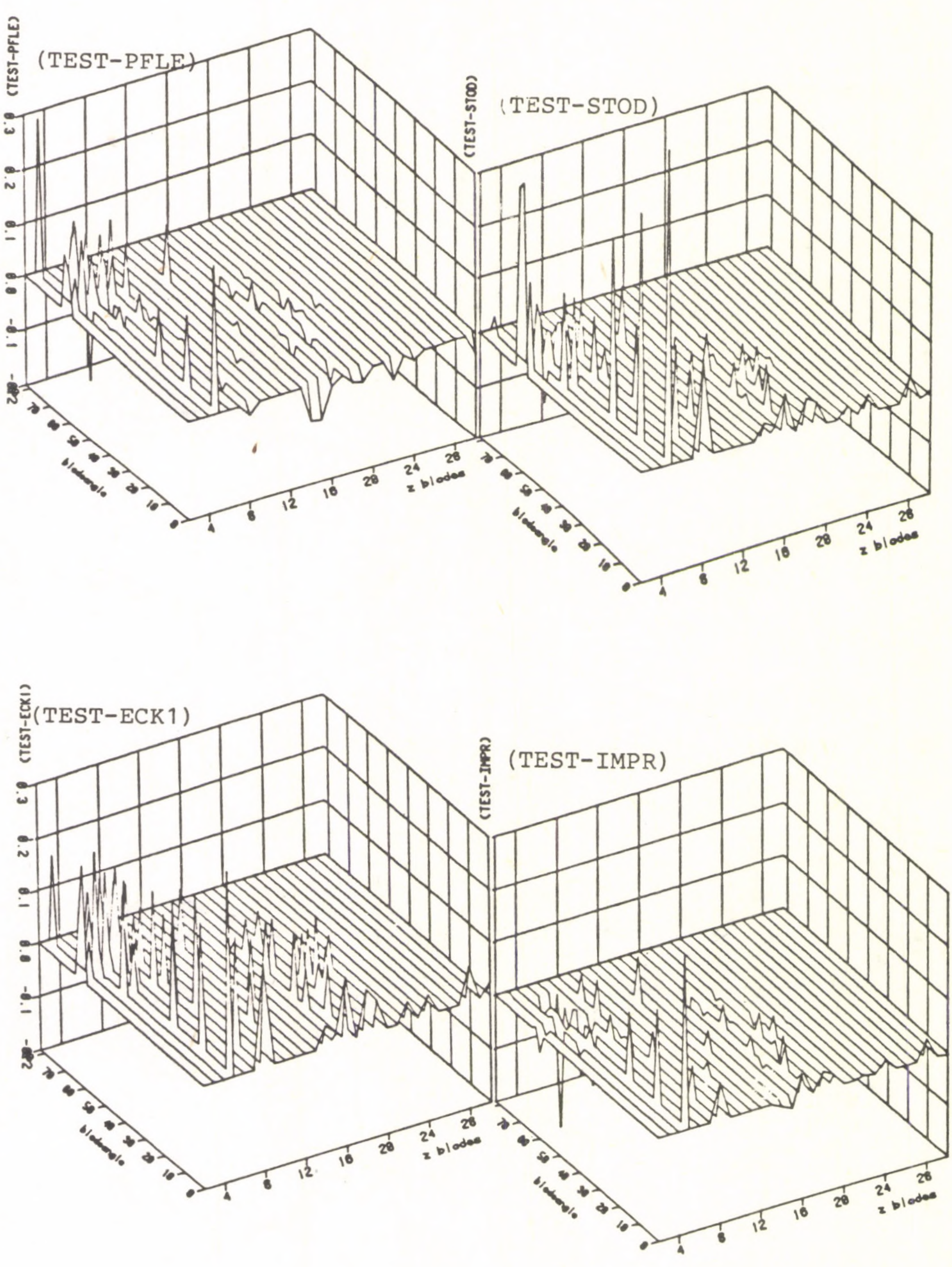

Figure 6: Deviation of testresults from the methods

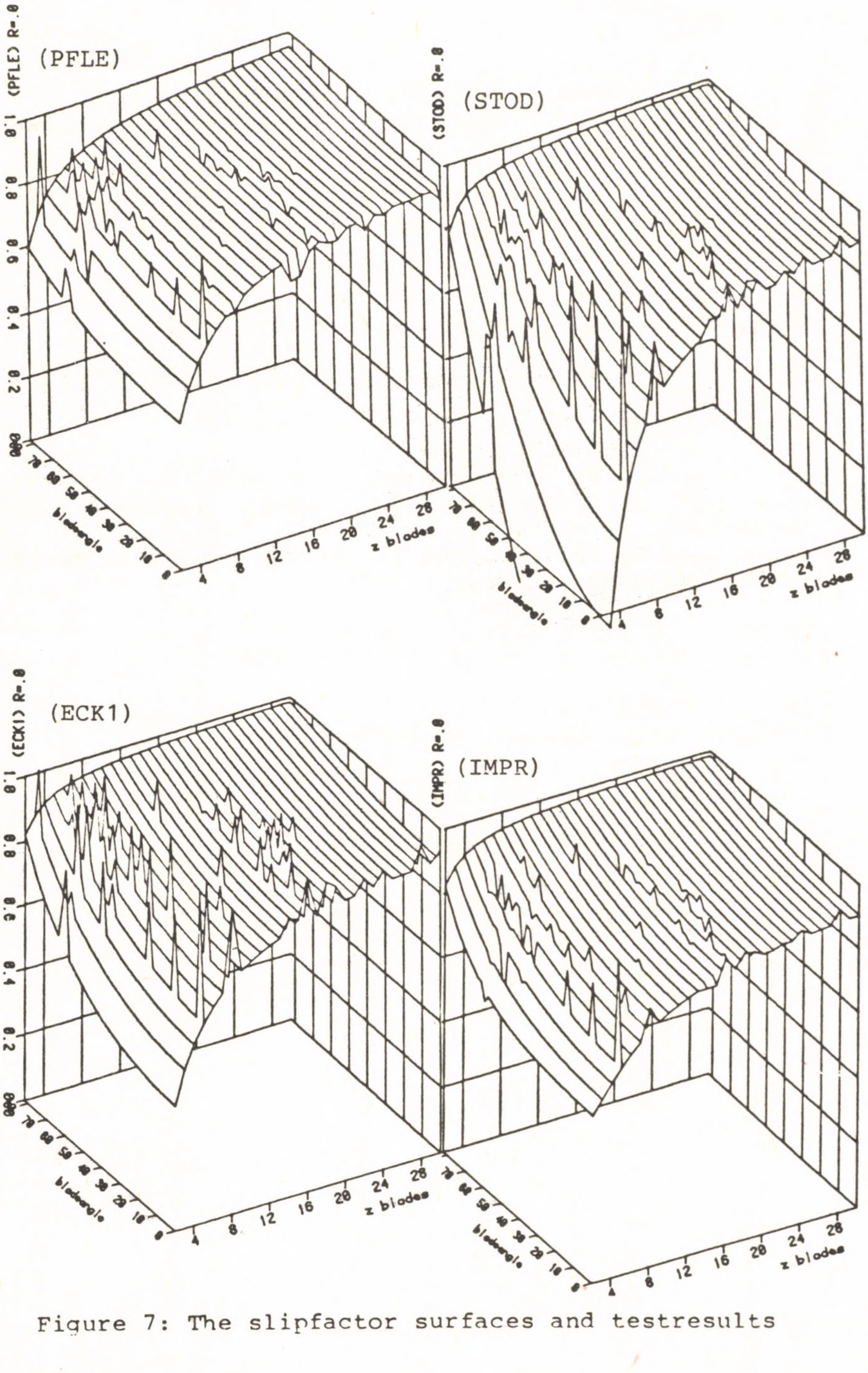

Figure 7: The slipfactor surfaces and testresults

List of References

(1) Qvale B., Bothmann V., NOTES IN TURBOMACHINERY. NE 82-2, Lab. f. energiteknik, Danmarks tekniske højskole, 1982

(2) Busemann A., Das Förderhöhenverhältnis radialer Kreiselpumpen mit logarithmisch-spiraligen Schaufeln. ZAMM, vol. 8, h. 5, 1928

(3) Stodola A., Steam and Gas Turbines. McGraw-Hill Book Company, New York, N.Y. 1927

(4) Dixon S.L., Fluid Mechanics, Thermodynamics of Turbomachinery. PERGAMON PRESS 1966

(5) Reffstrup J., En undersøgelse af metoder til bestemmelse af slipfaktorer ved pumper, blæsere og kompressorer. Master thesis, PE 76-2, Lab. f. Energiteknik, Danmarks tekniske højskole, 1976, 54 refs.

(6) Pfleiderer C., Die Kreiselpumpen. Springer Verlag Berlin, 3. Auflage, 1949

(7) Eck B. Ventilatoren. Springer Verlag Berlin, 5. Auflage 1972

Volker Bothmann (Ass. Prof.)
Jan O. Reffstrup (Ph.D.)
Laboratory for Energetics
The Technical University of Denmark
DK2800 Copenhagen-Lyngby
Bygning 303

PUMP PROPELLER PROPERTIES RELATING TO APPLICATION IN MIXERS AND FERMENTORS

Karel Brada

1 Introduction

The problem of providing sufficient food supplies for the world population results in the industrial production of food and the utilization of alternative, non-traditional resources for the production of food, namely valuable proteins. One possibility is the production of feed proteins /yeast/ by the fermentation of waste waters, e.g., from pulp mills. The equipment which safeguards the continuous production of yeast, i.e., the fermentor, operates according to the diagram shown in Fig. 1. The fill circulates symmetricalyy along the axis in a circular vessel - the fermetor F. We are concerned with a three-stage mixture /water - yeast - air/. The movement of the liquid is secured by impeller 1, which sucks the liquid slurry flowing over the control overfall 2. For separating the foam /air with consumed oxygen/ the liquid in the suction coupling is put into rotation by the pre-rotator 3 and partly by prerotation induced by the impeller 1. Oxygen needed for the biological process is driven into the fermetor by air pipe 4 and is dispersed by rotator 5. The rotator and impeller are driven by shaft 6. Impeller 1 must secure the continuous movement of the liquid and to induce the necessary discharge of the slurry with adequate specific energy /suction effect/ which will safeguard aeration /funnel/ in the suction coupling. Considering the magnitude of fermentors of up to several hundred [m^3] it is very important to provide the efficient conversion of mechanical energy in the impeller 1 to hydraulic energy /power input of several tens of [kW]/.

The above requirements were the basis for the design of the impeller which contrary to intuitive designs of impellers for mixers and fermetors applied the method of computation used in the design of impellers of hydrodynamic pumps. The designed proceeded from the assumption of constant specific energy for the blade span /cross-sectional area of flow/, the knowledge of the velocity field at inlet. The design also observed the possibility of modifying the operating element to changed working condidtions.

The difficulty of computing the impeller of the fermentor for arrangement shown in Fig. 1 was caused by the lack of exact

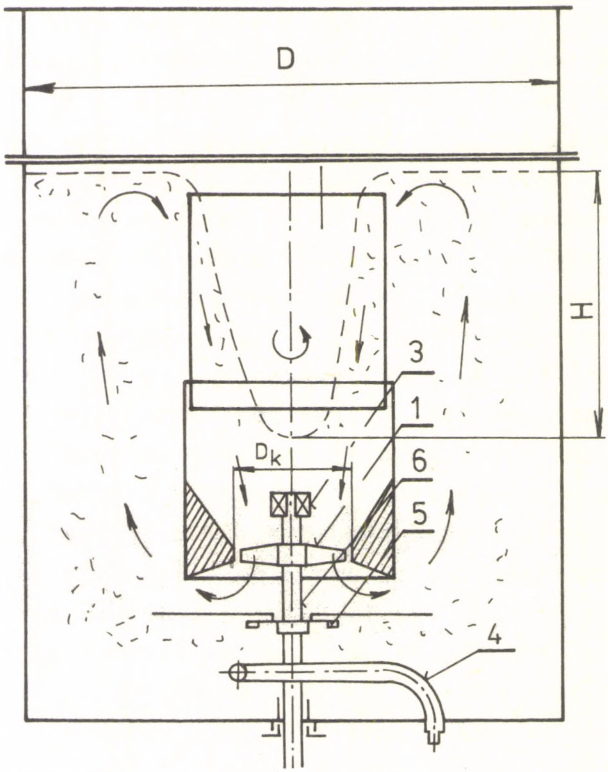

Fig. 1

Diagram of fermentor operation

D_k - Ø impeller

knowledge of the main hydrodynamic parameters, i.e., discharge Q and specific energy Y.

The required specific energy Y is given by the hydrodynamic losses /all power is used up by the fill of the fermentor/ and in the arrangement shown in Fig. 1 it necessary to design

in the fermentor head H needed for defoaming the slurry.
The indirect task of determining the main dimension of the impeller is complicated by the fact that the only given parameters are the power input to the impeller shaft P [W] and the specific weight of mixture ϱ .

$$P = Q \cdot Y \cdot \varrho/\eta \qquad [W] \qquad (1)$$

Q $[m^3\ s^{-1}]$ - discharge Y $[J\ kg^{-1}]$ - specific energy

ϱ $[kg\ m^3]$ - thickness of slurry η $[1]$ - total effciency of impeller

The relation between the main parameters of the hydrodynamic impeller and its power input may be expressed

$$Y = \left(\frac{P}{\varrho}\right)^{\frac{2}{5}} \cdot \left(\frac{n_s}{n} \cdot \frac{1}{1200}\right)^{-\frac{4}{5}} \qquad [J\ kg^{-1}]\ (2)$$

$$Q = \left(\frac{P}{\varrho}\right)^{\frac{3}{5}} \left(\frac{n_s}{n} \cdot \frac{1}{1200}\right)^{\frac{4}{5}} \qquad [m^3\ s^{-1}]\ (3)$$

where n_s is the specific speed determining the type of impeller.

$$n_s = 1200 \cdot Q^{0,5} \cdot Y^{-0,75} \cdot n \quad [s^{-1}] \quad (4)$$

Propeller type impellers are optimal for fermentors especially because the specific energy of fermentor impellers are relatively low with regard to the required discharge Q. The computations yielded the main dimensions of the impeller /important for the design of the fermentor/ and the principal kinematic values at inlet and outlet of the impeller which is important for the process of mixing.

2 Kinematic conditions of the impeller and indication of computation

In the fermentor the propeller operates under different conditions at the inlet of the blade than is the case with the pump /Fig. 1/. While with the pump we assume in the normal operating

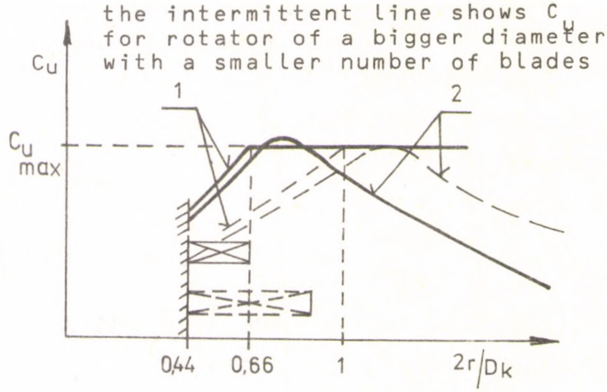

Fig. 2

Course of circumference of input velocity C_u into the impeller

1. computation /substitute course/
2. real course

point the axial inflow of the liquid, with the fermentor shown in Fig. 1 owing to prerotator 3 there is a considerable circumference of the liquid at inlet which has been determined by measurements made by a probe - see Fig. 2. At the prerotation of the inflow of the liquid this requirement will mean a bigger angle of profile β adjustment. This has two unfavourable consequences from the point of view of flow and hydraulic losses:

- the entry velocity and especially its circumference increases. As in the fermentor there is no diffuser behind the impeller the fermentor fill is put into rotation. Behind the impeller hydraulic losses are considerably higher than with a conventional pump. Values c_{u2} and c_2 should in all cases be less than u_2.
- the increase of the angle of adjustment of the blade cascade is biggest at the hub of the impeller where the circumference is biggest and the condition of constant specific energy for the blade range requires

$$\Delta C_u \cdot u = \frac{Y}{\eta_h} = \text{konst} \qquad (5)$$

The angle of adjustment of the hub profile should not exceed the value $\beta \leqq \frac{\pi}{2}$.

3 Experimental results and comparison with conventional mixers

The impeller with hydrodynamically profiled variable pitch

blades was investigated from the point of view of its hydrodynamic and homogenization properties in two arrangements: Arrangement I corresponds to fermentor in Fig. 1, arrangement II is usual in mixers.
The optimal position β of the impeller blade was investigated as was the distance of the mixer from bottom H_2. The measured results were compared with certain conventional impellers which were measured on the same measuring stand. The basic geometrical characteristics of the 6-blade and 3-blade reference impeller are shown in Fig. 3.

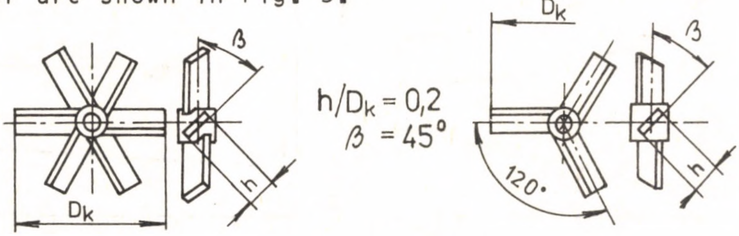

6-blade 3-blade

Fig. 3

Basic geometrical characteristics of convetional reference impellers

In the model impeller the angle of blade pitch was changed as follows: $\beta < 20 \div 50 >$ [deg] , the distance of the impeller from the bottom of the vessel $H_2 < 0{,}1 \div 0{,}75 > D_k$ we always chose the optimal adjustment of the model impeller and in the given arrangement was compared with the 6-blade and 3-blade impeller. The power characteristics are shown in Fig. 4. In arrangement I we have plotted the optimal adjustment of model impeller b, and the characteristic d - to show the impact of the increase of blade angle β . In arrangement II we chose as optimal variants of the model impeller cases which will show the most efficient mixing properties. This is shown in the following diagrams.
Mixing efficiency E as shown in Fig. 5 in Arrangement I unambiguously give preference to the propeller model wheel and is on the average troughout the whole course of operation double that of the better variant of the conventional 6-blade wheel.

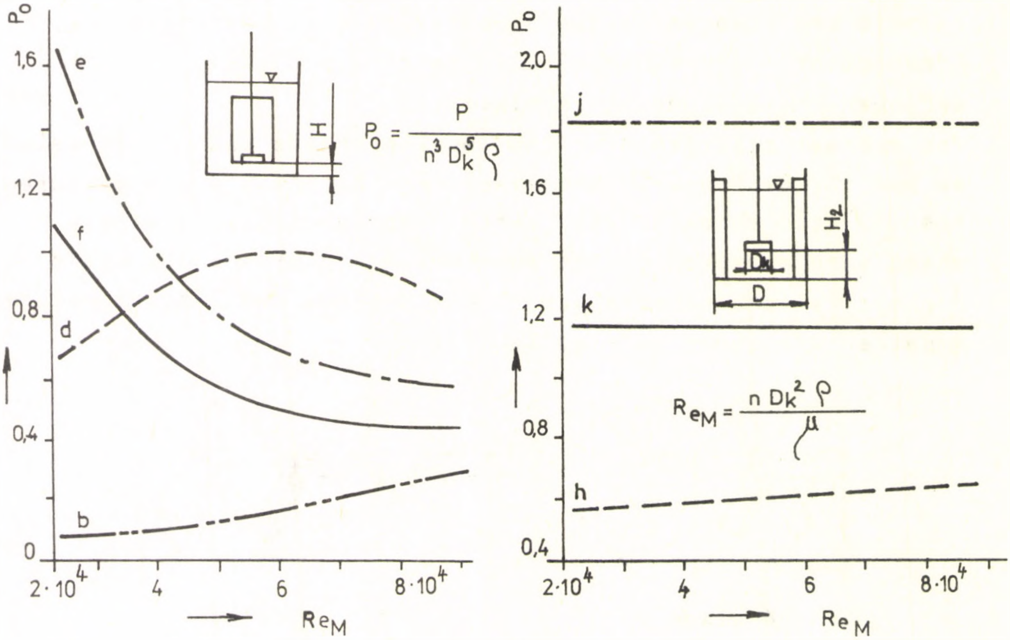

Arrangement I		Arrangement II	
b-model β = 30°	H_2 = 0.4 D_k	h-model β = 30°	H_2 = 0.75 D_k
d-model β = 50°	H_2 = 0.4 D_k	j-6-blade	H_2 = 0.75 D_k
e-6-blade	H_2 = 0.4 D_k	k-3-blade	H_2 = 0.75 D_k
f-3-blade	H_2 = 0.4 D_k		

Fig. 4
Comparison of power characteristics of model 6-blade and 3-blade impeller

P - power input of rotor [W]
n - rotor speed $[s^{-1}]$
D_k- impeller diameter [m]
ϱ - thickness of mixed liquid $[kg\ m^{-3}]$
u - dynamic viscosity of liquid [Pa.s]

As concerns variant II, with increasing R_e the optimal variant of the propeller impeller is equal to conventional wheels.

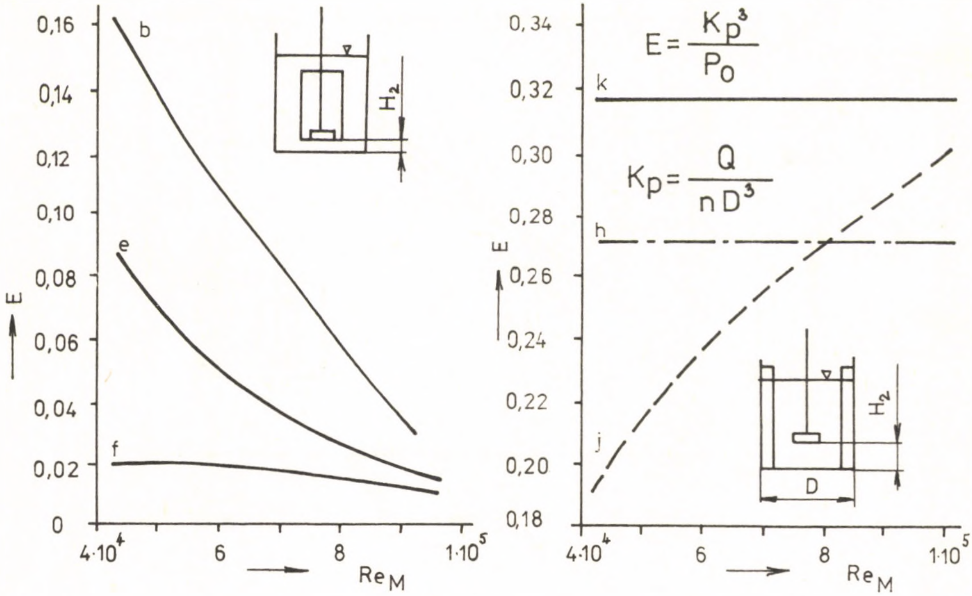

Arrangement I		Arrangement II	
b-model $\beta = 30^o$	$H_2 = 0.4\ D_k$	h-model $\beta = 30^o$	$H_2 = 0.75\ D_k$
e-6-blade	$H_2 = 0.4\ D_k$	j-6-blade	$H_2 = 0.75\ D_k$
f-3-blade	$H_2 = 0.4\ D_k$	k-3-blade	$H_2 = 0.75\ D_k$

Fig. 5

Comparison of mixing efficiency of model 6-blade and 3-blade impeller

Effectiveness of homogenization may be expressed by the proportion of exerted energy L for homogenization of the given volume of liquid.

$$\frac{L.t}{\mu.D^3} = \frac{P.t^2}{\mu.D^3} = P_o\,(n.t)^2 \left(\frac{D_k}{D}\right)^3 Re \qquad [1] \qquad (6)$$

In mixing technology mixing efficiency is usually represented in dependence on the criterion:

$$\frac{D^2.\rho}{\mu.t} = \frac{Re}{n.t} \left(\frac{D}{D_k}\right)^2 \qquad [1] \qquad (7)$$

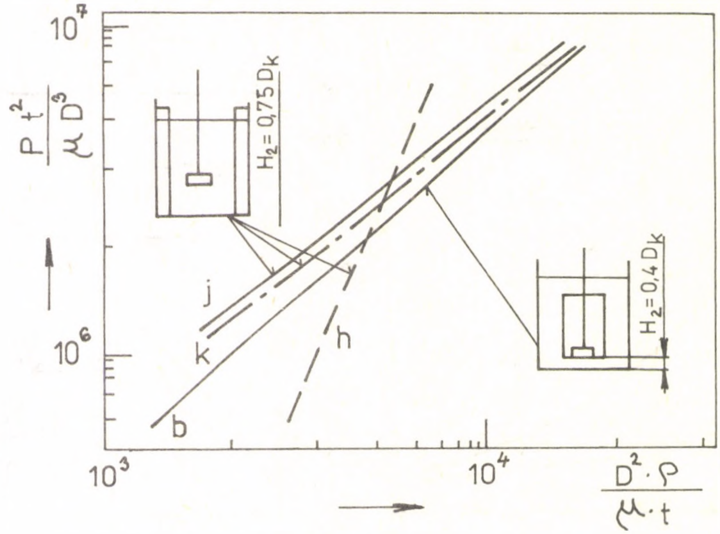

Fig. 6

Comparison of mixing efficiency of model 6-blade and 3-blade impeller

b - model impeller $\beta = 30^0$ $H_2 = 0.4\ D_k$ Arrangement I

h - model impeller $\beta = 30^0$ $H_2 = 0.75\ D_k$ Arrangement II

j - 6-blade impeller $H_2 = 0.75\ D_k$ Arrangement II

k - 3-blade impeller $H_2 = 0.75\ D_k$ Arrangement II

From the point of homogenization effectivness /Fig. 6/, variant b, i.e., the propeller impeller with the blades pitch at angle $\beta = 30^0$ and the distance from the bottom $H_2 = 0.4\ D_k$ in Arrangement I is better than in conventional wheels in arrangement II.

4 Conclusion

The assumption of a better conversion of mechanical energy in the application of the propeller impeller with hydro-

dynamically profiled blades for the fermentor was experimentally confirmed.
Energy saving for the drive is up to 50 % as against the impeller designed without considering the hydrodynamics of the flow along the blades of the impeller.
For the project of the rotor for the biggest fermentors this meant saving of power input of roughly 50kW per unit.
The dimensions of the impeller have been reduced in size as compared with the initialyy designed dimensions: D_k = 700[mm] to the present D_k = 500[mm]which means that the mass of the impeller will be roughly cut down to one half of the initial mass for a 200 $[m^3]$ fermentor.
The manufacture of this impeller is more labour demanding. This is, however offset by the variable pitch of the impeller blades and thereby the possibility of adjusting the discharge according to the demands of the mixing technology on a wide scale.

5 References

[1] Bláha J., Brada K.: Pump Atlas - text - book, TU Prague, 1976

[2] Bláha J., Brada K.: Choice and design of mixer impeller for fermentor, research report, TU Prague, K 217

[3] Strýček O.: Flow conditions in suction tanks od pumping installations, of the 3-rd Conference on fluid Mechanics and fluid machinery, Budapest 1969, P.446-453

[4] Strek F.: Mixing and mixing equipment, SNTL Praha 1977

[5] Medek J., Fořt I.: Mixing efficiency in monitoring volume flow rate of liquid through mixer, Chemický průmysl, 29/54, 1979, no 3

[6] Dohnal J., Novák V., Rieger F.: Basic processes of chemical and food production - hydraulic processes, TU Prague, 1979, text-book

STARTUP OF PROPELLER PUMP WITH A PARTIALLY SUBMERGED ROTOR

Karel Brada, Karel Matějka, Jan Vojtek

1 Introduction

The problem of startup of a hydrodynamic pump of which the rotor is only partially submerged is closely connected with the so-called selfpriming capacity of the pump, i.e., the capability of the pump to start up even if unfilled with water and in absence of simultaneous deaeration. In a typical situation the pump is located above the suction tank level, whereas both technical and investment cost problems will arise if it were to be located under the surface level.

One of the cases where the problems relating to the pump startup will influence the reliability of the entire pumping system is the floating pump station used in irrigation work. A schematic representation of the propeller pump arrangement can be seen in the Fig. 4. The suction elbow piece is provided with a valve and bar screen. The discharge piping is free from fittings. The submersed depth of the float and thus also the submersed height <u>h</u> of the pump rotor will fluctuate depending on the load carried on the one hand, and on how many out of the three assemblies present are operating or idle on the other hand.

The floating irrigation station SČS 11/8 is manufactured by ZTS, Czech Shipbuilding Co., of Prague.

The major design parameters of the pumping system incorporating the SIGMA 1200-AQT-977-68 pump are as follows: capacity $Q = 3{,}7\,[m^3/s]$, specific energy $Y = 78\,[J/kg]$, speed $n_c = 420\,[rpm]$, impeller diameter $D_k = 977\,[mm]$, discharge piping diameter $D_p = 1200\,[mm]$, and pump power input $P_c = 380\,[kW]$.

The problems relating to reliable pump startup under highly unfavorable and variable conditions of pump submergence were investigated on a model installation at the Hydraulic Machines Laboratory of the Mechanical Engineering Faculty of the Czech

Technical University in Prague, and the experimental results have made it possible to formulate recommendations for the manufacturer as well as for users.

2 Startup kinematics and dynamics

The transmission of energy in the set comprising a drive and a propeller pump is determined by the load. In the case of a propeller pump in the horizontal arrangement with a partially submerged rotor /schematically depicted in Fig. 1/ this

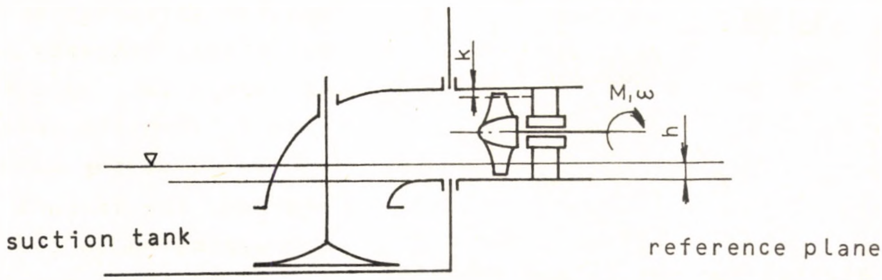

Fig. 1
Layout of the working part of the model propeller pump with a partially submerged rotor
h - submergence height taken from the lowest point of impeller casing

load varies due to the fact that the mass of water concentrated at the bottom part of the pump casing and reaching to an elevation h /also cf. Fig. 4/ will be distributed as a water-air mixture along the impeller circumference within an annular area of the thickness k under the influence of impeller rotation on the one hand, and due to the effect of pumping the impeller starts filling up with the water and air mixture and the load will rise further, already at constant rpm of the set, on the other hand.

2.1 Kinematics of startup of the set

The development of the kinematic values / ω , n, ε / and of the torque / M / is depicted schematically in the Fig. 2.

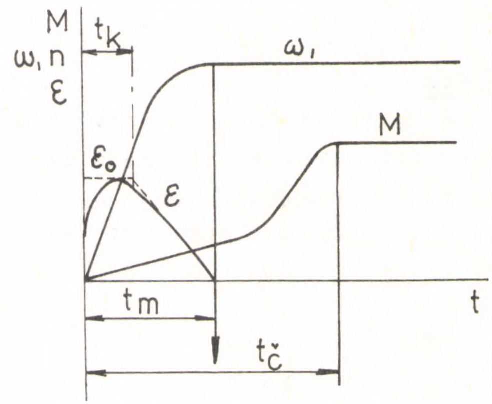

Fig. 2

Startup kinematics and dynamics of the set comprising motor and pump arranged as per Fig. 1

ω - angular velocity of rotor

n - frequency of motor rotation

ε - angular acceleration of rotor /dashed line for theoretical, solid line for experimental/

M - torque

t - time

t_k - duration of linear startup

t_m - startup time of set

$t_č$ - time of unsteady pump operation

The experimental rig made it possible to simulate a linear-parabolic startup where the angular acceleration was constant roughly up to half the steady-state value of rotation frequency, whereupon the angular acceleration kept decreasing linearly down to zero, i.e., till the time $\underline{t_m}$ when the operating rpm value of the pump was reached. The instant corresponding to the time $\underline{t_m}$ at which the constant value $\underline{M}$ was just attained was regarded as the onset of steady-state operation of the pump and as the initial time of pumping air-free water.

Angular acceleration will proceed as follows:

$$\varepsilon = \varepsilon_0 = \text{const} \quad <0,\ t_k> \quad [s^{-2}]$$

$$\varepsilon = \varepsilon_0\left(1 - \frac{t - t_k}{t_m - t_k}\right) \quad <t_k,\ t_m> \quad [s^{-2}]$$

/ 1 /

Then the angular velocity will be

$$\omega = \varepsilon_0 \cdot t \qquad <0,\ t_k> \qquad [s^{-1}]$$

$$\omega = \varepsilon_0\left[(t_k + t) - \frac{1}{2}\frac{(t - t_k)^2}{t_m - t_k}\right] \quad <t_k,\ t_m> \qquad [s^{-1}] \qquad / 2 /$$

2.2 Dynamics of startup of the set

The fundamental moment equation of the set assuming a constant moment of inertia J of the rotating masses can be written as

$$J\frac{d\omega}{dt} = M_M(\omega) - M_Z(\varphi, \omega, t) \qquad [Nm] \qquad /3/$$

where M_M is the motor moment and M_Z is the load moment. During startup, i.e., up to ω = const. or $t = t_m$, the motor moment exceeds the load moment thus accelerating the rotor of the set. The load moment is of a dynamic nature, i.e., the moment increases with the square of rpm:

$$M_Z = M_0 + (M_{Zn} - M_0)\left(\frac{n_Z}{n_n}\right)^2 \qquad [Nm] \qquad /4/$$

where M_0 is the moment of friction forces and passive resistances in case of the machine running without the impeller. In contrast to M_{Zn} /the load moment at design rpm n_n; ω_n/ its value is relatively very small.
At the instant of reaching design rpm it holds that $d\omega/dt$ = 0 and for $t > t_n$ we have $M_Z = M_M$. Then the torque value is given practically by the water level elevation /mass of water/ in the pump. Experimentally established M_Z values for various surface level elevations /pump submergences/ are given in Fig. 3. The torques were measured with the suction sealed off in order to obtain a steady state rather than a pumping effect. The values of these loading moments are maximum, inasmuch as the liquid is recirculating due to the stopped off suction /secondary flow/. With the suction open the pumping effect will occur /ordered flow/ and the load moments will be considerably reduced /see e.g. Fig. 5/.

3 Startup of propeller pump with a partially submerged rotor

The situation encountered in starting up a horizontal

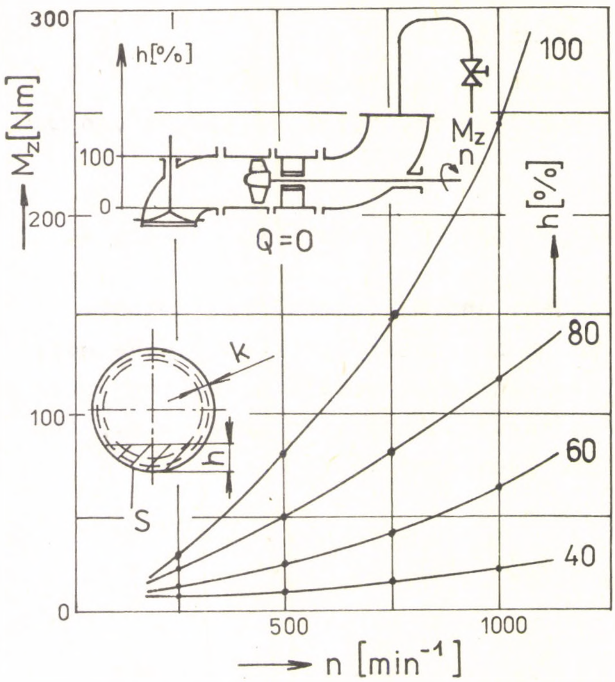

Fig. 3
The load moment of the horizontal propeller pump as a function of the rotor submergence depth h

propeller pump with a partially submerged rotor is depicted in the Fig. 4. The Figure represents the rotation surfaces as they occur in succession. The initial rotation ring 1 will allow for the flow of liquid from the suction inlet, it is expanded to the size 2 and, in case where the discharge can be water-locked /vertical piping/, the air present is gradually expelled into the discharge piping, the surface level 3 will close up, and the space within the pump will be filled up with water so that the pump will operate normally. The propeller pump arrangement described will thus make it possible to start the pump in absence of any additional fittings, making it to a selfpriming pump.

4 Conclusion

Experiments were run to investigate the startup of a propeller pump with a partially submerged rotor until normal full-load operation. The startup consists of two stages. At the first stage, the rotor will accelerate up to its design rpm within several seconds. The duration of this stage depends on the

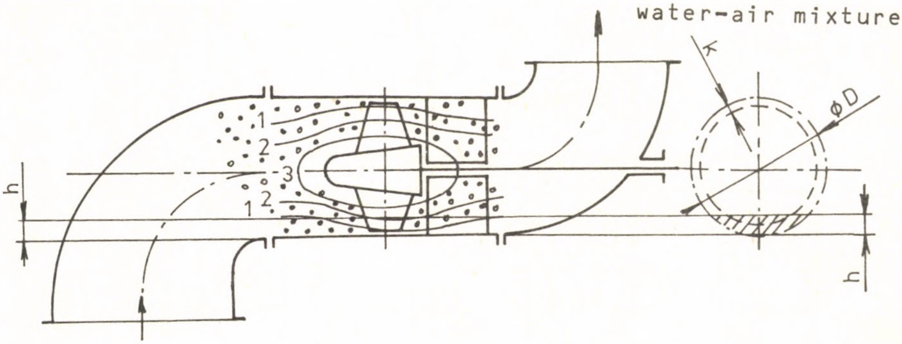

Fig. 4
Schematic representation of the selfpriming effect of the propeller pump /as observed in a transparent casing/

inertia forces of the rotor and on the dynamic characteristics of the drive and the propeller pump. The duration of the second stage is influenced by the configuration of piping and especially by the surface level elevation determining the depth of submergence of the rotor. The propeller pump operates in a way similar to that of most selfpriming pumps in that it keeps expulsing the water-air mixture until normal operation is established. The startup is reliable even at the submergence depth $h = 0.20\ D_k$ but in this case the startup time extends over several dozen seconds.

5 References

[1] Brada K., Hladiš V.: Development trends and certain current problems in pumping technology, Acta Polytechnica II, 8, 1982-2, Sci. conf.

[2] Kopáček J.: Hydraulic transmission mechanisms, SNTL Publishers, Prague /in press/

[3] Measurements on the model pump A-A-68-9,9, res. rept., Czech Tech. Univ., Mech. Engrg. Faculty, K 217, 1980

[4] A hydraulic model of the pump A-A-68-9,9, res. rept., Sigma Res. Inst., Olomouc, ZV-083/67-VZ, 1968

[5] The pump 1200-AQT-977-68, Czech Shipbuilding Co., Prague.

[6] Pump startup, the time dependence of the starting moments, res. rept., Sigma Lutin, VK 81-682, 1981.

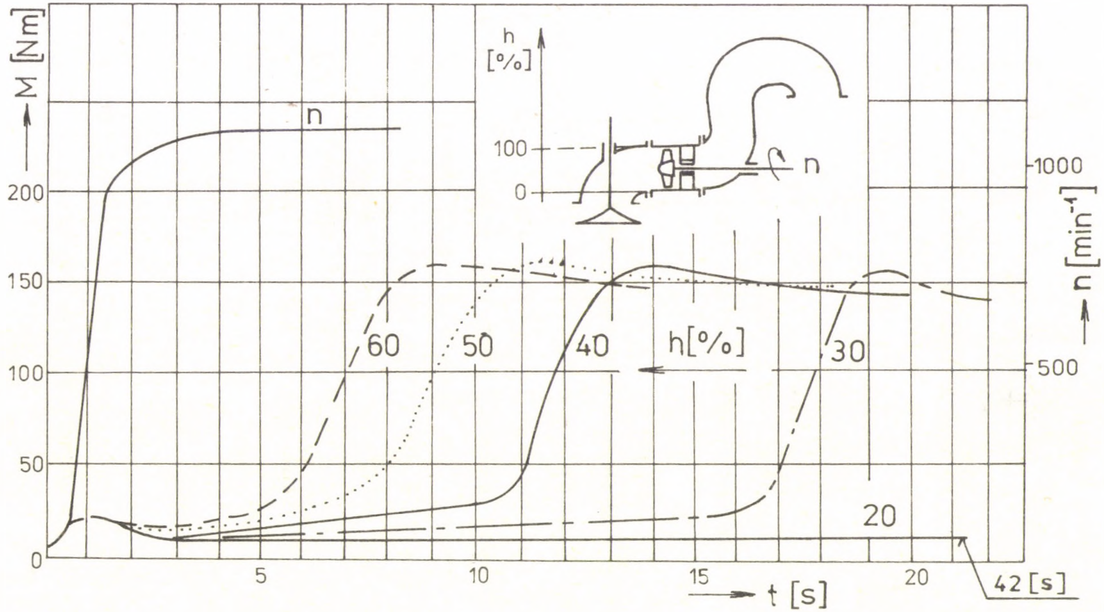

Fig. 5

Startup dynamics of the propeller pump with suction opened and with vertical discharge

INVESTIGATIONS OF CONICAL FLOWS THROUGH A HIGH TURNING TRANSONIC ROTATING ANNULAR CASCADE

W i l l y   B r a e u n l i n g

DFVLR - Institute for Experimental Fluid Mechanics, Goettingen, FRG

1. INTRODUCTION

Up to these days calculation methods used by industry for analyzing subsonic flows through axial turbomachines are often based on the assumption of coaxial cylindrical stream surfaces. Experimental and theoretical approaches based on this simplifying model have been quite successful in the past. Especially in the last stages of low pressure steam turbines and in high pressure turbines of jet engines the development of modern high-power axial turbines has led to transonic flow regimes. Consequently, the corresponding high expansion of the medium and the resulting increase of its volume requires an increase of the annulus cross section in downstream direction. Analogous to the model of coaxial cylindrical stream surfaces the model of conical stream surfaces may be an appropriate simplifying assumption for these flow conditions. The feature of conical cascade flow has some essential differences with respect to cylindrical cascade flow as follows :

(*) changes of the profile geometry

(*) changes of the cascade geometry (solidity, stagger angle)

(*) different pitches at inlet plane and outlet plane of the cascade

(*) different energies of rotation at inlet plane and outlet plane of the cascade, i.e. no constant total temperature in the relative system.

Up to now, only limited experimental results are available in the open literature for flows of this kind. Therefore, the aim of the investigations reported here has been to provide data which can be used as additional input values for today's calculation methods.

With respect to this goal the experimental work presented here does not include sophisticated investigations of the three dimensional flow structure in a conical flow annulus. The tests should be regarded as a simplified consideration of engineering practice to describe conical flow at different cone angles with respect to the basic characteristic aerodynamic quantities of a turbine cascade.

2. TEST CONFIGURATION

The measurements reported here have been carried out in the test facility for rotating annular cascades, <2>, of the DFVLR (German Aerospace Research Establishment), Research Centre Goettingen. The complete arrangement of the test facility is given in FIGURE 1 . In the closed cycle dried air is used as working fluid with its total pressure below atmosphere. A 4-stage radial compressor drives the fluid through a cooler to the settling chamber and the test section. Downstream of the test section the fluid moves through an outlet section and a pipe back to the compressor. The test wheel is coupled via two gearings to an electrical unit which can operate as motor or generator.

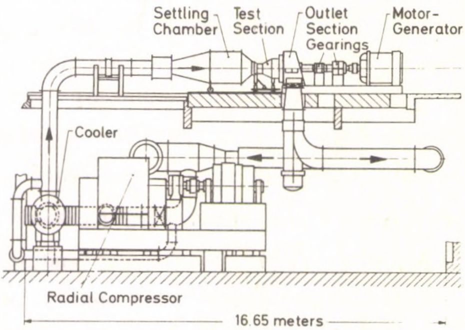

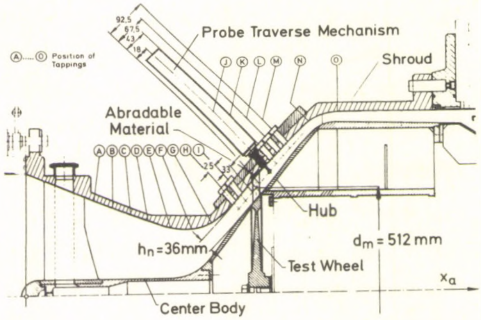

FIGURE 1 FIGURE 2

Investigations of the conical flow through rotating annular cascades have been performed for cone angles, σ ,of 30^o and 45^o . FIGURE 2 shows the 45^o - test section. Within the wheel region the contours of hub and shroud are parallel to each other and inclined to the axis at the cone angle. Downstream of the test wheel, where measurements have to be performed, the area of each annulus cross section is constant.

Together with its geometric data the investigated hub section cascade - built with VKI-1-profiles - is shown in FIGURE 3 . The significant changes caused by different cone angles may be seen clearly; for comparison, the cylindrical case is displayed too. With increasing cone angle the thickness of the trailing edge increases and both pitch to chord ratio and turning decreases. Moreover, the ratio of the smallest distance, e, to the inlet pitch, t_1, between two adjacent profiles becomes larger with cone angle, σ . The desired inlet flow conditions in the relative system are defined on a stream surface at medium height of the annulus. No torque-generating inlet guide vanes are used. Therefore, the circumferential velocity, u_1, of the test wheel has to correspond to the desired inlet flow angle, β_1 .

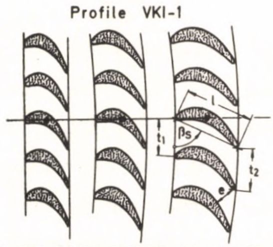

σ	0°	30°	45°
t_1/l	0,71	0,62	0,52
t_2/t_1	1,00	1,06	1,10
β_s	56,7	60,4°	65,1°
e/t_1	0,38	0,44	0,53

FIGURE 3

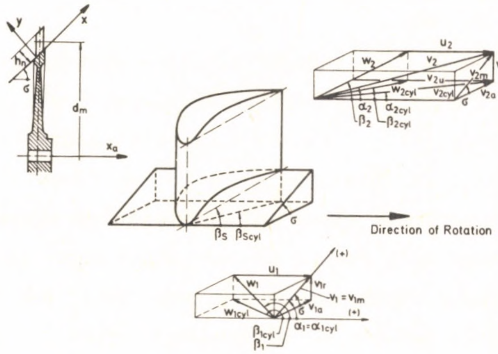

FIGURE 4

The relative inlet velocity, w_1, is given by the velocity triangle, shown in FIGURE 4 . For hub-section cascades - as is the case here - the direction of the flow-induced forces and the direction of rotation are opposite. Consequently, the test wheel has to be driven.

3. THE MEASUREMENT AND EVALUATION METHOD FOR CASCADE DATA

The measurement and evaluation method provides the determination of the characteristic aerodynamic cascade data, like relative inlet Mach number, Ma_{w1}, relative exit flow angle, β_2, loss coefficients of energy, ξ_w, and total pressure, ζ_w, which depend on the relative inlet flow angle, β_1, and the relative downstream Mach number, Ma_{w2} .

Such a method was developed earlier for cylindrical rotating annular cascades, <2>, and has now been extended and modified to deal with the current investigations of conical flows. Hereinafter this evaluation procedure will be termed First Method. The fundamental hypothesises of this method are two assumptions : first, flow particles are travelling on axially symmetric conical stream surfaces of constant thickness inclined with the cone angle, σ, within the wheel passages, and second, no heat exchange from the medium to the blades or vice versa occurs. The method was originally based on the experimental determination of the total pressure, p_{0v2}, and the total temperature, T_{0v2}, in the homogeneous absolute core flow in a measurement plane downstream of the test wheel. For current test conditions such temperature measurements have to be determined with an accuracy of about +/- .2 degree because of the small total enthalpy difference across the test wheel. If the flow quantities of the homogeneous inlet flow and the wheel's speed, n_t, are known, all required numbers for the evaluation of the characteristic cascade data can be determined.

Due to the required accuracy of temperature measurements in the downstream flow a detailed temperature probe calibration is absolutely necessary, <1> . The considerable expense attached thereto allowed only intensive calibrations in subsonic flows. The calibration characteristics in supersonic flows are described by approximated curves which have been derived only from some few points where probe calibrations could be done.

Under retention of the same basic assumptions as in the evaluation procedure before, an alternative method (termed Second Method) was developed in order to get results for comparison. The main difference to the First Method is in replacing the temperature measurements by measuring static wall pressures, p_{2p}, in the downstream flow field. A linear interpolation between values on hub and shroud leads to the current quantities at medium height in the annulus. The total temperature, T_{0v2}, in the absolute outlet flow can thus be derived independently by means of these two pressures and the quantities mentioned earlier. Applying the conservation laws of energy and mass together with Euler's turbine equation lead to a quadratic formula. The correct solution is given both for power input (sign +) and for power output (sign -) of the wheel :

$$(T_{0v2})_{I,II} = A/(A+BC)\ \{E + T_{0v1}\{1 \pm \sqrt{(1+E/T_{0v1})^2 - (1+BC/A)}\}\}$$

$$A = \gamma R\{u_{2p}(\gamma-1)\}^{-2} \qquad B = (R/\gamma)\{\rho_1 v_{1m}(\Delta F_1/\Delta F_{2p})\}^2 \qquad (1)$$

$$C = \{(1/p_{2p})(p_{0v2}/p_{2p})^{\frac{\gamma-1}{\gamma}}\}^2 \qquad D = (p_{0v2}/p_{2p})^{\frac{\gamma-1}{\gamma}} \qquad E = Ma_{v2p}^{\ 2}/2AD\ .$$

4. LOSS DEFINITIONS AND SIMPLE THEORETICAL RELATIONS

For conical flows, the coefficient of energy loss, ξ_w, in relative flow is defined as follows :

$$\xi_w = \frac{(p_{0w1}/p_{0w2})^{\frac{\gamma-1}{\gamma}}(T_{0w2}/T_{0w1}) - 1}{(p_{0w1}/p_2\ )^{\frac{\gamma-1}{\gamma}}(T_{0w2}/T_{0w1}) - 1}\ . \qquad (2)$$

The ratio of the kinetic energy in the exit plane to that in non-viscous flow is the basis for the definition (2) . The quotient of the relative total temperatures equals 1 in the case of cylindrical rotating annular cascade flows, which is a consequence of the conservation of energy. For this condition the term of the field forces (Coriolis force and centrifugal force) is equal to zero because radii upstream and downstream of the wheel are equal, <3> .

Another possibility to describe cascade efficiencies is to make use of the coefficient of pressure loss, ζ_w . Generally, for conical flow conditions it is defined as follows :

$$\zeta_w = 1 - (p_{0w2}/p_{0w1})(T_{0w1}/T_{0w2})^{\frac{\gamma}{\gamma-1}} \qquad (3)$$

Now, the ratio of the relative total pressure in the exit plane to the relative total pressure in case of isentropic flow is the basis for this loss definition. In the case of cylindrical flows for this equation the ratio of the relative total temperatures is unity as is the case for eq. (2) .

These two loss coefficients are established using values in the blade fixed relative system on a conical stream surface in the inlet and exit plane of the cascade.

In order to get a first estimation with a view to the experimental results, two simple theoretical relations can be derived. One of these relations gives a theoretical maximum choking Mach number, Ma_c . By developing the axially symmetric conical stream surfaces into a plane and then by assuming isentropic flow and a straight sonic line between two adjacent blades with perpendicular throughflow this calculation is possible. On medium height of the blades the equation of continuity is applied to a control surface between the inlet plane and the throat, e, see fig. 4 . Under these conditions the following expression is found :

$$Ma_c = \{ (1 + ((\gamma-1)Ma_c^{\,2}/2)) (2/(\gamma+1)) \}^{\frac{1}{2}\frac{\gamma+1}{\gamma-1}}$$

$$(\Delta h_e/\Delta h_1) (e/t_1) (1/\sin\beta_1) \qquad (4)$$

$$\{ \{1+(r_e\omega)^2/(2c_pT_{0v1})\} / \{1+(r_1\omega)^2/(2c_pT_{0v1})\} \}^{\frac{1}{2}\frac{\gamma+1}{\gamma-1}}$$

This equation can be solved iteratively. Using the same assumption as before and establishing a control surface between the exit plane and the throat an analogous equation for the relative exit flow angle, β_{2c}, is derived

$$\sin\beta_{2c} = \{ (1 + ((\gamma-1)Ma_{w2}^{2}/2)) (2/(\gamma+1)) \}^{\frac{1}{2}\frac{\gamma+1}{\gamma-1}} / Ma_{w2}$$

$$(\Delta h_e/\Delta h_2)(e/t_2)(1/(1-\zeta_w)) \qquad (5)$$

$$\{ \{1+(r_e\omega)^2/(2c_pT_{0v1})\} / \{1+(r_2\omega)^2/(2c_pT_{0v1})\} \}^{\frac{1}{2}\frac{\gamma+1}{\gamma-1}}.$$

In eq. (4) and (5), the term which includes the angular velocity, ω, has to be considered for high rpm's, small absolute temperature, T_{0v1}, and a high ratio of radii, r_e/r_1, only and is therefore neglected for the tests reported here, <1> .

5. EXPERIMENTAL RESULTS

5.1 Blade Surface Pressure Distribution Measurements in the Rotating System

For a better understanding of the physical behaviour of conical flows a device is used which allows measurements of blade surface pressure distributions from the rotating test wheel. The measurement configuration and its evaluation method including the correction due to the centrifugal acceleration is described in detail in <1> .

To present blade surface pressure distributions in transonic flows, it is approbiate to use the critical pressure coefficient :

$$c_{p1}^{*} = \{p(x/1)/p_{0w1}\}\{(\gamma+1)/2\}^{\frac{\gamma}{\gamma-1}} - 1 \quad . \qquad (6)$$

In this quantity subsonic flows are indicated for values greater than 0 and supersonic ones for values less than 0 . Sonic conditions correspond to $c_{p1}^{*} = 0$. The pressure distributions are measured in three radial positions which are 25% , 50% and 75% of blade height apart from the hub. For each of the three planes 14 tappings are distributed on pressure and suction side along the hypothetical conical stream surface. Here, only some typical results of these measurements are shown. In FIGURE 5 pressure distributions for three different Mach numbers are compared with results at three radial positions. In the subsonic case - shown in the left diagram - the profile loading near the hub is higher than the loading near the shroud which is in conformity with the radial distribution of the static pressures of the flow due to the angular momentum. With increasing Mach numbers this effect is inverted and the loading near the shroud is higher than the loading near the hub.

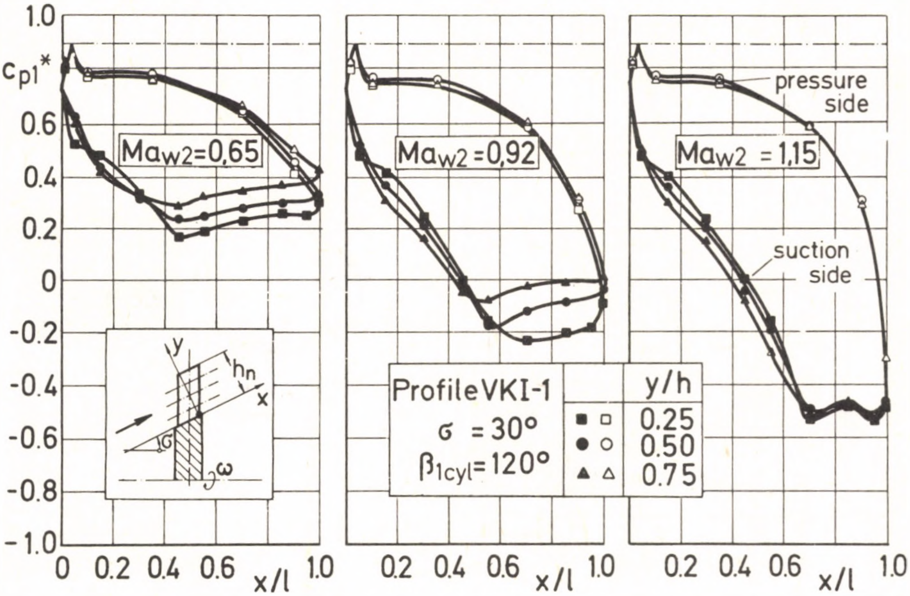

FIGURE 5

5.2 Measurements of the Downstream Flow

At the cone angles $\sigma = 30^{\circ}$ and 45° measurements have been performed at different relative inlet flow angles, β_1, and relative downstream Mach numbers, Ma_{w2}, from .4 to 1.3 . For the presented cascade the absolute downstream Mach number, Ma_{v2}, is larger than the relative one, see fig. 4 . In the range of Mach numbers mentioned the two evaluation methods - referred to in chapter 3 - were used. Up to a downstream Mach number of about $Ma_{w2} \cong .95$ no significant differences are to be seen. Considering larger Mach numbers, inconsistent results for cascade data often occured by using the First Method. Moreover, the homogeneous downstream Mach number, Ma_{w2}, in general was larger than the local maximum Mach number on the profile contour, determined from the blade surface pressure distribution measurements. The results of the Second Method do not show these discrepancies. Therefore, only results of this method will be plotted in the following figures.

As an example for one inlet flow angle, β_1, results are compared with tests of a rotating cylindrical annular cascade of the same profiles and geometry, <2,4>, FIGURE 6 .

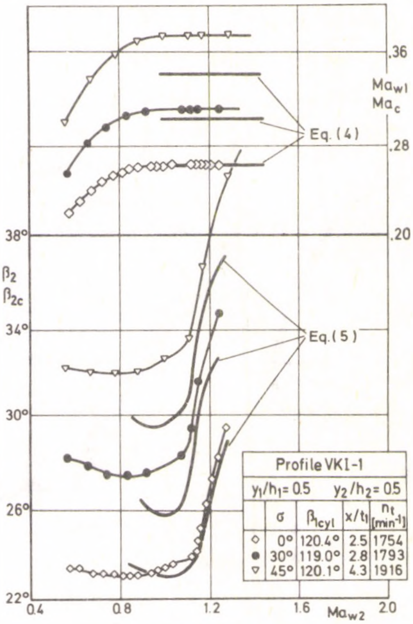

FIGURE 6

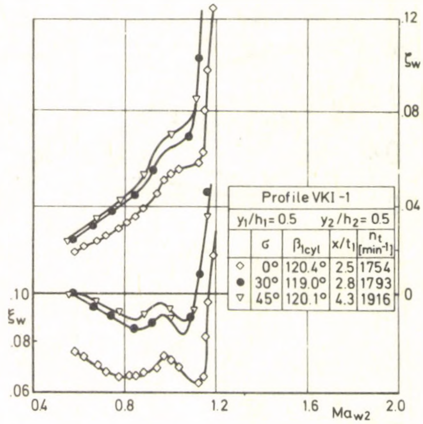

FIGURE 7

If the inlet flow angle is derived by the same way as is the case for the geometries of the profile and the cascade, inlet flow conditions for the cylindrical and the conical cascade can be compared. That means, that the inlet flow angle on a conical stream surface, β_1, projected onto a cylindrical surface is identical to the inlet flow angle, β_{1cyl}, of the cylindrical cascade, fig. 4 :

$$\beta_{1cyl} = (\pi/2) - \text{arc tan}\{\tan\{(\pi/2) - \beta_1\}/\cos\sigma\} \quad . \qquad (7)$$

In this figure further details of the geometric relations of the velocity triangles are given. Fig. 6 shows the inlet Mach number, Ma_{w1}, and the exit flow angle, β_2, plotted versus the downstream Mach number, Ma_{w2}, for the three cone angles, σ. All numbers are determinated in the cascade-fixed relative system. The results for the choked inlet Mach numbers, Ma_c, indicate differences in mass fluxes. The mass flux increases with increasing cone angle and so does the exit flow angle, β_2 .

Additionally, in fig. 6 theoretical curves from eq. (4) and (5) are plotted. The radius, r_e, in the middle of the throat is used for the calculation procedure. The ratio of the stream surface heights, $\Delta h_e/\Delta h_1$ resp. $\Delta h_e/\Delta h_2$, is set to unity. Obviously, theoretical results are always lower in comparison to the experiments which means that the experimental mass flux is larger than the theoretically predicted one. This is contrary to the physical assumptions used in the theoretical relations. Therefore, the sensitivity of the method is checked by enlarging the ratio, e/t_1, by only 1% . The discrepancies are reduced considerably, <1> . Such a small modification can occur, for example by a small difference between the cone angle of the actual flow and the hypothetical one. The effect is the same when changes in stream surface thickness along the current control volume occur. For the theoretical calculation of the outlet flow angle, β_{2c}, the losses according to eq. (3) plotted in FIGURE 7 are taken into account. Deviations can be explained in terms of the different mass flux rates. An increase of the differences between experimental and theoretical results corresponding to the increase of the cone angle is apparent.

In fig. 7 results for loss coefficients defined in eq. (2) and (3) are compared for the investigated cone angles. For $\sigma = 30^\circ$ and 45° losses are higher than for the cylindrical case. But there are obviously no considerable differences between the results for the two conical flow conditions. This means that the rate at which losses increase with increasing cone angle is reduced at larger cone angles.

Similar results are shown in the Turbine Atlas by DEICH <5>, but it should be considered that they depend on other geometrical conditions than the presented ones. There, two examples are shown in which the curves of losses have a continuous increase versus the cone angle, σ . In these figures results of some few measurements are particularly accentuated by symbols. In one of these examples, the symbols permit also another interpretation of loss increase as given by <5> . In this special example the Mach number was Ma = .6 . The losses increase considerably up to cone angles of about 30° . From here up to approximately 40° cone angle losses vary only slightly, and then they increase again. Up to cone angles of about 45°, this trend is quite similar to the presented loss increase. A better comparison of the results given in <5> and the presented ones would be provided by experiments for some more cone angles at the DFVLR test facility. However, the hitherto existing results do not allow to give a general conclusion for the loss increase due to increasing cone angles. Therefore, measurements in further test configurations with other geometrical conditions of both cascade and blading are desirable. In addition, more detailed insights to the real flow field can be achieved using Laser-2-Focus (L2F) measurements to derive the local flow quantities.

6. CONCLUSION

In this paper, first results from investigations of the influence of conical flows through a transonic rotating annular cascade have been presented. Main features of the test facility as well as those of the measurement and evaluation method have been described. Equations for the loss coefficients in conical flows, as well as some simple one dimensional theoretical relations have been given. A typical result from blade surface pressure distribution measurements in the rotating system is shown. Results of flow field measurements for different cone angles have been discussed and have been compared with the theory. Moreover, a comparison with a result published by DEICH has been given. The presented results show that it is possible to exploit the conception of conical stream surfaces in order to get a first insight into the real flow. But a more detailed analysis of such flows is necessary in the future, especially at other geometrical conditions and by using standard optical measurement methods like L2F .

7. NOMENCLATURE

Only those values are given, which are not defined in the text.

7.1 List of Symbols

$\Delta F_1/\Delta F_2$	ratio of areas	u	circumf. velocity
c_p	$\gamma R/(\gamma-1)$	v	absolute velocity
l	chord length	w	relative velocity
p	pressure	x, y	Cartesian coordinates
R	gas constant	β	relative flow angle
r	radius	β_s	stagger angle
T	temperature	γ	ratio of specific heats
t	pitch	ρ	density

7.2 Indices

c	choked	v	absolute system
cyl	cylindrical	w	relative system
e	position of throat	0	total condition
m	meridional direction	1	homogen. upstream flow
p	measurement plane	2	homogen. downstream flow

8. REFERENCES

<1> Braeunling W., Lehthaus F.
Konische Transschall - Turbinengitter.
Experimentelle und theoretische Untersuchungen ueber den Einfluss der Konizitaet auf die Stroemung durch Turbinengitter im transsonischen Geschwindigkeitsbereich.
DFVLR-AVA-Bericht : IB 222 82 A 01, April 1982 (internal report)

<2> Heinemann H.-J.
The Test Facility for Rotating Annular Cascades of the DFVLR and Its Measurements and Evaluation Method.
ICIASF 79 Record, IEEE publication, New York, 1979

<3> Traupel W.
Die Theorie der Stroemung durch Radialmaschinen.
Verlag G.Braun, Karlsruhe, 1965

<4> Ludwieg H., Amecke J., Heinemann H.-J., Kost F., Lawaczeck O., Lehthaus F.
Transsonische Turbinengitter.
Theoretische und experimentelle Untersuchungen zur Entwicklung allgemeiner Berechnungsverfahren fuer die Auslegung transsonischer Turbinengitter.
FVV-Forschungsbericht, Heft 221, Frankfurt/Main, 1977

<5> Deich M.E., Filippov G.A., Lazarev L.Ya.
Atlas of Axial Turbine Blade Characteristics.
Part I : Method of Profiling and the Aerodynamic Characteristics of Cascades.
Moscow : Mashinostroenie Publishing House, 1965

THE INFLUENCE OF GASKET TOLERANCE ON A [illegible] LOADED WITH FLANGED PIPE LENGTHS

W A BULLOUGH, M.Sc. C.Eng. M.I. Mech.E. A.F.R. Ae.Soc.

When the gasket of a flanged joint protrudes into a pipe by an amount less than 3% of the pipe internal diameter no perceivable loss in stagnation pressure is introduced. If the tolerance on the fitted gasket substantially exceeds this figure it is likely that the calculated pump load will be significantly underestimated if gasket losses are not included. This is especially so for a system made up from a series of pipes of small length to diameter ratio. Whilst the results presented are for fully developed flow upstream of the gasket, development lengths are such that interference between gaskets will occur when short pipe lengths ($\ell/D < 15$) are used.

INTRODUCTION

Flanged joints are in widespread use on pipe networks, sometimes because of the ease in which a pipe length may be removed so as to clean it or to replace it if it is corroded, and often because they ease assembly problems. They may be used in areas where welded joints are not allowed nor are they subject to such intensive inspection. Flanged joints are relatively inexpensive.

Wherever there is a bolted flanged joint a gasket will normally be used in order to make a pressure seal. In general the gasket will stand slightly clear of the bore, however, in some industries, such as food and chemical, it is necessary that little or no cavity be left at the joint so unhygenic

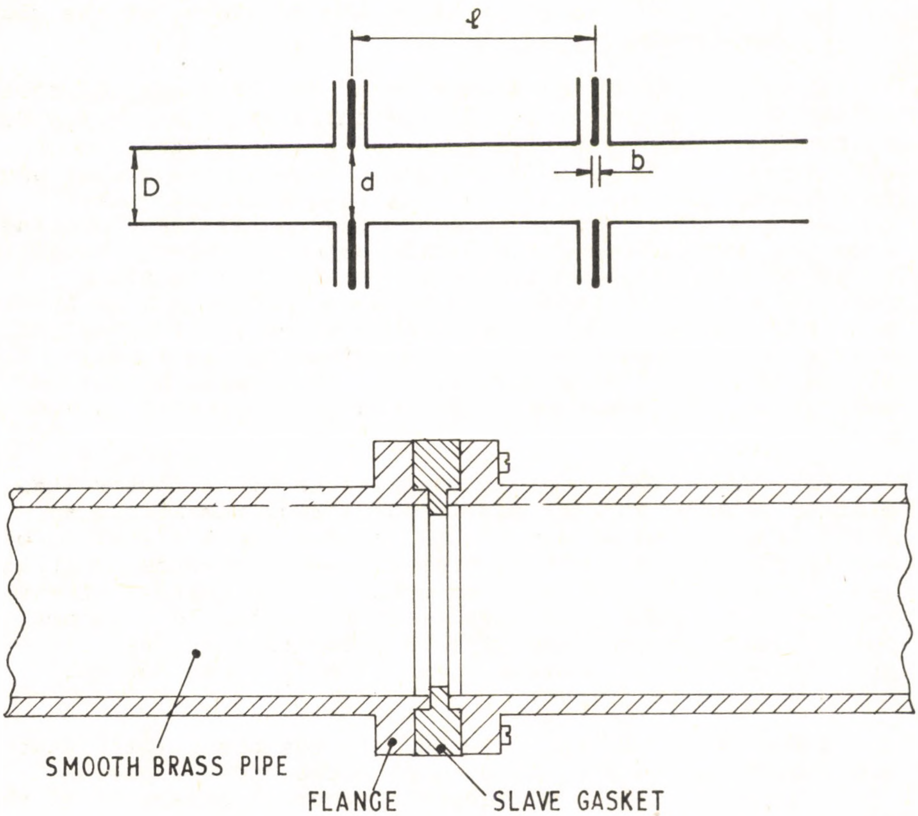

FIG. 1 - GENERAL ARRANGEMENT

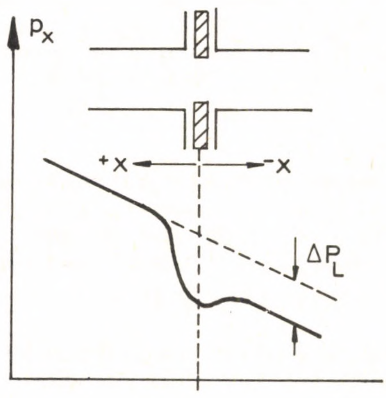

FIG. 2 - SYSTEM STAGNATION PRESSURE LOSS

debris may accumulate or where crystalisation and build up of the fluid can take place under the influence of the slow moving cavity eddies.

The function of the gasket is to create a seal by filling up the voids in the mating flange surfaces, these being due to surface finish imperfections and flange distortion or misalignment. The frictional force between the gasket and the flange (and not the tensile strength of the gasket) holds the gasket in place against the radial force arising from the pressurized fluid medium being conveyed. Thus, in order to effect the seal, and to retain it, the gasket material must flow under, and be subjected to a high initial assembly stress. The level of this stress, which has its origin in the bolt loads, is determined by the limiting flow stress of the gasket material, the pressure to be sealed against and any consequent hydrostatic end thrust on the bolts.

For even a low pressure conduit the first factor (the minimum seating stress) may impose a requirement for an axial compressive stress of 200 bar for say the sealing of a gas by the use of a common premium grade asbestos material [1]. In a highly pressurized conduit, the initial stress may be much higher than this (even for a liquid) subject only to the limiting crushing or relaxation stress properties of the material e.g. up to 200 bar for the asbestos material cited.

Given the above requirements and the possibility that the gasket may be subjected to pressure and thermal cycling by the fluid, differential thermal expansion of the flanges, pipe vibration, incomplete compatibility with the fluid, swelling due to attack by jointing compound etc., etc., and the presence of manufacturing tolerances on pipe and gasket, the possibility arises that the gasket will creep past the inside bore of the pipe. Thus the question of loss of stagnation pressure due to the protrusion of the gasket arises, Fig. 1. The aim of this paper is to quantify these losses in terms of the geometry of the gasket and the properties of the fluid and the flow.

EXPERIMENTATION

Defining the gasket stagnation pressure loss in system terms i.e. as the additional loss in the line due to the fitting of the gasket (Fig. 2) and by analysing the situation of Fig. 1, by dimensional methods it can be shown that:

$$\Delta P_L/0.5\ \rho V^2 = f(\rho VD/\mu,\ d/D,\ b/D) = K \quad \text{the gasket loss}$$

coefficient i.e. for a gasket concentric with the pipe, with fully developed (constant pressure gradient) flow upstream and downstream of the gasket.

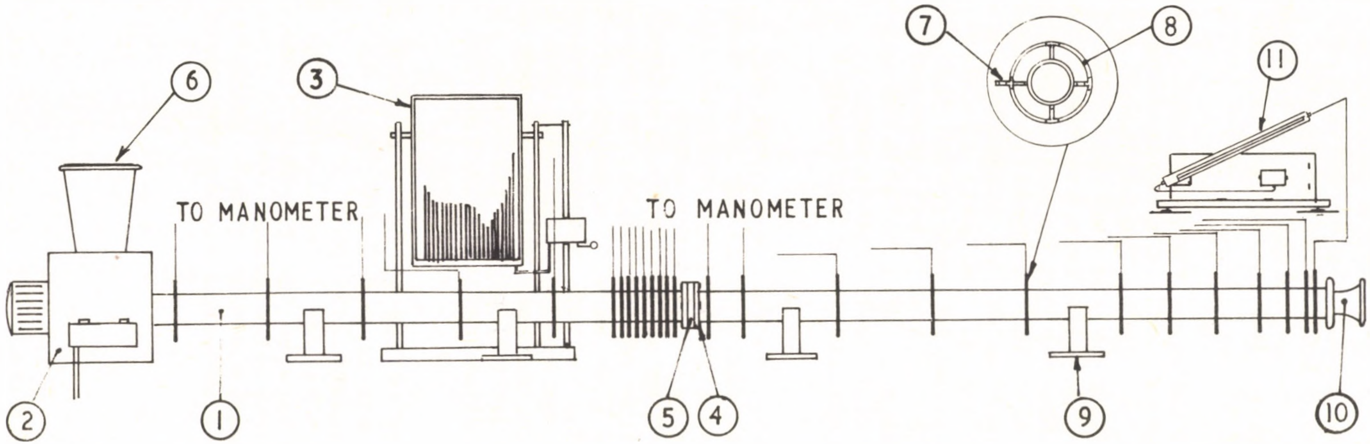

FIG. 3 - TEST RIG LAYOUT

1 - Pipeline
2 - Two-speed fan
3 - Multi-tube inclined manometer
4 - Pipeline flanges
5 - Gasket
6 - Variable opening throttle
7 - Connecting pressure line pipe to multi-tube manometer
8 - Peizometer rings
9 - Pipeline supports
10 - Bell-mouth inlet
11 - Inclined manometer (Bell-mouth throat)

Extrapolation of the low d/D value data of [2] indicated that the values of K to be encountered would be such that adequate, accurate and perspective pressure measurements could be achieved by using air at subsonic velocities as the test medium. That this could be undertaken in the industrial pipe Reynolds number range (order of 10^5) where K could be expected to be constant led to the use of the existing open circuit test rig of Fig. 3.

The requirement for measurement of the pressure distribution was met by the use of a multi tube inclined spriit manometer, volumetric flowrate by the bellmouth inlet throat tapping and flow regulation by the two speed fan motor and fan outlet throttle. Special care was taken to align the pipe and to ensure that the gasket was perpendicular to the pipe axis and co-axial with it. Initial leaks into the pipe were shown up on the manometer and subsequently rectified before readings were taken. Velocity profiles and turbulence levels were measured to ensure that the conditions in the test rig were compatible with the well established smooth pipe performance [3] i.e. at a range of Reynolds numbers. The friction coefficients were similarly checked and found compatible with the Moody Diagram.

For most jointing materials the stress relaxation property of the gasket material makes it sensible to choose as thin a gasket as the surface roughness and irregularities of the flanges will allow. There is also the added incentive that the area exposed to attack from agressive media is reduced [1]. The choice of test gasket thickness was based on this and so as to give as wide a range of b/D values as is consistent with the various national standards. This led to the use of square cornered gaskets machined from perspex (Fig. 1 insert) with thicknesses (b) of between ½ and 9 mm for use with a 79 mm dia (D) pipe. The lower limit of d/D was fixed by a maximum diametral tolerance of 20% ($d/D > 0.8$).

The effect of eccentricity of the gasket bore from the pipe bore was assessed from tests on a $d/D = 0.95$, 3 mm wide gasket ($b/D = 0.038$) at eccentricities ε of 0.25, 0.5, 0.75 and 1.0. i.e. the gasket bore was eccentric but not to the extent that it left a gap between the flanges. Tests were also carried out on a 4% oversize gasket ($d/D = 1.04$, $b = 3$ mm, $b/D = 0.038$). The maximum Mach number (based on the average pipe velocity V) encountered during the tests was 0.15.

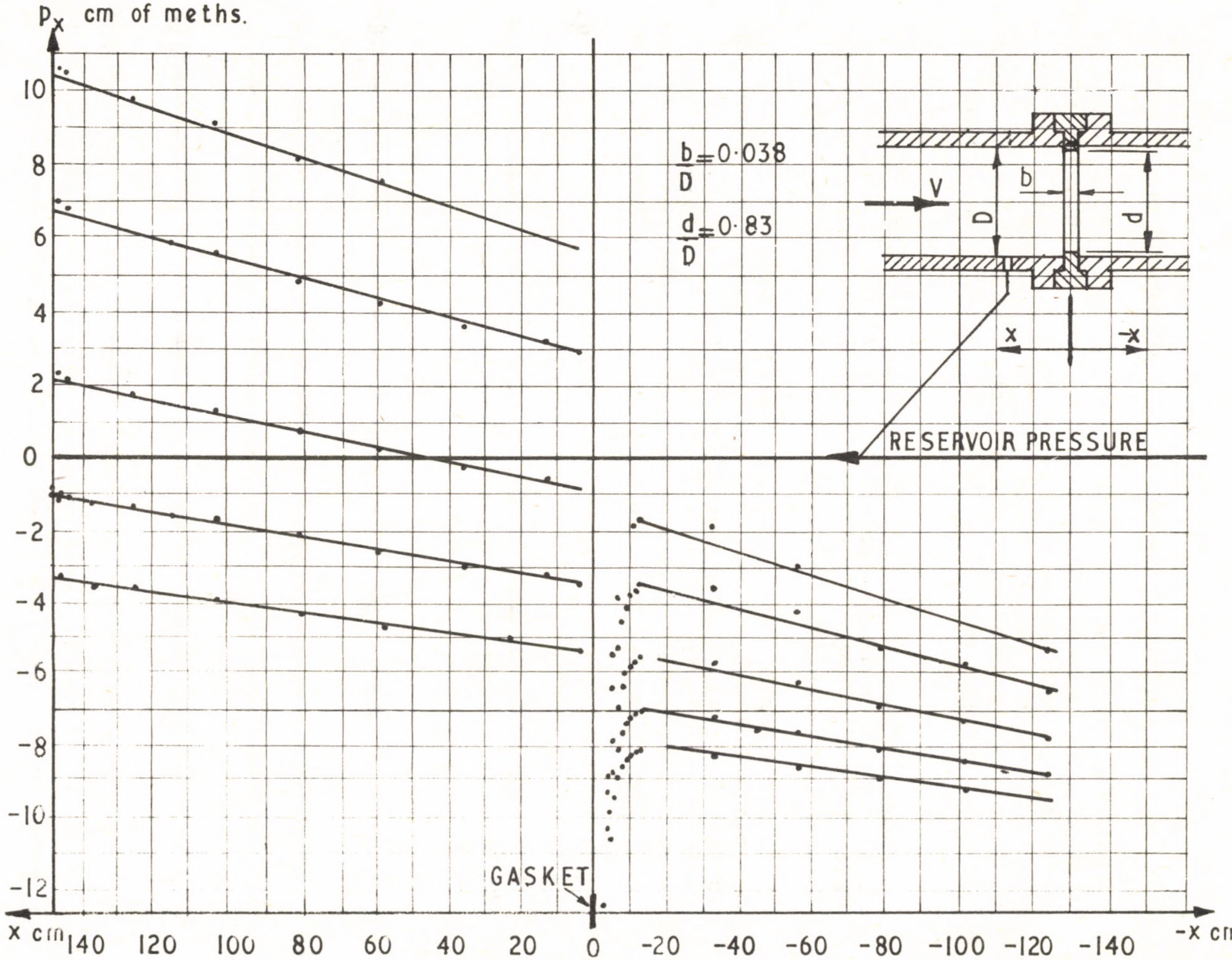

FIG. 4 - PRESSURE DISTRIBUTION

RESULTS

The distribution of static pressure along the pipe is exemplified in the specimen result of Fig. 4. The pressures are referred to the tapping directly upstream of the gasket which was connected to the common reservoir of the manometer.

On the lines in the fully developed pipe flow zone the scatter and pressure gradient are typical of what was obtained when the pipe was tested without a gasket but at the same Reynolds number. Whilst no divergence from the constant gradient is seen upstream of the gasket the flow redevelopment region is seen as typical of that for orifice meters of $d/D < 0.8$.

Fig. 5 shows a typical plot of the pressure loss coefficient K against Reynolds number ($\rho VD/\mu$). Within the degree of experimental error expected the loss coefficient can be said to be non Reynolds number dependent in this region.

The values of K from several graphs similar to Fig. 5 (for different b/D values) are plotted on Fig. 6. When the gasket had a larger diameter than the pipe ($d/D > 1$) no discernable loss in stagnation pressure was registered. Likewise the eccentric gasket showed the same results as the same gasket when mounted concentrically at the same Reynolds number.

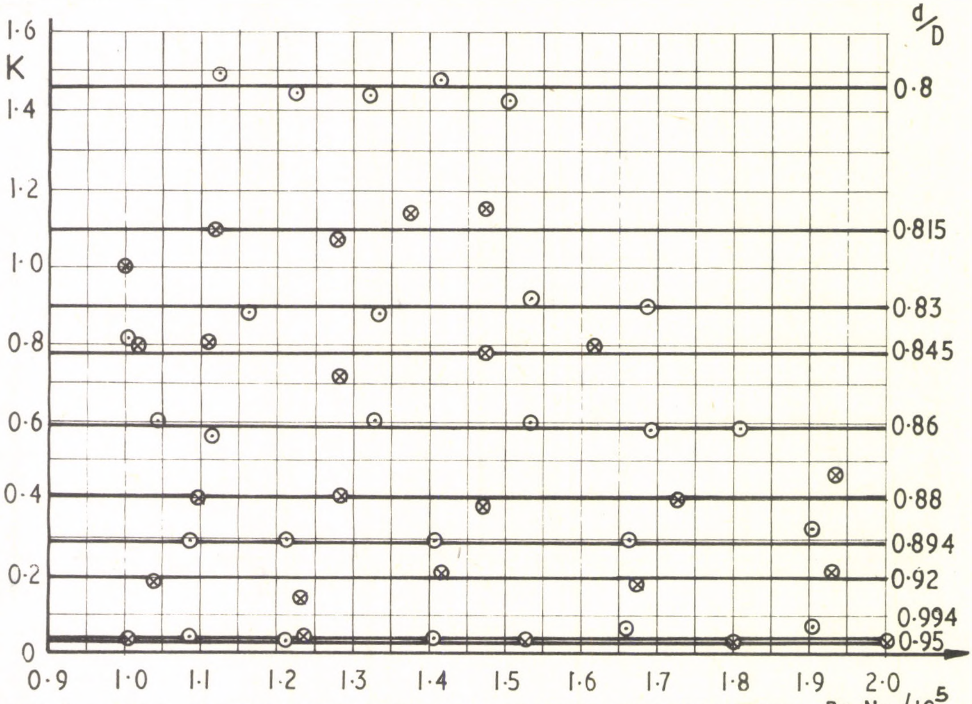

FIG.5. LOSS COEFFICIENT-REYNOLDS NUMBER RELATIONSHIP

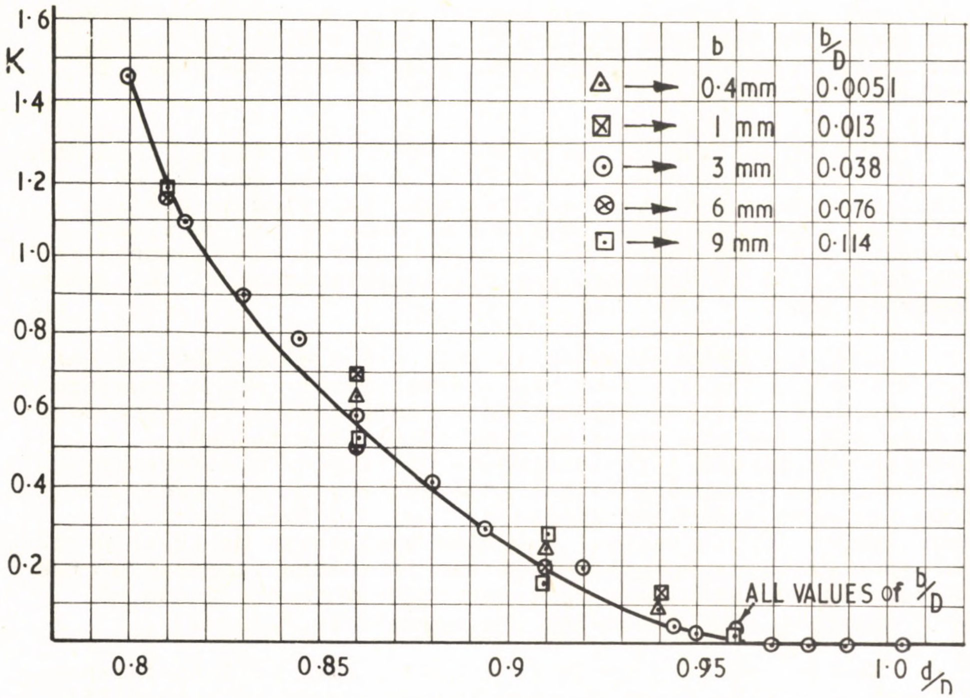

FIG.6. DEPENDENCE OF LOSS COEFFICIENT ON d/D

DISCUSSION

The results demonstrate that within the range of pipe Reynolds numbers encountered in industrial situations (order of 10^5) the stagnation pressure loss coefficient for a gasket of $0.8 < d/D < 1.0$ is constant. Moreover, where $d/D > 0.97$ no perceivable stagnation pressure loss occurs i.e. whatever the thickness of a practical gasket.

For a gasket of $d/D < 0.97$ the gasket loss may be significant as regards the pump load calculation. The magnitude of this effect will depend on $f\ell/D$ for the pipe length in question. The effect will be most severe for a system made up of large diameter pipes which tend to be supplied in short lengths, have small relative roughness and the most inaccurate flanges. For example, when $d/D = 0.91$, K equals 50% of $f\ell/D$ for a smooth pipe of $\ell/D = 20$ and Reynolds number of 10^5. If $\ell/D = 100$ then $KD/f\ell = 0.1$; if the pipe is rough then the significance of the gasket could be well below 10% of the total load per pipe length.

Anticipating the normal variation of loss coefficient with Reynolds number (for a fixed geometry restriction) it is unlikely that K will vary at Reynolds numbers higher than 2×10^5. In the low Reynolds number region where K may not be constant the stagnation pressure losses will be insignificant. When compared with the loss coefficient for square edged orifice plates [2] the gasket coefficient is $K = 1.5$ against 1.3 for the orifice at $d/D = 0.8$.

For $d/D > 0.95$ all b/D valves (Fig. 6) converge on to one line. In the region where $0.8 < d/D < 0.95$ the gasket thickness to bore ratio does have some effect but shows no systematic trend.

The definition of fully developed flow used in this work is that region where the pressure gradient is seen to be constant. Though it is possible that the velocity profile will continue to develop beyond the onset of the constant pressure gradient (this not discernable from the pressure line) the definition is adequate for the establishment of the system pressure loss.

One interesting result is that for a wide range of gaskets $0.8 < d/D < 0.95$, $b = 3$ mm the redevelopment length downstream of the gasket station appears to be independent of Reynolds number and, for the range of flow conditions tested, independent of d/D. It is however difficult to discuss exactly what the redevelopment length is even though more pressure tappings were made than appear on Fig. 3., i.e. for the development length tests. The flow appears to be fully developed for some distance upstream from the immediate vicinity of the gasket flange yet have a constant redevelopment length of approximately 15 D following the downstream flange.

Whilst the data tends to indicate that no interference effects will take place between joints placed more than 15 D apart the only way to be sure of this is to test such joints in series. This was not undertaken because the multiplicity of conditions of velocity profile and different diameter ratios of leading and trailing gaskets that would be encountered. In addition, provided d/D is greater than say 0.95 it is possible that the tolerance on pipe diameter, ovality and eccentricity of alignment may be a more significant factor than gasket loss.

CONCLUSIONS

Stagnation pressure loss coefficients for $d/D > 0.80$ do not depend on the Reynolds number or b/D over the range tested. For negligible loss the projection of the gasket into the pipe should be no greater than $d/D > 0.97$. For d/D values less than this attention should be paid to the relative values of K and $f\ell/D$ when calculating the pump load.

NOMENCLATURE

b	-	axial width of gasket
d	-	internal diameter of gasket
D	-	internal diameter of pipe
f	-	pipe friction coefficient (fully developed flow)
K	-	system loss coefficient $\Delta P_L/0.5\ \rho V^2$
ℓ	-	length of pipe between flanges
p_x	-	static pressure referred to that at manometer reservoir
ΔP_L	-	stagnation pressure drop
V	-	mean velocity of fluid in pipe
$\pm x$	-	distance along pipe upstream and downstream from gasket
ρ	-	density of fluid medium
μ	-	dynamic viscosity of fluid medium
ε	-	eccentricity of gasket from pipe axis as a fraction of (D-d)/2

REFERENCES

1. Childs, P. Take the guesswork out of Gaskets. Chartered Mechanical Engineer, November 1981, pp 23-29. Institution of Mechanical Engineers, London.

2. Engineering Sciences Data. Item No. 66030. Pressure Losses in Flowmetering Devices Oct. 1966. Engineering Sciences Data Unit, London.

3. Schlichting, H. Boundary Layer Theory. McGraw-Hill. New York 1968, 6th Edition, p 562.

W.A. Bullough,
Department of Mechanical Engineering,
The University of Sheffield,
Sheffield S1 3JD. U.K.

DOUBLE ACTING PUMP WITH INERTIA FLOW IMPROVES THE LOAD MATCHING OF WATER PUMPING WINDMILLS.

J. D. Burton

In recent years several designers have drawn attention to the poor load matching between a reciprocating water pump and wind turbine. The high starting torque associated with single acting pumps may be improved greatly by making the pump double acting, although with some risk of buckling in the pump rod as speed increases. A further feature of mismatch is due to the wind turbine power varying with the cube of speed, whereas a linear relationship tends to hold between the pump speed and its power absorption capability.

Starting with a pump used by Trevithick, for mine pumping at the end of the 18th century, the paper shows how these ideas led to the adoption of the double acting differential pump for windmill duties in Colombia, South America. More recently the design has been extended to incorporate the inertia flow principle, thereby improving the match between wind turbine and pump.

1. INTRODUCTION

As fuel prices have increased since 1973, so interest has grown in the possibility of using water pumping windmills for the provision of domestic and animal drinking water in isolated regions. Wind regimes in many tropical countries are not particularly good; however this need not be a problem unless the water has to be drawn from deep bore holes. Quite small cheap wind turbines, of up to 2 metre rotor diameter, have been successfully used in Colombia to supply 4-5 cubic metres of water per day. Sufficient to meet the minimum drinking needs of 400 people, or 100 head of cattle and sometimes irrigation of vegetable gardens.

2. PUMP MATCHING PROBLEMS

Considerable effort by designers has been expended on improving wind turbine blade shapes; however the efficiency gained in this way is not infrequently wasted through the poor load matching to final drive equipment.

Bragg & Schmidt (Ref 1) have examined the selection of both centrifugal and positive displacement pumps and in a most useful paper Dixon (Ref 2) has shown just how badly matched a reciprocating pump can become through the working speed range. Analysing a typical site Dixon shows that for a mean wind speed V_m, probably 90% of the available wind energy will fall between V_m and $3V_m$. If the system starts delivering water at $.8\,V_m$ and furling is set for $2.5\ V_m$ then the power captured by the turbine will increase by a factor of 30:1 between starting and furling. On the other hand the reciprocating pump's power absorption capability over the same speed range will vary by only 3:1; which means that at the higher speeds 90% of the wind energy will be wasted. Dixon also stresses the importance of peak pump torque T_p (which should be low for easy starting in light winds) compared with T_m the mean running torque. Significantly he shows that

$$\frac{T_p}{T_m} = \pi \quad \text{for a single acting pump}$$

$$\frac{T_p}{T_m} = \frac{\pi}{2} \quad \text{for a double acting pump} \qquad (1)$$

This means that for the same discharge rate per stroke a double acting pump will require only half the starting torque of a single acting pump.

3. TREVITHICK'S DOUBLE ACTING PUMP

Once Boulton and Watt's double acting steam engines became available for use in the Cornish mines around 1796 there was an immediate need to dispense with the simple bucket pump (which discharged only on the upstroke) and find a double acting pump. Trevithick's "temporary" solution (Fig.1 Ref 3) consisted of two pistons in parallel, one valved, as in the conventional bucket pump, and one solid. A common admission valve acted as the foot valve. With this pump Trevithick achieved an almost constant discharge on both the upward and the downward stroke. Significantly in some versions of the "temporary" pump, Trevithick made the solid piston of smaller size than the valved piston; almost certainly with the intention of reducing the possibility of pump rod buckling during the down stroke.

It is only a short step from Trevithick's "temporary" pump, to the double acting differential pump (Fig. 2) patented by Perkins (Ref 4) in the early 19th century. Here the plunger cross section area is increased to one half of the pump barrel cross sectional area. Like its predecessor this differential pump was able to sustain an almost constant flow. Unfortunately the increased size of the packed gland often led to increased leakage and sliding friction as the plunger moved back and forth.

4. THE DOUBLE ACTING PUMP APPLIED TO WINDMILL PUMPING

Early in 1977 (Ref 5) the author was involved in the testing of a Uniandes-Gaviotas sail windmill (rotor diameter 1.9m). The characteristics shown in Fig. 3 were obtained by mounting the rotor on the front of a jeep and measuring rotational speed and torque at different vehicle velocities.

Since the sail windmill was intended for shallow well pumping, where pump rod buckling would not be too big a problem, it seemed sensible to look at the possibility of improving starting torque by making the pump double acting. Examining the ideas of Trevithick and Perkins the author decided to dispense with the packed gland of Fig. 2 and extend the plunger to a level above the discharge tank Fig. 4. By making the plunger hollow it was also possible to further enhance the starting characteristics by making the moving parts of neutral buoyancy in the pumped water.

Taking a site with a mean wind speed of V_m = 2m/sec this windmill pump combination, on a combined lift of 10 metres would start discharge in a wind of 1.6m/sec ($\equiv .8 V_m$) and a friction disc would start to uncouple the pump in winds much over 5m/sec ($\equiv 2.5 V_m$). Typical output figures for pumping in a 5m/sec wind were 360 litres/hour or 4 cubic metres per 12 hour day. The power requirement of the pump has been superimposed on the wind turbine characteristics in Fig. 3.

Although the pump was built with $\frac{a}{A} = \frac{1}{2}$ to give equal discharge on both the down stroke and the upstroke; nevertheless a smaller differential can be used (as Trevithick sometimes did) so as to avoid buckling of the plunger rods. In general starting torque to running torque ratio will be:-

$$\frac{T_p}{T_m} = \left(1 - \frac{a}{A}\right)\pi \tag{2}$$

5. INERTIA PUMPING TO AVOID PUMP ROD BUCKLING

At higher speeds, when pumping through low lifts, reciprocating pumps generate quite high dynamic loads which could be a problem for the double acting pump. However the author has shown elsewhere (Ref 6) that these inertia effects may be used to advantage in greatly increasing the output of the pump.

One way of avoiding buckling at the higher speeds is to combine the differential pump with the inertia flow techniques presented at a previous Budapest Conference (Ref 7). Suppose that the differential pump of Fig. 4 is built with a bias such that $1/2 > a/A\,(=K)$, then at speed the flow will start to "free wheel", due to inertia of the fluid in the discharge, toward the end of each discharge pulse on both the upward and downward stroke (Fig.5a). If speed is further increased, and the bias is sufficient (Fig. 5b) then the down stroke will be missed out completely and <u>the pump will only power the flow on the upstroke</u>.

At the limiting condition in Fig. 5b, and expressing all flow velocities in terms of velocities in the rise pipe of area $A-a$, then λ and γ are related by:-

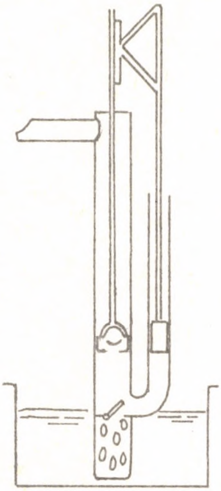

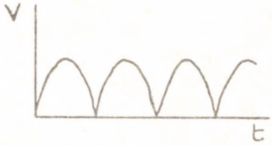

$$\frac{d}{D} = \sqrt{\frac{a}{A}} = \frac{1}{\sqrt{2}}$$

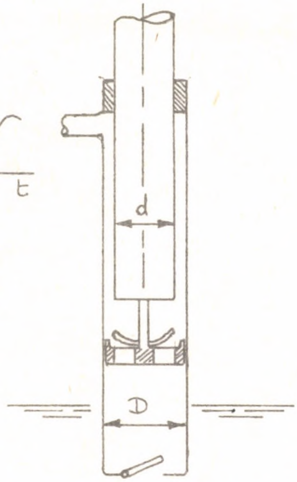

Fig. 1 Trevithick's "Temporary" Pump (Late 18th Century)

Fig. 2. Perkin's Differential Pump (Early 19th Century)

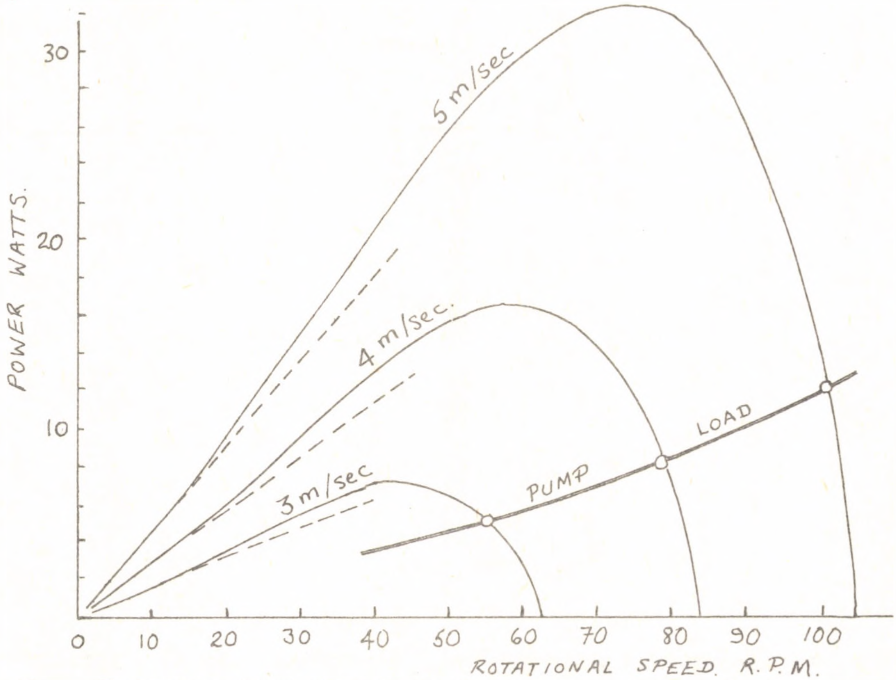

Fig. 3. Uniandes-Gaviotas Sail-Windmill and Double Acting Pump Characteristics

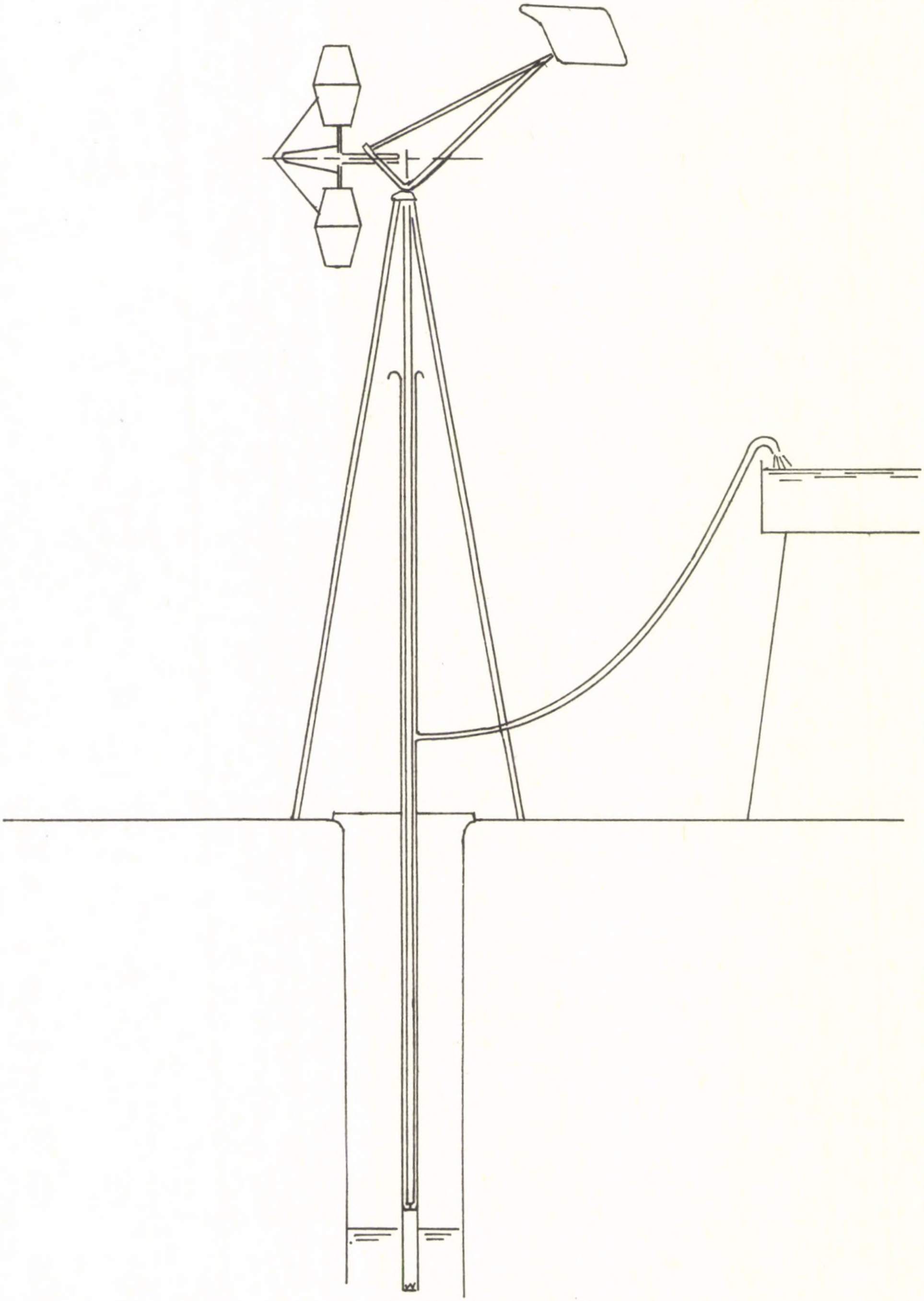

Fig. 4. Uniandes-Gaviotas Sail Windmill & Double Acting Pump.

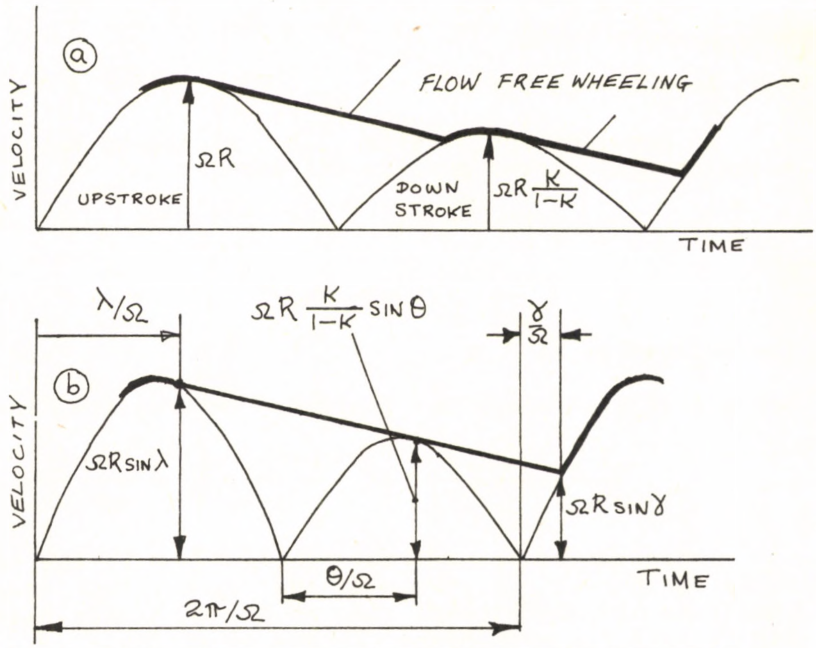

Fig. 5. Velocity-Time Curves fc Iner ia Pump before and at the point of Single Acting Operation.

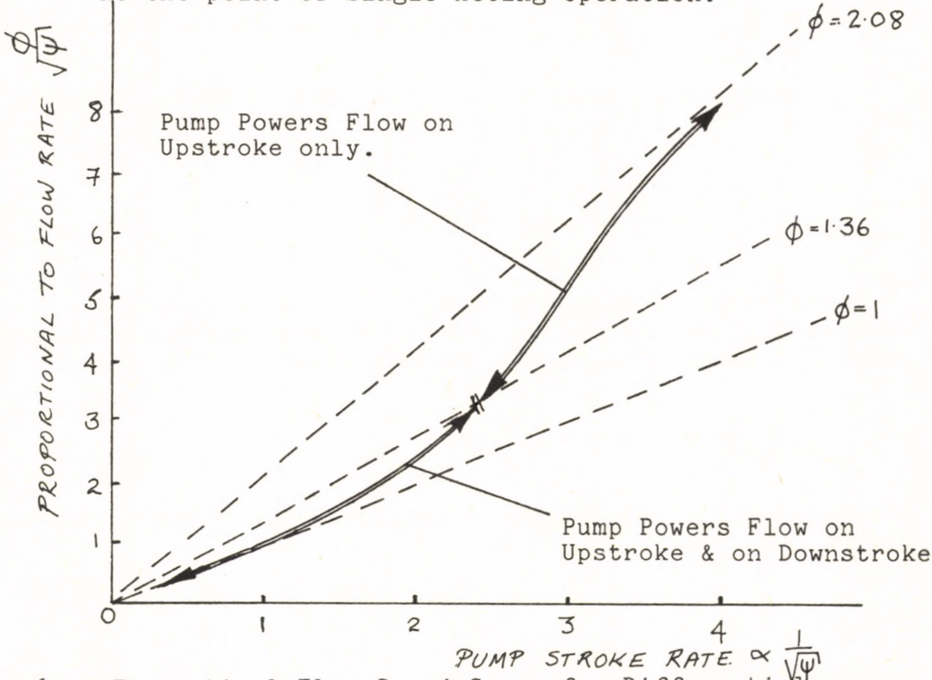

Fig. 6. Theoretical Flow-Speed Curve for Differential Inertia Pump

$$\frac{\sin\gamma - \sin\lambda}{\cos\lambda} = 2\pi - (\lambda - \gamma) \tag{3}$$

(see Appendix to Ref 7)

At the limiting condition, the slopes of the piston velocity time curves must be the same at

$$t = \frac{\pi + \theta}{\Omega} \quad \text{and} \quad t = \frac{\lambda}{\Omega} \quad \text{so}$$

$$\cos\lambda = \left(\frac{K}{1-K}\right)\cos\theta \tag{4}$$

The velocities at $t = \frac{\lambda}{\Omega}$; $t = \frac{\pi + \theta}{\Omega}$ and $t = \frac{2\pi + \gamma}{\Omega}$ are all related along the freewheel retardation line so that

$$\frac{\sin\lambda - \sin\gamma}{2\pi - (\lambda - \gamma)} = \frac{\sin\lambda - \left(\frac{K}{1-K}\right)\sin\theta}{\pi - (\lambda - \theta)} \tag{5}$$

Defining the volumetric efficiency ϕ as the volume of fluid discharged per stroke divided by the total swept volume (upstroke and downstroke) then at the condition shown in Fig 5b, and for even higher speeds of stroke:-

$$\phi = \frac{1}{2}(1-K)\left\{(\cos\gamma - \cos\lambda) + \frac{1}{2}(\sin\gamma + \sin\lambda)\left[2\pi - (\lambda - \gamma)\right]\right\} \tag{6}$$

Dimensionless head ψ will be defined as in Appendix to Ref 7:-

$$\psi = -\cos\lambda = \frac{g}{\Omega^2 R}\left(\frac{H}{L}\right) \tag{7}$$

The ratio of starting torque T_P (reduced by the differential double acting effect) to mean torque at maximum speed T_m (increased by the inertia flow) will be:-

$$\frac{T_P}{T_m} = (1-K)\frac{\pi}{\phi} \tag{8}$$

Resolving the above equations the condition shown in Fig 5b yields

$\gamma°$	$\lambda°$	$\theta°$	$\frac{K}{1-K}$	K	ϕ	T_P/T_m	ψ
15°	98.7	107.1	.51	.34	1.36	1.52	.15
30°	95.5	98.0	.70	.41	1.42	1.31	.10
45°	93.1	93.7	.83	.45	1.48	1.16	.05

With a differential plunger/piston area ratio $K \left(= \frac{a}{A}\right)$ of .34 T_P/T_m is quite close to the $\pi/2$ value (Equation 1) associated with the conventional double acting pump and this would seem to be a sensible design choice. The parameters $\phi/\sqrt{\psi}$ (proportional to pump flow rate) and $1/\sqrt{\psi}$ (proportional to stroke rate) have been graphed in Fig 6 for K = .34. At low speeds the volumetric efficiency $\phi \simeq 1$ whereas at very high speeds, way above normal furling, the theoretical maximum volumetric efficiency will be $\phi = (1-K)\pi = 2.08$. Between these extremes two contrasting operating zones can be distinguished, vis:-

$1.36 > \phi \geqslant 1$	Pump powers the flow on upstroke and downstroke
$2.08 > \phi \geqslant 1.36$	Pump powers the flow only on the upstroke

6. CONCLUSIONS

A production form of the differential pump coupled to a modern windmill has been on sale in Colombia now for about 3 years. In light winds the greatly reduced starting torque increases the utility of the machine, though this has to be set against the increased cost of the tower designed to withstand loads on both the upstroke and the downstroke. An inertia flow form of the differential pump has been tested at the University of Reading, U.K. (Ref 8)

7. ACKNOWLEDGEMENTS

The author wishes to thank the Centro Las Gaviotas (Colombia) for supporting the test work, on sail windmill and pump, undertaken in La Universidad Pontificia Bolivariana Medellin during 1977.

J. D. Burton, B.Sc. (Eng)., Ph.D., C.Eng.,
Department of Engineering,
University of Reading,
Whiteknights,
Reading,
Berks. U.K.

REFERENCES:-

1. BRAGG, G. M.; SCHMIDT, W. L. — 1978 University of Waterloo, Canada "Performance Matching of Windmills and Water Pumps".

2. DIXON, J. C. — 1977 Open University U.K. "Load Matching Implications for Wind Pump Design".

3. GREGORY 1806 "Mechanics" Vol. ii p.196

4. PARTINGTON, C.F. 1835. The British Cyclopaedia of Arts and Sciences Vol. 1 London.

5. FRANCO, J. B. 1978 Tesis de Grado Universidad Pontificia Bolivariana Medellin. p.p. 99-100

6. BURTON, J.D., LOBO-GUERRERO, J. 1972 Trans A.S.M.E. Vol. 94 Series D December p.p. 706-714 "Induced Flow Reciprocating Pump Theory Supported by New Performance Data".

7. SELWOOD, P.R., BURTON, J. D. 1975 Proceedings of 5th Conference on Fluid Machinery Budapest. p.p. 997-1009. "Induced Flow Reciprocating Pump with Rotodynamic Characteristics".

8. EISA, T. 1981. Ph.D Thesis University of Reading "Windpump System for the Sudan".

SYMBOLS

A	cross sectional area of piston
H	head across the pump
K	differential area a/A
L	length of discharge pipe of area $(A-a)$
R	half the stroke length i.e. crank throw
T_p	peak pump torque
T_m	mean pump running torque
a	plunger or pump rod cross sectional area
g	gravitational acceleration
t	time
γ	angular position in cycle at start of powered flow (upstroke)
λ	angular position in cycle at end of powered flow (upstroke)
θ	angular position in cycle on the downstroke

ϕ dimensionless flow (volumetric efficiency)

ψ dimensionless head

Ω angular velocity

A CONTRIBUTION ON THE VARIATION OF FLOW-PARAMETERS PUMPING HIGHLY VISCOUS FLUIDS

Ş. Çağlar

In the last few years the efforts are intensivated to extend the application of centrifugal pumps to the field of highly viscous fluids. It is well known, that with increasing viscosity the pressure head decreases, the required power rises and so the efficiency gets worse. Unnecessary costs for overdimensioned design or inefficient operation can be avoided, if the flow-parameters for pumping highly viscous fluids can be calculated by means of empirical or theoretical formulas from experiences on pumping — for example — water.

In this paper the effect of high viscosity on the flow parameters of centrifugal pumps is discussed. The analyzed data is based on some systematic experiments in the laboratories of the "Institut für Strömungslehre und Strömungsmaschinen" at the University of Karlsruhe [1]. The investigations were carried out on order and with cooperation of the "Forschungsfonds Pumpen im VDMA" and with the financial support of the "Arbeitsgemeinschaft Industrieller Forschungsvereinigungen e.V." (AIF-No: 4894, 5238).

POWER ANALYSIS ON A SINGLE STAGE PUMP

The energy to maintain the fluid flow in a plant is transmitted through the impeller onto the fluid. Thereby the losses of mechanical friction in the shaft-seals and in the pump-bearings (P_{mech}) and the losses of hydraulic friction between the impeller and the casing of the pump (impeller side friction) P_{Rsr} must be compensated through the expended shaft-power (P_W).

$$P_{Sch} = P_W - P_{mech} - P_{Rsr} \qquad (1)$$

The remaining power — so called "vane output" — P_{Sch}, is disposable for the increasing of the net energy level of the fluid.

The flow rate in the impeller $\dot{V}$, is higher than the flow rate at the inlet and outlet nozzles, $\dot{V}_N$, because of the leakages through clearance gaps, $\dot{V}_{Sp}$, and through balance holes, $\dot{V}_{Entl}$.

$$\dot{V}_N = \dot{V} - \dot{V}_{Sp} - \dot{V}_{Entl} \qquad (2)$$

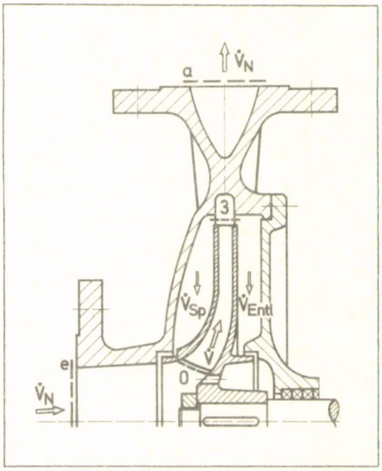

Fig. 1. Sketch of a centrifugal pump

The "vane output", P_{Sch}, is further reduced during the conversion of mechanical energy into hydraulic energy in the impeller and of the kinetic energy into potential energy in the volute casing because of the frictional dissipation and other hydraulic effects, P_V.

$$P = P_{Sch} - P_V \qquad (3)$$

Thus the remainin[illegible] the "vane output" is the available hydraulic power of the pump — pump output —, P, and corresponds to the product of the flow rate of the pump, $\dot{V}_N$, and the difference of the total pressure at the nozzles, $\underset{e\text{-}a}{\Delta}\bar{p}_{tot}$.

$$P = \underset{e\text{-}a}{\Delta}\bar{p}_{tot}\,\dot{V}_N \qquad (4)$$

In the further discussion it is postulated, that the leakage rate in the pump is neglectable, so that $\dot{V}_N = \dot{V}$ and the inlet and outlet nozzles have the same diameter, so that $\underset{e\text{-}a}{\Delta \bar{p}_{tot}} = \underset{e\text{-}a}{\Delta p_{pu}}$.

The pressure head of the pump $\underset{e\text{-}a}{\Delta p_{pu}}$ will be required — f.e. in a closed circuit — to cover up the pressure losses in the plant $\underset{a\text{-}e}{\Delta p_{pl}}$. (The energy to transport the fluid over a difference of altitude or against a difference of static pressure or to cover up the difference of the kinetic energy at the ends of a hydraulic line does not depend on the viscosity of the fluid, so that the discussion is limited to the pressure losses in a plant.)

$$\underset{e\text{-}a}{\Delta p_{pu}} = - \underset{a\text{-}e}{\Delta p_{pl}} \tag{5}$$

DIMENSIONLESS FLOW PARAMETERS

By using the following dimensionless parameters the flow quantities of a pump can be described independent of the actual values of the fluid density, of the angular velocity and of the impeller diameter. These are for the flow rate

$$\varphi_r = \frac{\dot{V}}{2\pi\, r_2^2\, b\, \omega}, \tag{6.a}$$

for the pressure head

$$\psi = \frac{\underset{e\text{-}a}{\Delta p_{pu}}}{(\rho/2)\, r_2^2\, \omega^2}, \tag{6.b}$$

for the "vane output" per flow rate

$$\psi_{th} = \frac{P_{Sch}/\dot{V}}{(\rho/2)\, r_2^2\, \omega^2} \tag{6.c}$$

and for the hydraulic efficiency — corresponding to $\underset{e\text{-}a}{\Delta p} \cdot \dot{V}/P_{Sch}$ —

$$\eta_h = \frac{\psi}{\psi_{th}}. \tag{6.d}$$

For the quantification of the kinematic viscosity of the fluid a Reynolds number is defined, which is proportional to the flow rate per blade number Z and impeller width b.

$$Re = \frac{\dot{V}/Z\, b}{\nu} \tag{6.e}$$

During the experiments the impeller width b was varied systematically, while all other geometric parameters were constant; thus

$$B = \frac{2\, b}{r_2}. \tag{6.f}$$

EXPERIMENTS

The experimental equipment allows the variation of the flow rate $\dot{V}$, of the angular velocity ω and of the fluid viscosity ν independent from each other. By systematic variation of these parameters and of the impeller width b the pressure head $\underset{e\text{-}a}{\Delta p_{pu}}$ and the "vane output" P_{Sch}, which is disposable to increase the net energy level of the fluid, were measured. Measuring P_{Sch} the driving torque at the impeller was registered with DMS, while the torque caused by the impeller side friction was eliminated for the measurement by means of additional synchron rotating disks on both sides of the impeller.

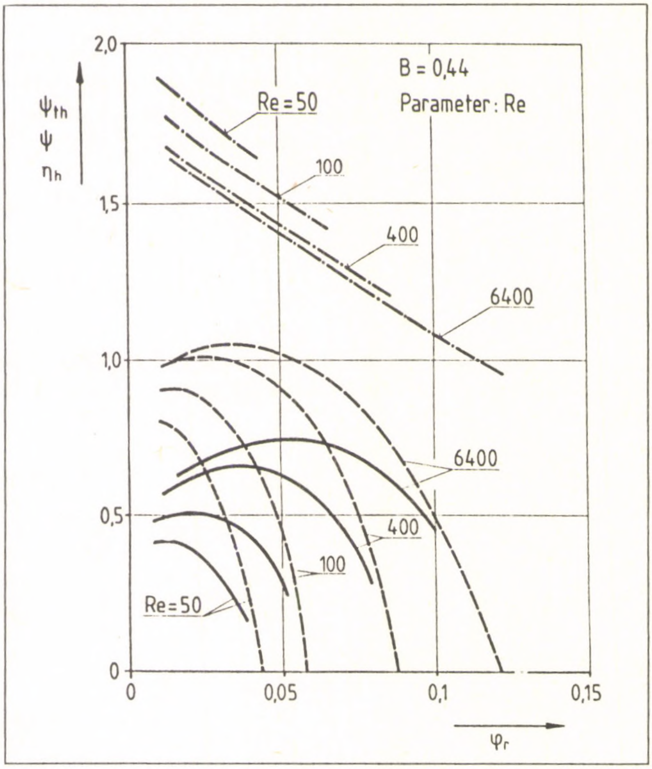

Bild 2. Flow coefficients of a pump

ψ_{th} (dash-dot), ψ (dashed), η_h (solid)

In figure 2 the coefficients ψ_{th}, ψ and η_h over φ_r are given exemplifying the other pumps for $B = 0.44$ at various Re. With descreasing Re — corresponding increasing viscosity — the hydraulic losses in the pump increase rapidly and cause a strong reduction of the pressure head ψ and of the hydraulic efficiency η_h. Also the optimum of the flow rate — corresponding to φ_r at the maximum of η_h — shifts to smaller values.

The growth of ψ_{th} is partially caused by the effects of secondary flows in the impeller channels [2].

APPLICATION

Applying these and other results on the flow of a highly viscous fluid in a close circuit, it is possible to predict the variation of the operation parameters as a function of the relevant quantities. With the assumption, that the pressure drop in the plant in a wide range of laminar flow can be calculated by

$$\Delta p_{pl} = -\sum_i \frac{K_i}{Re_{h,i}} \frac{l_i}{d_{h,i}} \frac{\rho}{2} \left(\frac{4\dot{V}}{\pi d_{h,i}^2}\right)^2 \qquad (7.a)$$

with

$$Re_{h,i} = \frac{4\dot{V}}{\pi d_{h,i} \nu} , \qquad (7.b)$$

where K_i is a value dependent only on the geometry, and considering (5) and (6.b), the following relation is obtained:

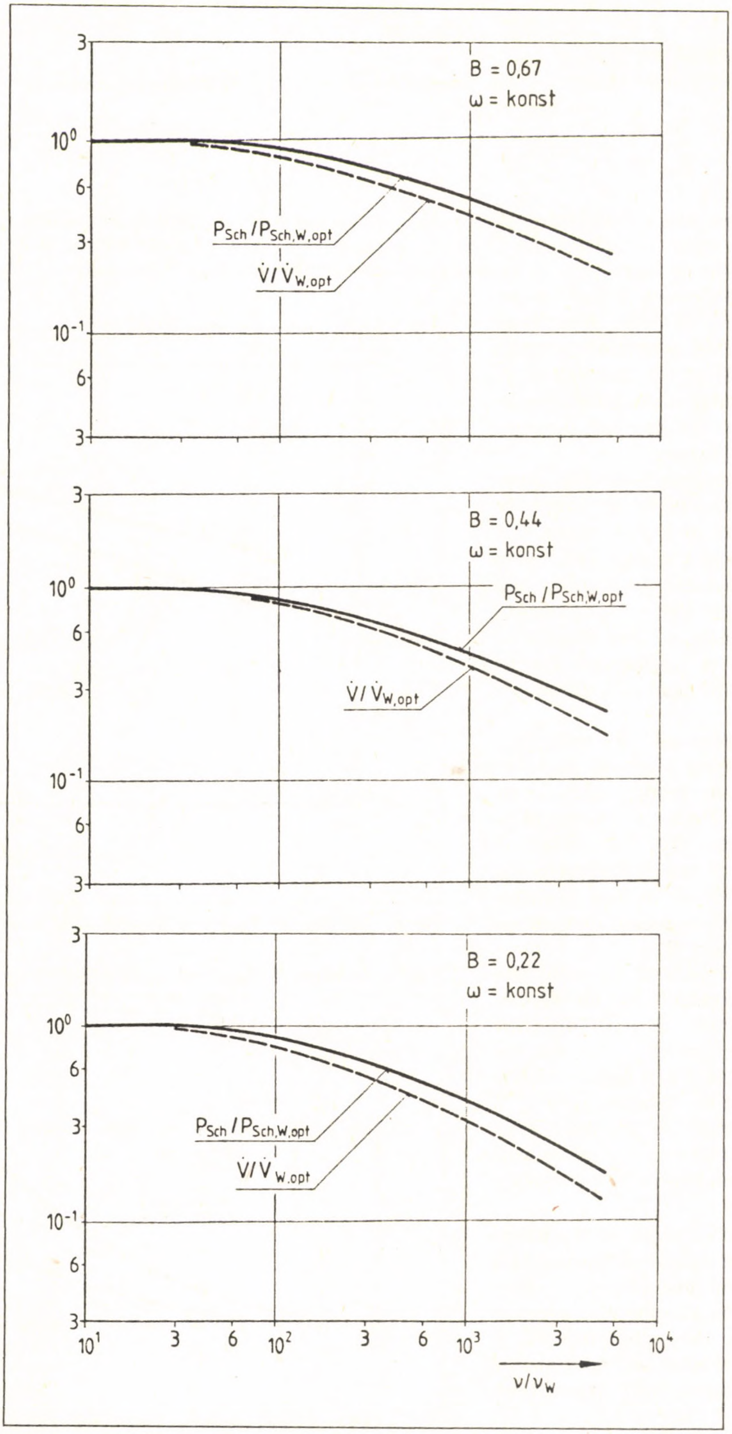

Fig. 3, 4, 5. Percentage change of P_{Sch} and $\dot{V}$ at varying viscosity

$$\psi \frac{\rho}{2} r_2^2 \omega^2 = \left(\sum_i \frac{4 K_i l_i}{\pi d_{h,i}^4} \right) \frac{\rho}{2} \dot{V} \nu \quad . \tag{8}$$

Rearranging (8) and considering the definitions (6.a) ÷ (6.f) equation (8) becomes

$$\frac{B}{Re} \frac{\varphi_r^2}{\psi} = \text{const} \quad , \tag{9}$$

which means, that all operating points for a given plant must obey this equation. The values for ψ and φ_r must be determined from the experimental data at given values of Re and B. The corresponding values of ψ_{th} allow the prediction of the required "vane output" P_{Sch}.

In the following three figures (Fig. 3, 4, 5) the percentage changes of the operation parameters — referred to the values at pumping water in designed operating point — are plotted over the kinematic viscosity.

These diagrams show for three pumps with different impeller widths, that in a given plant the flow rate and the required "vane output" decrease with increasing viscosity, if the driving speed is hold constant. The change of the values is neglectable up to viscosities of ca. 50 times of water.

The decrease of $\dot{V}$ and P_{Sch} with increasing viscosity is more significant in pumps with smaller B, as figure 6 shows at a constant viscosity. This effect is explicable, as the losses due to the secondary flows in the impeller channels are reduced percentage with increasing B.

If it is intended to hold the flow rate constant for all viscosities (Fig. 7 for B = 0.44), then the driving speed must be increased and a much higher driving power must be installed. (In Fig. 7 only the increase of the "vane output" is plotted. In a pump also the impeller-side-friction increases rapidly.)

As the mechanism of the variation of the operation parameters with varying viscosity is — contrary f.e. to varying the angular velocity — very complicated, a simple mathematical relation to describe these effects can not be extracted.

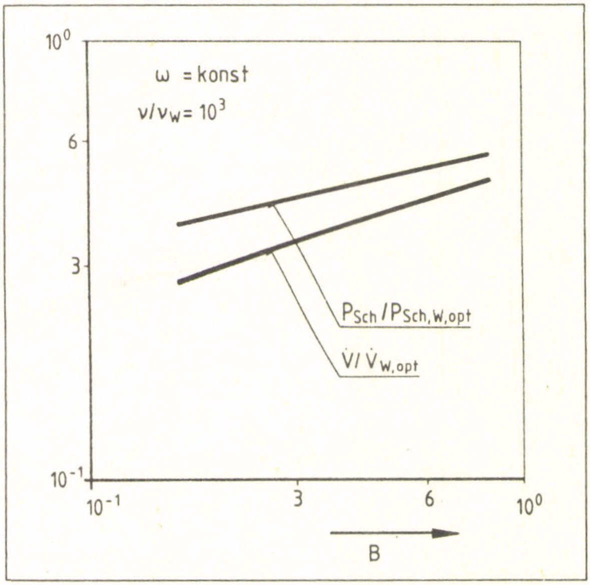

Fig. 6. Variation of P_{Sch} and $\dot{V}$ with B at a constant viscosity

Fig. 7. Variation of P_{Sch} and ω holding $\dot{V}$ = const

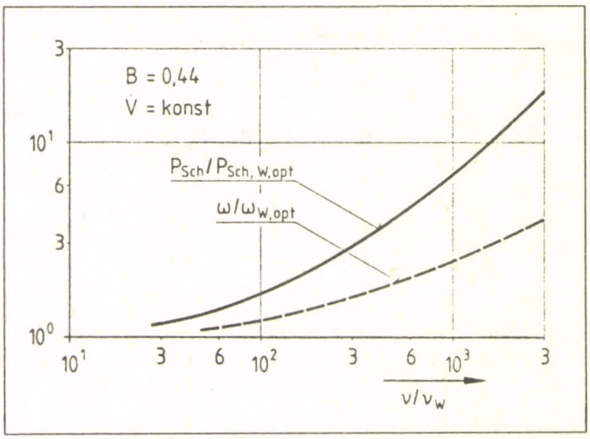

SYMBOLS

b	impeller width		Re_h	Reynolds number	(7.b)
B	dimensionless width	(6.f)	$\dot{V}$	flow-, leakage-rate	
d_h	hydraulic diameter		Z	blade number	
K	constant		ν	kinematic viscosity	
l	length		ρ	density	
P	pump output	(3), (4)	η_h	hydraulic efficiency	(6.d)
P_{Sch}	"vane output"	(1)	φ_r	coefficient for flow rate	(6.a)
p	pressure		ψ	coefficient for pressure head	(6.b)
r_2	impeller radius		ψ_{th}	coefficient for "vane output"	(6.c)
Re	Reynolds number	(6.e)	ω	angular velocity	

(Other indices are explained in the text.)

REFERENCES

[1] ÇAĞLAR, Ş.: Abhängigkeit der Strömungskenndaten von Kreiselpumpen bei der Förderung hochviskoser Flüssigkeiten. Konstruktion 4, Berlin: Springer, 1983.

[2] ÇAĞLAR, Ş.: Untersuchungen an Schaufelkanälen radialer Pumpenlaufräder bei laminarer Strömung. Karlsruhe, Universität (TH), Dr.-Ing.-Diss. v. 1980.

ÇAĞLAR, Şaban Dr.-Ing.
Institut für Strömungslehre und Strömungsmaschinen
Universität Karlsruhe (TH)
Kaiserstraße 12 · D 7500 Karlsruhe 1
Federal Republic of Germany

QUASI THREE-DIMENSIONAL FINITE ELEMENT FLOW CALCULATION IN PUMPS

By E. Carnevale, S. Giusti, G. Manfrida, F. Martelli
Istituto di Energetica - Università di Firenze

1. INTRODUCTION

The simulation of the flow in turbomachines by means of a recursive and interactive application of numerical codes solving the two-dimensional inviscid flow on the S1 (blade-to-blade) and S2 (meridional) flow surfaces, as defined by Wu [1], still presents some attractive features with respect to the application of direct three-dimensional and/or viscous computer codes. First of all, these two-dimensional calculations are much less expensive to be performed; moreover, with respect to inviscid potential flow 3-D calculation, they are able to deal with rotational flows; on the other hand, viscous effects in real turbomachines lead in most cases to turbulent flow separations, recirculating flows, which cannot be examined by "viscous" calculations as well as by inviscid ones. For many applications, an inviscid calculation with some experimental insight by the use of correlations able to predict the separation mechanism [2,3] can give better results than full viscous approaches.

These problems are particularly important in the pump field, ranging from axial to centrifugal designs, because of the large blade loadings commonly used by manufacturers, leading in many cases to large separations. Impeller pump geometries are often so complicated that a finite difference discretization is not able to describe the details; from this point of view, Finite-Element-based codes [4] are meeting a large popularity in the pump designer community. Two computer codes have been developed, respectively solving the S2 (meridional) and S1 (blade-to-blade) flow problem, which are based on this theory and able to interact between themselves in order to get a quasi three-dimensional picture of the flow.

2. THROUGH-FLOW CALCULATION (S2)

The through-flow analysis is done prescribing the stream surface and introducing a fictitious field of dissipative body forces giving at each point a force $\vec{D}$ tangent to the stream line and acting in opposition to the local velocity vector.

The S2 stream surface is defined by the following operations:

- use of blade geometric data for the construction of three-dimensional cubic splines defining the blade geometry as a grid of spatial curves.
- Evaluation of slip effect at the impeller outlet following the Wiesner model [5].
- Evaluation of the slip effect inside the impeller by means of empirical correlations of the type proposed in [5,6].
- Construction of the S2 geometry considering the cumulative slip effect on the blade geometry, starting from the blade inlet.

Such a procedure is by-passed when the S2 stream surface is given by a preceeding blade-to-blade calculation.

The condition that the flow takes place on a prescribed surface gives the possibility to substitute one of the motion equations with an equation of the type $f(r,\theta,z) = 0$, describing the S2 geometry. In this way it is possible to use the motion equation in the direction $\vec{N}$, tangent to the stream surface and normal to the local stream line. So dissipative and body forces disappear in the calculation and the internal loss effect results in an entropy gradient appearing in the final flow equation. [14,15]

For the evaluation of entropy gradient it is introduced a local loss coefficient as the ratio between the total pressure rise in the real flow and the total pressure rise in the corresponding isoentropic flow.

Combining the motion equation with geometric conditions, introducing Wu's special derivatives and the stream function ψ it is obtained a final flow equation of the type

$$\frac{\bar{\partial}^2\psi}{\partial r^2} + \frac{\bar{\partial}^2\psi}{\partial z^2} = q_I + q_E \tag{1}$$

where q_I depends on S2 geometry and on velocity components and q_E depends on entropy gradient, velocity components and S2 geometry.

Equation 1 is a non-linear Poisson-type equation and can be solved by an iterative procedure. The proposed numerical model is articulated in the following steps:

a) definition of S2 geometry starting from the machine geometric data.
b) Solution of equation (1) in the isoentropic case ($q_E = 0$).
c) Evaluation of dissipative effects in terms of entropy rise (evaluation of q_E).
d) Solution of equation (1) including loss model.

3. BLADE-TO-BLADE FLOW CALCULATION (S1)

The blade-to-blade calculation is performed on an axisymmetric stream surface and is based on the solution, by a Finite Element discretization, of the momentum equation orthogonal to the stream direction, which is written in stream function terms by the continuity equation.

This formulation in θ-m coordinates system can easily treat any geometry from axial to radial and by the variation of the streamtube thickness can take into account the effect of the meridional flow configuration.

For a complete description of the approach, the reader is referred to [7,8]. The main features are hereby recollected:

a) The impeller relative flow is examined on an axisymmetric S1 surface.

b) The flow is solved in the m(meridional abscissa)-θ(angular tangential abscissa) domain, thus allowing no discontinuities in the equations for mixed-flow or centrifugal geometries (as are encountered in some approaches [9]). The equation of motion is projected in the direction locally orthogonal to the streamwise direction; after the introduction of the stream function ψ, satisfying the continuity condition, one gets:

$$\frac{\partial}{\partial\theta}\left(\frac{1}{br^2}\frac{\partial\psi}{\partial\theta}\right) + \frac{\partial}{\partial m}\left(\frac{1}{b}\frac{\partial\psi}{\partial m}\right) = \frac{\rho\sin\alpha}{\dot{m}}\left(\frac{W\theta}{r} + 2\omega\right) + \frac{\rho}{\dot{m}W}\frac{\partial I}{\partial\eta} - \frac{\rho T}{\dot{m}W}\frac{\partial s}{\partial\eta} \qquad (2)$$

where: b is the local streamtube thickness (normal to S1)
r is the local radius
ρ is the fluid density
$\dot{m}$ is the mass flow
α is the angle of the S1 surface with the axial direction
ω is the rotational speed
I is rothalpy
η is the normal direction to the streamline, on the S1 surface
T is temperature
s is entropy

c) Eq. 2 is reformulated in a quasi-variational form suitable for the Finite Element Discretization; after application of this last, one gets a system of linear equations, which can be solved by a point relaxation algorithm, thus allowing a simple treatment of periodic boundaries; these are necessary in order to reduce the true flow problem to that around an isolated airfoil, and their presence actually leads to some numerical problems which are not encountered on the S2 surface.

d) As it is evident from Eq. 2 , large contributions to the rotationality of the flow field come from the radius variation ($\sin\alpha \neq 0$) in mixed-flow or centrifugal impellers); smaller ones are originated by non-constant rothalpy or entropy distributions at the inlet, as for the S2 calculations. These rotational terms are dealed with by means of an iterative procedure, which takes from 2 to 5 solutions of the system of linear equations described at point c).

e) A first guess to the impeller outlet angle is usually obtained by an improved Busemann slip factor correlation [5].

f) The final value of the outlet angle is calculated by imposing a closure condition at the trailing edge: this reduces to one the infinite solutions of the inviscid flow past an airfoil. This physical closure condition, ideally corresponding to the equality of pressure at the wake onset, is treated directly by Finite Element arguments [7].

g) The output consists in the ψ field inside of the domain;from this, the velocity distribution on the boundaries and the lines at constant ψ(streamlines) are determined.

h) Cubic spline interpolation routines allow the description of the geometry with a very limited set of input data; these can be easily interfaced with the S2-code output.

i) Off-design conditions in the neighbouring of the design point (i.e. as long as large separations are not physically expectable) can be examined by simply changing the value of the flow coefficient.

4. OVERALL COMPUTING SYSTEM

Several approaches are possible to the construction of the quasi-three-dimensional computing system by the use of meridional (S2) and blade-to-blade (S1) codes [10,11,12], according to the philosophy of the codes themselves. Considering that our blade-to-blade calculation is on an axisymmetrical surface, it is natural to build the flow by interacting one meridional calculation and various S1 calculations. In this sense the meridional code is an averaged calculation within the blade passages.

The two codes interact reciprocally because some output of each are the input of the other.

The S1 codes require the S1 surface definition, r(z), together with the associated blade geometry and the stream tube width from the S2 code, and the S2 requires the geometry of its calculation surface. This last is defined, according to the above considerations, by the mean streamline of each S1 calculation, i.e.: $\theta_m = \int_0^1 \theta d\psi$; the r,z are unchanged.

This curve can be slightly or strongly different from the streamline ψ = .5 depending on the geometry of the blade and of the meridional channel.

Then the whole procedure is the following:

- run the S2 code with its correlation

- run several S1 codes with the streamtube widths computed by S2 code
- run the S2 code with the mean surface from the previous calculation
- run new S1 codes with S2 output
- run S2 code with new surface.

The convergency in the calculation is always achieved after 2 coupled calculations, the last S2 code can represent an averaging process along the blade height. This procedure to describe the flow pattern within the blade passages, although approximate, nevertheless is able to give useful information in the design steps with low expenses of computer time.

5. RESULTS

The proposed quasi-3D calculation has been tested against the experimental results of Ref. [13], which represents one of the few examples of detailed flow investigations within a centrifugal impeller.

After a first S2 calculation with a slip correlation, a set of five S1 calculation was performed. The resulting blade-like surface geometry was fed into the S2-code, as described in part 4), and the new S2 streamlines were calculated. These are shown in Fig. 1, together with the mesh of quadrilateral isoparametric elements used for the discretization. As this set of stream lines agreed very closely with the previous one, which had been produced by the S2 calculation with the slip correlation, it was considered unuseful to perform a second set of S1 calculations: the resulting velocities and pressures of the blade-to-blade code are then those from the first set of calculations, with the S1 surface and streamtube heigth defined by the S2 calculation.

The pressure distributions on blade pressure and suction side are compared with experiments in Figs. 2-3-4, respectively for the hub, mean and shroud surface. A certain amount of separation on the blade suction side is present in the experimental data, which is low at the hub but becomes important at the mean and shroud stream surfaces; this separation is localized at the connection between the inducer and the radial part of the blade.

The calculation on the mean S1 stream surface yields very similar results to those of a S1 calculation (with the same code) effected on the [7] complete impeller with no coupling to the S2 code; nevertheless, important informations about the flow behaviour at the hub and shroud (which is the weak point of this impeller design, corresponding experimentally to a region of high total pressure loss) can be achieved only by means of an interactive quasi-three-dimensional procedure.

Results of theoretical calculations by other Authors are available only for the mean S1 stream surface, and are presented in Ref. [7]; with respect to other approaches, the present one is favoured by the possibility of a complete description of the pump in the region ranging from full axial to full radial.

The streamlines produced by the blade-to-blade code on the mean S1 surface are presented in Fig. 5. The mass-averaged blade-like surface for running the subsequent S2 code is also shown.

ACKNOWLEDGMENTS

The Authors are indebted to Mr. G. Battigaglia for his work during his degree thesis.

REFERENCES

[1] Wu, C.H., "A General Theory of the Two-Dimensional Flow in Subsonic and Supersonic Turbomachines of Axial, Radial and Mixed-Flow type", Naca TN 2604.

[2] Rodgers, C., "Impeller Stalling as Influenced by Diffusion Factor Limitations", Trans. ASME, J. of Fluids Eng., 1977.

[3] Howard, J.H.G., Osborne, C., "A Centrifugal Compressor Flow Analysis Employing a Jet-Wake Passage Flow Model", Trans. ASME, J. of Fluids Eng., 1977.

[4] Proceedings of the 11th AIRH Congress, Amsterdam, 1982.

[5] Wiesner, F.J., "A Review of Slip Factors for Centrifugal Impellers", Trans. ASME, J. of Eng. for Power, Oct. 1967.

[6] Salemi, C., Di Matteo, V., "Slip Factor Calculation in Centrifugal Pumps by Means of Evaluation of Wall Boundary Layer", in <u>Performance Prediction of Centrifugal Pumps and Compressors</u>, Ed. S. Golapakrishnan et al., ASME, 1980.

[7] Martelli, F., Manfrida, G., "Flow Calculation in Pump Impellers by Finite Elements", Hydroturbo '83 , Budapest.

[8] Martelli, F., Manfrida, G., "Studio del flusso interpalare in pompe assoradiali con il metodo degli Elementi Finiti", Proceedings of the 37th ATI Congress, Padova, 1982.

[9] Adler, D., Krimerman, J., "Calculation of the Blade-to-Blade Compressible Flow Field in Turbo Impellers Using the Finite Element Method", J. Mech. Eng. Science, vol.19 n°3, 1977.

[10] Krimerman, J., Adler, D., "A 2-D and 3-D Flow Analysis in Turbomachinery Using the Finite Element Method", VKI LS 05 - 1982.

[11] Novak, R.A., Hearsey, R.M., "A Nearly Three-Dimensional Intrablade Computing System for Turbomachinery", J. of Fluids Eng., Trans. ASME, March 1977.

[12] Bosman, C., El-Shaarawi, M.A.I., "Quasi Three-Dimensional Numerical Solution of Flow in Turbomachines", Trans. ASME, J. of Fluids Eng., March 1977.

[13] Mizuki, S., Ariga, I., Watanabe, I., "Investigation concerning the Blade Loading of Centrifugal Impellers", ASME Paper 74-GT-143, 1974.

[14] Carnevale, E., Giusti, S., "Analisi del flusso non isoentropico in giranti di pompe centrifughe con il metodo degli elementi finiti", XXXVII Congresso Nazionale ATI, Padova, 1982.

[15] Carnevale, E., Giusti, S., Angelo, G., "Analyse Théorique experimentale de l'écoulement réel dans les pompes assoradiales", 121ème Session du Comité Technique SHF, Paris, 1982.

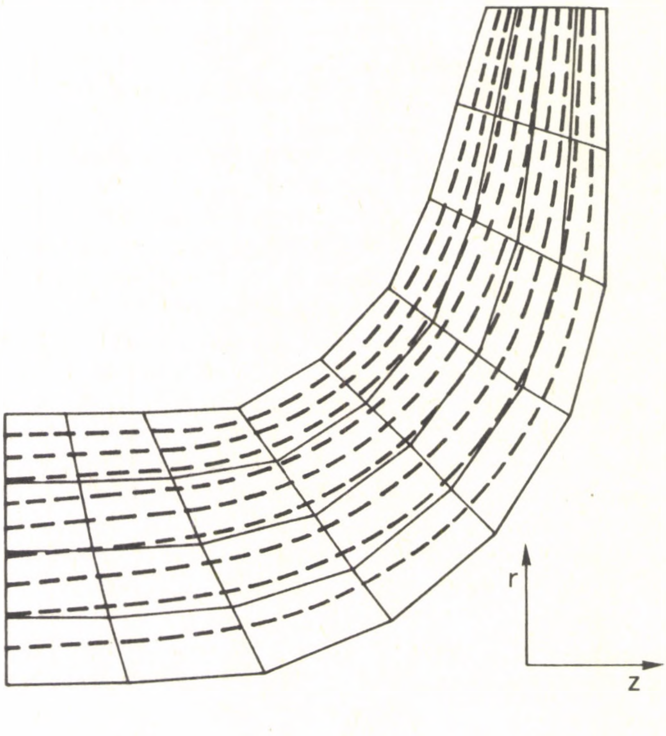

Fig. 1 - Meridional streamlines (S2)

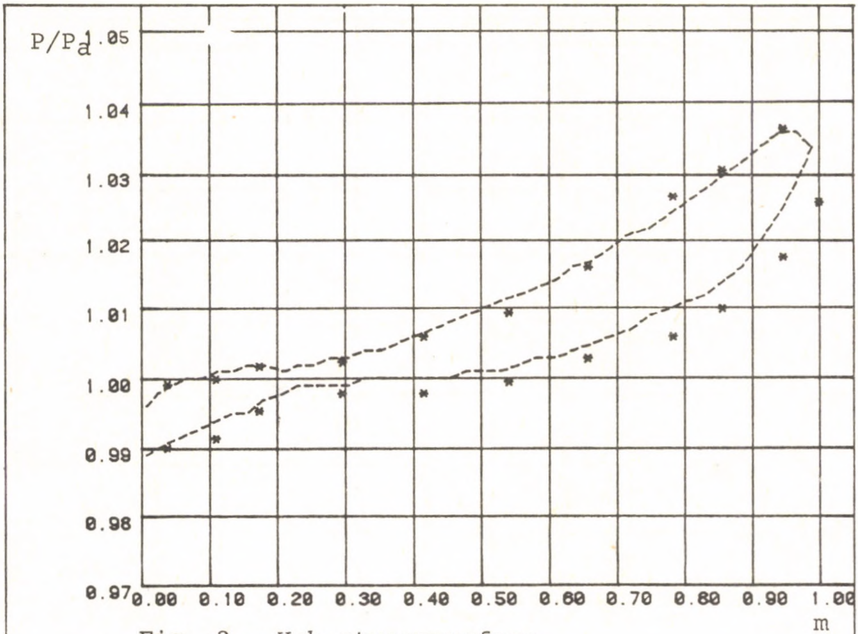

Fig. 2 - Hub streamsurface
* Experiment ----Present calculation

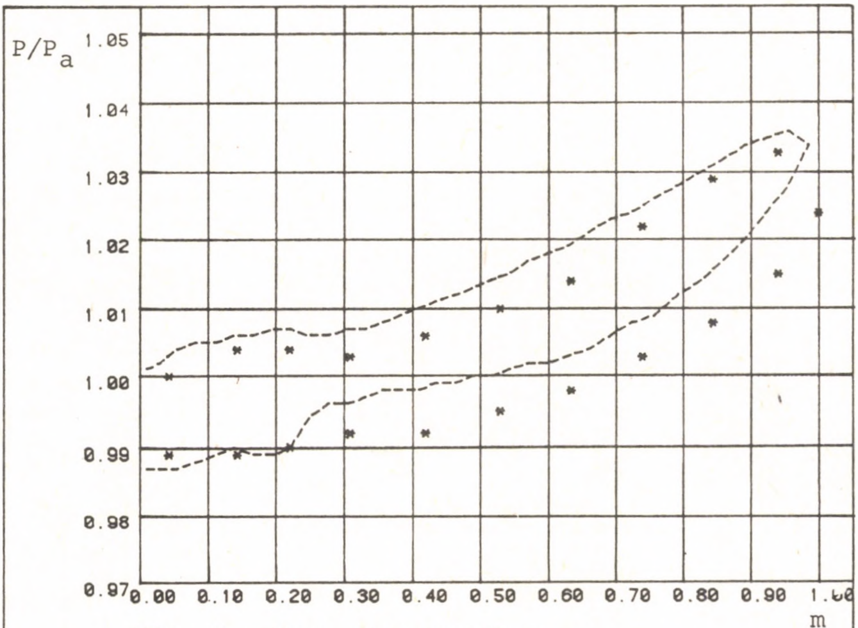

Fig. 3 - Mean streamsurface
* Experiment -----Present calculation

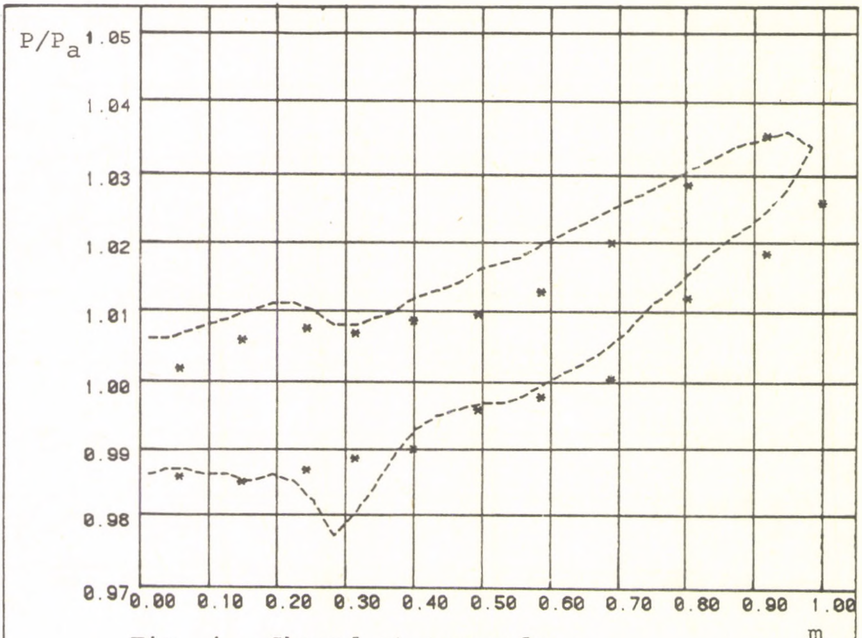

Fig. 4 - Shroud streamsurface
* Experiment ------ Present calculation

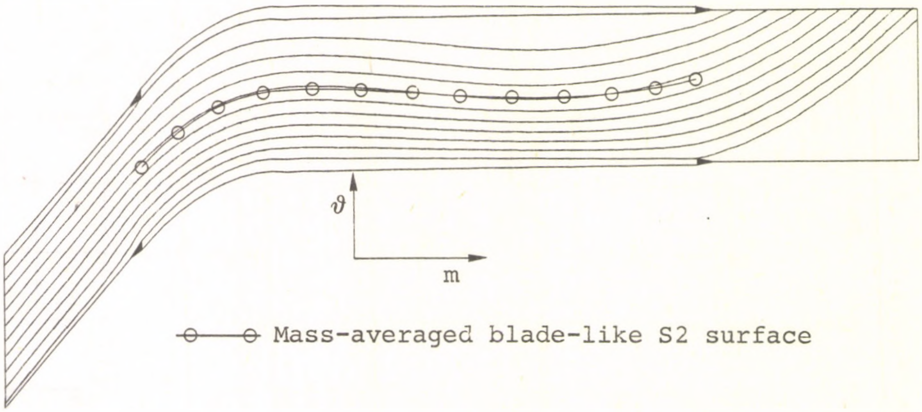

Fig. 5 - Blade-to-blade streamlines (S1) on the mean streamsurface

THE RETICAL AND EXPERIMENTAL DETERMINATION OF SURGE IN FAN SYSTEMS

Th.Carolus, L.Kullmann

A model with lumped parameter is used to describe a simple fan system. In order to determine the beginning of surge, the surge-amplitude and the frequency of the surge-cycles as functions of important parameters, a stability analysis and a numerical solution of the describing equations are carried out. Experimental results are obtained by measurements on a versatile test stand and are compared with theory.

MATHEMATICAL MODEL

Quite often pumping systems show instable behaviour of operating points with small or zero mass flux. Generally a pumping system consists of a turbomachine /pump, compressor, fan/,pipes, vessels, valves and throttles. If the pressure rise - mass flux characteristic of the turbomachine has a relative maximum, surge might occur. Surge not only causes noise and large mass-flux fluctuations but also can damage the whole system.

The unsteady Bernoulli equation along a stream tube s

$$\int_1^2 \frac{\partial c}{\partial t} ds + \frac{c_1^2 - c_2^2}{2} + \int_{p_1}^{p_2} \frac{dp}{\varrho} + g(z_2 - z_1) = 0$$

with the velocity c, the pressure p, the density ϱ and the gravitational acceleration g can be used to describe an important element of our system. For an incompressible flow through a pipe of length L and cross section A with $z_1 = z_2$ (fig.1) we get

$$\frac{L}{A}\frac{d\dot{m}}{dt} + p_2 - p_1 = 0 \qquad (1)$$

where the mass flux is $\dot{m} = c\,\varrho\,A$.

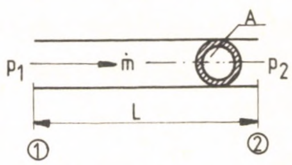

Fig.1: Pipe

If we apply the continuity, equation

$$c_1 \varrho_1 A_1 = c_2 \varrho_2 A_2$$

to a big plenum (fig.2) with the volume VOL, in which the pressure does not vary along any space coordinate and the fluid nearly rests, we get

$$\dot{m}_1 - \dot{m}_2 = \frac{d(\varrho \, VOL)}{dt}$$

or, if VOL = const.

and $$\frac{d\varrho}{dt} = \left.\frac{\partial \varrho}{\partial p}\right|_{isentropic} \cdot \frac{dp}{dt} = \frac{1}{a^2} \frac{dp}{dt}$$

finally:

$$\frac{dp}{dt} = \frac{\dot{m}_1 - \dot{m}_2}{VOL/a^2} \quad . \qquad (2)$$

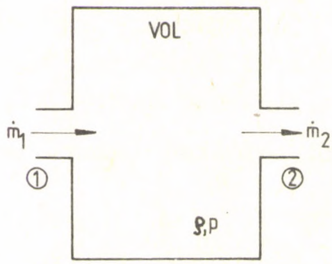

Fig.2: Plenum

For our purpose a fan can be described by its steady state mass flux - pressure rise characteristic $f(\dot{m})$. For dynamic problems, however, this is not completely correct. Greitzer [1] and Ohashi [2] proposed a simple model to take dynamic behaviour of the fan (at constant rotational speed of the impeller) in account. The non-steady pressure rise ϕ is modelled by a first order transient response

$$\frac{d\phi}{dt} = \frac{1}{T} \left(f(\dot{m}) - \phi\right). \qquad (3)$$

The time constant T depends on the impeller itself and its rotational speed and is found to be in the order of several rotor revolutions (fig.3)

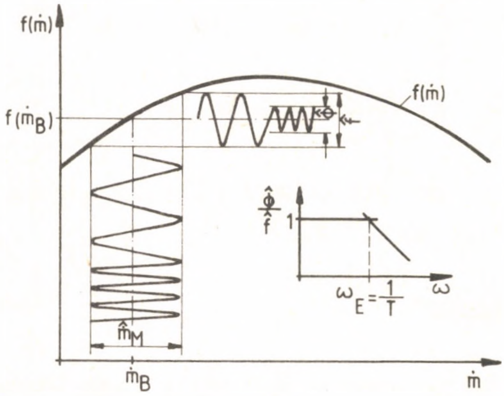

Fig.3: Model for the non-steady behaviour of the fan

A throttle used in our system always causes a pressure loss

$$\Delta p_D = \psi \,|\dot{m}_D|\, \dot{m}_D \,. \tag{4}$$

These four elements (pipe, plenum, fan, throttle) allow to describe the system shown in fig.4

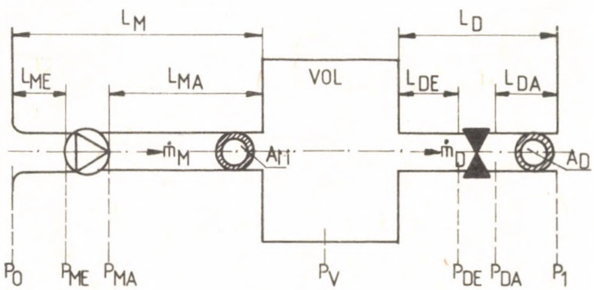

Fig.4: System

The adequate set of nonlinear (nonlinear, because of $f(\dot{m}_M)$ and $\psi|\dot{m}_D|\,\dot{m}_D$) but ordinary first order differential equations is:

$$\frac{L_M}{A_M}\,\frac{d\dot{m}_M}{dt} - \Phi + p_v - p_o = 0 \tag{5}$$

$$\frac{dp_V}{dt} - \frac{\dot{m}_M - \dot{m}_D}{VOL/a^2} = 0 \tag{6}$$

$$\frac{L_D}{A_D}\frac{d\dot{m}_D}{dt} + \psi\,|\dot{m}_D|\,\dot{m}_D - p_V + p_1 = 0 \tag{7}$$

$$T\frac{d\phi}{dt} - (f - \phi) = 0. \tag{8}$$

This system can be solved numerically by a Runge-Kutta or a predictor-corrector algorithm.

EXPERIMENTAL APPARATUS

The experiments were carried out on a test stand (fig.5) designed according to our model. The length L_M of the pipe and the volume VOL of the plenum can be varied. The pressure $p_V(t)$ in the plenum is measured with fast pressure probes, the mass-flux $\dot{m}_M(t)$ by means of an appropriate hot wire anemometer.

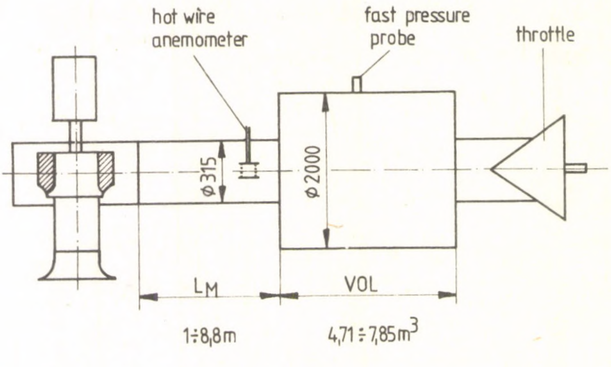

Fig.5: Test-stand

RESULTS

Theoretical surge-limit, stability

The set of equations (5) - (8) is nonlinear in the terms $f(\dot{m}_M)$

and $\psi|\dot{m}_D|\dot{m}_D = \psi\,\dot{m}_D^2$. In the second term we restrict ourselves to positive flux $\dot{m}_D$ through the throttle. These nonlinear functions are substituted by their series around the steady-state operational point. This steady-state point is defined by $d/dt = 0$ in Eqs. (5) - (8) and is denoted by the subscript "st". We have

$$\dot{m}_{Mst} = \dot{m}_{Dst}, \qquad \phi(\dot{m}_{Mst}) = f(\dot{m}_{Mst}) = \psi\,\dot{m}^2_{Mst} + p_1 - p_o$$

and

$$p_{vst} = f(\dot{m}_{Mst}) + p_o.$$

Using the following formulas and notations

$$x_1 = \dot{m}_M - \dot{m}_{Mst},\ x_2 = \dot{m}_D - \dot{m}_{Dst}, \qquad \alpha = \frac{df}{d\dot{m}_M}(\dot{m}_{Mst}), \tag{9}$$

$$x_3 = p_v - p_{vst},\ \ x_4 = \phi - f(\dot{m}_{Mst}),\ \beta = 2\,\psi\,\dot{m}_{Mst}$$

we have the transformed set of equations

$$\dot{\mathbf{x}} = A\mathbf{x} + \mathbf{g}(\mathbf{x}) \tag{10}$$

The dot denotes differentiation with respect to t, $\mathbf{g}$ stands for nonlinear terms, $\mathbf{x} = (x_1, x_2, x_3, x_4)$ and

$$A = \begin{pmatrix} 0 & -A_M/L_M & 0 & A_M/L_M \\ a^2/VOL & 0 & -a^2/VOL & 0 \\ 0 & A_D/L_D & -\beta A_D/L_D & 0 \\ \alpha/T & 0 & 0 & -1/T \end{pmatrix}.$$

According to a theorem (see p.314 [3]) the identically zero solution $\mathbf{x} \equiv 0$ of equation (10) is asymptotically stable if A is a real constant matrix with the characteristic roots all having negative real parts, $\mathbf{g}(\mathbf{x})$ is continuous and $\lim_{|\mathbf{x}|\to 0}\left|\frac{\mathbf{g}(\mathbf{x})}{\mathbf{x}}\right| = 0$. By the aid of the Routh-Hurwitz criteria one can determine the sufficient conditions of stability. As we found it too complicated to compute the Routh-Hurwitz criteria in the general case, we consider only three simple cases:

a./ $L_D = 0,\ T = 0$, i.e. $dx_3/dt = dx_4/dt = 0$

$$\alpha < \beta$$

and

$$\alpha\beta < \frac{a^2 L_M}{VOL.A_M}$$

are the conditions for stability in this case (see(9) for the notations α and β). The surge limit lies on the unstable branch of the fan's characteristic near to its maximum.

b./ $L_D = 0, \quad T > 0.$

In this case $\alpha < \beta$

$$\alpha\beta < \frac{a^2 L_M}{VOL.A_M}\left[1 + \frac{a^2}{VOL} T \left(\frac{A_M}{L_M} T + \frac{1}{\beta}\right)\right]$$

guarantee stability. The time constant T has a stabilizing effect.

c./ $L_D > 0, \quad T = 0.$ $\alpha < \beta$

is required again and also

$$\alpha\beta < \frac{a^2 L_M}{VOL.A_M}\left[1 + \lambda \frac{\alpha(1-\lambda)}{\beta - \alpha\lambda}\right]$$

where $\lambda = (L_D/L_M)(A_M/A_D)$. The existence of the second pipe between plenum and throttle is strengthening stability when $\lambda < 1$.

It has been impossible for us to compare theory with experiments because of errors in measuring surge limit.

Numerical results

Fig.7 shows typical numerically computed results. The dimensionless variables are defined as follows:

$$\dot{m}_M^* = \frac{\dot{m}_M - \zeta}{\Delta\dot{m}}, \quad p_V^* = \frac{p_V - \delta}{\Delta p}, \quad \tau = \omega_o t, \quad Dr = \frac{\Delta p}{\Delta\dot{m}^2}\psi^{-1}$$

where ζ, δ, $\Delta\dot{m}$, Δp are characteristica of the fan's steady state characteristic according fig.6.

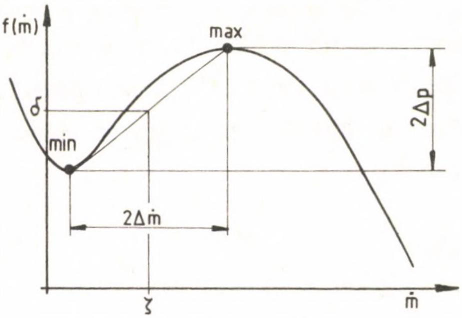

Fig.6: Characteristic of the fan

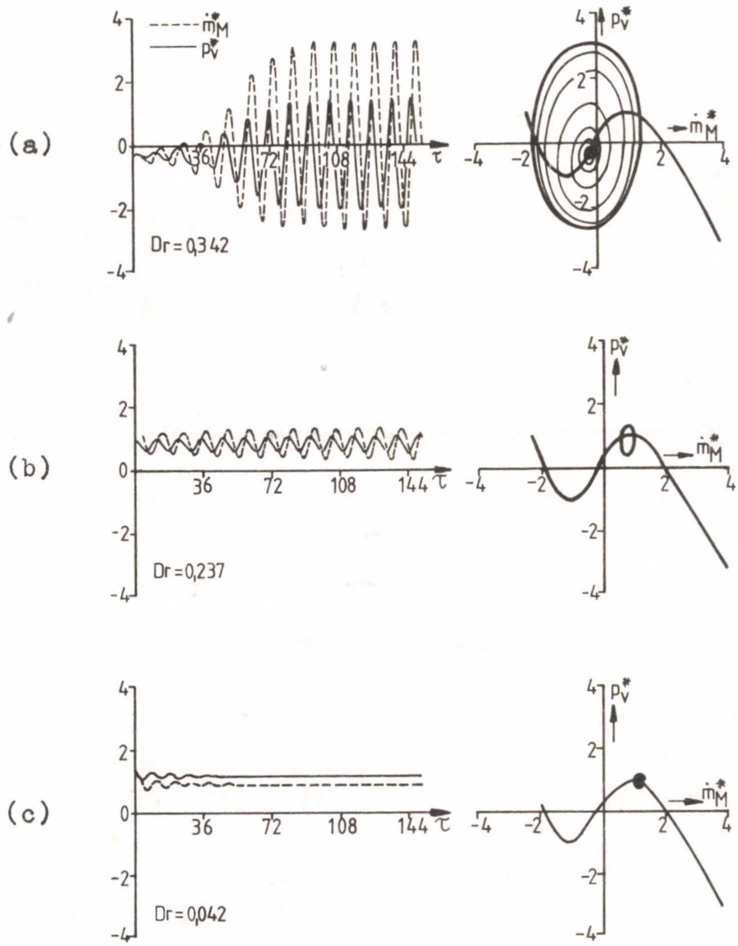

Fig.7: Typical numerical results

The same system is operated at three different operating points. If the operating point is stable, pressure and mass-flux return to the desired point on the characteristic after a small disturbance /case (c)/. If the operating point, however, is unstable, the system ends up in the so called limit cycle /case (a)/.

Experimental results

Fig.8 shows typical experimental results.

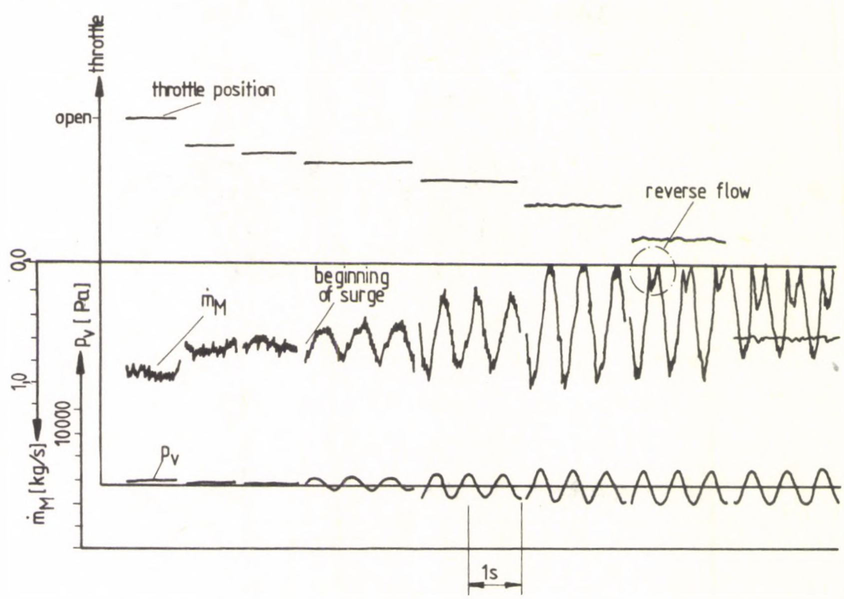

Fig.8 Typical experimental results

Pressure and mass-flux at eight points of operation are recorded for about three seconds. Clearly one can observe the beginning of surge. If the throttle is nearly completely closed,reserve flow through the pipe can be recognized.(The hot wire anemometer is not able to determine the flow direction.).

Fig.9 shows maximal pressure amplitude,the beginning of surge (Dr_{Krit}) and the surge frequency as a function of the pipe length L_M.Longer pipes stabilyze the system,the pressure amplitude, however, grows. Similarly, the influence of all other components of the system can be examined.

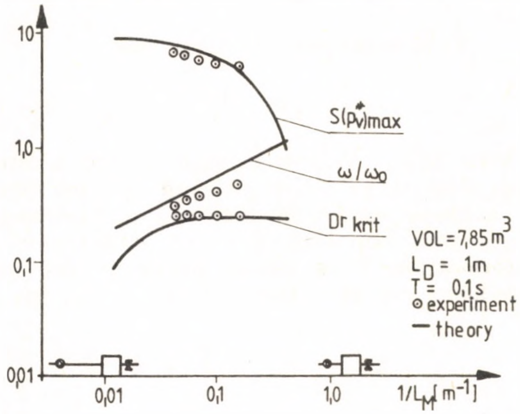

Fig.9: Maximal pressure amplitude, Dr_{Krit} and frequency as a function of L_M.

REFERENCES

[1] E.M.Greitzer: Surge and Rotating Stall in Axial Flow Compressors I and II, ASME Paper No. 75-GT-9 and -10,1975

[2] H.Ohashi: Analytical and Experimental Study of Dynamic Characteristics of Turbopumps, NASA Technical Note D-4298, 1968

[3] A.Coddington - N.Levinson:Theory of Ordinary Differential Equations, McGraw-Hill, New York, 1955.

Dipl.-Ing. Thomas Carolus
Institute of Fluid Mechanics and Fluid Machinery
T.U. Karlsruhe   Kaiserstrasse 12. D-7500 Karlsruhe 1

Kullmann László
Assistant
Department of Hydraulic Machinery T.U. Budapest
H-1521 Budapest, XI.

OPTIMAL STRUCTURAL DESIGN OF CENTRIFUGAL AND MIXED FLOW IMPELLERS

T. Chmielniak, G. Kosman

SUMMARY

The subject of this paper is the design of the centrifugal and mixed flow impellers. The base of optimizing the impeller is an adequate choice of criteria which in fan and compressor designing should above all take into consideration the criteria of thermodynamics, flow, stress and deformation. This paper presents the method of selection of the impellers constructional features in the aspect of strength.

INTRODUCTION

In the process of designing the fluid-flow machine it is necessary to select the following, main dimensions of the impeller (Fig. 1)

$$r_2,\ r_1,\ r_o,\ b = b(r),\quad h = h(r),\quad y = y(r),\quad e = e(r),$$
$$z,\ \beta = \beta(r),\quad s = s(r).$$

For the fan impeller (Fig. 1b) the description is simpler, since for example

$$e = 0,\quad h = \text{idem},\quad y = \text{idem}.$$

We assume that at first basing oneself on the thermodynamic-flow criteria, one calculates these dimensions which determine the parameters of flow of the designed machine. The remaining dimensions are calculated at the second stage of optimization taking into consideration the strength and technological criteria.

THE FORMULATION OF THE PROBLEM

We assume that basing oneself on the thermodynamic flow criteria the following dimensions were established

$$r_2,\ r_1,\quad b = b(r),\quad z,\ \beta = \beta(r) \tag{1}$$

The object of optimization remain

$$h = h(r), \quad x = x(r), \quad e = e(r), \quad s = s(r) \tag{2}$$

as well as the material of the impeller.

The application of mathematical programming to the considered problem requires the discrete description of the construction. To this end we represent the space of continuous independent variables $r \in (r_o, r_2)$ into the space of discrete variables r_i $(i=1,2,....,n)$ and instead of the function (2) we look for their values

$$h_i, y_i, e_i, s_i \qquad (i = 1,2,....,n) \tag{3}$$

in the points r_i (Fig. 2.I).

Let the variables (3) form the vector

$$\vec{X} = \left\{ h_1, h_2, ..., h_n, e_1, e_2, ..., e_n, ... \right\} = \left\{ x_1, ..., x_N \right\} \tag{4}$$

where N is the number of all the variables.

Assigning the axis of the coordinate system for each of the variables, we obtain the N dimensional space defined as the space of optimization. Sometimes the optimization is carried out only with reference to the dimensions for the assumed constructional form of the impeller. An example of such a defining of the space of optimization is shown in Fig. 2.II, 2.III and 2.IV.

As the objective function (the quality coefficient) we assume the mass of the impeller

$$m = \varrho \int_{r_o}^{r_2} (2\pi rh + zsb + 2\pi ry)\,dr \tag{5}$$

For the discrete description of the impeller shown in Fig. 2.I the objective function is the linear function of optimization variables

$$m = \varrho \frac{\Delta r}{2} \sum_{i=1}^{n-1} \left[2\pi (r_i h_i + r_{i+1} h_{i+1}) + z(s_i b_i + s_{i+1} b_{i+1}) \right] \tag{6}$$

If one is to assume the space of optimization as in Fig. 2.II and 2.III, then we obtain the non-linear objective function.

In detailed considerations we take into account two groups of constrains

a) strength constrains

$$g_{\sigma} = \sigma_{dop} - \sigma_{red,max} \geqslant 0 \tag{7}$$

or

$$g_{\omega} = \frac{\omega_g}{k} - \omega \geqslant 0 \tag{8}$$

The first condition postulates the maintaining of maximum stresses reduced below the permissible ones for a given material. The second condition concerns the bursting speed ω_g of the impeller,

b) technological, constructional constrains.

These constrains will be given separately for each analysed example. The exemplary constrains of this type are:

- the condition limiting the width of the impeller

$$g_l = l_{max} - (h_i + e_i + b_i + y_i) \geqslant 0 \tag{9}$$

- the condition limiting the thickness of the disk considering the production

$$g_h = h_i - h_{min} \geqslant 0 \qquad (i = 1,2,\ldots,n) \tag{10}$$

THE PROBLEMS CONCERNING THE SELECTION OF THE STRENGTH MODEL OF THE IMPELLER

The effective solution of the problem formulated earlier requires the acceptance of a suitable strength model of the impeller in order to define the condition (7) or (8). We shall consider three various approaches to this problem.

The disk-plated model

In order to calculate the stresses in the impeller one makes use of the theory of disks and circular plates with constructional orthotropy. It is assumed that the blades carry the loading and one takes into account the bending of the impeller. One assumes the hypothesis of plane sections according to which the cylindrical section of the unloaded impeller passes after the deformation to a cone.

The authors' own investigations in this domain were presented in the papers [1, 2].

The calculation of the stresses by finite elements method

At present there is a number of computer systems serving to solve strength problems by finite elements method. The Norwegian system SESAM-69 [3] may be given as an example. A number of programs serwing to analyse the stresses and strains of the construction enter into the composition of this system. Since the considered impeller disks are in most cases typical thin-walled constructions, the program denoted by the symbol NV331I was made use of to their analysis. The program is based on quadrangular or triangular plated, elements each having six degrees of freedom in every node.

The bursting speed of impeller

The problem concerning the valuation of bursting speed of the centrifugal impellers of fluid-flow machines was considered in the papers [1, 4]. The bursting speed of the impeller disk, is defined by the formulas:

- double-suction open impeller

$$\omega_g^2 = \frac{R_m \int_{r_o}^{r_2} h dr}{\varrho \int_{r_o}^{r_2} hr^2 dr + \frac{z m_1 r_s}{2\pi}} \tag{11}$$

- single-suction closed impeller

$$\omega_g^2 = \frac{\int_{r_o}^{r_2} (h^2 + 2by + 2hy + y^2) dr}{\varrho \int_{r_o}^{r_2} \left[r^2h^2 + \frac{zbsr}{\pi}\left(\frac{b}{2} + h\right) + 2r^2y\left(\frac{y}{2} + b + h\right) \right] dr} \tag{12}$$

THE SOLUTION OF THE FORMULATED PROBLEM BY MEANS OF MATHEMATICAL PROGRAMMING METHODS

In general case the problem formulated here is the non-linear problem of mathematical programming. Such a vector (4) should be calculated

$$\vec{X} = \vec{X}(x_1,\dots,x_N)$$

that

$$m(\vec{X}) = m_{min} \tag{13}$$

for the simultaneous satisfying of the conditions

$$g_r(\vec{X}) \geqslant 0 \qquad (r = 1,\dots,R) \tag{14}$$

where N is a number of variables, and R - a number of constrains.

In order to solve the formulated problem the iterative method of looking for the extreme with contraints was applied.

The method of calculations is based on Rosenbrock's algorithm which, however, was modified and enriched by including in it a number of positive features characteristic of other optimization algorithms, such as Powell's or Swann-Davies-Campey's algorithms.

The program in FORTRAN language, according to which the calculations were carried out, was given in the paper [5]. This program enters into the composition of the pack of the optimizing procedures of "OPTYMA" system.

In order to solve two-dimensional and simple three-dimensional problems the graphical method was applied. This method was treated as comparative for the iterative ones.

DESIGN OF THE DISK OF MIXED FLOW IMPELLER

Basing oneself on the thermodynamic - flow criteria the following values were received: (Fig. 3a)

$r_2 = 0{,}24$ m, $r_p = 0{,}048$ m, $r_o = 0{,}035$ m, $h_p = 0{,}065$ m,

the number of revolutions n = 8000 obr/min, $B = zV\,r_s/2\pi = 0{,}000061$.

The disk of impeller remain the object of optimization. The analysed constructional solutions of the disk were shown in Fig. 2.

The following limitations were taken into account:

- limitation (8) for k = 2,
- limitation (10) for $h_{min} = 0{,}004$ m.

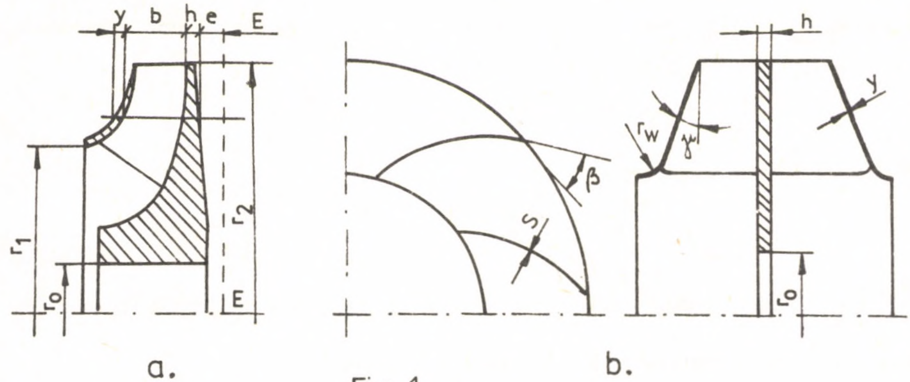

Fig.1

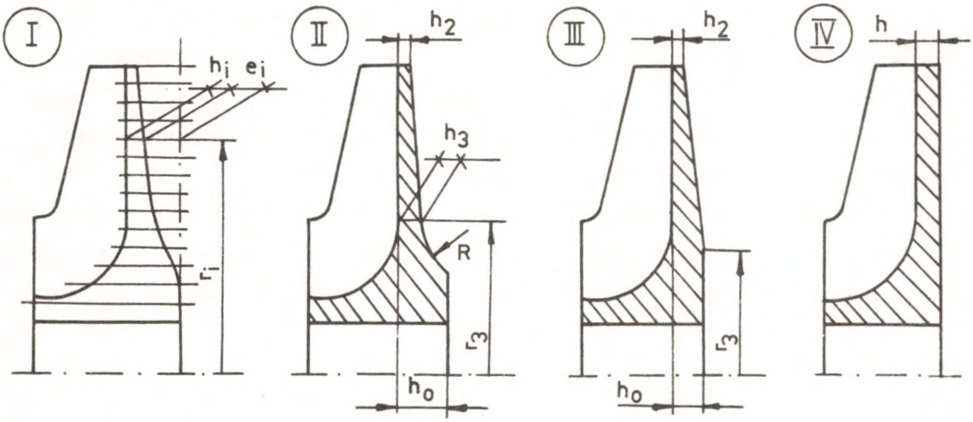

Fig.2

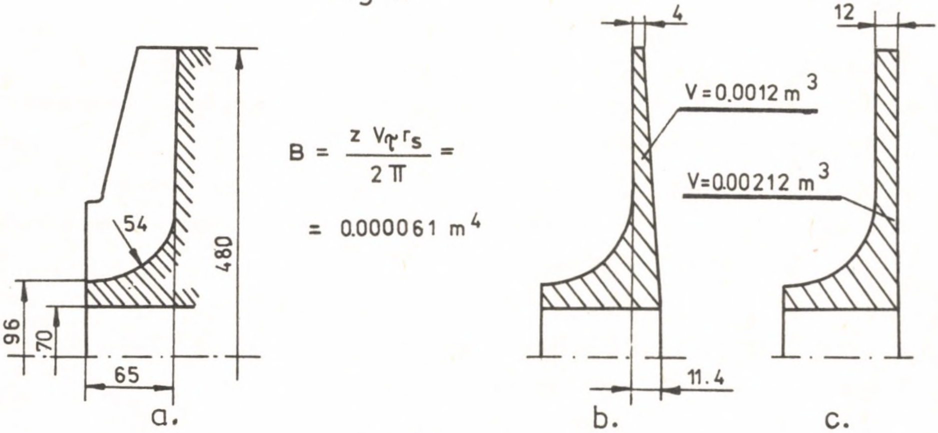

Fig.3

The results of optimization for version II and III (Fig. 2) were collected in Fig. 3b and for version IV in Fig. 3c. From the obtained results it follows that

$$m_{II} = m_{III}$$

and

$$\frac{\Delta m}{m} = \frac{m_{IV} - m_{III}}{m_{III}} * 100 = 75\%$$

AN EXAMPLE OF THE DESIGN OF THE FAN IMPELLER

The designed fan has a double-suction impeller.

Basing oneself on the thermodynamic-flow criteria the following values were received

$r_2 = 1{,}125$ m, $r_1 = 0{,}625$ m, $r_s = 0{,}81$ m, $r_w = 0{,}23$ m, $b_2 = 0{,}297$ m, the number of blades $z = 12 + 12$, the number of revolutions $n = 985$ obr/min, the mass of the blade $m_ł = 23{,}5$ kg.

There is a possibility of making the disks from the following materials St0, St35, 15HM, 18G2A.

The back disk is the disk with the constant thickness h and the radii r_2, r_o (Fig. 1b). Both h and r_o remain the object of optimization for various materials. The objective function (5) assumes the form

$$\bar{V} = \frac{m}{\pi\varrho} = h(r_2^2 - r_o^2) \tag{15}$$

The following limitations were taken into consideration

a. Limitation (8) for k = 2,

b. $$g_o = r_{o,max} - r_o \geqslant 0$$

where $r_{o,max} = 0{,}42$ m is determined by the radius r_1.

c. Considering the standardization of hubs r_o assumes descrete values from the set

$$\{0{,}26;\ 0{,}3;\ 0{,}34;\ 0{,}36;\ 0{,}38;\ 0{,}4;\ 0{,}42\}$$

d. Considering the standardized thicknesses of sheets h assumes discrete values from the set

$$\{0{,}001;\ 0{,}002;\ 0{,}003;\ 0{,}004;\ \ldots\}$$

Three versions of optimization were analysed in which the following limitations were taken into consideration:

Version 1 - limitations a and b,

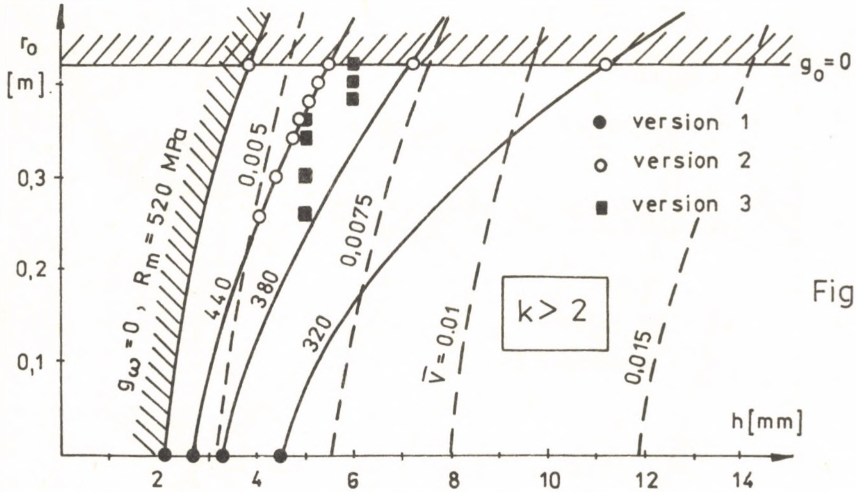

Fig.4

Table 1

Version 1, $h = f(R_m)$

R_m	MPa	320	380	440	520
h	m	0.0045	0.0033	0.0027	0.0021
r_0	m	0			
m	kg	139.6	102.4	83.3	65.2

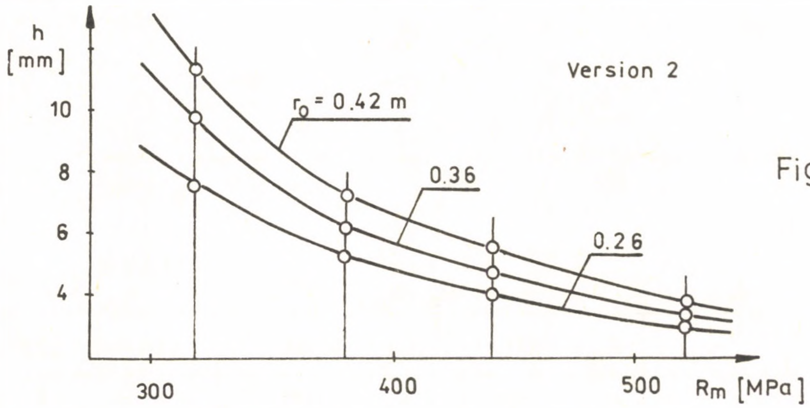

Fig.5

Table 2

Version 3 , $h = f(r_0)$ for $R_m = 440$ MPa

r_0	m	0.26	0.30	0.34	0.36	0.38	0.4	0.42
h	mm	5	5	5	6	6	6	6
k	–	2.11	2.07	2.02	2.04	2.07	2.05	2.03
m	kg	147.6	144.9	141.7	140.0	165.8	163.5	161.1

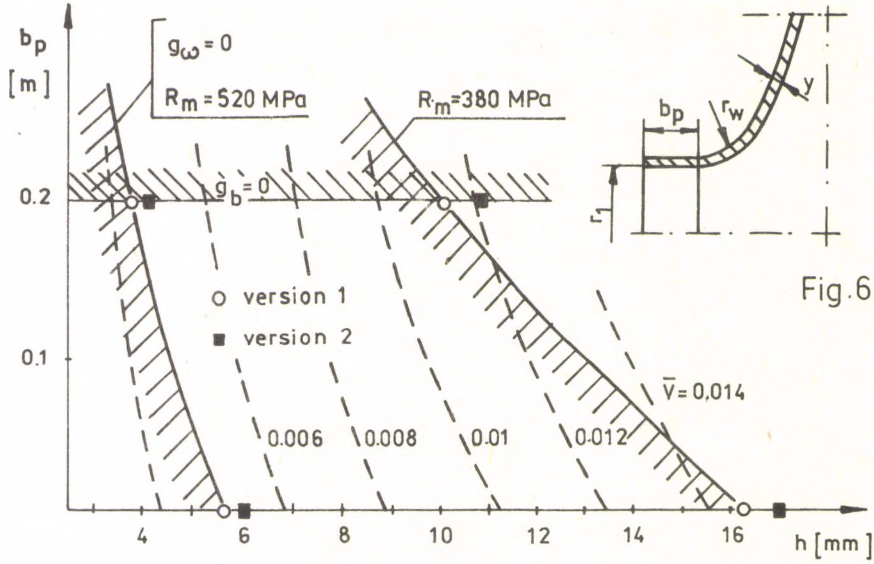

Fig.6

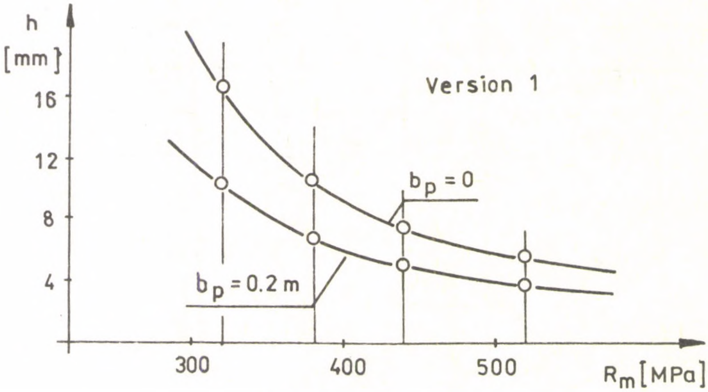

Fig.7

Table 3

Version 2 $\quad h = f(R_m, b_p)$

	R_m	MPa	320	380	440	520
$b_p = 0$	y	mm	17	11	8	6
	k	–	2.05	2.08	2.06	2.03
	m_t	kg	366.6	237.2	172.5	129.4
$b_p = 0.2$ m	y	mm	11	7	6	4
	k	–	2.09	2.06	2.11	2.02
	m_t	kg	305.0	194.1	166.4	110.9

Version 2 - limitations a, b and c,

Version 3 - limitations a, b, c and d.

The space of optimization was shown in Fig. 4. The results of optimization were collected in the table 1 and 2 and in Fig. 5.

From the obtained results it follows that the optimum thicknes of the disk increased together with the increase of the radius r_o. Also the mass of the disk corresponding to the optimum thicknes increases.

The analysed constructional solutions of the cover disk were shown in Fig. 6. The thickness y and the width of the ring b_p remain the object of optimization. Two versions of optimization were considered in which the following limitations were taken into account:

Version 1 - limitations a and

$$g_b = b_{p,max} - b_p \geqslant 0 \quad \text{for} \quad b_{p,max} = 0{,}2 \quad \text{m.}$$

Version 2 - limitations as in version 1 and the limitation d.

The space of optimization was shown in Fig. 6. The results of optimization were collected in the table 3 and Fig.7. Only the extreme values concerning the width of the ring were compared.

REFERENCES

1 KOSMAN G.: Thermostrength of fluid-flow machine. Gliwice 1982.

2 KOSMAN G.: The disk models in the calculation of the stresses in centrifugal impellers. Conference "The Industrial Fans", Gliwice 1974.

3 HORN S., MAGNUCKI K.: Stress determination in fans rotors by the finite elements method. Trans. of the Silesian Technical University, Gliwice 72/1979.

4 CHMIELNIAK T., KOSMAN G., WERBOWSKI T.: Analysis of the bursting loading of the radial fans impellers. Trans. of the Silesian Technical University, Gliwice 47/1973.

5 KERN F., SERAFIN D.: The program of Rosenbrock' method in Fortran language. Gliwice 1976.

CHMIELNIAK Tadeusz, Prof. dr hab. KOSMAN Gerard, Doc. dr hab.
Silesian Technical University
44-100 Gliwice, ul. Konarskiego 18
POLAND

AN ACOUSTIC CORRELATION METHOD FOR DETECTING CAVITATION EROSION

Pierre Courbière

Commissariat à l'Energie Atomique (CEA), France

ABSTRACT

For many years the CEA has conducted an on-going basic research program to characterize the parameters of sodium cavitation. The results of this effort have been used for the hydraulic design aspects of the Super Phenix fast breeder reactor assemblies.

The program was then oriented towards the analysis of cavitation erosion phenomena, which must be better understood to optimize the design and reliability of components such as valves and mechanical pumps.

This paper discusses work undertaken by the Fast Breeder Reactor Department at Cadarache in the context of this research and development program.

INTRODUCTION

The high-volume sodium flows required in fast breeder reactors have led to the design of flow lines and components, including valves and pumps, in which cavitation is liable to occur. This phenomenon must be avoided, not only because of the resulting acoustic noise but especially because of the erosion that can accompany it.

The Commissariat à l'Energie Atomique (CEA) therefore undertook a research program on sodium cavitation erosion motivated essentially by the importance of the phenomenon in the development of sodium pumps for French fast breeder reactors. Up to now, excessive safety margins on pump design specifications and restricted operating ranges have be considered necessary both because of the lack of a criterion characterizing incipient cavitation and because of the difficulties encountered in discriminating between potentially erosive cavitation flow and non-destructive cavitation flow conditions.

The research program covers two broad areas.

. Fundamental research using a sodium cavitation tunnel to characterize and determine the physical and dynamic parameters liable to produce cavitation erosion.

. Applied research on reduced-scale and full scale mockups to develop a measurement technique capable of detecting incipient cavitation at the pump impellers. Optical methods are not feasible in sodium, and an acoustic technique was therefore developed using the Cadarache sodium cavitation tunnel and subsequently adapted for industrial operation.

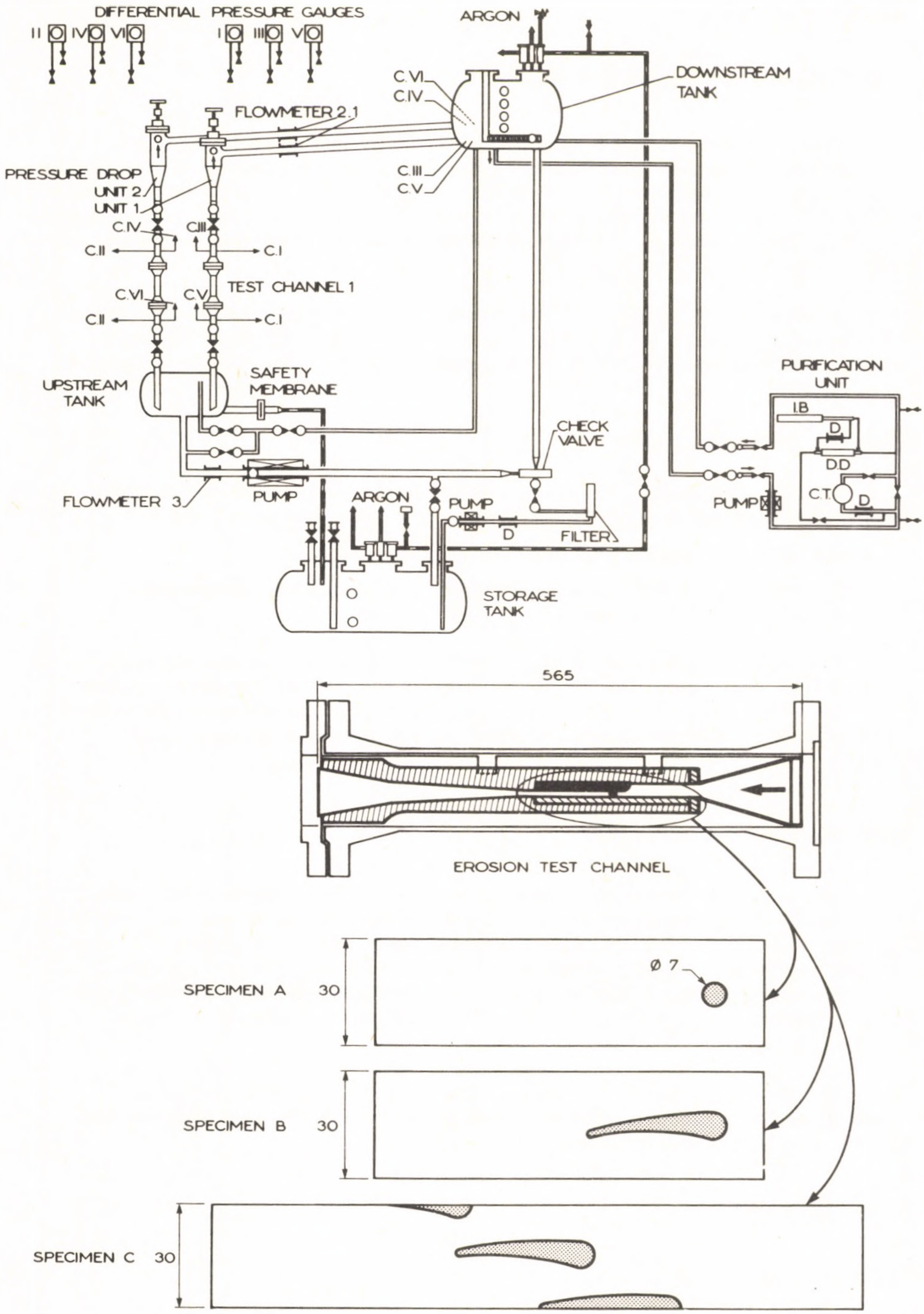

Fig. 1 CANADER CAVITATION TUNNEL

TEST EQUIPMENT

Sodium Cavitation Tunnel (CANADER)

The cavitation tunnel is shown schematically in Figure 1, and has already been described in references [1] and [2]. The test loop includes a pressure reducing unit at the test channel outlet, designed to set up a variable pressure drop, with a maximum pressure of 4 bars in the downstream tank and 15 bars in the upstream tank. The sodium temperature can be stabilized between 200° C and 550° C.

In addition to the conventional measurement instruments (flowmeters, fluid level probes and temperature sensors) the tunnel includes a bypass equipped with a system (PEGASO) designed to measure the sodium-entrained gas content.

Acoustic Detection System

The acoustic detection system can be used in both water and sodium loops. Two types of acoustic sensors were developed and are in use :

. barium titanate sensors wall-mounted on wave guides ;

. lithium niobate (TUSHT) sensors, capable of withstanding temperatures of up to 600° C, immersed in the fluid flow line.

The sodium flow noise level is monitored by an instrument package (CANASTA) that quantifies the sound level as the sum of the output pulses from a voltage-frequency converter ; this value is proportional to the sum of the integrals of all the signals recorded during each measurement cycle [2] [6].

SODIUM TEST PROCEDURE

Initially, the sodium cavitation tunnel erosion tests were conducted with flat test specimens on which cylindrical obstacles were placed. SHALNEY (URSS), VARGA and SEBESTYEN (Hungary) have already described this type of test procedure in water. Their findings showed that at high Reynolds numbers the type of cavitation erosion observed downstream from the cylindrical obstacle was equivalent to the erosion found in hydraulic systems [3] [4] [5].

In the second phase, the sodium flow obstacle was replaced by a vane-shaped test piece, and in the third phase by a triple vane assembly to study various forms of turbulent flow (Figure 1).

TEST RESULTS

Cavitation Threshold

Figure 2 plots the flow noise level, from subcavitating conditions to beyond the onset of cavitation, versus the Thoma number :

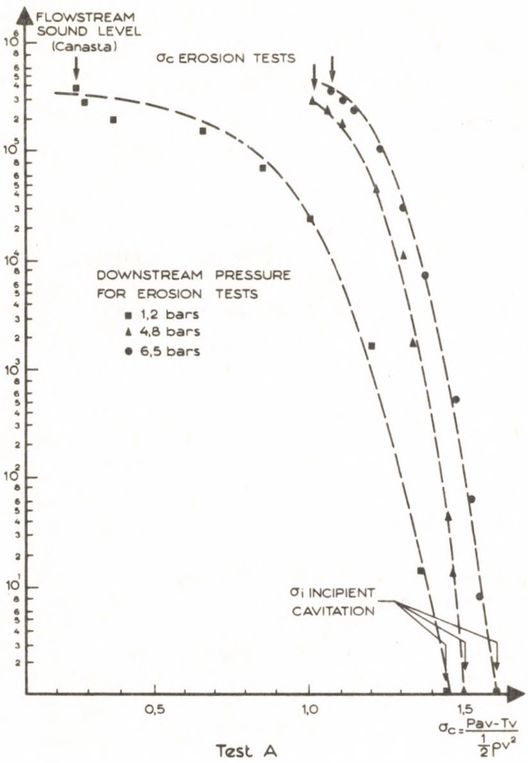

Test A

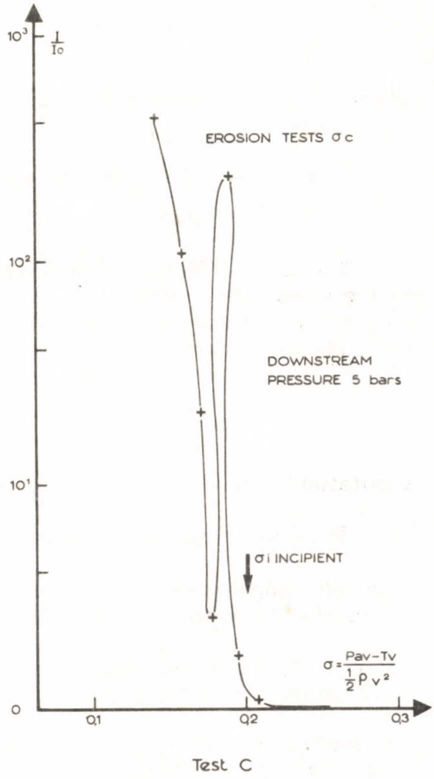

Test C

Fig. 2 CANADER _ SODIUM CAVITATION TUNNEL _ EROSION CHANNEL

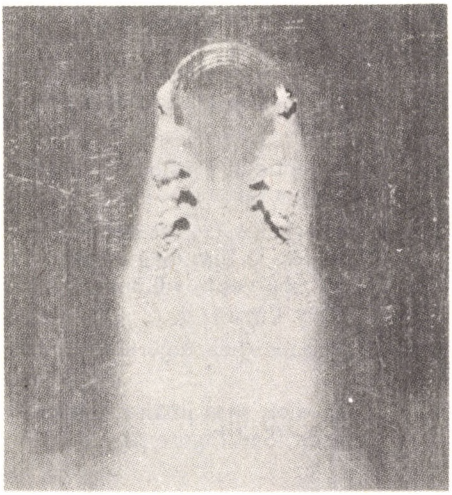

Upper specimen

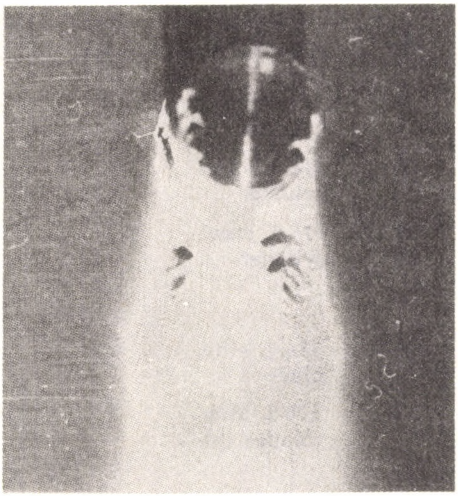

Lower specimen

Fig. 3 TEST A

$$\sigma = \frac{P_{av} - T_v}{\frac{1}{2}\rho V^2}$$

where P_{av} : pressure measured downstream from the test channel,

V : sodium flow velocity past the obstacle,

T_v : sodium vapor pressure ,

ρ : sodium density.

The CANASTA system was used to monitor the flow noise as a function of the sodium flow velocity. This system revealed a characteristic point of incipient cavitation, and made it possible to define the experimental conditions for erosion testing.

Cavitation Erosion

The experimental conditions were the following :

- sodium temperature : 400° C, corresponding to the pump operating temperature in the Phenix and Super Phenix reactors,
- Pav, sodium pressure downstream from the test channel : variable from 1.2 bar to 6 bars for differer⁺ .‹periments,
- V, sodium flow velocity through the necked-down sections : 33m/sec for a flow rate of 6l/sec.

The test results are summarized in the following chart.

TEST N°	TEST SPECIMEN	P_{av} (bars)	DURATION (hours)	REMARKS
A1	316 steel cylinder	1.2	1500	No erosion ; trace of wake zone
A2	316 L steel cylinder	4.8	1500	Superficial erosion ; incipient pigmentation
A3	316 L steel cylinder	6.5	560	Erosion with pitting in a recess 2.5cm long ; max pitting depth : 0.9mm (See Figure 3)
B	316 L steel blade	6	1000	Erosion (See Figure 4)
C	316 L steel blades (3)	5	1000	Erosion with pitting 0.8mm deep (See Figure 5)

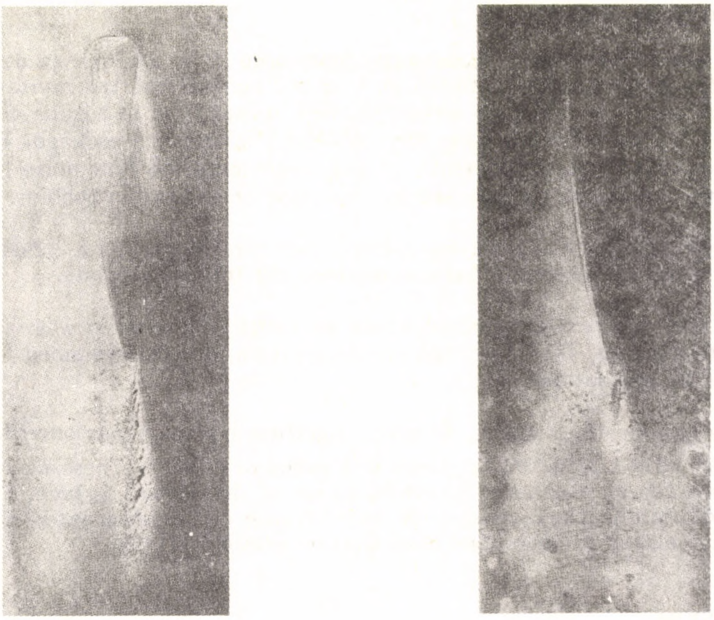

Upper Lower

Fig. 4 TEST B

Upper Lower

Fig. 5 TEST C

Cavitation Noise Analysis

The experiments were acoustically monitored in an attempt to develop a means for discriminating between erosive and non-destructive cavitating flow. Noise spectrum integrals were recorded in real time at regular intervals throughout the experiments using the CANASTA instrument package. The resulting quantified noise spectrum integral represents the flow noise intensity and thus the sound energy released by implosion of cavitation bubbles.

Observations of the resulting energy spectrum integral in a ±2kHz frequency band centered on 40kHz confirmed the following points.

- for the 1500-hour experiments in which no destructive erosion was visible on the test pieces, the cavitation noise spectrum integral remained constant throughout the test ;

- for experiments A3, B and C, in which significant erosion was observed, the noise level fluctuated as shown in Figures 6, 7 and 8. These noise variations can be attributed to modification of the eroded surface. The phases of stabilization, attenuation and increase in the noise intensity are certainly related to variations in cavitation erosion. [2] [3].

CONCLUSION

While the cavitation erosion mechanism is far from being elucidated, especially in sodium flow, the research program discussed in this paper has revealed a number of points not previously emphasized.

- The pressure is as important as the velocity in cavitating flow conditions.

- Acoustic detection methods are capable of discriminating between erosive and non-destructive cavitating flow. This result alone is enough to justify the current effort on sodium cavitation erosion in order to develop industrial-scale applications.

On the basis of the findings obtained with sodium, the on-going research program is now concentrated in three major areas :

- scale effects, for which no basic law is available for water or sodium flow ;

- the effects of various parameters, including pressure, sodium temperature and fluid velocity ;

- the influence of the entrained gas content in the sodium on cavitation erosion.

Fig. 6 Test A3

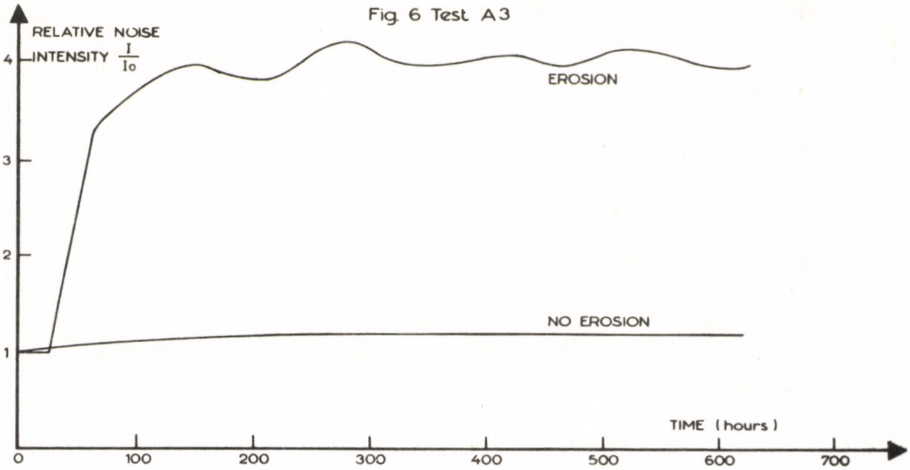

Fig. 7 Test B

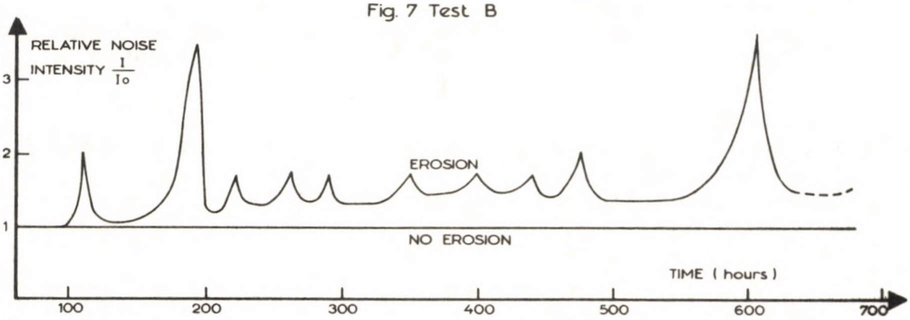

Fig. 8 Test C

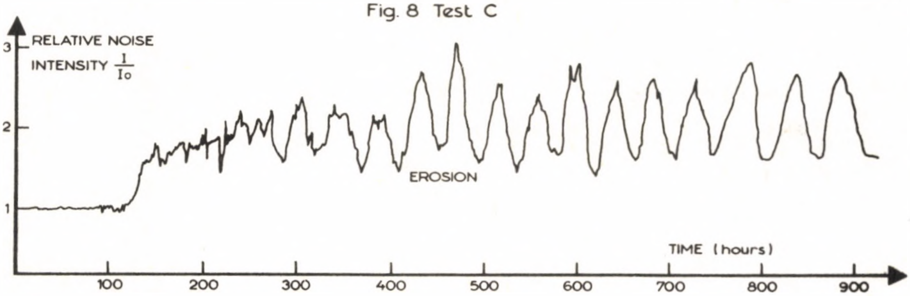

CAVITATION NOISE INTENSITY VERSUS TIME

REFERENCES

1 P. COURBIERE
Sodium Cavitation Testing
6th Conference on Fluid Machinery, Budapest, 1979

2 P. COURBIERE
Cavitation Erosion in Sodium Flow
ASME Meeting, Boulder, June 1981

3 K.SHALNEY, J. VARGA, G. SEBESTYEN
Scale Effect Investigation of Cavitation Erosion Using the Energy Parameter
Proceedings of the ASTM Symposium ASTM N° 408
Atlantic City, N.J., June 26-July 1, 1966, pp. 221-235

4 K. SHALNEY
PMTF, USSR, (1962)4, 121-128

5 J. VARGA, G. SEBESTYEN
Experimental Investigation of Some Properties of Cavitating Flow
Periodica Polytechnica Engineering, Budapest, Vol 9, N° 31965

6 P. COURBIERE
Acoustic Methods in Sodium Flow for Characterizing Pump Cavitation and Noise-Erosion Correlations
ASME Winter Meeting, Phoenix, Nov 14-19, 1982

P. COURBIERE

C.E.N. Cadarache

DRNR/STRA

B.P. 1

13115 SAINT PAUL LEZ DURANCE

FRANCE

CALCULATION OF PUMP EFFICIENCY FROM MODEL TEST RESULTS

J. Csemniczky

Applying the scaling up formule one has to take into account that these are related to the hydraulic efficiency only. The change of volumetric efficiency can be disregarded when a carefully designed model is tested. Correction is needed, however, due to the dissimilarity of constructions, namely additional hydraulic losses, mechanical losses and possibly additional volumetric losses have to be considered. A procedure for determining the efficiency and performance parameters of a full-size pump is presented and the estimation of mechanical losses is discussed in detail.

INTRODUCTION

The prediction of the performance characteristics of a full-size pump from model test results means - strictly taken - the calculation of H(Q), P(Q) curves at constant speed n above the whole pumping zone, that is from Q=0 to H=0. Cavitation-free operation is considered and the case of liquids of high viscosity is not examined. Turbulent flow inside the pump, typical at large Re numbers is assumed.

Publications widely discuss the scale effect problem, internationally coordinated efforts are made to develop the accuracy and reliability of the prediction methods. One has to keep in view, however, that the scaling up formule are valid for the hydraulic efficiency only and for working conditions not very far from the b.e.p. of the pump. The good estimation of additional losses is not elaborated thoroughly.

A procedure for determining the efficiency and performance parameters of full-size pumps is presented in the following, which is based on the literature and on a few reasonable consideration.

HEAD, POWER AND HYDRAULIC EFFICIENCY

In the region of turbulent flow, at higher Re numbers, the affinity law is true with very good approximation for the head [1], [3], [6]. The better efficiency appears due to the decreasing of power P.

For the head:

$$H = H_m \cdot \frac{D^2 \cdot n^2}{D_m^2 \cdot n_m^2} \qquad \dots (1)$$

where index m denotes the model parameters. D is a characteristic diameter and n is the speed in RPM.

The discharge calculated also with affinity law:

$$Q = Q_m \cdot \frac{D^3 \cdot n}{D_m^3 \cdot n_m} \qquad \dots (2)$$

For the boundaries of pumping zone:

$H=0$	where	$H_m=0$
$Q=0$	where	$Q_m=0$

and therefore

$\eta=0$	where	$\eta_m=0$

The hydraulic losses are caused by eddy, separation and by skin friction. The latter depends on the Re number /or on the surface roughness/ while the first group of losses is practically independent of the Re number of turbulent flow. These facts are explained by the formula known from literature [2], [5]:

$$\frac{1-\eta}{1-\eta_m} = 1 - V + V \cdot \left(\frac{Re_m}{Re}\right)^{1/\alpha} \qquad \dots (3)$$

where V and α do not depend much on the pump type, however, V has to change when the working point moves off the b.e.p. As $\eta=0$ at $\eta_m=0$, the value of V must be zero, too at this condition.

Let us consider the common simple method by which the scaling up is calculated for the b.e.p. and the ratio of efficiencies is kept constant:

$$\eta = \eta_m \cdot \frac{\eta_{opt}}{\eta_{m\,opt}} \qquad \ldots (4)$$

where index opt denotes the values at b.e.p.
Be V_{opt} is the value of V at the b.e.p. then the changing of V can be expressed as follows:

$$V = V_{opt} \cdot \frac{\eta_m}{1 - \eta_m} \cdot \frac{1 - \eta_{m\,opt}}{\eta_{m\,opt}} \qquad \ldots (5)$$

The lower is the model efficiency, the smaller is the value of V. The simple formula (4) gives well the nature of parameter V.
The power for the full-size machine:

$$P = \frac{\varrho \cdot g \cdot Q \cdot H}{\eta} \qquad \ldots (6)$$

ADDITIONAL LOSSES

There may be differences between the construction of model and real pump, which take place as additional hydraulic losses, for example: loss in column pipe and elbow at vertical propeller pump, the loss due to diffusor placed after the volute case of a radial pump, etc. The geomatrical similarity is not fulfilled for these parts. A "pump bowl" is defined to overcome this difficulty. The pump bowl is the main part of the pump for which the similarity is valid and the further parts are taken into account by additional hydraulic losses which vary as the square of the flow for a given machine. The separation of volumetric loss from hydraulic losses can be avoided when the similarity is approximated well for the clearances inside the pump. The same is true for the disc friction losses. When a small fraction of pump capacity is used for cooling the pump bearing, this part is considered as additional volumetric loss. Differences on the clearances or on other details effecting

volumetric loss can be taken into account approximately also in form of additional volume' '~ 'oss.
The scaling up formule can not be .ppl:ed for the mechanical losses. Up-to-date model measurements do not involve mechanical loss or, at last, the mechanical loss of the model is kept at a minimum and "filtered out" by calculation. This net model power is taken at scaling up and the mechanical loss of full-size machine is added to the power calculated by equations (1)÷(6).
The components of mechanical losses; the stuffing box and bearing losses can be calculated well when the operating conditions and the details of construction are exactly known. When these informations are not available, a simple empirical formula can be applied, which is based on a few measured data found in literature and on some tendencies, considerations as follows:

a/ One part of mechanical loss depends on the hydraulic forces, the second part is the function of speed only. The first part can be represented by a torque assumed proportional to the square of speed, the torque for the second part is constant.
b/ When a pump is running at lower speed, than the designed one, the mechanical efficiency decreases.
c/ Mechanical loss is increasing with the number of stages at multistage pump. The "characteristic power" of a pump from the aspect of mechanical loss is the power required by one impeller.
d/ The higher is the rated power of a certain pump type, the better is the mechanical efficiency, usually. The constructional possibilities are more favourable for a larger pump.
The following equation meets the requirements above.

$$1-\eta_{mech}=K_2\left[0{,}5+0{,}5\sqrt[3]{\frac{K_1}{P_n}}\cdot\left(\frac{n_n}{n}\right)^2\right] \quad \dots (7)$$

where P_n is the nominal power of one impeller at the designed speed n_n and n is the actual speed. For the parameters:

$$K_1 = 50\ \text{kW} \qquad \text{and} \qquad K_2 = 0{,}005 - 0{,}020 \qquad \dots (8)$$

where the lowest value for K_2 is attached to pumps with mechanical seal and with perfectly lubricated bearing. The highest K_2 value belongs to pumps with conventional shaft packing and with loaded bearings running submerged in the delivered water.

REFERENCES

[1] Csanady, G.T. — Theory of Turbomachines, McGraw - Hill, 1964

[2] Hutton, S.P., Fáy, Á. — Scaling-up head, flow and power curves for water turbines and pumps, IAHR Symposion, 1974 Wienna

[3] Fáy, Á. — Theory for the Reynolds number effect on the head and power of hydraulic machines, V-th Conf. of Fluid Machinery, 1975 Budapest

[4] Csemniczky, J. — Közelitő módszer radiális és félaxiális szivattyuk valóságos jelleggörbéinek meghatározására, Kandidátusi disszertáció, 1975 Budapest

[5] Fáy, Á. — High-accuracy modelling of hydraulic machinery, Diamond Jubilee Symposium, 1976 Poona

[6] Csemniczky, J. A simple flow pattern for computing the boundary layer on the performance characteristics of radial and mixed-flow pumps
Conference HYDRO-TURBO 76
1976 Brno

[7] Csemniczky, J. Léptékhatás figyelembevétele örvényszivattyuknál
Ganz-MÁVAG VKT 79. sz.
1978 Budapest

dr J. Csemniczky
Ganz-MÁVAG
H-1967 BUDAPEST
HUNGARY

ON THE FOUR QUADRANT CHARACTERISTICS OF CENTRIFUGAL PUMPS

J. Csemniczky

Analysing the hydraulic transients of a pumping statio , complete pump characteristics are needed. Some of them found in literature are compiled in a unified form and a few characteristics not published earlier are presented. The runaway working conditions as an important part of abnormal pump operation are shown by collecting data from various sources including GM test results.

INTRODUCTION

The starting or stopping of pumps causes transients in the pipeline of pump station. In order to calculate this phenomenon, the complete pump characteristics are needed. There are not many four-quadrant characteristics available in the literature. For a long period Kittredge, Swanson and Knapp's data were found merely in different forms of presentation. A suitable method for storing characteristics in digital computer has been developed by Suter[3]. The same method is applied here in a somewhat modified form. By using the dimensionless variables, cavitation-free conditions and the validity of affinity laws are presumed.

Strictly taken, the four-quadrant characteristics measured at stationary conditions are approximations only, when the speed and/or discharge are changing[10]. Comparisons of the calculations and test results show, however, that the approximation is good in practical cases and the deviations may be attributed to the simplifications of the calculation of other parts of the system.

FOUR-QUADRANT CHARACTERISTICS

The relation between the performance parameters is shown in Fig.1.

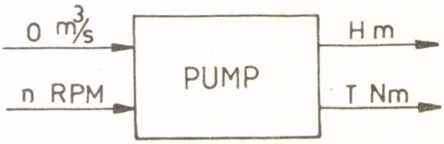

Fig.1

The discharge Q, speed n, head H and shaft torque T are used here in dimensionless form related to the rated values /index R/.
An angle γ is defined as

$$\gamma = \operatorname{atan} \frac{Q/Q_R}{n/n_R} \qquad \ldots /1/$$

for characterising the working point in the four quadrants.
The head may be written as

$$H = H_R \cdot h^*(\gamma) \cdot \frac{(Q/Q_R)^2 + (n/n_R)^2}{2} \qquad \ldots /2/$$

The torque

$$T = T_R \cdot \tau^*(\gamma) \cdot \frac{(Q/Q_R)^2 + (n/n_R)^2}{2} \qquad \ldots /3/$$

The specific head h^* and torque τ^* depend on the angle γ only. At the b.e.p. of the pump /at the rated values/:

$$\gamma = \pi/4 \qquad h^* = 1 \qquad \tau^* = 1 \qquad \ldots /4/$$

There are pump /P/, turbine /T/ and energy dissipation /D/ zones according to the signs of Q.H and n.T products /the fourth sign combination would be perpetuum mobile/. Taking the b.e.p. of pumping zone and changing the sign of Q and n we get a point of the turbine zone [11]. At the boundaries of pumping zone one factor of Q.H product becomes zero. Similarly the n=0 and T=0 give the boundaries of turbine regime. The pump and turbine zone must be separated by a dissipation zone, it comes from the existence of loss at energy conversion.
The operation zones are demonstrated in Fig.2. The axial flow pump differs from a radial one in the position of reversed pump zone /at about $\gamma = \pi$ /. For good measure

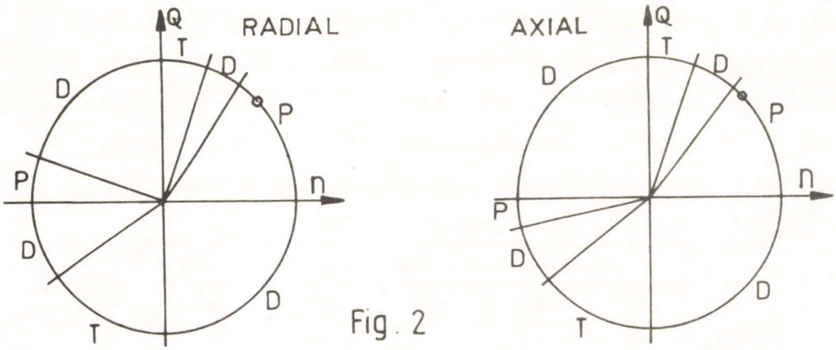

Fig. 2

one can add that the figures are related to backward curved impeller vanes. Assuming forward curved vanes, we would get two new figures, which differ from the previous ones in the position of the reversed turbine zone /at about $\gamma = \pi/2$ / [8].

PUMP CHARACTERISTIC DATA

$\gamma°$	$n_q = 25$		$n_q = 147$		$n_q = 261$	
	h^*	τ^*	h^*	τ^*	h^*	τ^*
-180	1.26	-1.36	-1.38	-2.78	-4.30	-4.40
-165	1.27	-0.48	-0.67	-1.64	-2.47	-2.77
-150	1.13	0.04	-0.03	-0.85	-1.10	-1.43
-135	1.01	0.46	0.38	0.00	0.13	-0.15
-120	1.02	0.98	1.00	1.06	1.11	1.00
-105	1.17	1.45	2.39	2.50	1.42	1.11
- 90	1.38	1.72	4.37	4.23	2.16	1.32
- 75	1.58	1.74	5.65	5.37	3.27	2.60
- 60	1.75	1.50	6.00	5.30	4.60	3.98
- 45	1.98	1.04	5.26	4.18	6.33	5.52
- 30	2.23	0.70	4.85	3.70	7.14	6.00
- 15	2.48	0.70	4.50	3.48	6.76	5.05
0	2.58	0.98	3.85	2.97	5.60	3.95
15	2.38	1.14	2.73	1.94	3.94	2.83
30	1.80	1.22	1.72	1.39	2.56	1.65
45	1.00	1.00	1.00	1.00	1.00	1.00
60	0.15	0.46	-0.20	0.12	-0.55	-0.32
75	-0.58	-0.15	-1.59	-1.20	-1.64	-1.16
90	-1.06	-0.70	-3.12	-2.85	-2.00	-1.20
105	-1.30	-1.83	-3.55	-4.50	-3.17	-2.85
120	-1.17	-2.63	-3.28	-5.15	-4.42	-4.62
135	-0.80	-3.02	-2.62	-4.85	-5.40	-5.80
150	0.00	-2.88	-2.20	-4.25	-5.72	-6.20
165	0.80	-2.28	-1.88	-3.72	-5.50	-5.82
180	1.26	-1.36	-1.38	-2.78	-4.30	-4.40

Table I.

The data contained in Table 1. are taken from Ref [1] and can be found in various forms in literature. Additional data in Table II. are taken from Ref [2] and Ref [4]. Some portions of the characteristics are missing, however, the most important parts are given. Table III. contains data not published earlier.

γ°	$n_q = 33$		$n_q = 48$		$n_q = 91$	
	h^*	τ^*	h^*	τ^*	h^*	τ^*
-180	-	-	0.98	-0.90	-	-
-165	1.15	-0.28	1.07	-0.33	-	-
-150	1.08	0.20	1.05	0.18	0.75	-0.31
-135	0.97	0.75	1.06	0.57	0.80	0.43
-120	1.07	1.30	1.10	0.91	1.23	1.15
-105	1.33	1.85	1.18	1.09	1.78	1.88
- 90	1.57	2.22	1.27	1.20	2.22	2.40
- 75	1.74	2.28	1.43	1.28	2.58	2.75
- 60	1.85	2.03	1.68	1.35	2.70	2.76
- 45	1.90	1.42	2.00	1.27	2.67	2.43
- 30	1.95	0.90	2.36	1.10	2.60	1.83
- 15	2.05	0.78	2.72	1.01	2.80	1.68
0	2.15	0.98	2.83	1.23	2.80	1.60
15	2.02	1.08	2.49	1.43	2.47	1.52
30	1.63	1.11	1.85	1.35	1.57	1.20
45	1.00	1.00	1.00	1.00	1.00	1.00
60	0.12	0.68	-0.14	0.42	-0.28	0.35
75	-	-	-	-	-	-
90	-	-	-	-	-	-
105	-	-	-	-	-	-
120	-	-	-	-	-	-
135	-	-	-1.57	-	-	-
150	-	-	-0.40	-1.90	-	-
165	-	-	0.52	-1.41	-	-
180	-	-	0.98	-0.90	-	-

Table II.

RUNAWAY SPEED

The runaway speed appears at the limit of turbine regime where the torque is zero. With the γ_0 angle belongs to this point:

$$\tau^*(\gamma_0) = 0 \qquad \ldots /5/$$

γ°	$n_q = 135$		$n_q = 188$		$n_q = 249$	
	h^*	τ^*	h^*	τ^*	h^*	τ^*
-180	-1.18	-1.81	-2.60	-3.95	-2.91	-2.91
-165	-0.45	-1.12	-1.58	-2.50	-1.77	-1.99
-150	0.11	-0.53	-0.63	-1.00	-0.75	-1.04
-135	0.76	0.45	0.56	0.28	0.46	0.11
-120	1.88	1.98	2.18	1.90	2.16	1.77
-105	3.38	3.78	3.98	3.83	4.15	3.72
- 90	5.05	5.40	5.74	5.78	6.76	5.85
- 75	6.05	6.06	7.05	7.20	9.08	7.45
- 60	6.10	5.92	7.92	7.62	10.16	8.00
- 45	5.68	5.33	8.23	7.67	10.29	8.00
- 30	4.94	4.37	7.90	7.20	9.85	7.50
- 15	4.15	3.32	6.77	6.22	8.73	6.27
0	3.34	2.44	5.20	4.79	6.66	4.66
15	2.55	1.90	3.57	3.12	4.20	3.22
30	1.89	1.58	2.30	1.90	2.42	2.15
45	1.00	1.00	1.00	1.00	1.00	1.00
60	-0.66	-0.05	-0.80	-0.30	-0.94	-0.57
75	-3.15	-1.33	-3.75	-2.57	-3.50	-2.78
90	-5.43	-2.61	-6.43	-4.52	-5.36	-4.76
105	-6.46	-3.72	-7.17	-5.35	-6.40	-5.94
120	-6.56	-4.24	-7.12	-5.60	-6.70	-6.35
135	-5.80	-4.05	-6.41	-5.55	-6.32	-6.03
150	-3.95	-3.42	-5.15	-5.31	-5.33	-5.12
165	-2.27	-2.60	-3.77	-4.80	-4.12	-4.00
180	-1.18	-1.81	-2.60	-3.95	-2.91	-2.91

Table III.

Fig.2. shows two runaway conditions according to the two turbine regimes. The negative runaway speed where the flow is negative, too, has greater practical significance.

The runaway speed itself is defined as the speed at rated head and zero torque.

$$H_0 = \pm H_R \qquad \dots /6/$$

From equations /1/,/2/ the runaway speed related to the rated value:

$$n_0/n_R = \frac{1}{\cos \gamma_0} \sqrt{\frac{2}{|h^*(\gamma_0)|}} \qquad \dots /7/$$

The flow in this point:

$$Q_0/Q_R = n_0/n_R \cdot \tan \gamma_0 \qquad \dots /8/$$

Data from various publications and from GM tests are given in Table IV. The lines 1-9 originate from the

No	τ_0^*	h_0^*	n_0/n_R	$\tau_0^{\bullet}$	$h_0^{\bullet}$	n_0/n_R	Pump type	n_q	Ref
1	-150	1.10	-1.17	71.7	-0.46	0.65	D	25	1
2	-135	0.40	-1.58	61.0	-0.35	1.16	M	146	"
3	-133	0.30	-1.76	56.5	-0.22	1.66	P	261	"
4	-155	1.10	-1.22	-	-	-	S	33	4
5	-156	1.05	-1.26	69.3	-1.07	0.48	D	48	5
6	-144.5	0.76	-1.32	-	-	-	MS	71	4
7	-140.8	0.42	-1.69	59.4	-0.58	0.95	P	135	Aut.
8	-138.1	0.33	-1.83	57.3	-0.39	1.22	P	188	"
9	-136.5	0.30	-1.87	55.3	-0.21	1.76	P	249	"
10	-140.7	1.11	-1.04	-	-	-	MS	23	1
11	-144.9	1.15	-1.08	-	-	-	MS	24	"
12	-	-	-1.17	-	-	-	MS	25	"
13	-153.9	1.43	-1.06	73.3	-0.68	0.49	S	34	"
14	-149.0	0.94	-1.25	73.3	-0.73	0.48	S	38	"
15	-154.0	1.07	-1.23	-	-	-	S	41	"
16	-157.9	1.13	-1.23	-	-	-	S	41	"
17	-147.4	0.91	-1.25	63.4	-0.64	0.79	D	68	"
18	-152.8	1.81	-0.93	-	-	-	S	15	7
19	-148.1	1.51	-0.98	-	-	-	S	18	"
20	-150.0	1.25	-1.10	-	-	-	MS	20	"
21	-148.7	0.89	-1.28	-	-	-	S	48	"
22	-154.1	0.79	-1.43	-	-	-	S	57	Aut.
23	-149.0	0.68	-1.47	-	-	-	M	91	"
24	-142.6	0.63	-1.42	-	-	-	M	94	"
25	-138.1	0.54	-1.43	-	-	-	P	128	"
26	-137.0	0.43	-1.58	-	-	-	P	155	"
27	-	-	-	57.6	-0.35	1.28	P	172	"
28	-	-	-	57.4	-0.32	1.35	P	177	"
29	-	-	-	56.1	-0.25	1.58	P	218	"

D = double suction, M = mixed flow, P = propeller,
S = single suction, MS = multistage

Table IV.

four-quadrant characteristics in Table I-III. The same data are presented in Fig.3. and Fig.4.

CONCLUSIONS

Complete pump characteristics are rarely available, nevertheless the data for pumping zone are usually given.
To "synthetise" a four-quadrant characteristic for water hammer calculation the following procedure can be suggested.

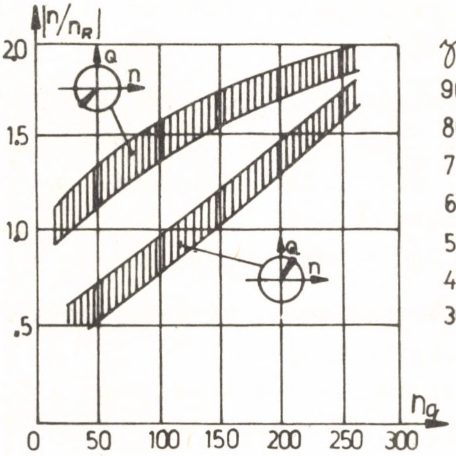

Fig.3.

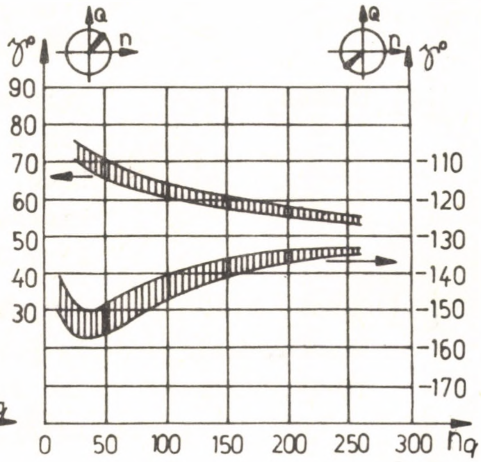

Fig. 4.

a/ To draw the known part /usually the normal pumping zone/ in the form presented here

b/ To determine the parameters of the runaway conditions with help of statistical relations given in Fig.3. and Fig.4.

c/ To complete the curves by interpolating the four--quadrant characteristics of pumps with similar specific speed n_q.

REFERENCES

[1] Stepanoff, A.J. Centrifugal and Axial Flow Pumps
John Wiley and Sons Inc.
1957 New York

[2] Kovats, A. Design and Performance of Centrifugal and Axial Flow Pumps and Compressors
Pergamon Press
1964

[3] Marchal, M.
Flesch, G.
Suter, P. The Calculation of Waterhammer Problem by Means of the Digital Computer

Int. Symp. Waterhammer in Pumped Storage Project, ASME
1965 Chicago

[4] Thomas, G.O. Determination of Pump Characteristics for a Computerized Transient Analysis
Proc. of the 1st Int. Conf. on Pressure Surges
1972 Canterbury, England

[5] Sheer, T.J., Baasch, R.J., Gibbs, M.S. Computer Analysis of Water Hammer in Pumping Systems
The South African Mech.,Eng. 130
1973

[6] Codrington, J.B., Witherell, R.G. The Use of Inpedance Concepts and Digital Modelling Techniques in the Simulation of Pipeline Transients
Proc. of the 2nd Int. Conf. on Pressure Surges
1976 London, England

[7] Diederich, H. Verwendung von Kreiselpumpen als Turbinen
KSB Technische Berichte 12.
1976

[8] Csemniczky, J. Szivattyuk négynegyedes jelleggörbé-iről
Ganz-MÁVAG VKT 81. sz.
1979

[9] Chaudry, M.H. Applied Hydraulic Transients
Van Nostrand Reinhold Co.
1979 New York

[10] Füzy, O., Sebestyén, A. Matematisches Modell zur Untersuchung des dynamischen Verhaltens einer Kreiselpumpe
4. Symp. Pumpen und Verdichter
1981 Magdeburg, DDR

[11] Nyiri, A. On the theoretical full characteristics of the hydraulic machines
Proc. of the 6th Conf. on Fluid Machinery
1979 Budapest

dr J. Csemniczky
Ganz-MÁVAG
H-1967 BUDAPEST
HUNGARY

OPTIMIZATION OF PLAIN STRAIGHT SLOTTED BLADE CASCADES BY PRESCRIBED VELOCITY DISTRIBUTIONS

Klaus Döge

Summary

This paper deals with the following problems: what minimum values can the loss coefficients of plain straight one-row and two-row cascades have? What kind of conditions must be met for achieving lower losses with slotted blade cascades than with conventional one-row and tandem cascades and what are the values to be found for the velocity distributions, blade chord length ratios on designing the cascades? To solve these problems the velocity distribution is optimized by calculated profile losses for prescribed Reynolds-numbers, states of boundary layers and flow angles without exactly knowing the geometry of the cascade.

1. Introduction

Fundamental knowledge to utilize the effect of the slot in slotted blade cascades was gained by Ihlenfeld /1/, /2/. Based on the experiences of Sheets /3/ and Ohashi /4/ Ihlenfeld-s slotted blade cascade design was improved by the soap-film analogy. The loss coefficients of those slotted blade cascades measured in the wind tunnel were very low and the question arises if the loss coefficients are low because of a large extension of the laminar boundary layer on the surfaces of the blades. Sheets /3/ indicates that the boundary layers in his investigations were laminar to a great extent and therefore extremely high efficiency rates of 96% were reached in a compressor stage. Strongly reduced losses in slotted blade cascades are subject of more recent papers, too. For diffusion and acceleration cascades in tandem arrangement Pal /5/ calculated and measured a reduction in loss up to 25% due to interference. Tschakirow /6/ determined the velocity distribution of a fan in prescribed slotted blade cascades at non-viscous flow the efficiency rate of which amounted to 85%.

In theoretical and experimental optimizing prescribed tandem cascades of compressor blades Bammert and Staudte /7/ reduced the profile loss by 18 - 22% by favourably arranging the two blade rows.

In all experiments very low loss coefficients for slotted blade cascades were achieved. However, so far it is not known what minimum loss coefficients can be achieved, what kind of conditions must be met for achieving lower losses with slotted blade cascades than with conventional ones and tandem cascades as to the occuring flow losses, and what kind of velocity distributions, blade chord length ratios, geometric form of the slot are the optimum ones and must be found in designing the cascades.

To answer all these questions, in the following the velocity distribution will be optimized for prescribed inflow and outflow angles, for prescribed Reynolds- numbers and prescribed fully turbulent or transitional boundary layers. The loss coefficient is to be calculated for

- plain conventional cascades (one-row cascades)
- plain tandem cascades (two-row cascades, the two blade rows having low mutual influence) and
- plain slotted blade cascades (two-row cascaedes, the two blade rows havings a considerable mutual influence).

In all the three variants the relations are to be investigated

- for a fully turbulent boundary layer on the pressure side and suction side
- and for a laminar boundary layer on the pressure side and on the suction side up to the diffusion's start as well as at a following turbulent boundary layer up to the trailing edge.

It is supposed that for each velocity distribution at least one cascade can be determined approximatively. At present by computing programs double cascades can be designed and analysed without considering frictional influences. The design of cascades belonging to optimum velocity distributions, however, is not subject of this paper.

In optimizing slotted blade cascades the reaction of the secondary flow can be neglected so far, as according to Ihlenfeld's measurements of strongly diffusing cascades, nearly the same parameters of the slotted blade cascade for the profile losses and side wall losses are practicably used.

2. Prescription of the velocity distributions

It is known from theoretical papers on conventional cascades, e. g. by Pascher /8/, Hackeschmidt /9/ and Čitaví /10/ that cascades have a low profile loss coefficient when their velocity distributions show a characteristic course. This course is marked by a constant velocity W_P with a following maximum diffusion without separation up to the velocity $W_{HK} = W_2$ on the suction side and by a constant velocity $W_{DS} = W_{HK} = W_2$ on the pressure side, see Fig. 1a.

The velocity distributions in tandem cascades on the fin (upstream profile of the slotted blade) and on the rudder (downstream profile of the slotted blade) at a prescribed blade chord length ratio and at prescribed velocities W_{PFl} and W_{PR}, see Fig. 1b, are prescribed in analogy to the velocity distributions in single cascades. However, it must be taken in consideration that the medium velocity between the two blade rows W_{12} depends on the prescribed velocities, when the inflow and outflow angles are prescribed. Hence an iteration must be carried out as the condition $W_{DS\ Fl} = W_{HK\ Fl} = W_{12}$ must be met.

In slotted blade cascades the two blade rows strongly

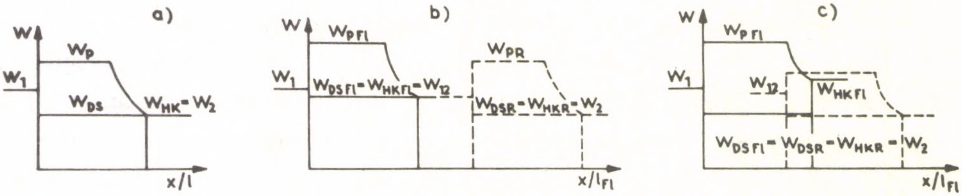

Fig. 1 -prescribed velocity distributions to optimize the conventional (a), the tandem cascade (b) and the slotted blade cascade (c)

influence each other. As to the velocity distributions the velocity at the trailing edge of the fin profile may be higher than the medium velocity W_{12}. The velocities on the suction side of the fin and the rudder are equal to the outflow velocity $W_2 = W_{DS\ Fl} = W_{DS\ R}$ except in the range of the slot. Therefore for the optimization on the trailing edge of the fin as a further variable the velocity must be described. No iteration to determine W_{12} is to be carried out. Near the slot the chosen velocity distributions are to be seen as an extreme simplification. But they are sufficient to describe the principal effects in slotted blade cascades.

In Fig. 2 the velocity distribution of a favourably designed slotted blade cascade determined in the wind tunnel and the idealized velocity distributions at fully turbulent and transitional boundary layer used for calculating the loss-coefficients are compared. As to the variant with

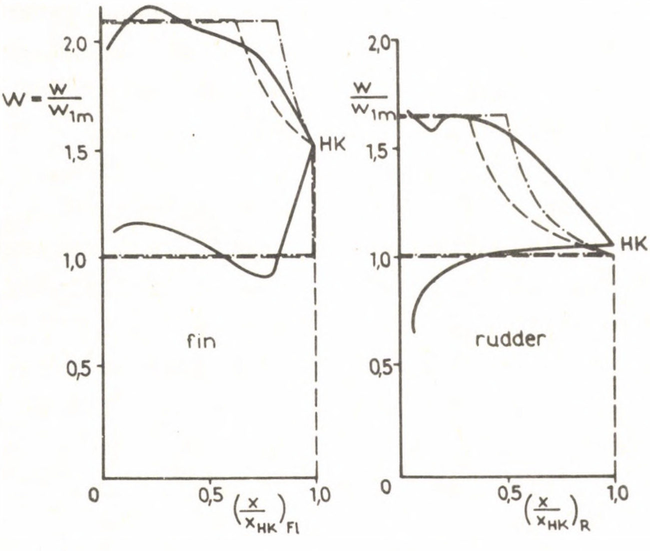

$t/l_{Fl} = 1{,}5$

$\beta_{Fl} = 55^\circ$

$\beta_R = 84^\circ$

$\beta_1 = 39{,}5^\circ$

$\beta_2 = 87{,}8^\circ$

$s/l_{Fl} = 0{,}05$

$a/l_{Fl} = -0{,}067$

$Re = 1{,}47 \cdot 10^5$

$\zeta'_e = 0{,}037$

$l_R = l_{Fl}$

Fig. 2 -velocity distributions at the slotted blade cascade
——— measurement according to Ihlenfeld /1/
— — — taken as a basis to calculate the loss of fully turbulent suction side boundary layer
— · — · taken as a basis to calculate the transitional boundary layer

transient boundary layer the diffusion start because of the thinner boundary layer is nearer to the trailing edge compared with the variant with a pure turbulent boundary layer. The velocity W_{PR} on the suction side of the rudder is higher on the cascade measured by Ihlenfeld than the velocity $W_{HK\ Fl}$ on the trailing edge of the fin. Great differences between the measured and the idealized velocity distributions occur in the near of the slot, as mentioned above, but the acceleration on the pressure side of the fin and also the very low acceleration at the stagnation point of the rudder are not considered in the following.

3. Determination of the loss coefficient and of the pitch chord ratio

To determine the loss coefficient of one-row and two-row cascades by the velocity distribution already mentioned, laminar or turbulent flat plate boundary layers are used, when the velocity is constant. In the range of turbulent boundary layer at maximum diffusion aquations will be used according to Nestler /11/. Additionally it is presumed:

- the wakes of the fin and the rudder do not influence each other, so the total loss coefficient can be determined by taking the boundary layer values at the blade trailing edges.
- the displacement effect of the boundary layers is included in the prescribed velocity distributions.

So in analogy to the ratios of Scholz /12/ the loss coefficient can be determined. The correlation between the pitch-chord ratio, the inflow and outflow angle and the given velocity distribution is described by the momentum equation, the velocities depend on the coordinate of the path s. The correlation between the coordinate of the path s and the coordinate x normal to the cascade's entrance - see Fig. 3 - varies for each prescribed velocity distribution and is not known. Therefore the profiles are approximatively replaced by the tangents to the profiles. The stagger angles β_{Fl} and β_R as against the profile tangent can only be determined approxi-

Fig.3 - parameters concerning geometrical form and fluid flow of the two-row cascade idealized for the calculation

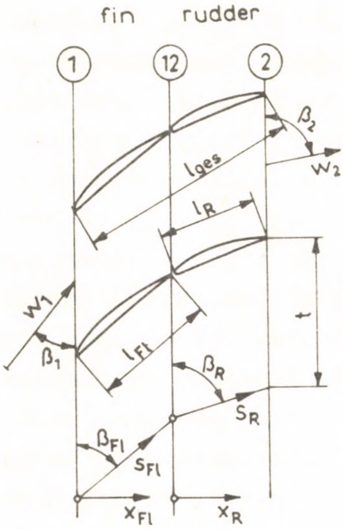

matively. At first a circular arc center line is determined for the total profile with non-viscous flow and a blade angle correction. After subdividing the center line according to the prescribed blade chord length ratio the stagger angles are found. For angle correction factor according to Eckert /13/ a simple approximate relation will be used.

Because in the practical calculation many iterations must be carried out and a great number of variants is to be investigated, a computer program has been elaborated [x)].

4. Optimization results

To test the applicability of the proposed calculating technique at first the measured loss coefficient is compared with the calculated loss coefficients of the slotted blade cascade investigated by Ihlenfeld /1/.

The results confirm that it is necessary to distinguish fully turbulent and transitional boundary layers. Only the calculated values for transitional buondary layer coincide sufficiently with the measurements. Thus the suggestion of Ihlenfeld is confirmed that the blade boundary layers are extensively laminar.

In optimizing the different types of cascades the same flow angles and the same Reynolds-number are prescribed as in the Fig. 2. The calculations can easily be repeated under other conditions. Starting from the calculated loss coefficients which can be compared either at the same Reynolds-number

[x)] This work was accomplished by Dipl.-Ing. Andreas Jahnke

$Re = w_{1m}\ l_{Fl}\ /\nu$ based on the chord length of the fin or the Reynolds-number $Re = Re(1+l_R/l_{Fl})$ based on the total blade chord length the following statements can be made:

1. At fully turbulent boundary layer on the profiles, see Fig. 4, optimum tandem cascades have a higher loss coefficient ($l_R/l_{Fl} = 1$) or nearly the same loss coefficient ($l_R/l_{Fl}=2$) as optimum one-row cascades. The loss coefficient of optimum slotted blade cascades is by 1/3 smaller than the coefficient of optimum tandem cascades and of one-row cascades.
2. At mixed transitional suction side boundary layer and laminar pressure side boundary layer, see Fig. 5, the same statements can be made as in the case of fully turbulent boundary layer. However, in the critical Reynolds- number-range tandem cascades have lower loss coefficients than one-row cascades because it is possible on the pressure side

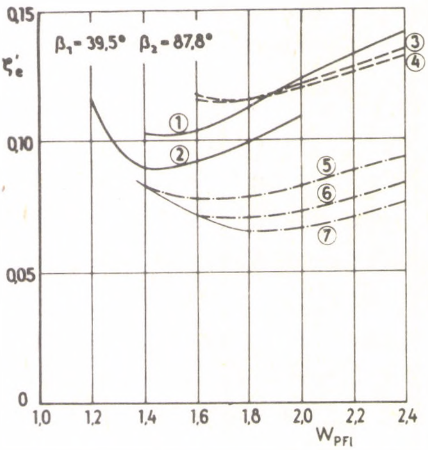

type of the c. Nr.	Re	l_R/l_{Fl}	W_{PR}	W_{HKFl}	W_{PFl}^+
conventi.c.—— 1	$1{,}5\cdot10^5$	0	–	1,0	1,5
2	$3\cdot10^5$	0	–	1,0	1,5
tandem c.– – 3			1,4	1,2	1,7
4			1,6	1,3	(1,8)
slotted blade c—· 5	$1{,}5\cdot10^5$	1	1,4+	1,4	(1,4)
6			1,4+	1,6	(1,6)
7			1,4	1,8	1,9

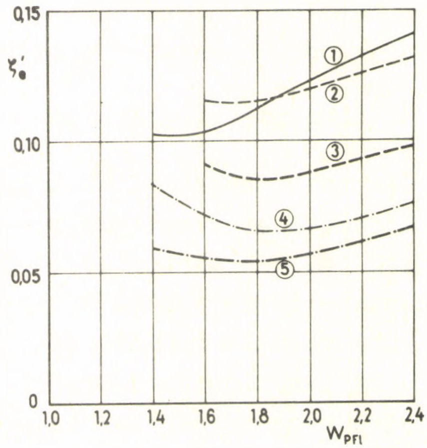

type of the c. Nr.	l_R/l_{Fl}	W_{PR}^+	W_{HKFl}^+	W_{PFl}^+	$\zeta'_{e\,min}$
conventi.c.—— 1	0	–	1,0	1,5	0,102
tandem c.– – 2	1	1,4	1,2	1,7	0,115
– – – 3	2	1,6	1,3	1,8	0,085
slotted blade c.—· 4	1	1,4	1,8	1,9	0,066
—·—·— 5	2	1,6	1,8	1,8	0,055

$Re = 1{,}5\cdot10^5$, $l_{sp}/l_{Fl} = 0{,}1$

+ optimized with regard to ζ'_e

Fig. 4 - calculated loss coefficient for fully turbulent profile boundary layer

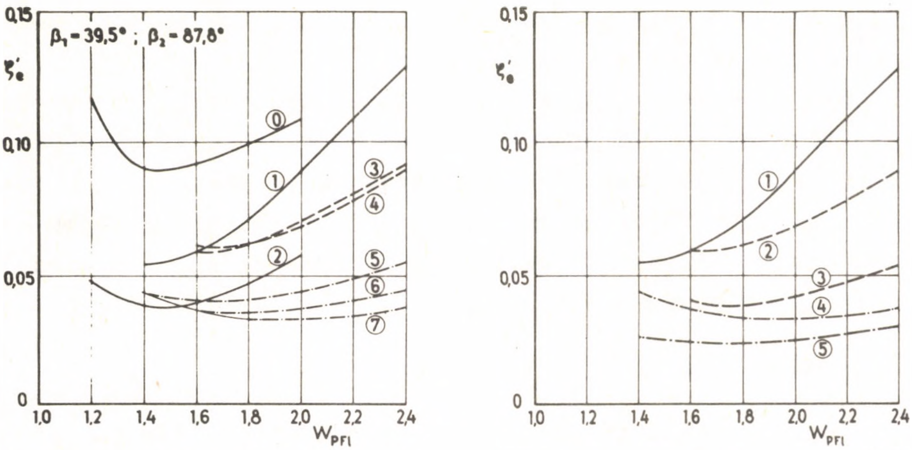

type of the c. Nr	Re	l_R/l_{Fl}	W_{PR}	W_{HKFl}	W_{PFl}^+
conventi.c. —— 0	$1{,}5\cdot10^5$	++			
1	$1{,}5\cdot10^5$	0	–	1,0	1,4
2	$3\cdot10^5$	0	–	1,0	1,5
tandem c. – – 3			1,4	1,2	1,6
4			1,6	1,4	(1,7)
slotted blade c. –·–5	$1{,}5\cdot10^5$	1	$1{,}4^+$	1,4	(1,7)
6			$1{,}4^+$	1,6	(1,8)
7			$1{,}4^+$	1,8	1,9

type of the c. Nr	l_R/l_{Fl}	W_{PR}^+	W_{HKFl}^+	W_{PFl}^+	$\zeta'_{e\,min}$
conventi.c. —— 1	0	–	1,0	1,4	0,055
tandem c. – – 2	1	1,4	1,2	1,6	0,059
– – 3	2	1,6	1,3	1,8	0,038
slotted blade c. –·–4	1	1,4	1,8	1,8	0,033
–·– 5	2	1,6	1,7	1,7	0,024

; $Re = 1{,}5\cdot10^5$, $l_{sp}/l_{Fl} = 0{,}1$

+ optimized with regard to ζ'_e

++ fully turbulent profile boundary layer

Fig. 5 -calculated loss coefficient for transitional suction side and laminar pressure side boundary layer

and on the suction side to maintain laminar boundary layers up to higher Reynolds-numbers Re_{ges}. The loss coefficient of optimum slotted blade cascades is also smaller in the transition region than that of tandem cascades.

3. As tandem cascades and slotted blade cascades are concerned, it is preferable to choose a blade chord length of the rudder which is greater than the blade chord length of the fins.
4. Optimum velocity distributions of one-row conventional cascades and tandem cascades in each profile row have a diffusion ratio of $W_P/W_{HK} \approx 1{,}5$. Optimum velocity distributions of slotted blade cascades are present, when the velocity on the suction side of the fin $W_{P\,Fl} \approx 1{,}8$ and there will be only a small diffusion up to the trailing edge of the fin. The optimum velocity distribution of the

rudder is similar to the distribution of the one-row cascades and of the tandem cascades.

5. Another advantage of slotted blade cascades not shown in the figures is the greater pitch-chord ratio as compared to conventional cascades and tandem cascades.
6. The slotted blade cascade designed by Ihlenfeld shows a velocity distribution deviating to some extent from the optimum velocity distribution at $l_R/l_{Fl} = 1$.

5. Conclusion

The optimization of plain straight slotted blade cascades by variation of the prescribed velocity distributions showed that optimum slotted blade cascades at great deviations can have loss coefficients lower by 1/3 than optimum one-row cascades and tandem cascades. This is due to the fact, that the optimal velocity distributions on slotted blades, having no strong pressure rise on the suction side of the fin, result in high pitch- chord-ratios and thus in low loss-coefficients. It was printed out by the calculations that the blade chord length of the rudder must be greater than the blade chord length of the fin as optimum slotted blade cascades and tandem cascades are concerned.

Two-row cascades are especially favourable in the critical Reynolds-number-range, because laminar boundary layers are formed on the fin and on the rudder whereas largely turbulent boundary layers are formed at comparable one-row cascades with equal total blade chord length.

References

/1/ Ihlenfeld, H. Strömungsvorgänge an geraden, stark verzögernden Spaltflügelgittern. Diss. TU Dresden, 1961

/2/ Ihlenfeld, H. Strömungsvorgänge an geraden, stark verzögernden Spaltflügelgittern. Maschinenbautechnik 14 (1965) H. 7, S. 361-65; 14 (1965) H. 8, S. 420-24

/3/ Sheets, H.E. The Slotted Blade Axial-Flow Blower. Transactions of the ASME 78, 1956, S. 1683

/4/ Ohashi, H. Theoretische und experimentelle Untersuchungen an Tandem-Pumpengittern starker Umlenkung. Ing. Archiv 27. Band,4. Heft, 1959, S. 201-26

/5/ Pal, P. Interferenzeinfluß bei Strömungen durch Tandem-Schaufelgitter. Ing. Archiv 34. Band, 1965, S. 173-93

/6/ Tschakirow, T.M. Untersuchung von Doppelschaufelgittern mit dem Ziel ihrer Anwendung in Axialventilatoren für große Druckerhöhung. Diss. Referat Sofia,1975 (bulgárisch)

/7/ Bammert, K.; Staudte, R. Experimentelle Untersuchungen an ebenen verzögernden Tandemgittern. VDI-Berichte Nr. 264, S. 81-89, 1976

/8/ Pascher, W. Ein Beitrag zur Entwicklung stark umlenkender Gitterprofile. Diss. TH Dresden, 1959

/9/ Hackeschmidt, M. Zum Entwurf optimaler, stark umlenkender Gleichdruckgitterprofile unter Verwendung der Elektroanalogie. Diss. TU Dresden, 1961

/10/ Čitavý, J. Ebene Verdichtergitter mit optimalen Geschwindigkeiten auf den Profilen. Diss. TU Prag, 1965 (tschech.)

/11/ Nestler, W. Inkompressible turbulente Wandgrenzschichten mit maximaler Verzögerung. Diss. TU Dresden, 1969

/12/ Scholz. N. Aerodynamik der Schaufelgitter, Band 1. Verlag G. Braun, Karlsruhe, 1965

/13/ Eckert, B.; Schnell, B. Axial- und Radialkompressoren. Springer Verlag Berlin ,Göttingen, Heidelberg 1961, S.265

Symbols and indices

$W = w/w_{1m}$	nondimensional velocity
w_{1m}	meridional component of the inflow velocity
β_1 , β_2	inflow angle, outflow angle
ζ_e'	loss coefficient related to $\varrho \cdot w_{1m}^2/2$
SS, DS	suction side, pressure side
Fl, R	profile of the fin, profile of the rudder

Döge, Klaus Dr. sc. techn.,wissenschaftl. Oberassistent
Technische Universität Dresden, Sektion Energieumwandlung
Bereich Strömungstechnik, Bereichsleiter: Prof. Dr.-Ing. habil. Vollheim , 8027 Dresden, Mommsen Str. 13,DDR

VIBRATION TEST OF CENTRIFUGAL PUMPS

Dömötör, Ferenc

The vibration test of rotating machinery is based on the concept that by the individual machine parts signals of frequency characterizing the parts are emitted, which can be measured by means of instrumental frequency analysis or determined theoretically through calculations. The vibration intensity of the machine and within this the amplitude of the individual vibration components is not constant but it varies with aging of the machine. In this article a survey on the individual frequencies will be given with the aid of relationships described in the bibliography and then a multistage centrifugal pump will be examined. From the variations conclusions will be drawn in relation to the reason causing the increasing of the resulting vibration intensity of the machine.

INTRODUCTION

If a centrifugal pump is considered to be a vibrating system of several degree of freedom, then the input signals are the residual unbalance, the interaction of impeller blades and volute tongue, the vibrations of antifriction bearings etc., while the output signals are the displacements of optional points of the pump casing.

The aim of vibration tests is to determine the variation of the input signal from the variation of the output signal and mainly to draw conclusions for the reason of the input signal variation.

However, this is not possible only in theoretical way. In vibration testing of rotating machines it is a common practice that the amplitude-frequency diagram of the new machine is plotted by measurement and it is compared with the curves plotted later during the course of the operation. From the variations occuring at the various frequencies, conclusions can be drawn in relation to the changes taking place in the interior of the machine. In majority of the cases it is assumed that the exciting forces are varying harmonically or rather from time to time the variation of the first few harmonics is examined. In the higher frequency domain, due to densification of the various components and their harmonics, it is very difficult to discriminate them from each other. This is the main reason why the basis of the estimation is referred not to the individual frequencies but by means of the

$$V_e = \sqrt{\frac{1}{T} \int_0^T v^2/t/dt}$$

formula to the effective vibration velocity, which must be measured in a certain frequency domain. If V_e reaches a certain value, then the machine is qualified faulty needing maintenance and as such it is excluded from operation.

1. CALCULATION OF THE CHARACTERISTIC FREQUENCIES

Frequencies of exciting forces acting on the pumps can be relatively unambigously determined. There are difficulties in the high frequency domain.

The so-called basic frequency is the frequency corresponding to the operating speed, caused partly by the residual unbalance and partly by dirt possibly depositing between the blades or occassionally by the mechanical damage of the rotor

$$\omega_o = \frac{n_{op}}{60} \quad /Hz/$$

The frequency originating from the interaction of impeller blades and the volute casing tongue is

$$\omega_1 = Z \times \frac{n_{op}}{60} \quad /Hz/$$

where Z denotes the number of impeller blades. However this effect is not one of harmonic-type, but it is much more of impulse nature. That's why the higher harmonics should be examined in this case.

Frequencies characteristic to the antifriction bearings can be attributed partly to the bearing structure itself and, on the other hand, to the manufacturing deficiencies of bearing elements.

The one part is depending on the operating speed, while the other part is independent of it. The majority of these frequencies is in the high domain and thus their separation from each other is troublesome.
/Formulae required for calculation of the individual typical frequencies can be found in the bibliography /4//
To the vibrations derivable from other reasons belong the vibrations occuring due to inaccurate adjustment of the shaft ends to be coupled. Uniaxiality errors cause vibrations on one hand, whose frequencies according to /9/ are as follows

$$\omega_2 = 2 \times \frac{n_{op}}{60} \text{ /Hz/}$$

and

$$\omega_3 = 3 \times \frac{n_{op}}{60} \text{ /Hz/}$$

and, on the other hand it increases the load on the bearings which results in early wearing of them, that is, in increasing of high-frequency vibrations.
The effect of the wearing rings, according to bibliographical data /8/ can be observed at the

$$\omega^* = /0,4 \div 0,6/ \times \frac{n_{op}}{60} \quad \text{/Hz/}$$

frequency.
Mention has also to be made on the vibrations originating from the electric motor, which can be correlated partly to the operational speed and partly to the mains frequency, and on vibrations caused by cavitation. The examination of these vibrations will, however, be disregarded in this paper.

2. VIBRATION TEST OF A MULTISTAGE PUMP

2.1. Main features of the pump

The pump subjected to testing was an 8 stage, electric motor driven machine used for delivery of 85°C petrol. The main data relating to the operating point are as follows:

Q = 1oo cu.m/h

H = 6oo m

n = 3ooo r.p.m.

There were in the pump 2 pcs. single-row deep-groove bearings on the coupling side and 2 pcs. single-row bearings of inclined influence line, on the opposite side.

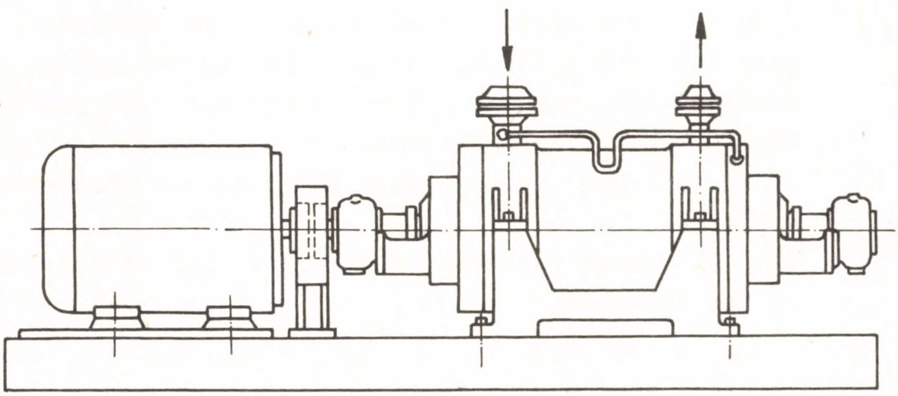

Fig.1. Contour drawing of the pump tested

2.2 Vibration measurent

Measurements had been carried out in the plane of the bearings, perpendicularly to the shaft in both horizontal and vertical directions as well as at a suitable point of the bearing housing axially, according to the specifications of ISO 2372, ISO 3945. For the measurement a piezoelectric accelerometer was used and the signal was made visible, after having it passed through a frequency analyser, by means of a level recorder.

The simplified diagrams of the measuring results are given in Figs. 2 and 3. Test point 1 represents the bearing box on the coupling side of the pump, while test point 2 refers to the opposite side.

The vibration pattern shown in Fig. 2 relates to a pump being in use for several years but running with freshly replaced rotor and bearings. In Fig.3. the condition set in after 8 months of continuous operation is recorded.

2.3. Evaluation of the diagrams, operational experiences

As seen on the plotted vurves, intensive change of the vibrations took place mainly in the high frequency domain. Although the total level of the vibrations was less influenced by this change than by the change manifesting itself at the lower frequencies, the smaller amplitudes of the high-frequency components have worth of attention as mainly these indicate the wear of the bearings.

The calculated frequencies are /for explanation, refer to the foregoing/

ω_0 = 5o /Hz/ ω_2 = 1oo /Hz/

ω_1 = 4oo /Hz/ ω_3 = 15o /Hz/

Frequencies, characteristic to the antifriction bearings are as follows:

Test point 1 Test point 2

Passing frequency of the rolling elements

ω_4 = 25o /Hz/ ω_4 = 167 /Hz/

Resonance frequencies of the outer ring /Hz/

$\omega_{51} = 111o$	$\omega_{54} = 9743$	$\omega_{51} = 1256$	$\omega_{54} = 11o31$
$\omega_{52} = 3143$	$\omega_{55} = 14294$	$\omega_{52} = 3558$	$\omega_{55} = 16183$
$\omega_{53} = 6o25$		$\omega_{53} = 6821$	

Residual unbalance of the cage

$\omega_8 = 25$ /Hz/ $\qquad\qquad \omega_8 = 21$ /Hz/

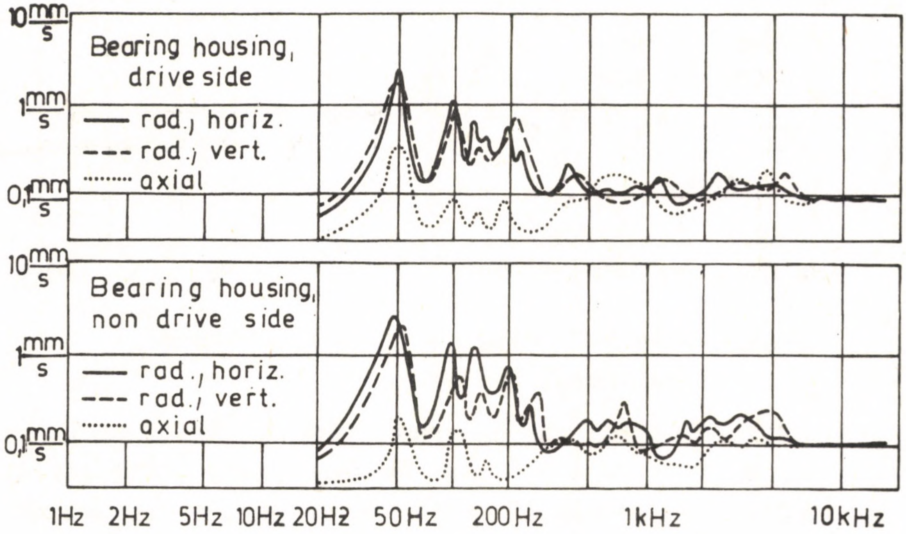

Fig. 2 Frequency diagram after installation of the new rotor and bearing replacement

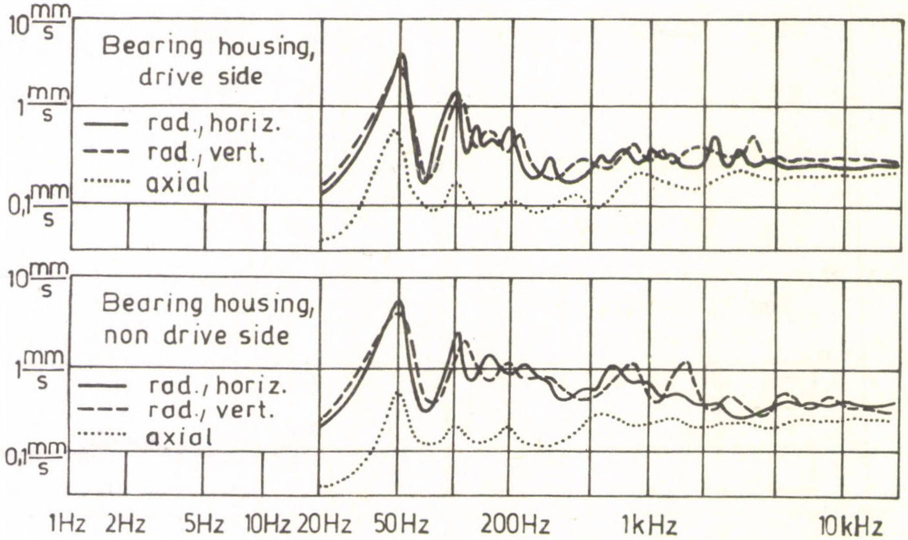

Fig. 3 Frequency diagram after 8 months of continuous operation

After plotting the diagram shown in Fig. 3 and subsequent to a repeated bearing change, the attention of the users was attracted by intensive vibrations appearing at the ω_0 frequency.

They were sure that this phenomenon could not be caused by improper balancing because it was carefully checked. They came to the explanation when it was revealed that the ball bearings of inclined influence line were mounted by the fitters, instead of the specified "O" pairing, in "X" pairing. The critical speed of the rotor /the first, lowest critical speed is in question/ has got reduced and the machine was brought into vibration by the exciting force of the nearest frequency.

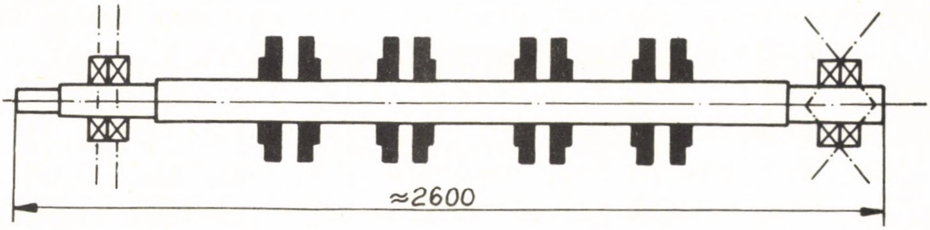

Fig. 4. Rotor of the pump

The phenomenon mentioned above could also be traced by calculation. For calculation of the critical speed the so-called transfer matrix method was used. In the mechanical model the shearing forces were not taken into account and the stiffeninc, stabilizing effect of the wearing rings and the shaft protecting sleeves was disregarded. According to bibliographical data /3/, the error caused in this manner in the case of the first critical speed is less than 5 %. In the case of bearing mounting in compliance with the specifications the calculated value was $n_{crit} =$ $= 4860$ r.p.m. while in the improperly mounted case this reduced to $n_{crit} = 3350$ r.p.m., that is, according to the calculations the operating speed was approached by 10-15 %, which resulted in the above mentioned intensive vibration.

DÖMÖTÖR, Ferenc M.Sc. mechanical engineer
Ganz-MÁVAG, Hydraulic Machinery and Compressor Design Dept.
1967-BUDAPEST, VIII. Könyves Kálmán krt. 76.
HUNGARY

BIBLIOGRAPHY

/1/ R. Nordmann: Modal Analysis of Rotating Machinery /Unpublished lecture notices of an intensive course/ CISM International Centre of Mechanical Sciences UDINE /Italy/ 2o-24 Sept., 1982.

/2/ A.J. Stepanoff: Radial und Axialpumpen Springer Verlag, Berlin 1959.

/3/ Ponomarjov: Mechanical strength calculus in the mechanical engineering /In Hungarian/ Technical Publishing House, Budapest, 1966.

/4/ Molnár - dr. Varga: Designing antifriction bearing supports /In Hungarian/ Technical Publishing House, Budapest, 1977.

/5/ Lipovszky-Sólyomvári-Varga: Vibration testing and maintenance of machines /In Hungarian/ Technical Publishing House, Budapest, 1981.

/6/ Márialigeti: The critical speed /manuscript/ Ganz-MÁVAG, Budapest, 1971. /In Hungarian/

/7/ Dömötör-Lechner: Some problems of pumps vibrations Techniche Nuove Milano, Il Progettista Industriale 9/82, pp. 8o-86.

/8/ E. Makay: Survey of Feed Pump Outages EPRI, FP-754, Project 641, April 1978. Morrisville, Pennsylvania

/9/ Vibration Trouble Shooting Chart /Brüel & Kjaer Publication/

THE BEHAVIOUR OF A CENTRIFUGAL PUMP IN A STEADY PULSATING HYDRAULIC SYSTEM. EXPERIMENTAL RESULTS.

M. Fanelli ENEL - Research and Development Division Center for
G. Angelico Hydraulic and Structural Research - Milano, Italy

P. Escobar CFE - Development and General Engineering Division
Mexico D. F., Mexico

SUMMARY

A pump model was included in a closed hydraulic circuit where a stationary regime of pulsating discharges (and pressures) was superposed to a mean flow (and to a reference pressure). An electric device allowed to control and vary the pulsation frequency. The angular velocity of the runner was very nearly constant during the tests.

Pressure oscillations were measured with the usual membrane and strain-gauge transducers. Flow oscillations were measured with a new technique: the laser - Doppler velocimetry. Experimental results were interpreted with a mathematical model based on the transfer-matrix method.

From experimental measurements, the "hydraulic impedance" of the pump has been obtained, that is the complex ratio between the difference in pressure oscillations at the two sides of the pump, and the discharge oscillation: $Z_p = (h_1 - h_2)/q_2$. This parameter summarizes the pump behaviour in a steady pulsating state, provided that there is no cavitation and the runner has a constant angular velocity. It has been found that Z_p value changes with the pulsation frequency.

The results obtained are remarkable because they are deemed to be more reliable than previously obtained ones.

1. TEST FACILITY AND INSTRUMENTATION

The test facility used in this investigation is a closed-loop hydraulic circuit. A sketch is shown in fig. 1. Its components are described hereunder.

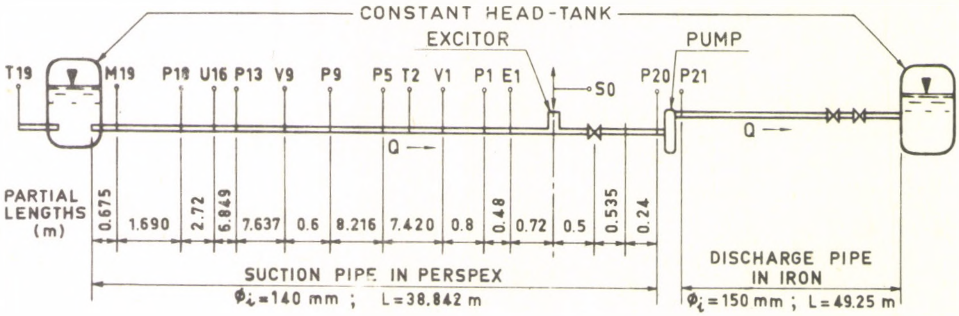

Fig. 1 - The experimental hydraulic circuit

The constant-head tank - It can be kept at a reference pressure, higher than the atmospheric one. It contains a heat exchanger whose purpose is to stabilize water temperature when it tends to increase because of the running pump.

The suction line - It is 38.8 m long, made of perspex, in 2 m long, 5 mm thick sections. The internal diameter is 140 mm. The couplings are in perspex too and have taps for pressure transducers.

The excitor - It is branched in derivation on the suction line and consists of two pistons ($\emptyset$ = 3 cm) that plunge into the circuit water. The frequency of the piston alternate motion is precisely controlled and can be varied by a regulation electric device from 0 to 50 Hz. The purpose of this perturbing system is to generate locally small sinusoidal flow pulsations that cause pressure and discharge perturbations all over the test facility and therefore also at the pump. Perturbations are superposed to average discharge and pressure conditions.

The pump - It is a model pump with a centrifugal impeller and a single discharge volute. There is no conical diffuser at the high-pressure end of the pump. The drive motor is asyncronous and runs at the very nearly constant velocity of 1500 r.p.m.

The discharge line - It is 49.25 m long, made of steel pipe 5 mm thick; the internal diameter is 150 mm.

Dynamic pressure measurements are made with membrane and strain-gage pressure transducers placed at the seven P-locations shown in fig. 1.

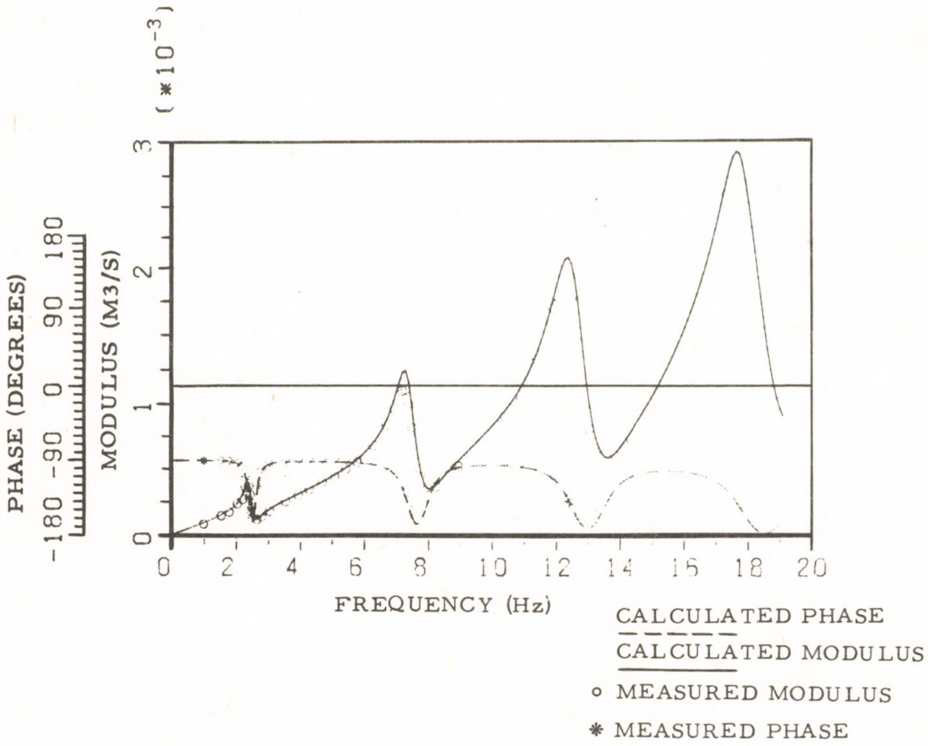

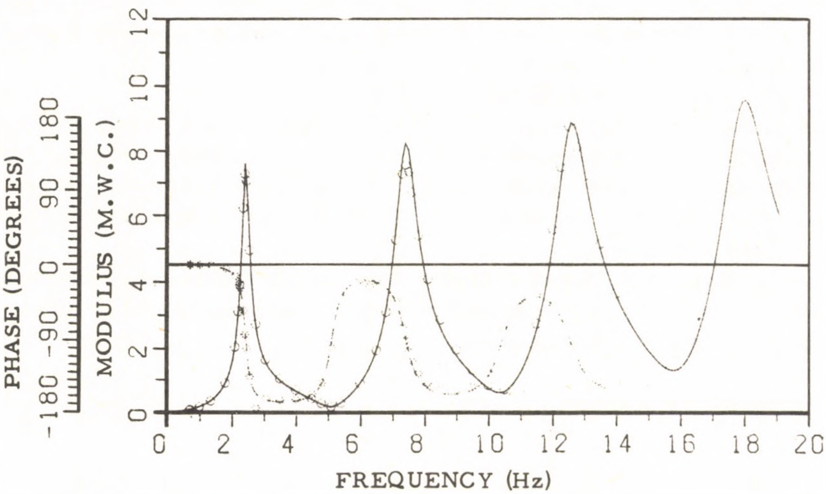

Fig. 2 - Calibration test ($Q = 0.0\ m^3/s$).
Measurement values versus calculated ones (frequency responses):
a) Discharge oscillations at V1 (see fig. 1);
b) Pressure oscillations at P1 (see fig. 1).

A Laser Doppler Velocimeter (see ref. /1/) is used to measure both average local flow velocities and velocity oscillations at the two V locations shown in fig. 1.

Electrical signals from the dynamic instrumentation are treated by a Signal Analyzer. Phase data are obtained by comparing the signal to be analyzed to the reference signal coming from a sensor that measures dynamic displacements of the excitor pistons.

All electric signals are also registrered to be further analyzed, if necessary.

2. CALIBRATION TEST

These tests were performed to study the dynamic behaviour of the suction line and define its mathematical model.

In the first test a closed valve excluded the pump and the discharge line: the mean discharge was zero. Pressure and discharge oscillations were measured and the celerity of the suction line was found by trial and error for the best fit to experimental measurements (see fig. 2)*

$c = (367 + 1.3\ f) + i\ (16.5 - 0.1\ f) \quad [m/s]$

[f = frequency of the perturbations (quasi-stationary waves), in Hertz]

The complex value and the frequency dependance are in agreement with former test results (see ref. /2/). They are due to the hysteretic and dynamic behaviour of perspex.

The second calibration test was performed in steady - non pulsating - conditions to find the friction losses in the suction line. The excitor was stopped, the valve opened and the pump run. The discharge was $0.0553\ m^3/s$. Pressure measurements and Reynolds number showed that head losses were of the kind "smooth pipe":

$j = 1.165 \cdot 10^{-3}\ U^2 + 4.7124 \cdot 10^{-3}\ U^{1.763}$

This formula had to be linearized to put it in the linear mathematical model of the pipe (on the basis of transfer-matrix method: see ref. /3/). A rather interesting linearization based on the "energetic equivalence" criterion was used that was deemed to be more advisable and proper than the usual one (see ref. /6/).

As a conclusion celerity and head loss characteristics of suction line defined the line transfer matrix necessary to check and complete the following dynamic pump-test.

---

* The agreement between experimental and theoretical frequency response (for pressure and velocity oscillations) shown in fig. 2 for two positions along the suction line, is consistently of the same excellent degree for all other positions checked.

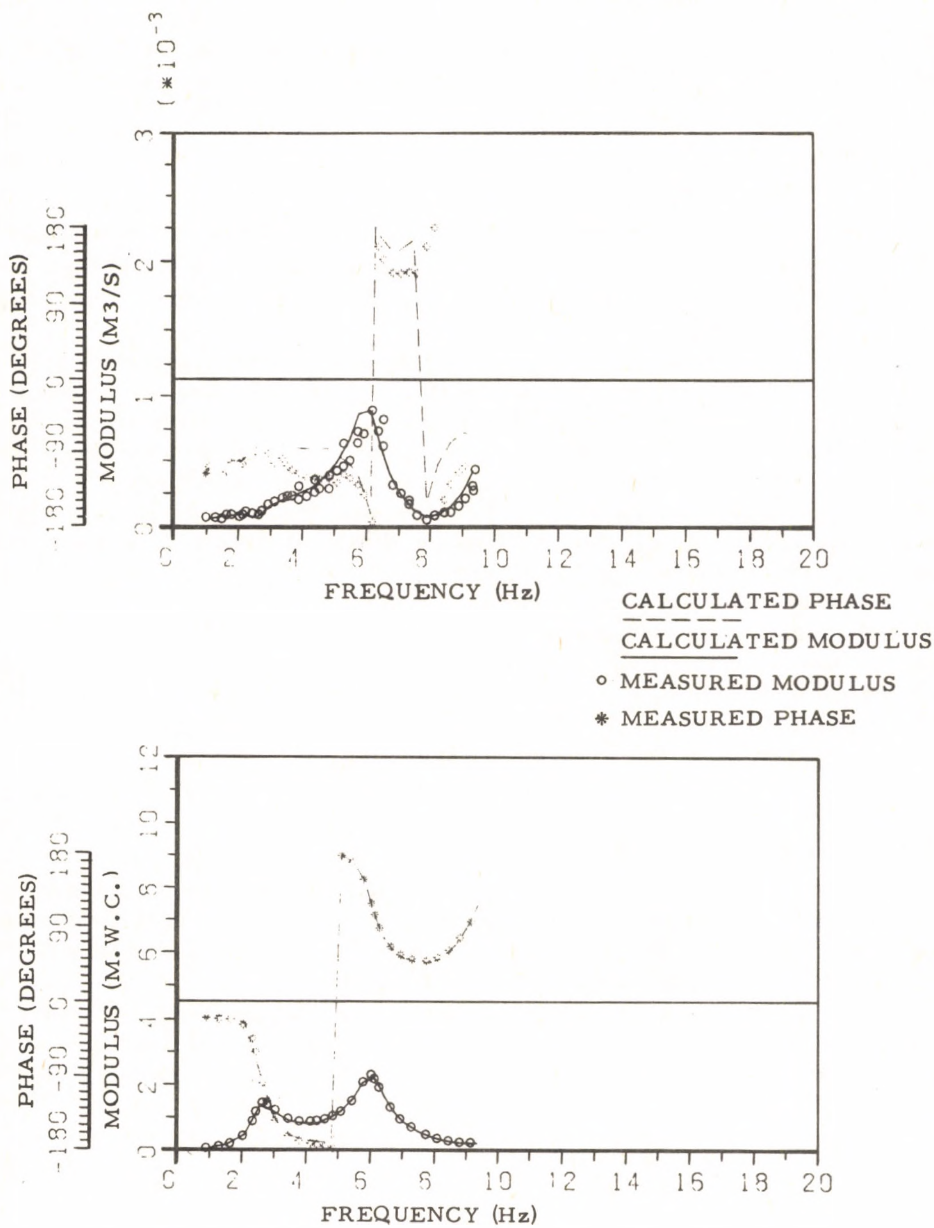

Fig. 3 - Pump test ($Q = 0.0553\ m^3/s$).
Measurement values versus calculated ones (frequency responses):
a) Discharge oscillations at V1 (see fig. 1);
b) Pressure oscillations at P1 (see fig. 1).

3. PUMP IMPEDANCE

The dynamic response of a pump is described by a simple complex impedance Z_p, provided that the flow is non cavitating and the runner has a constant angular velocity:

$$Z_p = \frac{h_{20} - h_{21}}{q_{20}} \qquad (1)$$

Z_p is the complex ratio between the difference in pressure oscillations at the two sides of the pump and the discharge oscillation at the suction side. In this very simple case the pump is a dipole and it is supposed that $q_{20} = q_{21}$ (see ref. /4/).

The mean discharge during dynamic pump test was $0.0553\ m^3/s$. The excitor frequency range was $0 \div 10$ Hz. Pressure oscillations in P20 and P21 (see fig. 1) were measured. Discharge oscillations in P20 were calculated by the calibrated mathematical model of the suction line. Calculation accuracy is good, as far as appears from the comparison in fig. 3.

From (1) Z_p values were obtained that are shown in the complex plane in fig. 4. Z_p values corresponding to different frequencies are interpolated by a curve in that figure. The resulting trend can be explained as a sum of three main components (see ref. /5/):

a) the quasi-steady impedance Z_p $(f = 0) = R_0$;
b) the inertia of the fluid inside the turbine;
c) the delay effects in angular momentum transport.

The qualitative contribution of each of them is shown in fig. 5. Quantitative evaluations are under way.

4. CONCLUSIVE REMARKS

The dynamic response of a model pump was determined - as a characteristic impedance - by measurements of pressure oscillations and by computed discharge oscillations. The pump impedance was found to be a frequency - dependent complex value.

Research development pointed out that the pump behaviour would have been studied in a reliable way only if measurements were composed with results from a proper mathematical model of the whole hydraulic circuit.

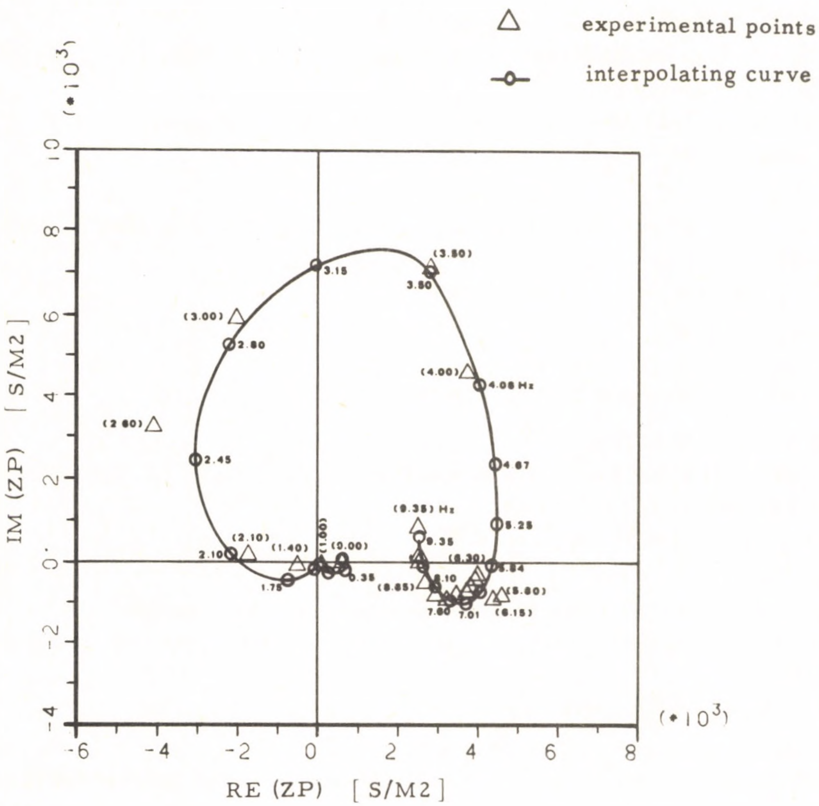

Fig. 4 - Frequency dependance of pump impedance.

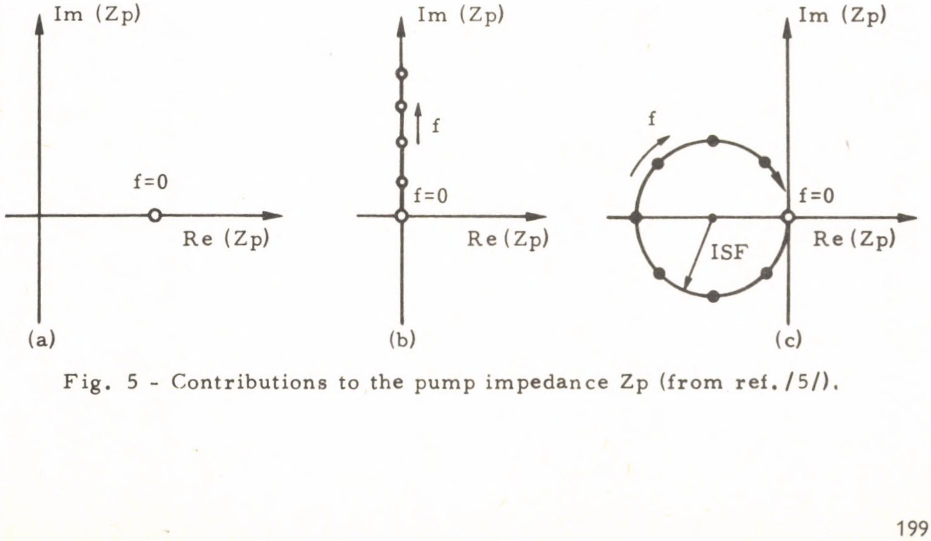

Fig. 5 - Contributions to the pump impedance Zp (from ref. /5/).

BIBLIOGRAPHIC REFERENCES

/1/ Corti M., Barberis A., Martinelli A.
A Laser Doppler Velocimeter for Zero Average Flow in Resonant Hydraulic Circuits
5th International Meeting on Water Column Separation, Obernach, September 28-30, 1981

/2/ Fanelli M.
Dynamic response of a pressure pipe having damping elastic wall in Italian)
L'Energia Elettrica n. 1, 1973

/3/ Chaudhry M.H.
Applied Hydraulic Transients
Van Nostrand Reinhold Co., 1979

/4/ Fanelli M., Siccardi F.
Response of a hydraulic turbomachine to fluctuation of dynamic circuit parameters (in French)
La Houille Blanche n. 1/2, 1980

/5/ Doerfler P.
System dynamics of the Francis turbine half load surge
11th IAHR Symp. on operating problems of pump stations and power plants
Amsterdam, September 13-17, 1982

/6/ Fanelli M., Angelico G., P.Escobar
Comprehensive experimental confirmation of transfer matrix theory for uniform pipelines under steady pulsating conditions. Presented for acceptance at the 4th Int. Conf. on "Pressure Surges"
Bath, England, Semptember 21-23, 1983

DEPENDENCE OF THE ACCURACY OF MAIN WATER METERS OF WATER WORKS ON ENVIRONMENT POLLUTION

Csaba FÁY

Summary:In the individual meters, the positive error developing due to effect of the deposit develops in 5-10 years between 2-4 %.

1.WATER METERING AT THE WATER WORKS OF BUDAPEST

The Water Works of Budapest has supplied the urban population with drinking water by pipes since 1868.The water is produced from the gravel deposits beside the Danube bed,from the so-called gravel terraces by wells,thus this is a naturally filtered running water.

Steam-driven piston pumps operated at the pumping stations built in the 19th century,these required no water-meter, it was enough to measure the number of strokes of the piston. As early as the turn of the century, pumping stations with centrifugal pump operation (with first lifting stage) sucking the individual well groups were built.With these,a Venturi meter was installed in the pressure pipe for water-metering at the time.

When between 1932-34 the main pumping stations were converted for electric drive and centrifugal pumps were located, Venturi-meters were installed at all stations for the metering of the water volume [1].

The first induction-meter was installed by us in 1973, and since then we have applied them in an ever growing number because of their significant advantages [2] .

At present, the water volume forced into the basepressure pipe network of Budapest is metered by 22 meters, of which 15 are old Venturi-meters, 7 are new inductions-meters.

2.VARIATION OF WATER QUALITY

Due to the effect of environment pollution,the water quality of the Danube also deteriorated,but besides this, because of various interferences in the bed of the Danube, such as e.g. gravel production for construction works,etc., silt deposited in the place of the natural filtering layers of the wells, the filtering process slowed down on this,the oxygen contained in the water was used up during filtering, the water became aggressive,it elutriated iron-manganese compounds from the soil.In some wells, the deterioration of well water quality exceed the limit values of the standard specifying the quality of drinking water,therefore such wells had to be stopped.

Of the bank-filtered wells, in 1973 the wells of Csepel (Pipe Factory),in 1975 the wells of Palotasziget were stopped. Since the pollutants (below limit value) appeared in the stopped wells already earlier, it can be estimated that the deterioration of water well quality started 5-7 years earlier: in 1966-68.The change of water quality is such a slow process that it is hardly perceivable, at first we noticed only its unfavourable effects: due to the effect of chlorinations,pumping (contact with air at places with water surface),the iron-manganese compounds precipitated and appeared on the wall of the pipeline inside in the form of a black deposit.

When the operating condition suddenly changed (e.g. well gruops stopped at the same time because of current failure), the oscillation in the pipes swept the black deposit off the wall and it reached the consumers in the form of scum.The first such deposit separation on a larger scale occured in 1976 , and even though we have increased the space of the washing and flushing of the system since then, we have been unable to eliminate it until now,which indicates that quality continues to deteriorate.

3.DEPOSIT IN THE METERS

At first we presumed that where the liquid accelerates - thus in the constriction of the Venturi meter - no deposit is formed.This was a reasonable assumption because no cleaning holes manholes were made in the environment of the old meters,thus control (with continous operation) was not possible.This assumption was based on the fact that in the pumps disassembled for repair we did not find deposits in the stators either.

The first indication that something is wrong in metering were observed around the end of the year 1976 because the openings of some Venturi-meters became clogged,it was necessary to clean them more frequently. However, these meters were not the meters of the mains,but the meters of the individual producing well-groups, where air instrusion under hihg vacuum frequently occured anyway, thus the operating troubles here were more frequent, therefore we did not attach great importance to this.

Since 1976, we began to use induction meters in the metering of producing well groups (in the case of newly located well groups),and later, during the reconstruction of well groups, we began to replace the old Venturi meters by induction meters.In 1979, we found a uniform 3-5 mm thick deposit layer inside the replaced Venturi-meter of one of the well groups, and this was the first warning, that this is possible, thus it may also cause a metering error. At the beginning of 1982, we replaced the Venturi-meter of such a well plant by induction meter, which had been operating since 1894 and in this the thickness of the deposit was 6-9 mm.By the way, in the case of this well group, the deterioration of water quality was also greater, one of the 7 wells already had to be stopped.Following this,we examin ed one of the main mains meter ,in wich a 3 mm deposit layer was found.This was metered before and after cleaning, and from this data are available concerning the magnitude of the metering error.

4.THEORETICAL VALUE OF THE METERING ERROR

Both the Venturi-meter and the induction meter used as main water-meter measure average velocity,which is multiplied by the area of the known cross-section.If the area is reduced because of the deposit, then the same water flow brings about a higher average velocity in a smaller cross-section.If this is multiplied by the original (unreduced) cross-section, the metered water flow will be greater than the real one.

a/Error of the induktion meter

With an induktion meter, an error occurs only because of the reduction of the original mouth diamater D to $D' = D-2s$, where s is the thickness of the deposit layer.
It can be written that the relative error

$$\Delta Q/Q = (D/D')^2 - 1$$

If the expression of D' is substituted in this, after raising to the second power:

$$\frac{\Delta Q}{Q} = \left(\frac{1}{1-\frac{2s}{D}}\right)^2 - 1 = \frac{1}{1-\frac{4s}{D}+\frac{4s^2}{D^2}} - 1$$

Since the value s/D is small, the square if this can be neglected, likewise 4s/D is small compared to the unit, therefore the approximation $1/1-(4s/D) \cong 1 + 4s/D$ can be applied. By these, the approximative relationship is:

$$\Delta Q/Q \cong 4s/D \qquad (1)$$

The error of the approximation can be taken from Table 1. If a more accurate approximation is required, then the relationship :

$$\Delta Q/Q = 4s/D.(1+3s/D) \qquad (2)$$

can be used. Apparently, this approximates the accurate value to abt. maximum 3 % deposit within 1 % error.

Table 1.

s/D =	0,01	0,02	0,03
$\Delta Q/Q$ accurate	0,041232	0,085069	0,131733
$\Delta Q/Q$ approx.(1)	0,04	0,08	0,12
approx(1)/acc.	0,9701	0,94047	0,91091
$\Delta Q/Q$ approx.(2)	0,0412	0,0848	0,1308
approx(2)/acc.	0,999225	0,99684	0,99291

b/Error of the Venturi-meter

If the pipe diameter D_1 is reduced to D_2 and the reduction ratio is $n=D_2/D_1$, the loss factor of the mouth is γ without deposit and the sames marked with comma with deposit, then the positive relativ error of metering is:

$$\frac{\Delta Q}{Q} = \left(\frac{D_2}{D_2'}\right)^2 \left(\frac{1+\zeta' - n'^4}{1+\zeta - n^4}\right)^{1/2} - 1$$

Similarly to the induktion meter the substitution $D_2' = D_2 - 2s$ in the first factor of the first term of the right side of the relationship may be used here too, but here a consideration should be still made concerning the other factor of the term.

Analyzing the extent of the dep sits, we observed that a thicker layer deposited in the larger diameter than in the part having a smaller diameter. Reality is approximated well by the the fact that $n' \cong n$. Making use of this, moreover raising $(1-n^4)$ out of the factor, it can be written that :

$$\frac{1+\zeta' - n'^4}{1+\zeta - n^4} \cong \frac{1+\zeta'}{1+\zeta}$$

Since the value of ζ is estimated anyway, it is indifferent, by what identical number standing near to one it is divided in the usual $n = 0,5-0,7$ range ($1-n^4 = 0,75-0,935$). With confusor the value of ζ varies between 0,02 and 0,03. Increase of roughness to about two-fold $\zeta' = 0,04-0,06$. Let us approximate the above expression, since $\zeta \ll 1$ and $\zeta' \ll 1$:

$$\left(\frac{1+\zeta'}{1+\zeta}\right)^{1/2} \cong (/1+\zeta'/./1-\zeta/)^{1/2} = (1+\zeta' - \zeta - \zeta'\zeta)^{1/2} = 1 + \frac{\zeta' - \zeta}{2}$$

With these and to the analogy of (1):

$$\frac{\Delta Q}{Q} \cong \left(1+\frac{4s}{D_2}\right)\left(1+\frac{\zeta'-\zeta}{2}\right) - 1 = \frac{4s}{D_2}\left(1 + \frac{\zeta'-\zeta}{2}\right) + \frac{\zeta'-\zeta}{2} \qquad (3)$$

or with more accurate approximation to the analogy of (2)

$$\frac{\Delta Q}{Q} \cong \left(1+\frac{4s}{D_2}\left/1+\frac{3s}{D_2}\right/\right).\left(1+\frac{\zeta'-\zeta}{2}\right) - 1 = \frac{4s}{D_2}\left(1+\frac{3s}{D_2}\right).\left(1+\frac{\zeta'-\zeta}{2}\right) + \frac{\zeta'-\zeta}{2} \qquad (4)$$

If $\zeta' = 0,06$, $\zeta = 0,03$, $(\zeta'-\zeta)/2 = 0,015$, then the extent of the approximation of the above relationships is presented in Table 2 . It is to be seen that here too (4) approximates the accurate value within 1% in the usual $s/D_2 < 0,03$ range.

Table 2.

s/D_2	0,01	0,02	0,03
$\Delta Q/Q$ accurate	0,0568505	0,101345	0,1487089
$\Delta Q/Q$ approx.(3)	0,0556	0,0962	0,1368
approx.(3)/accurate	0,978	0,94923	0,919918
$\Delta Q/Q$ approx.(4)	0,056818	0,101072	0,147762
approx.(4)/accurate	0,9994283	0,9973	0,993632

5. CONTROL OF THE METERING ERROR

In the individual meters, the positive error developing due to effect of deposit develops in 5-10 years (although even the slightest increase of roughness in the Venturi-meter may already cause an initial starting error value by means of the last term of relationship (3) and (4), respectively), thus the utilization difference of the water works increases to such a small extent annualy because of this (0,3-0,4 % annualy) that it cannot be determined from this subsequently.

Since the meter is installed in the mains after the pump, that possibility appears to be feasible that the characteristic curve of the pump is measured by the meter having deposit, then the meter is cleaned, the measurement of the characteristic curve is repeated and we infer the error caused by the deposit from the shift of the characteristic curve.

An s=3 mm layer was observed in the D_1=900mm, D_2=450 mm Venturi-meter located in the common pressure pipe of pumps No.3 and 4 of power room I. of Káposztásmegyer. The theoretical error, wich can be calculated from this by (4) is 4,26 % (with values ζ and ζ' of the end of the previous point). The metering yielded a 3,04 % error, but since here two Q values standing very near to each other were measured with approx. 1,0 % error each and the value of ΔQ was obtained from the difference of the two measurements, the metering error committed in this is $\pm 2\%$, that is, the metered $\Delta Q/Q = 3{,}04 \pm 2\%$. Thus, the theoretical value falls within the metering error band.

The experiences with the characteristic curve controls regularly repeated on machine No.1 of power room I.of Káposztásmegyer also provide a basis concerning the time of the depositions.This machine was measured in Noveber 1975 and in November 1979 with the same method.If it is presumed that in the meantime the gaps of the pump did not wear and the surface of the hydraulic parts did not smoothe out, then the shift of the characteristic curve can be due only to the reduction of the Venturi-meter.At the time we obtained a 4,2 % positive error from the 4 years' shift of the characteristic curve (unfortunately, at the time we did not yet suspect the Venturi-meter, but we presumed that the pump impeller channel was worn broader).If from this we calculate back layer thichness by relationship (4) and presume, that in 1975 there was no deposit yet,that is, ζ was equal to 0,03, then in 1979 s=2,935 mm layer thickness is obtained with ζ'=0,06, that is, practically so much wich was measured in the other pipe after 3 years. (It is to be noted that the measurement of layer thickness is also uncertain because the surface is uneven, the thickness of the layer varies as much as $\pm$1mm in the interest of some degree of accuracy data can be formed from average of 10-20 points).

6.ANALISIS OF THE RESULTS

If the same water flow Q is to be metered, e.g. in a 900 mm-diameter mains, the narrow cross-section of the Venturi-meter is selected at D_2=450 mm,whereas if the same is to be achieved by induction flow meter,it is selected (in order to save costs) at D=600 mm.The justification of this is the instrument deflection: at half water quantity the Venturi-meter produced quarter effective pressure,while the induction meter produces half voltage, that is, the accuracy of measurement does not deteriorate to such an extent than there.

From this measuring mouth selection it follows, that because of deposition s of the same degree the error of the induction meter will be a priori less than that of the Venturi-meter because the relationships (1-4) include D in the denominator.

The water producing and the further pressure system of the water works of Budapest is such that several hundred wells operate connected in parallel for a low-pressure collecting system and the high-pressure pumps suck the water from this, which they force into the urban main pipe network.Water-flow is measured at the wells too, by many small-diameter meters and water-flow is measured also in the mains. For example 94 meters measure well water in the north producing area of Budapest, while of the main meters 12 measured further pressure. The size of the well meters is between 200-350 mm.If a deposition s of the same degree is presumed everywhere (which is not true because it depends also in the water quantity differing by plant and besides this the deposition is greater at the wells, the wall of the collecting pipe system located between them - as a deposit storage - delays the development of deposition in the main water-meters) the error of the large number of small meters is necessarily greater than that of the few main meters.In recent years, we have concerned ourselves very much with this deviation, which can be always measured because we tried to find the defect, the flow-off in the low pressure collecting system.The differences measured meant such an extraordinary water flow (3-6 thousand m^3 per hour), the traceless dessication of which was improbable. The deposition and its delay at the meters explained this contradiction.

7.CONCLUSION FOR PLANT MANAGEMENT

Because of environment pollution, it is necessary to form cleaning openings beside the meters and to organize the regular internal cleaning of the meters at such intervals that the metering error should remain within the specified limits.

BIBLIOGRAPHY

1 Zalán,B:Technical economic aspects of water quantity metering at the Water Works of Budapest (in Hungarian) Hidrológiai Közlöny,1975.p.98-102

2 Nagy,M. Várszegi,Cs.:Latest results of liquid quantity metering not based on differential pressure (in Hungarian)
Épületgépészet, 1978.No.1.p.16-21.

Dr.Ing.Csaba FÁY, Direktor's Advisory
Address of Author :
Fővárosi Vizmüvek, H-1566.P.O.B.512
Budapest XIII.Váci ut 23-27.

EXPERIMENTAL RESEARCHES OF FLOW IN HYDRODYNAMIC TORQUE CONVERTERS

W. Fister and F.-W. Adrian

Measurements with the Laser-Two-Focus method and the Spark Tracer method in flow circuits of two geometrically identical and hydrodynamically similar torque converters are described and partly compared with theoretical results.

1. INTRODUCTION

So far flow circuits of hydrodynamic torque converters have been basically dimensioned by means of the one-dimensional theory. Losses occurring in the circuit (e.g. losses due to friction and angular deviation) have been taken into account by means of experimental coefficients or appropriate estimations [1]. A more efficient calculation seems to be possible, if the details of the three-dimensional flow patterns in the torque converter circuit, or rather the relationship between the elements carrying flow and the operating behaviour, are known [2]. As to this problem, the Lehrstuhl für Fluidenergiemaschinen at Ruhr-Universität Bochum has been trying to research the actual three-dimensional flow within the components of the torque converter circuit, both theoretically and experimentally, and to establish its relationship to the operating behaviour.

Besides conventional methods - e.g. by means of probes - two new measuring methods, the Laser-Two-Focus method (L2F) [3] and the Spark Tracer method [4] are applied for the experimental research of the distributions of velocities. For the theoretical computation of the three-dimensional flow a partially parabolic method of calculation has been developed in order to compute the turbulent, incompressible flow, including friction and secondary flow [5]. This method was first programmed for non-bladed, rotationally symmetrical deflection channels [6], and at present it is being extended for bladed channels.

2. DESIGN OF THE TESTING STANDS

The experiments were carried out with two testing converters with geometrically indentical circuits and hydrodynamically similar flows. When designing the testing stands it was taken into account that the L2F-method using sight-holes can only be applied in transparent fluids of a low optical absorption rate, whereas the Spark Tracer method can only be applied in gases and requires transparent and electrically non-conductive walls. Therefore one of the converters contains water as operating fluid (water-torque-converter), whereas a second one entirely consists of transparent plastics and contains air as operating fluid (air-torque-converter) (fig. 1 and 2).

The chosen arrangement of coaxially positioned shafts with impellers of centrifugal flow and the centripetally flown through reactor with rather large non-bladet gaps in front of and behind it ensures good access to the flow circuit, in accordance with the chosen method of measurement, and simplifies the fitting of particular elements carrying flow, if their geometry is to be varied. Such a basic type of a hydrodynamic torque converter is chosen, because essential theoretical and experimental findings are expected to be applicable to other types of torque converters, too.

It is only possible to compare and thus to mutually supplement the experimental findings of both converters, if flows are similar. Geometrical similarity is given by identical construction of the elements carrying flow. A comparison of the characteristic curves yields information about the hydrodynamic similarity. In this respect the optimum efficiency points η_{opt} and the torque ratios μ_o, established for the turnine at stall ($N_T = 0$), measured for different pump speeds, yield the following correlations: $\eta_{opt} = f(Re_u)$ and $\mu_o = f(Re_u)$ (fig. 4). The presented measurement results show the dependence of the optimum efficiencies on the Reynolds-number (Re_u), know from relevant literature [7].

The complete characteristic curves of efficiency and of torque ratio, measured for both converters, with identical Reynolds-numbers $Re_u = 1{,}8 \times 10^6$, confirm hydrodynamic similarity of the flow throughout the whole range of operation (fig. 5).

3. MEASURING METHODS

The L2F-method used in the water torque converter allows a non-disturbing and concentrated measurement of velocity and direction of the flow. The method is based upon dividing a laser-beam into two parallel beams and then focussing it in such a way that two focus points with a known distance occur at the measuring point (fig. 6). If a particle (speck or s.th. similar), carried by the flow, passes the two focus points, two dispersion impulses are reflected towards and registered by photo-multipliers. Averages of the particles velocity data, which are practically identical with the flow velocity, can be deduced from the known geometrical distance of the focus points and the time difference of measured dispersion impulses. The velocity cannot be determined merely by measuring one single particle but through a statistical analysis of all occurrences measured in a defined period.

The L2F equipment is adjusted to the relevant measurement points within the flow circuit by means of a five-dimensional traversing equipment with the aid of electronically controlled stepping motors. To determine the velocity distribution behind the rotating pump and turbine respectively, the measuring processes are interrupted during the rotation of the impeller and released by an impeller-controlled triggering equipment at the requested measuring point.

In addition to conventional probe measurements the Spark Tracer method is used in the air torque converter. The method is based on the procedure of applying high tension to two electrodes in the flow channel. At the point of the lowest electrical resistance - the shortest distance between the two electrodes - during the first ignition a luminescent discharge occurs which leaves an ionized plasmatube. This tube is carried by the flow and deformed according to the flow pattern. Further sparks caused by a high tension of high frequency in defined intervals regenerate and visualize the plasmatube. A photo of all successive sparks provides a so-called spark tracer curtain (fig. 7). It is possible to calculate particular velocities from the known intervals of the sparks and the distance which can be seen on the photo. With the aid of a special electronic appliance for digital picture analysis averages of the particular velocities are determined from a variety of pictures through statistical analysis.

By means of a rotating birefractive prism (Doveprism) it is possible to produce a picture of an impeller which is optically standing still, so that the relative velocity in rotating impellers can successfully be presented with the Spark Tracer method, too [4].

4. TEST RESULTS

Measurements of the total pressure with multihole probes in characteristic flow cross-sections of the torque converter circuit have shown that the losses in the reactor, according to the operating point, are higher by the factor 4-7 than the losses in the two deflections of 180° and 90°, respectively. In order to obtain further information about the losses within and in the surrounding of the reactor the flow in this part has been scrutinized with the L2F-method and the Spark Tracer method, for different operating points. The additional determination of the flow pattern in front of the pump by means of the L2F-method should provide further analysis of upstream effects possibly caused by the pump.

Fig. 3 presents the measurement planes A_1 - A_4 and A_I - A_{III} within the torque converter circuit specified for both measuring methods.

The spark tracer pictures (fig. 8) of the flow in the reactor blades show that with the turbine at stall (N_T = 0) and near the point of idle speed ($M_T \to 0$) the flow is separated on one side of the blade surface, due to the angular deviation of the flow. For the point of optimum efficiency (ν = 0.55) the spark tracer pictures show a flow pattern without any separation in the reactor blade channel. Further spark tracer pictures have shown that a flow without separation between the reactor blades only exists for the operating points $0.35 \leqq \nu \leqq 0.75$.

As the measuring time of the L2F-method increases considerably with increasing turbulence the flow velocities in the water-torque-converter have only been measured in the indicated measurement planes (fig. 3) for the operating points $\nu = 0.4$, $\nu = 0.55$ and $\nu = 0.7$. Fig. 9 shows the isotachs of the meridional velocities, referred to the circumferential speed at the pump outlet, measured at a distance of 5 mm in front of (A_1) and behind (A_3) the reactor blade channel as well as in the channel (A_2) and in front of the pump inlet (A_4).

For all the three operating points the maximum velocity is located at the inner channel wall of the blade inlet. The stagnation line in front of the reactor blades shifts according to the flow direction at the three different operating points. For $\nu = 0.4$ the vector of the inflow to the reactor blades is shifted to the blades' pressure side (fig. 11). For $\nu = 0.55$ (point of maximum efficiency) the flow follows, at least partly, the blade contour, whereas for $\nu = 0.7$ the vector of the inflow is shifted to the blades' suction side. In the middle of the channel the maximum of the velocity has shifted towards the blade's suction side. During all of the three operating points the flow is properly guided by the blades. At the reactor blade channel's outlet (A_3) the wakes are visible at the lateral edges of the isotach-graphs by the gradients of flow velocities. The velocity maximum at the outlet shifts back towards the inner channel wall and changes into a flow profile (A_4) which is typical of the plane in front of most pump impellers and compressor impellers. As these measurements were carried out without triggering the resulting velocity profile could only occur rotationally symmetric. Further measurements with the L2F- and Spark Tracer methods have shown that the shift of the velocity maximum already begins in the last quarter of the reactor blade channel.

A comparison of the flow data obtained by both measuring methods in both torque converters now confirms that flow similarity is given concerning local velocity distributions (fig.10).

The velocity vectors in fig. 11 referred to the circumferential speed of the pump (u_2), illustrate very efficiently the flow towards, between and behind the reactor blades. In contrast to the presupposition of the one-dimensional-theory, the inflow direction along the blade height is not even constant at the point of maximum efficiency. Since angular deviations of the flow towards a blade always lead to flow losses, blades which are twisted according to the measured direction of inflow would reduce such losses.

In fig. 12 the difference between the average flow angle $\bar{\alpha}$ and the flow angle measured in the channel's centre along the blade height is shown. According to the operating points (ν = 0.4, 0.55, 0.7) the curves through the five measuring points of the angle differences show different gradients. Therefore twisted reactor blades would lead to an improvement of the flow pattern and would reduce losses only for one operating point or for a small environment of the operating point. An optimal flow towards the reactor blades, without losses over the whole operating range, could therefore only be achieved by spatially adjustable blades.

5. COMPARISON OF COMPUTING AND MEASURING

At first, flow was experimentally researched as well as theoretically computed in the outer deflection channel with the turbine at stall (N_T = 0). Starting data for the computer program are the distribution of velocities behind the turbine measured with the L2F-method, and the distribution of pressures in front of the reactor measured with probes.

The computed and measured isotachs of meridional velocities of the flow in the outer deflection channel are shown in fig. 13. The influence of the wakes due to the turbine blades (cross-section 1) has faded out after a short distance (cross-section 6) and the flow shows rotational symmetry after a 90°-deflection. In the straight part of the 180°-deflection a comparison of computing and measuring results shows good correspondence. In cross-section 17 the computed and the measured results correspond in the section A-A, whereas in the isotachs of the measured velocities the influence of the following reactor, which so far has not been taken into account for the computation, is reflected.

6. CONCLUSION

In order to establish the relationship between the geometry of the torque converter circuit, the occurring losses, and the operating behaviour with more efficiency than heretofore possible, it has been tried to determine the flow in two geometrically identical and hydrodynamically similar test torque converters at characteristic cross-sections of the circuit. Measurements carried out for this purpose with the L2F-method in the water-torque-converter and with the Spark Tracer method in the air-torque-converter have proved applicable and efficient. The experimental researches are expected to yield basic information about the flow pattern. Additionally they are to serve as a means of countercheck and improvement of the partially-parabolic computing model, which is being developed at present. The combination of experiments and computations is to ensure that these procedures can be applied to other types of torque converters.

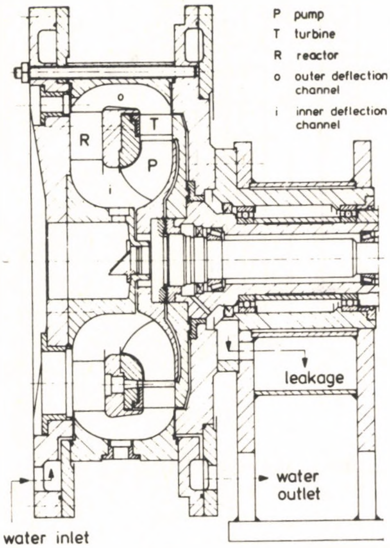

Fig. 1 Section of the hydrodynamic torque converter (water-torque-converter)

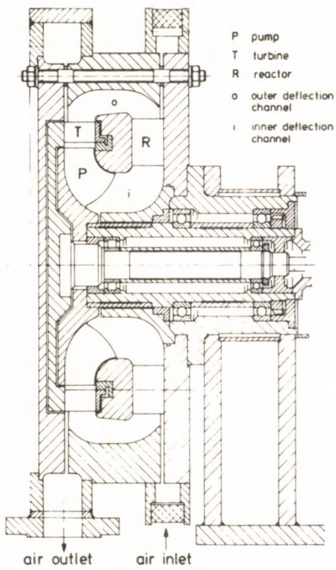

Fig. 2 Section of the hydrodynamic torque converter (air-torque-converter)

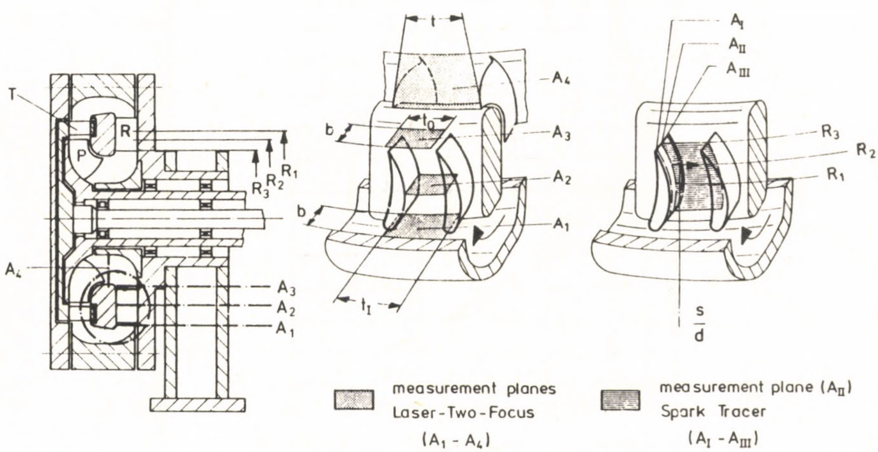

Fig. 3 Measurement planes of Laser-Two-Fokus- and Spark Tracer -method

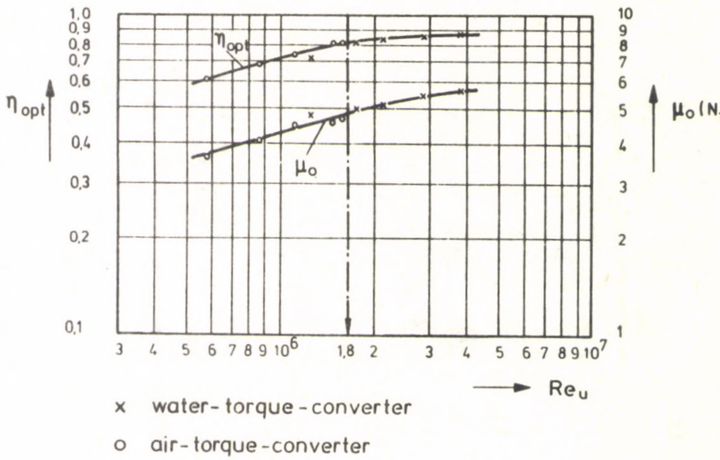

Fig. 4 Influence of Reynolds number on optimum efficiency and torque ratio

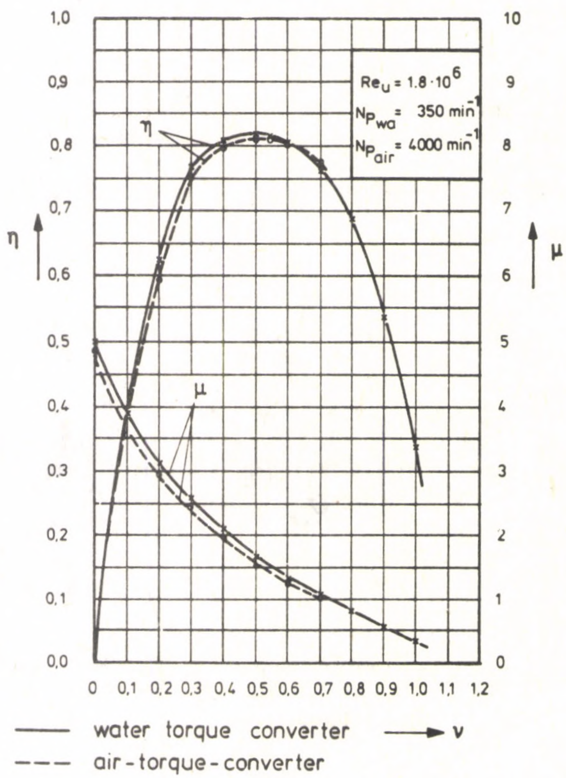

Fig. 5 Comparison of characteristics of the air- and the water-torque-converter

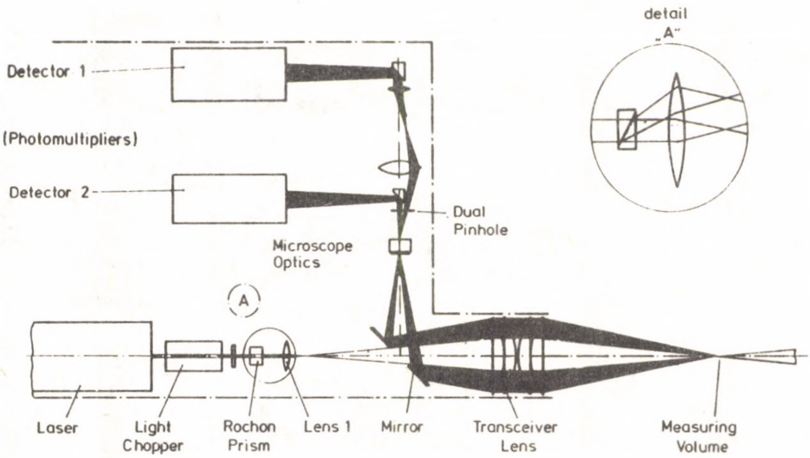

Fig. 6 Course of laser beam of Laser-Two-Fokus-method

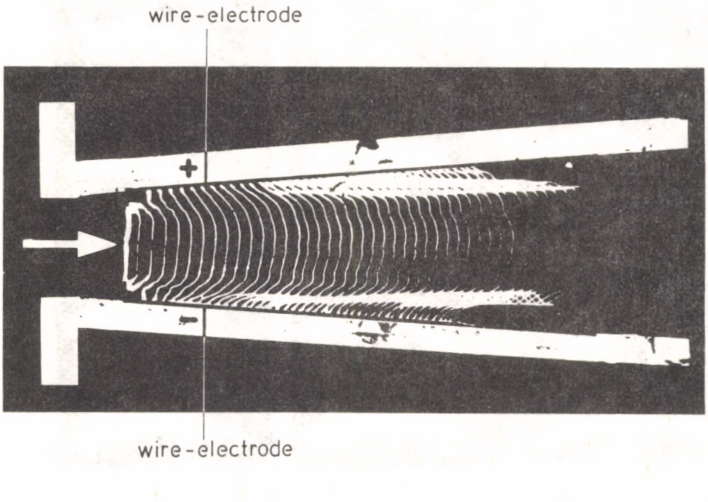

Fig. 7 Spark Tracer photo in a diverging diffuser

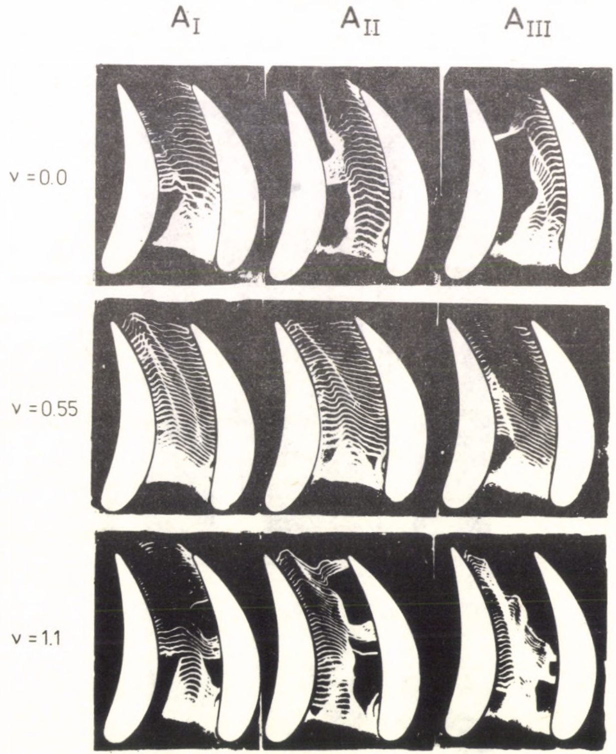

Fig. 8 Spark Tracer photo of the flow through the reactor blades for the operating points
ν = 0.0, ν = 0.55 and ν = 1.1

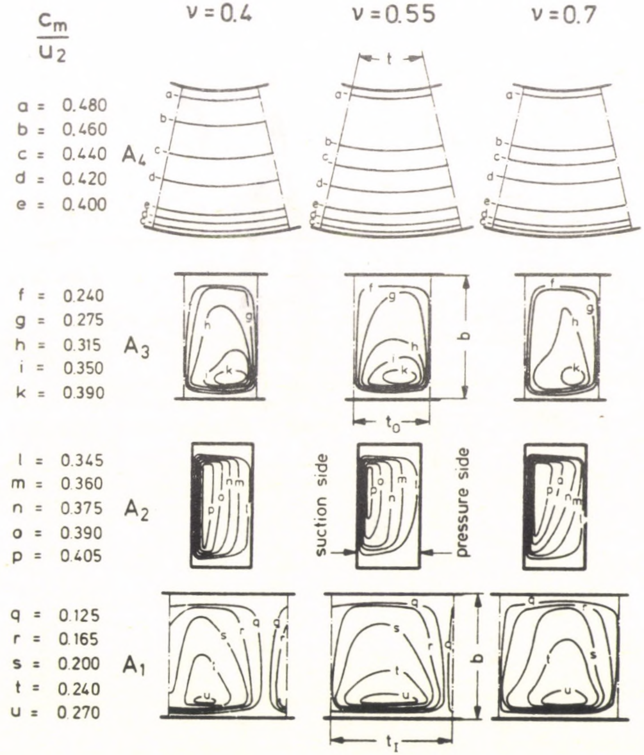

Fig. 9 Isotachs i.e. meridional velocities, referred to the circumferential speed of the flow through the reactor blades (A_1 - A_3) and of the flow in front of the pump (A_4)

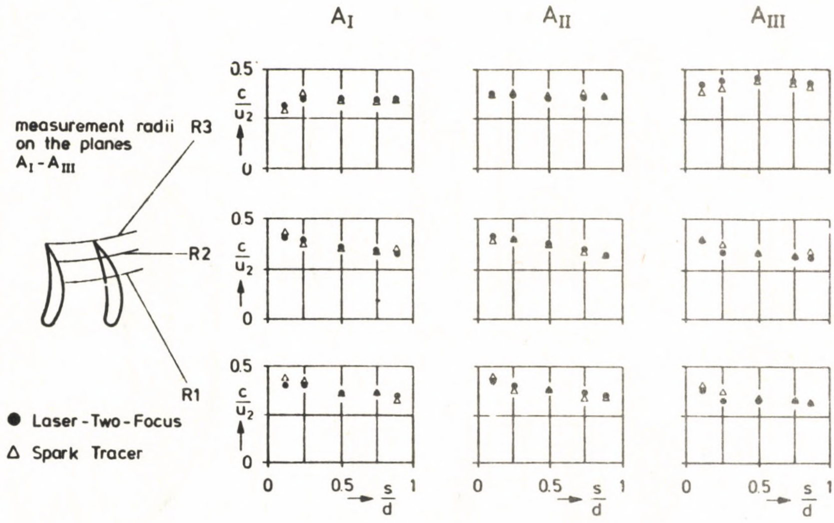

Fig. 10 Comparison of Laser-Two-Focus- and Spark Tracer measurements of the flow through the reactor blades

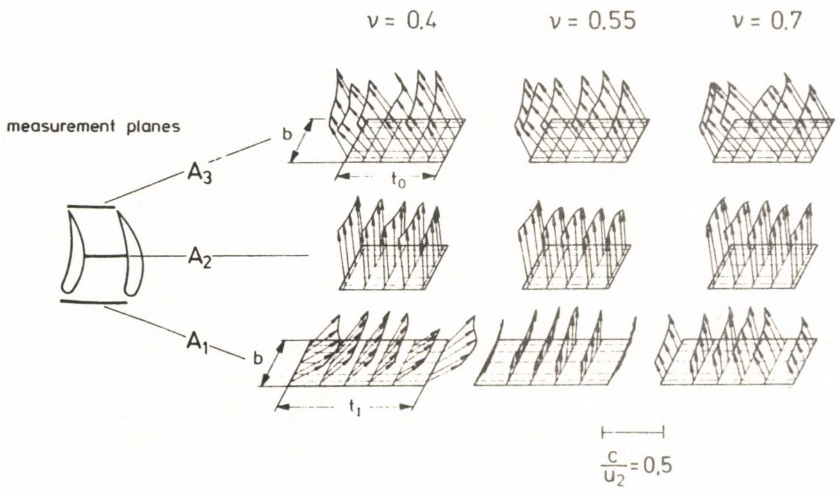

Fig. 11 Vectors of the absolute velocity through the reactor blades at different operating points

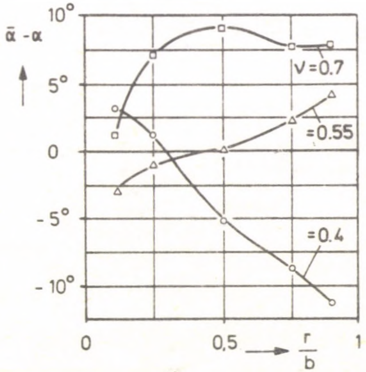

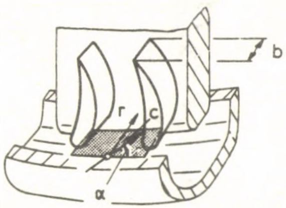

	ν	$\bar{\alpha}$
○	0,4	42°
△	0,55	75°
□	0,7	106°

Fig. 12 Angular differences between averaged and local direction of the flow in front of the reactor blades

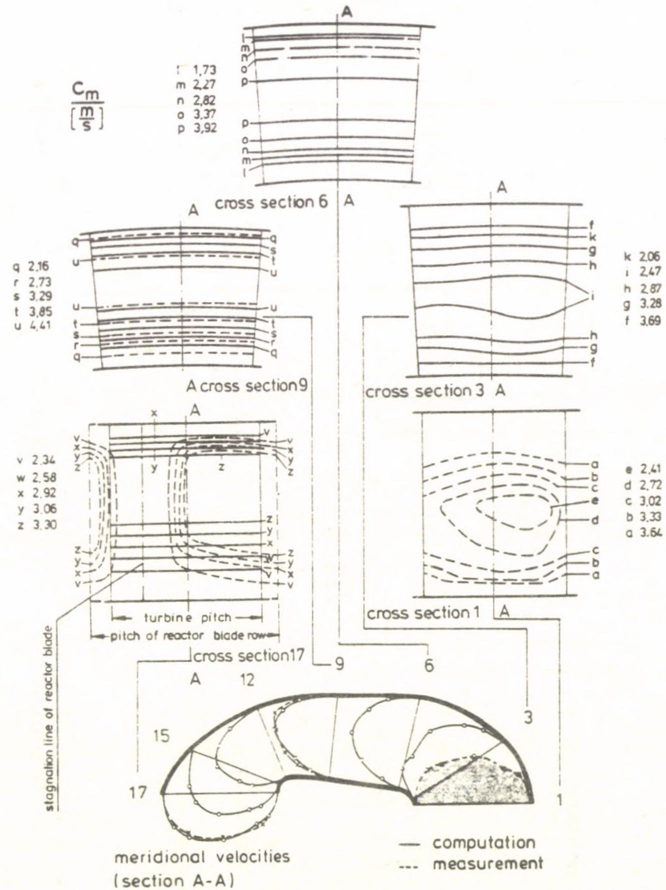

Fig. 13 Computed and measured meridional velocities in the outer deflection channel

7. REFERENCES

[1] TOMO-O-ISHIHARA: A study of hydraulic torque converter
Doc.th., University Tokio, 1955

[2] FISTER, W.; TASCHE, J. and F.-W. ADRIAN: Strömungsuntersuchungen an hydrodynamischen Wandlern im Hinblick auf eine gezielte Kennlinienanpassung
Sonderforschungsbereich 117, Ruhr-Universität Bochum, Arbeits- und Ergebnisbericht 1980/81

[3] SCHODL, R.: Entwicklung des Laser-Zwei-Fokus-Verfahrens für die berührungslose Messung von Strömungsvektoren, insbesondere in Turbomaschinen
DFVLR, Forschungsbericht DLR-FB, Köln, 1977

[4] FISTER, W.: Sichtbarmachung von Strömungen in Radialverdichterstufen, besonders der Relativströmung in rotierenden Laufrädern durch Funkenblitze
BWK, 18 (1966), 9, S. 425-429

[5] MOORE, J. and J.G. MOORE: A calculation procedure for three-dimensional, viscous compressible duct flow
Part I and Part II
Transactions of the ASME, Journal of Fluids Engineering, VOL 101, Dec 1979

[6] ZAHN, G.: Theoretische und experimentelle Strömungsuntersuchungen in Umlenkkanälen von Turbomaschinen
Diss., Ruhr-Universität Bochum, 1982

[7] ROHNE, E.: Der Einfluß von Baugröße, Fluidzähigkeit und Antriebsdrehzahl auf den optimalen Wirkungsgrad von Föttinger Wandlern
Voith Forschung und Konstruktion, Heft 21, Mai 1979

NOMENCLATURE

b	height of reactor blade
c	absolute velocity
c_m	meridional velocity
D_2	outer diameter of the pump
d	local distance between reactor blades
M	torque
N	speed
P	power
Re_u	Reynolds number u_2D_2/ν
r	coordinate of measurement
s	coordinate of measurement
t	pitch
α	flow angle
$\bar{\alpha}$	averaged flow angle
η	efficiency P_T/P_P
μ	torque ratio M_T/M_P
μ_o	torque ratio at stall of the turbine
ν	speed ratio
ν	fluid viscosity

SUBSCRIPTS

air	air-torque-converter
I	inlet
O	outlet
o	operating point $N_T = 0$
opt	point of optimum efficiency
P	pump
R	reactor
T	turbine
wa	water-torque-converter

adress:

Professor Dr.-Ing. W. Fister, Ruhr-Universität Bochum,
Lehrstuhl für Fluidenergiemaschinen, 4630 Bochum 1

THE FLOW THROUGH A SYSTEM OF PROFILE CASCADES

Petr Fleischner

INTRODUCTION

There are mostly more than one blade system in a turbomachine: in a single stage pump is one impeller and one diffuser device, a multistage type pump consists of more impellers, diffuser devices and back blades, a single stage water turbine has two or three blade systems, etc.

A possible method of determining the flow conditions in a blade system will be discussed here.

Let us suppose that a nonviscous incompressible ideal fluid, which elements do not rotate in the absolute space, flows through a turbomachine. This three-dimensional flow is unsolvable, therefore the problem will be transferred in a two-dimensional one if we suppose the flow of the fluid on co-axial stream surfaces in layers of a variable width b.

The flow will be investigated as stationary for certain positions of cascades. The flow surfaces can be transformed in planes by a conformal mapping. One obtains a system of straight cascades for each flow surface (Fig. 1). The cascades are numberred from the left to the right ($j = 1, \ldots, G$). The system is periodical in the direction of the axis η with the period T. The cascade of the number j contains ν_j profiles in one period; they are numberred in the direction of $+\eta$. The profiles of the whole system are numberred consecutively beginning with the first profile in the first cascade.

The flow of the fluid in the plane ζ is a two-dimensional motion in a layer of the variable width $b = b(\xi)$. The basic flow is the parallel one of the velocity $\bar{c}_\infty$; it flows from $\xi \to -\infty$ to $\xi \to +\infty$. The influence of profiles is modelled by elementar sources $q.dL$ and vortices $\gamma.dL$ on central lines of profiles. The variable width is modelled by elementar sources of magnitude

$$dQ = -\frac{1}{b} \cdot \frac{db}{d\xi} \cdot c_\xi . d\xi . d\eta . \tag{1}$$

THE INDUCED VELOCITIES

The velocities induced by singularities on central lines of profiles

The complex conjugate velocity in the point ζ_p on the investigated profile p induced by the singularity $(q_k' + i . \gamma_k') dL_k'$ in the point ζ_k' on the profile k is

$$d\bar{c}_i = \frac{q_k' + i \cdot \gamma_k'}{2\pi} \cdot \frac{dL_k'}{\zeta_p - \zeta_k'} . \tag{2}$$

The flow is periodical with the period iT. All the same singularities $(q_k' + i \cdot \gamma_k') dL_k'$ induce in the point ζ_p the complex con-

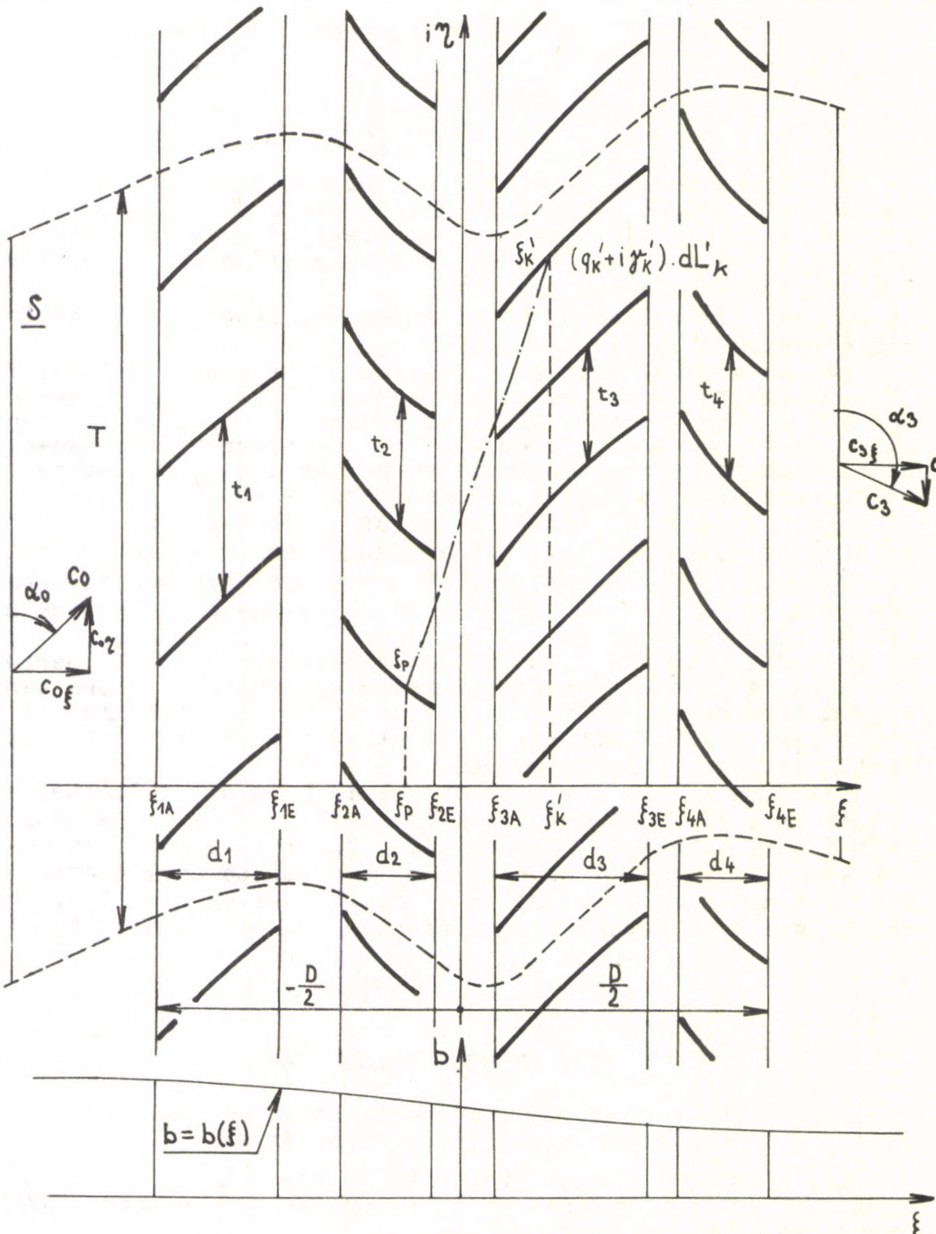

j =	1	2	3	4 = G
ν_j =	4	5	6	5
N_j =	4	9	15	20

Fig. 1.

jugate velocity

$$d\overline{c}_i = \frac{q_k' + i.\gamma_k'}{2T} . dL_k' . \coth \frac{\pi}{T}(\xi_p - \xi_k'). \tag{3}$$

The complex conjugate velocity in the point ξ_p induced by all singularities on all profiles, which are flowed round in the same way, is

$$\overline{c}_i = \frac{1}{2T}\int_{L_k'} (q_k' + i.\gamma_k').\coth \frac{\pi}{T}(\xi_p - \xi_k').dL_k'. \tag{4}$$

Introducing: $q^* = \frac{q}{\cos\chi}$; $\gamma^* = \frac{\gamma}{\cos\chi}$; $dL = \frac{d\xi}{\cos\chi}$, (5)

the equation (4) can be written in the form:

$$\overline{c}_i = \frac{1}{2T}\int_{\xi_{kA}}^{\xi_{kE}} (q_k^{*\prime} + i.\gamma^{*\prime}).\coth \frac{\pi}{T}(\xi_p - \xi_k').d\xi'. \tag{6}$$

If $k \neq p$:

$$\overline{c}_i = \overline{c}_{ik} = \frac{1}{2d_k}\int_{\xi_{kA}}^{\xi_{kE}} (q_k^{*\prime} + i.\gamma^{*\prime}).F_k.d\xi', \tag{7}$$

where $F_k = \frac{d_k}{T}.\coth \frac{\pi}{T}(\xi_p - \xi_k')$. (8)

If $k = p$: introducing the function

$$H_p = (\xi_p - \xi').\coth \frac{\pi}{T}(\xi_p - \xi_k') \tag{9}$$

we obtain $\overline{c}_i = \overline{c}_p = \overline{c}_{pR} + \overline{c}_C + \overline{c}_\pm$, (10)

where $\overline{c}_{pR} = \frac{1}{2d_p}\int_{\xi_{pA}}^{\xi_{pE}} (q_p^{*\prime} + i.\gamma_p^{*\prime}).F_p.d\xi'$, (11)

$$\overline{c}_C = \frac{1}{2\pi}.e^{-i\chi_p}.\cos\chi_p \oint_{\xi_{pA}}^{\xi_{pE}} (q_p^{*\prime} + i.\gamma^{*\prime})\frac{d\xi'}{\xi_p - \xi}, \tag{12}$$

$$\overline{c}_\pm = \frac{\gamma_p - i.q_p}{2}.e^{-i\chi_p}, \tag{13}$$

$$F_p = \frac{d_p}{T}\left[H_p - \frac{T}{\pi}.e^{-i\chi_p}.\cos\chi_p\right].\frac{1}{\xi_p - \xi'}. \tag{14}$$

The resulting velocity is the sum of velocities induced by all singularities on all profiles. Introducing

$$\overline{c}_R = \sum_{k=1}^{N_G} \frac{1}{2d_k}\int_{\xi_{kA}}^{\xi_{kE}} (q_k^{*\prime} + i.\gamma_k^{*\prime}).F_k.d\xi' \tag{15}$$

where F_k is given by (8) when $k \neq p$ and by (14) when $k = p$, we can write the resulting complex conjugate velocity:

$$\overline{c}_i = \overline{c}_R + \overline{c}_C + \overline{c}_{\pm}. \tag{16}$$

The velocities induced by sources in the domain S

The complex conjugate velocity induced by a source of the magnitude (1) is

$$d\overline{c}_B = \frac{dQ}{2\pi} \cdot \frac{1}{\xi_s - \xi_s'}. \tag{17}$$

The iteration process must be used if the velocity c_B is calculated by a two-dimensional integration. Using an average value of c_B the computation has one step only. The velocity

$$\hat{c}_\xi = c_{\infty\xi} + \hat{c}_{B\xi} + \hat{c}_{i\xi} \tag{18}$$

is independent on η for certain ξ. The value of $\hat{c}_\xi$ follows from the flow rate of the basic flow and the flow rate caused by elementar sources on profiles:

$$c_m . T . b_R = \hat{c}_\xi . T . b - \sum_{k=N_{g-1}+1}^{N_g} \int_{\xi_{kA}}^{\xi_k} q_k^{*'} . b' . d\xi' \tag{19}$$

The average velocity follows immediate:

$$\hat{c}_\xi = \frac{b_R}{b}\left(c_m + \frac{1}{T}\sum_{k=N_{g-1}+1}^{N_g} \int_{\xi_{kA}}^{\xi_k} q_k^{*'} \cdot \frac{b'}{b_R} . d\xi'\right). \tag{20}$$

The velocity $\hat{c}_{i\xi}$ is the mean value of velocities $c_{i\xi}$; they are given by the formula (15) with the function F (8); the point ξ_P must be replaced by a common point ξ_S. It is possible to write:

$$\hat{c}_i = \frac{1}{T}\int_{\eta_P - \frac{T}{2}}^{\eta_P + \frac{T}{2}} \left[\sum_{k=1}^{N_G} \frac{1}{2d_k} \int_{\xi_{kA}}^{\xi_{kE}} (q_k^{*'} + i.\gamma_k^{*'}).F_k . d\xi'\right] d\eta'. \tag{21}$$

The integration in the direction of η is independent on the integration in the direction of ξ. Therefore:

$$\hat{c}_i = \frac{1}{T}\sum_{k=1}^{N_G} \frac{1}{2d_k} \int_{\xi_{kA}}^{\xi_{kE}} \left[(q_k^{*'} + i.\gamma_k^{*'}) \int_{\eta_P - \frac{T}{2}}^{\eta_P + \frac{T}{2}} F_k . d\eta'\right] d\xi'. \tag{22}$$

The internal integral is: $$\int_{\eta_P - \frac{T}{2}}^{\eta_P + \frac{T}{2}} F_k . d\eta' = \begin{cases} d_k & \text{for } \xi' < \xi, \\ -d_k & \text{for } \xi' > \xi. \end{cases} \tag{23}$$

The following expression can be now written:

$$c_{\infty\xi} + \hat{c}_{B\xi} = \frac{b_R}{b}\left(c_m + \frac{1}{T}\sum_{k=N_{g-1}+1}^{N_g} \int_{\xi_{PA}}^{\xi_P} q_k^{*'} \frac{b'}{b_R} . d\xi'\right) \mp \frac{1}{2T}\sum_{k=1}^{N_G} \int_{\xi_{kA}}^{\xi_{kE}} q_k^{*'} . d\xi'; \tag{24}$$

the upper sign is valid for $\xi > \xi'$, the lower one for $\xi < \xi'$.

APPROXIMATION OF SOURCE AND CIRCULATION DENSITIES

Introducing the angle θ :

$$\xi = \frac{1}{2}(\xi_{kA} + \xi_{kE}) - \frac{d_k}{2}\cdot\cos\theta \tag{25}$$

the modified densities of elementar sources and circulations of the profile number k are

$$q_k^* = 2c_m \sum_{\mu=1}^{n_k} B_{k\mu}\left(k_{k\mu}\cdot \mathrm{cotg}\frac{\theta}{2} - \sin\mu\theta\right), \tag{26}$$

$$\gamma_k^* = 2c_m\left(A_{k0}\cdot \mathrm{cotg}\frac{\theta}{2} + \sum_{\mu=1}^{n_k-1} A_{k\mu}\cdot \sin\mu\theta\right) \tag{27}$$

the coefficients $k_{k\mu}$ follows from the closed contour of the profile:

$$k_{k\mu} = \frac{\int_0^\pi \frac{b}{b_R}\cdot\sin\mu\theta.\sin\theta.d\theta}{\int_0^\pi \frac{b}{b_R}\cdot(1+\cos\theta).d\theta}. \tag{28}$$

The dimensionless velocities can be expressed by using of the source and circulations densities. The components of c_C are:

$$\frac{c_{C\xi}}{c_m} = \cos\chi_p\left[\cos\chi_p \sum_{\mu=1}^{n_p} B_{p\mu}(k_{p\mu}+\cos\mu\theta) + \sin\chi_p\left(A_{p0} - \sum_{\mu=1}^{n_p-1} A_{p\mu}\cdot\cos\mu\theta\right)\right], \tag{29}$$

$$\frac{c_{C\eta}}{c_m} = \cos\chi_p\left[\sin\chi_p \sum_{\mu=1}^{n_p} B_{p\mu}(k_{p\mu}+\cos\mu\theta) - \sin\chi_p\left(A_{p0} - \sum_{\mu=1}^{n_p-1} A_{p\mu}\cdot\cos\mu\theta\right)\right]. \tag{30}$$

Introducing the coefficients

$$m_{k\mu} = \frac{1}{d_k}\int_{\xi_{kA}}^{\xi_{kE}} \mathrm{Re}(F_k).f(\theta').d\xi' \;;\; \overline{m_{k\mu}} = \frac{1}{d_k}\int_{\xi_{kA}}^{\xi_{kE}} \mathrm{Im}(F_k).f(\theta').d\xi', \tag{31}$$

where
$$f(\theta') = \begin{cases} \mathrm{cotg}\frac{\theta'}{2} & \text{for } \mu=0, \\ \sin\mu\theta' & \text{for } \mu>0. \end{cases} \tag{32}$$

the components of the velocity c_R (15) can be expressed in the form:

$$\frac{c_{R\xi}}{c_m} = \sum_{k=1}^{N_G}\left[\sum_{\mu=1}^{n_k} B_{k\mu}(k_{k\mu}\cdot m_{k0} - m_{k\mu}) - \sum_{\mu=0}^{n_k-1} A_{k\mu}\cdot\overline{m_{k\mu}}\right], \tag{33}$$

$$\frac{c_{R\eta}}{c_m} = -\sum_{k=1}^{N_G}\left[\sum_{\mu=1}^{n_k} B_{k\mu}(k_{k\mu}\cdot\overline{m_{k0}} - \overline{m_{k\mu}}) + \sum_{\mu=0}^{n_k-1} A_{k\mu}\cdot m_{k\mu}\right]. \tag{34}$$

Two integrals must be calculated for expressing the velocity (24). The first one is:

$$I_1 = \frac{2c_m}{T}\int_{\xi_{pA}}^{\xi_p} \frac{q_k^{*'}}{2c_m}\cdot\frac{b'}{b_R}\cdot d\xi' =$$

$$= c_m \frac{d_k}{T}\sum_{\mu=1}^{n_k} B_{k\mu}\int_0^{\theta}\left(k_{k\mu}\cdot \cot g\frac{\theta'}{2} - \sin\mu\theta'\right)\frac{b'}{b_R}\cdot \sin\theta' d\theta' \tag{35}$$

This integral must be solved numerically. The second integral of (24) is

$$I_2 = \pm \frac{c_m}{T}\int_{\xi_{kA}}^{\xi_{kE}} \frac{q_k^{*'}}{2c_m} d\xi' \tag{36}$$

It is solved for three alternatives. It can be demonstrated that for $\xi_{kE} < \xi_{pA}$:

$$I_2 = c_m \frac{\pi}{2}\cdot\frac{d_k}{T}\sum_{\mu=1}^{n_k} B_{k\mu}\left(k_{k\mu} - \frac{1}{2}\right), \tag{37}$$

for $\xi_{kA} < \xi_k < \xi_{kE}$:

$$I_2 = c_m \frac{d_k}{T}\left\{\sum_{\mu=1}^{n_k} B_{k\mu}\cdot k_{k\mu}\left(\theta + \sin\theta - \frac{\pi}{2}\right) - B_1\left(\frac{\theta}{2} - \frac{\pi}{2} - \frac{\sin 2\theta}{4}\right) - \right.$$

$$\left. - \sum_{\mu=1}^{n_k} B_{k\mu}\left[\frac{\sin(\mu-1)\theta}{2(\mu-1)} - \frac{\sin(\mu+1)\theta}{2(\mu+1)}\right]\right\}, \tag{38}$$

for $\xi_{pE} < \xi_{kA}$: $I_2 = -c_m \frac{\pi}{2}\cdot\frac{d_k}{T}\sum_{\mu=1}^{n_k} B_{k\mu}\left(k_{k\mu} - \frac{1}{2}\right)$. (39)

Using these formulae in (24) the velocity $\hat{c}_{B\xi}$ obtains the form:

$$\frac{c_{\infty\xi}}{c_m} + \frac{\hat{c}_{B\xi}}{c_m} = \frac{b_R}{b} + \sum_{k=1}^{N_G}\sum_{\mu=1}^{n_k} B_{k\mu}\, m_{k\mu}^{*}. \tag{40}$$

The components of the mean velocity on the central line can be now expressed:

$$\frac{c_\xi}{c_m} = \frac{b_R}{b} + \sum_{k=1}^{N_G}\left[\sum_{\mu=1}^{n_k} B_{k\mu}\left(k_{k\mu}\cdot m_{ko} - m_{k\mu} + m_{k\mu}^{*}\right) - \sum_{\mu=0}^{n_k-1} A_{k\mu}\cdot \overline{m}_{k\mu}\right] +$$

$$+\cos\chi_p\Big[\cos\chi_p\sum_{\mu=0}^{n_p} B_{p\mu}(k_{p\mu}+\cos\mu\theta)+\sin\chi_p\Big(A_{p0}-\sum_{\mu=1}^{n_p-1} A_{p\mu}\cos\mu\theta\Big],\tag{41}$$

$$\frac{c_\eta}{c_m}=\varkappa-\sum_{k=1}^{N_G}\Big[\sum_{\mu=1}^{n_k} B_{k\mu}(k_{k\mu}\overline{m}_{k0}-\overline{m}_{k\mu})+\sum_{\mu=0}^{n_k-1} A_{k\mu}m_{k\mu}\Big]+$$

$$+\cos\chi_p\Big[\sin\chi_p\sum_{\mu=1}^{n_p} B_{p\mu}(k_{p\mu}+\cos\mu\theta)-\cos\chi_p\Big(A_{p0}-\sum_{\mu=1}^{n_p-1} A_{p\mu}\cos\mu\theta\Big)\Big].\tag{42}$$

THE KINEMATIC CONDITIONS

The kinematic conditions are satisfied approximately: in a **finite** number of pivot points.

The first kinematic condition

The mean relative velocity on the central line must be tangential to it (Fig. 2):

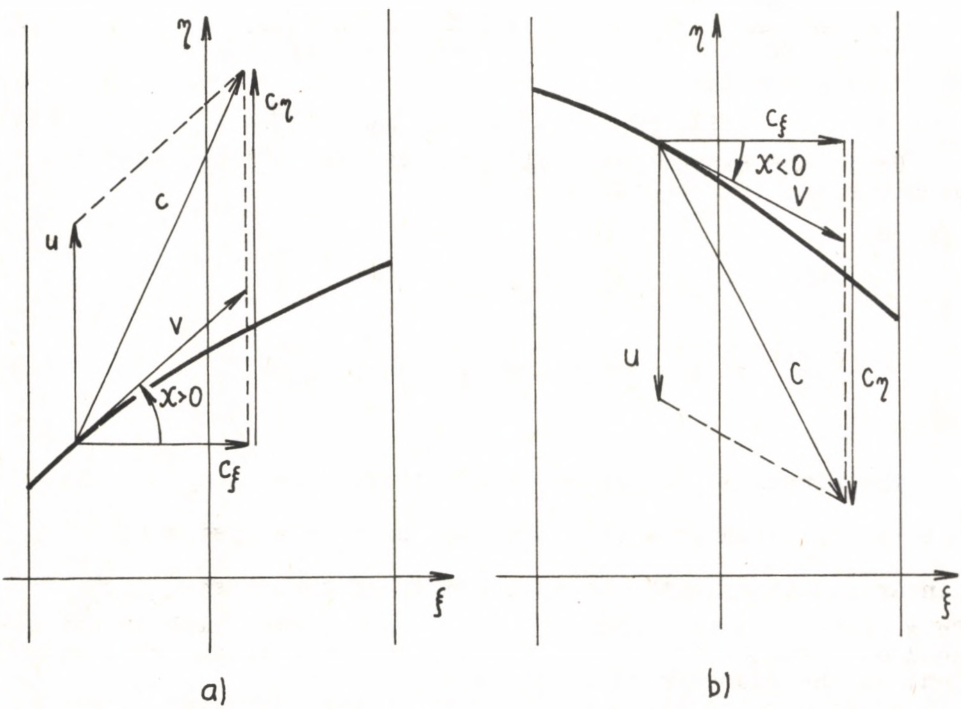

Fig. 2.

$$\frac{c_\xi}{c_m}\, tg\, \chi_p = \frac{c_\eta}{c_m} - sign\ \omega_p\, \frac{|u_p|}{c_m}, \tag{43}$$

where: $sign\ \omega_p = 1$ for u_p in the direction of $+\eta$,
$sign\ \omega_p = 0$ for a stator cascade,
$sign\ \omega_p = -1$ for u_p in the direction of $-\eta$.

The expression $\frac{|u_p|}{c_m}$ can be modified in:

$$\frac{|u_p|}{c_m} = \frac{\omega_p}{\Omega} \cdot \frac{1}{\varphi}\left(\frac{r}{R}\right)^2. \tag{44}$$

Every cascade can have an own angular velocity.

If the expressions (41) an (42) are introduced in (44), then we obtain:

$$\sum_{k=1}^{N_G} \sum_{\mu=1}^{n_k} (A_{k,\mu-1} \cdot \alpha_{k,\mu-1} + B_{k,\mu} \cdot \beta_{k,\mu}) = -\frac{b_R}{b}\, tg\, \chi_p + \varkappa - sign\, \omega_p \frac{\omega_p}{\Omega} \cdot \frac{1}{\varphi}\left(\frac{r}{R}\right)^2 \tag{45}$$

The second kinematic condition

It respects the equation of continuity on an element of profile:

$$\frac{v}{c_m}\Delta = \frac{q^*}{2c_m} \qquad \text{where} \qquad \Delta = \frac{d\delta}{d\xi} + \frac{1}{b} \cdot \frac{db}{d\xi}. \tag{46}$$

The velocity v is:

$$v = \cos \chi_p [c_\xi + tg\, \chi_p (c_\eta - |u_p| . sign\ \omega_p)]. \tag{47}$$

Using the expressions (41) and (42) in (47) and (46) the second kinematic condition is:

$$\sum_{k=1}^{N_G} \sum_{\mu=1}^{n_k} (A_{k,\mu-1} \cdot \overline{\alpha}_{k,\mu-1} + B_{k,\mu} \cdot \overline{\beta}_{k,\mu}) =$$

$$= [-\frac{b_R}{b} - \varkappa . tg\, \chi_p + sign\, \omega_p \frac{\omega_p}{\Omega} \cdot \frac{1}{\varphi}\left(\frac{r}{R}\right)^2 tg\, \chi_p]\Delta \tag{48}$$

The kinematic conditions are satisfied in $\sum_{k=1}^{N_G} n_k$ pivot points. The equations (45) and (48) creates a system of $2\sum_{k=1}^{n_G} n_k$ linear equations with the same number of unknowns: $A_{k,\mu}$; $B_{k,\mu}$.

This system can be decomposed in three systems which do not depend on $\varkappa$ and $\overline{\varphi}$; the coefficients of these systems are dependent on the geometry of cascades only.

After solving the systems of the linear equations the circulation and the velocity distribution on every profile can be determined.

This method was programmed for a special case: a radial pump impeller with main blades and intermadiate ones. The infinite thin blades had the forms of logarithmic spirals. The calculation shown it is not possible to achieve the shockless flow on both systems of blades. For our case, the impeller with one system of blades is more advantageous than the impeller with two ones.

SYMBOLS

Quantities

c absolute velocity
$\hat{c}$ average absolute velocity
L central line
n number of pivot points
N_G number of the last profile in the whole system
R refer radius
r radius
U peripheral velocity on the radius R

u peripheral velocity
v average relative velocity on the central line
δ half of the profile thickness
$\zeta = \xi + i.\eta$ complex plane
$\varkappa = \frac{c_{\infty\eta}}{c_m}$
$\overline{\varphi} = \frac{c_m}{U}$ velocity number
Ω angular velocity on the radius R

Subskripts

A on the leading edge
C contens an integral in the sense of Cauchy´s main value
E on the trailing edge
m average meridian velocity on the radius R

R on the radius R
R contens an integral in Riemann´s sense
S in an interior point of the domain S
η in the direction of η
ξ in the direction of ξ

REFERENCES

[1] Czibere T.: Über die Berechnung der Schaufelprofile und die Strömung um die Schaufeln von Strömungsmaschinen. Ingenieur-Archiv, Band 33 (1964), Seiten 215-230.

[2] Boros G.: Computation of the Theoretical Characteristics of Axial Flow Pumps Based on the Theory of Adjacent Cascades. Proceedings of the Sixth Conference on Fluid Machinery, Budapest, 1979, pages 127-136.

Doc. Ing. Petr Fleischner C.Sc.
Faculty of Mechanical Engineering
Department of Hydraulic Machines
and Equipments
Technical University
Obránců míru 65
602 00 B r n o .
Czechoslovakia.

INVESTIGATION OF CAVITY PULSATIONS BEHIND THE BODY IN A PLANE FLOW

A.P. Frolov, The Institute of Water Problems, the USSR Academy of Sciences, Moscow, U.S.S.R.

Analysis of the various ways of controlling the cavitation erosion of hydraulic turbines shows that all the conceivable methods of improving the cavitation stability of components have been investigated thoroughly enough and most of them have been used in practice /8/. However, elimination of the reasons responsible for cavitation erosion themselves bears a potential for turbine protection which has not yet been resorted to sufficiently. The ways to do this include mounting the turbine at a deep enough level or designing the turbine duct with allowance for displacement of the cavity collapse zones to an area behind the blade cascade.

Initially, a cavitation zone consists of periodically arising free vortices and surging cavities carried away by the flow. The regions of the most intensive erosion coincide with the regions where the cavity pulsation amplitudes are highest.

Comparison of the location of secondary erosion sites with the location and shapes of cavities may be done only with the help of high-speed filming of the cavitation zone, since the cavity generation process in these regions occurs within small volumes and with a high repetition frequency. It was found that the pulsation frequency of the cavity responsible for the generation of secondary erosion sites cannot be calculated by the formula for natural pulsations of a unit cavity in an unbounded liquid /1/.

Pulsations of a cavitation vortex behind a blunt body have not been studied thoroughly yet. In /2/ a solution of the problem of a flow past a steady-state vortex in a channel (the plane problem) was given. Pulsations of a vortex cavity in a boundless liquid have been discussed in /3/. It may be of interest to study the effect of channel walls on the pulsation period of a vortex-cavity.

With a view to analytically determine the pulsation period of a cavity wave behind the blunt body mounted in a plane-parallel working chamber of a cavitation tunnel, we will study the dynamics of a gas-filled circular cavity within a certain finite volume of an incompressible ideal liquid. The outer boundary of the liquid volume in question consists in part of impermeable solid straight sections and in part of surfaces on which a constant pressure, different from that in the gas-filled cylindrical cavity, is maintained. In a cavitation tunnel the constant-pressure surface is the surface of the liquid bed in the surge tank.

1.- Consider the radial vibrations of a liquid layer enclosed between two coaxial circular cylinders of radii $R(t)$ and $R_1(t)$. Differently formulated, this problem was considered in /4/. Since the motion of liquid is symmetrical relative to the cylinder axes, it follows from the continuity equation:

$$\frac{\partial}{\partial r}(r v_r) = 0 \tag{1.1}$$

that

$$v_r = C(t)\, r^{-1} \tag{1.2}$$

where r is the distance from a point in the flow to the cylinder axis;
$C(t)$ is a yet undefined function of time t,
V_r is radial velocity of liquid.

Introducing a velocity potential $\varphi(r,t)$ as

$$v_r = \frac{\partial \varphi}{\partial r} \tag{1.3}$$

we can find from (1.2) that

$$\varphi(r,t) = C(t) \ln r \tag{1.4}$$

Since on the inner boundary of the liquid at $r = R(t)$,

$$v_r = \dot{R}(t)$$

we have from (1,2)

$$C(t) = R\dot{R} \quad , \quad \dot{R} = \frac{dR}{dt}$$

For finding the law governing the variation of the internal cylinder radius $R(t)$ in time we write the Lagrange-Cauchy /5/ integral for unsteady potential liquid flow

$$\frac{\partial \varphi}{\partial t} + \frac{1}{2}\left(\frac{\partial \varphi}{\partial r}\right)^2 + \frac{p}{\rho} = F(t) \tag{1.5}$$

Here, p is pressure in the liquid
ρ is liquid density,
$F(t)$ is an arbitrary time function.

The boundary conditions will be the following:

$$\begin{aligned} p &= p_2 = p_H & \text{when} \quad r &= R(t) \\ p &= p_1 & \text{when} \quad r &= R_1(t) \end{aligned} \tag{1.6}$$

From eqs. (1.4)-(1.6) we obtain an equation from which $R(t)$ can be found:

$$(\dot{R}^2 + R\ddot{R})\ln\left(\frac{R_1}{R}\right)^2 + \dot{R}^2\left(\frac{R^2}{R_1^2} - 1\right) + z = 0$$

$$z = \frac{2(P_1 - P_H)}{\rho}, \quad R_1^2 = R^2\left(\frac{Q}{\pi R^2} - 1\right) \tag{1.7}$$

Here, Q is the volume of liquid per unit cylinder length. Assuming that for t=o, $R=R_0$, $\dot{R}=0$, we find

$$\frac{dR}{dt} = \left\{\frac{2P_1 R_0^2}{\rho R^2} \cdot \frac{1 - \frac{R^2}{R_0^2} - \frac{P_0}{P_1}\cdot\frac{1}{1-n}\left[1 - \left(\frac{R_0}{R}\right)^{2(n-1)}\right]}{\ln\frac{Q+\pi R^2}{\pi R^2}}\right\}^{1/2} \tag{1.8}$$

where p_0 is gas pressure for $R(t) = R_0$,
n is the adiabatic exponent.

In case of isothermal pulsation of a gas cavity,

$$\frac{dR}{dt} = \left\{\frac{2P_1 R_0^2}{\rho R^2} \cdot \frac{1 - \frac{R^2}{R_0^2} - \frac{P_0}{P_1}\ln\left(\frac{R_0}{R}\right)^2}{\ln\frac{Q+\pi R^2}{\pi R^2}}\right\}^{1/2} \tag{1.9}$$

It should be noted that real cavities are usually filled with a mixture of liquid and gas bubbles. As the heat capacity of water is high, cavity pulsations will be substantially isothermal /6/. The pulsation period of such cavities will be found from (1.9)

$$T = 2\int_{R_0}^{R_{min}} \frac{R}{R_0\sqrt{\frac{2P_1}{\rho}}}\left[\frac{1 - \left(\frac{R}{R_0}\right)^2 - \frac{P_0}{P_1}\ln\left(\frac{R_0}{R}\right)^2}{\ln\frac{Q+\pi R^2}{\pi R^2}}\right]^{-1/2} dR \tag{1.10}$$

where R_{min} is the root of equation ($R_{min} \neq R_0$):

$$1-\left(\frac{R}{R_o}\right)^2-\frac{P_o}{P_1}\ln\left(\frac{R_o}{R}\right)^2=0 \qquad (1.11)$$

The time of collapse of an empty cavity ($p_0 = 0$) is:

$$T=\int_0^{R_o}\frac{R}{R_o\sqrt{\frac{2P_1}{\rho}}}\left[\frac{1-\left(\frac{R}{R_o}\right)^2}{\ln\frac{Q+\pi R^2}{\pi R^2}}\right]^{-1/2}dR \qquad (1.12)$$

2.- Cavities are formed behind blunt bodies on the vortex strip axes in a liquid flow /7/. It may, therefore, be reasonable to take into account the flow vorticity caused by oscillations of the cylindrical cavity. The potential of such a flow is a vortex source and will depend both on r and the polar angle θ /5/ in the following manner:

$$\varphi=\frac{1}{2\pi}\left[m\ln r+\Gamma\theta\right]$$
$$v_r=\frac{m}{2\pi r}, \quad v_\theta=\frac{\Gamma}{2\pi r} \qquad (2.1)$$

Here, $m = 2\pi R\dot{R}$ is the source profusion,

Γ - is velocity circulation along the contour encompassing the cavity.

Using the Lagrange-Cauchy integral (1.5) and conditions (1.6) we obtain an equation for cavity radius R(t):

$$z+(\dot{R}^2+R\ddot{R})\ln\left(\frac{R_1}{R}\right)^2+\dot{R}^2\left(\frac{R^2}{R_1^2}-1\right)+\frac{\Gamma^2}{4\pi^2}\left(\frac{1}{R_1^2}-\frac{1}{R^2}\right)=0 \qquad (2.2)$$

Hence, taking into account the initial conditions (1.8) we find the cavity pulsation period:

$$T=2\int_{R_o}^{R_{min}}\frac{dR}{f(R)} \qquad (2.3)$$

Here, R_{min} is the root of equation ($R_{min} \neq R_0$):

$$1-\left(\frac{R}{R_o}\right)^2+\frac{P_o}{P_1}\ln\left(\frac{R_o}{R}\right)^2-\frac{\rho\Gamma^2}{8\pi^2P_1R_o^2}\ln\frac{R^2\left(1+\frac{\pi R_o^2}{Q}\right)}{R_o^2\left(1+\frac{\pi R^2}{Q}\right)}=f_1(R)=0$$

$$f^2(R)=f_1(R)\left[\frac{\rho R^2}{2P_1R_o^2}\ln\frac{Q+\pi R^2}{\pi R^2}\right]^{-1} \qquad (2.4)$$

It is easy to see that in the case of a rotational flow an empty cavity ($p = 0$) can no longer collapse. There is thus a certain minimum cavity radius R_{min}.

3.- To estimate the effect of solid impermeable flow boundaries on the vibrations of a cylindrical cavity in an ideal incompressible liquid, consider vibrations of a cavity whose center is located at a midpoint between two endless straight lines. It will be assumed, besides, that the maximum cavity diameter is small compared to the distance H between walls.

If the cavity radius $R \ll H/2$, the complex flow potential will be little different from the complex potential of the source (drain) located symmetrically in the duct. The velocity potential of such a flow is known to have the form:

$$\varphi=\frac{m}{4\pi}\ln 4\left(\sin^2\frac{\pi y}{H}+\operatorname{sh}^2\frac{\pi x}{H}\right)$$

$$m=2\pi R\dot{R} \qquad (3.1)$$

The Lagrange-Cauchy integral (1.5) is

$$\frac{1}{2}(R\ddot{R}+\dot{R}^2)\ln 4\left(\sin^2\frac{\pi y}{H}+\operatorname{sh}^2\frac{\pi x}{H}\right)+$$

$$+\frac{1}{2}\left(\frac{\pi}{H}\right)^2(R\dot{R})^2\frac{\operatorname{sh}^2\frac{\pi x}{H}\cdot\operatorname{ch}^2\frac{\pi x}{H}+\sin^2\frac{\pi y}{H}\cdot\cos^2\frac{\pi y}{H}}{\left(\sin^2\frac{\pi y}{H}+\operatorname{sh}^2\frac{\pi x}{H}\right)^2}+\frac{p}{\rho}=F(t)$$

$$(3.2)$$

For simplicity, we will consider this integral only along the streamline (trajectory) with $y = 0$ under the conditions:

$$x=R(t) \qquad p=p_H;$$

$$x=L(t) \qquad p=P_1=\text{const}. \qquad (3.3)$$

$$L=\frac{Q+\pi R^2}{2H}$$

The appearance of the length L means that instead of an infinite channel we are considering cavity pulsations in a limited liquid volume Q: The assumption is all the more accurate the higher the ratio L/H.

Finally, from (3.2) and (3.3) we obtain a nonlinear equation for R(t):

$$(R\ddot{R}+\dot{R}^2)\ \ln \frac{sh^2 \frac{\pi}{H}\cdot\frac{Q+\pi R^2}{2H}}{sh^2 \frac{\pi}{H}R} + \frac{2(P_1-P_H)}{\rho} +$$

$$+\left(\frac{\pi}{H}\right)^2 R^2\dot{R}^2\left(cth^2 \frac{\pi}{H}\cdot\frac{Q+\pi R^2}{2H} - cht^2 \frac{\pi R}{H}\right) = 0 \tag{3.4}$$

Solution of (3.4) can be found in the double quadrature form. Thus taking

$$f_2(R) = 2\left[\ln\left\{Sh\frac{\pi}{H}\cdot\frac{Q+\pi R^2}{2H}\right\} - \ln Sh\frac{\pi R}{H}\right];$$

$$g_2(R) = \left(\frac{\pi}{H}\right)^2 R^2\left\{cth^2\frac{\pi}{H}\cdot\frac{Q+\pi R^2}{2H} - cth^2\frac{\pi R}{H}\right\};$$

$$v(R) = u^2(R)\ ; \qquad u(R) = \frac{dR}{dt} \tag{3.5}$$

we reduce (3.3) to a first-order equation

$$\frac{1}{2}\frac{dV}{dR} Rf(R) + v\left[f(R)+g(R)\right] + \frac{2(P_1-P_H)}{\rho} = 0 \tag{3.6}$$

whence we find the cavity radius variations with time:

$$t = C_2 + \int_{R_0}^{R} \frac{dR}{\sqrt{F(R)}} \tag{3.7}$$

where $$F(R) = R^{-2}e^{-2\varphi}\left[C_1 - \frac{4}{\rho}\int\frac{P_1-P_H}{f_2} Re^{2\varphi}dR\right]$$

$$\varphi(R) = \int\frac{g_2(R)\,dR}{R f_2(R)}$$

The integration constants C_1 and C_2 are found from the initial conditions (1.8).

References

1. Hund M. Zur näherungweisen Berechnungen den Eigen frequenzen von Gasblasen in Flüssigkeit, Acustica, 1969, No 1, pp. 54-56.
2. Gurevich M.I. Ideal Liquid Jet Theory. Fizmatgiz Publishers 1961, p. 65 /in Russian/.
3. Bykovtsev G.I., Kuznetsov G.N. Investigation of cavity pulsations in a vortex. In: Trans. of the Acoustics Institute, 1969, Issue No. 6, p. 129.
4. Sterne T.E. A note on collapsing cylindrical shells. J. of Applied Physics, 1950, vol.21, No. 2.
5. Kochin N.E., Kibel I.A., Rosè N.V. Theoretical Hydromechanics. Part 2, Fizmatgiz Publishers, Moscow, 1963 /in Russian/.
6. Batchelor G.K. Compression waves in a suspension of gas bubbles in liquid. In: Mechanics, 1968, No. 3, pp. 65-84.
7. Shalnev K.K. Cavitation region structure, Izv. AN SSSR, 1954, No. 5.
8. Shalnev K.K., Varga J., Sebestyen Gy. Accurate determination of the scale effect formula for cavitation erosion. Acte Technica Academiae Scientarum Hungaricae, 1969, t.66, No. 4, pp. 347-367.

ON THE INERTIAL DEFORMATION OF A PIPE MADE OF AN ELASTIC MATERIAL IN CASE OF SUDDEN SHUTDOWN OF THE PUMP

A.P. Frolov, The Institute of Water Problems, the USSR Academy of Sciences, Moscow, U.S.S.R.

Many authors /1-3/ have pointed out the importance of taking into account the shear forces, bending moments and inertia forces produced in pipe wall material by a hydraulic shock. The effect of the above factors on the hydraulic shock propagation velocity in a real pipe for the practically attainable pipe closing times is not large /4/, but their dynamic contributions to the average (stationary) pressure and deformed pipe diameter behind the hydraulic shock front may be tangible. Because of the inertial nature of the deformations caused in the pipe wall material, dangerous pipe vibrations may arise. Determination of the pipe vibration frequencies behind the hydraulic shock front may help in investigations of the stability of hydraulic systems in service.

1. A sudden stop of the flow of a weakly-compressible liquid moving in an elastic pipeline with a velocity of v_0 gives rise to a pressure wave

$$P = P_1 - P_0 = \rho_0 v_0 V \tag{1.1}$$

propagating with the velocity

$$V = C_0\left(\frac{hE}{hE + 2\rho_0 C_0^2 R_0}\right)^{1/2} \tag{1.2}$$

Here, C_0 is the speed of sound in unperturbed liquid,
E^0 is the Young's modulus of the pipe material,
ρ_0 is the liquid density,
h^0 is the pipe wall thickness,
R_0 is the pipe radius,
p_0, p_1 are pressures in liquid before and after the passage of the hydraulic shock wave.

The mean value of the deformed pipe radius is given by:

$$R_1 = R_0 + \frac{P \cdot R_0^2}{hE} \tag{1.3}$$

However, taking into consideration that pipe wall deformation is inertial, we obtain that the liquid and pipe walls behind the hydraulic shock front perform vibrations about a stationary (average) state characterized by zero liquid velocity, pressure p_1 and pipe radius R_1.

For a real pipeline ($E = 9,x\ 8 \times 10^{10}$ N/m^2, $R_0 = 0.05$ m, $h = 0.0085$ m) and hydraulic shock of considerable strength ($P = 98$ N/m^2), the relative increase of the mean pipe radius will not be greater than:

$$\frac{R_1 - R_0}{R_0} = 10^{-3} \qquad (1.4)$$

In this case the small motions of liquid are given by:

$$\frac{\partial^2 \varphi}{\partial r^2} + \frac{1}{r}\frac{\partial \varphi}{\partial r} + \frac{\partial^2 \varphi}{\partial x^2} = \frac{1}{C_1^2}\frac{\partial^2 \varphi}{\partial t^2}; \qquad p = p_1 - \rho_1 \frac{\partial \varphi}{\partial t},$$

$$C_1^2 = \frac{K}{\rho_1} \qquad (1.5)$$

where φ (x,r,t) is the liquid velocity potential,
t is time,
x,r are cylindrical coordinates in which x is directed along the pipe axis and r along the pipe radius,
K is elasticity modulus of the liquid.

Pipe deformation and liquid vibrations are assumed to be axisymmetrical.

Considering the pipe as a thin-walled cylindrical shell, we may write down the equation for axisymmetrical pipe vibrations under effect of internal pressure $p-p_1$ /5/:

$$\frac{d^4 R}{d x^4} + 2\alpha^2 \frac{d^2 R}{d t^2} + \beta^4 (R - R_1) = \frac{1}{D}(p - p_1) \Big|_{r = R_1} \qquad (1.6)$$

Here, $2\alpha^2 = \frac{\varkappa h}{D}$, $\beta^4 = \frac{12(1-\nu^2)}{h^2 R_1^2}$, $D = \frac{h^3 E}{12(1-\nu^2)}$,

$\varkappa$ is pipe wall material density,
ν is the Poisson's ratio.

On the pipe wall ($r = R_1$) the radial velocity of liquid must be the same as wall velocity:

$$\frac{\partial R}{\partial t} = \frac{\partial \varphi}{\partial r}\Big|_{r = R_1} \qquad (1.7)$$

Hereby we exclude the case of a permeable pipe wall and the possibility of liquid separation from the pipe wall (cavitation).

The problem of the vibrations of a liquid-filled pipeline behind a hydraulic shock front is thus reduced to solving eqs. (1.5)-(1.7). Introducing dimensionless variables:

$$z = \frac{x}{R_1}, \quad y = \frac{r}{R_1}, \quad u = \frac{R - R_1}{R_1}, \quad \eta = \frac{V}{R_1}t, \quad \Phi = \frac{\varphi}{V R_1} \qquad (1.8)$$

and re-writing the set of eqs. (1.5)-(1.7) in the form:

$$\frac{\partial^2 \Phi}{\partial y^2} + \frac{1}{y}\frac{\partial \Phi}{\partial y} + \frac{\partial^2 \Phi}{\partial z^2} - \frac{V^2}{C_1^2}\frac{\partial^2 \Phi}{\partial \eta^2} = 0$$

$$\frac{E\varepsilon^3}{12(1-\nu^2)\rho_1}\frac{\partial^4 u}{\partial z^4} + \frac{\gamma}{\rho_1}\varepsilon V^2 \frac{\partial^2 u}{\partial \eta^2} + \frac{E}{\rho_1}\varepsilon u + V^2 \frac{\partial \Phi}{\partial \eta}\bigg|_{y=1} = 0 \qquad (1.9)$$

$$\frac{\partial \Phi}{\partial y}\bigg|_{y=1} = \frac{\partial u}{\partial \eta} \qquad \left(\varepsilon = \frac{h}{R_1}\right)$$

Assuming that no other limitations are imposed on the velocity field of the liquid except the condition of periodicity along Z-axis, we will find the solution of eqs. (1.9) in the following form:

$$\Phi = D_1 B(z) \sin\mu(x + Vt) = D_1 A(y) \sin\mu R_1 (z + \eta)$$

$$u = D_2 \cos\mu(x + Vt) = D_2 \cos\mu R_1 (z + \eta) \qquad (1.10)$$

Substituting (1.10) into the first equation of the system (1.9) we find that

$$A(y) = I_0(ny), \qquad n^2 = \left(1 - \frac{V^2}{C_1^2}\right)(\mu R_1)^2 \qquad (1.11)$$

where $I_0(ny)$ is a modified first-order Bessel function, since the hydraulic shock propagation velocity is smaller than the velocity of sound in the liquid.

The last two equations of (1.9) give

$$D_2\left[\frac{E\varepsilon^3}{12(1-\nu^2)\rho_1}\lambda^4 - \frac{\gamma\varepsilon}{\rho_1}V^2\lambda^2 + \frac{E\varepsilon}{\rho_1}\right] + A(1)V^2\lambda D_1 = 0 \qquad (1.12)$$

$$\lambda D_2 + A'(1) D_1 = 0, \qquad \lambda = \mu R_1$$

Since the constants D_1 and D_2 cannot become zero, it is the determinant of the system (1.12) which must be equal to zero. Hence we obtain the following characteristic equation for λ :

$$\frac{E\varepsilon^3}{12(1-\nu^2)\rho_1}\lambda^4 - \left[\frac{\gamma\varepsilon}{\rho_1} + \frac{A(1)}{A'(1)}\right]V^2\lambda^2 + \frac{E\varepsilon}{\rho_1} = 0 \qquad (1.13)$$

Using (1.11), eq. (1.13) can be transformed to:

$$\frac{E\varepsilon^3}{12(1-\nu^2)\rho_1}\lambda^4-\left[\frac{\gamma\varepsilon}{\rho_1}+\frac{I_0(n)}{n I_1(n)}\right]V^2\lambda^2+\frac{E\varepsilon}{\rho_1}=0 \tag{1.14}$$

where $n^2=(1-\frac{V^2}{C_1^2})\lambda^2$, and $I_0(n)=\sum_{K=0}^{\infty}\frac{1}{(K!)^2}\left(\frac{n}{2}\right)^{2K}$

and $I_1(n)=\frac{n}{2}\sum_{K=0}^{\infty}\frac{1}{K!(K+1)!}\left(\frac{n}{2}\right)^{2K}$

are modified first-order Bessel functions /6/.

To see if the transcendent equation (1.14) has any roots we introduce two new functions:

$$f(\lambda^2)=\left[\frac{E\varepsilon^3}{12\rho_1(1-\nu^2)}\lambda^4+\frac{E\varepsilon}{\rho_1}\right]\frac{1}{V^2\lambda} \tag{1.15}$$

$$g(\lambda^2)=\frac{\gamma\varepsilon}{\rho_1}+\frac{I_0(n)}{n I_1(n)}$$

whereafter the equation may be written as

$$F(\lambda^2)=g(\lambda^2)-f(\lambda^2)=0 \tag{1.16}$$

In the vicinity of point $\lambda^2=0$, the functions $f(\lambda^2)$ and $g(\lambda^2)$ have the form:

$$f(\lambda^2)=\frac{\alpha_1}{\lambda^2}+\alpha_2\lambda^2,\quad g(\lambda^2)=\frac{\beta_1}{\lambda^2}+\beta_2+\beta_3\lambda^2+\cdots \tag{1.17}$$

$$\alpha_1=\frac{E\varepsilon}{\rho_1 V^2},\quad \alpha_2=\frac{E\varepsilon^3}{12\rho_1(1-\nu^2)},\quad \beta_1=\frac{2}{n^2},\quad \beta_2=\frac{1}{4}+\frac{\gamma\varepsilon}{\rho_1}$$

Hence,

$$F(\lambda^2)=a\lambda^{-2}+\beta_2+\alpha\lambda^2+\cdots \tag{1.18}$$

where, in view of (1.2), the coefficient $\alpha=\beta_1-\alpha_1>0$

Therefore, near $\lambda^2=0$, the function $F(\lambda^2)>0$.

In the vicinity of an infinitely remote point the function $F(\lambda^2)<0$. Thus eq. (1.16) has at least one root $F(\lambda_*^2)=0$.

Writing eq. (1.16) in the form

$$\lambda^2 = G^{\pm}(\lambda^2) = \frac{1}{2\alpha_2}\left[g(\lambda^2) \pm \sqrt{g^2(\lambda^2)-4\alpha_1\alpha_2}\right] \tag{1.19}$$

we find that, since the function $g(\lambda^2)$ is monotonous, it has one root $\lambda^2=\lambda_*^2$ corresponding to the plus sign in (1.19), since

$$\left.\frac{dG^-}{d(\lambda^2)}\right|_{\lambda^2=0} = \frac{\alpha_1}{\beta_1} < 1$$

The analytical iterative method of finding the root of eq. (1.16) consists in solving consecutively a number of equations using the tables of /7/:

$$\lambda_K^2 = \frac{1}{2\alpha_2}\left[g(\lambda^2_{K-1}) + \sqrt{g^2(\lambda^2_{K-1})-4\alpha_1\alpha_2}\right] \tag{1.20}$$

where $$g(\lambda_0^2) = \frac{\gamma\varepsilon}{\rho_1}, \qquad (K=1,2,3.....)$$

For the particular example under consideration ($\gamma=7.8\rho_1$, $C=1435$ m/sec, $\nu=0.25$) we find:

$\lambda_1=6.39$, $\lambda_2=7.77$ $\lambda_3=7.41$,

$\lambda_4=7.56$, $\lambda_5=7.54$

The five-fold solution of (1.20) gives an error of less than 0.3%. For rougher estimates the first approximation, resulting in an error of not more than 15%, may be enough.

Using the condition of the hydraulic shock front:

$$x=t=0 \qquad R=R_0 \tag{1.21}$$

we find the constant $D_2=R_0-R_1$ and the deformed pipe radius

$$R=R_1+(R_0-R_1)\cos\lambda_*(z+\tau) \tag{1.22}$$

Using (1.5), (1.7) and (1.10), we determine the pressure on the pipe wall:

$$P = P_1 + (R_o - R_1)\rho_1 V^2 \lambda_*^2 \frac{A_1(1)}{A'(1)} \cos \lambda_* (z + h) \tag{1.23}$$

The relative dynamic pressure amplitude is

$$\delta_p = \frac{\varphi_1 V^2 \lambda_*^2 R_o^2 A(1)}{h E A'(1)} = \frac{P_{max} - P_1}{P_1 - P_o} \tag{1.24}$$

For the example under consideration, $\delta_p = 0.281$.

It is seen thus that the shear forces, inertia forces and bending moments causing pipeline deformation behind the hydraulic shock front produce a considerable rise of local pressures of liquid in the pipe. Obviously, in a real pipeline the liquid pressure and pipe radius tend with time, due to various dissipation factors, to assume stationary values given by formulas (1.1) and (1.3).

References

1.. Ginzburg I.P. Hydraulic shock in pipes of a visco-elastic material. Vestnik LGU, 1956, No. 13, Issue No. 3.
2. Dvukhsherstov G.I. Hydraulic shock in pipes of non-circular cross-section. Uch. Zap. MGU, 1948, Issue No. 122, Mechanics, vol. 2.
3. Surin A.A. Hydraulic Shock in Water Pipelines and Ways to Control it. Gostekhteoretizdat Publishers, Moscow, 1946 /in Russian/.
4. Zhukovsky N.E. On the hydraulic shock in water pipelines. GITTL, 1949.
5. Niordsen F.L.N. Tekniska Hogskolan Handlingar, No. 57, 1952.
6. Gray A., Mathews G.B. A treatise on Bessel functions. IIL, 1953.
7. Tables of the values of Bessel functions of an imaginary argument. An AN SSSR Publication, 1950.

THE INFLUENCE OF AUXILIARY BLADES ON THE CHARACTERISTICS AND EFFICIENCY OF CENTRIFUGAL PUMP IMPELLERS

T. Fryml, V.Heisler, L. Pavluch

ABSTRACT

This paper presents the results of experimental investigation of the influence of auxiliary blades added at critical points of model radial impellers for the sake of improvement of their characteristics and efficiency, especially under non-nominal conditions.

1. INTRODUCTION

It follows from the detailed measurements of flow in centrifugal pumps that in the working space of the impeller may occur flow separation, whirling in the regions of flow separation or secondary flows, heterogeneous cavitation zones etc. It is often the case that the flow picture of real liquid differs, to a considerable extent, from the picture of the ideal liquid flow that used to be the basis for pump design and dimensioning or for various mathematical methods of solution which do not take into account real properties of liquids, viscosity in the first place. These phenomena are especially conspicuous in regions outside the nominal operating point which leads to higher losses and thus to lower hydraulic efficiency of the pump in non-nominal operating conditions.

2. TESTING EQUIPMENT

Air was used for the tests in an open aerodynamic experimental apparatus. Two basic models (designed I and II) of the impeller of Ø 300 mm were made. The meridional profile in both the alternatives was designed as purely radial, see fig.1 , i.e. with parallel inner walls of both the hub and the front shroud normal to the axis of the shaft. The inlet and outlet edge of single-curvature blades were parallel to the axis of rotation. The number of blades in both the alternatives was 7, the inlet angle of the blade $\beta_{L1} = 20^o$, the outlet angle $\beta_{L2} = 30^o$. Also the other geometrical parameters were identical in both the alternatives. There was only a difference in the shape of the course of blade angle between the inlet and outlet edge, as is shown in figs.2 and 3. The characteristics were measured at the speed of 4000/min that is under operating conditions when on one hand the velocity of air is low enough to neglect its compressibility, on the other hand Reynolds number is high enough to apply the data collected in model testing to real pumps.

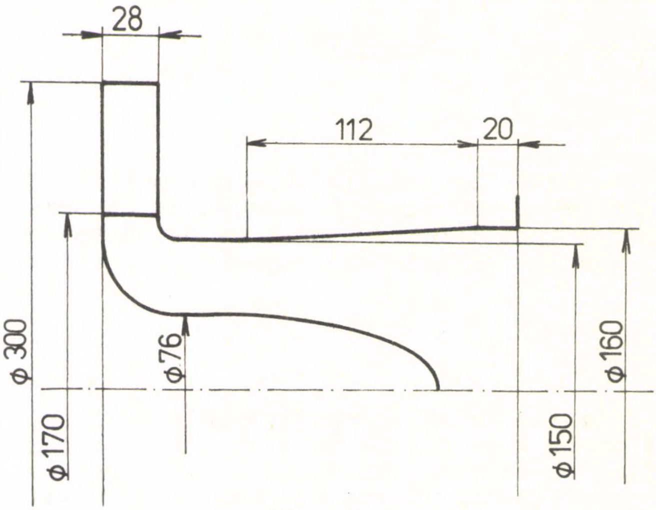

Fig. 1

Preliminary tests of both the model impellers (without the auxiliary blades) have shown that, as far as the quality of energy transfer in the impeller is concerned, the impeller I according to fig.2 may be considered really good while the impeller II according to fig.3 is not quite satisfactory. The qualitative differences in the measured curves $\psi - \varphi$ and $\eta - \varphi$ are demonstrated in fig.4 . In this as well as in the following diagrams the flow coefficient φ

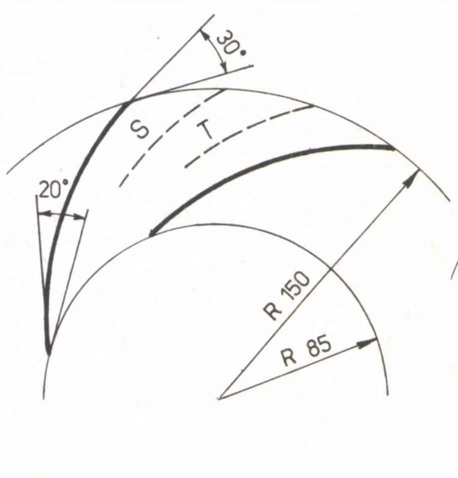

Fig. 2

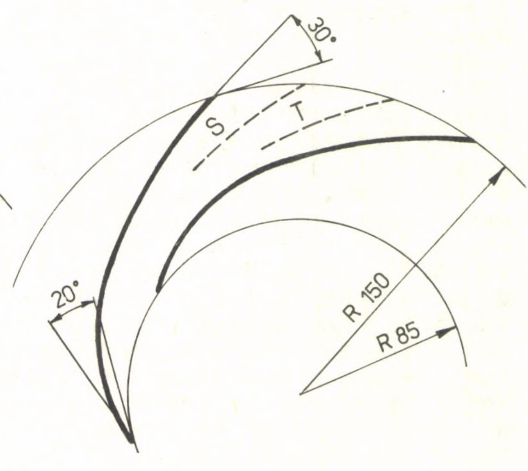

Fig. 3

is defined by the relation

$$\varphi = \frac{Q}{\pi D_2 b_2 u_2} \quad , \tag{1}$$

the pressure coefficient ψ by the relation

$$\psi = \frac{Y}{u_2^2} \tag{2}$$

and the efficiency η by the relation

$$\eta = \frac{\rho Q Y}{P} \quad . \tag{3}$$

Here Q ($m^3.s^{-1}$) is flow rate, $D_2 = 0.3$ m outlet diameter of the impellers, $b_2 = 0.028$ m meridional width of the impellers, u_2 ($m.s^{-1}$) peripheral velocity on the outlet diameter of the impeller, Y ($J.kg^{-1}$) specific energy, ρ ($kg.m^{-3}$) density of air and P (W) power input on the shaft.

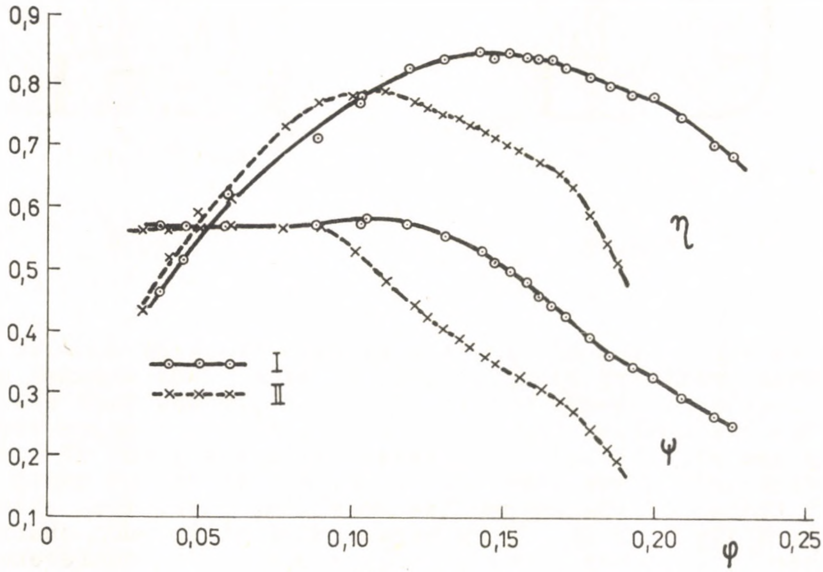

Fig. 4

3. AUXILIARY BLADES

Auxiliary blades are those elements which enable to influence, in the desirable direction, the losses in the impeller and thus the efficiency of a centrifugal pump.

In one series of experiments a fixed, annular, arched and profiled guide blade was used as such element. This element was placed coaxially in the impeller eye near the curvature where the wall of the front shroud turns from axial direction into radial. The influence of this element combined with new design of the wearing ring on the front shroud. The loss flow from the wearing ring was not guided, contrary to the common usage in design, normally to the main flow entering axially the impeller (see fig.5) , it was discharged in the direction of the main flow into the boundary layer behind the bending of the inner wall of the front shroud. This nonconventional design of the wearing ring is outlined, in combination with annular guide blade, in fig.6 . In the following test the conventional design will be denoted K , the nonconventional one with annular blade by N .

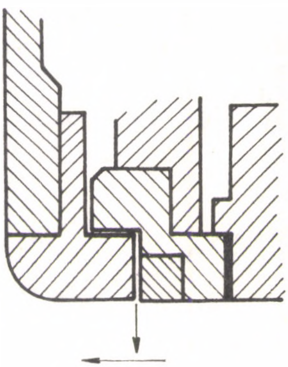

Fig. 5

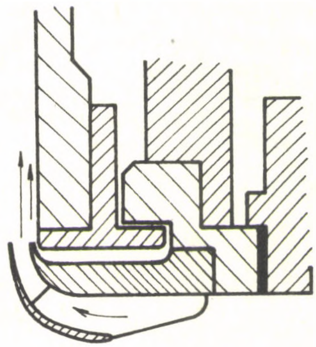

Fig. 6

The second series of experiments were tests of shorter and thinner auxiliary blades, added to each blade channel of the impeller, always between two main blades. Such auxiliary blades are applied in design of radial turbo-compressors. They are also called interblades. From the point of view of geometric shape they were congruent to outlet parts of the main blades of the respective model impeller, i.e. either alternative I or II. They were installed in each channel, either by 2 pieces symmetrically along the circumference as is shown by a dash line in figs.2 and 3 , or non-symmetrically only by 1 piece, in this case, however, alternatively into two different positions: either into position S i.e. nearer to the suction side of the preceding blade, or into position T i.e. nearer to the pressure side of the following blade.

The third series of experiments investigated the simultaneous effect of both types of auxiliary blades described above on the characteristics and efficiency of model impellers.

4. RESULTS OF MEASUREMENTS

It has been proved that the annular blade of a chosen shape and in a chosen position in combination with nonconventional design of loss flow outlet from the wearing ring according to fig.6 is advantageous, in comparison with the classical design of the wearing ring according to fig.5 , in its beneficient influence on the characteristics and efficiency curves. Fig.7 shows a comparative diagram of the curves $\varphi - \psi$ and $\varphi - \eta$ of the model impeller in the alternative I while fig.8 shows a similar diagram for the model impeller II.

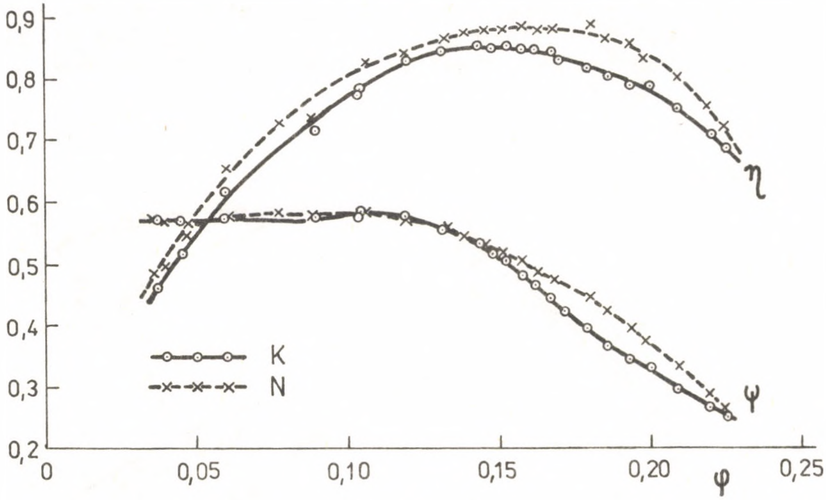

Fig. 7

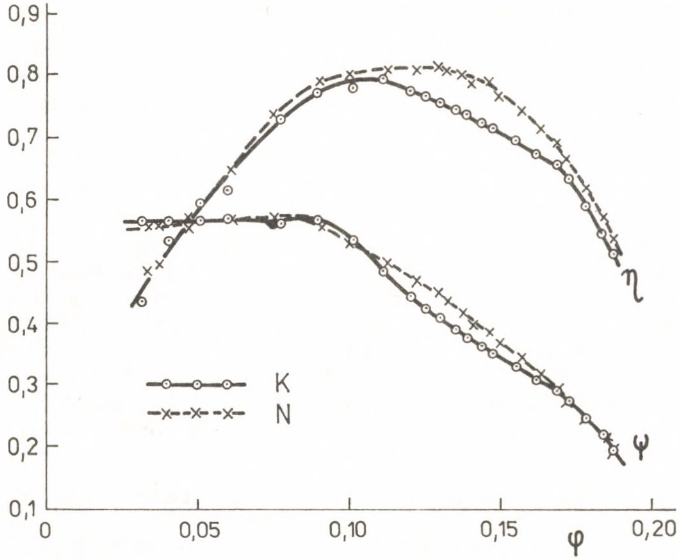

Fig. 8

The annular blade caused in both the alternatives of the impeller (i.e. either the impeller with favourable shape of the blades or the impeller with unsuitable course of blade angle) an increase of the pressure coefficient ψ and an increase of efficiency η in a wide range of values of flow coefficient φ .

It should be noted for the sake of accuracy that within the frame of the experimental program also the influence of the nonconventional design of the wearing ring according to fig.6 has been tested, however not with the added annular blade. Contrary to the data available in literature no remarkable improvement of the parameters ψ and η was observed for the given position, configuration and dimensions of the discharge slit. Only in combination with the annular blade a more remarkable effect of this nonconventional design was brought out.

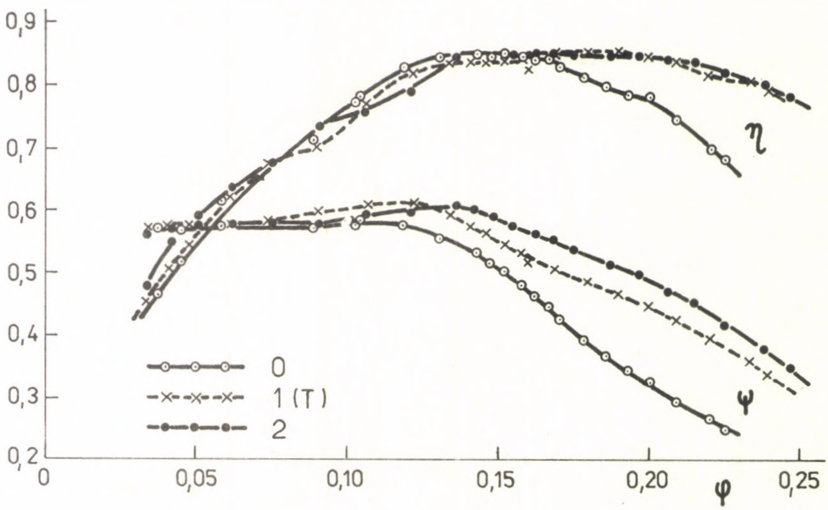

Fig. 9

The results of the measurements on impellers with interblades are demonstrated in figs.9 and 10 . The influence of the interblades on the course of the characteristics $\varphi - \psi$ is in both the alternatives of the impeller rather conspicuous in the direction towards higher values of φ . Obviously, two interblades in the channel have greater effect than a single one placed non-symmetrically. The diagram shows only the results for the position T i.e. nearer to the pressure side of the following main blade.

The results of the measurements on impellers without interblades (the basic model) are designated 0 , the model impeller with one interblade nearer the pressure side of the following blade 1 (T) , and the model impeller with two symmetrically placed interblades 2 . Fig.9 demonstrates alternative I and fig.10 alternative II.

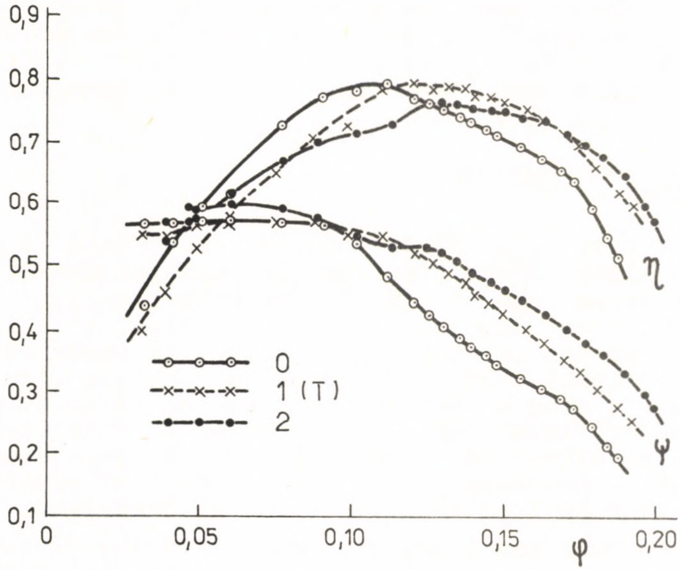

Fig. 10

Alternative I rendered approximately the same maximum values of efficiency $\eta_{max} \approx 0.85$ both with interblades or without them. However, the difference was in that the influence of the interblades caused a considerble flattening of the curve $\varphi - \eta$ and shifting of the maximum of this curve towards the higher values of φ .

Although in alternative II the maximum of efficiency is shifted towards higher values of φ and the curves $\varphi - \eta$ are flattened at the same time, their peaks are falling to some extent. This increase of losses around the nominal point seems to be caused by excessive increase of surface velocities due to further decrease of cross-sectional area of flow by the added interblades in the narrow blade channel of the basic variant of alternative II.

The existence of tendencies, observed separately, has been proved in the third series of experiments when the combined effect of both the systems of auxiliary blades, i.e. interbaldes and inlet annular blades was tested. Beneficient influence was observed especially in case of combination of one interblade in position T with an annular blade, in both the basic alternatives of the impeller.

More ambiguous were the results of measurements in combination of two interblades in each channel with an annular inlet blade. In alternative I due to the influence of the annular blade the parameters ψ and η around the nominal point of operation were further improved, the maximum value $\eta_{max} \approx 0.875$ was achieved. On the other hand, when two interblades were installed in each channel of the impeller with less suitable design of main blades according to alternative II the influence of the annular blade was practically nonexistent: there was no further improvement on the curves $\varphi - \psi$ and $\varphi - \eta$.

5. CONCLUSIONS

If a suitably arched, profiled annular guide blade is placed in the right place in the pump impeller suction eye of the low-specific speed type it may lead to better output parameters and lower losses. Beneficient effect of this annular blade at the inlet has been tested in combination with nonconventional design of the outlet of loss flow beam from the wearing ring on the front shroud which is directed into the boundary layer behind the bending from the axial into the radial direction. Improvement of the parameters ψ and η is due to decrease or elimination of flow separation behind this bending from axial into radial direction.

Shorter and thinner auxiliary blades named interblades situated by one or by two pieces into each channel between the main blades of the impeller have remarkably beneficient influence both on the characteristic and the efficiency curve of the impeller. Due to these blades the maximum efficiency shifts towards higher values of the flow coefficient φ , the peak of the efficiency curve widens and the stable part of the characteristic $\varphi - \psi$ also shifts towards higher values of φ .

By simultaneous effect of both the above mentioned types of blades, i.e. interblades in the channels and an annular blade in the impeller eye, further improvement of the parameters ψ and η may be achieved in some cases.

REFERENCES

[1] Wood, J.R.: "Secondary Flows in a Centrifugal Impeller" , MSc Thesis, MIT, 1969.

[2] Lennemann, E.: "Sekundärströmungen in umlaufenden Radialrädern" , BWK, Bd. 24, Nr. 7, Juli 1972.

[3] Timshin , A.Y.: "Flow Structure in Relative Motion at the Outlet of Centrifugal Pump Impeller" (in Russian), Gidravlicheskie mashiny, No. 6, 1972.

[4] Hellmann, D.H.: "Sekundärströmung in gekrümmten rotierenden Schaufelkanälen einer radialen Arbeitsmaschine", TU Berlin, 1975.

[5] Brdichka, M. - Samek, L. - Taraba, O.: "Cavitation" (in Czech), SNTL, Praha, 1981.

[6] Petermann, H.: "Der sekundäreinfluss des Spaltverlustes bei radialen Kreiselpumpen und Verdichtern mit Deckscheibe" , VDI-Zeitschrift, Nr. 11, April 1959.

[7] Pfleiderer, C. - Petermann, H.: "Strömungsmaschinen" , Springer-Verlag, Berlin-Heidelberg-New York, 1972.

[8] Anisimov, S.A. - Rekstin, F.S. - Seleznev, K.P.: "Investigation of Efficiency of Centrifugal Compressor Impellers with two Rows of Blades" (in Russian), Trudy LPI, No. 221, 1962.

[9] Pavluch, L.: "Influence of Geometrical Parameters of Radial Impellers on Characteristic and Efficiency" (in Czech), SVÚSS 79-04007, Praha, 1979.

[10] Pavluch, L.: "Directions for Design of Centrifugal Pump Stages" (in Czech), SVÚSS 80-04013, Praha, 1980.

FRYML, Tomáš, Ing.
Research Engineer

HEISLER, Václav, Ing.CSc.
Research Engineer

PAVLUCH, Lev, Ing.CSc.
Research Engineer

SVÚSS (National Research Institute for Machine Design),
Praha 9 - Běchovice, Czechoslovakia

GENERALIZATION OF THE DOWNWASH CONDITION FOR A DYNAMIC CASE

O.Fűzy - A.Sebestyén

SYNOPSIS

Several, practically proven methods are available for determining the velocity distribution of steady-state inviscid flow around a profile given by its geometry. Except some solutions applied with success in special cases, no general downwash condition valid for unsteady flow is known. Generalization of the flow condition to involve also unsteady flow is attempted, and its effect is illustrated in a dynamic example.

SYMBOLS

c	absolute velocity	Δt	time step
F	surface	t	time
g	gravity acceleration	u	peripheral velocity
G,S	refer to general curves	w	relative velocity
K	contour line	$\mathcal{T}$	tangential component of absolute velocity on the profile
p	pressure	Γ	circulation
$\underline{r}$	place vector	δ	profile end thickness
$\underline{s}$	arch element	ρ	density
		ω	angular velocity

SUBSCRIPTS

dyn	dynamic	ω	gyratory
k	mean	o	in steady-state operation
l	blade	$\sim$	in the meantime
q.st	quasi-steady		

1. INTRODUCTION

Downwash condition in unsteady flow is an essential, still not concluded research subject. Determination of downwash condition in steady flow [1] may start from stipulating the profile downwash direction, or from applying the JOUKOWSKY condition to mark out the rear ram point, or, at last, from defining the difference between bilateral relative velocities close the profile outlet edge based on the KUTTA condition. For the dynamic analysis of a radial-flow single-stage pump [2] none of these conditions may be specified.

VAN de VOOREN and VAN de VEL [3], KÜSSNER and GORUP [4], as well as HEWSON-BROWNE [5] have been concerned with the phenomenon of unsteady downwash from a detached, thin, somewhat arched upright profile with angular outlet edge. KELVIN's theorem let them conclude on a timely variable vortex to leave the profile. Thus, velocities bilaterally of the profile are different and timely variable. The downwash vortex was assumed to float away along a path parallel to the rear tangent of the skeleton line. GIESING [6] determined the path of vortex downwash again for fixed profiles by composing the timely variable field of velocities in the order of instants. Theoretical considerations supported the important fact that the profile downwash direction cannot point outside the domain inside the bilateral tangents of the profile tip end. Accordingly, the rear ram point migrates within a clearly definable arched section, obviously measuring zero for an angular outlet edge. Accordingly, GIESING concluded from his calculations on a potential flow model with angular outlet edge that downwash was on the side of the higher contour velocity, of a velocity that is the mathematical average of velocities leaving either side of the profile end.

LIENHART [7] analysed the unsteady flow from two, parallel grids of angular outlet edge. Relying on GIESING's results, and confronting his results with those of other authors, he has found a close agreement. In the following, a convenient formulation of the downwash condition developed for dynamic analysis [2] will be presented.

2. THE DOWNWASH CONDITION

Determination of the downwash condition will start from the fundamental equations of fluid mechanics.

The time dependent variation of the circulation of the relative velocity on a moving curve S(t) surrounding the profile, applying the rule of differentiation of parametric integrals with variable boundaries, is expressed by:

$$\frac{d}{dt}\oint_{S(t)} \underline{w}\,d\underline{r} = \oint_{S(t)} \left(\frac{d\underline{w}}{dt} + W\frac{\partial \underline{w}}{\partial \underline{r}}\right) d\underline{r} \tag{a}$$

Euler's equation for relative flow, assuming g_w to be potential, becomes:

$$\frac{d\underline{w}}{dt} + \frac{1}{\rho}\frac{\partial p}{\partial \underline{r}} - g_w + \left(\nabla\times\underline{u}\right)\times w = 0 \tag{b}$$

Hence:

$$\frac{d}{dt}\oint_{S(t)} \underline{w}\,d\underline{r} = -\oint_{S(t)} \frac{1}{\rho}\frac{\partial p}{\partial \underline{r}}\,d\underline{r} + \oint_{S(t)} g_w\,d\underline{r} - \oint_{S(t)} \frac{\partial}{\partial \underline{r}}\left(\frac{w^2}{2}\right) d\underline{r} - 2\oint_{S(t)} \underline{\omega}\,\underline{w}\,d\underline{r} \tag{c}$$

The way of integration being closed, first three terms in the right-hand side are zero. Hence:

$$\frac{d}{dt}\oint_{S(t)} \underline{w}\,d\underline{r} = -\oint_{S(t)} 2.\underline{\omega}\,\underline{w}\,d\underline{r} \tag{1}$$

Now, Eq. (1) will be transformed for computer treatment into a difference equation, extending the right-hand-side integral to a curve S(t) at a meantime $\tilde{t}$. In the following, let $S(\tilde{t})$ be the profile contour line itself, at no further restriction. Let us interpret timely variable curve G according to Fig.1:

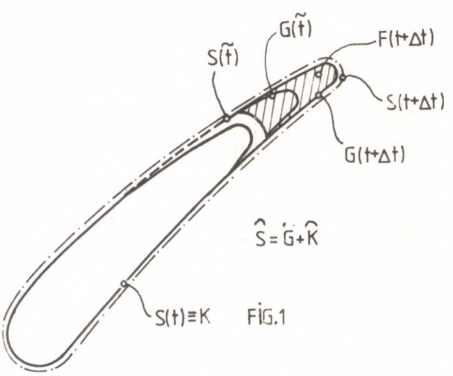

FIG.1

Accordingly, Eq. (1) may be written as:

$$\frac{1}{\Delta t}\left[\oint_{S(t+\Delta t)} \underline{w}\,d\underline{r} - \oint_{K(t)} \underline{w}\,d\underline{r}\right] = -2\oint_{S(\tilde{t})} \underline{\omega}\,\underline{w}\,d\underline{r} \tag{d}$$

Since at any instant on the profile contour $\underline{w} \times d\underline{r} = 0$, the right-hand-side integral becomes:

$$\oint_{S(\tilde{t})} \underline{\omega}\,\underline{w}\,d\underline{r} = \oint_{K(\tilde{t})} \underline{\omega}\,\underline{w}\,d\underline{r} + \oint_{G(\tilde{t})} \underline{\omega}\,\underline{w}\,d\underline{r} = \oint_{G(\tilde{t})} \underline{\omega}\,\underline{w}\,d\underline{r} \tag{e}$$

Since $\underline{w} = \underline{c} - \underline{u}$, the first term in the left-hand-side difference becomes:

$$\oint_{S(t+\Delta t)} \underline{w}\,\underline{dr} = \oint_{S(t+\Delta t)} \underline{c}\,\underline{dr} - \oint_{S(t+\Delta t)} \underline{u}\,\underline{dr} = \oint_{K(t+\Delta t)} \underline{c}\,\underline{dr} + \oint_{G(t+\Delta t)} \underline{c}\,\underline{dr} - \tag{f}$$

$$- \oint_{K(t+\Delta t)} \underline{u}\,\underline{dr} - \oint_{G(t+\Delta t)} \underline{u}\,\underline{dr}$$

Applying the Stokes theorem on the last term in the right-hand -side of this expression in the plane $F(t + \Delta t)$ spanning curve $G(T + \Delta t)$:

$$\oint_{G(t+\Delta t)} \underline{u}\,\underline{dr} = \int_{F(t+\Delta t)} (\nabla \times \underline{u})\,\underline{dF} = 2 . \omega(t+\Delta t) . \int_{F(t+\Delta t)} \underline{dF} \tag{g}$$

lending Eq. (1) the form:

$$\frac{1}{\Delta t}\left[\oint_{K(t+\Delta t)} \underline{c}\,\underline{dr} + \oint_{G(t+\Delta t)} \underline{c}\,\underline{dr}\right] = \frac{1}{\Delta t}\left[\oint_{K(t)} \underline{c}\,\underline{dr} + \oint_{K(t+\Delta t)} \underline{u}\,\underline{dr} - \right.$$

$$\left. - \oint_{K(t)} \underline{u}\,\underline{dr} + 2 . \underline{\omega}(t+\Delta t) \int_{F(t+\Delta t)} \underline{dF}\right] - 2 . \oint_{G(\tilde{t})} \underline{\omega}\,\underline{w}\,\underline{dr} \tag{2}$$

In Eq. (2):

$$\oint_{K(t+\Delta t)} \underline{c}\,\underline{dr} = \oint_{K(t+\Delta t)} \underline{\gamma}\,\underline{ds} = \Gamma(t+\Delta t) \tag{3}$$

and

$$\oint_{K(t)} \underline{c}\,\underline{dr} = \oint_{K(t)} \underline{\gamma}\,\underline{ds} = \Gamma(t)$$

not to be transformed again.

Computation of integrals for circumferential velocities (involving the Stokes theorem) takes advantage from

$$\oint_{K} \underline{u}\,\underline{dr} = \int_{F_\ell} (\nabla \times \underline{u})\,\underline{dF_\ell} = 2\int_{F_\ell} \underline{\omega}\,\underline{dA_\ell} = 2\omega F_\ell \tag{h}$$

for radial flow pumps at any time; namely throughout $\underline{\omega} \parallel \underline{dF_\ell}$.

Thereby $\frac{1}{\omega}\oint_{K} \underline{u}\,\underline{dr} = 2F_\ell$ = constant at any time.

Denoting

$$\frac{1}{\omega_0}\oint_{K(t_0)} \underline{u}\,d\underline{r} = \left(\frac{\Gamma u_0}{\omega_0}\right) \qquad (j)$$

to be obtained from steady-state operational data, it is:

$$\oint_{K(t+\Delta t)} \underline{u}\,d\underline{r} = \omega(t+\Delta t)\cdot\left(\frac{\Gamma u_0}{\omega_0}\right)$$

and (4)

$$\oint_{K(t)} \underline{u}\,d\underline{r} = \omega(t)\cdot\left(\frac{\Gamma u_0}{\omega_0}\right)$$

Let us consider Fig.2, enlarging the surrounding of curves G in Fig.1.

In Fig.2, be $\underline{\delta} = \overrightarrow{A\,B}$ ($\underline{\delta}$ being a vector pointing from A to B).
Be $\underline{\Delta s} \cong \underline{w}_k\cdot \Delta t$, where the velocity at leaving the profile is assumed as:

$$\underline{W}_K = \frac{1}{4}\left[(\underline{W}_A+\underline{W}_B)\Big|_{t+\Delta t} + (\underline{W}_A+\underline{W}_B)\Big|_{t}\right] \cong \frac{1}{2}\left[\underline{W}_A(t)+\underline{W}_B(t)\right] \qquad (k)$$

that is, $\underline{w}_k \cong \underline{w}_k(t)$

From Fig.2, at a fair approximation:

$$\int_{F(t+\Delta t)} d\underline{F} \cong \underline{\delta}\times\underline{\Delta s} \qquad (\ell)$$

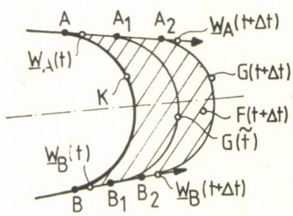

FIG. 2

Thus:

$$2\omega(t+\Delta t)\int_{F(t+\Delta t)} d\underline{F} \cong 2\underline{\omega}(t+\Delta t)\cdot$$

$$\cdot(\underline{\delta}\times\underline{\Delta s}) = -2\underline{\omega}(t+\Delta t)\,\underline{\Delta s}\,\underline{\delta} \qquad (5)$$

In computing integral $\oint_{G(\tilde{t})} \underline{\omega}\ \underline{w}\ d\underline{r}$, parts taken from the profile end, as well as from curves $\overset{\frown}{A\,A_1}$ and $\overset{\frown}{B\,B_1}$ are zero. Value of the integral taken from curve $\overset{\frown}{A_1\,B_1}$ is approximated by the timely mean value:

$$\oint_{G(\tilde{t})} \underline{\omega}\,\underline{w}\,d\underline{r} = \int_{A_1}^{B_1} \underline{\omega}\,\underline{w}\,d\underline{r} \cong \underline{\omega}(t+\Delta t)\,\underline{W}_K(t)\,\underline{\delta} \qquad (6)$$

In calculating integral $\oint_{G(t+\Delta t)} \underline{c}\,d\underline{r} = \oint_{G(t+\Delta t)} \underline{\tau}\,d\underline{s}$, we use an approximation, in which the value of the integral expression is computed on an average $\underline{\Delta s_K} \cong \underline{\Delta s_K}(t)$ line.

According to this:

$$\oint\limits_{G(t+\Delta t)} \underline{c}\,d\underline{r} = \oint\limits_{G(t+\Delta t)} \gamma\,ds \cong \gamma_a(t+\Delta t)\,\underline{\Delta s_K}(t) + \gamma_B(t+\Delta t)\,\underline{\Delta s_K}(t)$$

Thus:

$$\oint\limits_{G(t+\Delta t)} \underline{c}\,d\underline{r} \cong \left[\gamma_a(t+\Delta t) - \gamma_B(t+\Delta t)\right] \cdot W_K(t) \cdot \Delta t \tag{7}$$

Substituting Eqs (3), (4), (5), (6) and (7) into (2) and arranging leads to the downwash condition of unsteady grid flow:

$$\Gamma(t+\Delta t) + \left[\gamma_A(t+\Delta t) - \gamma_B(t+\Delta t)\right] W_K(t) \cdot \Delta t =$$

$$= \Gamma(t) + \left[\omega(t+\Delta t) - \omega(t)\right]\left(\frac{\Gamma_{u_0}}{\omega_0}\right) - 4\,\omega(t+\Delta t) \cdot \delta \cdot W_K(t) \cdot \Delta t \tag{8}$$

Figure 2 shows circulation $\Delta\Gamma$ leaving the profile in a time Δt in case of a fixed grid:

$$\Delta\Gamma = \oint\limits_{G(t+\Delta t)} \gamma\,\underline{ds} = \int\limits_{F(t+\Delta t)} (\nabla \times \gamma)\,\underline{dF} \cong 2\,\frac{\gamma_A - \gamma_B}{\delta} \cdot \delta \cdot \frac{\gamma_A + \gamma_B}{2} \cdot \Delta t \tag{n}$$

that is, the vortex leaves the profile at a translation velocity $\frac{\gamma_A + \gamma_B}{2}$, in argeement with Giesing's finding.

The same results by simplifying downwash condition (8) for a fixed grid.

Again, specifying steady-state flow (hence, $\Delta\Gamma = 0$) leads to Kutta's downwash condition $\gamma_A = \gamma_B$

Steady-state flow and rotating grid yield the downwash condition

$$\gamma_A - \gamma_B = -4\,\omega\,\delta \tag{9}$$

permitting to determine the blade circulation in steady-state operation.

3. EXAMPLE OF APPLICATION

Simulation of the run-out, that is, of the dynamic operation of a radial-flow, single-stage pump in [2] comprised the following test. Curve Ψq.st in Fig.3 is the steady-state

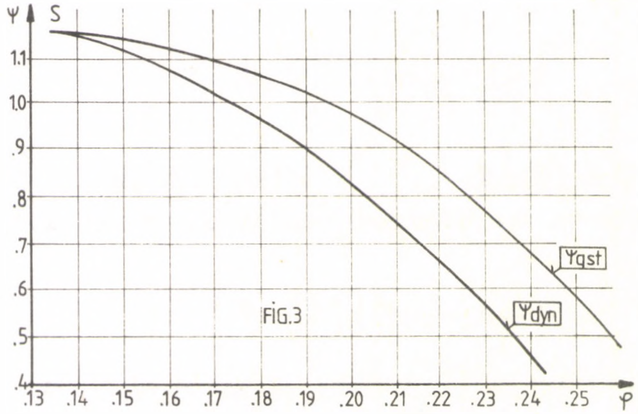

FIG.3

measured characteristic curve of the tested pump. Applying Eq. (9) as boundary condition in simulation [2], the mentioned curve resulted. For downwash condition (8) as boundary condition of the dynamic simulation, curve Ψ_{dyn} results. Thus, dynamic downwash condition applied in a dynamic analysis points to an other than steady-state characteristic of the phenomenon, namely that steady-state grid conditions may much change in unsteady operation.

REFERENCES

[1] BASU,B.C. - HANCOCK,G.J.: The unsteady motion of a twodimensional aerofoil in incompressible inviscid flow. Journal of Fluid Mechanics. Vol.87. part 1. 1978.

[2] FŰZY,O. - SEBESTYÉN,A.: Simulation of the dynamic behaviour of pumps. Proceedings of the Seventh Conference on Fluid Machinery,Budapest, 1983.

[3] VAN DE VOOREN,A.I. - VAN DE VEL,H.: Unsteady profile theory in incompressible flow. Archiwum Mechaniki Stosowanej. Vol.XVI.Warszawa, 1965.

[4] KÜSSNEP,H.G. - VON GORUP,G.: Instationare linearisierte Theorie der Flügelprofile endlicher Dicke in incompressibler Strömung. Mitt. Max Planck Inst. für Strömungsforschung Göttingen, 1960.

[5] HEWSON-BROWNE,R.C.: The oscillation of a thick aerofoil in an incompressible flow. The quart. J. Mech. Appl. Math. 1.16.1963.

[6] GIESING,J.P.: Vorticity and Kutta condition for unsteady multienergy flows. Trans. of the ASME Sept. 1969.

[7] LIENHART,W.: Berechnung der instationaren Strömung durch gegeneinander bewegte Schaufelgitter und der Schaufelkraftschwankungen. VDI Vorschungsheft, 562. VDI Verlag Düsseldorf, 1974.

Fűzy, Olivér Dr. techn. Cand. of Techn. Sci.
Professor
Sebestyén, András Dr. techn.
Scientific Research Worker

Dept. of Hydraulic Machinery
T.U. Budapest
H - 1521 Budapest Stoczek u. 2/D.

SIMULATION OF THE DYNAMIC BEHAVIOUR OF PUMPS

O. FŰZY - A. SEBESTYÉN

SYNOPSIS

A simulation method for testing the transient work of pumps in hydraulic networks will be presented, possibly taking dynamic conditions into consideration. Test results obtained in the described simulator will be confronted to those obtained in a quasi-steady simulator.

SYMBOLS

a	sound velocity	α^*	similarity invariant
B,C	quasi-constant quantities	γ	component of the absolute velocity tangential on the profile
H	delivery head		
i	similarity invariant		
L	length of delivery pipe	Γ	circulation
M	moment	η	efficiency
n	r.p.m	Θ	moment of inertia
N	number of blades	λ	friction coefficient
p	pressure	μ	similarity invariant
Q	volume flux	ρ	density
s	coordinate of place	φ	volume number
s'	running point coordinate	ψ	pressure number
T,t,Δt	time, time step	ω	angular velocity
T_o	time constant		
v	pipe velocity		

SUBSCRIPTS

0	steady-state	q.st.	quasi-steady
dyn	dynamic	Q	referring to volume flux
theo	theoretical		
h	hydraulic	pump	pump
meas	measured in steady-state operation	v	volume
		v'	loss
ö	vortex	Γ	circulation multiplier
		ω	referring to angular velocity

1. INTRODUCTION

Hazardeous pressure changes in hydraulic systems invariably arise in transient operation. Transient operation is mostly due to pump run-out caused by power cut (or to another cause) off . In course of a pump run-out, a depression wave starts from the pressure tap. The so-called first main period of the wave phenomenon is the time of return of the reflection of the starting depression wave to the pressure tap. In most of practical cases, to this time, the pump gets disconnected from the system. Thus, in examining the system behaviour, knowledge of the transient operation due to pump run-out in the first main period of the wave phenomenon is of outstanding importance.

Calculation methods for assessing the dynamic behaviour of pumps have been suggested by Knapp [1] and Kaufmann [2].Knapp checked his method in laboratory tests for the case of run-out of a pump-motor complex of relatively high inertia. In comparison of measured and calculated data of revolution vs. time showed a fair agreement.

Graphic methods for the pump run-out have been suggested, among others, by Bergeron [3], Parmakian [4].

Computer simulation of the dynamic behaviour of pumps has been described by Fűzy, Halász and Kullmann [5], Czibere, Kalmár és Tolvaj [6].

All pump run-out analyses involved the assumption of invariability of non-dimensional characteristic curves calculated from pump steady-state operation values in course of the transient work (at least, in given range ranges). This would mean the possibility to have recourse to the law of affinity in calculation. Calculations relying on steady-state non-dimensinal characteristic curves, this method may be termed quasi-steady, and simulation of the phenomenon quasi-steady simulation. It will be attempted to establish a dynamic pump model for testing pump run-out. The dynamic model is expected to be a closer approximation to the dynamic behaviour of the machine than does the quasi-steady one. Accordingly:

- Velocities induced by the trailing vortex back onto the profile have to be reckoned with.
- A dynamic flow condition has to be formulated to reflect conditions of the dynamic phenomenon, steady-state flow conditions [7] being unfit to dynamic analyses.
- The effect of leaving vorticies onto the moments braking the impeller should be taken into consideration.
- In pressure-rise between pump stubs the slowing down effect may not be negligible.

Conception of the dynamic model in this study aims at meeting the three latter requirements. Velocities induced by the trayling vortex will be ignored.

2. THE TEST MODEL

The test model is seen in Fig.1 to consist of three connected units, where

- condition in the inlet chamber does not change during the phenomenon;
- pump feed is spin-free;
- the pump is a single-stage, radial-flow one;
- the delivery pipe is horizontal, of zero hydraulic resistance, and length

$$L \geq \frac{1}{2} a \cdot T,$$

where T is the testing time.

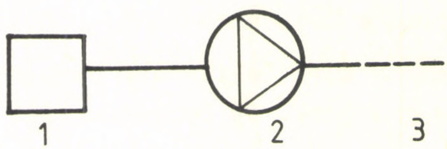

1 INLET CHAMBER
2 PUMP
3 DELIVERY TUBE

FIG.1

Thus, the test model corresponds to the case of pump connected to a long pipeline. The stipulation on the pipe length results in a testing time not exceeding the first main period of the phenomenon. Thus, any conclusion drawn from computations on the test model can only refer to the first main period of the phenomenon.

3. THE MATHEMATICAL MODEL

Solution of the model is reduced to testing the flow in the impeller. Mathematically this means the solution of an elliptic boundary value problem. The solution is expected from a Fredholm integral of second order equation in the form convenient for our analysis:

$$\gamma(s,t+\Delta t)+\int_K^C C(s,s')\cdot\gamma(s',t+\Delta t)ds'=C_Q\cdot Q_{theo}(t+\Delta t)+C_\omega\cdot\omega(t+\Delta t) \qquad (1)$$

Solution of the elliptic boundary value problem depends on boundary specifications. Conception of the mathematical model attempts to relate the solution to equations of boundary conditions adequately reflecting dynamic conditions under 1. Thus, velocity distribution along the profile obtained from the integral equation will correspond to dynamic operation.

Accordingly, the mathematical model comprises Eq.(1) and the three boundary conditional equations.

The first one is the downwash condition as uniqueness equation of the integral equation ([7], also see for legend):

$$\Gamma(t+\Delta t)+[\gamma_A(t+\Delta t)-\gamma_B(t+\Delta t)]W_K(t)\cdot\Delta t=$$

$$=\Gamma(t)+[\omega(t+\Delta t)-\omega(t)]\cdot\left(\frac{\Gamma_{u_0}}{\omega_0}\right)-4\omega(t+\Delta t)\cdot\delta\cdot W_K(t)\cdot\Delta t \qquad (2)$$

The other two boundary conditional equations are boundary specifications for Q_{theo} $(t+\Delta t)$ and $\omega(t+\Delta t)$ in the right-hand-side of the integral equation, obviously convenient in function forms:

$$Q_{theo}(t+\Delta t)=Q_{theo}(\Gamma(t+\Delta t)) \qquad (2a)$$

and

$$\omega(t+\Delta t)=\omega(\Gamma(t+\Delta t)) \qquad (2b)$$

Subsequently, determination of convenient functions $Q(\Gamma)$ and $\omega(\Gamma)$ from further physical equations will be endeavoured.

4. PRACTICAL RELATIONSHIPS FOR SIMULATION

4.1 Kinetic motion equation of the impeller

Relationship for angular velocity $\omega(\Gamma)$ is derived from the kinetic motion equation of the impeller, where determination of the pump moment aims at taking real machine losses into consideration. Thus, in writing(braking) moment in the motion equation

$$M_{pump} = -2\pi\Theta \frac{dn}{dt} \tag{a}$$

relationship

$$M_{pump} = M_h + M_{v'} + M_{\ddot{o}} \tag{b}$$

is applied, where $M_{v'}$ indicates loss moments (mechanical and disc friction), $M_{\ddot{o}}$ being impeller moment change due to separating vortices in dynamic operation

$$M_{\ddot{o}} = \frac{\rho N}{2\pi} \cdot Q_{theo} \cdot \Delta\Gamma \tag{c}$$

$\Delta\Gamma$ being size of a vortex leaving the blade during time Δt. Loss moment relationships have been taken from publications [8] and [9]. For calculating the theoretical circulation in the term of hydraulic moment, t auxiliary functions α_1 and α_2 have been taken from the ression for hydraulic efficiency

$$\eta_h = \frac{H}{H_{theo}} = \frac{\Gamma_{meas}}{\Gamma} \cdot \frac{\Gamma}{\Gamma_{theo}}$$

$$\alpha_1 = \frac{\Gamma_{meas}}{\Gamma} \quad \text{and} \quad \alpha_2 = \frac{\Gamma}{\Gamma_{theo}} \tag{d}$$

Steady-state operation characteristic curves lead to auxiliary function α_2. Any efficiency varying along the dynamic phenomenon, and the auxiliary functions above have been assumed to depend exclusively on volume number φ, permitting to determine the actual efficiency and auxiliary functions belonging to φ varying along the phenomenon. Transforming the kinetic motion equation of the impeller to a difference equation, and taking timely average moments, angular velocity of the impeller becomes:

$$\omega(t+\Delta t) = B_\Gamma(t+\Delta t) \cdot \Gamma(t+\Delta t) + B_\omega(t) \tag{3}$$

4.2 Effect of dynamic disturbance on the pipeline

The equation for volume flow $Q(\Gamma)$ (in the first main period of wave phenomenon) has been derived from the expression of the effect of dynamic disturbance on the pipeline. Depression wave passing through the delivery pipe at pump run-out is of a size:

$$p(t)-p(t_o)=\rho\cdot a\left[v(t)-v(t_o)\right] \tag{3a}$$

or, in terms of pump characteristics:

$$H(t)-H(t_o)=\frac{a}{gA}\left[\eta_v\left(\varphi(t)\right)\cdot Q_{theo}(t)-\eta_v\left(\varphi(t_o)\right)\cdot Q_{theo}(t_o)\right] \tag{3b}$$

In the expression for the real pump delivery head:

$$H(t)=\eta_h\left(\varphi(t)\right)\cdot H_{theo}(t)-h(t) \tag{3c}$$

where $h(t)$ is the change of the real delivery head due to rather short-time velocity variations [10].

Product $\omega\cdot\Gamma_{theo}$ in the expression of theoretical delivery head

$$H_{theo}=\frac{\omega}{2\pi g}N\cdot\Gamma_{theo} \tag{3d}$$

has been linearized by omitting the small term of second order. Adopting the above expressions in the wave equation yields a convenient expression for the volume flow:

$$Q(t+\Delta t)=C_\Gamma(t+\Delta t)\cdot\Gamma(t+\Delta t)+B_Q(t+\Delta t) \tag{4}$$

5. SIMULATOR BUILD-UP

The problem is solved by digital simulation starting from the known condition at time "t" to determine condition at time "$t+\Delta t$".

Mathematical framework of the dynamic simulator is system of Eqs (1) to (4) where coefficients of (3) and (4) have to be recalculated in each time increment of simulation.

Thus, the simulator writes the four equations and solves them for each time increment Δt, to yield velocity distribution $\gamma(s)$ at the new time. Thereupon the blade circulation at the new time

$$\Gamma(t+\Delta t)=\oint_K \gamma(s,t+\Delta t)\,\underline{ds} \tag{h}$$

can be calculated and substituted into Eqs (3) and (4) to yield angular velocity and volume flow at the new time. Now, pump delivery head at the new time can be calculated. Thereby $\Gamma(t)$, $\omega(t)$, $Q(t)$ and $H(t)$ as well as functions $\varphi(t)$ and $\Psi(t)$ can be determined at discrete points (for each time increment Δt).

6. SOME CALCULATION RESULTS

Results obtained by means of the dynamic simulator have been confronted to published measurement results. The tested pumps were exposed to dynamic effects expected to lead to relationships between input and output characteristics, to the phenomenological description of the dynamic work. Comparison the transfer matrix elements of the test measurements and calculated results shows a marked similarity of trend in the range of low frequencies [11].

Our results have been compared to those obtained by the classic quasi-steady model. theoretically made possible by making dimensionless the kinetic motion equation for revolving masses, the kinetic equation mathematically modelling the elastic pipe, as well as the equation of material conservation. Coefficients of the non-dimensional equations are similarity invariants:

$$T_o = \frac{2\pi n_o \Theta}{M_o}\,;\quad \alpha^* = \frac{v_o}{a}\,;\quad \mu = \frac{a \cdot v_o}{g \cdot H_o}\,;\quad i = \frac{\lambda \cdot v_o}{a} \tag{i}$$

Since $\lambda = 0$, $i = 0$, furthermore, in examining identical systems, $\mu = 10$, $\alpha^* = 1{,}51 \cdot 10^{-3}$, while time constant T_o was given values in the range 0,056 ~ 2,8. The variation rate of time constant is indicated by ratio

$$\frac{T_o}{0{,}56} = .1\,;\ .2\,;\ .4\,;\ \text{and } 5. \tag{j}$$

seen in the figures as parameters.

Variations of non-dimensional rpm and delivery head are seen in Figs 2 and 3.

Quasi-steady simulation is seen to produce results independent of time constant T_o. Namely, quasi-steady simulation relies on the assumed invariability of curve $\Psi/\varphi/$ calculated from

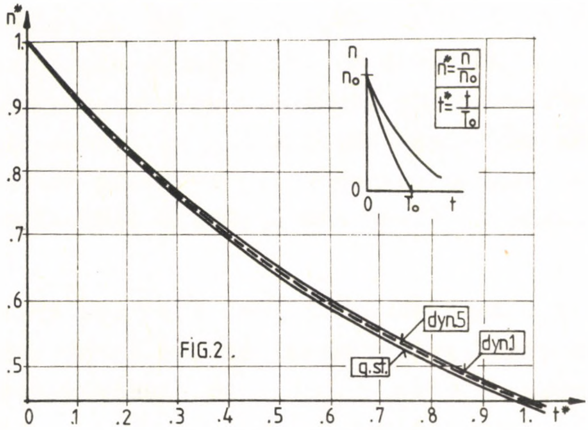

FIG.2

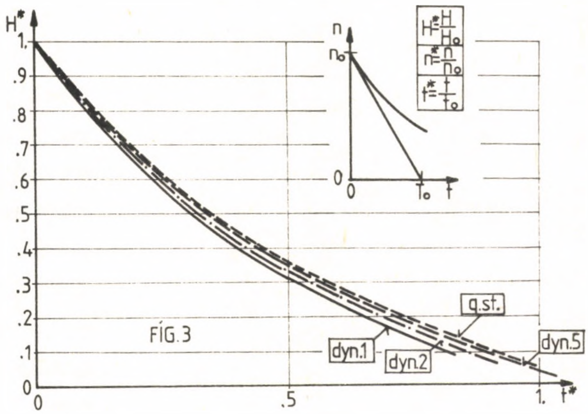

FIG.3

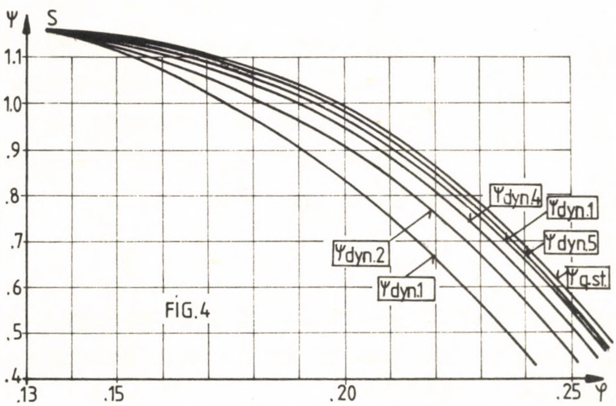

FIG.4

steady-state pump operation data in pump run-out. In the dynamic model, course of $\Psi/\varphi/$ depends on the T_o value (Fig.4). Curves $\Psi/\varphi/$ produced by the dynamic simulator tend to that of the quasi-steady simulator with increasing T_o, in compliance with the empirical expectation to reduce the system sensitivity to dynamic phenomena by reducing the moment of inertia of the machine in fixed steady-state operation (n_o, M_o).

Dynamic pump model tests have shown the not absolute truth of the assumption in the quasi-steady model of the invariability of characteristic curves $\Psi(\varphi)$, $\varepsilon(\varphi)$ in steady-state operation in course of pump run-out.

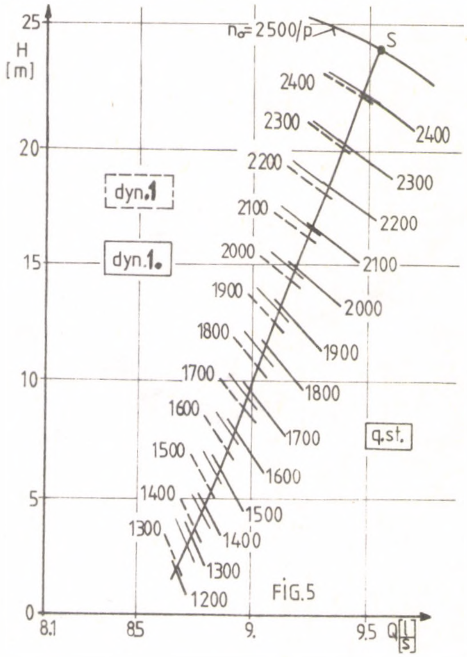

FIG.5

Characteristic curve sections $H(Q)_{n=const}$ for different numbers of revolution have been plotted in Fig.5 relying on affinity. In the quasi-steady model, these affin curves mark out working points moving along the wave line at the given rpm. Work point characteristics for the same numbers of revolution produced by the dynamic simulator have been plotted for two different time constant quotients ($\vartheta = T_o/0,56s$). For half of the steady-state operational numbers of revolution, this deviation is about 3 % for $\vartheta = 1$, while over 10 % for $\vartheta = 0,1$.

REFERENCES

[1] KNAPP,R.T.: Complete Characteristics of Centrifugal Pumps and Their Use in the Prediction of Transient Behaviour. Trans. of the ASME Nov. 1937.

[2] KAUFMANN,K.: Instationare Vorgange beim Betrieb von Pumpen

in Rohrleitungssystemen. Pumpentagung, Karlsruhe, 1973.

[3] BERGERON,L.: Waterhammer in Hydraulics and Wave Surges in Electricity. New York, Wiley, 1961.

[4] PARMAKIAN,J.: Waterhammer Analysis. New York, Prentice-Hall, 1955.

[5] FÜZY O. - HALÁSZ G. - KULLMANN L.: Simulation of pressure oscillations in pipelines. Proc. of the 5th Conference on Fluid Machinery, Vol.1. Budapest, 1975. Akadémiai Kiadó

[6] CZIBERE T. - KALMÁR L. - TOLVAJ B.: Computation of transient flows in pipelines. Proc. of the 6th Conference on Fluid Machinery Vol.1. Budapest, 1979. Akadémiai Kiadó

[7] FÜZY O. - SEBESTYÉN A.: Generalization of the downwash condition for a dynamic case. Proceedings of the Seventh Conference on Fluid Machinery. Budapest, 1983.

[8] DAILY,J.W. - NECE,R.E.: Chamber dimension effects on induced flow and frictional resistance of enclosed rotating disks. J.of Basic Engineering, March 1960.

[9] CSEMNICZKY J.: An Approximate Method for the Determination of Real Characteristic Curves of Radial and Semiaxial Pumps.* Candidate's Thesis, Budapest, 1975.

[10] SEBESTYÉN A.: Dynamic behaviour of pumps in long pipelines Doctor's Thesis.

[11] FŰZY O. - SEBESTYÉN A.: Theoretical investigations on the dynamic behaviour of pumps. Intercambio International sorbe Transientes Hidraulicos et Cavitocao. Vol.2. Sao Paulo, 1982.

* In Hungarian

Fűzy, Olivér Dr. techn. Cand. of Techn. Sci. Professor
Sebestyén, András Dr. techn. Scientific Research Worker

Dept. of Hydraulic Machinery T.U. Budapest
H - 1521 BUDAPEST Stoczek u. 2/D.

DETERMINATION OF THE VELOCITY DISTRIBUTION OF BLADING GIVEN BY ITS GEOMETRY

Füzy, O. - Steck, E. - Tánczos, L.

For calculation of the meridional velocity distribution -the second principal problem- a known method [1] , [2] is applied. According to it the blading is replaced by a field of forces depending on the form and load of the blades. After specifying the steady flow in front of the impeller and the possible general boundary conditions, behind the impeller, only the curvature of the meridional streamlines is prescribed.

There is a deviation from the known method, in two essential respects;

- Partly the natural co-ordinate system is replaced by a nearly similar curvilinear orthogonal co-ordinate system using spline functions,
- partly also spline functions are applied for determining the derivatives, the curvatures and the intersection angles.

Cubic spline functions are suited especially well for the production of surface oriented, orthogonal co-ordinates. As an example for a control volume the circular region of rotational symmetry between hub and shroud is shown in Fig. 1. Without restriction to generality z= const. was taken for the inlet and r= const. for the outlet.

With a suitable parameter t for co-ordinates $r_{\substack{h\\s}}$ and $z_{\substack{h\\s}}$ of the hub (h) and shroud (s), the following polynomials of third order may be written:

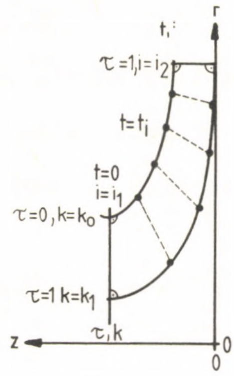

Fig.1

$$r_{\substack{h\\s}}(t) = a_{i,\frac{1}{2},1}(t-t_i)^3 + b_{i,\frac{1}{2},1}(t-t_i)^2 + c_{i,\frac{1}{2},1}(t-t_i) + d_{i,\frac{1}{2},1},$$

$$z_{\substack{h\\s}}(t) = a_{i,\frac{1}{2},2}(t-t_i)^3 + b_{i,\frac{1}{2},2}(t-t_i)^2 + c_{i,\frac{1}{2},2}(t-t_i) + d_{i,\frac{1}{2},2}.$$

Herewith it was supposed that the number of discrete points on the hub and shroud were equal and the parameter values of the correlating points i = const, were identical. Specifying, in addition, acceptable boundary conditions at the inlet and outlet of the control volume, e.g. slope of the curves at these points, the mathematical problem for the cubic spline functions is completely formulated, see also [4].

Coefficients

$$\begin{aligned}
A_{i,k,l} &= a_{i,1,l} + (a_{i,2,l} - a_{i,1,l}) \cdot f_l(t, \tau),\\
B_{i,k,l} &= b_{i,1,l} + (b_{i,2,l} - b_{i,1,l}) \cdot f_l(t, \tau),\\
C_{i,k,l} &= c_{i,1,l} + (c_{i,2,l} - c_{i,1,l}) \cdot f_l(t, \tau), \qquad l = 1,2\\
D_{i,k,l} &= d_{i,1,l} + (d_{i,2,l} - d_{i,1,l}) \cdot f_l(t, \tau),
\end{aligned}$$

(where $f_l(t, \tau)$ determines the co-ordinate distribution especially in the inlet and outlet cross section) yield a set of meridional co-ordinate lines in parametric representation with an additional set-parameter τ, $0 \leqq \tau \leqq 1$:

$$r(t, \tau) = A_{i,k,1}(t-t_i)^3 + B_{i,k,1}(t-t_i)^2 + C_{i,k,1}(t-t_i)+D_{i,k,1},$$

$$z(t, \tau) = A_{i,k,2}(t-t_i)^3 + B_{i,k,2}(t-t_i)^2 + C_{i,k,2}(t-t_i)+D_{i,k,2}.$$

It can be shown that this set of curves consists again of spline functions and at their supports the proper continuity and differentiability properties exist.

Determination of the orthogonal trajectories of the spline set (1) becomes understandable from Fig.2.

Starting form parameter values $t=t_a$, and $\tau = \tau_a$, integration should be carried out till the co-ordinate line $\tau = \tau_b$ with $\tau_b - \tau_a = \Delta\tau \ll 1$. Unknown of the problem is the magnitude $t=t_b$. As an approximation let the ortogonal trajectory (2) between a and b be a straight line with a slope $\left(\frac{dr}{dz}\right)_{(2)}$. Nodes (t_a, τ_a) and (t_b, τ_b) are subject to orthogonality relationships

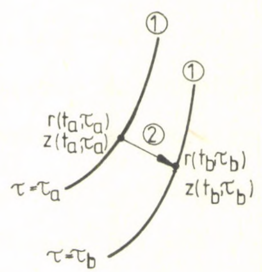

Fig. 2

$$\left(\frac{dr}{dz}\right)_{(1)} \left(\frac{dr}{dz}\right)_{(2)} + 1 = 0 \ : \ \tau = \tau_a$$

$$\left(\frac{dr}{dz}\right)_{①}\left(\frac{dr}{dz}\right)_{②} + 1 = 0 \quad : \quad \tau = \tau_b \; .$$

With these two equations for the unknown t_b, however the problem became redundant. This can be helped by accepting as solution the arithmetic mean $t_{b.m}$ of parameter values $t_{b.1}$ and $t_{b.2}$, calculated from both equations.

The characteristic equation being implicit, the Newton-Raphson iteration method is applied. Simultaneously it has to be tested during each iteration step, whether subscript i decreases or increases at the transition from τ_a to τ_b.

Putting spline functions also through the intersections of the obtained orthogonal co-ordinate lines, two sets of approximately orthogonal spline functions result in the domain $G = \left\{ t, \tau : 0 \leq t \leq 1, 0 \leq \tau \leq 1 \right\}$. Especially length of arch and curvature in the co-ordinate intersection points may be computed very easily.

The running time (CPU-time) needed for the numerical computation in a computer Typ Siemens 7864 for 21 x 21 lines is in the order of a few seconds.

In domain $G = \left\{ t, \tau : 0 \leq t \leq 1, 0 \leq \tau \leq 1 \right\}$ according to Fig.1 the elementary length of arch of the curves τ= const. are denoted dm, and t= const. db, the corresponding co-ordinate-line curvatures by G_m and G_b respectively. Let the meridional velocity components be c_m and c_b. Thus the differential equation system to be solved is

$$\frac{\partial c_m}{\partial b} + c_m G_m = \frac{\partial c_b}{\partial m} - c_b G_b + F(t, \tau) = H(t, \tau) \qquad (1)$$

and

$$\operatorname{div} \underline{c} = 0 \qquad (2)$$

For the solution a somewhat modified iteration method, based on [1] , [2] is suggested. Practically the iteration can never be avoided when the three -dimensional problem is examined as a set of two-dimensional ones. Namely the meridional streamlines define those stream surfaces being surfaces of revolution on which the second principal problem [3] of the hydrodynamic cascade theory has to be solved. The set of solutions gives the field of forces-and part of the vorticity - whose knowledge allows a better approximation of the meridional streamline.

To cut it short determination of the meridional streamlines is discussed, for sake of simplicity only in an environment without blades. In case of blading the right side of equation (1) increases with two more terms according to [1] and [2]. These can be determined in the above mentioned iteration process. In present case according to [1]

$$F(t, \tau) = C_1 r - \frac{C_2}{r}$$

where C_1 and C_2 are constants along a streamline and depend only on the value of parameters at t=1:

$$C_1 = \frac{1}{r_\phi\, c_{\phi m}} \left[\frac{\partial}{\partial b} \left(\frac{c^2}{2} + \frac{p}{\varrho} \right) \right]_\phi$$

$$C_2 = \frac{c_{\phi\varphi}}{c_{\phi m}} \left[\frac{\partial}{\partial r} \left(r\, c_\varphi \right) \right]_\phi$$

where subscrit ϕ refers to section t = 1.

For the solution of equation system (1) - (2) also an iteration process is suggested. This is based on the fact that in case of a properly chosen co-ordinate system the first two terms in the right-hand side of Eq.1 are of a smaller order than are the left-hand side terms, thus the error committed in them hardly disturbs distribution $c_m(b)$. Therefore curves t=const. and τ= const. of the curvilinear orthogonal co-ordinate system are plotted according to Fig.3 to have a constant volume flow ΔQ_j between surfaces of revolution defined by two adjacent curves τ= const. as meridional curves, in conformity with the velocity distribution assumed in sections t=0. At t=1 only the above mentioned stream-line curveture has to be specified. Starting from an approximation of the right-hand side of Eq.1 considering the distributions $H(t, \tau)$ on the curves t= const. as known, the differential equations along curves t= const.

$$\frac{dc_m}{db} + c_m(b)\, G_m(b) = H(b)$$

are solved.

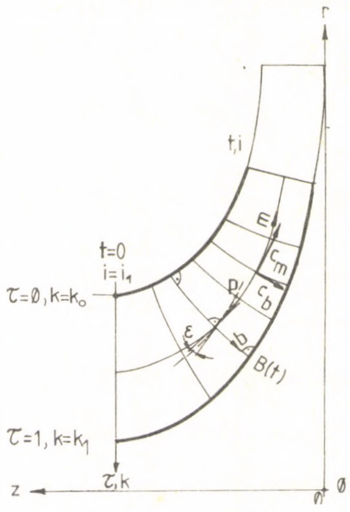

Fig. 3

The solution is:

$$c_m(t,\tau) = c_m(b) = K_1(b).K_2(b) + c_m(\emptyset) \cdot K_1(b)$$

where

$$K_1(b) = e^{-\int_{\emptyset}^{b} H(b')db'}$$

$$K_2(b) = \int_{\emptyset}^{b} \frac{H(b')}{K_1(b')}\, db' \qquad \text{and}$$

$c_m(\emptyset)$ - **integration** constant.

The obtained distributions $c_m(b)$ are applied to define the intersection (P) of meridional lines corresponding to ΔQ_j flow rates and lines t= const. For our purpose, instead of directly using Eq. 2 the relationship

$$\Psi(b) = \int_{\emptyset}^{b} r(b')\, K_1(b')K_2(b')db' + c_m(\emptyset) \int_{\emptyset}^{b} r(b')K_1(b')db'$$

is applied. The integration constant becomes

$$c_m(\emptyset) = \frac{\frac{Q}{2} - \int_{\emptyset}^{B} r(b)\, K_1(b).K_2(b)\, db}{\int_{\emptyset}^{B} r(b)\, K_1(b)\, db}$$

denotin $B(t) = b(t,1)$ and taking into consideration that $\Psi(B) = Q/2\pi$ (where Q is the total volume flow rate). Now, for any value Ψ, the intersection of an optional line t= const. and the streamline belonging to this Ψ can be defined. Describing each meridional streamline by spline functions, intersection angles ε are obtained, yielding approximate values

$c_b = c_m \operatorname{tg}\varepsilon.$

With the repeated use of spline functions all terms of the functions H(b) and with them a new approximation of H(b) itself can be determined. From here the procedure may be repeated until a suitable accordance is obtained in the H(b) distribution for two consecutive steps.

Essentially the same method is to be used if there are blades in the space. In determining distribution $c_m(t, \tau)$ the right-hand side of Eq.1 gets evidently supplemented according to [1], [2] and the entire procedure becomes incorporated into an iteration taking blade loading into consideration.

REFERENCES

[1] O. Füzy: Design of Mixed Flow Impeller (Periodica Polytechnica, M. VI/4.)

[2] O. Füzy: Consideration of Flow Conditions at Rotor Inlet in Blading Design (Periodica Polytechnica, M. VII/1. 1964.)

[3] Füzy, O. and Thuma, A.: Calculating the Velocity Distribution of a Plane Airfoil Cascade Given by its Geometry, Proceedings of the Third Conference on Fluid Mechanics and Fluid Machinery, 1969.

[4] Stiefel, E.: Einführung in die numerische Matematik. Stuttgart: Teubner, 1978.

Prof.Dr-Ing. FÜZY, O. - Ing. TÁNCZOS, L. Dept. of Hydraulic Mach. T.U. Budapest, H-1521 BUDAPEST, Stoczek u. 2/D.

Dr-Ing. STECK, E. Inst. für Strömungslehre und Strömungsmaschinen, Univ. Karlsruhe D-7500 KARLSRUHE, Kaiserstrasse 12.

CALCULATIONS OF THE FLOW IN PERIPHERAL BLOWERS

M. Gabi

SUMMARY

The flow in the side-channel of peripheral blowers is calculated. Solving the Navier-Stokes-equations numerically by a finite difference method, the case of fully developed, laminar and incompressible flow in a side-channel with rectangular cross-section ist treated. Starting from important dimensionless parameters the flow field and the characteristics of peripheral blowers are calculated. To proof the assumptions and theoretical results, characteristics and flow field also are investigated experimentally.

1. INTRODUCTION

Peripheral blowers and pumps are types of fluid machinery, which are used for special applications, when great increase of pressure is requested. The hydraulic efficiency is small (max. 40 %), so they are only built in small sizes.

In Fig. 1 the operating conditions of several types of fluid machinery are compared by plotting the coefficients of pressure and volume flow rate of axial, mixed-flow, radial and peripheral blowers in the point of operation of the best hydraulic efficiency.

The fundamental construction of a peripheral blower with one and two side-channels is shown in Fig. 2. The great increase of pressure in peripheral machines is caused by the fact, that the fluid multiply passes the blading of the impeller on its way through the machine, so that there is a kind of "multistage" increase of pressure. Fig. 3 schematically shows the principle of energy transfer between impeller and side-channel flow. The circumferential velocity component c_φ is accelerated in the blading of the impeller and retarded in the side-channel by the increase of pressure.

There are several experimental and theoretical investigations to examine the behaviour of peripheral pumps and blowers in the literature, calculating the characteristics using various unidimensional methods [1, 2, 3, 4, 5].

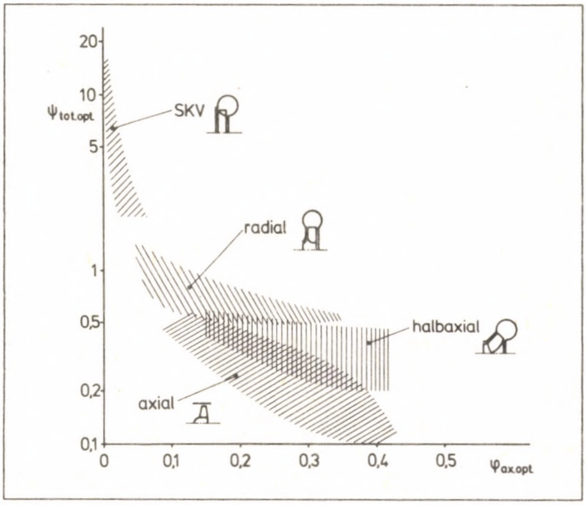

Fig. 1.

Fig. 2.

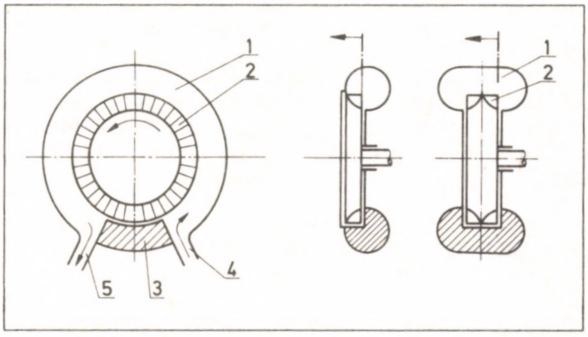

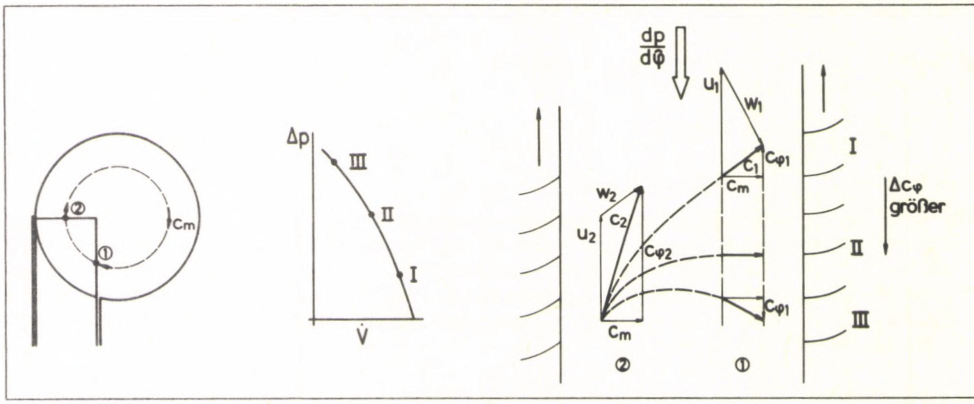

Fig. 3.

Fig. 4.

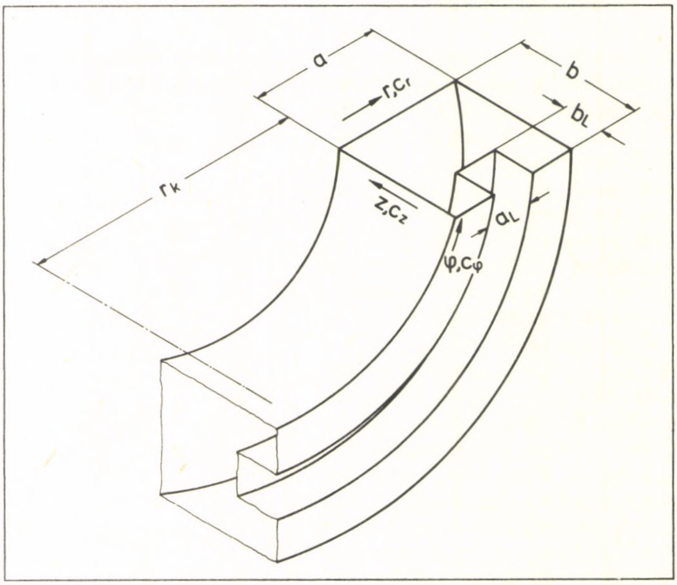

2. DESCRIPTION OF THE CALCULATION-MODEL

To calculate the flow in a peripheral machine, it is necessary to introduce a convenient calculation-model. The side-channel is superseded by a curved channel with rectangular cross-section (Fig. 4).

The cross-section of the impeller-blading also is rectangular and the blading is similar to that of a Sirocco-impeller. The boundaries of the impeller are treated as a part of the boundaries of the side-channel, where convenient boundary-conditions are to find.

The following premises are introduced: laminar, stationary and fully developed flow of an incompressible and Newtonian fluid.

3. METHOD OF CALCULATION

3.1. Set of equations

The flow field in the side-channel is described by the Navier-Stokes-equations:

$$\frac{d\vec{c}}{dt} = \vec{f} - \frac{1}{\rho}\,\text{grad}\,p + \nu\,\Delta\vec{c} \tag{1}$$

and the continuity equation:

$$\text{div}\,\vec{c} = -\frac{1}{\rho}\frac{d\rho}{dt}\ . \tag{2}$$

Using the formulation of the stream-function ψ and the vorticity-function ξ:

$$c_r = -\frac{1}{r}\frac{\partial\psi}{\partial z}\ ; \qquad c_z = \frac{1}{r}\frac{\partial\psi}{\partial r}\ ; \qquad \xi = \frac{\partial c_r}{\partial z} - \frac{\partial c_z}{\partial r}$$

and the dimensionless expressions:

$$X = \frac{r_K\,\hat{\varphi}}{d_h\,Re} \qquad R = \frac{r - r_K}{a} \qquad Z = \frac{z}{b}$$

$$U = \frac{c_\varphi}{\bar{c}_\varphi} \qquad V = \frac{c_r}{\bar{c}_\varphi}\frac{Re\,d_h}{a} \qquad W = \frac{c_z}{\bar{c}_\varphi}\frac{Re\,d_h}{b}$$

$$CP = c_p\frac{d_h\,Re}{r_K\,\rho\,\bar{c}_\varphi^2} \qquad A_K^* = \frac{A_K}{a\,b} \qquad \Omega = \xi\,\frac{d_h}{\bar{c}_\varphi}\,Re\,\frac{a}{b}$$

$$\Psi = \frac{\psi}{\bar{c}_\varphi\,d_h\,r_K}\,Re\,\frac{a}{b} \qquad Re = \frac{\bar{c}_\varphi\,d_h}{\nu} \qquad S = \frac{a}{b}$$

$$\sigma = \frac{a}{2\,r_K} \qquad De = Re\sqrt{\sigma} \qquad D = 2\,\frac{1 - AB}{1 + S + B}$$

the following set of equations is to be solved for U, Ω, Ψ, CP:

$$\frac{\partial}{\partial R}(V\,U) + \frac{\partial}{\partial Z}(W\,U) + \frac{4\sigma}{1+2\sigma R}\,V\,U =$$

$$= -\frac{CP}{1+2\sigma R} + D^2\left\{\frac{\partial}{\partial R}\,\frac{\partial/\partial R\,[(1+2\sigma R)\,U]}{1+2\sigma R} + S^2\,\frac{\partial^2 U}{\partial Z^2}\right\} \tag{3}$$

$$\int_{A_K^*} U\,dA^* = 1 \tag{4}$$

$$\frac{\partial}{\partial R}(V\,\Omega) + \frac{\partial}{\partial Z}(W\,\Omega) - \frac{4\,D^2\,S^2\,De^2}{1+2\sigma R}\,U\,\frac{\partial U}{\partial Z} =$$

$$= D^2\left\{\frac{\partial}{\partial R}\,\frac{\partial/\partial R\,[(1+2\sigma R)\,\Omega]}{1+2\sigma R} + S^2\,\frac{\partial^2\Omega}{\partial Z^2}\right\} \tag{5}$$

$$-(1 + 2\sigma R)\,\Omega = D^2\left\{(1 + 2\sigma R)\frac{\partial}{\partial R}\left(\frac{1}{1+2\sigma R}\,\frac{\partial\Psi}{\partial R}\right) + S^2\,\frac{\partial^2\Psi}{\partial Z^2}\right\} \tag{6}$$

$$V = -\frac{D^2}{1+2\sigma R}\,\frac{\partial\Psi}{\partial Z} \qquad W = \frac{D^2}{1+2\sigma R}\,\frac{\partial\Psi}{\partial R} \qquad (7),\ (8)$$

3.2. Boundary conditions

There are two different types of boundaries circumscribing the integration area (Fig. 5):

(1) Side-channel-walls (I — IV): no-slip condition is valid here.

$$U = V = W = 0, \quad \Psi = 0.$$

$$\text{I, III:} \qquad \Omega_W = -\frac{D^2}{1+2\sigma R}\frac{\partial}{\partial R}\left(\frac{1}{1+2\sigma R}\frac{\partial \Psi}{\partial R}\right)_W$$

$$\text{II, IV:} \qquad \Omega_W = -\frac{D^2\,S^2}{1+2\sigma R}\left(\frac{\partial^2 \Psi}{\partial Z^2}\right)_W$$

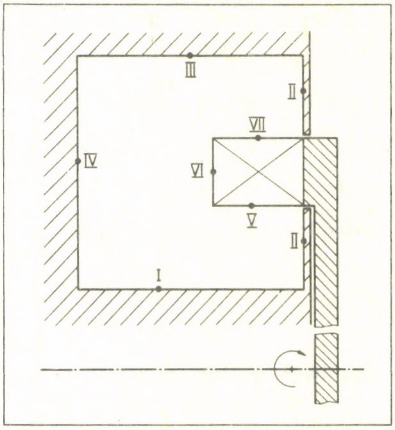

Fig. 5.

(2) Boundaries of the impeller (V — VII):

VI (blade end):

$$U = U_L(R), \qquad V = W = 0, \qquad \Psi = \Psi(B)$$

$$\Omega = -\frac{D^2\,S^2}{1+2\sigma R}\left(\frac{\partial^2 \Psi}{\partial Z^2}\right)_B$$

V, VII (inlet, outlet):

$$U = U_{1,2}\,(\varphi_L,\,\psi_L), \qquad V = V_{1,2}\,(\varphi_L), \qquad W = 0$$

Volume flow rate $\varphi_L = \bar{c}_{r2}/u_2$ and deflection of the impeller $\psi_L = 2\,(c_{\varphi 2} - (r_1/r_2)\,c_{\varphi 1})/u_2$ depend on the geometry of side-channel and impeller and the point of operation $\varphi = \bar{c}_\varphi/u_2$ [6].

$$(\varphi_L,\,\psi_L) = f\left\{\varphi,\ Re,\ \sigma,\ S,\ D,\ A,\ B,\ \beta_{S1},\ \beta_{S2}\right\}$$

3.3. Numerical solution

The set of equations is solved by using a finite-difference-method of the second order. A rectangular co-ordinate map grid is applied [7]. The computation is started from a set of dimensionless parameters and initial values for the flow field.

4. TESTING STAND

To proof the assumptions and theoretical results, a testing stand was built with a pattern of the side-channel and the impeller similar to the calculation-model (Fig. 6). Its dimensions are:

$d_o = 0.886$ m	$d_2 = 0.954$ m	$a = 0.1$ m
$b = 0.105$ m	$a_L = 0.034$ m	$b_L = 0.041$ m
$\beta_{S1} = 45°$	$\beta_{S2} = 135°$	

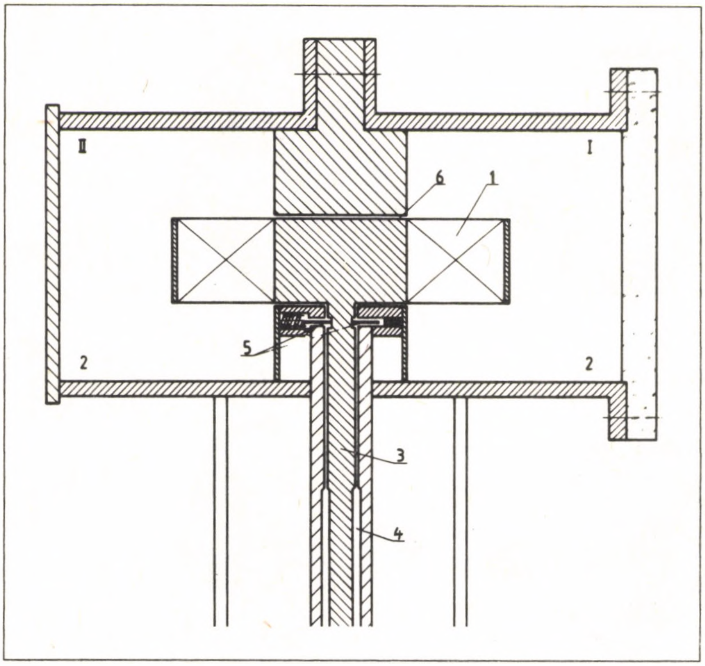

Fig. 6.

1 impeller-blading
2 side-channels
3 impeller
4 radial gap
5 seals
6 axial gap

5. RESULTS

Calculating the increase of pressure $\psi = \Delta p/(\rho/2)\cdot u_2^2$ for several values of the volume flow rate, the characteristic curve of a side-channel blower can be determined. Fig. 7 shows the characteristics for a variation of the curvature σ.

The figure also yields points of measurements in the testing stand. For increasing curvature σ the characteristics become more shallow.

Fig. 8, 9, 10 show the pattern of the flow field in the cross-section of the side-channel for a variation of the volume flow rate φ. In some regions of the side-channel reverse flow can be observed at strongly throttled points of operation (Fig. 8).

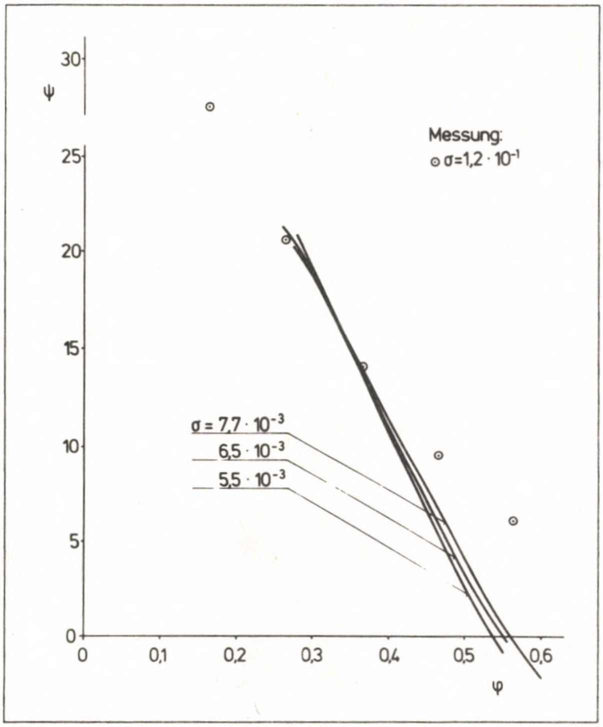

Fig. 7.

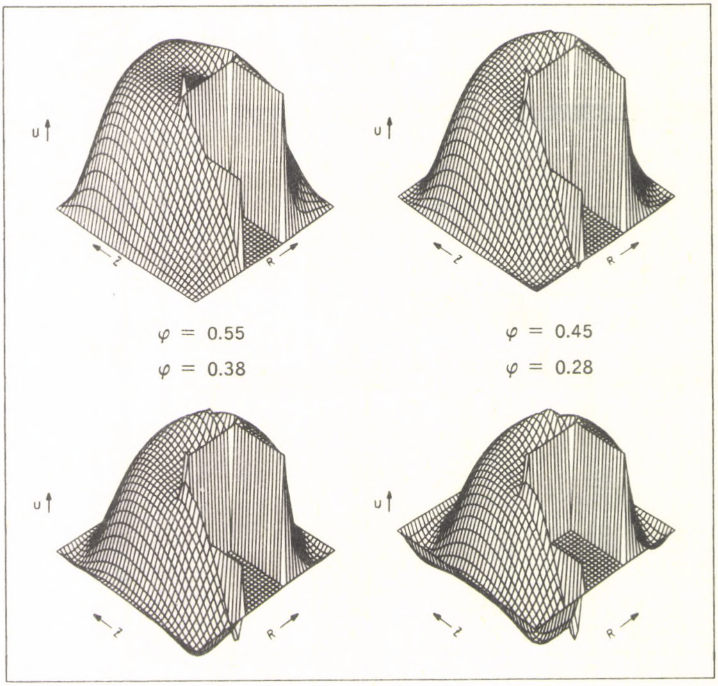
u
Z
R
φ = 0.55
φ = 0.45
φ = 0.38
φ = 0.28

Fig. 8.

Fig. 9.

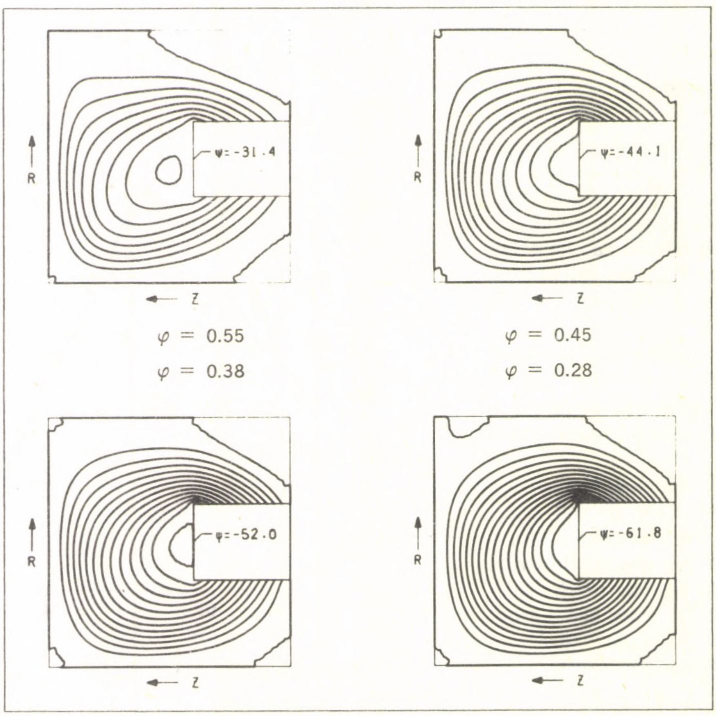
R
Z
ψ=-31.4
ψ=-44.1
ψ=-52.0
ψ=-61.8
φ = 0.55
φ = 0.45
φ = 0.38
φ = 0.28

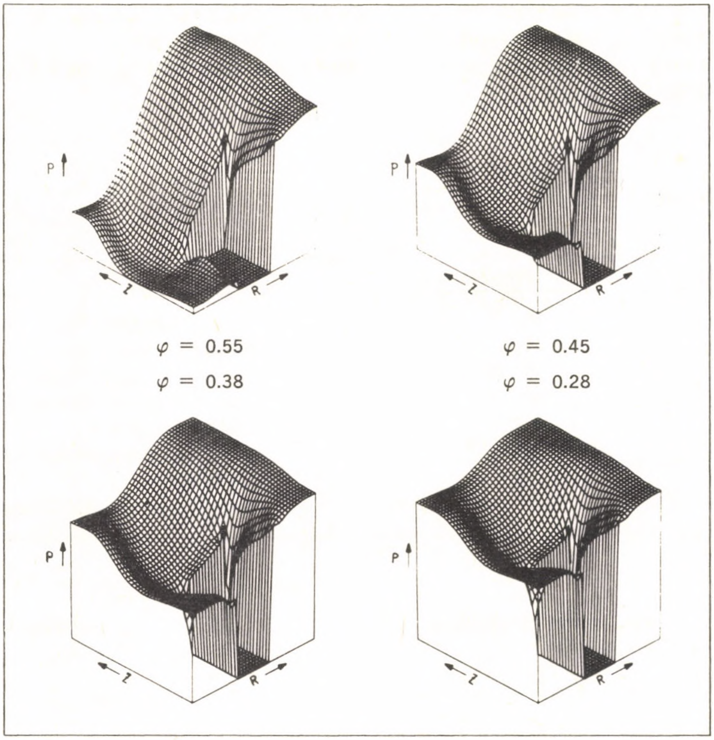
P
Z
R
φ = 0.55
φ = 0.45
φ = 0.38
φ = 0.28

Fig. 10.

Fig. 11.

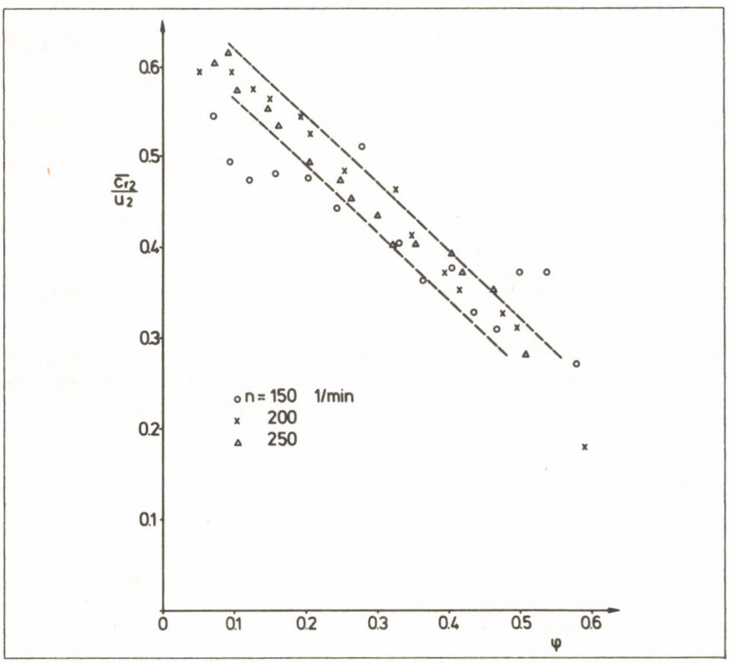
$\frac{\overline{c_{r2}}}{u_2}$
0.6
0.5
0.4
0.3
0.2
0.1
0
0.1
0.2
0.3
0.4
0.5
0.6
φ
o n = 150 1/min
x 200
Δ 250

The intensity of the secondary flow, represented by the stream function Ψ, increases (Fig. 9) and the pressure field becomes more uniform for throttling (Fig. 10).

Fig. 11 shows measurements of the impeller-volume flow rate φ_L as a function of φ. φ_L nearly is a linear function of φ.

6. SYMBOLS

with dimension	dimensionless	
a, b	A, B	size of side-channel and impeller
d_h	D	hydraulic diameter
$r, \widehat{\varphi}, z$	R, X, Z	cylindrical coordinates
c_r, c_φ, c_z	U, V, W	components of flow velocity
c_p	CP	pressure gradient
Δp	Ψ	pressure, pressure coefficient
β	—	blade angle
ρ, ν	—	density, kinematic viscosity

Subscripts

1, 2	inlet, outlet of impeller	L	impeller
K	side-channel	W	wall

7. REFERENCES

[1] IVERSEN, H.W.: Performance of the Periphery Pumps. Trans. ASME, 1955.

[2] WEINIG, P.S.: Analysis of Traction Pumps. Hydr. Div. ASME, Nr. 55-SA-35, 1955.

[3] SENOO, Y.: Researches on Peripheral-Pumps. Rep. Res. Inst. Appl. Mech., Vol. 3, 1954.

[4] ENGELS, H.: Untersuchungen an Ringpumpen. Hannover, Techn. Universität, Dr.-Ing.-Diss. v. 1940.

[5] WILSON, W.A.; SANTALO, M.A.; OELRICH, J.A.: A Theory of the Fluid-Dynamic Mechanism of Regenerative-Pumps. Trans. ASME, 1955.

[6] GABI, M.: Theoretische und experimentelle Untersuchung der Strömung in Seitenkanalverdichtern. Karlsruhe, Universität (TH), Dr.-Ing.-Diss. v. 1982.

[7] SCHILLING, R.; SIMON, R.: Berechnung der ausgebildeten Strömung in gekrümmen Kanälen mit rechteckigem Querschnitt. In: Theoretical and Experimental Fluid Mechanics. Hrsg. von U. Müller, K. Roesner, B. Schmidt. Heidelberg: Springer, 1979.

GABI, Martin Dr.-Ing.
Institut für Strömungslehre und Strömungsmaschinen
Universität Karlsruhe (TH)
Kaiserstraße 12 · D 7500 Karlsruhe 1
Federal Republic of Germany

TURBULENT FLOW STRUCTURE WITHIN A BEND OF A CIRCULAR TUBE

N.G.Gontzov, O.A.Marinova, A.V.Tananayev

A bend in a pipeline is one of the common elements of a hydraulic system. It is known [1] that within curvolinear parts of a pipe-line a considerable transformation of the pressure and the velocity profile takes place, there arise secondary flows and separation zones are possible. Studies of this kind of flow structure are necessary for obtaining efficient methods of flow design. Though bends with large radius of curvature have been the subject of investigation [2], there are, practically, no data on the measurements of flow parameters within bends of $R/d \leq 2$ in spite of the fact that such bends are widely used in industry.

The paper presents results of an experimental study of the isothermic turbulent flow structure in the zone of a 90° bend of a circular tube. The radius of curvature of the bend is $R/d = 1$, $d = 206$ mm. It was made of an acrylic plastic of 6 mm.

For pressure sampling holes were drilled in the pipeline walls as well as in the walls of the bend. The hole diameter is 0.7 mm. The pressure was measured by a differential micromanometers filled with alcohol. The air discharge was defined by the differential pressure in the inlet nozzle. The velocity vector and pressure in the flow were measured by a five-hole spherical probe. The diameter of the probe is 5 mm. The investigation was carried out on an open aerodynamic stand. Air flow was studied under $Re = U d/\nu = 9\cdot10^4 \div 4\cdot10^5$, where U is the mean discharge velocity.

Velocity and pressure distribution measurements in the flow show that the bend influences the profile of these parameters starting from the section of the inlet pipe-line situated 2.2d upstream to the bend inlet. Mean velocity profile is axially symmetric and corresponds to the fully-developed turbulent flow. The pressure is constant across the flow. The chosen coordinate system is shown in Fig.1. Non-dimentional pressure distribution on the bend walls is presented in Fig.2,

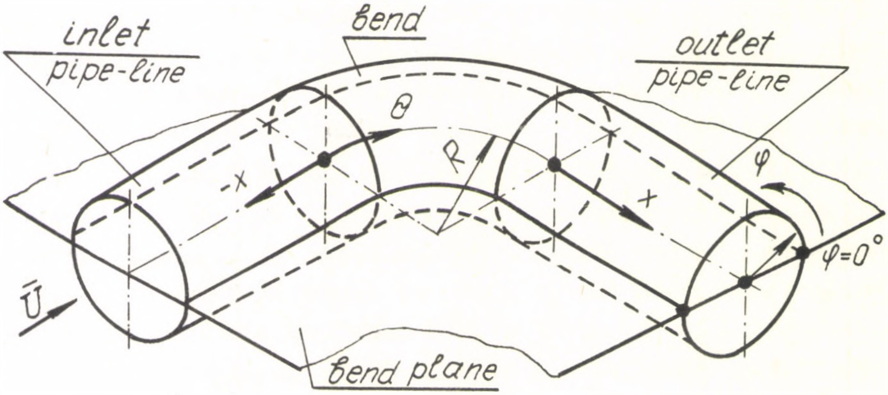

inlet
pipe-line
bend
outlet
pipe-line
θ
R
-x
x
φ
φ=0°
Ū
bend plane

Fig.I

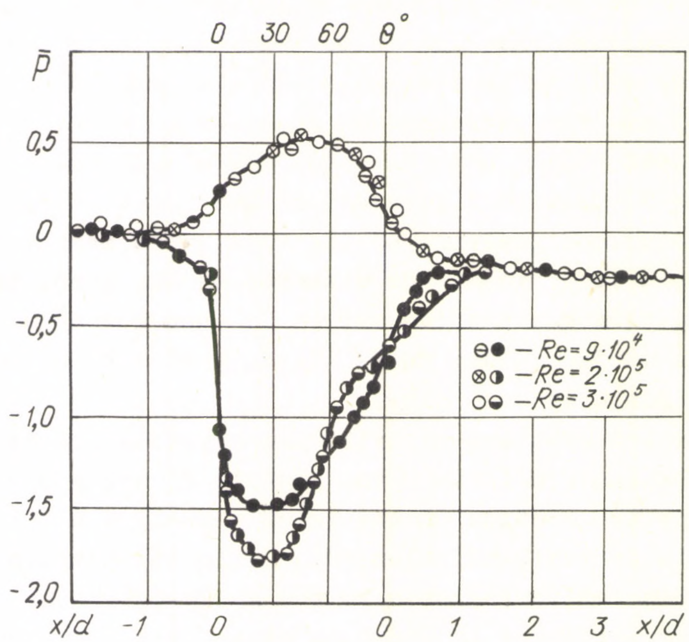

0 30 60 θ°
P̄
0,5
0
-0,5
-1,0
-1,5
-2,0
x/d -1 0 0 1 2 3 x/d
⊖● – Re=9·10⁴
⊗◑ – Re=2·10⁵
○◒ – Re=3·10⁵

Fig.2

where $\bar{p} = (p - p_o)/0,5\rho U^2$, p_o is the pressure upstream the bend distortion zone.

For the inlet pipe-line section the pressure is constant around the cross-section perimeter up to $\bar{X} = 1.5$. Nearer the bend the pressure on the external (concave) wall increases and decreases on the internal (convex) wall, which agrees with the earlier results [3,4,5]. The maximum pressure drop on the internal wall makes up approximately $1.8\rho U^2/2$, the value of the increase for the external wall being $0.5\rho U^2/2$. The maximum value for the external wall pressure is observed with $\theta = 55^o$, the minimum value for the internal wall occures with $\theta = 25^o$.

The pressure distribution on the internal wall within the bend plane turned out to be asymmetric with respect to the bisector of the bend angle. Experiments [3] revealed symmetric pressure distribution on the internal wall of a rectangular bend with the non-dimentional curvature radius 1.5. In case of an inviscid flow the flow parameter distribution is also symmetric with respect to the bisector of the bend angle. The most plausible cause of the asymmetry must be secondary flows developed within the bend. The stagnation of the flow opposite tangential motion near the internall wall displaces the pressure increase upstream. A viscous flow with the uniform inlet velocity profile is known to retard the development of the secondary flow [4]. In such cases the pressure distribution is symmetric [3]. In our investigation the velocity profile at the inlet had fully-developed near-wall shear layers making the development of the secondary flow more intensive. The pressure distribution turned out to be asymmetric. The pressure distribution along the generating line displaced for 90^o from the bend plane remains constant up to $\theta = 65^o$, then it slowly decreases to the outlet pressure. Such pressure distribution occures with the range of $9 \cdot 10^4 \leq \mathrm{Re} \leq 4 \cdot 10^5$. Comparison of the curves for the pressure distribution on the walls within the bend plane, corresponding to different values of the Reynolds Number, showes that on the external wall the pressure distribution follows its pattern, while on the internal wall it changes essentially with the increase of Re from $9 \cdot 10^4$ up to $2 \cdot 10^5$; after that it remains constant. The changes in the pressure distribution on the internal wall of the bend are evidently connected with the appearance of the separation zone. A wall pressure distribution for a non-separation flow within a bend is presented in [3]. We obtained similar distribution for Re = $9 \cdot 10^4$. Here, the positive pressure gradient occures on reaching the minimum pressure value and remains constant up to the bend outlet. Separation at the internal bend wall starts under Re > $9 \cdot 10^4$, the pressure distribution on the wall changing its shape. With the increase of the Re the separation point moves upstream. The effective flow geometry including the separation zone changes,bringing about the corresponding changes in the pressure distribution on the internal wall. Thus, the pressure distribution shows whether the separation or non-separation flow developes within the bend. The influence of the bend on the pressure distribution on the walls ends throughout the cross-section perimeter 1.5d downstream from the bend. Changes in the flow pressure profile begin as far as the inlet pipeline (Fig.3). In the bend zone the pressure distribution essentially differs from the generally assumed linear distribution. Sharp decrease of pressure takes place near the internal wall under $\theta = 0 \div 45^\circ$.The maximum pressure drop makes up $\sim 1.7 \rho U^2/2$ for $\theta = 25^\circ$. When the flow turns from $\theta = 0$ to $\theta = 65^\circ$ minimum $p = f(r)$ is situated on the internal wall. Starting from $\theta = 65^\circ$ the minimum moves into the flow, which is, evidently, brought about by a separation zone, emmerging, as the velocity measurement showed, under $\theta = 65^\circ$. The levelling of pressure profile in the flow is comming to an end in the outlet section with $\bar{X} = 1.5$. The bend does not influence the pressure distribution in the inlet pipe-line along the diameters normal to the bend plane. There occures a slight increase in pressure near the pipe-line axis with $\theta = 5 \div 45^\circ$. Starting with $\theta = 65^\circ$ the pressure becomes constant along the diameter.

Under the influence of the negative pressure gradient as far as in the inlet pipe-line section the flow accelerates

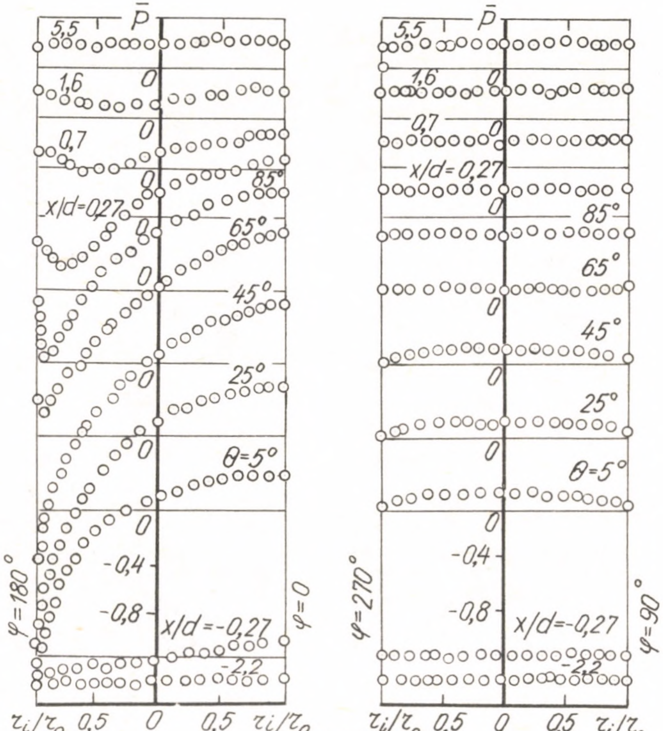

P̄
5,5
1,6
0,7
x/d=0,27
85°
65°
45°
25°
θ=5°
-0,4
-0,8
x/d=-0,27
-2,2
φ=180°
φ=0
φ=270°
φ=90°
r_i/r_o 0,5 0 0,5 r_i/r_o

Fig.3

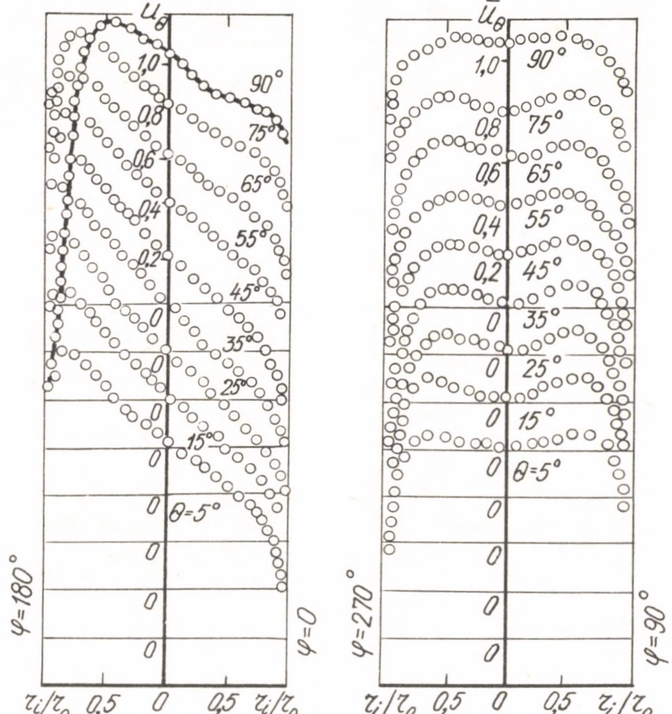

$\bar{u}_\theta$
1,0
0,8
0,6
0,4
0,2
0
90°
75°
65°
55°
45°
35°
25°
15°
θ=5°
φ=180°
φ=0
φ=270°
φ=90°
r_i/r_o 0,5 0 0,5 r_i/r_o

Fig.4

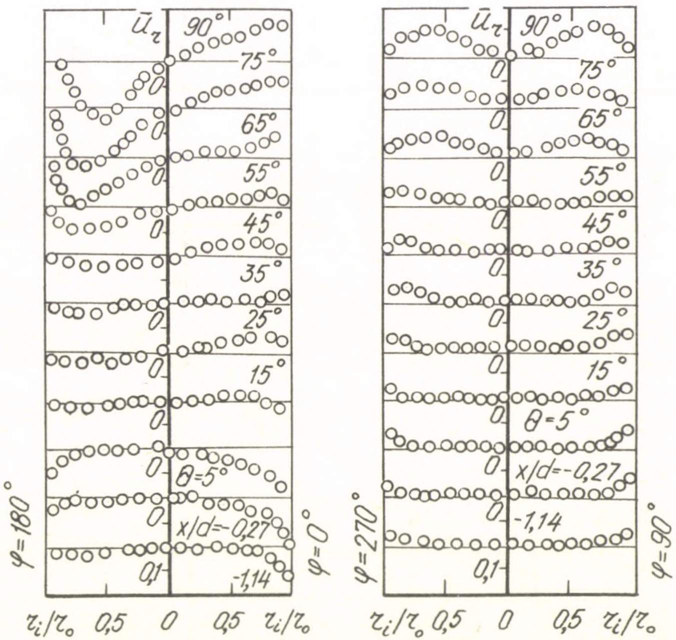

$\bar{u}_r$
90°
75°
65°
55°
45°
35°
25°
15°
$\theta=5°$
x/d=-0,27
-1,14
0,1
$\varphi=180°$
$\varphi=0°$
$\varphi=270°$
$\varphi=90°$
r_i/r_o 0,5 0 0,5 r_i/r_o

Fig.5

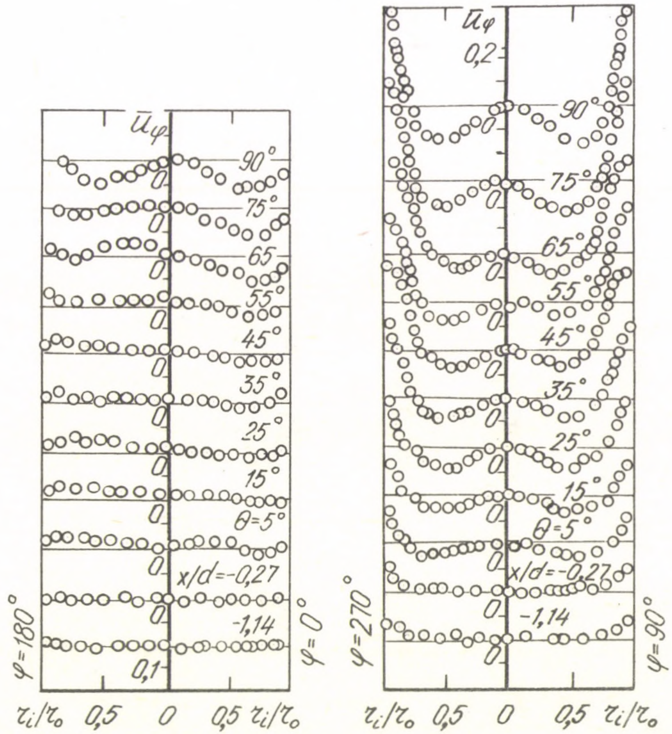

$\bar{u}_\varphi$
0,2
90°
75°
65°
55°
45°
35°
25°
15°
$\theta=5°$
x/d=-0,27
-1,14
0,1
$\varphi=180°$
$\varphi=0°$
$\varphi=270°$
$\varphi=90°$
r_i/r_o 0,5 0 0,5 r_i/r_o

Fig.6

near the internal wall. At the entry of the flow into the bend the increasing negative pressure gradient results in the further flow acceleration within the zone of internal wall, so that under $\theta = 5^{\circ}$ the maximum longitudinal velocity component makes up $1.35\,U$ with $\theta = 15^{\circ}$ - $1.45\,U$, $\theta = 35^{\circ}$ - $1.5\,U$ (Fig.4). The maximum velocity profile moves to the internal bend wall. Then under the action of the increasing positive pressure gradient, the flow in the zone of the internal wall begins to slack with $35^{\circ} < \theta < 60^{\circ}$ and with $\theta = 65^{\circ}$ the flow separates from the internal wall. The zone of separation gradually widens and propagates downstream to the end of the bend. It reaches its maximum transverse dimension in the outlet pipe-line with $\bar{X} = 0.27$. Then the separation zone begins to diminish, and with $\bar{X} = 0.56$ the flow attaches the internal wall. After that the flow in the region of internal wall undergoes intensive acceleration, the highest acceleration taking place directly within the vicinity of the internal wall $0.8 < r_1/r < 1$.

In the region of the external wall the flow at the bend inlet essentially slows down under the action of the positive pressure gradient. At a 45° bend the pressure gradient becomes negative, the flow near the external wall accelerates. In the outlet pipe-line within the wall zone, facing the external wall of the bend, the velocity profile undergoes slight changes to $\bar{X} = 1.23$. Further downstream there appears a well-developed maximum of the velocity profile which gradually moves to the axis of the tube.

The velocity profile along the diameter normal to the bend plane acquires M-shape, starting from the $\bar{X} = -1.14$. Within the inlet pipe-line and the bend, the M-shape is actually constant. The relation of maximum velocity $U_{\theta\,max}$ to pipe axis velocity $U_{\theta o}$ equals approximately 1.06, the distance of the maximum profile from the wall is about 0.5 r. In the outlet pipe-line the M-shape of the velocity distribution strongly increases, reaching maximum value $U_{\theta_{max}} / U_{\theta_o} = 1.37$ with $\bar{X} = 1.23$, after that it begins to diminish, actually disappearing with $\bar{X} \approx 10$. Pressure and velocity measurements,

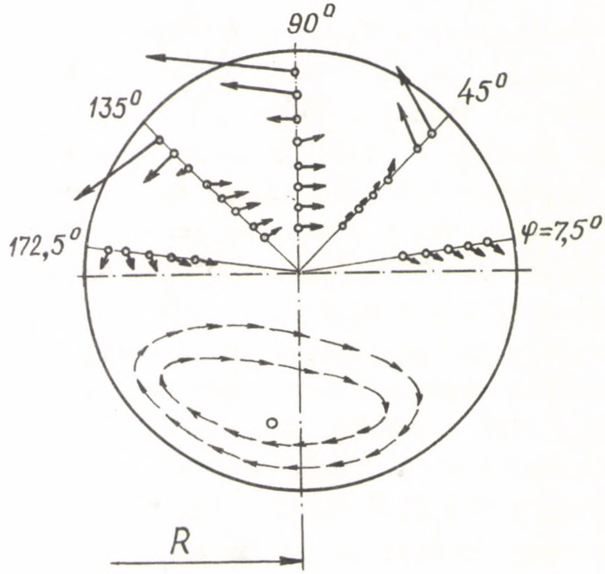

Fig.7

taken for diameters of different inclination to the bend plane, showed that the flow is symmetric with respect to the plane.

Radial and tangential velocity component distribution (Figs.5,6) fully corresponds to the progress of the changes of the longitudinal component profile. The maximum values of U_r and U_φ constitute about $0.5\,U$. From the measurement of the mean velocity vector field (Figs.4,5,6) the secondary flow structure is defined within the bend zone. According to the theoretical speculation and the visual investigation data the secondary flow has the appearance of the "paired-vortex" (Fig.7) which appears only at the inlet of the flow in the bend.

Our investigation revealed the complete symmetry of the flow with respect to the bend plane, the nature of the pressure profile changes, the longitudinal, radial and tangential mean velocity vector component the structure of the secondary flow and the zone of the disturbing effect of the bend upstream and downstream.

References

1. Tananayev A.V. Flows in MHD-channels. M., 1979.
2. Agrawal B., Talbot L., Cony K. Lazer anemometer study of flow development in curved pipes. J.Fluid Mech. 1978, v.85, N 3, p.497-578.
3. Nippert H. Über den Strümungsverlust in gekrümten Kanälen. Ferschungsarbeiten, 1929. H.320.
4. Heskestad I. Flow in a rectangular bend. The Journal of Basic Engineering, 1971, N 3, p.86-98.
5. Hawthorne W.R. Secondary Circulation in Fluid Flow. Proc. Roy.S . 1951, ser.A, V-206, p.374-387.

COMPARISON OF RADIAL AND AXIAL TYPE REGENERATIVE BLOWER

Gerd Grabow, Freiberg GDR

Summary

A comparison is made between radial and axial type regenerative blower. Calculations show the possibility for considerable increase of the dimensionless total head coefficient for the axial type up to the 6-fold compared to the dates of the usual radial type. A theoretical dimensionless total head coefficient of

$$(\psi_{th\,\infty})_{\varphi=0} \cong 116{,}5$$

referring to $\dot{V}=0$ resp. $\varphi=0$ (no discharge) and infinite number of vanes is obtainable. The performance characteristics can be adjusted to that of a Roots blower with the tendency to increase the energy density for regenerative blowers.

1. Nomenclature

A	m^2	- area
r	m	- radius
l	m	- length of side channel
c	m/s	- velocity
$u = r\omega$	m/s	- tangential velocity
p	Pa	- pressure
w	Nm/kg	- specific work
$\dot{V}$	m^3/s	- flow rate
ρ	kg/m^3	- mass density
s	m	- traced way in the channel
β	o	- vane angle
ψ	1	- dimensionless total head coefficient

Subscripts

a	- outer
i	- inner
K	- channel
L	- rotor
m	- meridional; mean
St	- shock
Z	- circulation
th	- theoretical
∞	- infinite
1	- inlet
2	- outlet
R	- friction

φ	1	- dimensionless flow coefficient
τ	1	- circulationfactor
ξ	1	- factor for stripper region
ν	1	- radius ratio ($\nu = r_i/r_a$)
dp/dl	Pa/m	- pressure gradient in the side channel

2. Comparison of the two types

Based upon the one-dimensional circulation theory the relations for circulatory velocity c_m, dimensionless total head coefficient $\psi_{th\infty}$ and pressure gradient in the side channel dp/dl are given below. Radial type (fig. 1).- The following assumptions are made: inlet and outlet losses in the suction and discharge region, the losses at the stripper and the losses due to rotor wall friction and rotor-casing clearance leakage are neglected. An energy balance involves the terms

- theoretical specific work of the rotor vanes $(w_{th})_L$
- specific energy increase in the centrifugal field $(w_{th})_K$, deriving from the rotating gas ring in the side channel
- energy losses caused by the shock at the vane entrance $(w_{St})_L$
- hydraulic energy losses of the circulatory process w_R, consisting of rotor losses(change of the cross-sectional area at the rotor entrance, friction and turning of the flow in the blade passage) and mixing losses in the side channel due to the interaction between the boundary layer regions of the circulatory and the meridional flow.

The energy equation yields

$$(w_{th})_L = (w_{th})_K + (w_{St})_L + w_R \qquad (1)$$

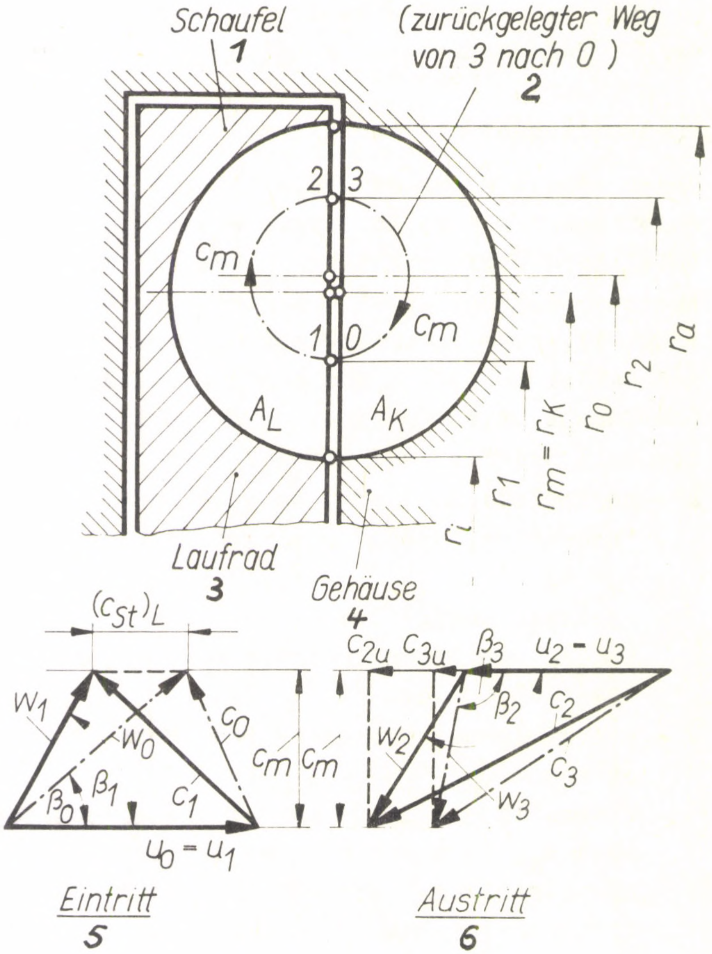

Fig. 1 : Velocity triangles and meridional section of the radial type
1 - vane; 2 - traced way from 3 to 0;
3 - rotor; 4 - casing; 5 - entry; 6 - exit

Assuming an infinite number of vanes with $\beta_2 = 90^\circ$ (pure radially) the circulatory velocity referring to $\varphi = 0$, is obtained from /1/ and /2/

$$\left(\frac{c_m}{u_m}\right)_{\varphi=0} = \frac{r_2}{r_m}\sqrt{\frac{1}{\zeta_R}\left[1 - \left(\frac{r_1}{r_2}\right)^2\right]} \qquad (2)$$

The dimensionless total head coefficient is

$$(\psi_{th_\infty})_{\varphi=0} = 16\frac{(r_2/r_m)^2\xi}{(1-\nu)^2}\left(\frac{c_m}{u_m}\right)_{\varphi=0}\left[1-\left(\frac{r_o}{r_a}\right)^2\right]\left(1+\frac{r_1}{r_2}\right) \times$$

$$\times\left[1+\frac{r_m}{r_2}\left(\frac{c_m}{u_m}\right)_{\varphi=0}\right] \qquad (3)$$

with $(c_m/u_m)_{\varphi=0}$ from eq.(2).
The relation for the pressure gradient along the side channel follows from /2/ and /3/

$$\left(\frac{dp}{dl}\right)_{\varphi=0} = \frac{\varrho}{s}\left(\frac{r_2}{r_m}\right)^2 u_m^2\left(1-\frac{r_1}{r_2}\right)\sqrt{\frac{1}{\zeta_R}\left[1-\left(\frac{r_1}{r_2}\right)^2\right]} \qquad (4)$$

<u>Axial type</u>(fig. 2).- The energy balance of the circulatory flow for axial type regenerative blower with infinite number of vanes and $\varphi = 0$, but with inlet vane angle $\beta_1 = 45^\circ$ and outlet vane angle $\beta_2 = 135^\circ$ corresponding with /1/ and /2/ leads to

$$\left(\frac{c_m}{u_m}\right)^*_{\varphi=0} = \frac{1}{\zeta_R}\left(1 + \sqrt{1 + 3\zeta_R}\right) \qquad (5)$$

The dimensionless total head coefficient is

$$(\psi_{th_\infty})_{\varphi=0} = 4\,\frac{r_m}{r_K}\,\frac{\xi\pi r_a^2(1-\nu^2)}{A_K}\left(\frac{c_m}{u_m}\right)^*_{\varphi=0}\left[1 + \left(\frac{c_m}{u_m}\right)^*_{\varphi=0}\right] \qquad (6)$$

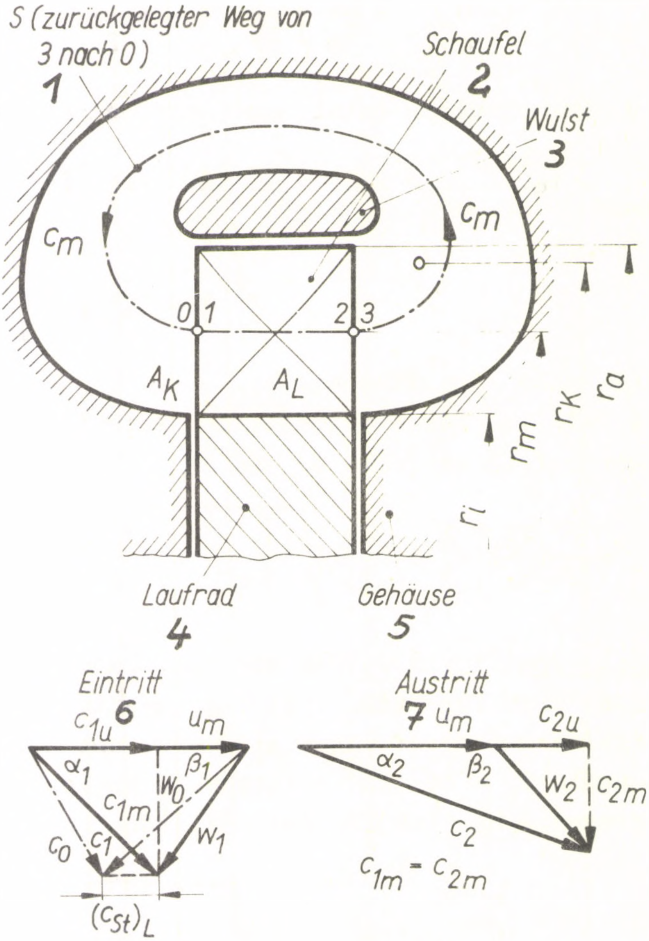

Fig. 2 : Velocity triangles and meridional section of the axial type
1 - traced way from 3 to O; 2 - vane;
3 - collar; 4 - rotor; 5 - casing; 6 - entry;
7 - exit

with $(c_m/u_m)^*_{\varphi=0}$ from eq.(5).

Finally the pressure gradient in the side channel in accordance with /2/ and /3/ is

$$\left(\frac{dp}{dl}\right)^*_{\varphi=0} = 2\,\frac{\rho}{s}\,u_m^2\left(\frac{c_m}{u_m}\right)^{*2}_{\varphi=0} \qquad (7)$$

3. Numerical calculation

Assuming for the radial type regenerative blower vane angle $\beta_2 = 90^0$; dimensionless flow coefficient $\varphi=0$ (no discharge!); radius ratio $\nu=0{,}75$ and circulation factor $\zeta_R = 4$, then with the designed

radius ratios $r_1/r_2=0{,}868$ and $r_2/r_m=1{,}075$

the dimensionless circulatory velocity follows from eq.(2)

$$(c_m/u_m)_{\varphi=0} = \underline{0{,}267}$$

The pressure gradient is determined from eq.(4) with the mass density of air $\rho = 1{,}293$ kg/m^3

$$dp/dl = 0{,}049 . u_m^2/s$$

The dimensionless total head coefficient is according to eq.(3) and with the factor for the stripper region $\xi \cong 1$

$$(\psi_{th\ \infty})_{\varphi=0} = \underline{39{,}7}$$

For the axial type regenerative blower eq.(5)yields, with $\beta_1 = 45^0$ and $\beta_2 = 135^0$

$$(c_m/u_m)^*_{\varphi=0} = \underline{1{,}152}$$

that indicstes a 4,32 fold increase of the circulatory velocity compared with the value for the radial type.

The pressure gradient referring to $\varphi=0$ follows from eq.(7)

$$(dp/dl)^*_{\varphi=0} = 3{,}31 . u_m^2/s$$

The dimensionless total head coefficient for $\xi \cong 1$ and the designed radii $r_i = 262$ mm, $r_a = 350$ mm, $r_m = 306$ mm is derived from eq.(6)

$$(\psi_{th_{\infty}})^{*}_{\varphi=0} = 13{,}7 \; \frac{r_m}{r_K} \; \frac{r_a^2}{A_K}$$

Supposing a design with $r_a^2/A_K = 10$ and $r_m/r_K = 0{,}85$ the dimensionless total head coefficient is

$$(\psi_{th_{\infty}})^{*}_{\varphi=0} = \underline{116{,}5}$$

That indicates the pressure rise to be the 2,94 fold of that of the radial type.
With the pressure gradient in consideration and with

$$s_{axial} \approx 10 . s_{radial}$$

for the length of the circulatory flow way according to fig. 1 and 2 a 6,73 fold pressure rise is attainqble.
The consequence is, that the axial type regenerative blower has to be designed with the conditions

s - small and A_K - small

if large dimensionless total head coefficient should be the result of the new blower type.

Substituting the usual(radial)type of regenerative blower by the new design with pure axial blade rotor a considerable increase in energy density is possible. The characteristics, fig. 3, of such a blower therefore is approaching the characteristics of the Roots blower. Finally the economic-technical characteristics like required specific mass, volume and area of the products are better.

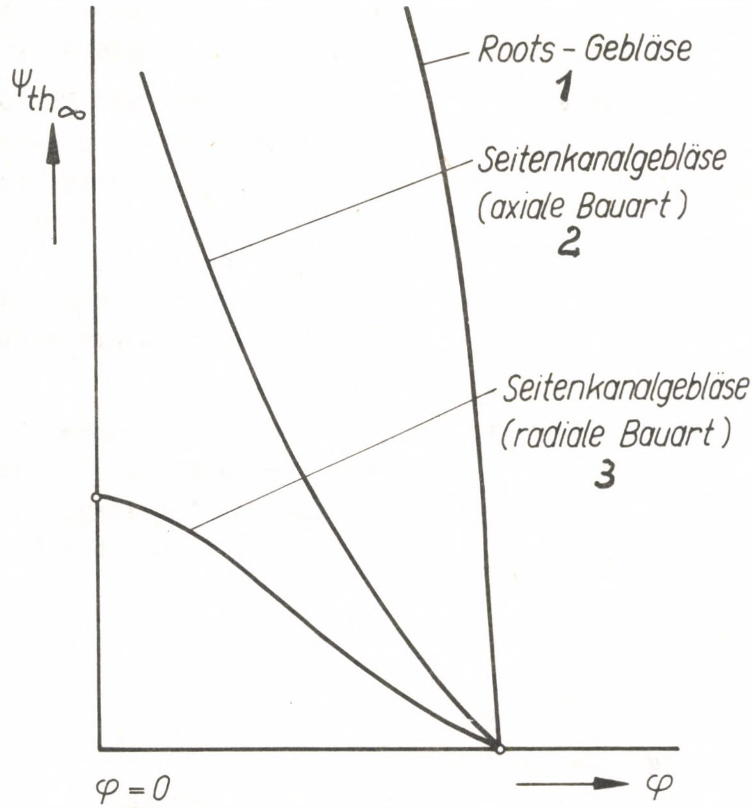

Fig. 3 : Characteristics of different blower types

1 - Roots blower; 2 - regenerative blower (axial type); 3 - regenerative blower(radial type)

4. Bibliography

/1/ Grabow, G. Einfluß der Schaufelform auf das Kennlinienverhalten von Peripheral-Seitenkanalpumpen und hydrodynamischen Strömungskupplungen("Föttinger-Prinzip"), Diss. B, TH - Magdeburg,(1971)

/2/ Grabow, G. Untersuchungen über Peripheral-Seitenkanalpumpen und -gebläse sowie Vergleichsbetrachtungen zwischen Maschinen radialer und axialer Bauart, Bergakademie Freiberg, Sektion Maschinen- und Energietechnik, (1982)

/3/ Sixsmith,H. Altmann,H. A regenerative compressor,Trans ASME, Reihe B, Journal of Engineering for Industry, 99(1977) 3, August, S. 637 bis 647

Prof.Dr.sc.techn. Gerd Grabow
Bergakademie Freiberg
Sektion Maschinen- und Energietechnik
Grundlagen der Energieumwandlung

IMPROVING THE PARAMETERS OF CENTRIFUGAL PUMPS FOR WATER-SOLID PARTICLE MIXTURES

Grozev G. , Ivanov S., Lazarov M., Pasheva V.

Introduction

The operation of centrifugal pumps for hydromixtures in the mining and power industry applications involves a number of problems, such as the comparatively low efficiency of the new machines; fast wear of their operating parts and the corresponding increased worsening of all their parameters.

You will find here presented the results obtained by our research team in our efforts to improve the parameters of a slurry pump using a wheel without a front disk(PG 125) the parameters of which correspond to those of a DENVER5" pump.

Wearing out of the Pump Investigated Here and its Improvement Using the Channel Theory

The wearing out of the above mentioned pump when in use in the mining industry is distributed ina typical way on the blade surface as shown in Fig. 1. The presence of increased wear on the front blade surface and leakage traces in the front clearance in the same place are evidence of the possible stagnation point shift of the flow due to incorrect operating conditions. It is true that the manufacturing firm specifications imply that the pump is intended for use in a wide range of flow rates without any significant decrease in its efficiency; but the actual range of those values at which the flow through the blades retains the stagnation point on the profile nose is comparatively limited. The same thing was shown by applying the two-dimensional cascade theory to the flow analysis of the above mentioned blade system.Those facts have led us to make our first attempt at designing a new impeller having a design point suitable for the required applications. In other words we have developed a more detailed nomenclature of impellers having the same meridional section and dimensions with a view to making an adequate choice of a blade cascade.

In accordance with those considerations a new blade cascade was made using the conventional channel theory method. At the same time the influence of some design parameters was tested for the improvement of the efficiency, the rear disk cutting and the running clearance. The developed samples underwent complete model tests. The best version obtained in this way is shown in Fig. 2. Fig. 3 shows efficiency curves the parameter of which is the diameter of the rear disk cutting.

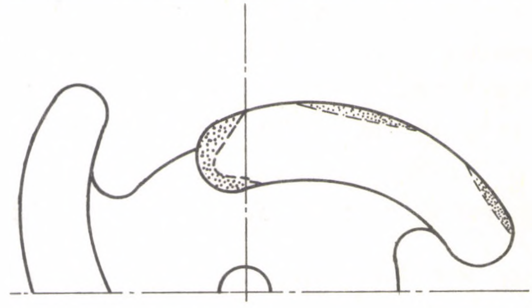

Fig. 1

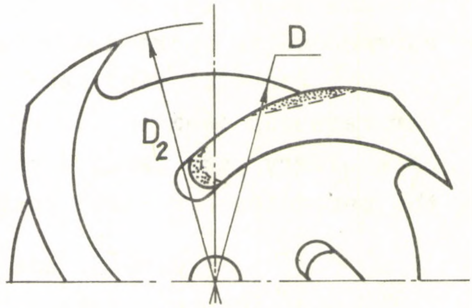

Fig. 2

The results obtained here show a 10% efficiency improvement at optimum rear disk cutting $D/D_2=0.75$. With impeller wear tests

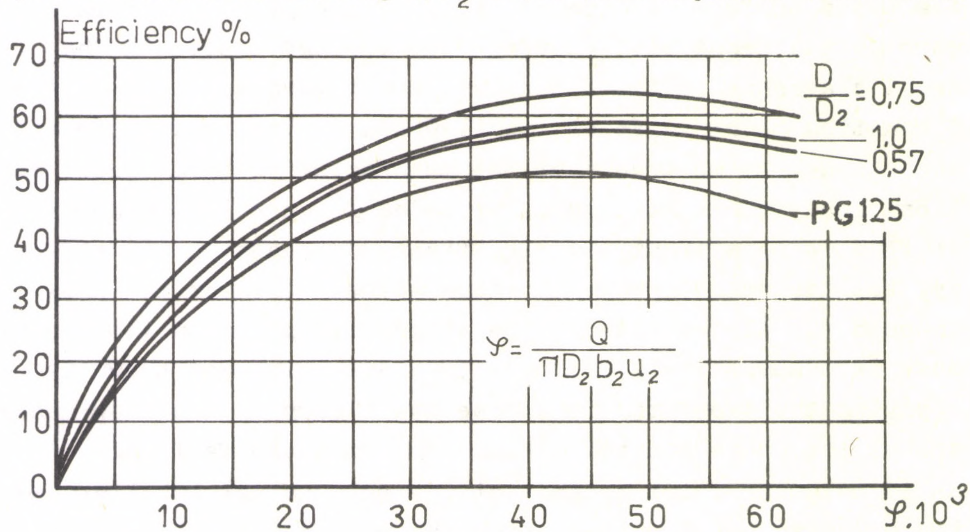

Fig. 3

using hydromixtures increased wearing out has again been observed on a limited surface of the front blade (see Fig. 2). The numerical flow analysis of this particular type of cascade has again shown localization of the front stagnation point in the same area which can be seen from the velocity distribution along the blade contour / Fig. 4 /.The obtained design data have permitted us to conclude that when using the channel theory, the rubber impeller dimensioning results in a blade cascade whose design parameters are far behind the requirements concerning the flow kinematics.For example, when the front stagnation point is on the profile nose of the same blade cascade,

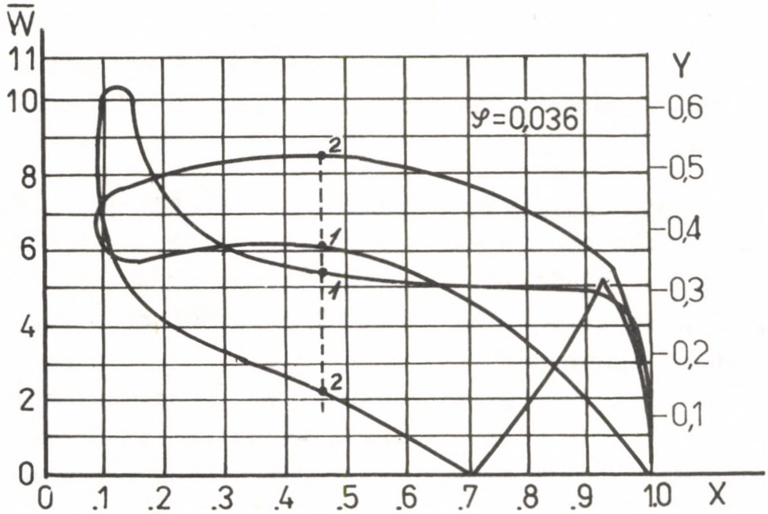

Fig. 4

by using the two-dimensional theory, the   coefficient obtains a value three times greater than the design point. Probably the reasons for such discrepancy lie in the decreased blade number and the great relative blade thickness compared with those of the traditional pumps having the same specific speed where the use of the channel theory yields good results.

Experimental and Theoretical Investigation of the Solid Particle Paths through an Impeller

Further studies have been made in two directions, viz. first, theoretical and experimental investigation of solid particle movement in the blade-to-blade channel of centrifugal pumps and second, seeking a new philosophy and methodology for dimensioning impellers for hydromixtures.

What determined the first direction in our researches was the still unknown nature of the wearing process. The preliminary investigations have shown the existence of impact as well as friction wear due to the solid particles present in the fluid. Moreover, the wearing life of a pump depends on its type and the specific for each particular pump operating conditions.The idea of developing a mathematical model for the solid particle paths in a blade-to-blade channel seemed attractive since we had available extensive experimental data. The model could further be employed for determining the mutual position of particle paths, the particles being of different sizes and initial velocities.

Experimental Photographing of Solid Particle Paths.- A high-speed film camera was used to photograph the consecutive positions in the blade-to-blade channel of particles of different size and density at an interval of 0.001 sec. The limited distinguishing camera ability necessitated the taking of greater than life pictures. In this case the aim was not the study of the movement of the slurry but that of isolated particles, thus acquiring the necessary experimental data for checking the mathematical model of the "particle-flow" type which we are going to use. In addition,it must be pointed out that among the photographed paths were such that showed an impact in the predicted zone of maximum wear which was a visual confirmation of the conjectures about the nature of the flow around the blades.

Mathematical Model of the "Particle-Flow" Type.- The pump under consideration transfers hydromixtures of low volume concentration of the solid phase and small particle size. This allows us to employ a mathematical model of the "particle-flow" type /1/, developed on the basis of the following considerations; the stream of the carrying fluid is of the flat potential type; the particle movement does not affect the fluid movement; the particles are spherical in shape. Because of the comparatively close values of the solid particle density and that of the carrying fluid, the resultant force on one single particle is the sum total of a great number of forces differing in origin, none of which can be overlooked. Thus the solid particle motion equation can be written down as follows

$$m\vec{a} = \vec{F}_d + \vec{F}_p + \vec{F}_b + \vec{F}_{rm} + \vec{F}_M , \tag{1}$$

where m - particle mass and $\vec{a}$ - particle acceleration. The right hand side of the equation consists of: $\vec{F}_d$ - drag force, $\vec{F}_p$ - pressure force, $\vec{F}_b$ - Basset's force, $\vec{F}_{rm}$ - extra force due to relative acceleration of the fluid around the particle, $\vec{F}_M$ - Magnus force.

For the separate forces expressed by means of $\vec{V}$, i.e. the relative fluid velocity (or its derivatives) with respect to the particles, we obtain

$$\vec{F}_d = \zeta S \rho_f \frac{V^2}{2} \vec{V}^0 ,$$

where

$$\zeta = \frac{24}{Re_p} f(Re_p) , \quad Re_p = \frac{dV}{\nu} , \quad S = \frac{\pi d^2}{4} .$$

Here ρ_f - fluid density, d - particle diameter, ν - kinematic viscosity, ζ - drag coefficient. For the function $f(Re_p)$ different expressions are given depending on the range of values. We have used

$$f(Re_p) = \begin{cases} 1 \quad \text{for} \quad Re_p \le 0{,}2 \\ (5Re_p)^{0{,}0694\,[\lg_{10}(5Re_p)]^{1{,}2348}} \quad \text{for} \quad 0{,}2 < Re_p < 5000 , \end{cases}$$

which approximates the values of ζ with an error less than 2.7% shown in /2/.

$$\vec{F}_p = \frac{\pi d^3}{6} \operatorname{grad} p ,$$

where p is the fluid pressure in the range under consideration.

$$\vec{F}_b = \frac{3}{2} \sqrt{\pi \nu}\, \rho_f d^2 \left[\frac{\vec{V}(0)}{\sqrt{t}} + \int_0^t \frac{d\vec{V}(\tau)}{\sqrt{t-\tau}} \right] ,$$

where t is the current moment and τ - the integration variable.

$$\vec{F}_{rm} = -\frac{1}{2}\varrho_f \frac{\pi d^3}{6}\frac{d\vec{V}}{dt},$$

$$\vec{F}_M = -\frac{\pi d^3}{8}\varrho_f \vec{\omega}_p \times \vec{V},$$

where $\vec{\omega}_p$ is the current velocity of particle rotation expressed by

$$\vec{\omega}_p(t) = -\vec{\omega}\, e^{-\frac{60\mu t}{\varrho_p d^2}},$$

where $-\vec{\omega}$ is the initial angular particle velocity with respect to the fluid, a normal vector to the flow plane; ω - the blade system angular velocity; t - time measured from the moment when the particle enters the impeller. We obtain a differential equation system for particle motion after expressing the absolute acceleration $\vec{a}$ from (1) by means of its components relative to cylindrical coordinate system which is linked with a rotating wheel as well as by solving the equations concerning the relative velocity and its derivatives.

$$\frac{dr}{dt} = w_r$$

$$\frac{d\theta}{dt} = \frac{w_\theta}{r}$$

$$\frac{dw_r}{dt} = D(w_{fr} - w_r) + P\left(r + \frac{1}{2}\frac{\partial(w_f^2)}{\partial r}\right) + B\int_0^t \frac{\left[\frac{d}{dt}(\vec{w}_f - \vec{w})\right]_r}{\sqrt{t-\tau}}d\tau +$$
$$+ R\left[\frac{dw_f}{dt}\right]_r + M(w_{f\theta} - w_\theta) + G\left(\frac{w_\theta^2}{r} + 2w_\theta + r\right) \qquad (2)$$

$$\frac{dw_\theta}{dt} = D(w_{f\theta} - w_\theta) + P\left(\frac{1}{2r}\frac{\partial(w_f^2)}{\partial\theta}\right) + B\int_0^t \frac{\left[\frac{d}{dt}(\vec{w}_f - \vec{w})\right]_\theta}{\sqrt{t-\tau}}d\tau +$$
$$+ R\left[\frac{dw_f}{dt}\right]_\theta + M(w_r - w_{fr}) + G\left(-2w_r - \frac{w_\theta w_r}{r}\right).$$

The system (2) has been written down after expressing the term of $\vec{F}_p$ by means of the fluid velocities in Bernoulli's equation for a rotating channel. The forces have been compared with the particle unit mass, the accelerations made dimensionless by $\frac{D_2\omega^2}{2}$, where D_2 is the wheel diameter; w - relative velocities; the r and θ indices show the components of the cylindrical coordinate system; the f indicates the fluid parameters; p particle parameters. The coefficients are $D=\frac{36\lambda f(Re_p)}{(2+\lambda)Re_\omega}$ where $\lambda=\frac{\rho_f}{\rho_p}$ is the relationship between the fluid and particle densities.

$$Re_\omega=\frac{d^2\omega}{\nu}, \quad P=-\frac{2\lambda}{2+\lambda}, \quad B=\frac{18\lambda}{(2+\lambda)\sqrt{Re_\omega}},$$

$$R=-\frac{\lambda}{2+\lambda}, \quad M=\frac{3}{2}\frac{\lambda}{2+\lambda}e^{-\frac{60\lambda(t_0+t)}{Re_\omega}}, \quad G=\frac{2}{2+\lambda}.$$

The system coefficients depend on the dimensionless λ, Re_ω which have been accepted as basic criteria of dynamic similarity. The problem initial conditions are $r(0)$, $\theta(0)$, $W_r(0)$, $W_\theta(0)$ and t_0 - the time from the moment the particle enters the rotating channel until the moment when $t=0$. The right hand side of the system (2) includes the fluid velocities W_{fr} and $W_{f\theta}$ which are the coordinate functions and result from the solution of the analysis problem.

The flow through the circular blade cascade is modelled by means of vortex layers on the blade surface /3/. The expression of the non-permeability contour condition by means of the stream function yields the integral equation

$$p(s)+\left(\frac{\tilde{\Psi}}{4\varphi}-ctg\alpha_0\right)q(s)+\frac{1}{2\tau\varphi}e^{-2\tau q(s)}-\frac{1}{4\pi}\int_S\gamma(\sigma)F(s,\sigma)d\sigma=const, \tag{3}$$

which is about the density $\gamma(\sigma)$ of the vortex layer. Here $p(s)+iq(s)$ is a point on the blade surface in a plane conformly transformed; τ - the angular cascade step; $\tilde{\Psi}$ - dimensionless theoretical pressure; φ - dimensionless flow rate; α_0 - angle of the preliminary flow revolution. For the kernel of the equation we get

$$F(s,\sigma)=ln\left(ch\,2\pi(q(\sigma)-q(s))-cos\,2\pi(p(\sigma)-p(s))\right).$$

After solving (3) with respect to $\gamma(\sigma)$, the velocities in each point of the area may be determined from

$$w_{f\theta}(p,q)=\left[\frac{\tilde{\Psi}}{4\varphi}-ctg\,\alpha_0-\frac{e^{-\tau 2q}}{\varphi}-\frac{1}{2\pi}\int\gamma(\sigma)\frac{sh(2\pi(q-q_\sigma))}{ch(2\pi(q-q_\sigma))-\cos(2\pi(p-p_\sigma))}d\sigma\right]\frac{\varphi}{r}$$

$$w_{fr}(p,q)=\left[1-\frac{1}{2\pi}\int\gamma(\sigma)\frac{\sin(2\pi(p-p_\sigma))}{ch(2\pi(q-q_\sigma))-\cos(2\pi(p-p_\sigma))}d\sigma\right]\frac{\varphi}{r}.$$

Numerical Experiments.- The mathematical model was specified on the basis of the initial conditions of the experiment. You will find here determined the initial velocities of the particles entering the channel as well as the time t_0 during which the particles have been acquiring a rotary motion until the initial moment $t=0$ .A series of calculations was made for the different particle sizes and a different particle behaviour was found out depending on the particle size. The impact action of the different size particles was confirmed in the case when they happen to hit the front blade surface in the vicinity of the stagnation point.

A New Impeller of a Non-Traditional Design

It has been accepted that the hydromixture pumps should have a wider blade-to-blade channel. This requirement can be neglected in many cases when the pump transfers a mixture of a guaranteed granulometric composition. The avoidance of a large blade-to-blade channel permits the creation of a new blade shape ensuring better streaming of the flow only a slight flow change in the blade system when changing the flow rate. As a result of all this there occurs a localization of the impact wear zone in the rubber lining only on the profile nose, where the lining can be made thicker.On the rest of the blade surface there is predominantly an evenly distributed friction wear. This results in a longer operating life of the impeller without any change of the manufacturing material and the way of production.

Fig. 5 shows a blade cascade in accordance with the above mentioned requirements using methods based on the design problem concerning the neutral line. The profile contour is determined having in mind the design and technological considerations and the analysis problem is applied to the profile.

The initial and the meridional section are the same as those of the pump under consideration. Fig. 6 shows the efficiency curve comparison between the two different impellers tested under the same conditions. The maximum wear zone of the new blade has also been examined.

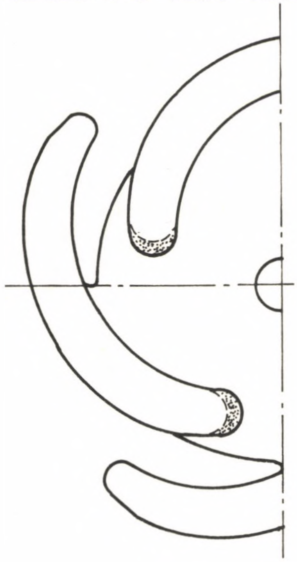

Fig. 5

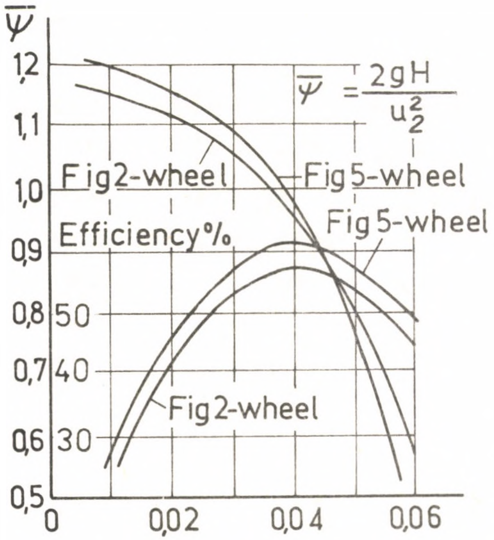

Fig. 6

The blade cascade obtained in this way has better hydraulic and wear parameters and differs from the traditional one in inlet and outlet angle, in the blade spacing and in the channel width.

Conclusions

The research and design activity on the problem of improving a particular type of pump for hydromixtures has led us to make the following conclusions

1. Both the wear resistance and the efficiency of rubber lined impellers can be significantly improved using a suitably designed blade cascade.
2. In order to obtain optimum surface wear of the blades it is important to operate the impeller in suitable conditions. The development of a series of blade cascades is recommended , having the same meridional section for one and the same type of pump thus ensuring the exact correspondence between the

operating conditions and the most suitable impeller.

Bibliography

1. Murakami M., Minemura K., "A Theoretical Study on Air Bubble Motion in a Centrifugal Pump Impeller". Trans. of the ASME, ser.D, 1980, 102, N4.

2. Boothroyd R. G., "Flowing Gas-Solids Suspensions" Chapman and Hall Ltd., London , 1971.

3. Panov L., " A Unified Approach to Investigation of Potential Flows in Multiconnected Domains". Proc. of Euromech 129, Varna , 1980.

ON THE BOUNDARY LAYER - POTENTIAL FLOW INTERACTION FOR AXISYMMETRIC BODY IN DUCT

A.J.HAIMOV

1. Introduction

It is well known that in order to obtain better information about the differential characteristics of incompressible high Reynolds number flow, the interaction of the outer inviscid stream with the boundary layers on the surfaces has to be taken into account .

For isolated body, this approach has been successfully used by many authors. The idea of Prandtl for the displacement effect of the boundary layer is usually applied by two procedures. In the first one, more frequently used, the displacement thickness is added directly to the body contour and the inviscid computations are repeated for the modified geometry. Another procedure is the inverse solution of the boundary layer equations and the normal velocity obtained is used to modify the boundary condition on the original body. The latter is especially preferable when the solution is performed by a grid method .

The present paper describes briefly some results of the computerization of a method proposed in [2] to account for the viscous effects in the inner problems, related to turbomachinery by formulating a boundary layer growth on the tunnel wall

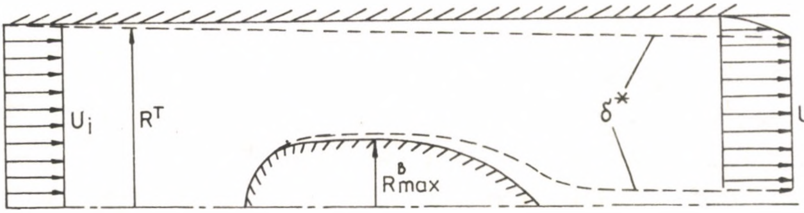

Fig.1

as well as on the body .

2. Theoretical Solution

A sketch of the flow region is presented in Fig. 1. The dashed line indicates the boundary layer displacement growth on the body and duct walls .

Inviscid Analysis

The potential axisymmetric calculations were done with a program which solves a couple of integral equations for the velocity distribution over the body and the duct. This method is described in details in reference [1]. Modifications have been performed in order to account for the wake behind the body. Particularly the induced velocities from an additional vortex cylinder have been included in the equations.

Viscous Analysis

In the present computer program , the Rott - Crabtree's [3] method for laminar boundary layer on the nose part of the body and Patel's method for axisymmetric turbulent boundary layer on the body and duct are used .

The turbulent boundary layer method solves the momentum integral equation and the entrainment equation, assuming a simple power - law family of velocity profiles . The skin - friction coefficient is related to the other integral parameters by the Thompson's formula .

Simple criteria are used for the laminar turbulent transition and turbulent separation prediction.

Iteration Procedure

The solution is carried out by an iterative method . First the potential - flow velocity distribution on the body and duct surface is calculated with all effects of the boundary layer and wake neglected. Using the velocity distribution determined in such a way , the boundary layer on the body and the duct are calculated. The displacement thickness distribution δ^* is added normally to the original surfaces of the body and the duct thus forming the so-called displacement body. The wake of a closed body is represented approximately by a cylinder of constant radius, which in the case of separation of the turbulent boundary layer begins from the separation point. The potential flow analysis is repeated for the semi - infinite displacement body including the modified contour of the duct. The velocity distribution obtained is attributed to the original body - duct surfaces and the procedure is repeated until convergence is obtained .

It was found that the solution is almost insensive to the initial conditions for the turbulent boundary layer on the duct So in the case that no experimental data are available, the transition values of the Reynolds number based on the momentum thickness is taken to be 320 - 500 as suggested by Patel for a body of revolution .

3. Results and Discussion

The computer program, called BXSCBL was tested to a different tube - body configurations. As shown on Fig. 2 , the increase of pressure coefficient ΔCp_{min} , computed with and without boundary layer interaction of the tube for a casing-boss configuration of a blower is more pronounced for high blockages. With the purpose of verification of the theoretical model, experiments were carried out in the cavitation tunnel of the Bulgarian Ship Hydrodynamics Centre . The pressure distribution on bodies of revolution of hemispheroidal (No. 1), standard ITTC (No.2) and semi -

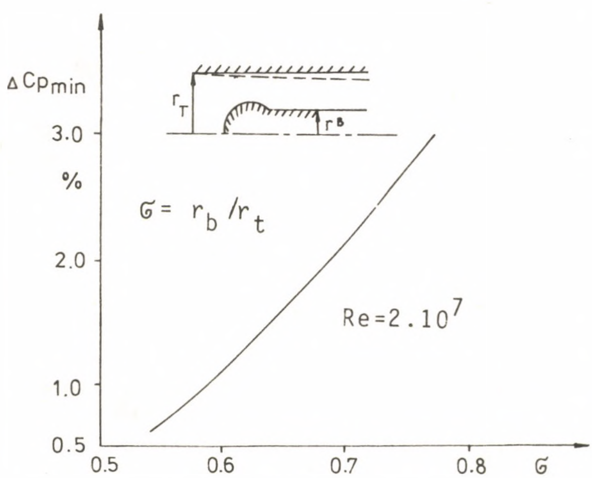

Fig. 2

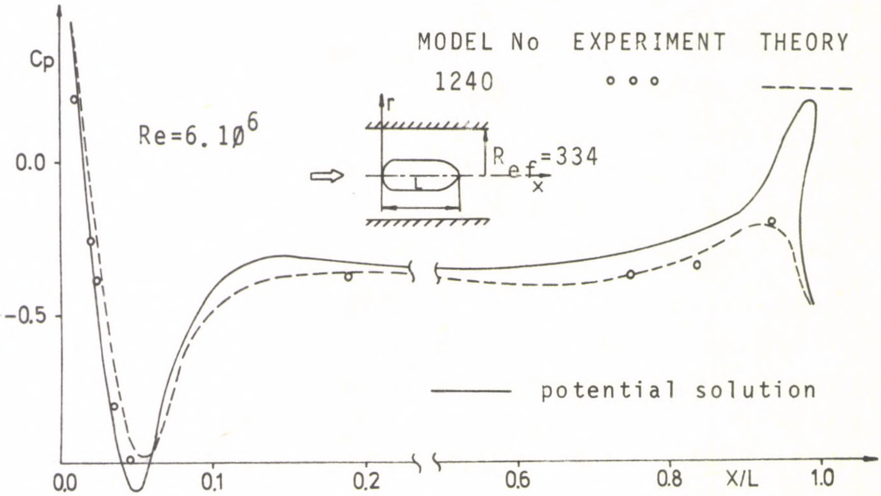
MODEL No EXPERIMENT THEORY
1240
Cp
Re=6. 1Ø⁶
r
Ref=334
x
L
0.0
-0.5
potential solution
0.0
0.1
0.2
0.6
0.8
X/L
1.0

Fig. 3

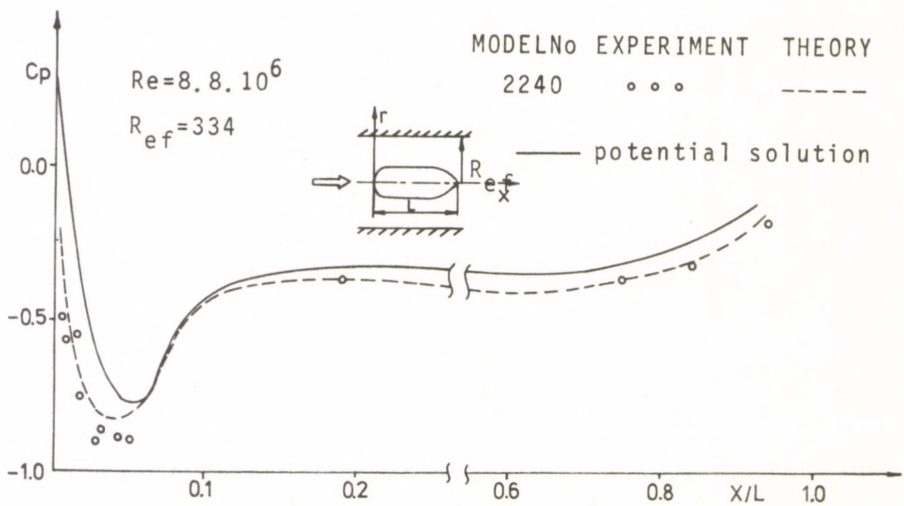
MODELNo EXPERIMENT THEORY
2240
Cp
Re=8. 8. 10⁶
Ref=334
r
potential solution
Ref
x
L
0.0
-0.5
-1.0
0.1
0.2
0.6
0.8
X/L
1.0

Fig. 4

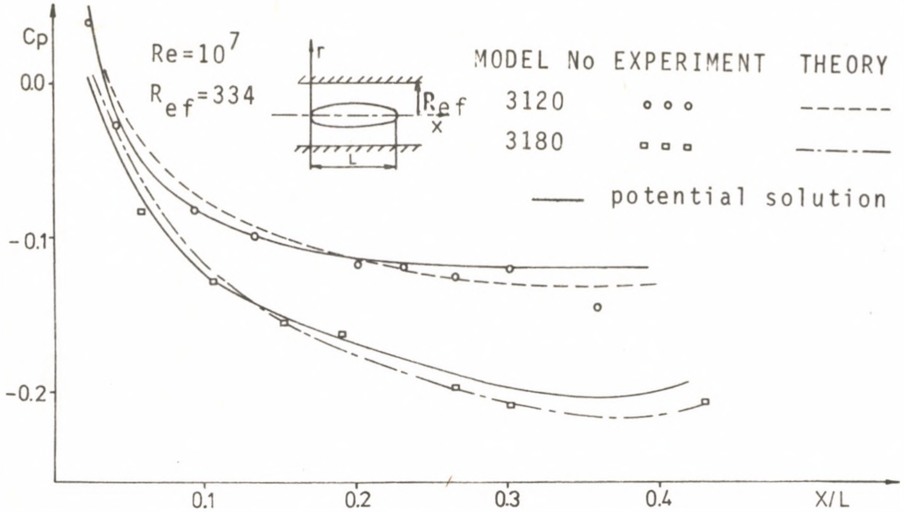

Fig.5

ellipsoidal (No-3) heads was measured and comparison with the numerical results is shown on Figs. 3, 4, 5 .

As can be seen, the agreement is satisfactory showing the need of accounting for the inviscid - viscous interaction and also the applicability of duct boundary layer approach for enginee - ring purposes .

References

1. Varsamov K., Haimov A. " Axisymmetric Potential Flow About a Multiply Connected Body in Duct ", Proc. Sixth Conf.on Fluid Machinery,Budapest 1979.

2. Haimov A. " A Study on Blockage Effect in Cavitation Tunnel ", Rep. of BSHC , 1980 (in Bulgarian)

3. Rott N. , Crabtree L. " Siplified Laminar Boundary Layer Calculations for Bodies of Revolution ", Journal of Aeronautical Sciences, vol.19, No.8 , 1952 .

4. Patel V.C. " A Simple Integral Method for the Calculations of Thick Axisymmetric Turbulent Boundary Layers ", The Aeronautical Quarterly, vol.XXV 1974 .

Anri Haimov, Research Officer , Bulgarian Ship Hydrodynamics Centre , Varna 9003 , BULGARIA

FLOW CONDITIONS IN WATER RESERVOIRS

GEORG HAJDU

SUMMARY.It was proved by the model measurements and field tests, that the reservoir having an oblong ground plan,which can be rapidly constructed from the prefabricated wall elements, satisfies the settling task just as well as the piano-shaped one if there are no deflecting walls in it.The inlet of the water into the reservoir can be realized by a carefully designed distribution system in such a manner that such a vortex which agitates the sediment should not develop in the reservoir.

1.THE NECESSITY OF THE RESERVOIR

Water supply is made reliable by the water and energy reserves in the system.The water reserve can be realised by reservoir located on the ground level, in a hilly region it is possible to form an energy reserve with an elevated reservoir as well.

2.FACTORS INFLUENCING DEVELOPMENT

According to the earlier view, it is necessary to bring about piston-like flow in the reservoir in order that the dwelling period of the individual water particles should not be too long in the reservoir and that an accidental deterioration of the quality of the water should not occur, the risk of which exists whenever the water is unable to change and because of this the organic impurities may become enriched. For example, in reservoirs having an oblong ground plan this was to be achieved by forcing the water by deflecting walls to make a long distance through narrow channels, at a relatively high flow velocity (Figure 1.):

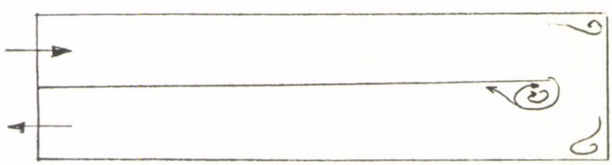

Figure 1.

Later on it was suggested that it is expedient to bring about as intensive mixing as possible to avoid the settling of organic matters [1,2].Under the effect of the pollution of the environment, for example, iron and manganic oxides appeared also in the drinking water of Budapest, which deposited on the pipe wall in the form of black colloidal sediment, where the water came into contact with air or chlorine. Sometimes this sediment separated from the wall and appeared in the water as scum.If possible, this scum should not be let out to the consumer, but it must be caught in the reservoir. Thereby, the settling character of the reservoir came into prominence, which necessitated low flow velocity and freedom from mixing (vortex).

Since the reservoir volume in Budapest fell behind the necessary extent compared to the daily consumption,we tried to find such a reservoir form which meets the requirements and such a construction technique for this where the easily cleanable, smooth internal surface, the impermeable concrete wall having a small mass and thickness, can be constructed rapidly, faultlessly also without the application of subsequent layers.The first step was the reduction of the wall thickness, with was realised on the basis of the Dywidag-type patent, by the application of prestressed concrete.The second step was that the prestressed elements were prefabricated and these were assembled by a patented sealing method. At first, this new reservoir type was still made with deflecting wall-type construction, however, this does not satisfy the settling purpose.Nevertheless, the last reservoir having 10 thousand m^3 volume already has a large space, and by the appropriate constuction of the inlet element it was possible to bring about such a flow in it by which we were able to approximate the dead space-free flow conditions of the so-called piano-shaped reservoirs.

3. THE CHARACTER OF FLOW IN THE VARIOUS RESERVOIRS

In the flow-tipe reservoirs, where both feed and eduction are continous, it is understandable that efforts are made to achieve mixing-free, but always continous flow [3] .This was realized most ideally by the socalled Munich (piano-shaped) reservoir type,where great width and low velocity are realized by slot-wall distibution and from this point the reservoir space is continously reduced, bring about a continously accelerating flow [4,5] (Figure 2.).

In the counterpressure-type reservoir, there is either feeding or eduction.From this point of wiew, in the old reservoirs the deflecting wall-type solution was considered to be good, however, the small model tests performed at Budapest Technical University showed that vortexes some into being at the ends of the deflecting walls, which with the large-scale construction manifested itself in the form of increased suspended matter quantity during the discharge period because in such a case the vortexes agitated the already settled material [6,7] .Therefore, we considered the piano-shaped form favourable in this case too, and this was proved by the careful model experiment [8] ,then in one of the already completed 10 thousand m^3 reservoirs we controlled the flow coming into being, which will be discussed below [9] .

The piano-shape proved to be excellent from a hidrological point of wiew as a counterpressure reservoir as well,but it is very difficult to construct its form from prefabricated elements stressed together.This is why we returned to the oblong ground plan, also with the consideration that if it proved to be good as a flow-type reservoir in Neusiedlen and the piano-shape is suitable either as a flow-type or as a counterpressure-type reservoir, then the one without deflecting wall, having an oblong ground plan must be also suitable as a counterpressure-type reservoir, if it is possible to make the inlet and outlet of the water similar to that which was realized in the case of the piano-shaped reservoir.

By the way, in the counterpressure-type reservoirs the fundamental character of flow is that at one end of the reservoir the finite horizontal velocity becomes 0 at its other end, whereas vertically a finite uniform velocity lower by one order of magnitude can be observed.

4.COMPARISON OF MODEL AND MAIN CONSTRUCTION IN THE CASE OF PIANO-SHAPE

The results of model measurements were already published earlier [8] .In the completed reservoir, we constructed a footway system suspended on the colums supporting the roof, and from here we observed the character of the surface flow and the velocity distributions in the vertical sections.

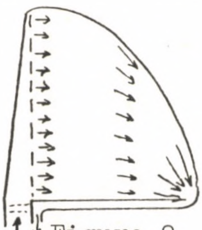

Figure 2.

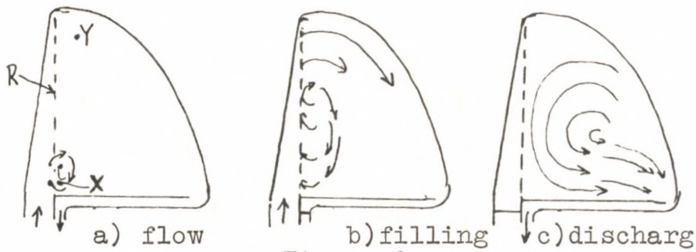

a) flow b)filling c)discharge
Figure 3.

In the publication of 1974,experiments were made with several versions from the distribution space: there was no slot-wall, there was a uniformly perforated wall, an unevenly distributed slotted wall and a reduced distribution channel at its end.There was vortex -free movement during filling only according to this last version, there was turbulence during filling in the case of all other versions, while there was no vortex in either case during discharge.

Prior to the construction of the 2x40.000 m^3 twin reservoir built on Gellért Hill, one 5000 m^3 and one 10000 m^3 reservoir ware constructed by us with this form.We made the control measurements in 1977 with the latter.The distribution slot-wall of this reservoir (marked with R in Fig.3/a.) had a completly uniform slot distribution, thus it corresponded to the uniformly perforated wall of the small-scale model.(It was not possible to take into consideration the results of the small-scale model measurement here because the reservoir was already under construction when the measurement was completed).The flow pattern of this main construction essentially corresponded to the results of the model experiment,namely, both the surface and depth flow patterns showed turbulence, too (Figure 3.): during flow, the slot-wall inhausted the water into the distribution channel to its 0,25 length (Fig.3/a) and during filling this inhaustion length became longer to about 0,67 part (Fig.3/b),whereas during discharge a vortex having an opposite sense of rotation developed (Fig.3/c).However the speed of the rotation is very low, the value of the number of revolutions per hour is as folows:

flow:	1,5 r.p.h.	
filling:	0,5 r.p.h.	at the edge of reservoir,
	6,0 r.p.h.	in the middle.
discharge:	0,5 r.p.h.	uniformly at the edge and in the middle of the reservoir.

Thus, this rotation can be neglected.

Another conclusion drawn during the experiment was,that the rotation-damping effect of the slot wall is also negligible.The velocityes developing in the reservoir are of 1-3 m/min = 0,016-0,05 m/s magnitude in the distribution channel during flow behind the slot-wall and during filling (depending on the level).The velocity of inflow on the slot-wall near the inlet (at the point marked with X in Fig.3/a) is 0,001 m/s during flow, 0,04 m/s during filling, whereas the velocity of outflow through the slot-wall at its end is of 0,03 m/s order of magnitude.The velocity distibution in depth at the point marked with Y in Fig.3/a is shown in Figure 4. At such low velocities, the slotted wall cannot have a considerable damping effect. These conclusion were utilized by us later in the design of the distribution space of the rectangular reservoir.

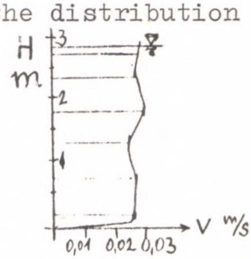

Figure 4.

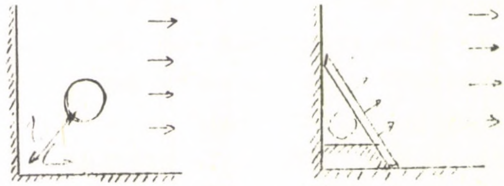
a)distribution pipe b)slots on coverplates
Figure 5.

5. EXPERIENCES WITH MODEL MEASUREMENT WITH THE OBLONG FORM

It is worth construction a reservoir having an oblong ground plan from the prefabricated wall elements. If the ground plan of the reservoir is square, then is the minimum wall len length necessary for the given footing area. The wall length K can be expressed compared to the minimum length K_o measurable with the square by the relationship

$$\frac{K}{K_o} = \frac{1}{2}\left[\left(\frac{a}{b}\right)^{1/2} + \left(\frac{a}{b}\right)^{-1/2}\right]$$

(where a is the long, b is the short side), the side relation and the wall length ratio are as follows:

a/b	1,0	1,2	1,4	1,6	1,8	2,0
K/K_o	1,0	1,0042	1,0142	1,0277	1,0435	1,0607

In the interest of minimum increase of costs, we envisaged to realize an a/b = 1,5 ratio (K/K_o = 1,021). We extended the model experiments only to the design of the inlet element. We designed two different kinds of inlet element: a distribution pipe running parallel to the narrow side of the reservoir with a row of distribution openings on it, and a row of prefabricated cover plates leaning obliquely against the corner of the reservoir, respectively (Figure 5.) [10] .

The method of the model measurement was practically the same as the one published in [8] , with the addition that photoelectric smoke-detector was installed in the blow out stub after the flow rectifier valves installed in the suction and pressure pipe of the reservoir model having a plexiglass wall, moved over the water seal, and by this could be also established after how many filling-discharge cycles the smoke leaves the model completely (Figure 6.).

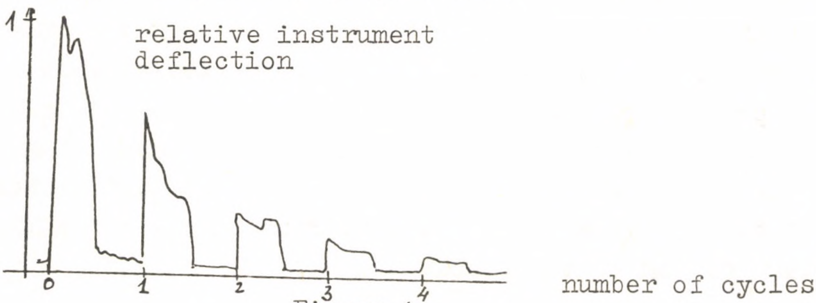

Figure 6.

The insertion of the slot-wall was also investigated in the model with all versions,however, it had no effect whatever, as it was to be expected on the basis of the antecedents.The two versions tested:both the distribution pipe-type and the slotted cover plate-type, appeared to be good alike, although in the perforated pipe version minor differences, back-flows appeared,while with the cover plate-type these were not observed. Since similar cover plates are placed on the discharge side of the reservoir,this appears to be more suitable becau e of typifying, however, during the washing of the reservoir these cover plates must be lifted one by one by crane,whereas in the case of the horizontal pipe located at 1 m height above the bottom, this work is omitted.Because of this, ultimately the distribution pipe was installed in the main construction.

6.EXPERIENCES WITH THE SEDIMENT TESTS OF THE MAIN CONSTRUCTION

In the case of the reservoir having a high specific change of water (with a single daily filling-discharge cycle), the small backflow has no serious significance.We did not make flow-measurements in the constructed reservoir,but we tested the layer thickness of the sediment settled after 1 year's operation (all the more because accordihg to the tests of the Technical University, there is a critical layer thickness from the point of view of bacterium growth which must not be exceeded).

While in the piano-shaped reservoir (according to point 4) a 4-5 cm thick sediment layer appeared in 1 year at about 3 m distance in the entire width of the reservoir, and the thickness of this decreased approx uniformly as far as the outlet opening, in the oblong reservoirs the sediment formed a uniform 1-1,5 cm thick layer on the bottom of the whole reservoir, which proved that there was nowhere such a turbulence (as at the end of the deflecting wall in the turn according to Fig.1.) where the vortex agitates the sediment during every discharge,sweeping the bottom clean,deteriorating the quality of the water getting to the consumers.

ACKNOWLEDGMENTS
Thanks are due for the careful performance of the model experiments to the Dep.of Water Supply of the Hydraulic Institute of Budapest Technical University,to prof.Dr.Öllős and first assistant Dr.Mészáros, moreover for the field measurements of the piano-shaped reservoir to Hydraulic Institute II of the Scientific yResearch Centre VITUKI, the head Dr.Starosolszky and Mr.Muszkalay in charge of the project.

BIBLIOGRAPHY
1.Schubert,Maier:Untersuchungen über den Wasseraustausch in Trinkwasserbehältern. GWF-WASSER/ABWASSER 117(1976)H.7.S 290.
2,Liepsch:Untersuchungen der Strömungsvorgange in Grossbehältern für Trinkwasser BBR 28 (1977) H.9. S.327.
3.Geilhofer: Der neue Wasserbehälter und seine Bedeutung für die Wasserversorgung Wiens - Neusiedl am Steinfeld MONOGRAPHIENREIHE DER AUFBAU H.11.Wien 1959.
4.Lohr:Der neue Hochzonenbehälter Forstenrieder Park für die Münchener Wasserversorgung GWF-WASSER/ABW.109(1968)H.2.S.39.
5.Hajdu:Der Trinkwasserbehälter am Gellért-Berg in Budapest, Inhalt 80000 m^3 GWF-WASSER/ABW. 115(1974) H.1.S.1.
6.Mészáros:Hydraulic aspects of the reconstruction of drinking water reservoirs (in Hungarian).- 6th Seminar of Hungarian Hydrological Society,Miskolc 23.05.1980.
7.Fáy:Reconstruction of pover-rooms and water reservoirs (in Hungarian).- Summary of subjekts in the publication of the Seminar of the Hungarian Hydrological Society,Miskolc,1980.
8.Gruber,Preszler,Lajos:Modellversuche für einer Trinkwasserspeicher GWF-WASSER/ABW. 115(1974)H.1.S.8.
9.Starosolszky,Muszkalay:Field hydrological test of the Dywidag type drinking water reservoir (in Hungarian) Unpublished Report, VITUKI 1977,Budapest.
10.Öllős,Mészáros:Hydraulic laboratory test of prefabricated drinking water reservoir (in Hungarian) Unpublished Report,Budapest Technical University,1980.

Author's address:

Georg Hajdu M.M.E.

H-1025,Budapest,Józsefhegyi ut 13

Hungary

EVALUATION OF THE MEASUREMENTS OF CHARACTERISTIC CURVES

by

G.Halász

SUMMARY

In the course of measuring the characteristic curves, the unknown relationship between the variables is revealed by measurements. The measurements involve errors. Based on the analysis of measurement inaccuracies, the paper presents a method by which the points of the desired characteristic curve can be determined numerically.

INTRODUCTION

Measurements in the engineering practice are in most cases aimed at revealing the relationship between the variables observed. Processing the results is not finished by plotting the obtained set of points, it is often necessary to express the relationship between the variables by formulas. In practice, relying on the ready procedures [1] of the program system of up-to-date computers, the method of least squares is exclusively used. Seldom is the validity of those conditions analysed which, beyond the well-known numerical application of the method, ensure the statistical good quality of the obtained estimations [2]. The fact that the numerical application of the method results in a curve running across the measured points even if other conditions are lacking, leads to uncritical applications.

In the publication [3] a method was presented the main point of which is as follows: It is desired to reveal an unknown functional relationship y(x) by measurement. With the use of the measurement results an approximating function g(x) is determined. By means of our method one can determine that band along g(x) which contains the unknown function y(x) with given probability.

In the present paper a method will be presented by means of which discrete points of the unknown function y(x) can be determined.

FORMULATION AND SOLUTION OF THE PROBLEM

It is desired to reveal by measurement a function relationship $y = y(x)$ the mathematical structure of which is known insufficiently or not at all. The measurements will be carried out in the discrete points $\{x_i\}_{i=1}^{n}$ of the interval $x \in [a, b]$ (see Figure 1). Let the following assumptions be made:

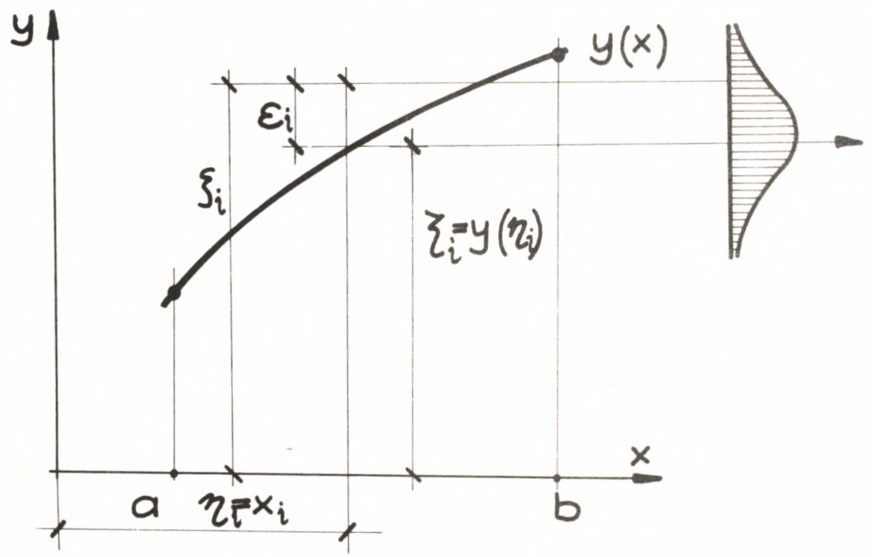

Figure 1.

a) $y = y(x)$ is a monotonic function and can be derived. (This strict condition will be mitigated later.)

b) Let η be a random variable interpreted in the interval $[a,b]$, the density function of which is e(x). The base points $\{x_i\}_{i=1}^{n}$ of the measurement constitute an n-element sample with respect to the variable η. The base points $\{x_i\}_{i=1}^{n}$ can accurately be adjusted. (They are free from measurement errors.)

c) In the base points $\{x_i\}_{i=1}^{n}$ the result of the measurements performed for the dependent variable is the set $\{\xi\}_{i=1}^{n}$, which is considered to be an n-element sample assumed for a variable ξ. Based on Figure 1:

$$\xi_i = y(x_i) + \varepsilon_i \tag{1}$$

where the realization of random errors $\varepsilon \in N(0,\sigma)$ is ε_i.

d) A single value pair (x_0, y_0), $x_0 \in [a,b]$ from the function $y(x)$ is known.

The object is to determine, in the case limited by the above four conditions, some points of the unknown function $y(x)$. As a first step, let the density function $f(z)$ of variable ξ be determined.

Let ζ denote the random variable assigned to η by function $y(x)$:

$$\zeta = y(\eta) \tag{2}$$

Of the conditional expected value and standard deviation of the random variable ξ representing the measurement results one can write on the basis of Figure 1:

$$M(\xi \mid \zeta = y) = y(x)$$

$$D(\xi \mid \zeta = y) = \sigma$$

Based on relationship (1), with the condition $\zeta = y$, it can be stated that ξ is a variable having normal distribution,an expected value y and standard deviation σ; thus its conditional density function will be

$$f(z \mid y) = \frac{1}{\sigma\sqrt{2\pi}} \exp\left\{-\frac{(z-y)^2}{2\sigma^2}\right\}. \tag{3}$$

After this, the task is to calculate the density function $f(z)$ from the conditional density function $f(z \mid y)$. From the probability theory [2] it is known that, if $r(y)$ denotes the density function of ζ, then

$$r(y) = \frac{e(x(y))}{\left|\frac{dy}{dx}\right|} \tag{4}$$

where $x(y)$ is the inverse function of $y(x)$. Based on [2], the relationship between the functions stated in equations (3) and (4) is

$$f(z|y)=\frac{f(z)r(y|z)}{r(y)} \tag{5}$$

It will be easy to determine the desired function $f(z)$ from equation (5), since after reduction and integration of both sides with respect to y

$$f(z)=\int_{-\infty}^{+\infty} f(z|y)r(y)dy. \tag{6}$$

will be obtained. Expressed in words this means that $f(x)$ is a mixed density function, namely a mixture of the density functions $f(z|y)$ with the weight function $r(y)$.

It is known that $f(x)$ is the density function of the variable ξ, and the sample $\{\xi_i\}_{i=1}^{n}$ is the result of our measurements. By known methods [5], one can construct the empirical density function $f_n(z)$, from which - based on Kolmogorov's theorem [2] - one can state the confidence domain in which $f(z)$ proceeds with a probability $p<1$. Briefly: one has an approximation of the lefthand side of equation (6) and it is a mixed function. We know decomposition methods [5], [4] which determine from a known $f_n(z)$ the parameters of the essential mixture components: the expected value y_j, the standard deviation σ_j and the weight r_j. Suppose that the decomposition has been performed and the parameters

$$\{y_j, r_j, \sigma_j\}_{j=1}^{K} \tag{7}$$

were obtained.

Return now to equation (4). In order to resolve the absolut value of the derivative, let equation (4) be decomposed:

$$\frac{dy}{dx}=\frac{e(x)}{r(y)} \qquad \text{if } \frac{dy}{dx}>0 \tag{8a}$$

and

$$-\frac{dy}{dx}=\frac{e(x)}{r(y)} \qquad \text{if } \frac{dy}{dx}<0 \tag{8b}$$

Our measurement results show that an increasing or decreasing function is being examined. Consider, e.g., the case of the positive derivative: integration of equation (8a) will yield

$$\int r(y)dy = \int e(x)dx + C \tag{9}$$

which is the implicite form of the relationship $y(x)$ between x and y.

With the use of the values (7) obtained from the decomposition, the numerical approximation of the lefthand integral can be calculated in the form

$$\sum_j r_j \Delta y_j \quad . \tag{10}$$

$e(x)$ on the right side is a density function chosen by us. Thus an x_j can be calculated to each y_j ; j = 1, 2, ... K. The integration constant C can be determined on the basis of condition d).

SUPPLEMENTARY REMARKS

If often occurs that a characteristic curve $y(x)$ having an extreme value is to be examined, and here the condition of monotonicity is not fulfilled. In this case the procedure is to choose a completely known auxiliary function $s(x)$ with the assumption that, in the case of $u(x)=y(x)-s(x)$ one can write

$$\frac{d}{dx}u(x) \neq 0 \qquad \text{if } x \in [a,b]$$

After this, the previous reasoning is applied to the function $u(x)$. After calculating its discrete points, we return to the original characteristic curve $y(x)$ by means of the relationship

$$y(x) = u(x) + s(x) .$$

The knowledge of the interrelated value pair fixed in condition d) is necessary for the determination of the constant C. In a lucky case we know such a point theoretically: e.g., the curve $y(x)$ crosses the origo. Failing such knowledge, a point will be determined on the basis of measurements with a fixed value x_0, by statistical methods relative to the direct measurement of one parameter.

Finally, the steps of the proposed method can be summarized as follows:

- Determination of the base points of measurements: choice of $e(x)$ and the determination of sample $\{x_i\}_{i=1}^{n}$
- Measurement, its result is the sample $\{\xi_i\}_{i=1}^{n}$
- Construction of the histogram $f_n(x)$
- Decomposition: determination of $\{y_j, \sigma_j, r_j\}_{j=1}^{K}$
- Determination of the value pairs $\{x_j, y_j\}_{j=1}^{K}$

In the lecture at the Conference, a few examples will be presented to demonstrated the application of the method.

Important notations:

$N(m,\sigma)$ normal distribution with expected value m and standard deviation

$f(z|y), r(y|z)$ conditional density functions

$\xi, \zeta, \eta, \varepsilon$ random variables

$D(\xi|\zeta=y)$ conditional standard deviation

$M(\xi|\zeta=y)$ conditional expected value.

REFERENCES

1 Ambrózi - Jávor: Evaluation of measurement data Műszaki Könyvkiadó, Budapest, 1976.

2 Rényi, A.: Probability theory. Tankönyvkiadó, Budapest, 1954.

3 Halász, G.: Untersuchungen der auf Messergebnissen beruhenden Naherungsfunktionen. Periodica Polytechnica M. 17/4, 1974. pp 313-321.

4 Medgyessy, P.- Varga, L.: On the improving of a method for the numerical decomposition of mixtures

of Guassian functions. Publication of the Department of Mathematics and Physics. 18, 31. 1968. pp 31-39.

5 Vincze, I.: Mathematical statistics with industrial application. Műszaki Könyvkiadó, Budapest, 1968.

Halász, Gábor dr. techn.
First assistant
Department Hydraulic Machinery
Technical University of Budapest
1111. Budapest, Stoczek-u. 2.
Hungary.

LOW TEMPERATURE ORGANIC FLUID VAPOR TURBINE OF HIGH OPERATIONAL FLEXIBILITY

S. HAVAKECHIAN and R. REY

ABSTRACT :

In the present paper, the features of an organic fluid Rankine cycle (ORFRC) power plant designed for the purpose of low temperature waste heat recovery is briefly reviewed. Among the major components of the cycle, the detail design considerations of the 31 KW organic fluid vapor turbine, and the relatively simple manufacturing technique employed in its construction is described. Emphasis has been placed on the turbine detail component design to provide an economical construction of the turbine. The experimental results obtained have proved that the penalty in maximum efficiency is not serious. It is therefore, believed that this economical method can eventually provide a less expensive turbine for these plants.

INTRODUCTION :

The recovery of low temperature waste heat available from industrial process, gas turbine, diesel engine exhaust,... etc, can yield an important contribution in energy saving. The use of (ORFRC) power plant is considered to be one of the effective means of converting the vast amount low temperature waste heat into useful mechanical energy. In recent years considerable amount of invetigations have been devoted to the development of these plants (1, 2).
In this connection, a small (ORFRC) power plant has been designed and its construction is in the state of completion in the departement of energy at ENSAM (Ecole Nationale Supérieure d'Arts et Métiers). The heat input to this cycle is recovered from the cooling water of a diesel engine (shaft power $\approx$ 270 KW). The flow diagram of the combined cycle is illustrated in figure (1).

The (ORFRC) plant is characterized by its very low maximum design temperature, namely, Tmax : 72¤C. At the recovery exchanger outlet, the organic working fluid is in the state of saturate vapor 72¤C/2.135 bar, it is then expanded in the turbine to a pressure of 0,538 bar. After the condensation process, the fluid is pumped back to the recovery exchanger, and the cycle is repeated. The design features of the turbine is presented in the following :

ORGANIC FLUID TURBINE DESIGN

During the last ten years, attentions have been focussed over the design of the organic fluid vapor (ORFV) turbines for heat recovery applications (3, 4). One of the distinctive characteristics of these turbines is the poor inlet vapor conditions i.e, inlet temperature 120 — 300¤C. For this purpose one has fully taken advantage of the steam turbine design techniques and the extensive aerodynamic developments made over the years. Meanwhile, the investigations over a cost effective efficient design for the very low temperature (ORFV) turbines have been lacking. The objective of this paper is to present a simple design technique applied to an axial flow (ORFV) turbine adapted to the above mentioned recovery cycle.

In effect, while designing an (ORFV) turbine inspite of the potential difficulties associated with the characteristics of the organic fluid, the designers dispose one more degree of freedom, namely, the choice of the organic fluid. The selection of the working fluid is of great importance in the waste heat recovery cycle because for a given cycle temperature spread it determines the following parameters which highly influence the turbine design :

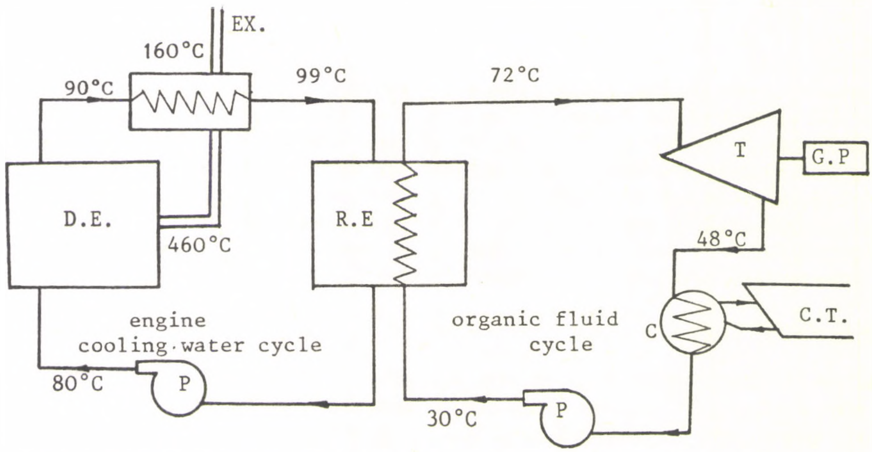

D.E. (Diesel Engine), Ex. (Exhaust Gases), R.E (Recovery Exchanger)
P. (Pump), T. (Turbine), C. (Condensor), C.T. (Cooling Tower)
G.P. (Gear Pump)

Fig. 1 - Schematic of Organic Fluid Rankine Cycle To Diesel Engine Cooling Water Circuit.

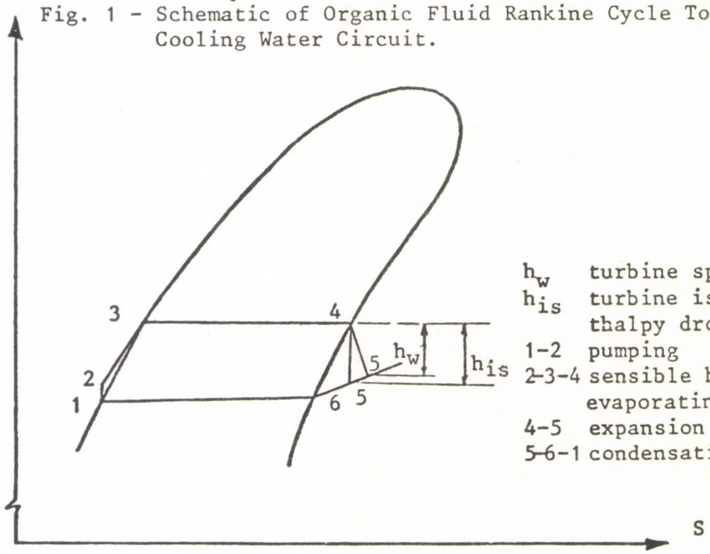

Entropy (KJ/Kg-°K)

Fig.2 - Temperature Entropy presentation of the freon Thermodynamic cycle

C = absolute velocity
W = relative velocity
U = tangential velocity
C_a = axial velocity component
α = absolute flow angle
β = relative flow angle
S, stator
R, rotor

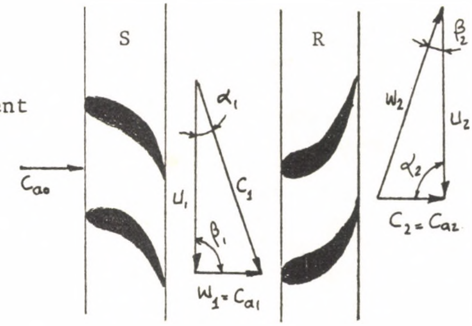

Fig. 3 - The Design Velocity Diagram of The 50% Reaction Turbine.

- Turbine inlet pressure (saturated vapor)
- Turbine outlet pressure (condenser pressure)
- Adiabatic enthalpy drop
- The type of flow (subsonic, transonic, supersonic)
- Turbine size and the required number of stages
- The effort exerted over the turbine elements
- Relative position of the expansion line end with respect to the vapor saturated line.

The main problems concerning the organic working (OW) fluids are associated with their characteristics such as, thermal stability, corrosion of materials, cost, availability of thermodynamic properties,...etc. Taking account of the above contraints a limited number of investigations for a certain number of organic fluid have been carried-out (5, 6), which can be used as a guide for optimal choice of the (OW) fluid for each application.

Thermal stability of the working fluid is primarily a function of cycle maximum temperature. In the present project, this temperature (72°C) is carefully determined to assure a safe operation of the cycle i.e. without fluid dissociation, and to yield maximum carnot cycle efficiency for the given waste heat cycle maximum, and recovery cycle condenser temperature (Tc = 30°C). The fluorocarbon F 113 was considered to be the appropriate fluid for our cycle. The imposed design conditions are :

- vapor inlet conditions 72¤C/2.135 bars
- condenser pressure 0.538 bar
- rotor angular speed 6000 RPM
- flow rate of 1,910 Kg/s

Our experience indicates that if high efficiency is the sole criteria the optimum flow coefficient (C_a/U) should be about 0.30 to 0.35. The value of flow coefficient chosen is 0.33. It is further assumed that this value remains unchanged during the expansion in the turbine.

In the preliminary design step a careful balance was made between the number of required stages (n), and the turbine size (Dm = mean diameter) to satisfy the following constraints :

a) blade height to diameter ratio (h_i/D_m) not too small (>0.025) for the first stage (to avoid high loss level)

b) h_i/D_m not too large (<0.13) for the last stages (this limitation has permitted to make a two dimensional, i.e., no radial diffusion, analysis based on the blade average diameter without introducing a significiant error in the calculation for all the stages, also the necessity of having the last stage blading twisted and tapered is avoided).

A double flow turbine arrangement was chosen for the following reasons :

1) to satisfy the above mentioned last stage blade height limitation

2) to eliminate the need for the thrust bearing,

3) to reduce stress level in turbine elements.

TURBINE CASCADE DESIGN :

The aerodynamic profile chosen is the NACA A_3 K_7 aerofoil. It was decided to design all the turbine stages at 50% degree of reaction. This decision was made to take advantage of slightly higher efficiency offered by a 50% reaction stage and to be able to use the same profile with identical aerodynamic parameters for both stationary and rotating blade rows Fig.3 .

The pitch/chord ratio was determined by the stage mechanical layout and aerodynamical considerations. The design of the stationary and rotating cascade of the first stage was carried out according to (7) coupled with a stage loss prediction method (8).

In order to lighten the volume of calculation, and to simplify the construction, the same profile with the same cascade parameters is used for all the remaining stationary and rotating blade rows of the turbine, in other words, it is assumed that the velocity triangles are conserved throughout the turbine stages. Therefore, with this imposed cascade, and by using the same performance prediction method, also with the aid of a program similar to (9) made to model the thermodynamic properties of F113 the aerothermodynamic state of the fluid is evaluated at the inlet and outlet of each rotating blades.

For the question of simplicity in construction, the same hub diameter is imposed for all the stationary and rotating blade rows and their blades'height (BH) have been correspondingly corrected, so as to satisfy the continuity equation. Then, by considering the variations of the BH, from the first stationary (FS) to the last rotating (LR) blade rows, it turned out that a linearly increasing approximation of the BH, by the line joining the inlet (FS) blade tip to the outlet (LR) blade tip (Fig.4) resulted in a maximum discripancies of less than 27% with respect to the calculated BH of the intermediate stages. According to the results obtained in (10) this descripancy is not supposed to cause serious efficiency degradation.

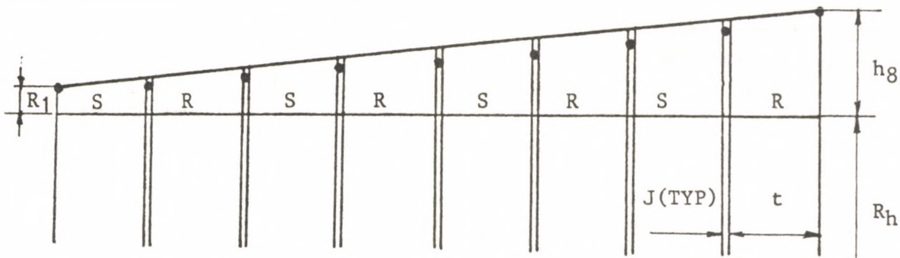

S : Stationary blade row, R : Rotating blade row,
R_h : Hub diameter, t : Disk thichness, J : axial clearance
• : Calculated blade (vane) tip position.

Fig.4 - Configuration of flowpath in the successive stages of the turbine, with the approximated linear blades height variation.

CONSTRUCTION :

Having adopted the same hub diameter for all the stationary, and rotating (SR) cascades, and making the assumption of linear height variation, have permitted to simplify the cascade fabrication as explained below.

A number of homogenous disks, (equal to the required number of (SR) blade row) with the same thickness and outer diameter (equal to the last stage blade tip diameter) have been taken. It was decided to produce the (SR) blades directly on their corresponding disks by a duplicating milling machine.

A master blade with the same profile as the required ones was mounted on a cylinder of the same outer diameter as the common hub diameter of the turbine disks. This assembly was used as the template to guide the cutter ; the work piece (disk) in its turn is held on a dividing head. In this way the suction and pressure side of all the stationary vanes and rotating blades have been machined (Fig.5).

The required number of the (SR) cascades have therefore, been machined all with the same hub diameter and height.

TABLE 1 SUMMERY OF LOW TEMPERATURE TURBINE DESIGN

Inlet Design Conditions	72¤C/2.135 bars
Exit Design Conditions	48¤C/0.538 bars
Mass Flow Rate (Kg/s)	1.918
Rotational Speed (rpm)	6 000
Number of Stages	4
Hub Diameter (mm)	210
Blade (vane) Chord (mm)	27
Number of Vane, Stator	31
Number of Blade, Rotor	32

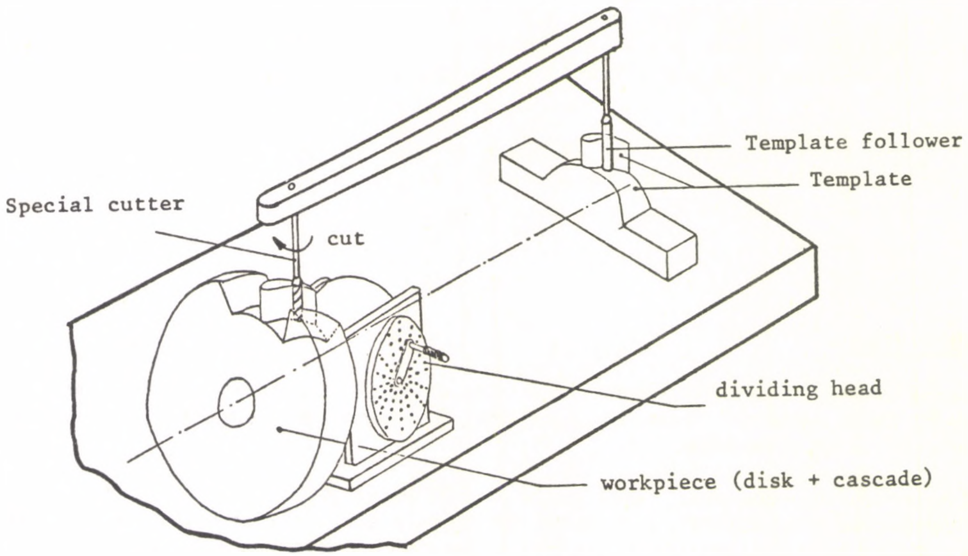

Fig. 5

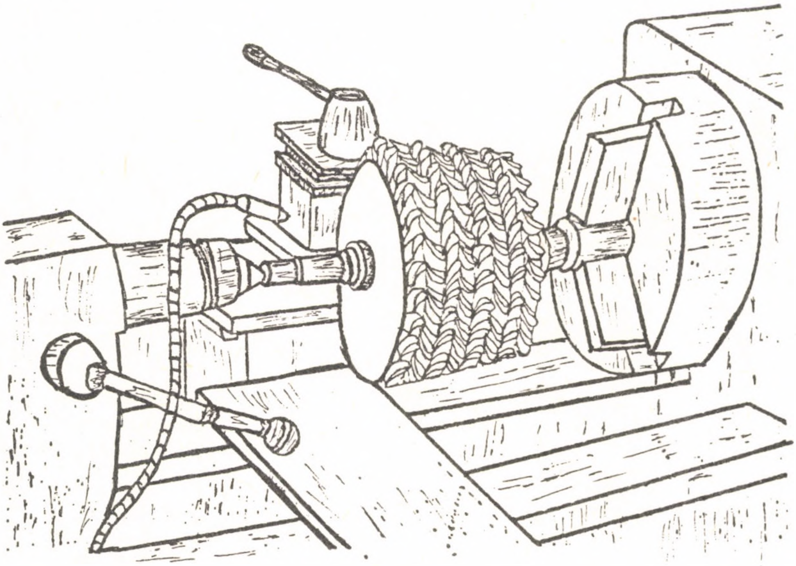

FIGURE (6) - Simultaneous sizing of stationary and rotating blade height of the four stages of the turbine by a simple tapering operation

Then, refering to Fig. (4), a simple tapering operation was sufficient to bring all the (SR) cascades to their desired height. For this purpose the (SR) disks are properly held on a lathe dog while conserving the necessary (SR) blade axial clearance by the standard gages. This assembly was then, mounted on a lathe machine for the tapering operation (Fig.6).

The material chosen for the fabrication of disks + bladings was AU4G (duralumine ; 4% copper, 0.6% magnesium and 0.4% silicium). The stress calculation and the dynamical analysis of the turbines'rotating elements have shown the adequacy of this material. Furthermore, with the cycle maximum operating temperature (i.e. 72°C) in the presence of F 113, it seems that the problem of fluid dissociation will not be critical.

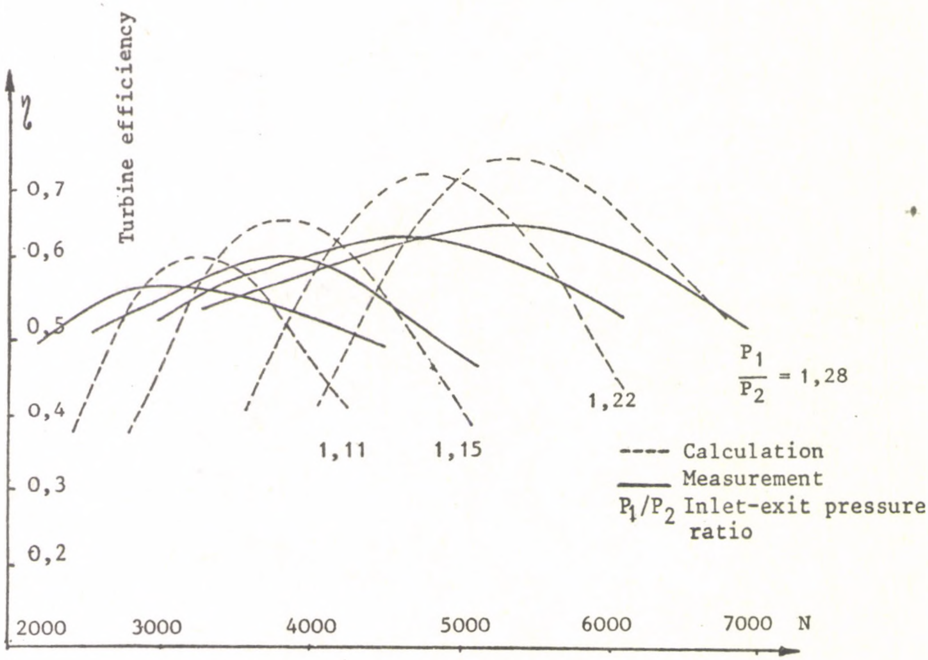

Figure 7 - Rotational speed (RPM)

EXPERIMENTAL VERIFICATION :

Despite the prototype nature of the above turbine, it has demonstrated a reliable and quiet operation. The first calculated torsional and transverse critical speed are 19 000 and 8 000 RPM respectively. It has been safely operated up to a speed of 7 400 RPM i.e.23% overspeed.

For the present time the erection of the complete cycle components is not completed. Therfore, the verification of aerodynamic behavior of the turbine has been performed by chosing the turbine parameters such as maximum flow rate, inlet pressure, power, rotating speed, to match the laboratory facilities and the design constraints. Also the energy developped by the turbines is delivered to two gear pumps specially mounted on each shaft extremities. This solution was temporarily adopted for experimentation with air (Fig.8). The measured turbine efficiency as a function of speed, for different ratios is shown in Fig. (7). A comparison is made with the employed performance prediction method, it is seen that the corresponding curves have approximately the same trend but, the discripancies at the points far from the maximum efficiencies are quite large. This is clearly due to the fact that the off design profile losses approximated by the Ainley Mathison correlation is over-estimating in this case. It also turned out that there is a systematic difference in the order of 6 to 9% between the measured and predicted maximum efficiencies. The optimum speed with air as the working fluids is estimated to be around 1 300 RPM, however, this speed cannot be attained because of the aforementioned constraints. Nevertheless, according to the comparative efficiency curves Fig.( ), a maximum efficiency of 72% is quite attainable at the design point.

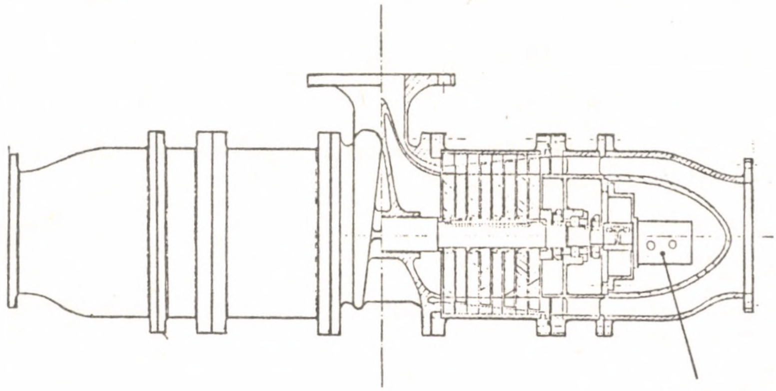

Fig. 8

CONCLUSIONS :

In summary, we have presented the design concept and the simple technology employed for the construction of a small organic vapor (ov) turbine. The primary purpose of the project was to provide a cheap (ov) turbine, which is capable of operating efficiently at a very low temperature and pressure. Although the partially confirmed maximum obtainable efficiency was promising, at this stage it is difficult to make a precise estimation of the economic advantage of the method. However, owing to the versatility of the heat recovery sources, the adaibatic enthalpy drop, and flow rate are evidently different from case to case. The most interesting advantage of this method resides on the fact that once the turbine for a specific application is designed, then for another design one can use exactly the same (SR) blade disks as the previous turbine. It is then sufficient to vary the number of stages, and the slope of the line which appoximates the BH variation (Fig.4) to allow for the required enthalpy drop, and flow rate respectively. This flexibility of utilizing exactly the same disks with the same blading for different cases permits the production of disk + blading in large quantities therefore, the overall cost of the turbine will be further reduced.

ACKNOWLEDGEMENTS :

The investigation presented in this paper has been carried out in the Department of Energy of Ecole Nationale Supérieure d'Arts et Métiers (ENSAM).
The authors are indebeted to the technicians of the hydraulic laboratory for their valuable suggestions in manufacturing processes. They are also grateful to the graduate students, J.Cl. Delhoume, J. Brunarie and Ph. Arnal for their invaluable help for the preparation of the test rig and experimentation.

1) Ubersickt von Ausgefuhrten ORC - Anlagen
von Ing. H.P. Corneille and Dr. Ing. S.Haaf, Koln

2) Systeme de Conversion de Rejet Thermique en Puissance par un Cycle de Rankine à Fluide Organique d'une Puissance de 600 KWe par AW. ADAM - Colloque Franco-AMéricain (1978)

3) Freon Turbine by Koji Sega Chem. Econ. Engng. Rev. Jap. (1974)

4) Cycles de Récupération d'Energie par Alain VERNEAU Entropie n¤ 84-1978

5) Selection of Rankine Cycle Fluid for Recovery of Waste From Heat at Moderate Temperature. David A. PALMER, SAE (1978)

6) Thermal stability data on six Fluorocarbons by John A. CALLIGHAN Heating/Piping/Air Condit ioning - Sept. 1971

7) Investigation of a Related Series of TURBINE-BLADE Profiles in Cascade by Jame C. Dunavant and John R. Erwin NACA 3802.

8) Les Turbines par André HOUBERECHT

9) Refregiration Equation R.R. Downings ASHRAE n¤ 2313

10) Axial Turbine Performance Evaluation, Part B, optimization with and without constraints O.E. Balje Journal of Engineering for Power Oct. 1968

S. HAVAKECHIAN
Ingénieur-Chercheur au
Laboratoire Hydraulique
ENSAM - PARIS

R. REY
Maître-Assistant au
Laboratoire Hydraulique
ENSAM - PARIS

A SIMPLE GRAPHICAL METHOD FOR CALCULATION OF MASS OSCILLATIONS IN A SYSTEM CONNECTED WITH A COMPRESSOR

V. Heisler, L. Pavluch

ABSTRACT

This paper points out the possibility to apply the classical graphical Schnyder-Bergeron's method also to calculations of medium oscillations in an aerodynamic system compressor - pipe - air vessel - discharge valve. If certain simplifying assumptions are adopted, this method may serve as an illustrative and efficient means for investigation of instability phenomena in the system.

1. INTRODUCTION

Even now, at the time when numerical methods and computers are increasingly used, in technical practice we may come across some cases when graphical solution of a certain technological problem is more advantageous from the point of view of economy, of brain work or for some other reasons. This is true especially in case of problems facile from the mathematical point of view and one-shot problems.

2. ASSUMPTIONS

Let us consider an idealized system according to fig.1, consisting of compressor 1, pipe 2, air vessel 3 and discharge valve 4. The compressor sucks in air from free atmosphere at the pressure p_b and blows it through the pipe

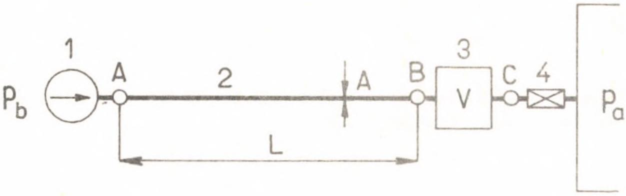

Fig. 1

into the air vessel. From there the air might be, if necessary, discharged through the discharge valve into the working space of certain pressure p_a which might generally differ from atmospheric pressure.

Let us suppose that in this system oscillations of air mass occur if by partial closure of the valve the nominal operating point of the system is shifted into the instable region of the compressor characteristic, see fig.2 . The throttling curve passes from position 1 to position 2 .

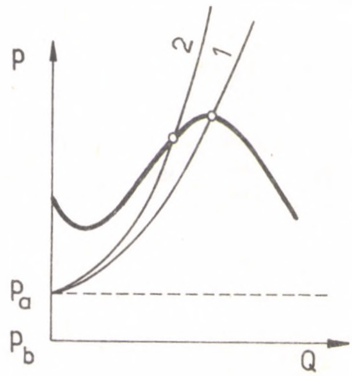

Fig. 2

The new point of intersection with pressure characteristic of the compressor is remarkable for that the decrease of flow causes pressure drops at the discharge nozzle of the machine.

As this is the case of a system with non-negligibly long pipe through which flows compressible medium it would be natural to apply in theoretical investigation of medium oscillation in this system also the classical graphical method which has been proved advantageous in calculations of transient operating conditions in hydraulic systems [1] , [2] . The solution outlined here is thus based on the same simplifications and ideas used by Schnyder and Bergeron in their work.

3. SURGE EQUATION

In the given case when air density and acoustic velocity in the process under consideration are not constant but are functions of the fluctuating pressure, let us use the differential form of the classical surge equation

$$dp = \varrho a \, dw \, . \qquad (1)$$

On assumption of adiabatic changes for acoustic velocity holds the well-known relation

$$a = \sqrt{\frac{\varkappa p}{\varrho}} \qquad (2)$$

which helps transform (1) into the form

$$dp = \sqrt{\varkappa \varrho p} \, . \, dw \, . \qquad (3)$$

Also if for adiabatic changes the state equation is adapted we will obtain the function

$$\varrho p = \varrho_0 p_0 \left(\frac{p}{p_0} \right)^{\frac{\varkappa + 1}{\varkappa}} . \qquad (4)$$

The zero index denotes the initial values of the given quantities. After substituting (4) into (3) and after another adaptation and integration within the limits from p_0 to p and from w_0 to w we will obtain the relation

$$\frac{p}{p_0} = \left(1 + \frac{\varkappa - 1}{2} \; \frac{w - w_0}{a_0} \right)^{\frac{2\varkappa}{\varkappa - 1}} . \qquad (5)$$

Obviously, the ratio of the instantaneous pressure p to its initial value p_0 is the function of increase (decrease) of velocity in the pipe for its sudden change by $w - w_0$ (for the sake of illustration we consider only the case of $w / w_0 > 1$).

The second term in brackets on the right side of (5) will be, as a rule, considerably smaller than 1. Therefore, after developing the right side into a series, very small terms with high powers may be omitted. If we limit our considerations to the first two terms of the series we will obtain the linear dependence

$$\frac{p}{p_0} = 1 + \varkappa \frac{w - w_0}{a_0} , \qquad (6)$$

valid exactly for the case of independence of medium density and acoustic velocity on pressure. To illustrate the influence of neglecting the fluctuation of these quantities on the value of the relative change of pressure p / p_0 both the dependences, i.e. according to (5) and (6), are plotted in fig.3 .

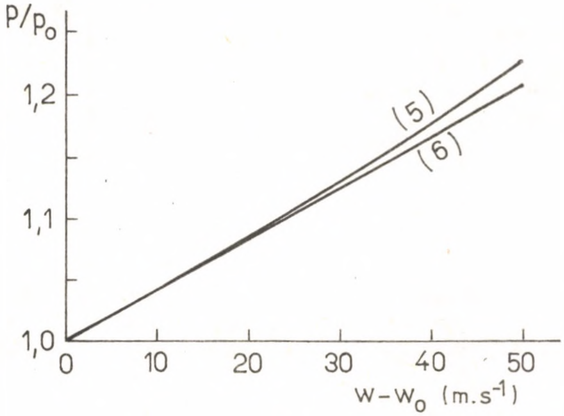

Fig. 3

For air $\varkappa = 1.4$ was substituted and when dimensioning the scale for $w - w_0$ we supposed that $a_0 = 340\ m.s^{-1}$. We can see that in the region of minor velocity changes the differences between the two lines are only slight. The line according to (6) is a tangent to the curve according to (5) at the point $w - w_0 = 0$. As the graphical solution according to Schnyder and Bergeron the velocity changes in the individual time steps (short time intervals) are as a rule relatively small, the linearization (5) is quite admissible and we can use surge lines in calculation diagrams.

4. CALCULATION USING TWO SYSTEMS OF STRAIGHT LINES

To follow further explications it is necessery to know the principles of Schnyder-Bergeron's method. A simplest case of resistanceless system with negligible component of kinetic energy in the pipe between the compressor and air vessel has been chosen to explain the new application of this method. For the sake of simplicity we consider the case when the pressure in the working space behind the discharge valve is equal to atmospheric pressure, i.e. $p_a = p_b$.

The procedure of the graphical solution will be explained with the use of normal Carthesian system of coordinates $Q - p$. The surge equation for the time step Δt will be used in the working form

$$p_{t+\Delta t} - p_t = \pm \frac{\varrho a}{A}\left(Q_{t+\Delta t} - Q\right) . \qquad (7)$$

For slight pressure changes within one time step we take $\varrho a/A \approx$ const. and the dependence (7) will then be expressed graphically by a straight line with the slope

$$\left|tg\gamma\right| = \frac{a\varrho}{A}\cdot\frac{M_p}{M_Q} , \qquad (8)$$

where M_p (m/Pa) and M_Q ($m/m^3.s^{-1}$) are the scales of the corresponding axes of the system of coordinates. If the expression $a\varrho/A$ is multiplied by the ratio of the two scales the right side will be dimensionless which is necessary here. With the use of (2) the slope of the surge lines may be defined also by the alternative relation

$$\left|tg\gamma\right| = \frac{\sqrt{\varkappa\varrho p}}{A}\cdot\frac{M_p}{M_Q} . \qquad (9)$$

Using this expression we can, in the individual steps of calculation, i.e. on slightly varying levels of pressure p, respect to an advantage the slight change of the angle γ.

The situation in the first step of calculation is illustrated by the diagram in fig.4 . After the sudden change of the throttling curve of the valve unsteady operational condition begins at time $t = 0$. There is unbalance with the input into the air vessel (point B_0) larger than cutput (point C_0). Due to the difference of flows $Q_0^B - Q_0^C$ the pressure in the air vessel gradually increases. Boundary condition for the dependence of flow on pressure at the point B must be in this case the surge line of the pipe (it is supposed that no influence of reflections from the opposite end of pipe occurs and thus holds $\Delta t \leqq 2L/a$).

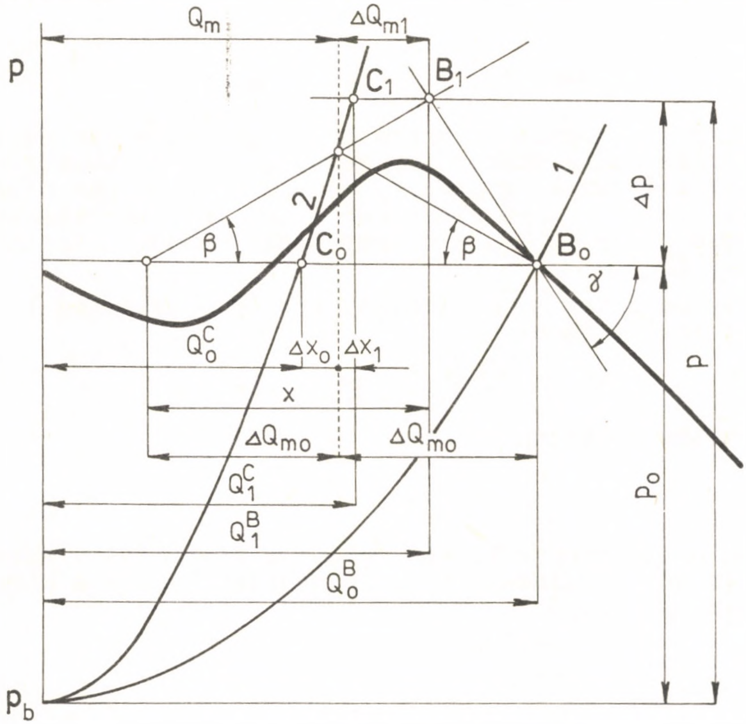

Fig. 4

A similar dependence at the point C is the throttling curve of the discharge valve at the new position 2 . In the end of the first step of calculation Δt the input into the air vessel will drop according to the surge line to the value Q_1^B while the output from the air vessel will reach according to the curve 2 , to the value Q_1^C . If the time step Δt is small enough, the curve between the points C_0 and C_1 may be replaced by a straight line and then for the volume of air that remained in the air vessel during this short time interval may be written

$$\Delta V_1 = \left(\frac{Q_0^B + Q_1^B}{2} - \frac{Q_0^C + Q_1^C}{2} \right) \Delta t \quad . \qquad (10)$$

With regard to the designation in fig.4 the expression in brackets may be rewritten into the form

$$\frac{1}{2}\left[(Q_m + \Delta Q_{mo}) - (Q_m - \Delta x_o) + (Q_m + \Delta Q_{m1}) - (Q_m + \Delta x_1) \right] \; .$$

If we admit that $\Delta x_0 \approx \Delta x_1$ this expression may be simplified and with certain approximation the following expression holds instead of (10)

$$\Delta V_1 \approx \frac{1}{2} \left(\Delta Q_{mo} + \Delta Q_{m1} \right) \Delta t \quad . \qquad (11)$$

The assumption mentioned above is in practice admissible in most cases. The throttling curve 2 in the investigated region of pressures is usually very steep. On the other hand, the time steps Δt are chosen so short that the absolute magnitudes of Δx_0 , Δx_1 are very small compared to the values of Q_m .

From the condition of continuity in the considered time interval in the form

$$\left(V + \frac{\Delta Q_{mo} + \Delta Q_{m1}}{2} \Delta t \right) . \varrho_o = V . \varrho \qquad (12)$$

and from the relation

$$\varrho - \varrho_o = \frac{d\varrho}{dp} \cdot \Delta p \qquad (13)$$

after an adaptation a linear relation will result which in the given coordinates will be represented by a straight line with the slope

$$\frac{\varrho_o \Delta t}{2V \dfrac{d\varrho}{dp}}$$

With a view to fig.4 we may write

$$tg\beta = \frac{\Delta p}{x} \cdot \frac{M_p}{M_Q} = \frac{\Delta p}{\Delta Q_{mo} + \Delta Q_{m1}} \cdot \frac{M_p}{M_Q} \quad . \qquad (14)$$

After substitution for $\dfrac{\Delta p}{\Delta Q_{mo} + \Delta Q_{m1}}$ we will obtain

$$tg\beta = \frac{\varrho_o \, . \, \Delta t}{2V \cdot \dfrac{d\varrho}{dp}} \cdot \frac{M_p}{M_Q} \quad . \qquad (15)$$

We will also introduce instead of $d\varrho / dp$ the derivative of the equation of adiabatic change of the state and after an adaptation we will obtain for the absolute value of $\operatorname{tg}\beta$

$$|\operatorname{tg}\beta| = \frac{\varkappa . \Delta t . p_0^{\frac{1}{\varkappa}}}{2Vp^{\left(\frac{1}{\varkappa}-1\right)}} \cdot \frac{M_P}{M_Q} \quad . \tag{16}$$

From what has been said here the following directions for graphical solution have been derived:

A straight line will be drawn from the point B_0 under the angle β, from the point of intersection with the throttling curve 2 the second line will be drawn also under the angle β but with the opposite sign. At the point of intersection of this second line with the surge line lies the state we are looking for in the end of the first time step at the point B_1.

With regard to the fact that the differences $\Delta p = p - p_0$ will not be very large in the individual steps, (16) might be simplified by means of developing it into a series and the following relation will be obtained

$$\frac{p_0^{\frac{1}{\varkappa}}}{p^{\left(\frac{1}{\varkappa}-1\right)}} \approx p\left(1 - \frac{\Delta p}{\varkappa . p}\right) \quad .$$

After substitution (16) will have the form

$$|\operatorname{tg}\beta| \doteq \frac{\varkappa . \Delta t}{2V} \cdot p\left(1 - \frac{\Delta p}{\varkappa p}\right) \cdot \frac{M_P}{M_Q} \quad . \tag{17}$$

This relation may be further simplified if the very small second term in brackets is neglected. In this case a most simple relation

$$|\operatorname{tg}\beta| \doteq \frac{\varkappa \Delta t}{2V} \cdot p \cdot \frac{M_P}{M_Q} \quad , \tag{18}$$

where p is the pressure around the computed point.

For preliminary calculation it is satisfactory to take for the time step Δt the whole surge period of the pipe, i.e.

$$\Delta t = \frac{2L}{a} \quad .$$

Then with a view to the relation (2) the slope of the auxiliary straight lines will be expressed in the form

$$|\operatorname{tg}\beta| \doteq \frac{L\sqrt{\varkappa \varrho p}}{V} \cdot \frac{M_P}{M_Q} \quad . \tag{19}$$

As far as form and content are concerned, this relation is very similar to the relation (9) for the slope of surge lines.

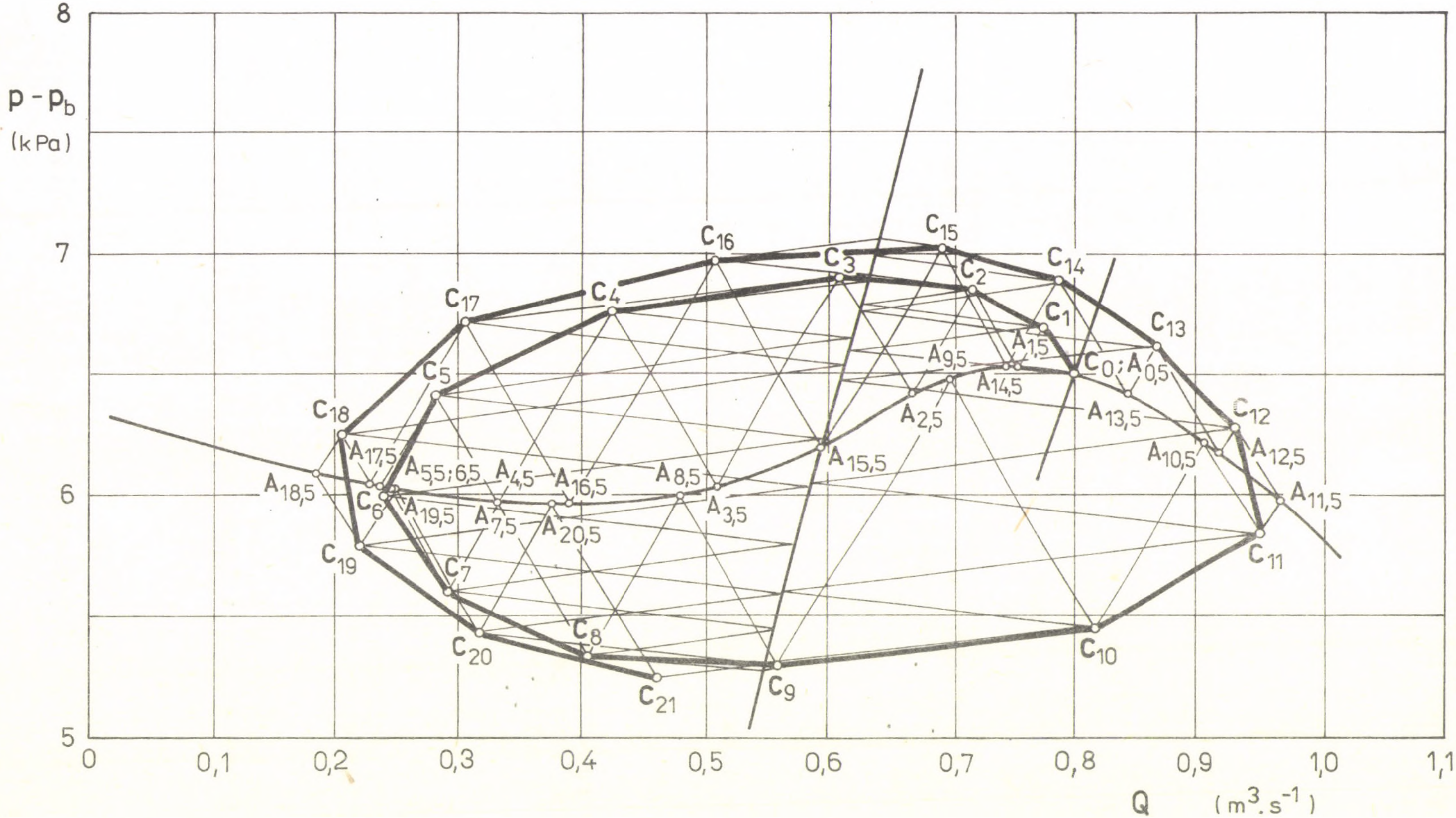

8
7
6
5
p - p_b
(kPa)
0
0,1
0,2
0,3
0,4
0,5
0,6
0,7
0,8
0,9
1,0
1,1
Q (m^3.s^-1)
C0 ; A0,5
C1
C2
C3
C4
C5
C6
C7
C8
C9
C10
C11
C12
C13
C14
C15
C16
C17
C18
C19
C20
C21
A1,5
A2,5
A3,5
A4,5
A5,5 ; 6,5
A7,5
A8,5
A9,5
A10,5
A11,5
A12,5
A13,5
A14,5
A15,5
A16,5
A17,5
A18,5
A19,5
A20,5

Fig. 5

It can be easily demonstrated that similar procedure in the second and following steps of the graphical solution leads to basically the same relations. The relation (9) holds unchanged, the relation (16) holds in a more general form

$$|tg\beta| = \frac{æ\,\Delta t\, p_t^{\frac{1}{æ}}}{2V\, p_{t+\Delta t}^{\left(\frac{1}{æ}-1\right)}} \cdot \frac{M_P}{M_Q} \quad , \tag{20}$$

and so do the simplified variants of (17), (18), (19).

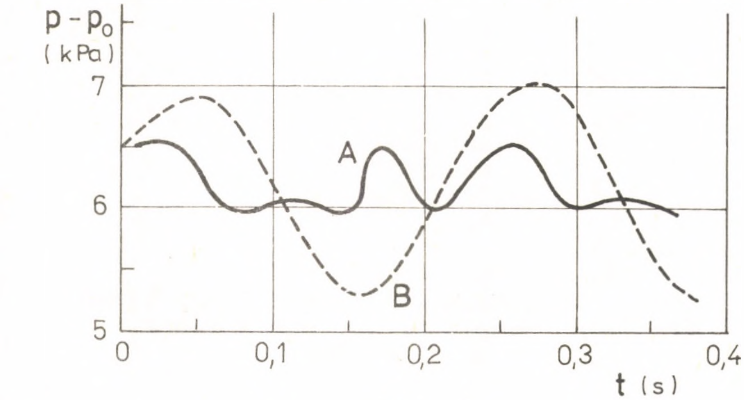

Fig. 6

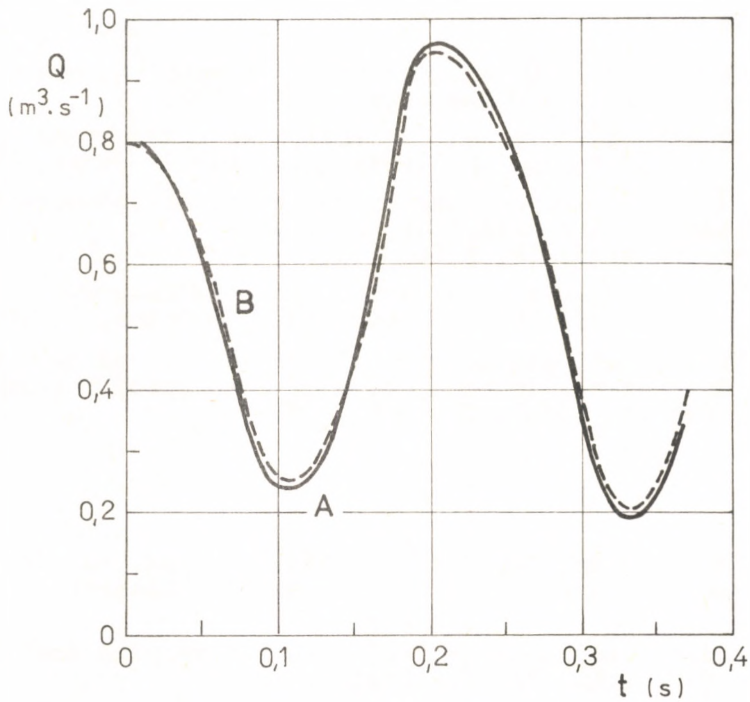

Fig. 7

For the sake of illustration fig.5 shows a part of graphical solution of air oscillations in the simple system whose diagram is shown in fig.1 . The result of this graphical calculation is presented in figs.6 and 7 in the form of time dependences of pressure and flow oscillations, for both the ends of the pipe: A is valid for the plane of the outlet nozzle of the compressor (beginning of the pipe) and B is related to the opposite end of the pipe near the air vessel. The calculation step in this case was the whole period of the pipe of the value 0.018 s.

SYMBOLS

A	(m^2)	cross-section area
a	($m.s^{-1}$)	acoustic velocity
L	(m)	length of the pipe
p	(Pa)	pressure
Q	($m^3.s^{-1}$)	volume flow
t	(s)	time
V	(m^3)	volume
w	($m.s^{-1}$)	velocity
β	(rad)	angle of the auxiliary lines
γ	(rad)	angle of the surge lines
æ		adiabatic exponent
ρ	($kg.m^{-3}$)	density

REFERENCES

[1] SCHNYDER, O.: Über Druckstösse in Rohrleitungen, Wasserkraft und Wasserwirtschaft, 1932.

[2] BERGERON, L.: Du coup de bélier en hydraulique au coup de foudre en électricité, Dunod, Paris, 1950.

[3] ERHART, F.: Pulsations in Pumps and Compressors with Unstable Characteristics (in Czech), Strojírenství, 12, 1956.

[4] STUDNITCHKA, J.: Gas Oscillations in Compressor Pipes, (in Czech), Technical Reports of ČKD Praha, 2, 1966.

[5] PAVLUCH, L.: Application of Schnyder-Bergeron's Method in Theoretical Investigation of Compressor Surges, (in Czech), SVÚSS, 79-04002, 1979.

HEISLER, Václav, Ing.CSc.
Research Engineer

PAVLUCH, Lev, Ing.CSc.
Research Engineer

SVÚSS (National Research Institute for Machine Design)
Praha 9 - Běchovice, Czechoslovakia

INVESTIGATIONS ON INTAKE ELBOWS FOR CENTRIFUGAL PUMPS

G. Hensel and C. Priesnitz

ABSTRACT
While the design of the intake has great importance for the mode of operation of turbomachinery it largely influences the costs of the unit. Therefore, the problem is not only to provide good hydrodynamic properties for intake elbows but small main dimensions, too. In order to restrict the experimental work for the design of intake elbows theoretical considerations can be dealt with beforehand. With the help of a cascade calculation method, the computational pre-optimization of elbow variants is described.

1. INTRODUCTION

The purpose of intake elbows for centrifugal pumps is to ensure favourable approach flow conditions for the turbomachinery in regard to the velocity and pressure distribution as well as prevention of vortex at the impeller inlet for an optimum power transmission and performance. Any infringement of these requirements may have detrimental effects on the mode of operation and reliability, in particular for machines of a high specific speed as in the case of cooling water pumps. By no means, these requirements can be met by a standard elbow pipe of uniform cross section. There are not only great differences in speed at outlet cross section and deviations from the axially parallel direction of flow but even more or less great separation regions along the inner contour of the elbow pipe. Thus, such an elbow will also exhibit a great pressure loss. It is clear that even the designing engineer for turbomachinery deals with this structural unit because of the great importance of the intake elbow for the function of a turbomachinery though, generally speaking, it is often considered as a part of the installation.

Elbows with an accelerated flow show essentially better properties as compared with those having an equal inlet and outlet cross section. In the first case the speed difference is smaller in the outlet cross section and no separation regions are formed because the thickness of the boundary layer remain small due to the accelerated flow.

The advantages of such elbows often designed with rectangular inlet cross section have been known. Therefore, they are widely used for great cooling water pumps and turbines.

Besides criteria of flow techniques the problem of costs derived from the geometrical dimensions of the inlet also play a role not to be underrated because of the required construction and depth of foundation. Therefore, it is desired to reduce the main dimensions of the intake elbow greatly, with the good properties of the flow technique being maintained. Work is done for this aspect and a review is given here from the very start.

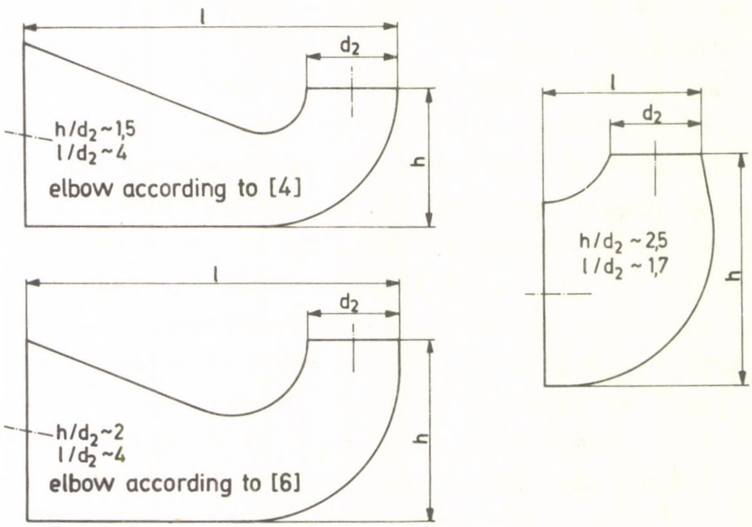

Fig. 1

When the intake is reduced as shown in Fig. 1 the acceleration of the flow within the elbow area and the deflection of the direction along the inner contour should be accomplished along an extremely short distance of flow. Apart from the fact that a reduction of the length of the elbow can easily be performed a decrease in the height is limited due to the geometrical shape of the intake cross section. Circular cross sections require greater heights than rectangular cross sections. It is, therefore, necessary to shape the contours of the intake elbow carefully.

2. INVESTIGATION METHODS

The quality of an elbow can be found reliably by experimental tests only. Nevertheless it is reasonable to make a pre-optimization or preselection, resp. of variants appearing favourably already by theoretical methods. A specific hydrodynamical computational process is not available for elbows. The use of FE methods well suitable for three-dimensional problems preliminarily fail due to the fact that all of these known methods do not take into consideration any frictional effect or secondary flow effect at all or insufficiently. However, these effects are required to be considered at any rate in order to comply with the real conditions. This has been shown by comparisons of measurements.

Therefore, the turbomachinery designer is attempted to apply one of the available cascade calculation processes for this task. The application on the elbow flow is rendered possible if the elbow is regarded as an individual duct of an axial cascade (see Fig. 2) and the particular situation is considered by appropriate boundary conditions:

- Calculation is made for a non rotating cascade ($\omega = 0$)
- the diameter of the cascade is selected in a very great size so as to approach the flat case as close as possible
- the blade number is obtained from the diameter of the elbow and the diameter of the cascade
- the cascade flow rate is obtained from the blade number and the elbow flow rate
- the shock-free approach flow to the cascade is obtained by providing with an appropriate inlet vortex

- the circular section of the elbow is substituted by a square cross section enclosing this circle.

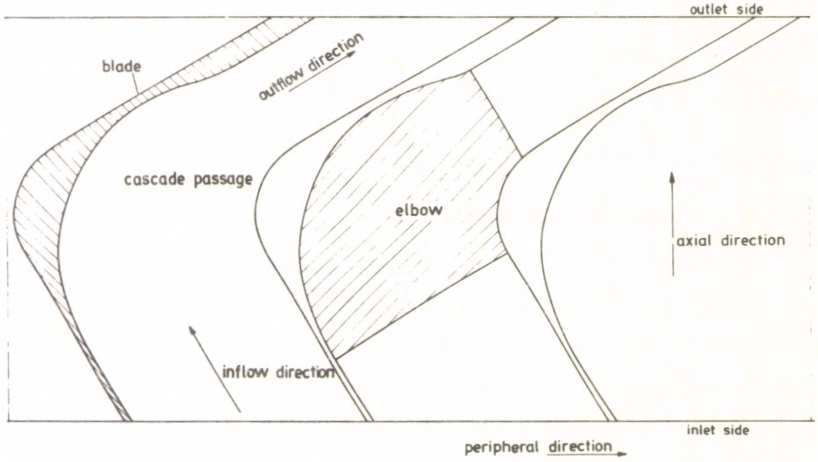

Fig. 2

The described process has already been tested for another application. Siphon pipes have been checked and a good agreement was reached between the calculated pressure distribution and the measuring results [2]. For this application a cascade calculation method [1] worked out in cooperation between Technische Universitaet Dresden and VEB Kombinat Pumpen und Verdichter, Scientific-technical centre, had been used as well as for the use of the elbow presented anew here. This method is based upon the comprehensive consideration of the frictionless main flow and the wall boundary layers and provides the subsequent statements:

- streamline flow and meridian velocity distribution
- development of boundary layers and shape parameters of boundary layers
- energy transfer, pressure losses.

These statements also include the essential criteria for the hydrodynamic evaluation of an intake elbow. The method is two-dimensional and provides the data for the plane of symmetry of the elbow. This is no restriction of the statements, for it has been found many a time that the gradients of the pressure and velocity distributions have been greatest in the bisector of the elbow [3, 4, 7]. Therefore, it may be expected that a minimization of the gradients in the bisector shall improve the conditions in the total cross section. Similarly, an elbow having a circular cross section will have a lower factor in the pressure loss than one with a rectangular cross section [3]. As the process [1] includes a calculation model for secondary flows of the boundary layer along smooth duct walls and the circular section for the calculation has to be replaced by a square cross section the calculation will probably show a loss factor that is too great.

3. CALCULATIONS MADE

Fig. 3 shows the intake elbow investigated in cast and welded construction. The illustration indicates the dimensions varied during the theoretical studies. Changes at the two elbows were made in height, length and the diameter ratio d_1/d_2. Moreover the cast elbow was calculated for different radii of bend of inner and outer contours and the welded elbow for various shapes and numbers of individual segments.

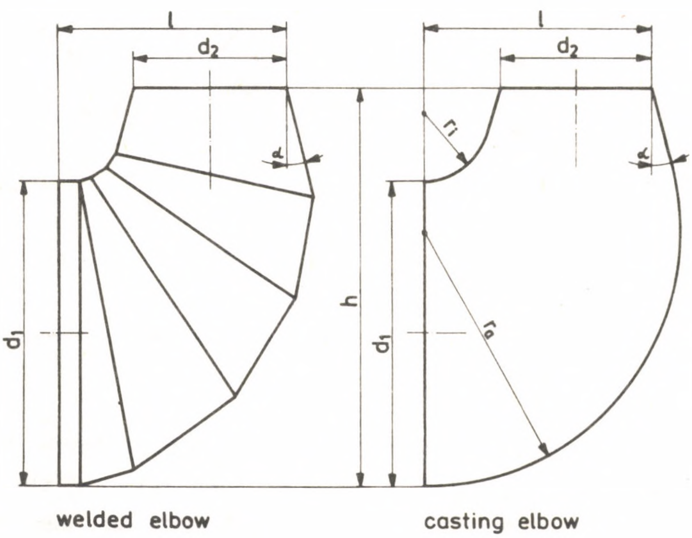

Fig. 3

The flare of the outer contour of the two elbows is obvious and it has been proved to be of advantage for an axially parallel flow direction at exit of the elbow. It is comparable with the angle correction at the exit of the cascade to balance the decreased deflection.

Fig. 4 shows the results of an elbow calculation. In the course of streamlines (Fig. 4a) it can be seen that the axially parallel flow directions at exit from the elbow is attained very well. From the calculated velocity along the streamlines (Fig. 4b) the velocity profile can be determined in any cross section and compared with the required one.

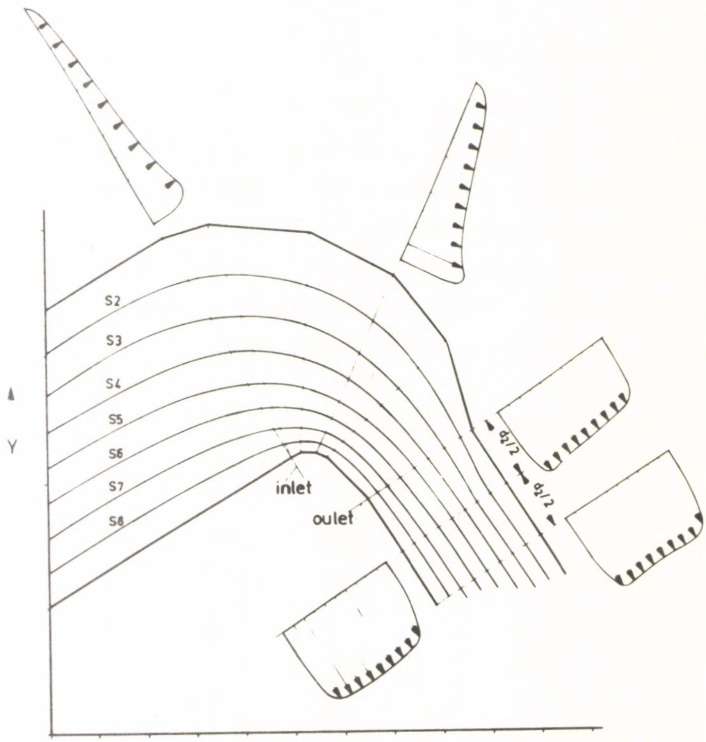

Fig. 4a

The profiles of five selected cross sections have been shown in Fig. 4a. The profile directly at the exit of the elbow is of greatest interest: it should be symmetrical as far as possible and it shall be balanced well. It can be seen that these requirements at the example considered are met in the cross section being situated at a distance of $0.5 \cdot d_2$ behind the elbow exit. In this plane the impeller inlet might be arranged in order to ensure optimum approach flow conditions. However, this, in turn, requires a greater foundation depth and thus higher costs for the construction. In various cases such a working length may be necessary for the sake of structure up to the impeller inlet plane, for example, if a corrugated pipe compensator, or a vortex regulator is installed between pump and elbow.

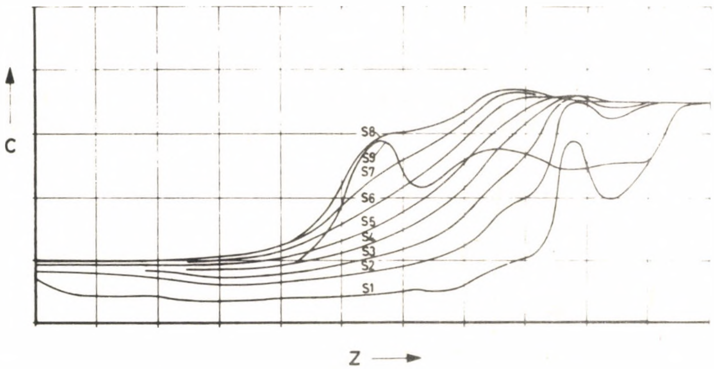

Fig. 4b

If the case is not the one given it should be tried to improve the profile at the exit cross sections, a possibility showing the use of a guiding rib. In Fig. 5 such an elbow is shown together with a guiding rib and the velocity profiles calculated for it. The guiding rib has been arranged so that the flow in the outer region of the elbow is accelerated more strongly than in the inner region. It can be seen from the velocity profile that the velocity differences at the exit cross section can be reduced approximately by half by means of an installation of such a guiding rib. Of course, this balanced velocity profile is attained in the exit plane only.

Another possibility to improve the velocity profile is the selection of a higher area ratio of cross sections A_1 and A_2. Fig. 6 shows the velocity profile at the

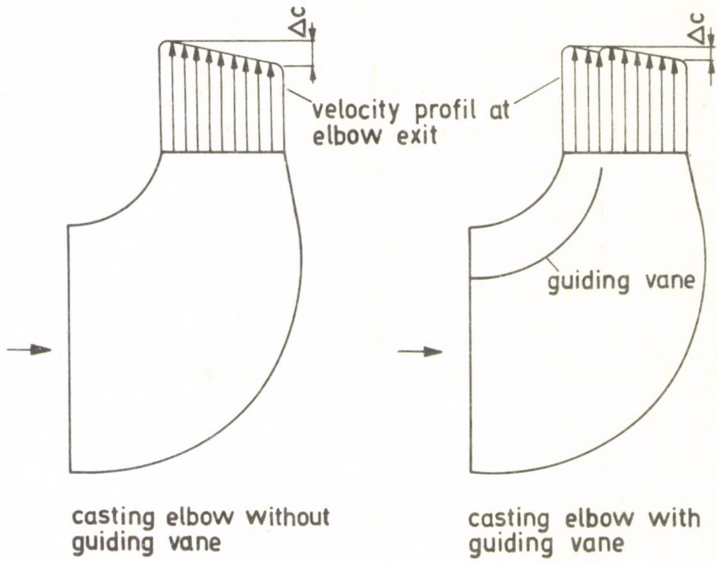

Fig. 5

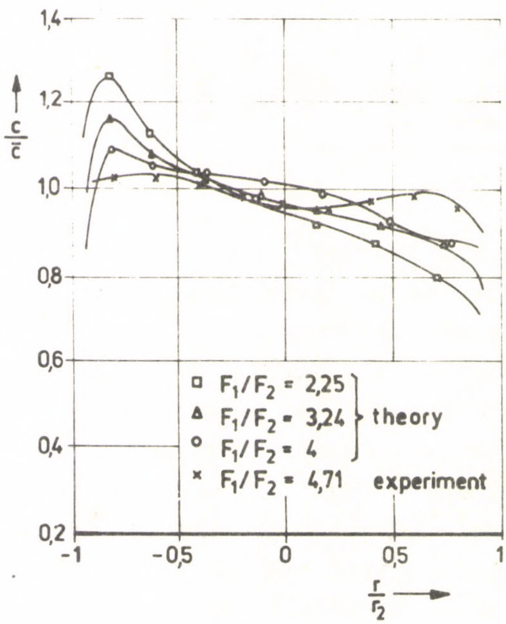

Fig. 6

exit for four area ratios from 2.25 to 4.71. While low area ratios exhibit strong velocity peaks at the inner contour a well balanced profile has already been given for $A_1/A_2 = 4$. Another improvement is to be expected for

$A_1/A_2 > 4$. This is confirmed by measurements which have been taken at an intake elbow having a area ratio of $A_1/A_2 = 4.71$. However, an accurate comparison of the first three profiles with the last one is not possible because the elbow at $A_1/A_2 = 4.71$ was provided with a rectangular inlet cross section and the original velocity profile of the elbow exit is superimposed by the hub effect of the followed impeller. This can be seen by the inward bulging of the velocity profile in the central region of the elbow exit. An unlimited enlargement of the area ratio is faced with the unwanted increase of the main dimensions of the intake elbow.

Besides the possible effects on the mode of operation of the followed turbomachinery the hydraulic losses of the elbow proper are an important criterium for evaluating the quality of the intake. For the best investigated elbow variants having an area ratio of $A_1/A_2 = 4$ pressure loss factors of ζ = from 0.034 to 0.038 were calculated (ζ referred to the dynamic pressure at the exit). These factors seems to be too low despite the statements given in par. 2 and will not quite meet the real conditions because the portion in the boundary layers only is considered for the calculation of the pressure losses. The main flow is regarded as frictionless in the cascade calculation method [1] and thus as lossfree though losses may also occur due to velocity and pressure gradients and turbulent motions in the main flow. This portion is not included in ζ. Morover, it should be taken into consideration that the calculation has been made for a hydraulically smooth surface, therefore expecting a very low pressure loss factor due to the great area ratio $A_1/A_2 = 4$. These results are compared with the data available in literatur of other authors in Fig. 7. In Fig. 7a pressure loss factors according to Nippert [5] have been plotted for equal inner contour radii of $r_i/b_1 = 0.5$ and various area ratios versus the outer contour radius. The elbow calculated in the present study (Fig. 3) has an outer contour radius of $r_a/b_1 = 0.85$. The calculated loss factor of $\zeta = 0.034$ fits well in a connecting line of the curve minima. A plotting versus the area ratio (Fig. 7b) also obtains a plausible

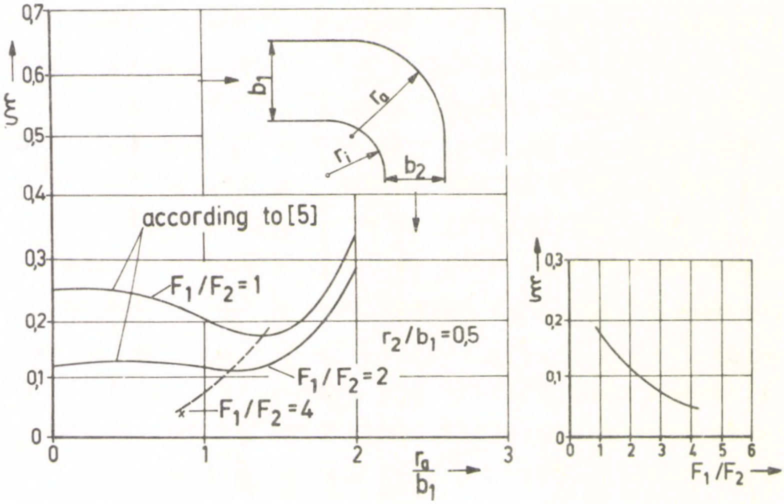

Fig. 7

course of dependence, the value theoretically obtained being, to be sure, already in an order of magnitude of a minimum limit value for ξ for acceleration elbows. This will not be obtained in the experiment due to the influence of roughness of the elbow surface alone.

4. CONCLUSIONS

The theoretical examinations carried out on intake elbows using a cascade calculation method indicate the possibility of a suitable pre-optimization for the design of elbows. Experimental studies on selected model elbows are required and in preparation to check and guarantee the theoretical results.

REFERENCES

[1] Will, G.
On the mathematical modeling of two-dimensional cascade flows.
Proceedings of the 4th Conference on Fluid Mechanics and Fluid Machinery, Budapest 1972

[2] Priesnitz, C.
Anwendung eines Berechnungsverfahrens fur die Gitterströmung zur Ermittlung des Druckverlaufs in Heberauslassen.
Pumpen- und Verdichterinformationen Halle (1979) 2, p. 22 - 25

[3] Fischer, G.
Einflussgrössen der Sekundärströmung in gekrümmten Kanälen.
Dissertation, Technische Universitat Dresden 1969

[4] Lottermoser, H.
Modellversuche an einem Einlaufkrümmer für Kühlwasserpumpen.
VDI-Berichte Nr. 193, 1973, p. 165 - 174

[5] Nippert, H.
Über den Strömungsverlust in gekrümmten Kanälen.
VDI-Forschungsheft Nr. 320, published in
Eck, B.
Technische Strömungslehre, Springer-Verlag 1966

[6] Hutarew, G.
Über die Ausbildung von Zuleitungen von Strömungsmaschinen, insbesondere von vertikalen Kreiselpumpen.
Energie (1961) 7, p. 289 - 292

[7] Report axial pumps
Research paper of the VEB Kombinat Pumpen und Verdichter Halle, unpublished.

Hensel, Gerhard Dr. rer. nat.
Priesnitz, Christoph Dipl.-Ing.
VEB Kombinat Pumpen und Verdichter
WISSENSCHAFTLICH-TECHNISCHES ZENTRUM
Halle (Saale)
Leninallee 90
DDR

LIFT AND DRAG COEFFICIENTS OF ROTATING RADIAL AND SEMIAXIAL CASCADES

P. Hergt

Summary:

The blades of a rotating radial impeller are replaced by discrete vortices arranged at the outer diameter. The velocities induced at the position of one of these discrete vortices by the source at the center and the remaining discrete vortices are added to the circumferential speed to give w_{oo}.

That in mind and with the definitions known from straight cascades, the formulas for the lift and drag coefficients are derived.

By introducing a virtual blade number, the relations are generalized to include cascades with any inclination of the meridional section to the axis, the straight cascades being contained as a limiting case.

With the help of the example of a free flow radial impeller measured in air it is shown that the relations found lead to values C_A and C_W and polars that are comparable with straight cascades.

1. Introduction

The design methods for impellers of radial or semi-axial pumps mainly base on empirically optimized coefficients, such as Ψ (nq); D_2/b_2 (nq); β_2 (nq), etc. Experience shows that these coefficients can be chosen within certain limits, without a considerable change of the hydraulic effiency of the pump. The hydraulic losses only rise considerably if the coefficients are selected far outside these limits.

In order to model these facts with the help of physical principles, several authors have tried to come to a criterion for optimum blade numbers and consequently to permissible blade loadings on the basis of geometrical considerations [1] or by means of assumptions for the losses occurring in impellers [2, 3].

The corresponding results very much depend on the type of loss assumptions used, which evidently can not describe the complex nature of the flow phenomena.

In analogy to straight cascades, other authors [4 to 9] have suggested, to use the lift coefficients as a measure of the blade loading, and to apply this loading as a characteristic hydrodynamic quantity when designing impellers. In [7] the cascade effect has been divided into two parts: a centrifugal part and a deceleration part.

All literature on this subject shows that the definition of basic flow W_{oo} causes difficulties due to the fact that contrary to straight cascades W_{oo} is not constant in the entire flow area of a radial or semi-axial cascade. With the procedure described hereafter, if is tried to avoid some of the past shortcomings.

2. Basic flow in the radial cascade

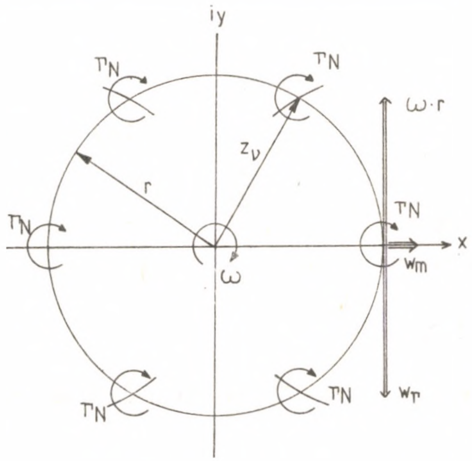

Fig. 1: impeller with 6 vanes replaced by 6 discrete vortices

The distributed circulation of N radial impeller blades is concentrated into N discrete vortices arranged at the radius r, according to Fig. 1.
In the case of an inflow without prerotation the circulation of such a discrete vortex is given by:

$$\Gamma_N = \int_0^l \gamma \cdot ds = \frac{2\pi}{N} \cdot r_2 \cdot c_{u_2} ;$$

The components of the velocity w_{oo} at the point of one of these vortices are (Fig. 1):

- the system velocity $u = (\omega \cdot r)$
- the velocity $w_m = E/2\pi \cdot r$ induced by the source E at the origin of the coordinate system
- and the velocity w_Γ induced by the remaining vortices, which for reasons of symmetry cannot have a radial component.

Consequently: $\vec{w}_{oo} = - \vec{u} + \vec{w}_m + \vec{w}_\Gamma$; (1)

The complex potential function of the vortices distributed at the z_ν points with z as pivotal point is:

$$F(z) = \frac{i \cdot \Gamma_N}{2\pi} \cdot \sum \ln (z-z_\nu) \qquad (2)$$

From this, the conjugate complex velocity is determined as follows:

$$\frac{dF(z)}{dz} = w_x - iw_y = \frac{i \cdot \Gamma_N}{2\pi} \sum \frac{1}{z-z_\nu} \qquad (3)$$

Where, according to Fig. 1,:

$$z = r \qquad (4)$$

$$z_\nu = r \cdot e^{i\frac{2\pi}{N}\cdot\nu} \qquad (5)$$

$$\nu = 1,2,\dots (N-1) \qquad (6)$$

After some transformations, equation (3) leads to:

$$w_x - i\cdot w_y = \frac{\Gamma_N}{4\pi r} \cdot \sum_1^{N-1} \left(i - ctg\frac{\pi}{N}\cdot\nu\right) \qquad (7)$$

When comparing the imaginary terms with $w_y = w_\Gamma$ we get:

$$w_\Gamma = \frac{r_2 c_{u2}}{2r} \cdot \frac{N-1}{N} \qquad (8)$$

(8) and (1) show that w_{oo} depends on the radius where the vortices are located.

It is the objective of this paper, to apply these considerations to the semi-axial and the axial cascade respectively, both having the same flow and pressure coefficients as the radial impeller. Thus the outer radius r_2 of the impeller can be taken as radius of the circle, where the discrete vortices are located.

Then we obtain: $w_\Gamma = \frac{c_{u2}}{2} \; \frac{N-1}{N}$ (9)

According to Fig. 1, the components of the basic flow then are:

$$w_{oo\,m} = c_{m_2} \qquad (10)$$

$$w_{oo\,u} = u_2 - \frac{c_{u2}}{2} \; \frac{N-1}{N} \qquad (11)$$

or: $$w_{oo\,m}/u_2 = \varphi \qquad (10a)$$

$$w_{\infty u}/u_2 = 1 - \psi_{th}\cdot(1-N)/4N \tag{11a}$$

$$\beta_\infty = \mathrm{arc\,tg}\,\frac{\varphi}{1-\psi_{th}\cdot(1-N)/4N} \tag{12}$$

$$\beta_{\infty_0} = \mathrm{arc\,tg}\,\hat{\varphi} \tag{13}$$

3. Lift coefficient C_A of a radial cascade

According to KUTTA-JOUKOWSKI, the lift force of a vortex is:

$$A = \rho \cdot b \cdot \Gamma_N \cdot w_{\infty} \tag{14}$$

Lift coefficient C_A can then be defined as:

$$C_A = \frac{A}{\rho/2 \; w_{\infty}{}^2 \cdot l \cdot b} \tag{15}$$

To simplify matters we assume a constant blade width $b = b_2$; eq. (15) in combination with eqs. (14), (10) and (11) as well as with $t_2 = 2\pi r_2/N$ will give:

$$C_A = 2 \cdot \frac{t_2}{l} \cdot \frac{c_{u_2}}{\sqrt{(u_2 - c_{u_2}(N-1)/2N)^2 + c_{m_2}^2}} \tag{16}$$

or, introducing dimensionless quantities:

$$C_A = \frac{t_2}{l} \cdot \frac{\psi_{th}}{\sqrt{(1-\psi_{th}\cdot(N-1)/4N)^2 + \varphi^2}} \tag{17}$$

Except for the factor (N-1)/N this expression is identical with that for straight cascades.

4. Drag coefficient C_W and glide angle ε

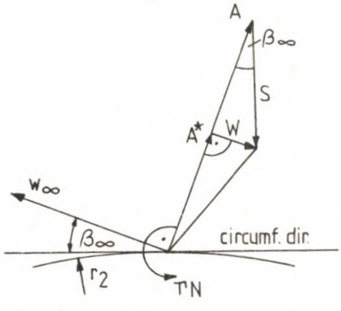

Fig. 2: Forces acting on the vortex

So far, all considerations have been based on a potential flow. Assuming the cascade has a pressure loss P_V, this only reduces the radial component of the lift (Fig. 2).

Taking $S = P_v \cdot t_2 \cdot b_2$, we obtain according to Fig. 2:

$$W = S \cdot \sin\beta_{oo} = p_v \cdot t_2 \cdot b_2 \cdot \sin\beta_{oo}$$

and with the definition analogous to C_A:

$$C_W = {}^{t_2}/_{1} \cdot \psi_v \cdot \frac{1}{\varphi^2} \cdot \sin^3\beta_{\infty} \tag{18}$$

the real lift coefficient then being:

$$C_A^* = C_A - C_W \cdot \operatorname{ctg} \beta_{oo} \tag{19}$$

and the glide angle :

$$\operatorname{tg}\varepsilon = \frac{C_W}{C_A - C_W \cdot \operatorname{ctg}\beta_{oo}} = \frac{C_W}{C_A^*} \tag{20}$$

5. Generalization of the derived formulas for cascades with any inclination towards the rotating axis

It can be exactly proven (see for example [10]) that a rotating cascade with an angle ϑ to the axis of rotation produces the same theoretical head - i.e. has the same blade circulation - as a radial cascade of same width and same radius ratio, but with a different number of blades N^*. This blade number can be expressed as:

$$N^* = N/\sin\vartheta$$

The fact that N^* can be a real number, is irrelevant from a mathematical viewpoint. By introducing this virtual blade number N^* instead of N, it is possible to generalize the above derived formulas and to find the connection to the straight cascade. Taking N^*, we obtain:

$$w_{\Gamma} = \frac{c_{u2}}{2} \cdot \left(1 - \frac{\sin\vartheta}{N}\right) \tag{9a}$$

$$w_{oo\,u}/u_2 = 1 - \frac{\psi_{th}}{4} \left(1 - \frac{\sin\vartheta}{N}\right) \tag{11b}$$

$$\beta_{oo} = \operatorname{arc\,tg} \frac{\varphi}{1 - \frac{\psi_{th}}{4}\left(1 - \frac{\sin\vartheta}{N}\right)} \tag{12a}$$

$$C_A = 2 \cdot \frac{t_2}{1} \frac{c_{u2}}{\sqrt{\left[u_2 - \frac{c_{u2}}{2}\left(1 - \frac{\sin\vartheta}{N}\right)\right]^2 + c_{m2}^2}} \tag{16a}$$

For $\vartheta = 0$, i.e. for the axial cascade, above formulas are similar to the formulas known from literature.

Thus we have found an approach which applies to all types of cascades. If we now look at a possible prerotation, a variable impeller width or a curved meridional section, the relations obtained become more complicated, but do not represent a serious problem.

6. Evaluation of the measurement of a radial impeller

Fig. 3 shows the characteristic curves of a free flow impeller measured in air with the following dimensions:

D_1 = 210 mm; D_2 = 395 mm; b_2 = 24 mm; $\beta_2 = 32^o$; N = 7; t_2/l = 0,68

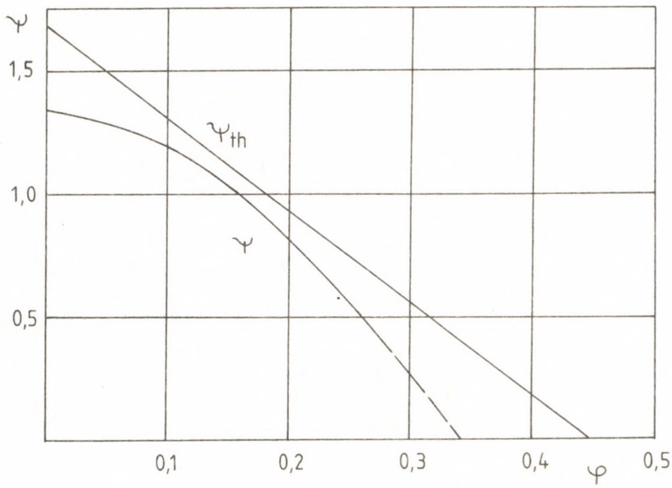

Fig. 3: Head characteristics of the tested impeller

The theoretical characteristic curve was determined by two different procedures the results of which agreeing very well:

- from the velocity distribution measured downstream of the impeller
- from the power input after subtracting the mechanical loss, the disc friction losses and the gap losses.

Fig. 4 shows the lift coefficients C_A acc. to (17), C_A^* acc. to (19) as well as the drag coefficient C_W acc. to (18) as a function of the difference of the basic flow angles ($\beta_{oo_o} - \beta_{oo}$).

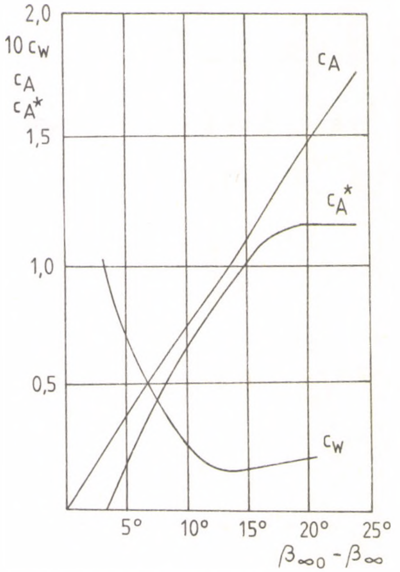

Fig. 4: Lift and drag coefficients

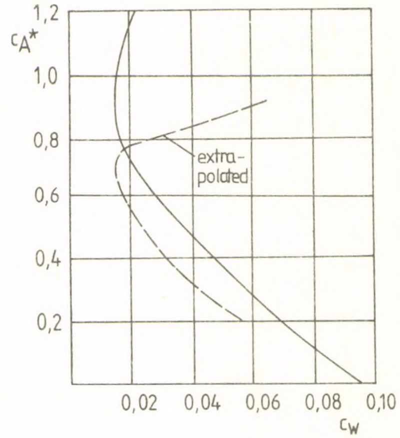

Fig. 5: polars of
——— radial and
----- axial cascades

The maximum attainable real lift coefficient is in the range of $C_A{}^* = 1.18$ and the lift coefficient corresponding to the min. drag coefficient lies at about $C_A{}^* \approx 0.9$.

Fig. 5 shows the cascade polar $C_A{}^*$ (C_W) together with the polars of a straight cascade with equal t/l and equal turning at $\varphi = 0.14$ measured on the basis of NACA-measurements. For the straight cascade the measuring values had to be extrapolated and, therefore, the curves can only be regarded as an approximation.

In view of the boundary layer conditions which certainly differ in the two cascades, the curves could not be expected to be identical.
It is, however, evident that the curves at small $C_A{}^*$-values are very similar. In case of high cascade loadings the drag coefficients of the straight cascade increase faster. The minimum C_W-values are identical.

P. HERGT
Head of hydr. res. and devel. dept.
KSB, Frankenthal (FRG)

7. Nomenclature

A	(N)	= lift
b	(m)	= width
c	(m/s)	= absolute velocity
c_A	(-)	= theor. lift coeff.
c_A^*	(-)	= real lift coeff.
c_W	(-)	= drag coefficient
D	(m)	= diameter
ds	(m)	= diffential length
F(z)	(m^2/s)	= flow potential
i	(-)	= imaginary unit
l	(m)	= blade length
N	(-)	= number of blades
N^*	(-)	= virtual number of blades
n_q	(Upm)	= specific speed
p	(N/m^2)	= pressure
r	(m)	= radius
t	(m)	= pitch
u	(m/s)	= circumf. speed
w	(m/s)	= relative velocity
W	(N)	= drag force
β	(°)	= angle
γ	(m/s)	= local circulation
Γ_N	(m^2/s)	= blade circulation
ε	(°)	= glide angle
ϑ	(°)	= angle of inclination
ϱ	(kg/m^3)	= density
φ	(-)	= flow coefficient
$\hat{\varphi}$	(-)	= flow coeff. at Ψ_{th} = o
Ψ	(-)	= head coefficient
ω	(1/s)	= angular velocity

Subscripts:

m	= meridional
N	= related to the blade number
th	= theoretical
u	= circumferential
o	= zero lift
2	= outer diameter
oo	= basic flow
ν	= index
v	= loss

8. Bibliography

[1] C. PFLEIDERER: Die Kreiselpumpen für Flüssigkeiten und Gase, Springer-verlag

[2] J. SUKUP: Uvaha o stanoveni vhodneho poctu lapadiek radialneho obezneho kolesa cerpadla. Cerpadla, Potrubi, Armatury-SIGMA-1980

[3] Y.R. REDDY, S. KAR: Optimum Vane Number and Angle of Centrifugal Pumps with Logarithmic Vanes. Journal of Basic Eng. No. 70-WA/FE-20.

[4] G.F. WISLICENUS: Fluid Mechanics of Turbomachinery. Mc Graw-Hill Book Company, Inc., New York and London.

[5] A. DE KOVATS, G. DESMUR: Pumpen, Ventilatoren, Kompressoren. Verlag G. Braun, Karlsruhe

[6] J. CSEMNICZKY: Selection of Blade Solidity for Runner of Hydraulic Machines. Proc. of the fifth Conf. of Fluid Mach. Budapest 1975.

[7] D.J. MYLES: A Design Method for Mixed-flow Fans and Pumps. NEL Report No. 177.

[8] A.D.S. CARTER: Blade Loadings for Hovercraft and other Radial Flow Fans. Journal of Mech. Eng. Science, Vol 9, No. 4, 1967

[9] W. WESCHE: Method for Calculating the Number of Vanes at Centrifugal Pumps. Proc. of the sixth Conf. on Fluid Mach., Budapest 1979

[10] N. SCHOLZ: Aerodynamik der Schaufelgitter, Braun-Verlag

AN ALTERNATIVE TO THE FAY PIPEFLOW ANALOGY FOR SCALING UP WATER TURBINE EFFICIENCY

S.P. Hutton

SUMMARY

Fay's analogy of two pipes of different sizes to represent the losses in model and prototype turbines, and thereby to simulate the Hutton scale formula, is examined and extended. It is shown that the questionable assumption of considering the runner blade passages as very short pipes can be avoided in the case of a Kaplan turbine if the blades are considered as flat plates. Using the Blasius formula for blade friction losses and typical geometrical runner data yields a simple equation for the ratio of hydraulic losses (and efficiency) which gives reasonable practical values. Moreover this flat plate analogy suggests how the proportion of kinetic to total losses may be expected to vary with turbine specific speed Ns.

1. INTRODUCTION

For scaling up the optimum efficiency of Kaplan turbines from model to prototype the author (Reference 1) evolved a formula which has since been widely used

$$\frac{1 - \eta h}{1 - \eta h'} = \frac{\delta}{\delta'} = (1 - V) + V\left(\frac{Re'}{Re}\right)^{\frac{1}{5}} \qquad \ldots (1)$$

where ' represents the model turbine. In this, V, is the proportion of losses influenced by Reynolds Number and (1 - V) is the remainder of the losses which are "kinetic" and therefore do not vary with Re. The general form of equation had been origiginally derived by Ackeret for Francis turbines where V = 0.5 but Equation 1 applies specifically to Kaplan turbines assuming:-

1. The principal sources of loss are in the runner and in the draft tube. (Losses in guide-vanes and spiral casing were neglected).
2. The model and the prototype are geometrically similar and the flow over the runner blades for both model and prototype is in the smooth turbulent regime.

3. The model and prototype Kaplan turbines are operating on the "cam curve" at optimum efficiency, i.e. the blade angle giving the overall highest efficiency.

In deriving the value of V in the formula it was calculated, using the above assumptions, that for the range of blade angles giving best efficiency at each flowrate, the mean value of the proportion of the frictional to total losses in the runner was about 90% and for the draft tube about 20%. Using these typical values it was shown that V = 0.3 was a good mean value at optimum efficiency and that Equation 1 became

$$\frac{\delta}{\delta'} = 0.3 + 0.7 \left(\frac{Re}{Re}\right)^{\frac{1}{5}} \qquad \ldots (2)$$

From practical experience this formula has been shown to be a useful guide and has therefore been used for Kaplan turbines ever since. It has even been applied (quite wrongly in principle!) to Francis turbines and pumps with some success. However we now know that it is an oversimplification because the flow over the prototype runner blades may not be "hydraulically smooth" but rather transitional (friction varies with Re and roughness k) or even in the fully rough regime (friction varies only with k). There are other sources of loss in addition to the runner and the draft tube as pointed out by Chevalier (2).

For this reason other researchers particularly Osterwalder (3, 4), and Fay (5), have suggested modifications to the Hutton formula to improve it and make it more applicable to modern commercial standards of surface finish used in the manufacture of water turbines. Osterwalder (4) showed that because of the large difference between Re for the model and for the prototype, α might vary considerably and that α = 5.84 was a better mean value than α = 5 in Equation 2. Also Osterwalder and others pointed out that the runner blades of the prototype might not be hydraulically smooth but might be operating in the transitional or fully rough regimes. Osterwalder (4) summarized the problem very clearly and suggested a new formula which, although correct in principle, was complicated and, at that time, lacked sufficiently precise information on the empirical constants to be used. Fay (6) has pointed out that because of the latter uncertainty it was perhaps not opportune to use such a complicated formula when a simpler one might give similar accuracy. Fay (6) ingeniously showed that one could use the analogy of two pipes of different sizes to represent the hydraulic losses in two turbines of different sizes. The losses in each pipe had to be separated into kinetic and frictional so as to be in the form $\frac{c^2}{2g}\left(1 + \lambda\frac{L}{D}\right)$ and it could be shown that

$$\frac{\delta}{\delta'} = \frac{1 + \lambda\frac{L}{D}}{1 + \lambda'\frac{L'}{D'}} \qquad \ldots (3)$$

where for the turbine case $\frac{\delta}{\delta'} = \frac{1 - \eta h}{1 - \eta h'}$ and $\frac{L}{D} = \frac{L'}{D'}$ for geometrically similar machines. In this way Equation 3 was a convenient form for allowing λ & λ' to take values appropriate to hydraulically smooth, transitional or fully rough flow.

Fay demonstrated that if Equation 3 were extended to

$$\frac{\delta}{\delta'} = \frac{1}{1 + \lambda'\frac{L}{D}} + \frac{\lambda\frac{L}{D}}{1 + \lambda'\frac{L}{D}} \left(\frac{Re}{Re'}\right)^{\frac{1}{\alpha}} \qquad \ldots (4)$$

the first term on the right hand side of Equation 4 is the fixed kinetic part of the total losses and the second term is the remainder of the losses, which vary with Re. Thus Equation 4 could be made identical with Equation 2 provided a pipe length equivalent to a turbine is chosen so that with reference to Equation 2,

$$\frac{1}{1 + \lambda'\frac{L}{D}} = 0.3$$

With this value of $\frac{L}{D}$ then Equation 4 becomes Equation 2 and the pipe analogy can be used. Fay pointed out for example that if λ' x 0.0176 then $\frac{L}{D} = 132$ would make Equation 4 into Equation 2.

However some people took this analogy too literally and thought that it was unjustifiable to consider runner blade passages as pipes particularly for Francis turbines where $\frac{L}{D}$ is too short to permit the "classical" values of λ established for long straight pipes to be applied. This was rather hard on Fay because his hypothesis was really concerned with the ratio of the losses, $\frac{\delta}{\delta'}$, and this might not be such an unreasonable assumption even if long pipe values of λ were applied to the short pipe equivalent of a runner blade passage.

2. AN ALTERNATIVE APPROACH FOR A KAPLAN TURBINE

For the Kaplan turbine it is possible to use an alternative analogy which avoids the short-pipe criticism. This is to assume that the runner blades are analogous to flat plates and that the friction coefficients for flat plates at the appropriate Reynolds Number based on blade chord and mean relative water velocity can be applied.

However to do this we must first make a slight modification to Fay's Equation 4 and assume that not all the kinetic energy in the pipe ($c^2/2g$) is lost but that some is regained, as in a draft tube. The pipe analogy should really be a pipe followed by a diffuser of efficiency ηd in which case Equation 4 becomes

$$\frac{\delta}{\delta'} = \frac{1 + \eta d}{(1 - \eta d') + \lambda' \frac{L}{D}} + \frac{\lambda' \frac{L}{D}}{(1 - \eta d') + \lambda' \frac{L}{D}} \left(\frac{Re'}{Re}\right)^{\frac{1}{\alpha}} \quad \dots (5)$$

Then we can proceed to use the flat plate analogy rather than the short pipe.

Using two dimensional cascade theory for a typical annular section of blade passage at radius r, it can be shown that the head loss (h_L) associated with blade drag for a spacing/chord ratio t/ℓ, and an angle β between the mean relative velocity, W, and the rotational velocity direction is given approximately by

$$h_L = \frac{W^2}{2g} \frac{\ell}{t} \frac{C_D}{\sin\beta} \quad \dots (6)$$

where C_D is the dimensionless blade drag coefficient, Drag Force/ $\frac{1}{2}\rho W^2.\ell.dr$.

Now from the velocity diagram for a Kaplan turbine operating at maximum efficiency it is approximately true that

$$W \sin\beta = C \quad \dots (7)$$

where C is the axial velocity component and W is the relative velocity.

Then combining Equations 6 and 7 gives

$$h_L = \frac{c^2}{2g} \cdot \frac{\ell}{t} \cdot \frac{C_D}{\sin^3\beta} \qquad \ldots (8)$$

and taking representative overall mean values for the runner blades Equation 5 becomes

$$\frac{\delta}{\delta'} = \frac{1 - \eta d + \frac{C_D}{\sin^3\beta} \frac{\ell}{t}}{1 - \eta d' + \frac{C_D'}{\sin^3\beta'} \frac{\ell}{t}} \qquad \ldots (9)$$

C_D and C_D' will depend on blade Reynolds number and we can use the flat plate analogy and the Blasius formula for two sides of a plate

$$C_D = \frac{0.144}{Re^{\frac{1}{5}}} \qquad \ldots (10)$$

As before in the case of Fay's pipeflow analogy if the Equation 9 is to be similar to Equation 2 and assuming that all the draft tube losses are kinetic and all the runner losses are frictional we must have

$$\frac{1 - \eta d}{1 - \eta d' + \frac{Cd'}{\sin^3\beta'} \cdot \frac{\ell}{t}} = 1 - V \qquad \ldots (11)$$

For example taking typical values as follows

$\eta d = \eta d' = 0.85$, $1 - V = 0.3$

$R'e_\ell = 2 \times 10^5$ and thus $C_D' = 0.012$

$\beta = 22^\circ$ and thus $\sin^3\beta = 0.052$

Equation 11 becomes

$$\frac{0.15}{0.15 + 0.012 . \frac{\ell}{t} . 19.15} = 0.3$$

Hence $\frac{\ell}{t} = 1.5$ which is of the right order for the blade spacing of Kaplan turbines.

It seems therefore that this simple flat-plate analogy may be worth exploring further, particularly because it also suggests that (1 - V), the proportion of kinetic losses to total in a Kaplan turbine, is a function of C_D', $\sin^3\beta'$ and ℓ/t, the last two terms being very much functions of specific speed Ns.

Let us therefore see how, from Equation 11, we might expect (1-V) to vary with typical values of β' and ℓ/t used for the range of specific speeds covered by Kaplan turbines (Ns metric from about 300 to 900).

TABLE 1

N_s metric	500	600	700	800	900
ℓ/t at periphery	1.67	1.20	0.93	0.75	0.61
β' at periphery	20.3	19.3	18.8	18.5	18.4
1 - V	0.21	0.27	0.31	0.35	0.39

Table 1 lists some typical values of ℓ/t and β at the outer periphery of the runner quoted by Anton (7). Inserting these values in Equation 11 suggests that, depending upon Ns, the fixed proportion of losses in the Hutton formula may vary from about 0.21 to 0.39. Such values have only been chosen for illustration and will vary depending on the design of runner and the typical representative mean values of ℓ/t and β' for the blades at all radii. However they do demonstrate how (1 - V) may vary with N_s and that a suitable mean value for (1 - V) is 0.3 which is the same as in Equation 3.

3. CONCLUSION

It should be remembered that the values of ℓ/t and β' used in the above example are only indicative of the mean values used by designers and that actual designs vary considerably above and below these. Nevertheless despite its considerable over-simplifications this simple model demonstrates that V in the original Hutton formula would be expected to vary with Ns. The same applies to V values used in similar scale formulae applied to Francis turbines but so far we do not have enough data to agree on the values of V to be used for each Ns, and Stille has made such a suggestion (8).

This is only a simple model to illustrate the validity of Fay's general approach and we must still remember the extra complications outlined by Osterwalder which have still not been adequately dealt with.

Nevertheless it is clear in principle that for both Kaplan and also Francis turbines V should vary with Ns.

REFERENCES

1. HUTTON, S.P. Component losses in Kaplan turbines and the prediction of efficiency from model tests. Proc. I.Mech.E. Vol. 68 No. 28 pp 743-762 1954.

2. CHEVALIER, J. "Contribution à l'étude de l'effet d'échelle dans les turbines Kaplan" La Houille Blanche, 1965, Vol. 20 p 663.

3. OSTERWALDER, J. Model testing for Kaplan turbine design including studies on efficiency scale tests. Water Power 1967 p 103.

4. OSTERWALDER, J. Considerations on the revalorisation behaviour of hydraulic turbomachinery. Trans. 6th IAHR Symposium Rome 1972.

5. FAY, A. On the efficiency scale formulae for hydraulic turbines. Kolloquium, Darmstadt May 1975.

6. FAY, A. On the high accuracy scaling up for pumps and turbines. Paper 2-5, International Conference on design and operation of pumps and turbines 1-3 Sept. 1976 at National Eng. Lab.

7. ANTON, I. Turbine Hidraulice (Figs. 7.26 & 7.35) Editura Facla, Timisoara, 1979.

8. STILLE, C.E. Water turbine scale-effects and efficiency majoration methods. I.Mech.E. Conf. on Scaling for Performance Prediction in Rotodynamic Machinery 6-8 Sept. 1977, University of Stirling.

UNSTEADY PRESSURE DISTRIBUTION AROUND THE STATOR BLADES IN AXIAL FLOW FAN

JAN JĘDRYSZEK

SUMMARY

The unsteady pressure distribution between the stator blades due to passing wakes shed by upstream moving rotor blades are measured. The number of moving thin aerofoil rotor blades was 6,7,8,9 and 10,and for stator row steady number 8 used. Measurements were made of the fluctuating pressures on the stationary blades for various axial-distances between rotor and stator rows, various radius ofmmeasured points by various rotor velocities. Measures were made for any number of rotor blades at three points of the characteristics for each number of rotational velocity.It is well known that the sound generated by an axial flow fan consists of a discrete noise and a broad band noise. As the cause of generation of the discrete noise, we can consider several factors, but in an axial flow fan with rotor and stator, it is mainly due to the pressure fluctuation on blade caused by the viscous interference between the blade rows. In this paper we report the results of some measurements of those phenomenons.

LIST OF SYMBOLS

Δc - velocity fluctuation,
c - main stream velocity,
f - frequency,
l - chord lenth,
L - sound pressure level,
n - number of rotational speed,
p - amplitude of pressure fluctuation,
r - radius of measured points (Fig.2),
x - distance between the moving and stationary rows,
z_w- number of rotor blades,
z_k- number of stator blades,

ϱ - density of the air,
ω - nondimensional frequency [2,5] or angular velocity,
φ - flow coefficient,
ψ - pressure coefficient,
$\Phi(\omega)$ - function represented $S(\omega)$, $F_{\alpha}(\omega)$ and $F_{f}(\omega)$ in [2].

INTRODUCTION

In an axial flow fans the effect of interference arises between moving and stationary blade rows if the axial distances between them are small. In this case, noise is generated and some unsteady forces act on the blades. On the other hand, if the axial distances are large, the rotor will be longer and the pressure rise for the same capacity becomes smaller. It seems necessary to choose a proper axial distance between moving and stationary blade rows, but the optimal distance is not determined yet. Each blade of a turbomachine has a viscous wake trailing behind it. Owing to the relative motion of adjacent blade rows, the wakes shed from an upstream blade row are encountered by the following row in an unsteady but periodic fashion. This phenomenon gives rise to an unsteady pressure distribution on each blade, which is a source of mechanical vibration as well as acoustic radiation.

The unsteady forces acting on the blades in the flow have been treated by many authors, mainly from a theoretical point of view, for example by Horlock [1], Naumann and Yeh [2], Murakami, Hirose and Adachi [5]. However many studies, which compared the theoretical results with the experimental ones, have been published, for example by Adachi and Murakami [4] or Ispas [3]. This paper investigated experimentaly the unsteady pressure acting on the stationary blades in an axial flow fan with the stationary blade row behind the moving rotor row in an attempt to clarify the causes of these interference. They made measurements of the unsteady pressure distribution on the stationary blades for various axial distances between the moving and stationary blade rows. For the same test fan five moving blade rows with 6,7,8,9 and 10 blades, each with the same stationary blade row /8 blades/ were used. A periodic row of oblique wakes is created exactly by upstream moving blade row. The measuring method utilizes a condenser microphone with oscilloscope. Comparing the results, discusion were made about the causes of unsteady pressures acting on the stationary blades. It is well known that the sound exist in an axial flow fan with rotor and stator is mainly due to the pressure fluctuation on blade generated. In this paper we report the results of some measurements of those sound level.

EXPERIMENTAL APPARATUS AND METHOD

The experimenthal apparatus is schematicaly shown in Fig.1.

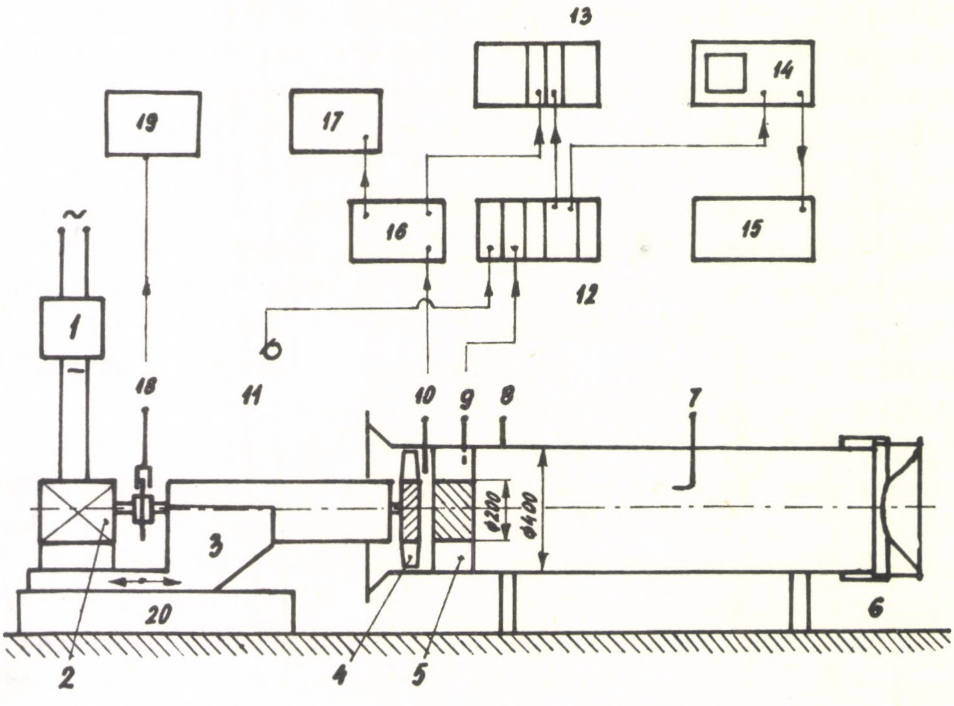

Fig.1. Schematic view of experimental apparatus: 1 - motor speed regulator, 2 - electric motor, 3 - moviable bearing housing, 4 - rotor blades, 5 - stator blades, 6 - throttle mechanism, 7 - Prandtl tube, 8 - static pressure tube, 9 - acoustic pressure transducer, 10 - hot-wire probe, 11 - microphone, 12 - two channel sound pressure level, 13 - two channel oscilloscope, 14 - real-time analyser, 15 - X-Y re-

corder, 16 - hot-wire anemometer, 17 - digital voltmeter, 18 - frequency probe., 19 - digital frequencymeter, 20 - support.

A test fan is mounted near the suction end of pipe, where an inlet bellmouth is installed. The diameter of the fan is 400 mm, and the rotor of the fan is mounted on the main bearing housing which is upstream of the impeler located. The electric motor is supported at the upstream end of the bearings shaft through the elastic coupling. The rotor of the fan may be available as the 6,7,8,9 or 10 blades. On the stator the number of blades is constantly 8. The arrangement of the stator blades used in the experiment are shown in Fig.2.

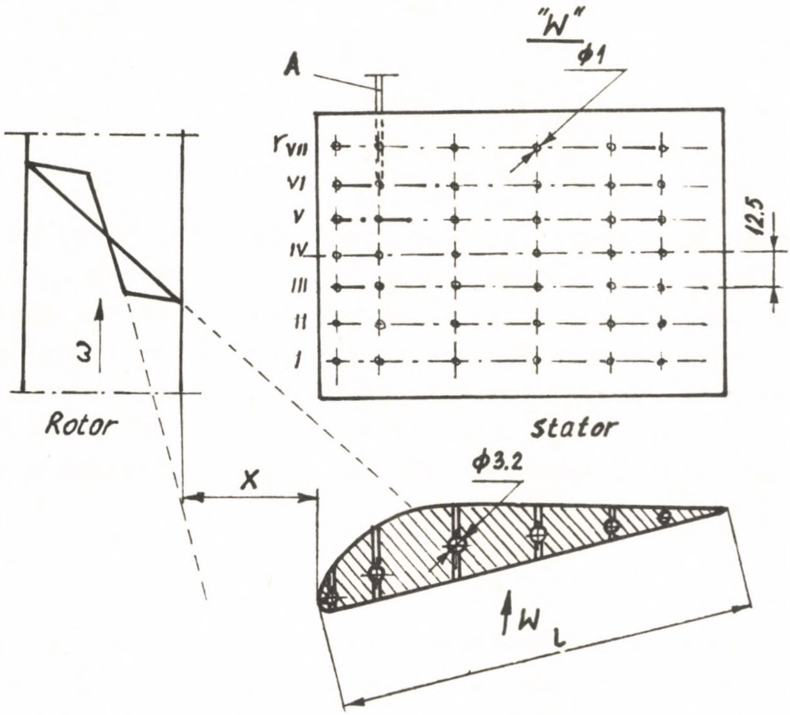

Fig.2. Reciprocal configuration of the rotor and stator blades, and pressure holes distribution on the stator blade surface. A - pressure probe.

This experimental may be varied in the spacing between the rotor and stator rows. The axial flow fan is driven by various rotational speed of the electric motor. Fig.3 shown the typical overal performance of the experimental fan used for various rotational speed /30 ÷ 50 Hz/ and for various resistance lines /O,I,II/.

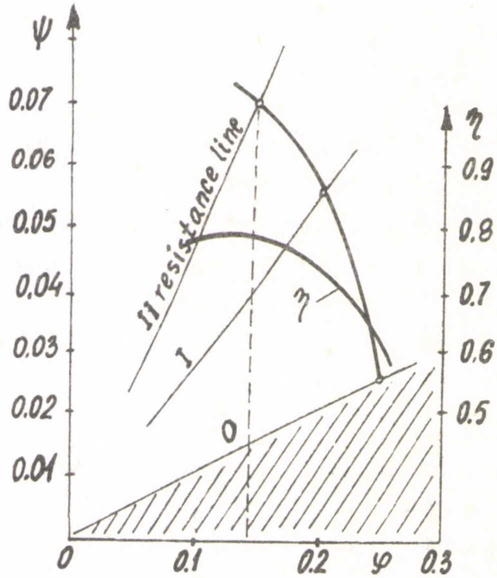

Fig.3. Performance field for axial flow fan used in experimental work.

In order to measure pressure fluctuation acting on the stationary blades, one of the stator blades was replaced by a special blade shown in Fig.2, on which pressure holes are distributed. To measure pressure fluctuation, a condenser microphone connected with special sounding-pipe of 3 mm diameter could be inserted in any of the holes of 3,2 mm diameter. Then the measured amplitude of pressure fluctuation was calculated by relation :

$$p = 2 \cdot 10^{L/20 - 5} \tag{1}$$

where L - measured pressure level in dB. For this purpose the experimental apparatus as shown in Fig.1 was used. The output voltage of the sound level meter is fed to a oscilloscope and could be pressure patterns observed and registrated. Calibration of output was done by the use of image on the oscilloscope when a definite pressure was applied to the sounding-pipe of the condenser microphone. The acoustical frequency of the condenser microphone an the pressure hole on the stator blade must be measured beforehand. The results shown that the measurement of pressure fluctuating was satisfactory up to frequency 600 Hz.

Measurement of the velocity distribution after rotating rotor blades is carried out by the hot-wire probe. The output voltage of the hot-wire anemometer is fed to a digital voltmeter for average value of the stream velocity and to oscilloscope for time-dependent components of the velocity. A schematic of the apparatus is shown in Fig.1. The results of the velocity measurements was used to theoretical calculation of the pressure distribution. Comparisons of the fluctuating pressure calculated following the method presented in papers [2,5]. On account of this papers, the pressure fluctuation can be written as follows:

$$p = 2.\pi.\rho.c.\Delta c.\Phi(\omega) \qquad (2)$$

The function $\Phi(\omega)$ were used to simplification.

The instrumentation of noise measurement consist of a condenser microphone of 25,4 mm diameter which is attached to two -channel sound level meter, a real-time analyser, and a X-Y recorder. The arrangement is shown also in Fig.1.

ANALYSIS OF EXPERIMENTAL RESULTS

Fig.4.shown results of the unsteady pressure distribution at the pressur side and the suction side of stator blades by rotational speed 40 1/s. In the paper [5] authors have reported a interference problem between moving and stationary blade rows due to wake effect by use of unsteady thin aerofoil theory. Acording to this theory, fluctuation of pressure was compared with experiment. This measurements and calculation was made at the mean radius of blade rows /r = 300 mm/. The agreement between the experimental results and theoretical results [2,5] is fairly good.

Fig.5 shown results of the fluctuating pressure distribution at the various radius /r_{II},r_{IV} and r_{VII}- see Fig.2/ at the pressure side of stator blades. From this experimental results, is was found that the magnitude of pressure fluctuation dependent much on axial spacing between abowe rows than on radius. It is obvious clear from the Fig.2 that the axial spacing between the stator and wakes of the rotor change more than radius from hub to tip in this case.

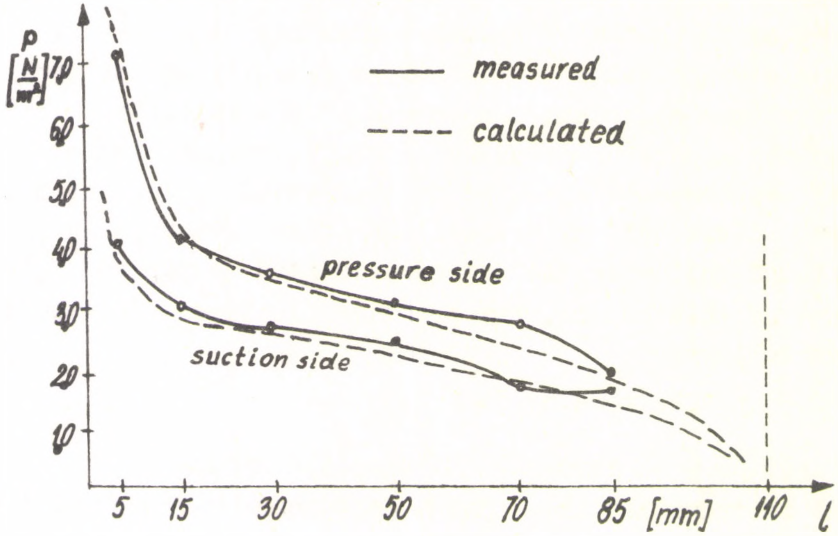

Fig.4. Unsteady pressure distribution on the stator blade for various profil sides /$z_w = z_k = 8$, $x = 15$mm, $n = 40$ 1/s, r_{IV} and resistance line II/.

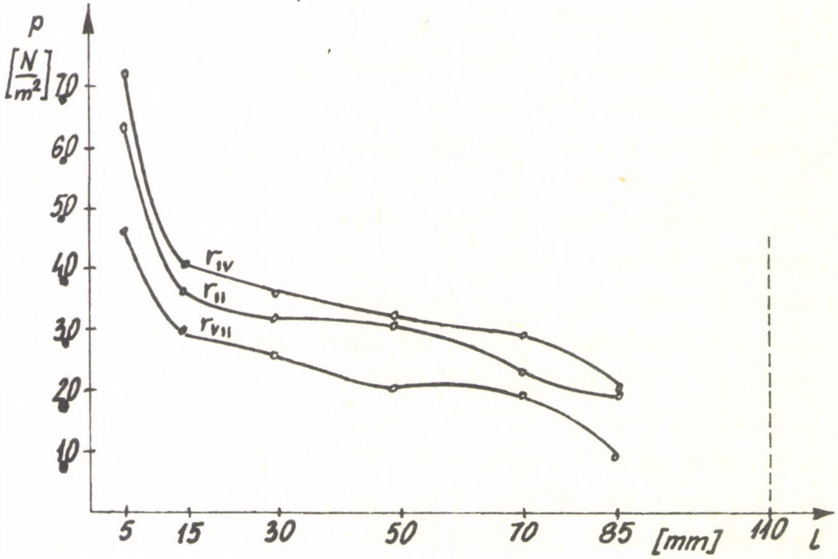

Fig.5. Unsteady pressure distribution for various radius on the stator blade /The rest parameters as abowe/.

The relation between the flow coefficient φ and the unsteady pressure distribution around the stator blade show Fig.6.

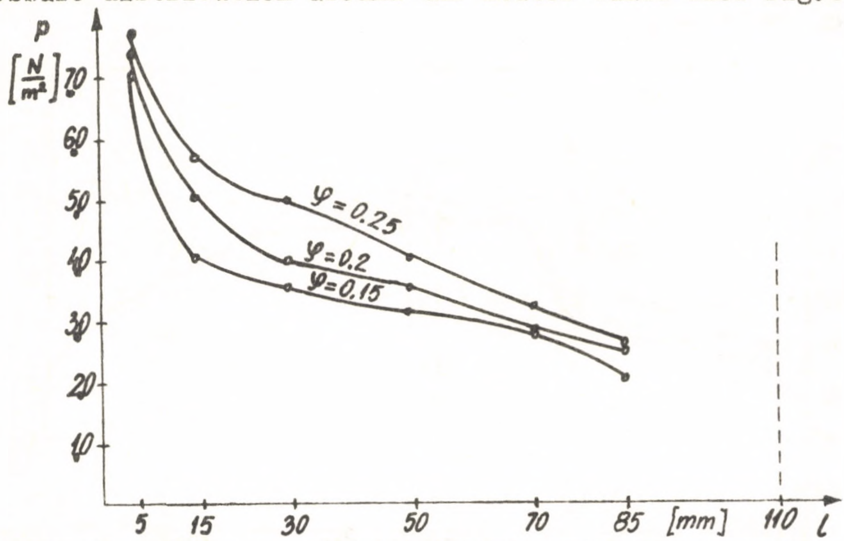

Fig.6. Unsteady pressure distribution for various flow coefficient /the rest parameters as in Fig.4/.

It is found from this figure that the magnitude of unsteady pressure have a minimum value at the point $\varphi = 0,15$, near the maximum efficiency.

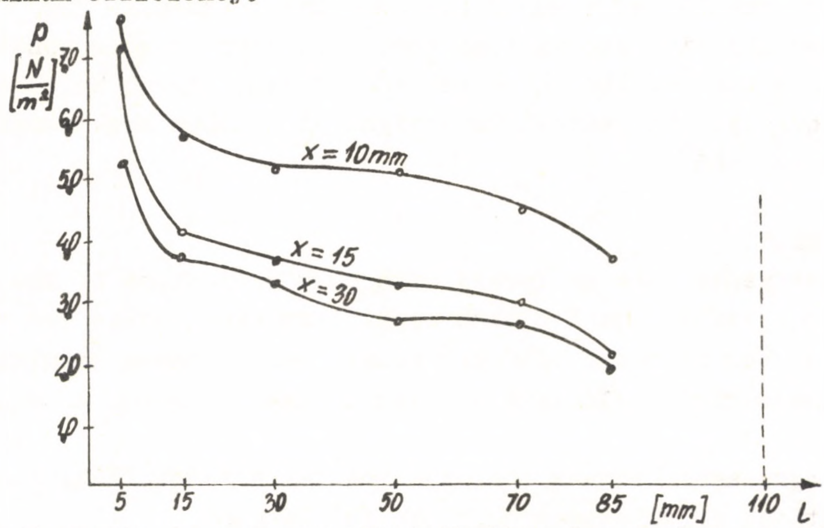

Fig.7. Unsteady pressure distribution for various spacing "x" /the rest parameters as abowe/.

The change in the amplitudes of the fluctuating pressure with variation of the spacing x is shown in Fig.7. On the stator blade /Fig.2/ the fluctuating pressure becomes smaller rapidly with an increase of x.

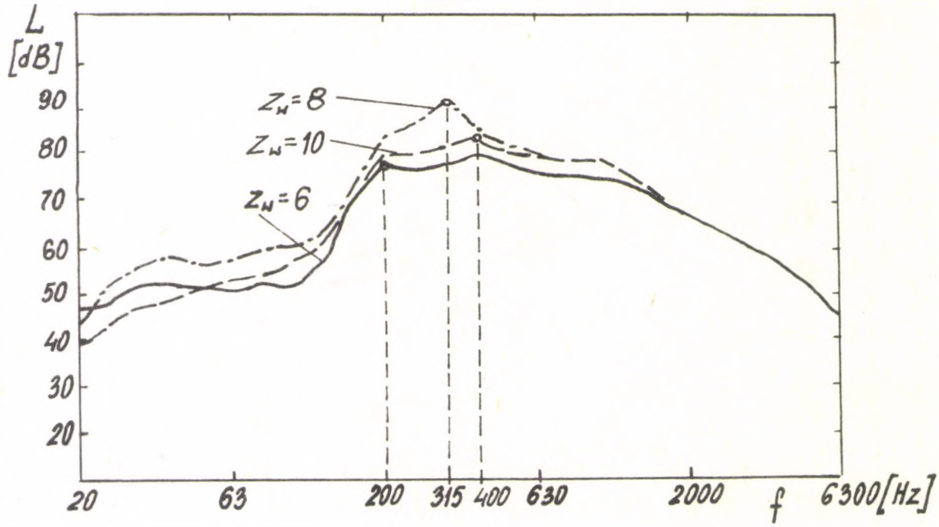

Fig.8. Measured frequency spectrum of the sound pressure level for various number of rotor blades /parameters as in Fig. 4 /.

From the results of a sound pressure level shown in Fig.8 it is found that the use various number of rotor blades considerably one can reduces the magnitude of sound level by the blade frequency. Theoretical investigation to them are presented in the work [6].

CONCLUSIONS

Experiments were performed with some variations of the single stage axial flow fan with equivalent performance for various number of rotor blades. Comparisons of there results and some theoretical calculations lead to the following conclusions :

- the agreement between the experimental results /Fig.4/ and theoretical calculations [2,5] is fairly good,
- the magnitude of pressure fluctuation dependent much from blade configuration /Fig.5 and 7/,
- the relation between the flow coefficient and the unsteady

pressure shown, that the minimum of pressure magnitude is obtain by the maximum efficiency,

- the sound level is much dependent from number of rotor blades /Fig.8/. The agreement between experiment and theories [6,7,3] confirm these results.

Presented results make introduction to next works in this domain. This paper is aimed at test answering some of the major questions about unsteady flow and noise in axial flow fans.

REFERENCES

[1] HORLOCK J.H.- Fluctuating lift forces on moving through transverse and chordwise gusts, Trans.ASME, series D, vol.90, nr 4, s.494-500, 1968

[2] NAUMANN H., YEH H.- Lift and pressure fluctuation of a cambered airfoil under periodic gusts and application in turbomachinery, Trans.ASME, series A, s.1-10, 1073

[3] ISPAS I.- Beitrag zur Berechnung der reibungsfreien Unterschallströmung durch Gitter und Stuffen von Axialen Turbomaschinen mit Hilfe eines Differencenferfahren, Dissertation, Technische Hochschule Aachen, 1974

[4] ADACHI T., MURAKAMI Y.- Three-dimensional velocity distribution between stator blades and unsteady force on a blade due to passing wakes, Bull.JSME, vol.22, nr170, s.1074, 1979

[5] MURAKAMI Y., HIROSE T., ADACHI T.- Unsteady pressure on a cambered blade under periodic gusts, Bull.JSME, vol.25, nr 206, s.1252-1257, 1982

[6] JĘDRYSZEK J.- Analiza hałasu generowanego przez wentylator osiowy powstałego wskutek oddziaływania palisady łopatkowej wirnika i kierownicy, Praca doktorska, Politechnika Wrocławska, I-20, nr 220, 1976

[7] JĘDRYSZEK J.- Mathematical model of acoustics sources for rotor-stator interaction in axial flow fans, INTER-NOISE 79 vol.1, s.95, 1979

Author: JAN JĘDRYSZEK Dr Eng.
I-20, Technical University of Wrocław, POLAND
ul.Wybrzeże Wyspiańskiego 27, 50-370 WROCŁAW

COMPUTER AIDED DESIGN OF COMPRESSOR-IMPELLERS

László Kalmár

This paper deals with the numerical computation procedure suitable to design of compressor-impellers. The computation is based on the solution of the indirect problem of hydrodynamic cascade theory. The flow in the bladed space is divided into flows in part-channels. Relations suitable to compute the velocity field are derived using the potential theory for the two dimensional flow on the mean stream surface of the part-channels. Discrete points of the blade surface and the velocity and pressure distributions there - in case of inviscid flow - are determined by using an iterative method.

1. INTRODUCTION

Requirements becoming higher and higher for turbomachinery made it necessary to use design methods applying higher mathematical means. They have to meet the requirements of technical demands, too [1,2,3]. In this paper a method is shown for designing of the blades of compressor-impellers. The paper deals with the solution of the cascade flow problem. First the main dimensions of the compressors and the meridional channel are determined then approximative surfaces of revolution are produced by partitioning the meridional channel into part-channels. Along these stream surfaces the cascade flow mentioned above can be solved and profile-sections of the blade surfaces can be determined [1,7].

2. ENERGY RELATIONS IN COMPRESSORS

When designing the impeller of a compressor the energy distribution is supposed to be known in the inner parts of the compressor . By knowing this it will be possible to determine the geometric dimensions of the impeller and the main physical parameters of the flow. At first the equation can be written which represents the mechanical energy variation between the points B and K /referred to inlet and outlet branches of the compressor, respectively/ and the first law of thermodynamics [6]. When writing these two equations the variation of potential energy is ignored, furthermore the compressor will be regarded as a thermo insulated system. Thus the change of state of the gas can be regarded polytropic in the compressor. Using the above equations the change of total energy in the compressor is:

$$Y_{BK} = Y_{BK,pol} + \frac{c_B^2 - c_K^2}{2} = \frac{m}{m-1}\frac{p_B}{\varrho_B}\left[1-\left(\frac{p_K}{p_B}\right)^{\frac{m-1}{m}}\right] + \frac{c_B^2 - c_K^2}{2} \qquad (1).$$

The specific value of the polytropic work $Y_{BK,pol}$ can be expressed using absolute temperature too as:

$$Y_{BK,pol} = \frac{m}{m-1} R\left(T_B - T_K\right) \qquad (2).$$

The relation of theoretical energy-variation and loss per unit mass provides a possibility to determine the theoretical change of energy per unit mass. Using the above equations we can write:

$$Y_{BK,e} = h_{BK} + \frac{c_B^2 - c_K^2}{2} = \frac{\varkappa}{\varkappa - 1} R\left(T_B - T_K\right) + \frac{c_B^2 - c_K^2}{2} \qquad (3).$$

Using the polytropic equations of state h_{BK} can be expressed in another form

$$h_{BK} = \frac{\varkappa}{\varkappa - 1}\frac{p_B}{\varrho_B}\left[1-\left(\frac{p_K}{p_B}\right)^{\frac{m-1}{m}}\right] \qquad (4).$$

By using the polytropic work $Y_{BK,pol}$ and the change of enthalpy h_{BK} the polytropic efficiency η_{pol} will have the form

$$\eta_{pol} = \frac{Y_{BK,pol}}{h_{BK}} = \frac{\varkappa - 1}{\varkappa}\,\frac{m}{m-1} \qquad (5).$$

Internal flow field can be divided into three parts: the first one extends from inlet branch to impeller, the second one is the flow in impeller and the third one is the region between impeller and outlet branch. In the knowledge of the initial set of data /flow rate Q_B, pressure p_B, density ϱ_B at the inlet branch of the compressor, the pressure ratio p_K/p_B referred to branches B and K and angular speed n/ the main dimensions of the compressor and its main hydraulic properties at the branches can be determined; furthermore the energy changes occuring in the above mentioned regions can be calculated as well. The meridional channel of impeller can be plotted. After having divided the meridional channel into part-channels velocity components at the leading and trailing edges of the blades on the mean stream surfaces of the part-channels can be determined. These with geometrical parameters of part-channels constitute the initial set of data for the design method to be presented.

3. THEORETICAL BACKGROUND OF THE DETERMINATION OF BLADE-SECTIONS

The real three-dimensional flow in the bladed space of impeller is devided into flow in part-channels by surfaces of revolution coaxial with rotating axis, and two-dimensional flow on the mean stream surface /F/ of these part-channels is investigated [1].

For the two-dimensional flow on the mean surface /F/ of an arbitrary part-channel of the impeller the equation of continuity is

$$\frac{\partial}{\partial \sigma}\left(\varrho_F b_F r_F c_{F\sigma}\right)+\frac{\partial}{\partial \varphi}\left(\varrho_F b_F c_{F\varphi}\right)=r_F\,\omega\,\frac{\partial}{\partial \varphi}\left(\varrho_F b_F\right) \tag{6}$$

and the differential equation expressing the condition of vortex-free absolute flow can be written as

$$\frac{\partial}{\partial \sigma}\left(r_F c_{F\varphi}\right)-\frac{\partial c_{F\sigma}}{\partial \varphi}=0 \tag{7}$$

The third equation is the Bernoulli's equation; it runs for isentropic flow in the impeller as

$$\frac{\varkappa}{\varkappa-1}\,\frac{p_{F1}}{\varrho_{F1}}\left[\left(\frac{\varrho_F}{\varrho_{F1}}\right)^{\varkappa-1}-1\right]=\frac{c_{F1}^2-c_F^2}{2}+\left(r_F c_{F\varphi}-r_{F1} c_{F1\varphi}\right)\omega \tag{8}$$

The absolute flow in the impeller can be determined as a solution of these three equations. In order to determine functions $c_{F\sigma}$, $c_{F\varphi}$ and ϱ_F it is sufficient to use the boundary conditions at the inlet of impeller $\sigma=0$:

$$c_{F\sigma}=c_{F1\sigma}\quad ; \quad c_{F\varphi}=c_{F1\varphi}$$

and at the outlet of impeller $\sigma=\sigma_L$:

$$c_{F\sigma}=c_{F2\sigma}\quad ; \quad c_{F\varphi}=c_{F2\varphi}$$

further equs. (6), (7) and (8).

The flow on the mean surface of the part-channel /F/ is conformally transformed to the one on a complex plane (ξ, η). Since the absolute flow in this image plane remains vortex-free the velocity potential Φ can be used and the problem is

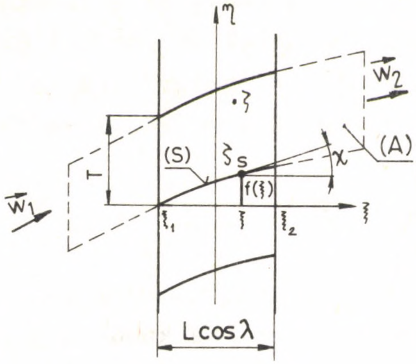

Fig. 1.

reduced to the solution of a Poisson-like partial differential equation. By using the theory of potentials the conjugate complex velocity [1] at an arbitrary point $\zeta = \xi + i\eta$ can be written as /Fig.1/.

$$\bar{C}(\zeta) = C_\xi - i\,C_\eta = \bar{C}_B(\zeta) + \bar{C}_D(\zeta) + \bar{C}_\infty \tag{9}$$

where:

$$\bar{C}_B(\zeta) = -\frac{1}{2T}\int_{(A)} \frac{1}{\varrho_F b_F}\left[w_\xi \frac{\partial}{\partial\xi}(\varrho_F b_F) + w_\eta \frac{\partial}{\partial\eta}(\varrho_F b_F)\right] \mathrm{cth}\frac{\pi}{T}(\zeta - \zeta')\,dA \tag{10}$$

$$\bar{C}_\infty = C_{\infty\xi} - i\,C_{\infty\eta} \tag{11}$$

in case of $\zeta \neq \zeta_S$:

$$\bar{C}_D(\zeta) = \frac{1}{2T}\int_{(S)} (q + i\gamma)\,\mathrm{cth}\frac{\pi}{T}(\zeta - \zeta')\,ds \tag{12.a}$$

in case of $\zeta = \zeta_S$:

$$\bar{C}_D(\zeta_S) = \pm\frac{\gamma - iq}{2}\,e^{-i\chi} + \bar{C}_E(\zeta_S) + \bar{C}_G(\zeta_S) \tag{12.b}$$

$$\bar{C}_E(\zeta_S) = \frac{1}{2\pi}\,\frac{1}{1 + i\frac{df}{d\xi}}\int_{(S)} \frac{q + i\gamma}{\xi - \xi'}\,ds = \frac{1}{1 + i\frac{df}{d\xi}}\left(C_{Eq\xi} - i\,C_{E\gamma\eta}\right) \tag{13}$$

$$\bar{C}_G(\zeta_S) = \frac{1}{2T}\int_{(S)} (q + i\gamma)\left[\mathrm{cth}\frac{\pi}{T}(\zeta_S - \zeta_S') - \frac{T}{\pi(\xi - \xi')}\,\frac{1}{1 + i\frac{df}{d\xi}}\right] ds \tag{14}$$

The upper one of the double signs refers to the suction side while the lower one to the pressure side.

The numerical solution of the indirect problem can be gained in such a way, that the skeleton-line belonging to singularity-distributions q and γ choosen suitable is determined, which is a streamline of singularity induced velocity field and at the same time it is carrying the singularities too. The determination of the singularity carrying skeleton-line is possible using the following equation

$$\frac{df}{d\xi}=\frac{c_{E\gamma\eta}+c_{G\eta}+c_{B\eta}+c_{\infty\eta}-u_{\eta}}{c_{G\xi}+c_{B\xi}+c_{\infty\xi}} \tag{15}$$

with the knowledge of velocity distribution. However the computation of velocity distribution requires the knowledge of the singularity carrying curve. It may be seen from the foregoing discussion, that the solution of the problem is possible only by an iterative procedure. At first the relative streamline of velocity field induced by singularities arranged along a curve choosen suitable must be computed, then the relative streamline of the new velocity field induced by singularities transformed to the above mentioned curve is to be determined. This computation procedure is to be repeated until the singularity carrying curve and the relative streamline induced by singularities arranged on it coincide with each other with prescribed accuracy. If the iteration's condition is fulfilled then the distributions of the physical characteristics along the skeleton-line can be calculated. At first the relative velocity distribution is computed along the skeleton-line on the basis of expression

$$\frac{w_S}{c_m}=\frac{1}{\sqrt{1+\left(\frac{df}{d\xi}\right)^2}}\left[\frac{c_{Eq\xi}}{c_m}+\frac{c_{G\xi}}{c_m}+\frac{c_{B\xi}}{c_m}+\frac{c_{\infty\xi}}{c_m}+\left(\frac{c_{G\eta}}{c_m}+\frac{c_{B\eta}}{c_m}+\frac{c_{\infty\eta}}{c_m}-\frac{u_{\eta}}{c_m}\right)\frac{df}{d\xi}\pm\frac{\gamma}{2c_m}\sqrt{1+\left(\frac{df}{d\xi}\right)^2}\right] \tag{16}$$

where: u_{η} the peripheral velocity in image-plane,

c_m the outlet meridional velocity in image-plane.

The dimensionless thickness distribution of the aerofoil section on image-plane is determined on the basis of the equation of continuity referring to the flow inside the profile

$$\delta_K(\xi)=\frac{1}{2}\,\frac{c_m}{w_S}\,\frac{\rho_{F2}}{\rho_F}\,\frac{b_{F2}}{b_F}\int_{\xi_1}^{\xi}\frac{q}{c_m}\sqrt{1+\left(\frac{df}{d\xi}\right)^2}\,\frac{\rho_F}{\rho_{F2}}\,\frac{b_F}{b_{F2}}\,d\xi' \tag{17}$$

Herewith the computations to be done during the design procedure on the image-plane are completed. Now the results obtained must be retransformed to the mean stream surface of the part-channel. The skeleton-line can be transformed in the following form

$$\varphi_F(\sigma) = a_L \frac{f(\xi)}{L\cos\lambda} \tag{18}$$

The profile thickness d_{FK} to be measured on the surface /F/ can be determined by

$$d_{FK}(\sigma) = a_L r_F \frac{\delta_K(\xi)}{L\cos\lambda} \qquad \left(\text{where}: a_L = \int_0^{\sigma_L} \frac{d\sigma}{r_F}\right) \tag{19}$$

while the contour velocity w_{FK} can be written as

$$\frac{w_{FK}}{c_{F2\sigma}}(\sigma) = \frac{r_{F2}}{r_F} \frac{1}{\sqrt{1+\left[\frac{d}{ds}(\delta_K)\right]^2}} \frac{w_S}{c_m} \tag{20}$$

Finally - by means of quantities at the inlet and an arbitrary sections of the part-channel - the pressure distribution at the suction and pressure side of the blade surface can be calculated by

$$\frac{p_F}{p_{F1}}(\sigma) = \left[1 + \frac{\varkappa-1}{\varkappa} \frac{\varrho_{F1}}{p_{F1}} \frac{w_{F1}^2}{2} \bar{p}_F(\sigma)\right]^{\frac{\varkappa}{\varkappa-1}} \tag{21}$$

where:

$$\bar{p}_F(\sigma) = 1 - \left(\frac{w_{FK}}{w_{F1}}\right)^2 + \left[\left(\frac{r_F}{r_{F2}}\right)^2 - \left(\frac{r_{F1}}{r_{F2}}\right)^2\right]\left(\frac{r_{F2}\omega}{w_{F1}}\right)^2$$

Herewith we came to the end of the numerical solution of indirect problem of the cascade theory. Carrying out the presented computational procedure for all of the part-channels the blade surface can be drawn up. The velocity and pressure distribution - in case of inviscid flow - is also available at the points of blade surface.

4. EXAMPLE OF APPLICATION FOR THE NUMERICAL EXECUTION OF THE DESIGN PROCEDURE

Initial data of the compressor to be designed are as follows:

Q_B=4,7 m³/s; ϱ_B=1,2 kg/m³; p_B=10^5Pa; p_K/p_B=2,6; n=14000 r.p.m.

Using the above values the main dimensions of the impeller can be determined and the meridional channel can be drawn up. The meridional channel of the impeller is regarded as only one part-channel. Blade sections obtained as results of the computation and the meridional section of the impeller are drawn up in Fig.2. The velocity and pressure distributions

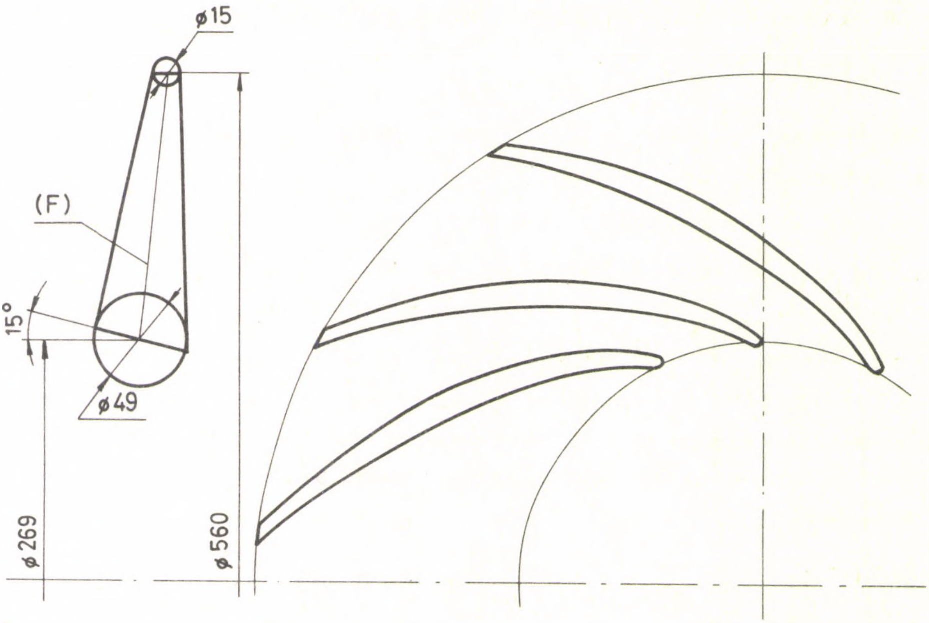

Fig. 2.

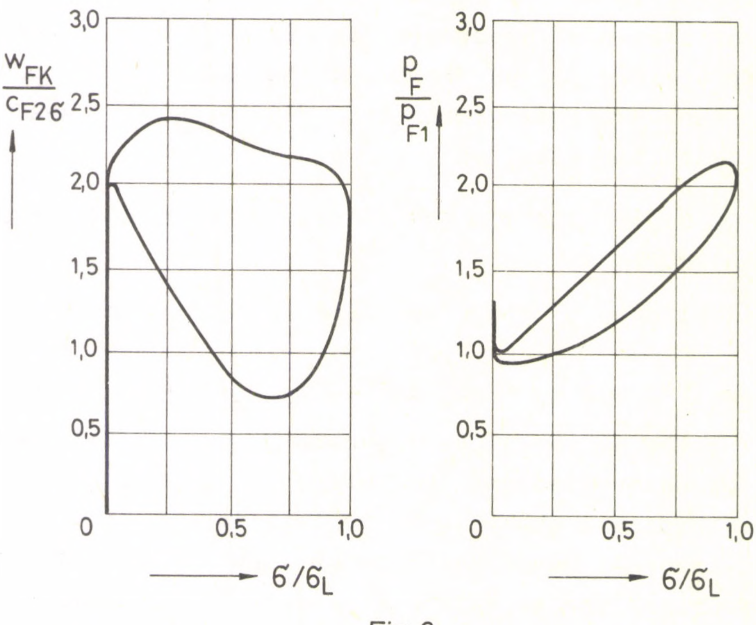

Fig. 3.

- in case of inviscid flow - at the points of blade section along surface /F/ can be seen on Fig.3.

REFERENCES

1 Czibere,T.: Solution of the Two Main Problems of the Hydrodynamic Cascade Theory by the Theory of Potentials
Thesis for D.Sc. Miskolc, 1965.

2 Wu, Ch.H.: A General Theory of Three-Dimensional Flow in Subsonic and Supersonic Turbomachines of Axial, Radial and Mixed Flow Types
Transactions of the ASME /1962/

3 Nyiri,A.: Potential Flow around Blades of Hydraulic Machines. The Second International ISME Symp. Tokyo /1972/

4 Eckert,B.: Axialkompressoren and radialkompressoren
Springer Verl. Berlin /Göttingen/ Heidelberg /1953/

5 Füzy,O.: Design of mixed flow impellers
Periodica Techn. /1962/

6 Czibere,T.: Fluid Mechanics
Tankönyvkiadó, Budapest /198o/

7 Kalmár,L.: Computer Aided Design of Turbomachines Handling Compressible Medium
Techn. Dr. Thesis Miskolc /1981/

Dr. László KALMÁR
Department of Fluid Mechanics and Heat Engineering
Technical University for Heavy Industry
H 3515 Miskolc - Egyetemváros

THE USE OF SURFACE APPROXIMATION IN PROCESSING OF WATER TURBINE TEST RESULTS

Vladimir Kercan

John Shawe Taylor

SUMMARY

This report deals with the possibility of approximation of measuring results distributed in space. The computer programme has been worked out to approximate the surface which should be used particularly for the computation the efficiency results of hydraulic machines.
The method is based on the principle of local approximation with second power polynomial and pondered function. By testing the programme for efficiency, the arbitrary use of method and its application for approximation of the other hydraulic and geometric parameters was ascertained.

1. INTRODUCTION

The use of process computers enabled tremendous development of the methods and the quality in testing the water turbines. All leading world turbine manufacturers, due to market competition, have placed great emphasis on the development, the equipment and introducing modern methods into their research institutions. The first stage of test rig modernization and the use of the computers enable very quick and reliable measurement of hydraulic, energy, cavitation and dynamic turbine characteristics with manifold increased number of measured data. In the second stage of the computer use the basic emphasis has been placed on the quick and qualitative processing of measured data by means of the method of numeric mathematics.

The use of numeric mathematics in the plane applied whether in the approximation, the interpolation, the numeric integration or any other process has many years' tradition. In all advanced research institutions the processing of measuring results is carried out by means of well known method of mathematic statistics and by method of numeric mathematics. The use of numeric methods in three dimensional distribution of test results is making its first steps and has since experienced the first success regardless the numerous possibilities tendered. Since all water turbine (hydraulic machines) characteristics are part of a certain surface, whatever the form, somehow, there has been an intention in the Institute for a long time that the processing of three dimensional distribution of test results should be computer aided.

Although there are several suitable approaches to three dimensional distribution of processing test results, the approach has been chosen which is applicable to the most various surfaces. Therefore, it has to be taken into account the fact, that measurement results of turbine characteristics should be very accurate and consequently, also the approximation of results must be accurate, particularly, in the vicinity of the optimum. To satisfy this requirement the method of partial (local) approximation has to be used what advantages express in measuring results with small error while it requires time - consuming computer with large memory.

The research of hydraulic machine characteristics is completed by defining the surface characteristics. Since three dimensional distribution cannot be presented in a plane, the isolines drawing is used what presents the section of the plane pa rallel to the coordinate plane and the surface itself. Thus the known topographic diagram is obtained when the isolines of constant efficiency are drawn. In the same diagram the turbine geometry is defined by opening of guide vane apparatus just as well as determined by the surface. Besides, the surface of power, axial forces, radial forces, critical cavitation, the torque, the amplitude and the frequency of pressure oscillation, etc, should be added. All these are surfaces of turbine behaviour at different running conditions. Although they can be hand - drawn, the development of computer - aided techniques for isolines drawing have been undertaken due to its objectivity and the speed of processing of measuring results.

2. SELECTION OF APPROXIMATION FUNCTION

Though there are several possibilities in selecting the approximation function according to the type or the form due to certain advantages, the polynomial function was accepted [1].

$$z = f(x, y) = ax^2 + bxy + cy^2 + dx + ey + f \qquad 1$$

Owing to the requirement for the most accurate approximation possible (local approximation) and because the measurement results are obtained with a certain error, the pondered function has been introduced and defined

$$w(x, y) = \begin{cases} 0 & d > r_x \\ \left(\dfrac{d - r_x}{d + d_w}\right)^2 & d \leq r_x \end{cases} \qquad 2$$

Outside the region defined by r_x the pondered function has the value 0 or in other words, in approximation only the points within the region r_x are taken into account. In Fig. 1 the parameters x_i, y_i are drawn being the values of a set of measured results and also the parameter r_x is denoted. As an input data it is inserted into the programme and it is so defined that x - coordinate scale is valid for it.
Since the greater emphasis has been placed on the points in the close proximity of the approximating point, the parameter r_x must be smaller.

The parameter d_w depends on the accuracy of the data being treated. At very accurate data $d_w = 0$ is chosen. In this instance, each point measured appears on the approximation plane, as the pondered function for $d_w = 0$ takes up the infinite value.

As the data are less accurate for d_w greater value should be taken, what allows larger discrepancy between the measured value and the approximated one. The value d defines the distance of the measuring point x_i, y_i from the point where the approximation is calculated while x, y is calculated by simple expression

$$d_i = \sqrt{(x_i - x)^2 + (y_i - y)^2} \qquad 3$$

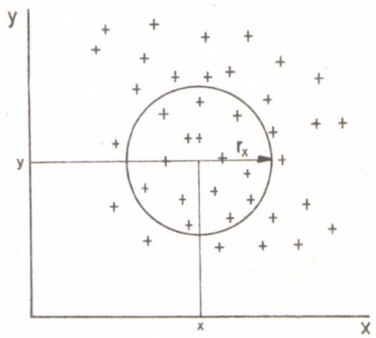

Fig. 1 Series of data to be approximated. r_x - radius of range of points taken into account for approximation.

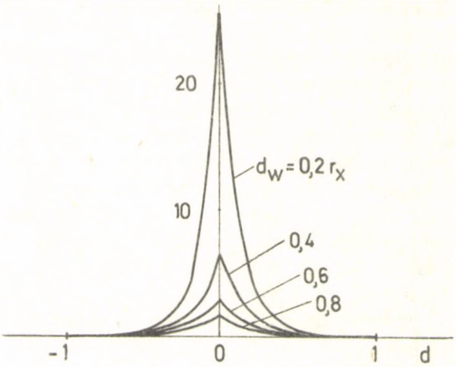

Fig. 2 Form and size of ponder function for various values of d_w.

For better appreciation the pondered function is drawn in Fig. 2. Evidently, the function is more.pointed and gaining all the greater value for d = 0, the smaller is d_w. The pointed pondered curve gives and exerts great influence of the points in the close proximity, what is favourable in case the data are reliable while it is absolutely unacceptable if the data are measured uncertainly. Too wide curve presents another extreme. Even in long distance from the approximating point, the errors in individual measuring points reflect on the approximation too much. The most acceptable solution is a compromise, therefore, the values d_w and r_x should be determined by experience.

By pondered function w_i the value of approximating function is calculated by the expression

$$Z(x, y) = \frac{\sum_{i=1}^{N} w_i\, z(x_i, y_i)}{\sum_{i=1}^{N} w_i} \qquad 4$$

where N denotes the number of measuring points. Actually, only the number of points within the radius r_x make sense, while out of it, the pondered function is equal to 0.

Unknown coefficients a, b, c, d, e and f from the equation 1 are determined by the method of least squares. Minimizing the expression

$$\phi = \sum_{i=1}^{N} w_i \left[ax_i^2 + bx_iy_i + cy_i^2 + dx_i + ey_i + f - z_i \right]^2 \qquad 5$$

leads to the system of linear equations wherefrom the coefficients are simply derived. The system of equations can be written in matric form

$$c \cdot x = K \qquad 6$$

where x - vector containing unknowns (coefficients) a, b, c, d, e and f
K - vector containing constant parts of the right side of equation
c - matrix of unknown coefficients

There is no problem to solve the system of linear equations, however, the problem is encountered at the computer-aided drawing of the isolines. The isoline level is set into the main programme as an input data. In order to enable the start of isoline drawing it is necessary to find one point on it. For this purpose over the region of measuring points a grid is set which is defined by a minimum and a maximum value of x and y and by number of partitions by x and y (Fig. 3).

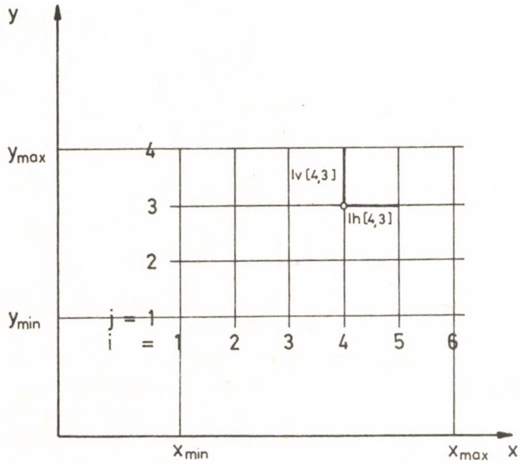

Fig. 3 Test grid

By lh [i, j] and lv [i, j] the grid joints are defined in the horizontal and the vertical directions. By the programme LOCATE for the chosen isoline level the point on the joint lv i, j or lh i, j of the same level is to be found. When the first isoline point is found by the subprogramme ROTATE the isoline direction in starting point is determined. The drawing of isoline is computer aided by subprogramme FOLCONTOUR and thus that by the iteration process the actual isoline position is determined until it is in starting point concluded in itself. In case the isoline reaches the edge of the diagram, the subprogramme FOLCONTOUR begins from the starting point but in the opposite direction from the previous one. When all the isolines are drawn whose main programme data required by the subprogramme VRH the maximum of surface is being determined (if it exists).

3. APPLICATION OF SURFACE APPROXIMATION ON MEASUREMENT RESULTS OF ENERGY CHARACTERISTICS

Topographic turbine diagram by which its energy characteristics are defined presents the hill mapped in the plane which form is changing according to the fuction of type and quality of tested turbine. In order to enable to form an opinion about the quality of approximation and about the deviation of hand - drawn isolines and the computer - aided ones, the measurement results of a bulb turbine runner are specially analysed in detail. From the measured data the flowrate coefficient, the specific energy coefficient and the efficiency values have been calculated.

In the Institute there has been common practice to present turbine characteristics in $\varphi - \psi$ coordinate system (φ - flowrate coefficient, ψ - head coefficient or energy coefficient) though the programme is applicable to any other way of presenting the energy characteristics - Q - H system, N_{II} - Q_{II} system etc.

The measured and calculated values respectively, 103 of them have been measured for topographic diagram, present a series of data in φ (x), ψ (y), η (z) coordinate system. Using the auxiliary cross-sections, the topographic turbine diagram shown in Fig. 4 is hand - drawn while the diagram in Fig. 5 is obtained by means of the approximation described in previous chapter. The analysis of approximation accuracy is carried out on the basis of comparison of measured efficiency

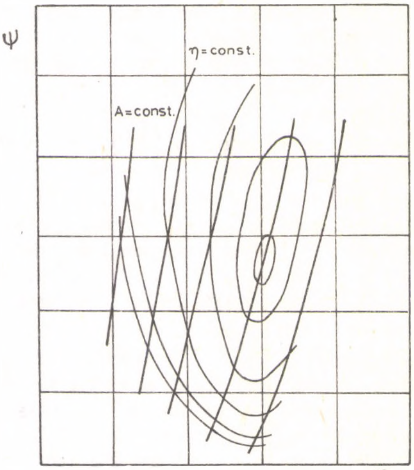

Fig. 4 Computer - drawn topographic turbine diagram

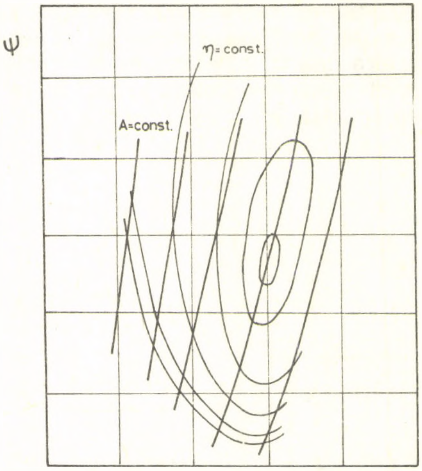

Fig. 5 Hand - drawn topographic turbine diagram

and the efficiency determined by the approximation function in the same points. The results of analysis of accuracy are shown in Table 1. In the analysis of accuracy the well known parameters of the theory of errors are taken into consideration. The average deviation value of approximated and measured value defined by the expression

$$\Delta\bar{\eta} = \frac{\sum_{i=1}^{N} (\eta_{APP} - \eta_{MEA})_i}{N} \qquad 8$$

indicates whether the approximation gives the greater of less efficiency values than the measured one. Mean square deviation of single point (standard deviation)

Table 1: The analysis of accuracy of surface approximation efficiency

Number of points	All points	Points $\eta > 0{,}75$	Points $\eta > 0{,}80$
N	103	31	13
σ	0,011925	0,009824	0,008385
σ_A	0,001181	0,001764	0,002326
$\Delta\bar{\eta}$	-0,001266	-0,000415	-0,005344

$$\sigma = \left[\frac{\sum_{i=1}^{N} \left[(\eta_{APP} - \eta_{MEA})_i - \Delta\bar{\eta} \right]^2}{N-1} \right]^{1/2} \qquad 9$$

and the deviation of real from the most probable value of difference $\Delta\eta_i$

$$\sigma_A = \frac{\sigma}{\sqrt{N}} \qquad 10$$

give sufficient arguments for the conclusion about the quality of approximation. On the basis of results from the Table 1, it is evident that the diagram by the approximation function is very precisely drawn. It can be concluded

1. the approximation function, as a rule, gives somewhat lower efficiency values than the measured ones. Irrespective of this small difference (it is merely - 0,12 % for all 103 points) it obviously increases in the proximity of the optimum and it reaches the value of - 0,5 % for the efficiency $\eta > 0{,}8$. This is rather unwelcome fact regarding that the accuracy of approximation is the most

claimed for just about the proximity of the optimum. This problem is being successfully solved by changing r_x parameter, particularly, by its continued increasing in the function of moving from the optimum.

2. Mean square deviation of the approximation efficiency from the measured one (σ_A) is very small, of order 0,1 ... 0,2 % what is very favourable as the measurement accuracy is $\approx$ 0,3 ... 0,4 %.

In addition to the analysis of approximation accuracy also the analysis of the influence of measuring results accuracy on the topographic diagram form was made. Further, the influence of eliminating the suspected incorrectly measured points, the effect of number of measuring points on the form and diagram accuracy were analysed. The results of the analyses accomplished have been already used a great deal in processing the results of model turbine tests in the Institute.

4. OTHER APPLICATIONS OF SURFACE APPROXIMATION

The surface approximation programme has been analysed from all points of view also on the other three dimensional distribution measurement results in order to ascertain its general application.

The surface geometry of guide vane apparatus in $\varphi - \psi$ coordinate system is a smooth uniform surface, essentially different from the surface efficiency. There has been no problem of drawing the section of this surface with the planes parallel to the coordinate plane (isolines). By the analysis of drawn isolines it has been established that they are drawn very precisely compared to the hand - drawn ones. Therefore, the programme can be very successfuly applied to smooth, uniform surfaces without the maximum what has been perfectly confirmed in drawing the surface of critical cavitation coefficient and the surface of Kaplan turbine blade. For the illustration of the results acquired, in Figs. 6 and 7 the surface geometry of guide vane apparatus has been drawn by hand (dotted line) and computer - aided respectively (full line) as well as the surface of critical cavitation coefficient.

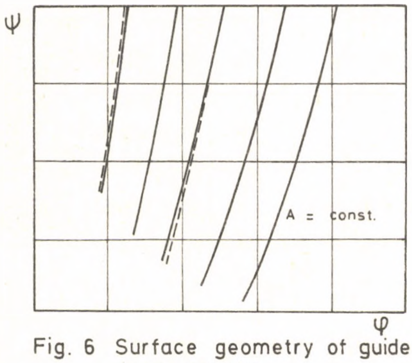

Fig. 6 Surface geometry of guide vane aparatur

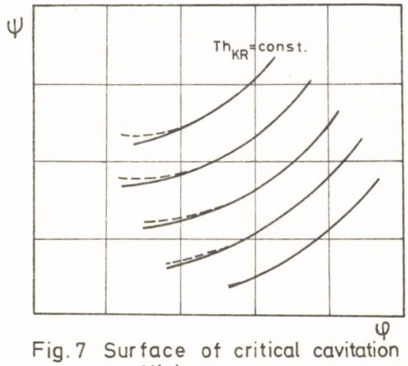

Fig. 7 Surface of critical cavitation coefficient

Computer - aided drawing of topographic diagram enable very simple presenting of characteristics in different coordinate systems. For the analysis of a turbine machine behaviour at certain running conditions many - sided knowledge of its characteristics is necessary. Although the measuring data might be the same the diagram form essentially depends on the choice of the coordinate system as well as the possibility of application of individual way of presentation. Thus, the turbine characteristics presentation in $\varepsilon - \vartheta$ coordinate system is very convenient for the analysis of turbine operation at various heads or constant speed of rotation. In case the turbine head is constant while the speed is changing it is more reasonable the presentation of characteristics in $\varphi - \psi$ system. Finally, if the characteristics are measured in several quadrants and it is necessary to approximate them by certain curve due to computer - aided calculation of water hammer, they are best presented in Suter's coordinate system. Among the before mentioned parameters there exists a relation for surface approximation application, so, it is very simple to show desired characteristics in different systems.

As for the illustration the measurement results are shown in detail for one Kaplan turbine runner diagram. The characteristic parameters relation in individual coordinate system is shown in the Table II. The computer - aided graphs by programme HRIB are presented in Fig. 8, for the same input data. All the graphs are drawn thus as first the surface geometry of guide vane apparatus is set (curve A = const.) and afterwards still the torque, axial force or the efficiency isolines are drawn. It is far easier to reach the optimum use of measuring results if the designer or turbine user is furnished with all graphs available. Hand drawing of all graphs for only one Kaplan turbine runner presents too trying, time - consuming and expensive process and, as a rule, practically not in use. The computer aided process is shortened to a few minutes.

It is worth mentioning that for the use of HRIB programme some experience is needed. Owing to the principle of local approximation application, the programme is rather sensitive to greater unaccuracy of individual point, therefore, the selection of r_x and d_w parameters should be optimized. The speed of gaining and graph drawing respectively enable quick time - saving optimisation of selected parameters r_x and d_w and the boundary points of the diagram.

Table II : Interrelation of parameters in different coordinate systems

			System		
			D, N	D, E	Suter
System	D, N	Flowrate coefficient	$\varphi = \frac{Q}{\pi^2/4\ N\ D^3}$	$\varphi = \frac{\varepsilon}{\vartheta}$	$\Theta = \pi + \arctan(\frac{\varphi}{\varphi_o})$
		Specific energy coefficient	$\psi = \frac{E}{\pi^2/2\ N^2 D^2}$	$\psi = \frac{1}{\vartheta^2}$	$W_\psi = \mathrm{sign}(\psi)\sqrt{\frac{\psi/\psi_o}{1+(\varphi/\varphi_o)^2}}$
		Torque coefficient	$\mu = \frac{M}{\rho\pi^3/8\ N^2 D^5}$	$\mu = \frac{\xi_M}{\vartheta^2}$	$W_\mu = \mathrm{sign}(\mu)\sqrt{\frac{\mu/\mu_o}{1+(\varphi/\varphi_o)^2}}$
		Force coefficient	$\sigma = \frac{F}{\rho\pi^3/8\ N^2 D^4}$	$\sigma = \frac{\xi_F}{\vartheta^2}$	$W_\sigma = \mathrm{sign}(\sigma)\sqrt{\frac{\sigma/\sigma_o}{1+(\varphi/\varphi_o)^2}}$
	D, E	Specific flowrate	$\varepsilon = \frac{\varphi}{\sqrt{\psi}}$	$\varepsilon = \frac{Q}{D^2\pi/4\ \sqrt{2E}}$	
		Specific rotational speed	$\vartheta = \frac{1}{\sqrt{\psi}}$	$\vartheta = \frac{N\ D\ \pi}{\sqrt{2E}}$	
		Specific torque	$\xi_M = \frac{\mu}{\psi}$	$\xi_M = \frac{M}{\rho\ D^3\pi/4\ E}$	
		Specific force	$\xi_F = \frac{\sigma}{\psi}$	$\xi_F = \frac{F}{\rho\ D^2\pi/4\ E}$	
N [s^{-1}], D [m], E [Jkg^{-1}], Q [$m^3 s^{-1}$], M [Nm], ρ [kgm^{-3}]					

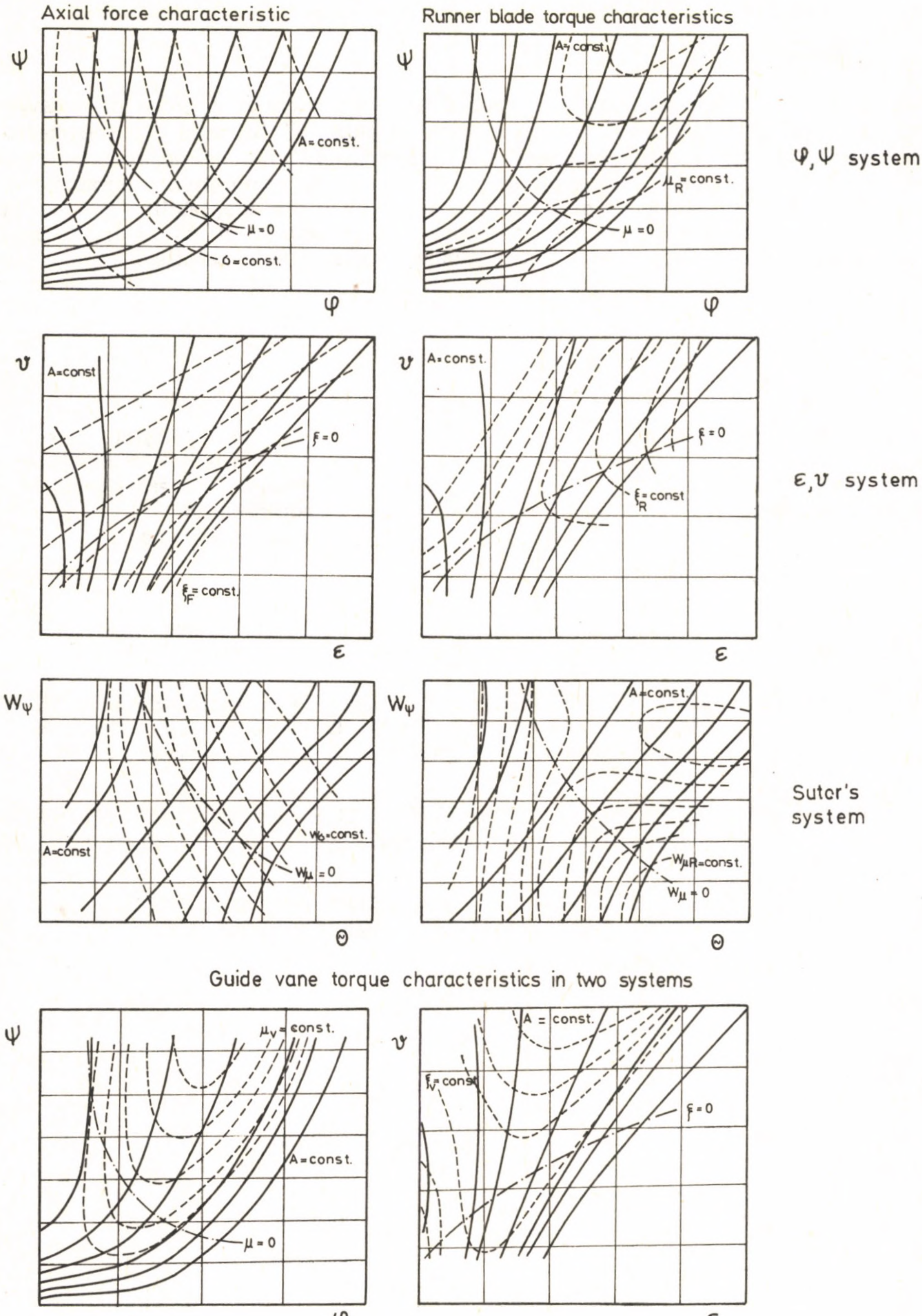

Fig. 8 Computer - aided graphs for the same input data (A - oppening of guide vane aparatus)

5. CONCLUSION

Although the problem of three dimensional approximation of a series of measured data has been tackled in the first place because of the need and the desire to approximate the surface efficiency of water turbine, the developed programme has shown considerably wider application. The basic approximation programme characteristics: the speed of drawing, the accuracy, the adaptability and the application for the most various surfaces show the possibility of its wider use in processing of three dimensional distribution of measurement results.

Vladimir KERCAN, M. sc.
Turboinštitut
Rovšnikova 7
61 210 Ljubljana

John Shawe Taylor, B. sc.
FNT, Matematika in Mehanika
Univerza "Edvard Kardelj"
Jadranska 19
61 000 Ljubljana

REFERENCES

1 V. KERCAN: SURFACE APPROXIMATION OF MEASURING RESULTS WITH EMPHASIS ON MEASUREMENT OF HYDRAULIC MACHINE CHARACTERISTICS, Turboinštitut, Internal Report No 1401, Ljubljana 1980

2 J. G. HAYES: NUMERICAL METHODS FOR CURVE AND SURFACE FITTING, National Physical Laboratory Report, NAC 50, April 1974, p. 34

3 C. W. CLENSHAW, J. G. HAYES: CURVE AND SURFACE FITTING, National Physical Laboratory, J. Inst. Maths Applics, 1965, 1, p. 164 - 183

UNSTEADY FLOW OF LIQUID IN A VISCO-ELASTIC PRESSURE PIPELINE

M.G. Khublaryan

The Institute of Water Problems, USSR
ACADEMY OF SCIENCES, Moscow, U.S.S.R.

Whereas a huge amount of works have been devoted to investigation of unsteady flow of liquid in pipes made of elastic materials there have been very few dealing with viscoelastic pipes. The latter do play an important part in industry, especially in construction, hydraulic engineering and machine-building where components made of polymer materials have been used on an ever increasing scale. By taking into account the viscoelastic properties of a material the engineer is able to design a structure without an excessive safety margin and thereby reduce its weight and cost.

The present paper is devoted to an investigation of unsteady motion of liquid in cylindrical pipes of both constant and variable cross-section, including flows in permeable pipes.

In the linear viscoelasticity theory the relationship between the stress (σ) and strain (ε) is expressed by a linear differential equation of the form:

$$a_0\sigma + a_1\dot{\sigma} + a_2\ddot{\sigma} + \cdots a_m\sigma^{(m)} = b_0\varepsilon + b_1\dot{\varepsilon} + b_2\ddot{\varepsilon} + \cdots + b_n\varepsilon^{(n)} \tag{1}$$

where $\dot{\sigma}, \ddot{\sigma}, \cdots \sigma^{(m)}, \dot{\varepsilon}, \ddot{\varepsilon}, \cdots \varepsilon^{(n)}$ are derivatives with respect to time t.

Equating to zero one or another pair of coefficients (a_i, b_i) of eq. (1) one obtains all the known rheological relationships. It can be easily seen that if an equation of the general form (1) is used for relating stresses and strains in viscoelastic media, the order of equation becomes higher on the one hand and each model will require a problem formulation and solution of its own. In view of the foregoing, we are using the hereditary theory of Boltzmann-Volterre in this work, which is equivalent to the differential equation (1) and describes with sufficient accuracy the strength characteristics of many polymer materials and metals.

Then we have

$$\varepsilon = G^*\sigma \tag{2}$$

where G^* is a linear integral operator:

$$G^*(\sigma) = G\left[\sigma(t) + \nu_\sigma \int_0^t G(t-\tau)\,\sigma(\tau)\,d\tau\right] \tag{3}$$

where $G = 1/E$ is the reciprocal of elasticity modulus,
ν_σ is the modulus defect,
$G(t)$ is the integral retardation nucleus.

Limiting consideration to the region of small deformations only, we have for the cross-sectional area:

$$f = f_0 \left(1 + 2\frac{r}{R_0}\right) = f_0 (1 + 2\varepsilon) \tag{4}$$

where f is cross-sectional area,
r is displacement of the initial radius R_0.

In accordance with (2) and (4), we have

$$\frac{f - f_0}{2 f_0} = G^* \sigma \tag{5}$$

For a thin-wall pipe of thickness δ_0, using the approximate equality

$$\sigma = \frac{P - P_0}{\delta_0} R_0 \tag{6}$$

we can write the formula 5 in the form:

$$f - f_0 = \frac{2 f_0 R_0}{\delta_0} G^* (P - P_0) \tag{7}$$

Here, P is mean pressure over the cross-section,
f_0 is cross-sectional area under pressure P_0.

After conventional assumptions and linearization, the differential equations for subsonic flow of a mobile liquid in pipeline and the continuity equation become:

$$-f_0 \frac{\partial P}{\partial x} = \frac{\partial M}{\partial t} + 2aM \tag{8}$$

$$\frac{\partial}{\partial t}(f\rho) + \frac{\partial M}{\partial x} = 0 \tag{9}$$

$$\rho = \rho_0 \left(1 + \frac{P - P_0}{K_m}\right) \tag{10}$$

where a is the reduced coefficient of linear friction of liquid

$$2a = \frac{1}{4}(\lambda V R_0^{-1}) = const.$$

K_m is the dilatation modulus of liquid,

$M = \int\limits_f \rho V dt$ is mass flow rate,

ρ is liquid density,
V is velocity average over a cross-section,
ρ_0 is liquid density at pressure P_0,
λ is friction loss.

Using eqs. (7) and (10) and ignoring, as we do in case of elastic pipes, the terms $2R_0(P-P_0)G^*(P-P_0)K_m^{-1}\delta_0^{-1}$, we reduce eq. (9) to the form:

$$\rho_0 f_0 \left(\frac{1}{K_m}\frac{\partial P}{\partial t} + \frac{2R_0}{\delta_0} G^* \frac{\partial P}{\partial t} \right) = -\frac{\partial M}{\partial x} \tag{11}$$

We have thus obtained a set of eqs. (8), (11) for finding the unknown functions P and M.

Consider now specific problems and examples.

1.- Liquid flow in short impermeable cylindrical pipes:
The initial conditions:

$$t = 0; \qquad M = 0; \qquad P = 0 \tag{12}$$

boundary conditions:

$$x = 0 \qquad P = \varphi(t)$$

$$x = \ell \qquad M + h\frac{\partial M}{\partial x} = \psi(t) \tag{13}$$

where $\varphi(t)$ and $\psi(t)$ are known prescribed functions of time,
h is a positive parameter representative of the liquid flow rate control.

The set of eqs. (8), (11) was solved, under the conditions (12) and (13), with the help of the Laplace transform.

Various models are used to simulate polymeric materials (such as Maxwell, Voigt, standard linear body, and other models). For instance, in the Maxwell model the solution of the problem (8), (11), (12) and (13) for P has the form /1/:

$$P(x,t) = \frac{f_0 \cdot B \cdot \theta\,[ch\,\theta(\ell - x) + h\,sh\,\theta(\ell - x)] - 2aA\,ch\,\theta x}{f_0\,\theta\,(ch\,\theta\ell + h\,sh\,\theta\ell)} -$$

$$-2e^{-(a+æ)t}\left\{B\sum_{n=1}^{\infty}\frac{\mu_n[(aæ)\sin\xi_n t + \xi_n\cos\xi_n t][\cos\mu_n(\ell-x) + h\mu_n\sin\mu_n(\ell-x)]}{\xi_n(\mu_n^2+\theta^2)[\ell + h + \ell(h\mu_n)^2]\sin\mu_n\ell} +\right.$$

$$\left.+\frac{A}{f_0}\sum_{n=1}^{\infty}\frac{[(a^2 - \xi_n^2 - æ^2)\sin\xi_n t + 2a\,\xi_n\cos\xi_n t]\sin\mu_n x}{\xi_n(\mu_n^2+\theta^2)[\ell + h + \ell(h\mu_n)^2]\sin\mu_n\ell}\right\}$$

where μ_n are the roots of equation $h\mu\,tg\,\mu\ell = 1$

$$\theta = 2\sqrt{ad\alpha}\,,\quad \xi_n = \sqrt{c^2\mu_n^2 - (a - æ)^2}\,,\quad æ = dc^2\alpha\,,\quad \alpha = \frac{1}{n}$$

$d = \rho R_0 \delta_0^{-1} E^{-1}$, C-is sound velocity in the medium.

It was assumed here that $\varphi(t) = B = \mathrm{const}$; $\psi(t) = A = \mathrm{const}$.

In cases where the boundary conditions for eqs. (8), (11) are functions of time, we may take into account that the boundary-value problem is linear and use the Duhamel integral permitting to apply boundary conditions expressed in terms of time functions instead of discontinuous conditions.

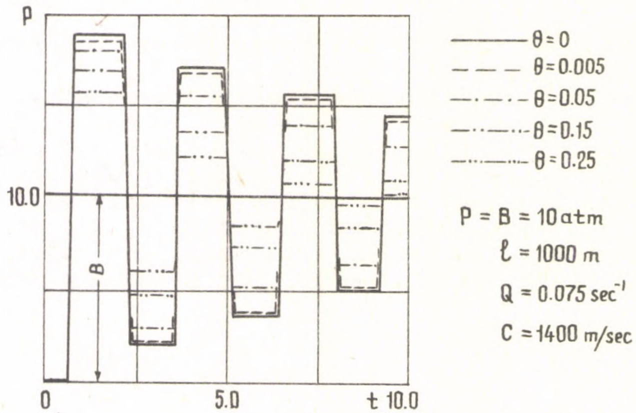

Fig. 1 shows curves of pressure variation in a viscoelastic pipe after a hydraulic shock. The calculation was for h = 0. The curves make it apparent that the hereditary properties of material considerably affect the unsteady process. In certain cases the hereditary properties of the material attenuated the wave process greater than the friction losses did. If we, furthermore, remember that mostly short pipes are used for machine-building applications, we may, in certain cases, ignore the friction term.

2.- Motion of liquid in a variable cross-section pipe.

In this case the pipe diameter is variable, i.e. R and f are functions of X. Analytical quadrature solutions may be obtained for the case of $K_m G \ll 1$ which is true for polymer pipes and when the wall thickness or elastic properties of the material vary in proportion with the diameter.

3.- Motion of liquid in a permeable pipe.

In practice it is often necessary to use porous or perforated pipes. In this case the liquid flow rate is variable along the liquid path. Many works have been published discussing the steady-state flow of liquid at a variable rate through pressure pipelines. In these works the motion equation was usually derived in accordance with the variable-mass body theory developed by I.V. Meshchersky. In /2/ it was shown that it was very convenient to determine the control of liquid flow in pipes with a variable flow rate along the path by averaging the hydrodynamic equations written in a cylindrical coordinate system x, r over the flow cross-section. In the general case of constant diameter permeable pipes these equations have the form:

$$\rho\left(\frac{\partial u f}{\partial t} + u\frac{\partial \alpha u f}{\partial x}\right) = \rho F_x f - f\frac{\partial p}{\partial x} - \frac{\lambda u|u|}{8\delta}\rho f - 2\pi\rho R V_{xR} V_R$$

$$\frac{\partial \rho f}{\partial t} + \frac{\partial \rho u f}{\partial x} = -2\pi\rho R V_R \qquad (15)$$

It was assumed that $V_R = 0$, for $r = 0$; $V_r = V_R$; $V_x = V_{xR}$ for $r = R$.

The above case is that of drain. In case of supply the lateral velocity has the negative sign and, therefore, in (15) the signs of the V_R-containing terms will be reversed. To simplify and linearize the equations we will use a number of assumptions in what follows. For example, we assume that $V_{xR} = 0$, i.e. that the liquid is drained at 90°, the convection term in the unsteady-state equation is negligibly small and that the friction term is linearized.

The flow in a polymer pipe is studied under two different conditions: when the drain rate is a constant value and when it is a first-order function of pressure (the case of porous pipe the flow in which follows the linear Darcy's law).

For a constant drain rate the set of linearized equations have the form:

$$\frac{\partial \rho f}{\partial t} + \frac{\partial M}{\partial x} = -qf \qquad \left(q = \frac{2}{R} V_R\right)$$

$$-f_0 \frac{\partial P}{\partial x} = \frac{\partial M}{\partial t} + 2aM \tag{16}$$

For viscoelastic pipes the equations transform to:

$$\rho_0 f_0 \left\{ \frac{1}{K_m} \frac{\partial P}{\partial t} + \frac{2R_0}{\delta} G^* \frac{\partial P}{\partial t} \right\} = -\frac{\partial M}{\partial x} - qf$$

$$-f_0 \frac{\partial P}{\partial x} = \frac{\partial M}{\partial t} + 2aM \tag{17}$$

Under the Maxwell model assumptions and boundary conditions:

$$\begin{array}{lll} t = 0 & M = 0 & P = 0 \\ x = 0 & P = P_0 & \\ x = \ell & M = M_0 & \end{array} \tag{18}$$

the solution of the problem is

$$P(x,t) = \frac{P_0 f_0 \theta \{ch\,\theta(\ell - x)\} - 2aM_0 sh\,\theta x}{f_0 \theta\, ch\,\theta\ell} -$$

$$-2e^{-(a+\varkappa)t}\left\{ P_0 \sum_{n=1}^{\infty} \frac{\mu_n \cos \mu_n(\ell - x)\left[(a+\varkappa)\sin \xi_n t + \xi_n \cos \xi_n t\right]}{\xi_n \ell \left[\mu_n^2 + \theta^2\right] \sin \mu_n \ell} + \right.$$

$$\left. + \frac{M_0}{f_0} \sum_{n=1}^{\infty} \frac{\left[(a^2 - \xi_n^2 - \varkappa^2)\sin \xi_n t + 2a\xi_n \cos \xi_n t\right] \sin \mu_n x}{\xi_n (\mu_n^2 + \theta^2)\, \ell \sin \mu_n \ell} \right\} +$$

$$+ \frac{2qc^2}{\ell} e^{-(a+\varkappa)t} \sum_{n=1}^{\infty} \frac{(-1)^{n+1}\left\{\left[a^2 - \xi_n^2 - \varkappa^2\right]\sin \xi_n t + 2a\xi_n \cos \xi_n t\right\}}{\mu_n \xi_n \sin \ell\mu_n \left[(a+\varkappa)^2 + \xi_n^2\right]} -$$

$$- \frac{2aq}{\theta^2}\left[1 - \frac{ch\,\theta(\ell - t)}{ch\,\theta\ell}\right]$$

where $\mu_n = \frac{(2n-1)\pi}{2l}$, $\xi_n = \sqrt{c^2\mu_n^2 - (a - dc^2\alpha)^2}$

For cases of drain rate being a function of pressure, the in eq. (17) is not a constant and assumes values $q=\alpha_1(P-P_1)$. Analyzing eq. (17) with regard to the pressure-dependent value of q, one may conclude that the solutions of the two problems under the same boundary conditions differ only by the values of q and ξ_n. Therefore, the solution (19) may be used for a porous pipe, provided it is assumed that

$$q = + \frac{P_1\alpha_1}{f_0} \qquad \xi_n = \sqrt{c^2\mu_n^2 - (a - dc^2\alpha)^2 - \frac{\alpha_1}{f_0}}$$

As one would expect, from the equations thus obtained it follows that both the hydraulic losses and the viscoelastic properties of the pipe material attenuate the flow unsteadiness, whereas the drain rate has a reverse effect.

When we considered the flow in permeable pipes we assumed that the liquid drain (supply) was spread over the pipe surface. In practice, however, one more frequently has to deal with situations where the liquid is drained (or supplied) at certain discrete points. Using the generalized functions (the Dirac δ -function and Heaviside function) one may simulate liquid flows in pipes for cases where the liquid is drained (supplied) over a limited portion of the pipe and over a limited time interval or the liquid is drained at discrete points during a certain limited time, as well as for cases of combined continuous and discrete drains (supplies) along the pipe.

In conclusion we should note that if it is the mass flow rate which is to be found, then, knowing P values and using an appropriate set of equations one may find M.

References.

1. Blitshtein Yu.M., Khublaryan M.G. Unsteady flows of liquid in pipes of a hereditary-elastic material. Izv. AN SSSR. Fluid Mechanics series, 1976, No. 2, pp. 178-182.

2. Khublaryan M.G. Investigation of unsteady flows in irrigation systems. In: Collected Scientific Papers on Modern Problems of Melioration, Moscow, 1979, pp. 183-192.

CAVITATION INTENSITY ESTIMATION IN HYDRAULIC MACHINES BY MEANS OF STRESS WAVES MEASUREMENT IN SOLID WALLS

by

Juliusz Kirejczyk

SUMMARY

Cavitation dynamic intensity may be expressed by its effects originated in flow systems, such as erosion and vibrations. Neverthless, a quantitative evaluation and prediction of phenomenon, needs a parameter which can express the intensity in form of energy supplied from a cavitation cloud to adjacent walls. One of the energy evaluation methods is the measurement of the pressure pulses distribution. This method, however, is not easy to be applied in machines operating in field conditions, though it may be useful in laboratories.

In the present work, another method has been used to estimate the dynamic cavitation intensity. The method is based on a measurement of cavitation acoustic effects - caused in walls adjacent to the cavitation cloud. The paper presents application grounds of the method and the usefulness for cavitation intensity estimation in hydraulic machines.

INTRODUCTION

Developing a simple practical method of cavitation intensity evaluation in an arbitrary machine is a fundamental trend in cavitation diagnostics. An ideal solution would be probably a portable device, which should afford possibilities for quantitative cavitation intensity evaluation after minimum set-up activities - best of all outside the machine. There arise many difficulties in developing such a solution. One of them is the multiaspect form of the phenomenon itself. It is well known that the operational parameters of hydraulic machines corresponding to the cavitation incipience, its most intense dynamic influence on the object /generating erosion and vibrations/ and the break-down point of efficiency curves do not coincide. Besides, the interdependencies between these parameters are not strictly defined and individual for each type of the machine.

Neverthless, not all the properties of the cavitation cloud in a machine should be known. In paper [1] , among other things an attempt has been made to prove that requirements which are raised before diagnostic methods concerned with the extent of the phenomenon are usually reduced to the problem of indication of its incipience conditions. For this purpose well suited are acoustic methods and in particular the observation of high frequency hydro-acoustic noise [2,3] .

Demands put before estimation methods of cavitation influence on the energy exchange conditions between liquid and the blade system of a hydraulic machine appear much the same. Their chief task is to indicate operation parameters by which such an influence occurs. The most efficient evaluation method of such conditions is the direct measurement of the machine efficiency. But this method shows an disadvantage in the case of huge machines. In this case it is necessary to take the characteristics of a machine.

Requirements put to diagnostic methods, related to dynamic intensity of the phenomenon, concern a quantitative evaluation. They come out from practical needs. On the one hand, permissible operating parameters of the machine should be found having in view the dynamic intensity of cavitation. On the other hand, possibilities should exist to foresee the possible erosive effects of the phenomenon at its permitted intensity.

This problem is so complex as cavitation erosion - the most important cavitation effect from the point of view of hydraulic machines operation /particularly the huge ones/ - is not an appropriate method to evaluate the phenomenon intensity. There are two basic reasons. The first one is the long waiting period till affects appear. The more, during this period - generally thousends of hours - the machine is operating in various conditions, characterized by various intensities of the cavitation phenomena.

The problem can be solved to some extent e.g. by coating the machine elements with easy erosive materials [4,5] or by special techniques as [6] .

The second reason is the complex character of the erosion itself, which depends not only on cavitation dynamic intensity but in the same extent on the properties of the eroded material, its surface condition or physical and chemical properties of the liquid.

It may be supposed, that the appropriate evaluation method of erosive cavitation threat should consist of two stages. The first one should comprise an evaluation of dynamic intansity of the phenomenon; the second should enable to evaluate the material response to the given erosive impingement.

A good evaluation method of cavitation dynamic intensity is the measurement of pressure pulses executed on the walls which are adjacent to the cavitation cloud. The method consists in replacing a wall element by a measuring sensor membrane. It assures good results [7,8,9] so far as high grade sensors are applied. The disadvantage of the method lies in the necessary access to the cavitation zone. This condition is difficult to fulfill in the case of low specific speed pumps and water turbines. Another disadvantage is the local information about the cavitation intensity. In order to estimate the phenomenon intensity in a machine, the location of the cavitation cloud should be known, and high number of measureng points should be applied.

In paper [1] another measureng method has been used. It is based on the measurement of high-frequency acoustic phenomena in walls of flow ducts being under the cavitation influence. The similar method has been used by O.Taraba [10] ,but his cavitation intensity test results are not widely accessible. An advantage of this method lies in its great simplicity. In the simpliest version, when applied for high specific speed machines with open impellers, the intensity of slot cavitation and the cavitation on blades which is in contact with the impeller casing, can be evaluated without any initial activities, on the external surface of the impeller casing.

Another advantage of this method is the informative possibility about dynamic cavitation intensity, acting directly on the machine walls /comparatively the hydroacoustic noise measurement informs about the overall cavitation intensity while only a part of the cavitation cloud acts dynamically on the flow limiting walls/.

The disadvantage of this method lies in the fact that the absolute read-out of energy is not possible.

PHENOMENON ANALYSIS

The phenomenon analysis giving grounds for application of measuring techniques has been divided into three parts concerning implosion and formation of shock waves, their propagation and measurement.

Implosion and shock wave

In principle, the application of acoustic phenomenon measurement in the walls, which enclose a cavitation zone in order to evaluate the phenomenon intensity, does not need any assumptions concerning the implosion course. However, if the measurement should determine the erosive part of cavitation energy flux, it should take into account the character of this energy.

Experimental investigations revealed that cavitation implosions occuring by the walls generate shock waves in the wall material[11]. Propagation velocity of those waves depends on the properties of the wall material and on the shock parameters /e.g. in [11] it has been stated, that in the case of the epoxy resin such a velocity is equal app. 2600 m/sec./.

The pulse duration depends on its highest amplitude and expansion wave velocity which in turn depends on the material properties. In case of shock wave the pulse duration does not depend on the stress increase velocity /because of the stress discontinuity/ [12] .

The pulse process in a chosen place of the cavitation cloud contact with the solid wall may be expressed as a pulse sequence

$$T(t) = \sum_{m=1}^{N} T_m \cdot e^{-(t - t_m)/\tau}$$

where: T_m denotes the maximum stress value, caused by the m-th pulse, t_m - starting point of the m-th pulse, τ - time constant of pulse decay. Those pulses appear in time according to the Poisson distribution [13;14] . Maximum amplitude values for each pulse are subordinated to a certain distribution depending on cavitation intensity. The spectral pulse characteristic is constant for frequencies (f) lower than $1/2\pi\tau$. When $f > 1/2\pi\tau$ it is reduced twice as the frequency is dubled [15] .

Experimentally determined time constants are of the order 10^{-5} - 10^{-6} sec. [14]. This means, that the energy spectrum of cavitation shocks should reach the frequency order of some megacycles per second. It can be assumed with high probability that no other phenomenon occuring in hydraulic machines besides cavitation, is able to generate in casing walls the acoustic effects of such a high frequency level. An important conclusion can be derived from the above: the measurement of those phenomena bears no error caused by the background noise or noises generated by other phenomena /which is the case during hydroacoustic measurements/.

Stress wave propagation in solid walls

The stress waves appear in the form of spherical shock waves, but they could propagate in such a form only in an infinite, isotropic, homogeneous and perfectly elastic medium. Practically there occur the propagation disturbances caused by [16] :

- surfaces, which create reflections and formation of surface waves /Rayleigh or Lamb/;
- grain boundaries, microcracks, inclusions etc., which create reflection and diffraction;
- anisotropy, which causes deformation of the spherical wave on account of the difference in wave velocity in different directions;
- inhomogeneities, which distort wavefronts;
- non-linear elastic behaviour, which is responsible for damping and dispersion /frequency dependence of the velocity/.

Due to circumstances mentioned above, it is extremely difficult to estimate in absolute figures the value of energy, which has been supplied to a certain place in form of pulses by measuring the wave energy in another place.

However, all the stress waves damping factors specified above remain constant in a define machine. This means that if the shock waves are generated at the same place in various stages of cavitation development and the measureng point also does not change, the value of signal obtained is proportional to the intensity of the process, generating the stress waves. This condition is not fulfilled if for example cavitation noise is measured in liquid, as the noise propagation conditions depend among others on the pressure; so they generally change with cavitation intensity changes.

Measurement

The measurement of the process intensity can be conducted using a simple set consisting of: a piezoelectric transducer, an amplifier and a gauge. The signal comes in a pulse form, which should be taken into account. There are two methods possible to apply. The first is the pulse energy measurement, the second one - the measurement of pulse amplitude distribution. The second method is easier to apply. In this case the process energy is proportional to the amplitude (T) square and to the number n(T) of pulses with the amplitude T:

$$E \propto \sum n(T) \cdot T^2$$

An important problem, not mentioned yet, is distinguishing between the surface and volume waves. It is of particular importance when defining the wave measurement method. Though the stress waves come from the same source they bring information in different ways: differently in the case of volume waves and in the case of surface waves. In the first stage of analysis this problem has been neglected.

In the next section the test results of cavitation intensity in pumps will be shown.

THE TEST STAND AND THE MEASURING METHOD

Experimental investigations have been executed on two high specific speed pumps with open mixed-flow impellers: a diagonal pump /with vaned diffuser/ having the specific speed n_q= 120 and a volute pump with n_q= 205.

Investigations have been carried out by kinematically constant flow conditions / $\varphi^* = \varphi/\varphi_x$ =const./ in few groups characterized by different values of the cavitation number σ . The angular velocity ω of the impeller was changed. The measurement conditions were chosen in such a way that the only varying parameter was the flow velocity.

The used measuring set consisted of a piezoelectric transducer and an amplifier having a pass-band of 0.8 - 5 MHz $\pm$ 3 dB, an amplitude analyser and a pulse counter. Vibrations /accelerations/ of a pump casing were measured too.

To estimate the intensity of a pulse process in walls of the machine the cavitation intensity factor was determined from a simple relationship:

$$IF = \frac{1}{t} \sum_{i=1}^{k} n_i \, T_i^2$$

where: T_i means the pulse magnitude in an i-th amplitude interval, n_i - pulse quantity in the i-th interval, k - the number of amplitude intervals, t - measurement time.

The more detailed test results of the diagonal pump are shown in paper [1] . Here we refer only to a part of them which may illustrate the usefulness of the presented method.

The investigations of the diagonal pump, beyond a measurement of acoustic phenomena in walls and of vibrations, comprised also a measurement of the energy flux density (I):

$$I = \frac{K}{2\varrho c} \cdot \frac{1}{t} \sum_{i=1}^{k} n_i \cdot p_i^2$$

where: p_i - pressure pulse magnitude in an i-th interval, K -correction factor $K \approx 5\ 10^{-5}$, ϱ - liquid density, c - sound velocity t,k and n_i - as before. Evaluation of this parameter, was based on a measurement of pressure pulses on the impeller casing [17].

Esential difference between measurements on both pumps lies in the fact, that in case of the diagonal pump the measurements were conducted on the outer side of the wall under cavitation. These were the best conditions to be obtained. In the same plane perpendicular to the impeller axis, the energy flux density (I) was measured. In case of the volute pump, the pulse precess was measured on a suction tube wall in a distance 110 mm before the impeller inlet.

TEST RESULTS

An example of test results of the volute pump is shown in Fig.1. It is the relationship IF(ω) by varying σ. The diagram shows that IF $\propto \omega^n$ and the exponent n varies in a range from 4.5 to 9 /adequate n values are shown in the figure/. In case of the diagonal pump, a similar relationship was obtained [1].

The presented results indicate the existence of relation

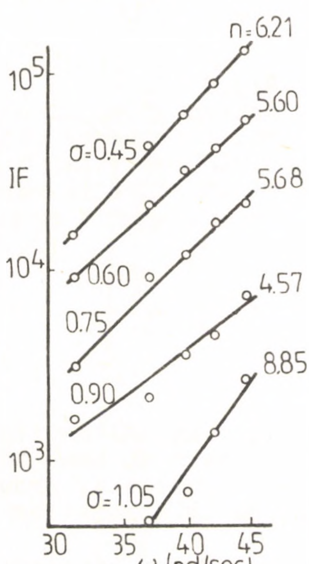

Fig.1. Cavitation intensity factor IF vs. angular velocity ω of a volute pump for various σ, $\varphi^* = 1$

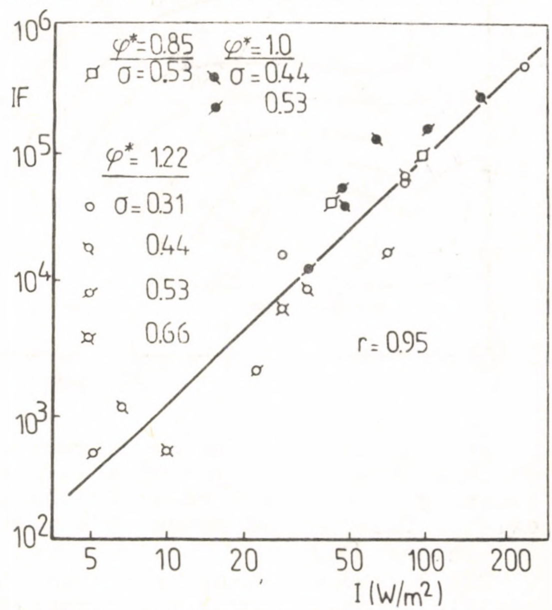

Fig.2. Cavitation intensity factor IF vs. energy flux density I for a diagonal pump σ, φ^*=var.

between the parameter IF and the cavitation intensity. To be sure that the factor IF is related to the cavitation dynamic intensity, we should compare it with another one, which also depends on the phenomenon dynamic intensity.

The most objective measure of the cavitation dynamic intensity seems to be the energy flux density (I). In Fig.2 the relationship IF(I) is shown, which has been obtained in course of the diagonal pump investigations by varying values of σ, φ^* and ω. A good correlation /r=0.95/ may prove the existence of relationship between those two processes in a wide range of values, reaching 2 - 3 orders of magnitude. This relationship is an exponential one; in this case it was obtained IF $\propto$ $I^{1.9}$.

Another diagram, which presents the relationship between the intensity factor IF and operating conditions of the diagonal pump, is shown in Fig.3. This characteristics has been obtained by putting the relationship IF(Q,ω) on the $\eta(Q,\omega)$ diagram. Both characteristics were taken by the constant suction head.

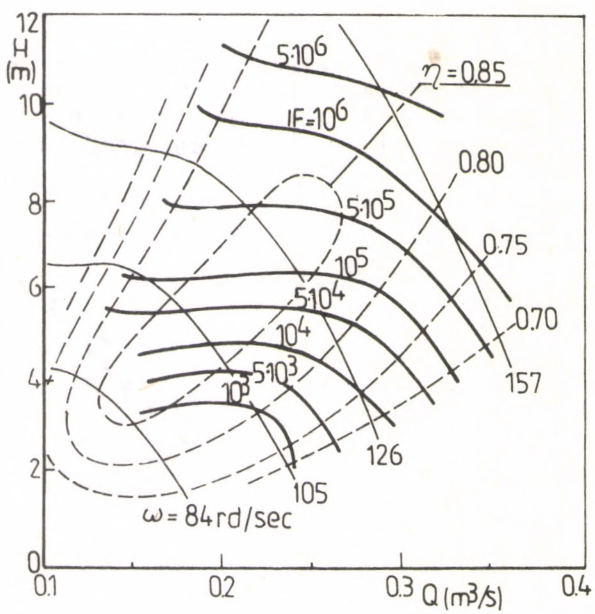

Fig.3.
Set-up of an universal efficiency characteristics η and a line of constant IF values in a diagonal pump.

It follows from the comparison of curves, that the cavitation dynamic intensity grows up with increase of the pump head and capacity. There is a range /by $Q < Q_{\wedge}$/ when an intensity growth exists. This is the range of a pump operation by a rotating detachment [18].

Fig.3 enables inspection into the changes of the cavitation dynamic intensity by varying operating parameters of a pump /by a constant suction head/. In order to discuss it let us consider three variation combinations of a pump operating parameters, assuming the initial values: Q = 0.23 m^3/sec., ω =105 rd/

/sec. and $I \propto \sqrt{IF}$:

a. capacity decrease down to $Q = 0.16\ m^3$/sec.by ω =const. causes app. a tenfold increase of the cavitation dynamic intensity;
b. an increase of capacity up to $Q = 0.35\ m^3$/sec. by an increase of an angular velocity up to $\omega = 157$ rd/sec./ $\varphi^* =$ const/, causes a 25-fold increase of the phenomenon intensity;
c. an increase of angular velocity up to $\omega = 157$ rd/sec., by a constant capacity causes an app. 100-fold increase of the cavitation dynamic intensity.

A comparison of test results of the pump impeller casing vibrations with the value of IF suggests the existence of vibration damping, which depends on the range of cavitation phenomena. A similar conclusion has been made previously in [1], in order to explain the relationship between the vibration accelerations and the energy flux density (I) in a diagonal pump. An assumption has been made there, that the damping is proportional to the cavitation cloud size. According to [19], in cases of flows by subcritical Reynolds numbers /in the diagonal pump, the Re value, related to the blade thickness, was equal $0.7 - 1.1 \times 10^5$/ there is a relationship between σ and the length L of the cavitation cloud in form of $L(\sigma)^{1.5} =$ const. In effect of taking together vibration accelerations (a), the cavitation number σ and the energy flux density (I), the following relationship has been obtained: $a^2 \propto I \cdot (\sigma)^3$ /with the correlation coefficient r = 0.96/ which means that elastic vibrations energy induced by cavitation is proportional to the excitation energy, expressed by (I), and to the damping factor, proportional to σ^3.

In case of the volute pump, the flow in an impeller was in the range of transient and supercritical Reynolds numbers /Re = $1.9 - 2.7 \times 10^5$/. According to [19], the length of cavitation cloud for a supercritical flow can be well described by a dependence $L(\sigma)^{2.5} =$ const.

To make sure about the dependence between vibrations and the intensity factor IF, the test results of the volute pump were set together in form of $a^2 \cdot \sigma^{-5}$ (IF), which is illustrated in Fig.4. The relationship which has been obtained from the diagram /by use of the least squares method/ is as follows:

$$a^2 \propto (IF)^{0.96} \cdot \sigma^5 .$$

Though, the correlation between $a^2 \cdot \sigma^{-5}$ and IF is satisfying /r = 0.95/ in the whole range of values, comprising two orders of magnitude, some discrepancies can be seen between the function values for various σ. It may be caused by the influence of transient Reynolds numbers; it may also mean, that the above mentioned relationship is only an approximation of a real relationship between vibrations, cavitation dynamic intensity and the cavitation number.

CONCLUSIONS

1. The measureng method of the cavitation intensity, which has been described, reflects well the dynamic intensity of the phenomenon, meant as the energy flux density, supplied in

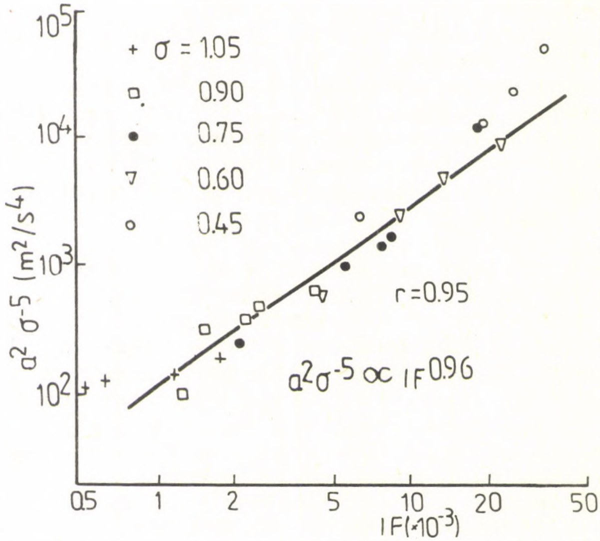

Fig.4. Relationship between the cavitation intensity factor (IF), vibration acceleration of the impeller casing (a) and the cavitation number (σ) in a volute pump.

form of pressure pulses from the cavtiation cloud to the walls limiting the flow.

2. Simplicity of the method used, promotes its application for evaluation purposes of the cavitation dynamic intensity in hydraulic machines in field. The method is capable to point out the most unfavourable machine operating conditions, with regard to the erosion threat.

3. However, the simplicity of the method is payed for by resigning of the energy flux density measurement in absolute values, which makes impossible its application e.g. for comparative purposes of the cavitation intensity in various machines or for predicting the cavitation damage extent. The future investigations should tend to formulate the quantitative relationships between the intensity factor IF and the real cavitation dynamic intensity in any flow system.

BIBLIOGRAPHY

1. Kirejczyk J.: Cavitation Signs in Rotodynamic Pumps; submitted to the Second Conf. on Cavitation, Edinburgh 1983.
2. Deeprose W.M. et al: Cavitation Noise, Flow Noise and Erosion; Conf. Cavitation, Edinburgh 1974, Publ. I.Mech.Eng. 1976.
3. Mellen R.H.: Ultrasonic Spectrum of Cavitation Noise in Water; J.Acoust.Soc.Am. 26, No 3, May 1954.
4. Kerr S.L., Rosenberg K.: An Index of Cavitation Erosion Means of Radioisotopes; Trans. ASME, 80, No.6, 1958.
5. Pylayev M.I., Edel Y.U.: Kavitacia v gidroturbinach; Mašinostroenie, Leningrad 1974.
6. Chincholle L., Guyomard D.: Detection de la cavitation erosive

et de l'abrasion; Proc.IAHR Symposium Tokyo 1980.
7. Hammitt F.G.: Cavitation Damage Prediction - Final Report; Report UMICH 014456-F-1, Univ.of Michigan, Nov.1981.
8. De M.K., Hammitt F.G.: New Method for Monitoring and Correlating Cavitation Noise to Erosion Capability; Trans.ASME, J.of Fluid Eng. 104, Dec.1982.
9. Steller K.: On Cavitation Intensity and Cavitation Erosion Prediction; Inst.Fluid-Flow Mach.Report 91/99/80 /in Polish/.
10. Taraba O.: Diagnostika kavitačních procesů rozborem emitovaného ultrazvukového pole a selektivní určení rozměru kavitační zony; Proc.Hydroturbo, Brno 1976.
11. Fujikawa S., Akamatsu T.: Effects of the Non-equilibrium Condensation of Vapour on the Pressure Wave Produced by the Collapse of a Bubble in a Liquid; J.Fluid Mech. 97 part 3, 1980.
12. Nunziato J.W.et al: Wave Propagation in Nonlinear Viscoelastic Solids; Handbuch der Physik, Band VIa/4, Springer-Verlag 1974.
13. AkuličevV.A., Olševskij V.V.: Niekotoryie statističeskie charakteristiki kavitacionnych javlenij; Akust.Żurn. XIV, 2/68.
14. Kirejczyk J.: Cavitation Diagnostics in Diagonal Pumps; D.Sc.Thesis, Gdańsk 1980 /in Polish/.
15. Pernik A.D.: Problemy kavitacii; Sudpromgiz, Leningrad 1963.
16. Licht T.: Acoustic Emission; Bruel Kjaer Techn.Rev.2/1979.
17. Kirejczyk J.: Cavitation Diagnostics in Diagonal Pumps; Proc.IAHR Symposium Amsterdam 1982.
18. Rey R.et al: Étude statistique sur les charactéristiques à débit partiel des pompes centrifuges et sur la détermination approximative du débit critique; La Houille Blanche 2-3/82.
19. Varga J., Sebestyen G.: Experimental Investigations of Some Properties of Cavitating Flow; Periodica Polytechnica 9, No.3, Budapest 1965.

MOST IMPORTANT NOTATIONS

a - vibration accelerations /RMS/
I - energy flux density
IF- intensity factor
NPSH- net positive suction head
Q - rate of flow
r - correlation coefficient
Re- Reynolds number
T - stress pulse amplitude
u - circumferential velocity

$$\sigma = \frac{NPSH}{u^2/2g}$$

$\varphi^* = \varphi/\varphi_{\wedge}$
φ - flow coefficient
ω - angular velocity
$\wedge$ - optimum point

Juliusz KIREJCZYK Dr.Eng.
Institute of Fluid-Flow Machinery
Polish Academy of Sciences
80-952 Gdańsk, ul.Fiszera 14
Poland

INVESTIGATIONS ON THE FLOW AND ENERGY CONVERSION IN THE IMPELLER AND IN THE CASING OF CENTRIFUGAL PUMPS

H.-J. Kleinert, G. Will, S. Nagork

SUMMARY

The flow condition in the impeller and in the casing of a single-stage radial pump has been investigated experimentally. Beside the velocity field the pressure distribution at the impeller's periphery and at the periphery of the volute was determined as well as the volume flow distribution in the impeller. The analysis used considers the friction approximately and provides the velocity distribution in the impeller and in the vaned diffuser. The calculation method described here can be used to assess the volute flow.

SYMBOLS USED

P_s	Shaft horsepower
P_m, P_d	Loss of efficiency due to mechanical and disk friction, respectively.
$\dot{V}$	Capacity
$\dot{V}_l$	Loss capacity
$\dot{V}_n$	Nominal Capacity
Y	Specific delivery
Y_{th}	Theoretical specific delivery
Y_l	Specific loss delivery
c_m, c_t	Meridian component and tangential component of the absolute velocity
u	Peripheral velocity
w	Relative velocity
r	Radius
t	Angular coordinate
$m = \int \frac{dx}{r}$	Radius related meridian coordinate
b	Cascade width

ρ Density of fluid

ψ Stream function

β Flow angle

1. AIM OF THE INVESTIGATION

To convert energy in a centrifugal pump stage the impeller and the casing are important. Obviously, the flow condition in the casing depends on the impeller's outflow. The presence of a radial force acting on the rotor is also evidence for a reaction of the casing on the impeller's flow.
The investigations carried out were to settle the question to what extent the interaction of the two components can be determined by hydraulic calculation and to obtain the performance of a stage by the summation of their individual characteristic features.
Especially the following problems should be investigated:

- How the flow and the power transmission differ in one and the same impeller with different casings?
- What kind of deviations from the axial symmetry occur in the impeller?
- What kind of methods must be used to determine the flow in non-axial symmetric casing?

To solve these problems experimental and theoretical investigations had to be carried out.

2. EXPERIMENTAL INVESTIGATIONS

The investigations were carried out with a radial centrifugal pump with a cylindrically vaned impeller, already used in previous investigations /1/.
Figure 1 shows the experimental pump to a large extent made of plexiglass to optically observe the flow.

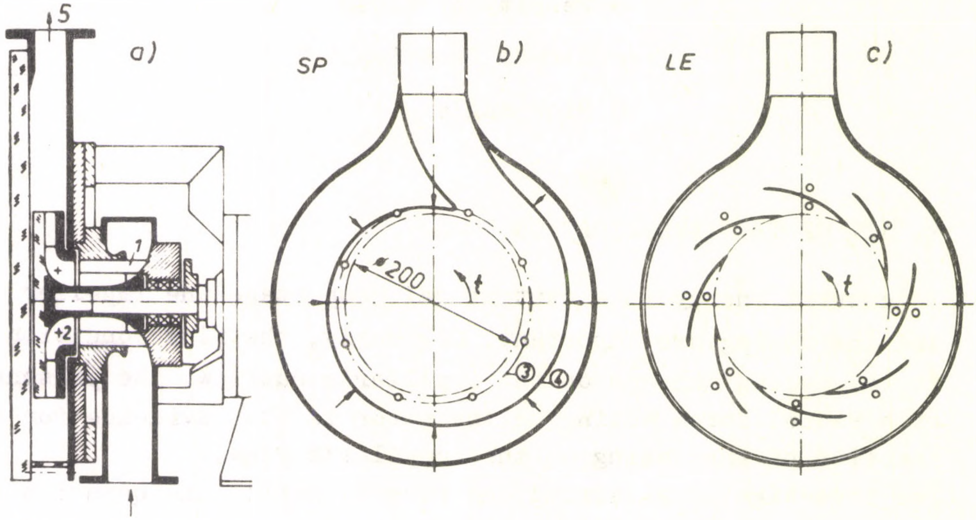

Fig.1 Experimental pump
a) Sectional view perpendicular to the axis of the component flowed by the fluid
b) volute c) vaned diffuser

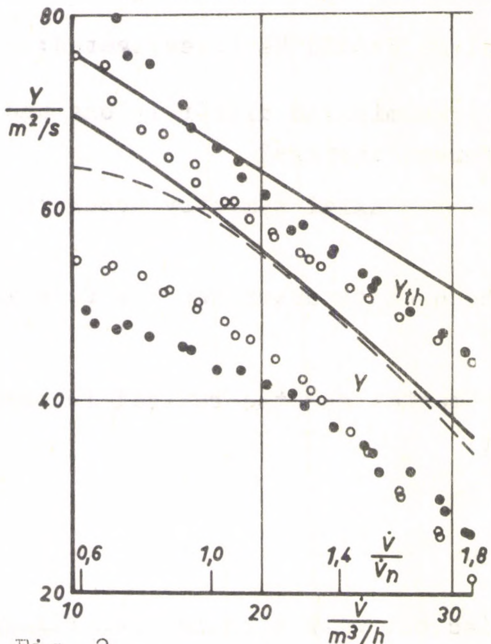

An almost rotationally symmetric and irrotational inlet flow to the impeller is achieved by the rectifier 1 inspite of the radially arranged suction connection. Following casings were used: vaned diffuser and an volute; both components were cylindrically contoured.

Figure 2 shows the characteristics $Y(\dot{V})$ and $Y_{th}(\dot{V})$ at $n = 1000\ \text{min}^{-1}$ for the impeller-vaned diffuser-combination and impeller-volute-combination.

Fig. 2

Characteristics of the experimental pump

measurement:
- o with volute
- ● with vaned diffuser

prediction:
- ——— Y_{th}, Y_{volute}
- - - - $Y_{vaned\ diffuser}$

Whereas the specific delivery Y was directly determined by the power increase between suction eye (2) and discharge connection (5) the theoretical specific delivery Y_{th} was obtained by the shaft horsepower in deducting the losses due to leakages, disc and mechanical friction according to equation(1).

$$Y_{th} = \frac{P_s - (P_m + P_d)}{\rho(\dot{V} + \dot{V}_R)} \qquad (1)$$

As to the theoretical specific delivery fundamental differences occur only under reduced-flow conditions. There are more significant differences in the course of the specific delivery. For the impeller-volute-combination at $\dot{V}/\dot{V}_n \approx 0{,}6$ a maximum of Y is present. The effective work of the impeller-vaned diffuser-combination decreases monotonically with $\dot{V}$, but is more increased for $\dot{V} > 1{,}4\ \dot{V}_n$ than the specific delivery determined with the impeller-volute-combination.
To estimate the flow condition in the impeller the velocity distribution was determined by the following principle. The flow was made visible by tracers and photographically registered by a camera rotating synchronously and coaxially to the pump. A double representation of each tracer is obtained by a double exposition by elektronic flash in a measurable time interval and by this representation its velocity can by obtained which nearly corresponds to the flow velocity.

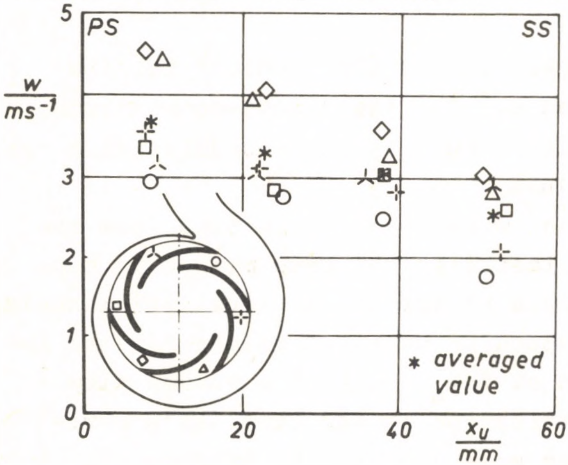

Fig. 3
Relative velocity distribution in the blade channels of the impeller with volute for the operating condition $\dot{V}/\dot{V}_n$ = o,6 in a medium radius range.

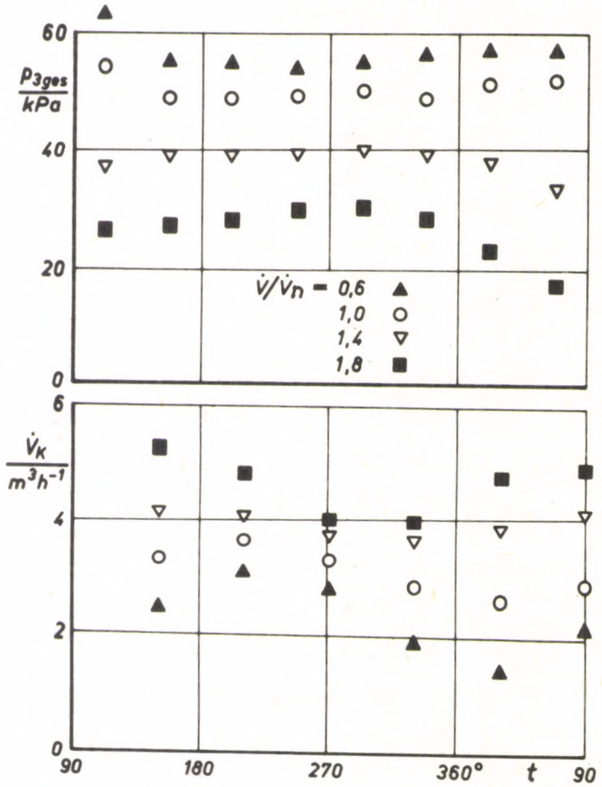

Fig. 4

Measured values of the total pressure at the impeller's outlet (a) and of the capacity in the blade channels (b) as a function of the angle for four operating conditions

With the interpretation to a large extent the informations of several photographs were superimposed and local average values are established for partial areas.

Figure 5a shows the averaged relative velocity values over all bladed channels in two radius-ranges for the flow rate $\dot V/\dot V_n$ = 1,4.

Also negligible differences between the w-values for the vaned diffuser-combination and for the volute-combination, respectively, are recognized, this is in accordance with the nearly coinciding Y_{th}-values.

As the impeller flow is concerned, the deviations from the axial symmetry can by estimated by the same method in considering the measured values of the single impeller channels. Figure 3 shows the corresponding measured values for the impeller-volute-combination at $\dot V/\dot V_n$ = 0,6. The volume flow - and total pressure - distribution at the impeller's periphery was measured for the same combination (figure 4).

The difference of the volume flow of the single channels become more significant by the increasing distance from the nominal capacity and correspond to the total pressure distribution, i.e. in the blade channel discharging against the greatest total pressure the smallest flow rate can be observed.

3. THEORETICAL ANALYSIS

In 1972 in the same bibliographical reference [2] it was reported on a method to calculate the flow by described blade cascades. By this method the real flow is decomposed in an inviscid core-flow and in boundary layers at the channel sides. The partial flows are iteratively and simultaneously calculated considering their interactions. The method was developed in the past and was used as a basis for the theoretical analysis. A comparison of the results of the velocity profiles in the impeller and in the vaneless diffuser measured and plotted against the grid spacing (figure 5) shows a good coincidence.
As to the theoretical specific delivery Y there is only a favourable coincidence.

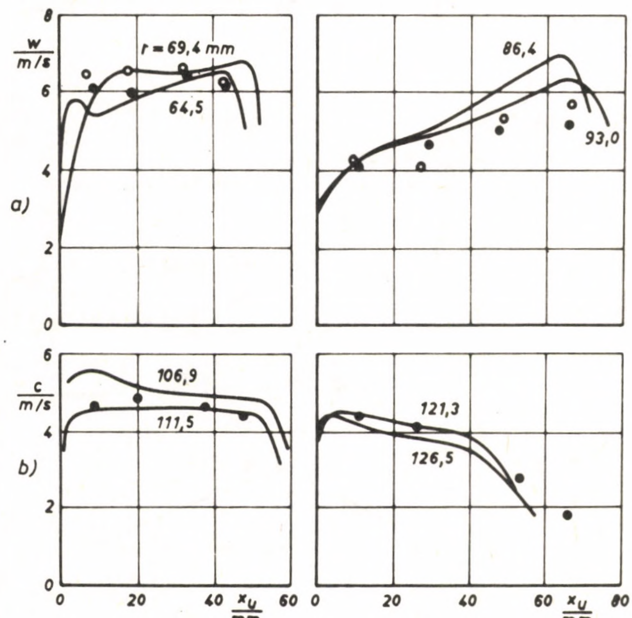

Fig. 5
Velocity distribution averaged over all channels between the pressure side and suction side near the cascade inlet and cascade outlet for the impeller and the vaned diffuser at
$\dot{V}/\dot{V}_n = 1,4$

In comparing the plots Y with the calculated values $Y_{th} - Y_{l\text{-}impeller} - Y_{l\text{-}casing}$ more significant difference are observed.

The causes for the underestimate of the losses are:

- it was supposed that inviscid core flow is present
- the mixing losses after the impeller were neglected
- the return flows into the impeller were not considered
- unconsidered losses after the vaned diffuser

In order to apply this method to calculate non-symmetrical casing like volute, the following facts were considered:

The volute can be understood as an annular cascade with the blade number N = 1. (figure 6) However, the inlet flow to this cascade is not to be seen as a rotationally symmetric one. The complicated interaction between the impeller and volute is approximated by a simple model. Only the relative velocity's direction is conferred by the impeller to the inlet. The amount may vary over the impeller's periphery and is obtained in calculating the volute-flows. To derive a corresponding boundary condition for the numeric integration of the stream function equation $\psi(m, t)$ the velocity triangle for the impeller's outlet is considered.

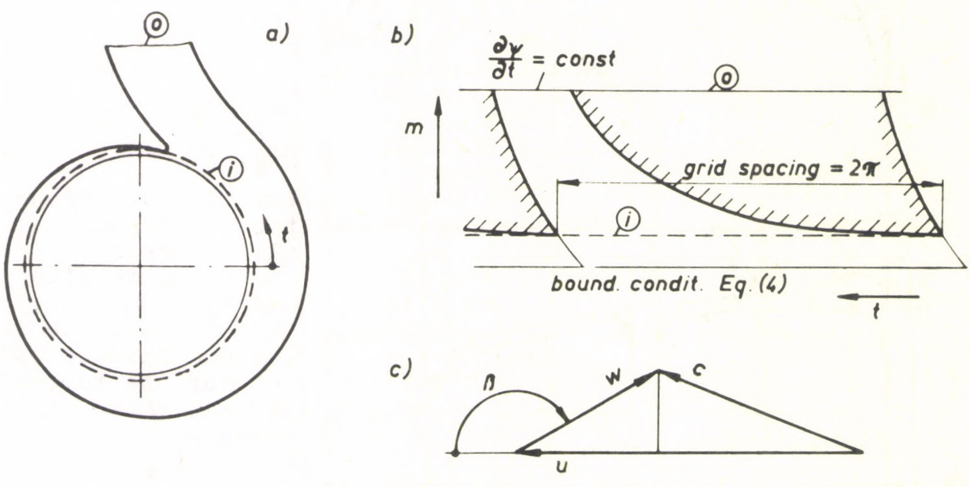

Fig. 6 Extension of the calculation method for a volute

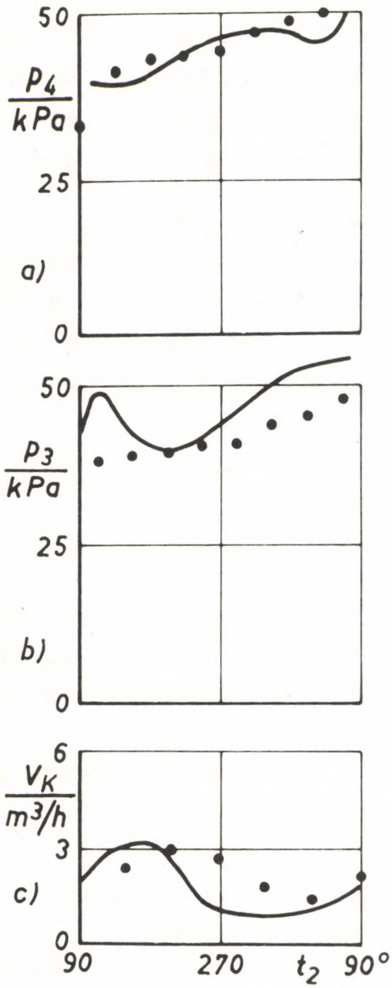

Fig. 7

Pressure distribution at the impeller's periphery (a) and at the volute (b), capacity distribution (c) for the operating condition $\dot{V}/\dot{V}_n = 0{,}6$

It holds:

$$c_t = u + w_t = u + c_m \cdot \cot \beta \quad (2)$$

According to the stream function's definition the velocity components c_t and c_m must be expressed by the derivation of the stream function:

$$c_t = -\frac{1}{\rho br} \quad \frac{\partial \psi}{\partial m} \qquad (3a)$$

$$c_m = \frac{1}{\rho br} \quad \frac{\partial \psi}{\partial t} \qquad (3b)$$

Substituting the equations (3) in (2) the boundary condition searched for at the impeller's outlet (m = 0) is obtained.

$$\frac{\partial \psi}{\partial m} = -\left(u \rho br + \cot \beta \frac{\partial \psi}{\partial t}\right) \quad (4)$$

The flow in the volute of the experimental pump for 4 operating conditions was checked by the extended method. The results are shown in figure 7 for the operating condition $\dot{V}/\dot{V}_n = 0{,}6$. Beside the pressure distributation at the impeller's periphery (3) and at the volute periphery (4) also the capacity rate of the single blade channels are obtained. A qualitative agreement with the measuring results was founded.

4. CONCLUSIONS

The flow condition and the power transfer casings in the impeller differ only negligibly with different can be calcu-

lated without considering the casing.
The specific delivery of the stage calculated in advance is higher than the measured one due to the insufficiant loss registering. Due to the assymmetry of the casing the single blade channels of the impeller are irregularly flowed through.

The averaged velocity distribution over all blade channels can be described satisfactorily by a axial symmetric theory in a certain operating range. The flow in an even volute can be determined by a modified method for the cascade flow analysis, giving also information on the unsymmetric impeller flow.

REFERENCES

[1] Kleinert, H.-J.; Will, G.; Nagork, S. — Experimental and theoretical investigations of the flow in radial impeller's of centrifugal pumps at cavitation. Proceedings of the 6th conference on Fluid Machinery, Budapest 1979

[2] Will, G. — On the Mathematicel Modeling of Two dimensional Cascade Flows. Proceedings of the 4th conference on Fluid Mechanics and Fluid Machinery, Budapest 1972

Kleinert, Hans-Joachim	Will, Gotthard	Nagork, Siegbert
Dr.-Ing.	Dr.-Ing.	Dipl.-Ing.
Professor	Oberassistent	Forschungsstudent

Technische Universität Dresden
Sektion Energieumwandlung
Wissenschaftsbereich Thermischer
und hydraulischer Maschinenbau
8027 Dresden
Mommsenstr. 13

PLANE POTENTIAL MOVEMENTS THROUGH CASCADES
COMPUTED WITH THE FINITE ELEMENTS METHOD

by

I.Kolati,I.Voia

INTRODUCTION

The potential movements, though representing an idealization of the real flow, are still used in the study of flows through the various parts of fluid machinery.

Laplace's equation describes the potential movement in any domain, but certain supplementary conditions should be imposed in order to obtain theoretical results in accordance with experimental measurements.

The finite elements method permits to solve Laplace's equation for any domains (simple or multiple connected domains) and admits supplementary conditions being imposed as well.

A "NON-LINEAR PLANE" program was elaborated, by making use of quadrilateral elements of second degree for the computation of the hydrodynamic field in plane cascade. The program permits the computation of the pressure distribution, of speeds and speed circulation, of the resulting forces and moments. In order to facilitate the user's work, the division into elements of the domain and the internal numbering is automatically achieved within the program. The program was implemented on a Felix C512 computer.

MATHEMATICAL ANALYSIS

The two-dimensional, irrotational and incompressible flow is shown by the following equations:

$$\nabla^2\phi = 0 \quad ; \quad \nabla^2\psi = 0 \tag{1}$$

for the velocity potential and stream function.

The flow domain is divided into quadrilateral elements with curved sides, like the one shown in Fig.1. The isoparametrical interpolation function of second degree which will describe the variation of unknown functions ϕ and ψ depending on their values in the nodes of the elements, has the following form:

$$\phi_n(\theta,\eta)=\frac{1}{4}(1+\theta\theta_n)(1+\eta\eta_n)(\theta\theta_n+\eta\eta_n-1) \qquad (n=1,2,3,4) \tag{2}$$

$$\phi_n(\theta,\eta)=\frac{1}{2}(1-\theta^2)(1+\eta\eta_n) \qquad (n=5,7) \tag{3}$$

$$\phi_n(\theta,\eta)=\frac{1}{2}(1+\theta\theta_n)(1-\eta^2) \qquad (n=6,8) \tag{4}$$

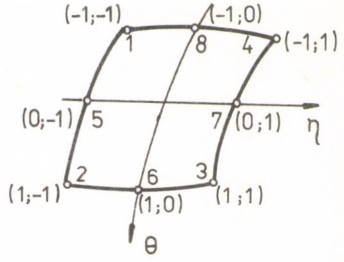

FIG.1.

The connection between the isoparametrical and Cartesian coordonates is done by means of the formulas:

$$x = \sum_{n=1}^{8} \Phi_n x_n \; ; \quad y = \sum_{n=1}^{8} \Phi_n y_n \tag{5}$$

It is admitted that the unknown ϕ and ψ functions are described inside an element by the expressions:

$$\phi = \sum_{n=1}^{8} \Phi_n \phi_n \; ; \quad \psi = \sum_{n=1}^{8} \Phi_n \psi_n \tag{6}$$

where: Φ_n -the interpolation function in the node $\underline{n}$;
x_n, y_n -the Cartesian coordonates of the node $\underline{n}$;
ϕ_n, ψ_n -the values of the respective functions in the node $\underline{n}$.

One supposes that the expressions (6) satisfy the equations (1) to a very small residue ε :

$$\nabla^2\phi = \varepsilon \; ; \quad \nabla^2\psi = \varepsilon \tag{7}$$

The Galerkin integral is written /1/:

$$(\varepsilon, \Phi_n) = \int_{\Omega} \nabla^2\phi \cdot \Phi_n \cdot d\Omega = 0 \tag{8}$$

By transformation through the Green-Gauss formula, it results that:

$$\int_{\Omega} \nabla\phi \, \nabla\Phi_n \, d\Omega = \int_{\Gamma} \nabla\phi \, \Phi_n^* \, d\vec{\Gamma} \tag{9}$$

After replacing the ϕ expression from (6), the matrix equation of a finite element is obtained:

$$\left[A_{nm}\right]\left[\phi_m\right] = \left[F_n^{\circ}\right] \tag{10}$$

and also in an analogue manner for ψ :

$$\left[A_{nm}\right]\left[\psi_m\right] = \left[F_n\right] \tag{11}$$

where the following notations have been used:

$$A_{nm} = \int_{\Omega'} \left(\frac{\partial \Phi_n}{\partial x} \frac{\partial \Phi_m}{\partial x} + \frac{\partial \Phi_n}{\partial y} \frac{\partial \Phi_m}{\partial y} \right) dx \cdot dy \tag{12}$$

$$F_n^{\circ} = \int_{\Gamma'} \nabla\phi \, \Phi_n^* \, d\vec{\Gamma} \; ; \quad F_n = \int_{\Gamma'} \nabla\psi \, \Phi_n^* \, d\vec{\Gamma} \tag{13}$$

The Ω' domain is the surface of a finite element and Γ' is its contour. The Φ_n^* function is the interpolation function on the Γ' contour.

$[A_{nm}]$ Matrices Computation

The integral in (12) is calculated numerically. One passes to the isoparametrical coordonates(θ , η):

$$\frac{\partial \phi_n}{\partial x} = \frac{1}{|J|}\left(\frac{\partial \phi_n}{\partial \theta}\frac{\partial y}{\partial \eta} - \frac{\partial \phi_n}{\partial \eta}\frac{\partial y}{\partial \theta}\right) = \frac{S_n}{|J|} \tag{14}$$

$$\frac{\partial \phi_n}{\partial y} = \frac{1}{|J|}\left(-\frac{\partial \phi_n}{\partial \theta}\frac{\partial x}{\partial \eta} + \frac{\partial \phi_n}{\partial \eta}\frac{\partial x}{\partial \theta}\right) = \frac{T_n}{|J|} \tag{15}$$

where: $|J|$-is the Jacobian of the transformation.

The x,y expressions and ϕ_n depending on θ , η are known, so the calculation of derivates from (14) and (15) presents no difficulty:

It is finally obtained that:

$$A_{nm} = \iint_{-1}^{1} (S_n\, S_m + T_n\, T_m)\frac{d\theta\, d\eta}{|J|} \tag{16}$$

The integration can be done by Gauss' quadrature in 3-4 points.

$[F_n]$ and $[F_n^o]$ Matrices Computation

Considering the formulas connecting the speed components with the ϕ and ψ functions:

$$v_x = \frac{\partial \phi}{\partial x} = \frac{\partial \psi}{\partial y} \qquad v_y = \frac{\partial \phi}{\partial y} = -\frac{\partial \psi}{\partial x} \tag{17}$$

these matrices can be transcribed in other forms.

One obtains for F_n :

$$F_n = \int_{\Gamma'} \phi_n^* (-v_y \vec{i} + v_x \vec{j})\, d\vec{\Gamma} \tag{18}$$

The boundary conditions for the velocity potential in (13) are transformed to:

$$F_n^o = \int_{\Gamma'} \phi_n^* (v_x \vec{i} + v_y \vec{j})(n_x \vec{i} + n_y \vec{j})\, dl \tag{19}$$

where: n_x and n_y are components of the outer normal at Γ' .

The integrals (18) and (19) cannot be computed in the general case except at input because for the rest the contour speeds are not known. From this reason, in both cases, an equipotential line (ϕ =constant) is chosen for the output boundary upon which the first integral is vanished and the second one is replaced by Dirichlet conditions. On the solid boundary the F_n integral is replaced by Dirichlet conditions and the F_n^o integral is vanished owing to the Neumann conditions($\vec{v}\,\vec{n} = 0$ on the wall). If an equipotential line is chosen for the boundary input, it results that:

$$[F_n] \equiv [0] \tag{20}$$

and Dirichlet conditions will be used on the inlet line.

The calculation of the Dirichlet conditions for ψ formulation is described below.

Taking into account the fact that after assembling (see fig.3.) the integral in (19) is vanished on the common sides of the neighboring elements,the computation is achieved on the inlet boundary only.

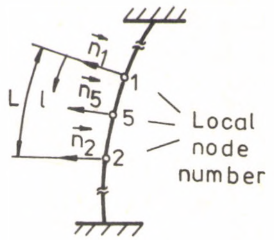

FIG.2.

For the calculation of the integral (19) one considers the side of an inlet element as in fig.2.The components of the outer normal are known (n_{xi},n_{yi}),as well as the speed components on the side of the elements (v_{xi},v_{yi}).

The interpolation function along the side is chosen as follows:

$$\phi_n^*(l) = a_n + b_n l + c_n l^2 \qquad (n=1,2,5) \tag{21}$$

The a_n,b_n,c_n coefficients are determined under the conditions:

$$\sum_n \phi_n^*(l) = 1 \quad \text{and} \quad \phi_m^*(l_m) = \begin{cases} 1 & \text{if } n=m \\ 0 & \text{if } n \neq m \end{cases} \qquad (n=1,2,5) \tag{22}$$

If it is admitted that n_x,n_y and v_x,v_y vary according to a second degree rule,one can state that:

$$n_x(l) = \sum_n \phi_n^* n_{xn} \quad ; \quad n_y(l) = \sum_n \phi_n^* n_{yn} \qquad (n=1,2,5) \tag{23}$$

$$v_x(l) = \sum_n \phi_n^* v_{xn} \quad ; \quad v_y(l) = \sum_n \phi_n^* v_{yn} \qquad (n=1,2,5) \tag{24}$$

With these notations,the integral for F_n^o will become:

$$F_n^o = \int_0^L \phi_n^* \left[\left(\sum_n \phi_n^* v_{xn}\right)\left(\sum_n \phi_n^* n_{xn}\right) + \left(\sum \phi_n^* v_{yn}\right)\left(\sum \phi_n^* n_{yn}\right)\right] dl \qquad (n=1,2,5) \tag{25}$$

After replacing the ϕ_n^* expression from (21) and effecting the integration,it results that:

$$F_n^o = A_o a_n L + \frac{B_n L^2}{2} + \frac{D_n L^3}{3} + \frac{E_n L^4}{4} + \frac{G_n L^5}{5} + \frac{H_n L^6}{6} + \frac{K_n L^7}{7} \qquad (n=1,2,5) \tag{26}$$

where the coefficients A_o,B_n,... will result from (25),arranging according to the exponents of l.

The column matrix $\lfloor F_n^o \rfloor$ is finally obtained,which is rendered horizontally ($[F_n^o]^T$ is the $[F_n^o]$ transposed):

$$[F_n^o]^T = [\, F_1^o \; F_2^o \; 0 \; 0 \; F_5^o \; 0 \; 0 \; 0 \,] \tag{27}$$

The Matrices Assembling

After the assembly of the matrices $[A_{nm}]^e$ of the finite elements $\underline{e}$,the global matrix $[A_{NM}]$ is obtained.This is tape-type square matrix having an equal dimension with the maximum number of nodes in the discretization being considered.

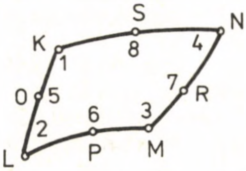

$$i;j = 1,2,3,4,5,6,7,8 \downarrow I;J = K,L,M,N,O,P,R,S$$

$$A^e_{ij} \to A^e_{IJ} \qquad A_{IJ} = \sum_e A^e_{IJ}$$

FIG.3.

The assembling method is shown in Fig.3.With capitals is put here the global numbering. Having the global matrices $[A_{NM}]$ and $[F^o_N]$ the matrix equation for the whole flow domain can be written:

$$[A_{NM}]\,[\phi_M] = [F^o_N] \qquad (N,M=1,\dots N_{max}) \tag{28}$$

$$[A_{NM}]\,[\psi_M] = [F_N] \qquad (N,M=1,\dots N_{max}) \tag{29}$$

where: N_{max} -is the maximum number of nodes of the global numbering.

These systems of linear equations can be only solved by computer,as for instance by using Gauss'replacing method. In the above system,the Dirichlet conditions are introduced, before solving,by the method indicated above.

Dirichlet Conditions Computation for ψ

One considers a portion of a line crossing the lines of ψ =constant (fig.4.).If the two points (1 and 2) are sufficiently close and one considers that the speed varies in a linear way between the two points,the following formula results for calculating the Dirichlet conditions:

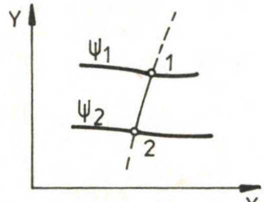

FIG.4.

$$\psi_2-\psi_1=(x_1-x_2)\frac{v_y^{(1)}+v_y^{(2)}}{2}+(y_2-y_1)\frac{v_x^{(1)}+v_x^{(2)}}{2} \tag{30}$$

By using this formula one calculates the Dirichlet conditions at inlet and on the inner foils.In this case it is necessary to solve first Laplace's equation with ϕ formulation,where from the speed components inside the domain are obtained.

The introducing of Dirichlet conditions is done in the following way.Let K_L be any Dirichlet condition in the node L.The L line in the matrix $[A_{NM}]$ and $[F^o_N]$ is annuled by putting:

$$A_{LL}=\begin{cases}1 & L=M\\ 0 & L\neq M\end{cases} \quad \text{and} \quad \begin{matrix}F_L=K_L\text{ , or}\\ F^o_L=K_L\end{matrix} \tag{31}$$

After introducing these conditions ,the equations systems (28) and (29) can be solved.

Special Boundary Conditions

Besides the Neumann and Dirichlet boundary conditions, Kutta-Jukovski conditions as well or flow conditions,can be imposed as it is shown below.

Kutta-Jukovski conditions-in order to avoid excessively great speeds at the trailing edge and in order to obtain circulation around the foil,nule speed on the trailing edge is imposed,which means that the streamline dressing the foil leaves it in the trailing edge(fig.5.).It can be observed that in point 1 the line of ϕ=constant should be perpendicular both on the foil upper surface and lower surface as well as on the ψ_K line.A compromise is always obtained so that the line of ϕ =constant,passing through point 1 will be bisectrix of the angle formed by the upper surface and ψ_K ,and by the lower surface and ψ_K respectively.(fig.6.).After the direction of ψ_K is chosen (usually as a prolongation of the camberline)the nodes n and p are positioned as shown in fig.6.It is imposed that the n-m-p line should be a line ϕ_c ,that is:

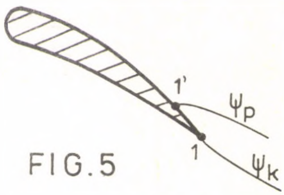

FIG.5

ψ_p- streamline without imposition of Kutta-Jukowski condition
ψ_K-streamline with imposition of Kutta-Jukowski condition

$$\phi_n = \phi_m = \phi_p \qquad (32)$$

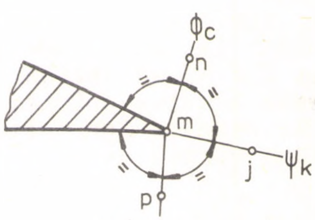

FIG.6.

$\phi_c$line = ϕ constant

The conditions (32) will be introduced in the system of matrix equations (28).They cannot be added as supplementary equations because more equations would result than unknown,which would lead to an incompatible system.
In principle the following operations will be done:

1)Choosing the equation m as a basis,the equations n and p will be added to it;

2)In all the equations differing from n,m,p, the coefficients of n and p will be added to the coefficient of the unknown m and zero is put instead;

3)Instead of n and p equations the conditions (32) will be used.

For the ψ formulation the procedure is similar to the following conditions (see fig.6):

$$\psi_m = \psi_j \qquad (33)$$

Flow Conditions

In the case of the straight cascades of foils the reduction of the infinite cascade to a finite cascade is imposed, including 1...3 foils. The straight lines limiting the domain form an elbow (see fig.7). The effect of the curve is manifested in the fact that in the region E the flow will be smaller than the one in the region I, to the same extent the α angle is larger. This fact means that the flows between the blades are not equal, which does not correspond to reality. In order to avoid this inconvenient it will be imposed that the value of ψ on the foil should be:

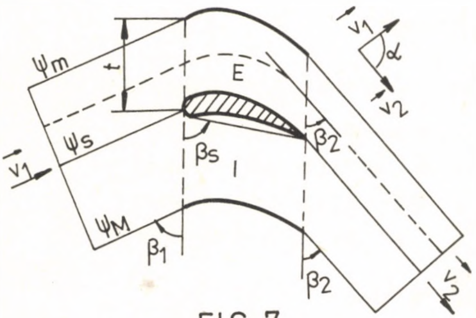

FIG.7.

$$\psi_s = \frac{\psi_m + \psi_M}{2} \tag{34}$$

The (34) formula is valable when the speed ($\vec{v_1}$) is uniform on the boundary input. The condition (34) is a Dirichlet condition and is introduced in the system in the way shown above.

Speeds Computation

In the calculation of the speeds one starts from the relations (17) where the expressions (6) of ϕ and ψ are replaced:

$$v_x = \sum_{n=1}^{8} \phi_n \frac{\partial \Phi_n}{\partial x} = \sum_{n=1}^{8} \psi_n \frac{\partial \Phi_n}{\partial y} \tag{35}$$

$$v_y = \sum_{n=1}^{8} \phi_n \frac{\partial \Phi_n}{\partial y} = -\sum^{8} \psi_n \frac{\partial \Phi_n}{\partial x} \tag{36}$$

Taking into account the relations (14) and (15), these relations become:

$$v_x(\theta,\eta) = \sum_{n=1}^{8} \phi_n \frac{S_n(\theta,\eta)}{|J(\theta,\eta)|} = \sum_{n=1}^{8} \psi_n \frac{T_n(\theta,\eta)}{|J(\theta,\eta)|} \tag{37}$$

$$v_y(\theta,\eta) = \sum_{n=1}^{8} \phi_n \frac{T_n(\theta,\eta)}{|J(\theta,\eta)|} = -\sum_{n=1}^{8} \psi_n \frac{S_n(\theta,\eta)}{|J(\theta,\eta)|} \tag{38}$$

By using these formulas the speeds upon the surface of one element are obtained, depending on the θ, η coordonates. The speeds differ in the nodes if calculated out of different elements. From this reason the arithmetic mean of the speeds calculated out of the common elements of the respective node, can be considered. Thus, one can assure the speed continuity at the elements boundary.

APPLICATIONS

Some examples are given below of computation effected by the "NON-LINEAR PLANE"program.The notations correspond to those of fig.7.The hydraulic line considered was similar to the one of fig.8.

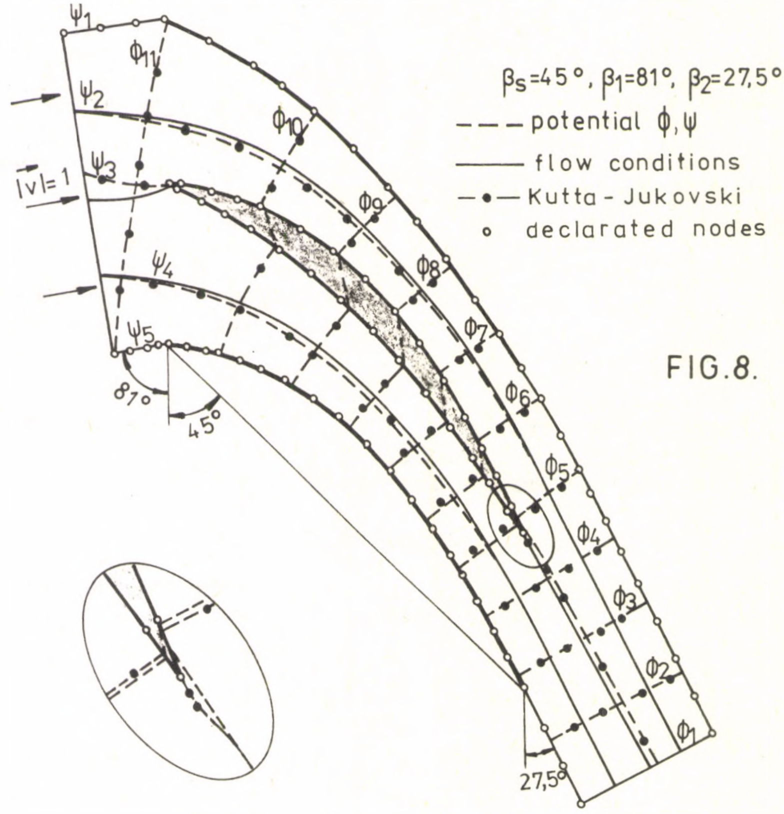

FIG.8.

The nodes existing in the figure were those declared as input data for the computer.The flow domain was finally divided into a second order discretization of 850 nodes.The computation time was about 28 minutes on a Felix C512 computer.The average lenght of the hydraulic line at input was considered to be t/2.This lenght was chosen because during the experimental tests,the direction of the current at input was determined at this distance.The straight lines limiting the domain at input are considered parallel to $\vec{v_1}$ (at the angle β_1).At the cascade output is chosen in such a way that the streamline at the cascade output should have the tangent at β_2 angle as well(see fig.7.). Some pure potential field lines are represented in fig.8,as well as the lines obtained by imposing

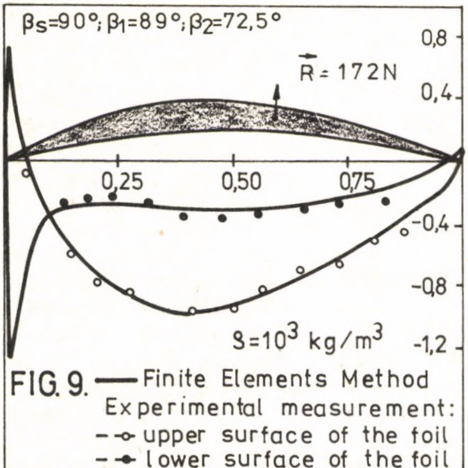

FIG. 9.

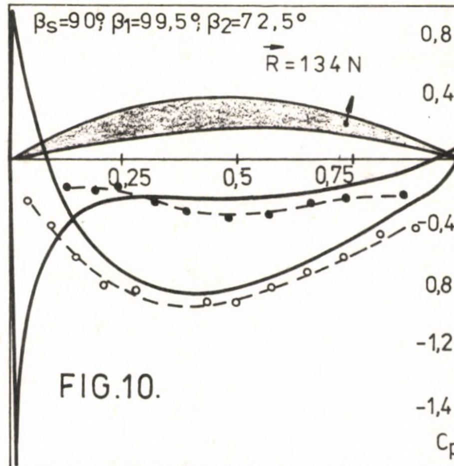

FIG. 10.

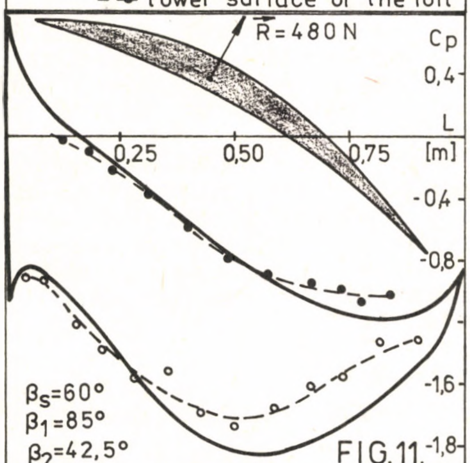

FIG. 11.

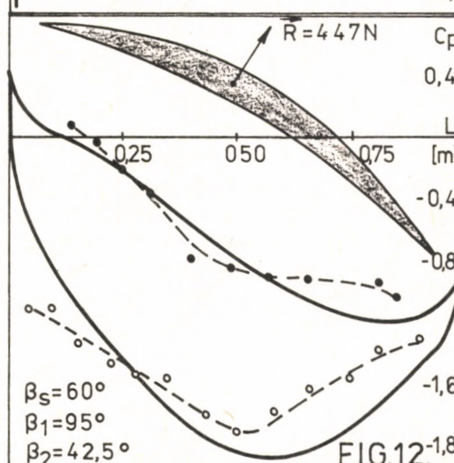

FIG. 12.

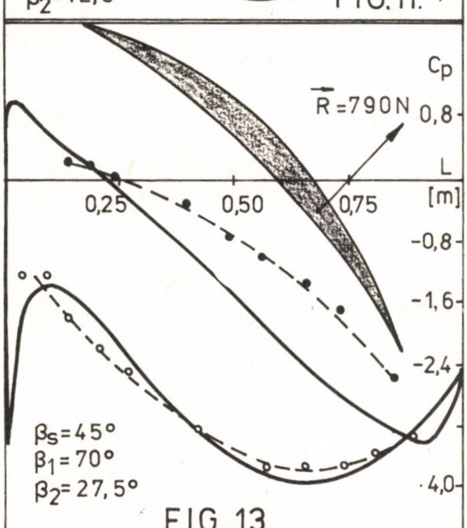

FIG. 13.

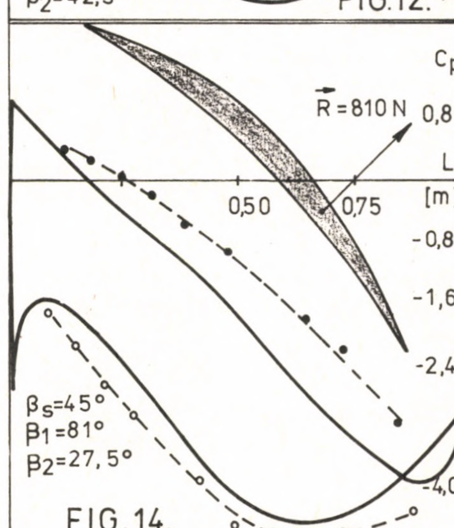

FIG. 14.

of Kutta-Jukovski condition.It can be noticed that the pure potential field line leaves the foil in the proximity of the trailing edge,although the blade is very inclined as compared to the input flow.The flow over the foil differs from the one flowing under the foil,the ratio between the flows being 1,31.The foil does not divide the flow into equal parts even after the Kutta-Jukovski condition has been imposed and it differs quite slightly from the pure potential case.

The pressure coefficient defined by $C_p=1-v^2/v_1^2$ was totally different,in both cases,from the experimental curves. In fig.9...14 the pressure coefficient obtained by imposing the condition of equal flows between the blades,was represented.By comparison,the experimental curves transposed from /3/ have also been traced.The Kutta-Jukovski condition was no more imposed for these curves and yet,the streamline leaves the foil on the output edge.The circulation as well was different. from zero.The foils in the computation position and the resulted theoretical forces were also represented in fig.9...14. For the angle $\beta_s=90^o$ and $\beta_1=89^o$ the theoretical calculus is in perfect accordance with the experimental measurement.At other angles of β_s and β_1 ,larger and larger deviations begin to appear.At $\beta_s=45^o$ the theoretical calculus is only for orientation as the deviations are too large.

As conclusion,one can state that by imposing equal flows between the foils,good enough results are obtained as compared to the experimental measurements.The research work should be continued in order to obtain a calculus correction for a better correspondance of theoretical and experimental results.The method can also be used in the computation of simple or multiple circular cascades.

Bibliography

1.Chung T.J.:"Finite Element Analysis in Fluid Dinamics" Mc.Graw Hill,New York,1972

2.Vries G.de,Norrie D.H.:"The Application of the Finite Element Technique to Potential Flow Problems",Journal of Applied Mechanics Transaction of the American Society of Mechanical Engineers,pp.798-802,1971.

3.Gheorghiu M.:"General Characteristic of Cascade",Politechnic Institute Traian Vuia Timişoara.

4.Kolati I.,Butaru I.:"Axial-simetric flow Computation with the Finite Element Method"-Journal of Machine Construction, no.1.Bucureşti,1983.

Iacob Voia -Dr.engineer,scientific researcher

Iuliu Kolati -Physicist,scientific researcher

Scientific Research and Technological Engineering Center for Hydroenergetic Equipement

Address: Calea Caransebeşului Nr.16

1700 Reşiţa-România

AXIAL THRUST IN PUMPS WITH MODERNIZED GUIDE VANES

Andrzej KORCZAK, Janusz LAMBOJ

SUMMARY

The paper deals with the measuring results of the axial thrust in centrifugal single-stage impeller pump with modernized centrifugal vanes. The parameters of the pump as well as the axial thrusts were measured, the pump having a built in stator with a typical inlet, guide vanes with a reconstructed inlet and a rotor with relief orifices. Measurements were taken for varying numbers of revolutions and for different positions of the rotor. Moreover, the structure of the tested pump was discussed, as well as the method of measuring the respective quantities.

1. DISCRIPTION OF THE INVESTIGATED SET OF PUMPS

In these investigations a reconstructed stage of a multistage pump with guide vanes was used. The fundamental dimensions of this stage may be gathered from Fig. 1.

Fig. 2 represents a diagram of a measuring position. The rotor 1 of the pump has been mounted on the shaft 2 sliding in the bearing body 3. The longitudinal bearing 4 of the impeller set has been mounted self-aligningly in the impeller arm 5 so that it became possible to measure the axial thrust could be measured making use of a hydraulic servo-motor 6.

The pump is driven over a sliding clutch 7 by a DC motor 8 bedded in a cradle 9. The 28 kW motor with a nominal number of revolutions n = 3000 min^{-1} is fed from a silicon-controlled rectifier. The momentum on the shaft was measured by measuring the reaction of the motor arm on a balance. The number of revolutions of the motor was measured by means of a photo-

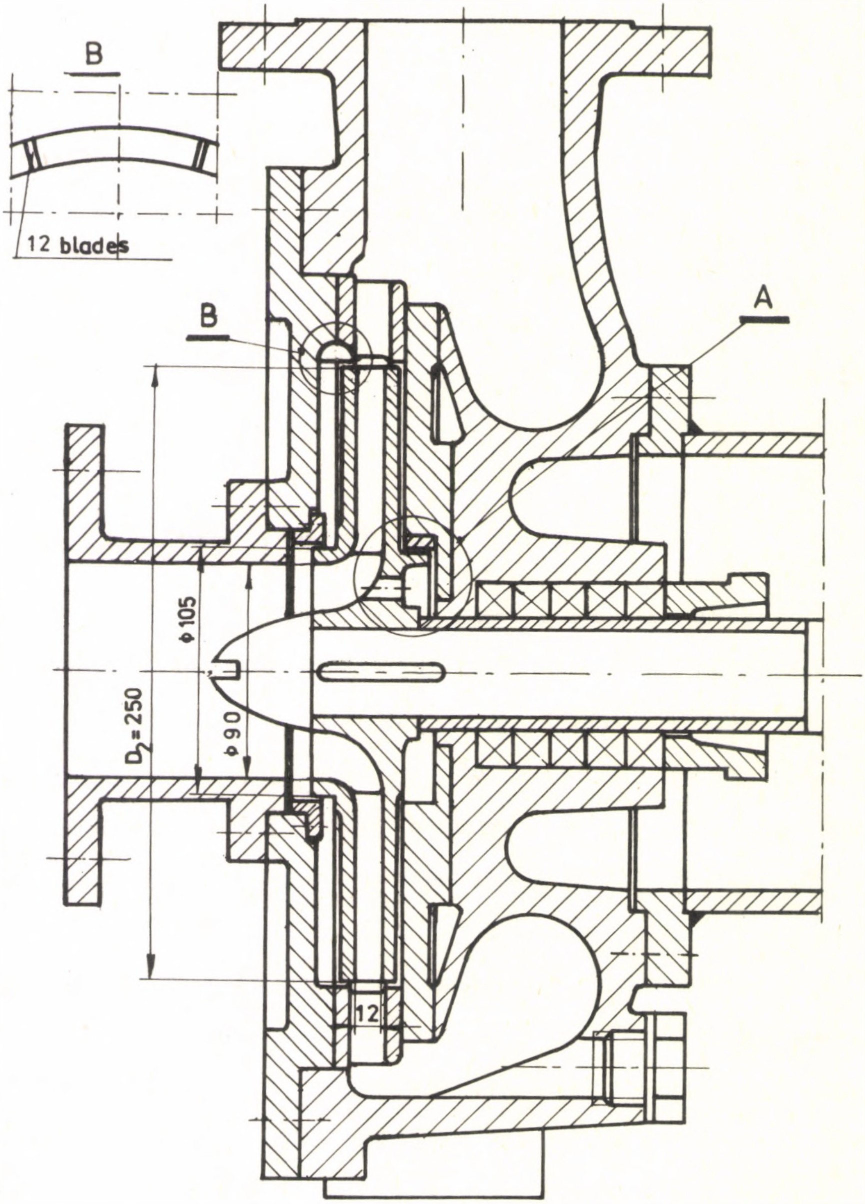

Fig. 1. Diagram of the investigated pump.

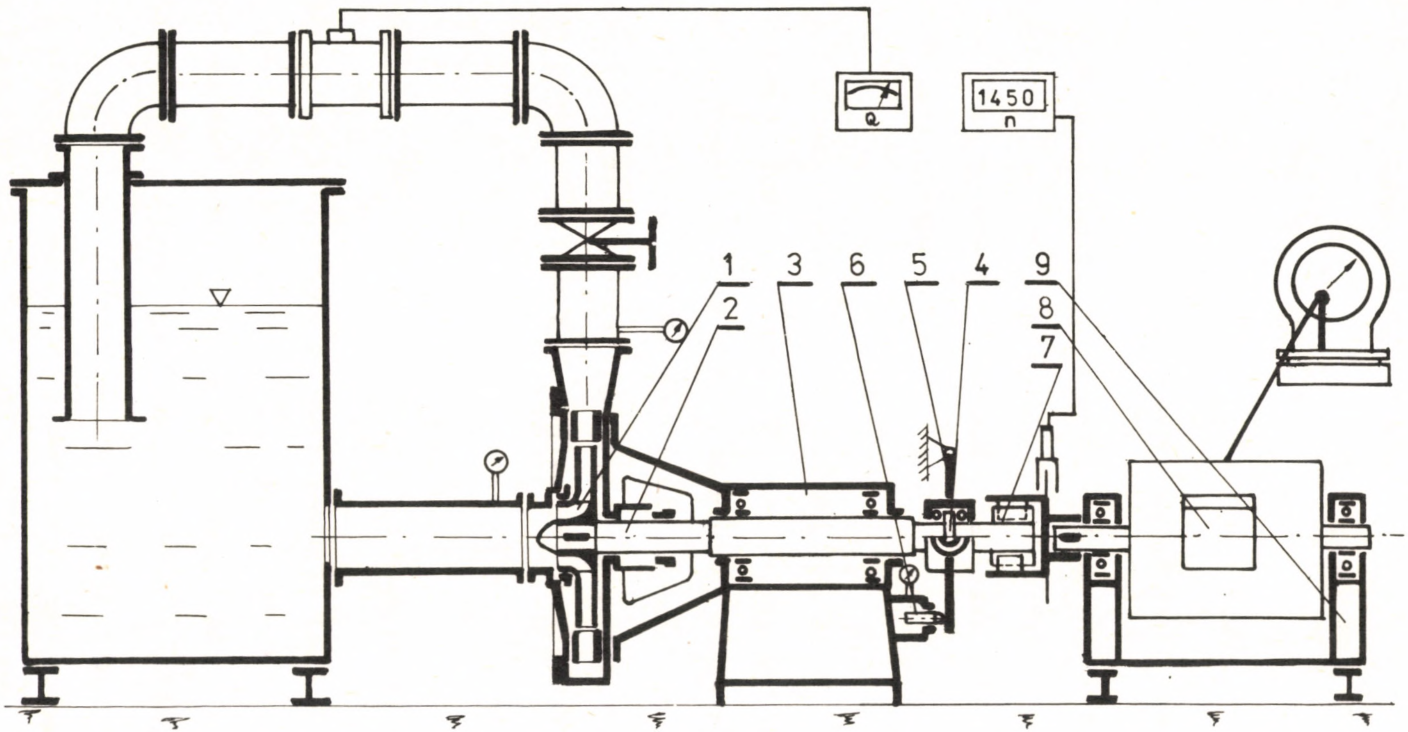

Fig. 2. Diagram of the measuring system.

electric converter. The pump was operated in a circulating pump system, the pressure and temperature being controlled at steady-state conditions.

2. MEASURING RESULTS

2.1. Measurements of an unloaded pump

Measurements of the shell characteristics and axial thrust $P = f(Q)$ of an unloaded pump within the rotational speed range $n = 1450$ to $2350\ \mathrm{min}^{-1}$ have made it possible to plot the characteristics presented in Fig. 3 and the curves a in Figs. 6 and 7.

It turned out that the axial thrust reaches values which are more than 100 % higher than the calculated ones, due to the shape of the space between the rotor disks and the walls of the casing, and also to the roughness of the walls. The measured characteristics of efficiency facilitate the evaluation of the effect of further reconstructions on the decrease of the efficiency of the pump.

2.2. Measurements of a pump with relief orifices

Fig. 4 shows a set of iso-efficieny curves of a pump with relief orifices. If we compare it with the diagram in Fig. 3, we see that due to the application of relief orifices the efficiency decreased by 4 %. The width of the sealing slot on the rear ring of the rotor was 0,25 mm.

Measurements of the axial thrust have made it possible to plot the curves b in Figs. 6 and 7. These diagrams show that at an

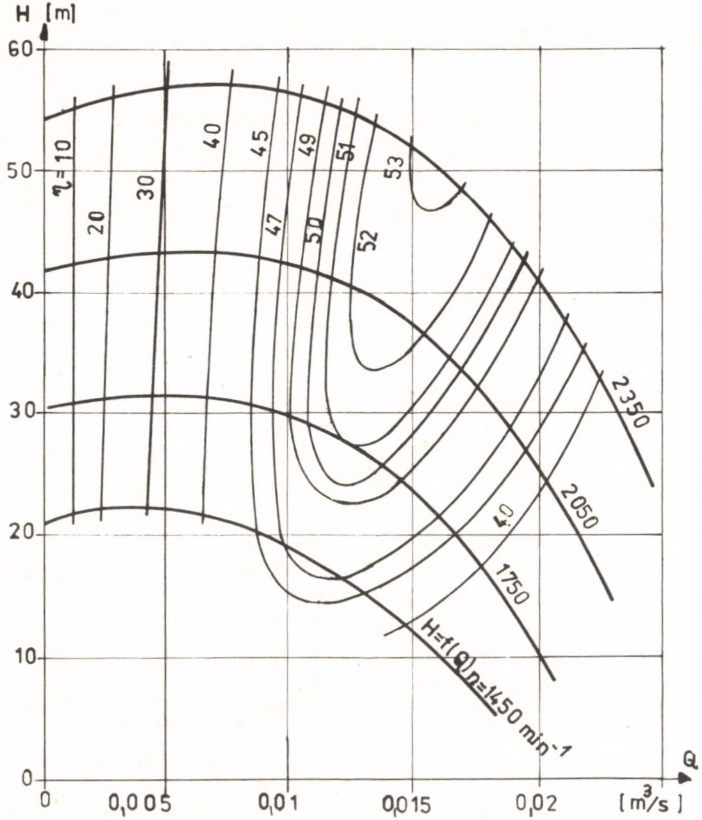

Fig. 3. Iso-efficiency curves of a pump without a relieved axial thrust.

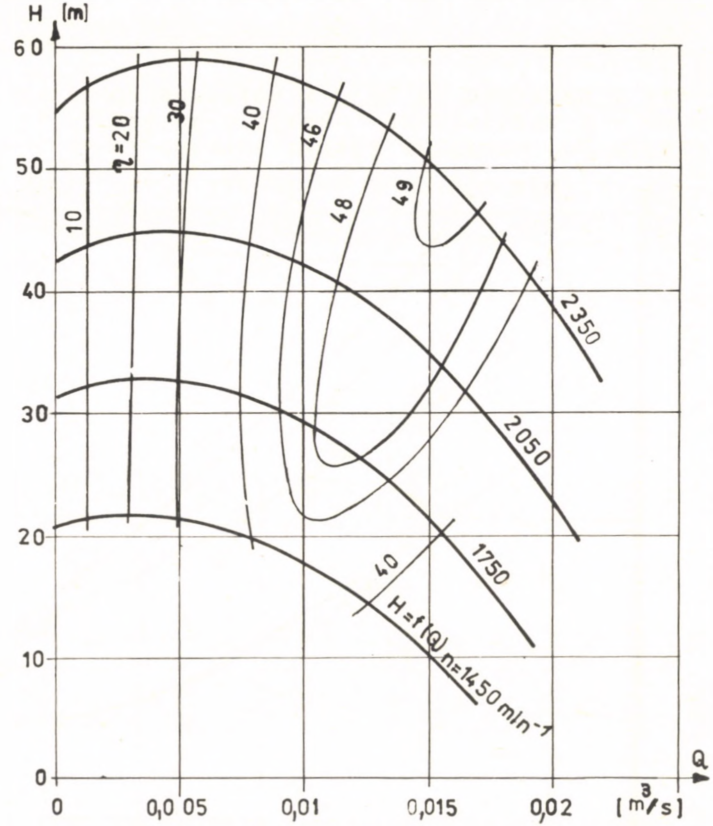

Fig. 4. Iso-efficiency curves of a pump with a rotor provided with relief orifices.

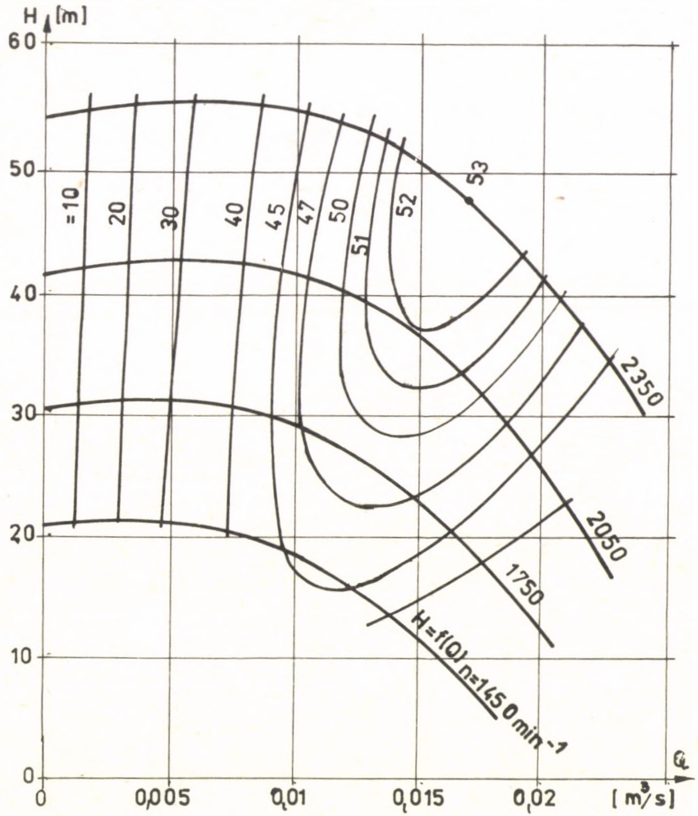

Fig. 5. Iso-efficiency curves of a pump with modified guide vanes.

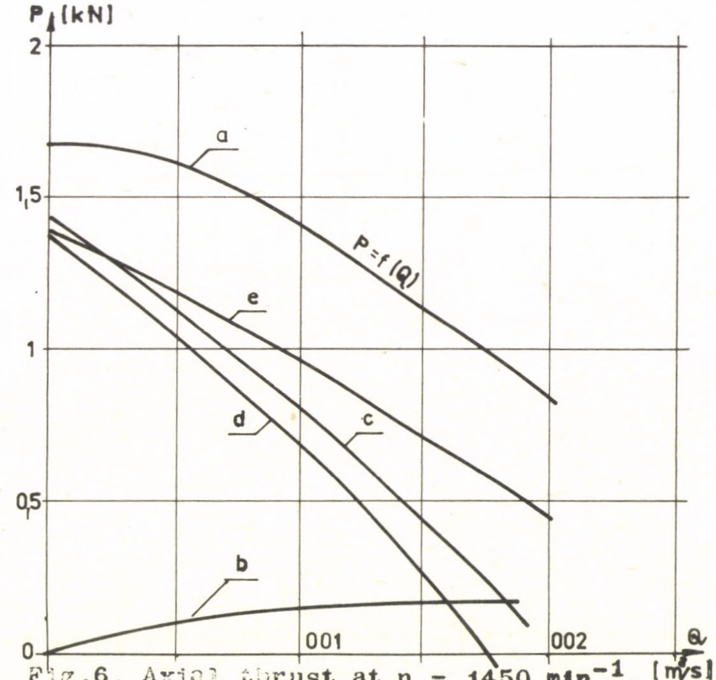

Fig.6. Axial thrust at n = 1450 min^{-1}.

a/ without relief orifices, b/ with relief orifices, c/ position x = -2, d/ position x = 0, e/ position x = 2.

efficiency of Q = 0 the axial thrust equalled zero, growing with the increase of the efficiency, without exceeding, however, 10 % of the thrust value in the case of a lack of relief.

2.3. Measurements of a pump with reconstructed centrifugal guide vanes

In order to set down the axial thrust centrifugal guide vanes were constructed as described in [1]. Its front disc is provided with a sharp edge to distribute the stream flowing out of the rotor. The dynamic pressure of the part of the stream directed into the space between the rotor and the cover of the pump increases the statical pressure at the front side of the rotor. An additional effect is brought about by the blades which are slowing down the circulation of the liquid. Measurements of the iso-efficiency curves /Fig. 5/ of a pump with reconstructed guide vanes proved that in the case of a coaxial positioning of the rotor and the guide vanes its influence on the reduction of the pump efficiency is small and may be neglected.

The application of new guide vanes resulted in a decrease of the axial thrust by about 50 % if the rotor and the guide vanes were positioned coaxially, as may be gathered from the curves shown in Figs. 6 and 7. When the rotor was shifted 2 mm towards the suction side, the axial thrust decreased /cf. curves d in Figs. 6 and 7/, if it was shifted backwards, the axial thrust grew /cf. curves e in Figs. 6 and 7/. Fig. 8 presents the non-dimensional coefficients of the axial thrust for

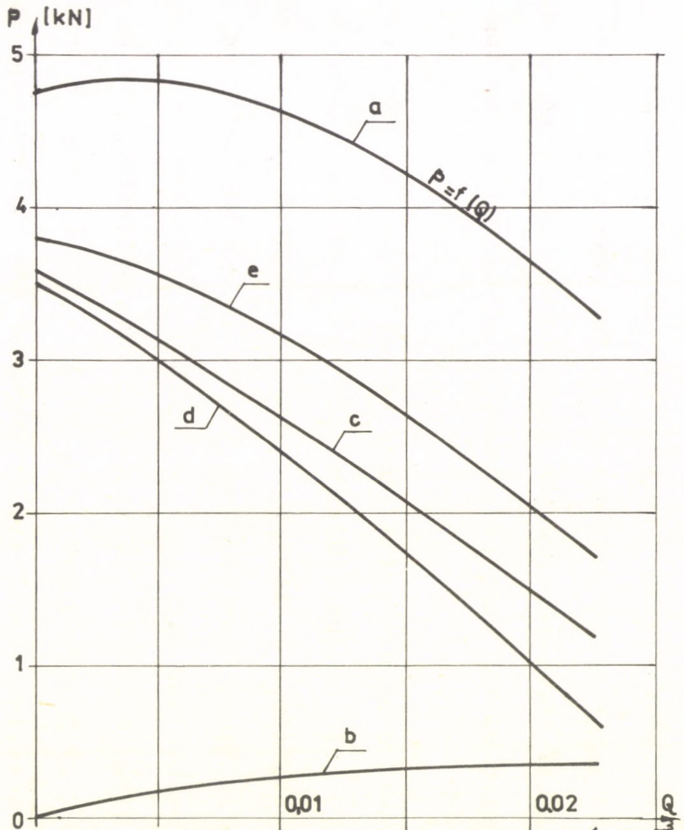

Fi.7. Axial thrust at n = 2350 $\min^{-1}$. a/ without relief orifices, b/ with relief orifices, c/ position x = -2, d/ position x = 0, e/ position x = 2.

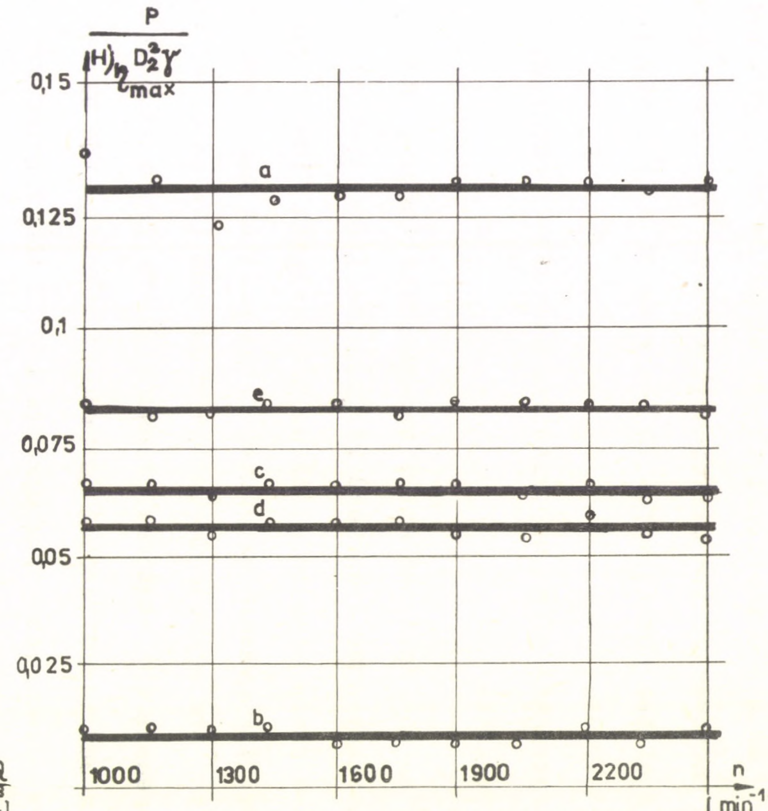

Fig. 8. Non-dimensional coefficient of the axial thrust in the rotational speed function.

the investigated cases of relief and positioning of the rotor.

3. CONCLUSIONS

As these investigations have shown, the adequate shaping of the space between the rotor discs and the walls of the casing makes it possible to reduce the axial thrust with a simultaneous permissible pressure drop. Such a method of relieving does not lengthen the pump stage, and thus it does not lead to a lengthening of the whole pump. Preliminary results justify the prediction that it might be possible to reduce the axial thrust to an indispensable minimum, i. e. to the values transmitted by the bearings. Relief achieved due to a reconstruction of the inlet to the centrifugal vanes leads to inherent regulation, which means that as the rotor is being shifted towards the suction side, the axial force will decrease. In the course of the investigations described in this paper a zero and even negative axial thrust have been achieved, though it was in the case of high capacities and low efficiencies.

REFERENCES

1. A.Korczak: Wlot kierownicy pompy wirowej odśrodkowej /The inlet of the guide vanes of centrifugal impeller pumps/, Polish patent No 231901, 1982.

KORCZAK Andrzej, Dr techn.
LAMBOJ Janusz, Dipl.Ing.

Silesian Technical University
44-100 Gliwice, ul. Konarskiego 18
POLAND

EFFECTS OF OPERATING CONDITIONS ON CENTRIFUGAL PUMPS WHEN CONVEYING LIQUIDS WITH GAS CONTENTS

by

KOSMOWSKI, I. and STEINHEIMER, K.-H.

1. Influence of Gas contents on the Performance Characteristics of Pumps

It is well known from existing literature that gas in the pumped flow has a very pronounced effect on the operating behaviour of centrifugal pumps. It shows itself in the drop of the pump characteristics as compared with a pure liquid operation. To estimate the influence of the gas on the operating behaviour of the pump it is useful to refer the head and flow coefficients to the appropriated head and flow coefficients at the point of the best efficiency of the liquid delivery. The result are the normalized head and flow coefficients (ψ_* and φ_*) as dimensionless parameters for the representation of the performance characteristics.

The influence of gas content existing at the pump inlet on the performance characteristic of an end-suction centrifugal pump is shown in Fig. 1.

In it for a dimensionless plotting of the dependence of the pump characteristics on the supplied amount of gas the gas columetric flow is related to the total volumetric flow of liquid and gas, i. e. $\dot{V} = \dot{V}_l + \dot{V}_g$. The result is the volumetric flow fraction of gas:

$$\overset{(\cdot)}{\varepsilon} = \frac{\dot{V}_g}{\dot{V}} \qquad (1)$$

which essentially is a function of pressure according to the compressibility of the gaseous phase. Therefore, the value of volumetric flow fraction refers to a fixed cross-section

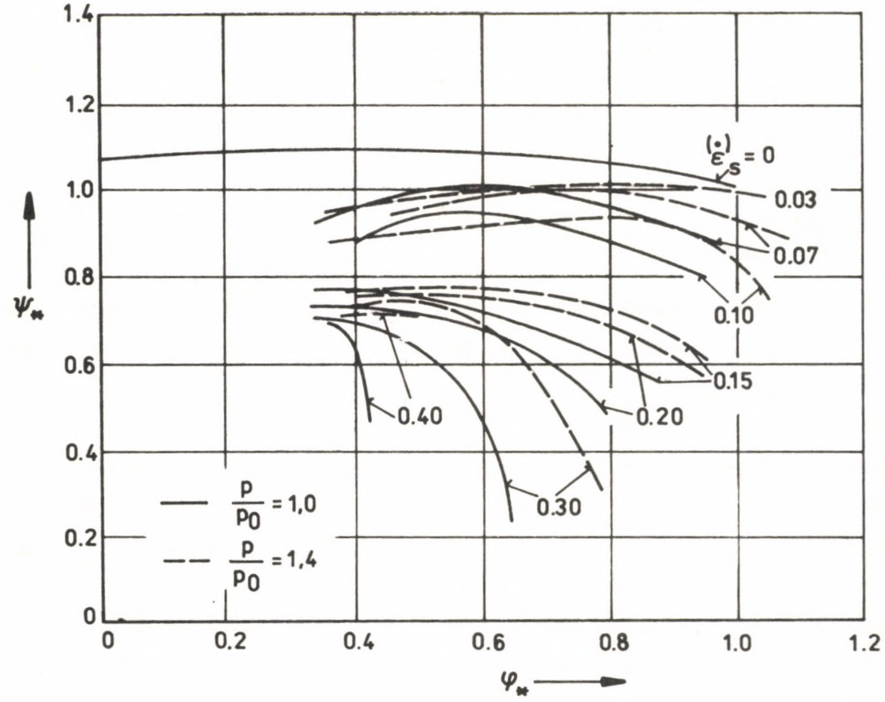

Fig. 1 Performance Characteristics of the Tested Pump in Dependence on the Volumetric Flow Fraction of Gas and the Pressure in the Suction Connection

with what according to the isothermic change of state of the gas phase a unique dependence on the pressure is determined. It is useful to represent the pump characteristics as a function of the pressure in the suction connection according to the conditions of the entry flow to the pump (Ref. 1).

For the representation of the performance characteristic the pump head is determined by the following equation:

$$H = \frac{v_d^2 - v_s^2}{2g} + \frac{1 - \overset{(\cdot)}{\mu}}{\varrho_l\, g} (p_d - p_s) + \frac{\overset{(\cdot)}{\mu}\, RT_g}{g} \ln \frac{p_d}{p_s} + (z_d - z_s) \qquad (2)$$

considering that the liquid-gas flow can be carried as approximatively adiabatic to the atmosphere. By it in comparison to the delivery of liquids the pressure term must be completed with the value of the compression work of the gas phase. For the mass flow fraction of gas the following relation is current:

$$\overset{(\cdot)}{\mu} \approx \frac{p_s \, \overset{(\cdot)}{\varepsilon}_s}{(1 - \overset{(\cdot)}{\varepsilon}_s \, \varrho_l \, R T_g} \qquad (3)$$

For the mean mixture velocities obtained by the energy term can be set the mean velocities of the liquid phase achieved in the same way.

On condition that the fluid density at the pump inlet remains unchanged, what is in conformity with a constant value of the volumetric flow fraction of gas, it follows from the equations (1) to (3) that the head increases with an increase of the pressure in the suction connection. This tendency may be proved to be true representing in Fig. 1 by the experiments upon the pump. The dotted drawn curves are results of measurements with a higher pressure level in the suction line of the pump. The influence of the rotational speed on the discharge and the pump head may be expressed as

$$\dot{m} \sim H^{1/2} \sim \omega \qquad (4)$$

where $\dot{m}$ is the mass flow.

2. The Output Limit with Liquid-Gas Mixtures

Only on the understanding that detailed informations on the phase behaviour in the mixture flow are known it is possible to interpret the specialities when conveying gas laden liquids (Ref. 2).

As the pressure raises in the impeller the volumetric flow fraction of gas decreases as a mean value over the cross-section of the passage in flow direction. Nevertheless locally there can be higher volume fractions of gas at the impeller outlet than at the inlet cross-section of the impeller. In direction to the impeller outlet there is a strong unregular phase distribution over the cross-section of the impeller channel because of the pressure field resulting from centrifugal and Coriolis forces. This phase distribution may lead to local gas accumulations in the impeller outlet.

Moreover, because of the rotating flow is caused a pressure field in the space between the impeller and casing wall which demixes the phases of very different density. A larger drop in the performance characteristic of the pump arises when the gas rim expands which was built up by phase separation in the space between the impeller and casing wall (Ref.3).

The tests have shown that the pump has almost reached the delivery limit at that moment when the gaseous area is near the impeller outlet diameter. The larger gaseous area extending to impeller outlet gives the possibility of connecting the gas accumulations and leads to the interruption of delivery.

The influence of the operating parameters on the output limit $\dot{\varepsilon}_{out}$, which is related to the pressure at the pump inlet, is shown in Fig. 2.

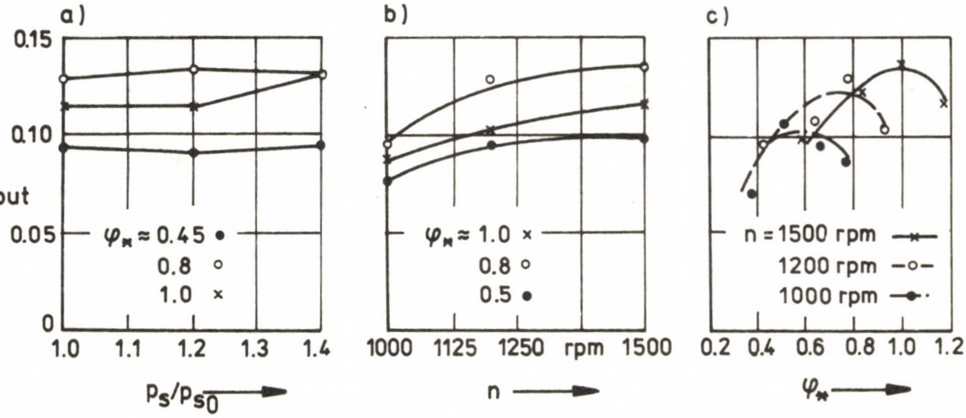

Fig. 2 Influences of the Operating Parameters on the Output Limit

Hence it is evident that neither the pressure at the pump inlet nor the rotational speed takes an important influence on the output limit. The small improvement of the characteristics results from the mixing influence of the impeller by an increase of the rotational speed. According to the proportionality

$$d_{bubble} \sim \omega^{-4/5} \qquad (5)$$

it follows that a higher angular velocity leads to smaller bubbles and with it to a more equal phase distribution.

It is doubtless noticed that the volume flow has a very pronounced effect on the output limit. This appaerance is explicable by the flow conditions in the channels of the pump because the position of the maximums correspond with the points of the best efficiency.

3. The Delivery Limit with Simultaneous Reduction of the Mass Flow Fraction of Gas in the Pumped Flow

Pumping of mixtures with higher volumetric flow fractions of gas can be realized by gas removing from the pump to the atmosphere where at the same time a reduction of the mass flow fraction of gas in the pumped flow takes place (Ref. 4). Since it is impossible to lead the gas unlimited out of the pump to the atmosphere the pump will reach with a certain volumetric flow fraction of gas its delivery limit $\overset{(\cdot)}{\varepsilon}_{del}$. This limit depends, what is described in Fig. 3, on the volume flow and the rotational speed.

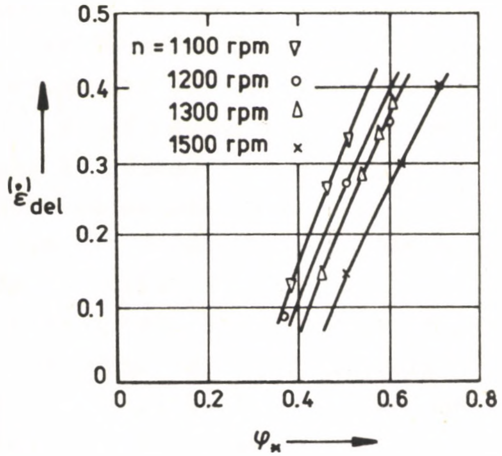

Fig. 3 Influences of the Volume Flow and the Rotational Speed on the Delivery Limit

4. The Barrage Limit in Conveying Liquid-Gas Mixtures

As shown with the performance characteristics in Fig. 1 pumps when conveying liquid-gas mixtures cannot work at operating points near to the zero value of the volume flow. Different to the delivery of a pure liquid the pumping of gas entrained liquids is limited by reaching a minimum volume flow. This limit described as barrage limit of the pump results from the flow conditions of liquid and gas phases. The motion of the phases surrenders itself by the value of the slip v_{rel}, i. e. the relative motion between gas and liquid phases, in proportion to the velocity of the mixture which is in conformity with the liquid velocity. The liquid velocity as transport velocity, whereby is decided the motion of the gaseous phase, can be expressed by the proportionality to $\dot{V}_1$. Consequently the transport velocity of the mixture is on the decrease by decreasing the liquid volume flow. In combliance with the proportionality

$$v_{rel} \sim (\text{grad}\, p)^{1/2} \sim \omega \qquad (6)$$

the pressure gradient depends on the centrifugal field and the slip cannot be strongly influenced by changing the volume flow. Therefore, with small values of volume flow the slip can be reach values in the order of the transport velocity whereby the pump get near to the barrage limit. Almost independent upon the volumetric flow fraction of gas related to the suction connection gas accumulations develop themselves in the impeller channels in areas which are marked by the formation of secondary whirls. Hence it follows that all the performance characteristics, which are ascertained with different volume flow fractions of gas, are directed to one and the same value of the head coefficient. The approach of the pump to operating points near to the barrage is connected with a partial working of the impeller according to which the pumping is realized by only some passages more. By further decreasing in the volume flow the pump reaches the barrage limit.

5. The Importance of the Sound Number in regard of the Liquid-Gas Delivery

The sound velocity of a liquid-gas flow depends according to the equation

$$a \approx \left[\frac{p}{\varepsilon(1-\varepsilon)\,\varrho_l}\right]^{1/2} \tag{7}$$

on the volume flow fraction of gas ε and the pressure. Therefore, it must be taken into consideration that it depends on the pressure in the suction connection wether the sound velocity can appear somewhere in the pump.
The Sound Number

$$N_{sound} = \dot{V}\omega^2\left[\frac{\varrho_l}{(1-\overset{(\cdot)}{\mu})\,p}\right]^{3/2} \tag{8}$$

as a term depending on the design of pump and the flow fraction of gas (Ref. 5) set the limit for it that the flow everywhere in the channels of the pump possesses a subsonic velocity. As an numerical example for the equation (8) it is shown in Fig. 4 which context exists between the volume flow, angular velocity and the pressure in the suction connection for a given pump with an appointed flow fraction of gas.

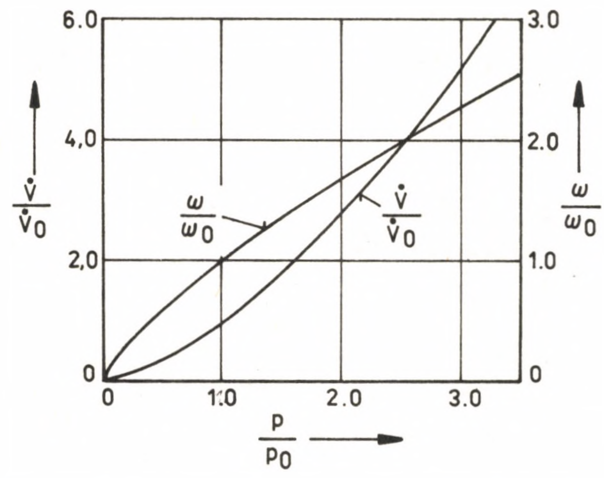

Fig. 4 Influence of the Pressure in the Suction Pipe on the Volume Flow and on the Possible Rotational Speed at the Sound Limit

In this way there will be a limit related to the pressure in the suction connection when conveying liquid-gas mixtures like it is known from the cavitation in the liquid delivery.

KOSMOWSKI, I. Prof. Dr. sc. techn.
STEINHEIMER, K.-H. Dr.-Ing.
Setion Diesel Engines, Pumps and Blowers
Department of Fluid Engineering
TH Otto von Guericke
Magdeburg, German Democratic Republic

References

1. Kosmowski, I.: Behaviour of Centrifugal Pumps when Conveying Gas Entrained Liquids, 7th Technical Conference BPMA, 1981, York

2. Steinheimer, K.-H.: Abreiß- und Fördergrenze bei der Förderung von Flüssigkeits-Gas-Gemischen mit Kreiselpumpen, Wiss. Z. TH Magdeburg 25 (1981), H. 4, S. 47 - 51

3. Kosmowski, I.: Problems when Conveying Liquid-Gas Mixtures and Conclusions for the Construction of Centrifugal Pumps, 11th Symposium IAHR, 1982, Amsterdam

4. Kosmowski, I.: Design of Centrifugal Pumps for the Delivery of Liquids with High Gas Contents, 8th Technical Conference BPMA, 1983, Cambridge

5. Steinheimer, K.-H.: Die Überschallgrenze bei Pumpen zur Förderung von Flüssigkeits-Gas-Gemischen, Wiss. Z. TH Magdeburg 26 (1982), H. 4, S. 17 - 20

A CONTRIBUTION TO THE CORRELATIONS BETWEEN CAVITATION EROSION AND MATERIAL MECHANICAL PROPERTIES

A. KOUTNÝ

SUMMARY

In this paper the results of investigations into cavitation erosion resistance of a selected group of materials being applied for the manufacture of hydraulic machines are presented. Tests were carried out under laboratory conditions in a test device with rotating disk in water and the objective was to determine primarily the relative resistance to cavitation erosion of the tested materials in dependence upon the cavitation intensity.

An attempt was made to determine the correlations between the rate of cavitation erosion and the ultimate resilience under altered test conditions - such as the peripheral velocity of the cavitation inducer holes in the disk which affected the cavitation intensity.

The laboratory test results are discussed and compared with the conclusions obtained from the testing of materials in pump under operating conditions.

1. INTRODUCTION

A great number of publications in the field of cavitation deal with the evaluation of materials resistance to cavitation erosion. Diverse test devices based upon different principles and test conditions are applied by various investigators. In spite of the implementation of many tests of virtually all technically applicable materials, no convenient guidelines recommending machine parts materials working under cavitation erosion conditions and thus not even sufficient data for an appropriate choice of material exposed to cavitation of different intensity are available.

According to recently gained experiences materials of various hydraulic machine parts show a different relative cavitation erosion resistance depending upon cavitation intensity which is to be taken into account in the evaluation of the cavitation erosion resistance of materials.

The cavitation erosion mechanism damaging materials even those of high strength, is a very complicated phenomenon. The mechanical effects of cavitation are presumed to be prevailing in general, even if corrosive affects are to be taken into account, as well. The investigation into this combined phenomenon appears to be, at the present state of knowledge, only too difficult. For this reason laboratory cavitation investigations are being carried out under conditions of cavitation intensities where mechanical effects are dominant.

Insufficiently precise knowledge of cavitation intensity and of other important cavitation effect characteristics reduces the significance of laboratory testing and frequently the application of the obtained results in the case of other conditions is virtually not feasible.

2. LABORATORY TESTS AND CORRELATIONS OF CAVITATION EROSION WITH MATERIAL MECHANICAL PROPERTIES

For the determination of the resistance to cavitation erosion under laboratory conditions, in the main four basic methods have been developed - in the cavitation area created in the Venturi-type device, in the cavitation area created behind the rotating disk hole, in the cavitation area created by the vibrations and by numerous impacts on water jet.

All laboratory methods show a common imperfection consisting in the impracticability of a uniform cavitation intensity assessment.

The experimental verification of cavitation erosion resistance seems to be, for the time being, the most appropriate method for any technically applicable material. The finding of a method facilitating a preliminary classification of materials from the standpoint of their cavitation erosion resistance, precise enough to achieve an overall reduction of laboratory tests number and costs, is considered to be very useful.

In the past half-century many papers relating to the correlations between cavitation erosion and different material properties were published. However, no good correlation valid for a wide number of different materials and test methods and conditions was determined hitherto. The reason why the measure of cavitation erosion resistance of materials cannot be correlated with mechanical properties consists without any doubt in the fact that there exist too many factors which are necessary to be involved.

Various investigators exerted to find the best material property which could be derived from conventional mechanical properties and would have the unit of energy per unit volume, since the maximum volume loss rate was presumed to be inversely proportional to the energy necessary for the removal of the unit volume from the material /1/.

So for example Hobbs /2/ ascertained that the best correlation was created by the ultimate resilience defined as

$$UR = \frac{R_m^2}{2E} \qquad (1)$$

where UR - ultimate resilience, R_m - ultimate tensile strength and E - modulus of elasticity in tension.

Hammitt /3/ verified this parameter and recommended a following relation expressing that the reciprocal maximum mean depth of penetration rate MDPR was direct proportional to ultimate resilience

$$MDPR_{max}^{-1} = C_o + C_1 . UR \qquad (2)$$

where $MDPR_{max}^{-1}$ - "erosion resistance", C_o, C_1 - constants and UR - ultimate resilience.

Parameter UR was implicated in experiments performed by other investigators /4/, /5/ and a good correlation between both quantities was confirmed. For that reason this parameter was employed for the evaluation of the cavitation intensity effect upon material resistance in the subsequent tests.

3. TEST DEVICE AND TEST CONDITIONS

For the experimental examination of the cavitation intensity effect upon the relative resistance of selected materials group a laboratory test device with rotating disk being applied for cavitation investigations in the SIGMA Research Institute was employed.

The principle of this device is well-known. In the given case a flat disk with a diameter of 275 mm is rotated in a water-filled chamber. The disk is provided with holes of 6 mm diameter generating cavitation and futhermore six specimens are inserted in the disk. A detailed description of the test device and test method is given in reference /6/.

The disk revolutions during testing was altered in the range of 5000, 4500, 4000 and 3500 rev/min which in the given case corresponded to the peripheral velocity of cavitation inducer holes 60,2, 54,2, 48,2 and 42,1 m/s. The static pressure of the liquid within the test chamber was 0,07 kPa and the fluid temperature 40 degC. As test fluid distilled water with a stabilized gas content was applied. The total test period was chosen to obtain the maximum rate of cavitation erosion and achieved 50-200 hours in dependence upon the disk revolutions.

4. TEST MATERIALS

For the given experiments altogether six stainless steels being applied in Czechoslovakia for the manufacture of hydraulic machines, were chosen. These steels have a different chemical composition, structure and mechanical properties. The chemical composition and structure are given in Table 1, the review of the observed mechanical properties in Table 2.

Steels manufactured according to Czechoslovak State Standard and designated ČSN 42 2904, ČSN 42 2905 and ČSN 42 2906 are stainless 13% Cr steels for castings employed in the production of water turbines and pumps. Steel ČSN 42 2931 represents the stainless 18-9 CrNi austenitic steels and steels designated Cr13Ni4 and Cr13Ni6 are low-carbon stainless steels of martensitic type applied in the manufacture of highly stressed machine parts. Hence for the given experiment solely stainless steels which have approximately the same corrosion resistance in the medium in question, were employed.

5. TEST RESULTS AND DISCUSSION

The numerical test results in dependence upon the peripheral velocity of the cavitation inducer holes (cavitation inten-

Table 1 Chemical composition and structural conditions of test materials

Materials reference	Steel designation	C	Mn	Si	Cr	Ni	Mo	Structural condition
		Chemical compositions (%)						
1	ČSN 42 2904	0,10	0,66	0,16	12,20	1,15		TM(+F)
2	ČSN 42 2905	0,12	0,40	0,48	13,30	0,11		TM(+F)
3	ČSN 42 2906	0,17	0,24	0,45	13,00	0,13		TM
4	ČSN 42 2931	0,11	0,32	0,81	20,10	9,96		A(+F)
5	Cr13Ni4	0,06	0,30	0,16	13,50	4,10	0,32	TM(+TA+F)
6	Cr13Ni6	0,06	0,38	0,39	11,28	5,60		TM(+TA)

Note: TM - tempered martensite
F - ferrite
A - austenite
TA - transf. austenite

Table 2 Some characteristic mechanical properties of test materials

Materials reference	R_m (MPa)	$R_p0,2$ (MPa)	A (%)	HV 30	E ($x10^5$MPa)	UR ($x10^{-3}J.mm^{-3}$)
1	600	359	24,9	191	2,19	0,822
2	618	390	15,8	184	2,19	0,872
3	731	508	21,4	223	2,19	1,220
4	577	226	41,0	170	1,95	0,854
5	859	675	13,2	282	2,07	1,782
6	849	633	19,2	299	2,07	1,741

sity), in the given case represented by the maximum mean volume loss rate MVLR and its reciprocal values are given in Table 3.

Table 3 Numerical results of cavitation erosion tests

Materials reference	v ($m.s^{-1}$)	$MVLR_{max}$ ($x10^{-3}mm^3.min^{-1}$)	$MVLR_{max}^{-1}$ ($x10^2 min.mm^{-3}$)
1	60,2	15,1	0,66
2		25,6	0,39
3		13,7	0,73
4		22,5	0,44
5		8,5	1,18
6		7,8	1,28
1	54,2	7,0	1,43
2		7,2	1.39
3		5,0	2,00
4		5,7	1,75
5		3,6	2,78
6		2,1	4,76
1	48,2	2,0	5,00
2		2,8	3,67
3		1,2	8,33
4		1,1	9,09
5		0,8	12,50
6		0,5	20,00
1	42,1	0,7	14,90
2		0,8	12,50
3		0,6	16,60
4		0,4	25,00
5		0,5	20,00
6		0,4	25,00

In order that an assessment of the effect of several mechanical properties on material resistance to cavitation erosion might be done calculations of equations of regression lines and correlation coefficients were made. Correlations with fundamental mecharical properties such as tensile strength, 0,2 proof stress, elongation and hardness presented in all cases lower values of correlation coefficients than the ultimate resilience. In Table 4 the regression line equations and correlation coefficients r_{xy} for the correlations of maximum MVLR and reciprocal maximum MVLR with UR are given.

In Fig. 1 the correlations of maximum mean volume loss rate and reciprocal maximum mean volume loss rate with the ultimate resilience for the given set of examined steels are illustrated. From the above mentioned results follows that the values of relative resistance to cavitation erosion of the

Table 4 Correlations of $MVLR_{max}$ and $MVLR_{max}^{-1}$ with UR (x)

Value (y)	v ($m.s^{-1}$)	Regression line $y = a + bx$	r_{xy}
$MVLR_{max}$	60,2	$y = 3,24.10^{-2} - 1,39.10^{-2}x$	-0,855
	54,2	$y = 1,01.10^{-2} - 4,02.10^{-3}x$	-0,928
	48,2	$y = 3,13.10^{-3} - 1,42.10^{-3}x$	-0,747
	42,1	$y = 8,06.10^{-4} - 1,97.10^{-4}x$	-0,541
$MVLR_{max}^{-1}$	60,2	$y = -1,78.10^{1} + 7,89.10^{1}x$	0,950
	54,2	$y = -5,82.10^{1} + 2,41.10^{2}x$	0,841
	48,2	$y = -3,81.10^{2} + 1,11.10^{3}x$	0,842
	42,1	$y = -1,21.10^{3} + 5,62.10^{2}x$	0,471

investigated stainless steels are altering in dependence upon the respective cavitation intensity at an overall decrease of cavitation erosion along with disk speed reduction which became evident above all in case of steels with different structure types. In case of cavitation intensity corresponding to peripheral velocity v = 60,2 m/s it was found that from the chosen material set, the stainless 18-9 CrNi austenitic steel showed a relatively low resistance. At a peripheral velocity reduction this steel manifests gradually from the standpoint of cavitation erosion resistance to be equivalent to martensitic structure steels. This steel ranks among the group of austenitic steels featuring good properties with regard to corrosion resistance and inclining considerably to work-hardening. The difference between the individual steel types of martensitic class is no more so evident.

The laboratory results and partial conclusions can be compared with results of operation tests performed in the past years /7/ with various types of weld stainless steels regarding the cavitation erosion resistance. The operation tests were carried out with a mixed-flow cooling pump impeller of 720 mm diameter manufactured of carbon steel for castings according to ČSN 42 2650. The impeller was considerably damaged by cavitation erosion in the area of the inlet and circumferential edges on the blade suction side already after 1 year of operation in a power station. The blades were repaired by overlaying (Fig. 2) according to indications in Table 5. In order that the same hydrodynamic conditions might be ensured a precisely equal geometric shape of all 3 blades was maintained.

The repaired impeller was put into operation and studied in certain repair intervals over a period of 5 years, i.e. after more than 30 000 working hours. Whilst the blades Nos 2 and 3 with an austenitic weld metal overlay virtually did not show any erosion, blade No 1 with a low-carbon stainless high strength martensitic steel overlay was already considerably

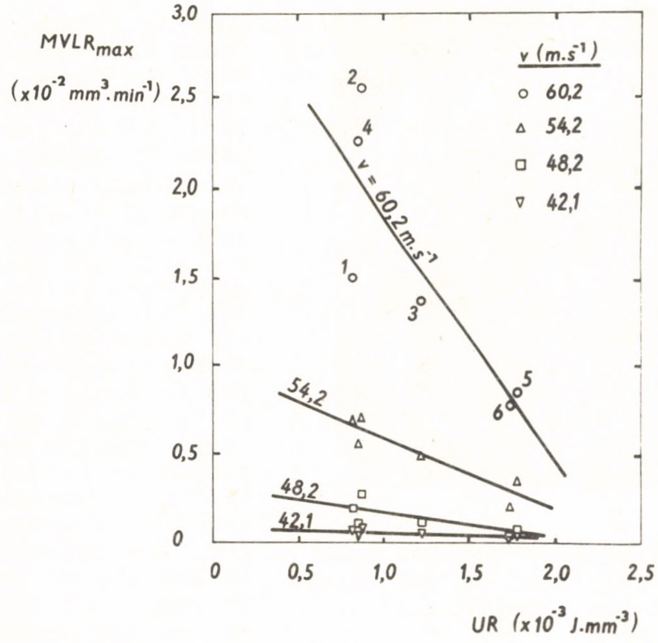

a)

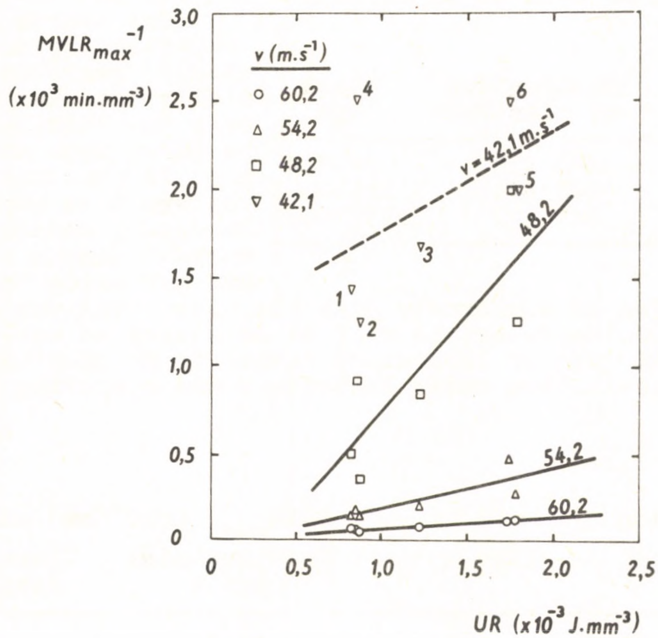

b)

Fig. 1 Correlations of maximum MVLR (a) and reciprocal maximum MVLR (b) with UR in dependence on peripheral velocity v

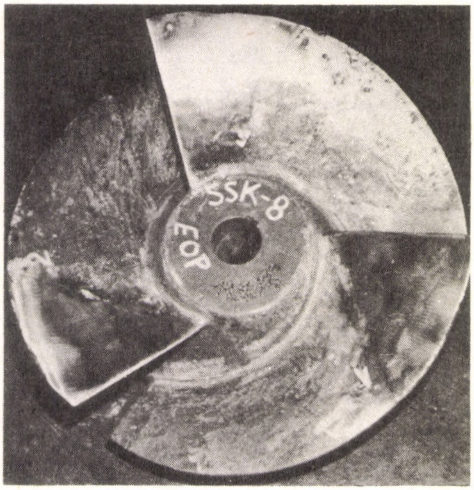

Fig. 2 Mixed flow cooling pump impeller after the repair of the damaged blades

damaged by cavitation erosion. These weld metals jointly with the basic material were evaluated as well with regard to cavitation erosion resistance by means of tests under laboratory conditions in the rotating disk test device with a peripheral velocity of $v = 60,2$ m/s and in the vibratory test device according to the ČSN standardized method /9/ corresponding to ASTM /10/. From the test results presented in Table 6 follows that on the basis of tests in the rotating-disk device and the vibratory device various resistance orders of the observed 3 weld metals were achieved. The material of electrode E-B 410 which appeared to be very good during laboratory testing showed the least resistance under operating conditions. Nevertheless, these results are presented here rather as a topic to be discussed and are not to be generalized.

Table 5

Blade No	Designation of electrode	Steel type
1	E-B 410	Cr13Ni4
2	E-B 472	Cr10Mn17
3	E-B 417	Cr18Ni8Mn5

The search for the correlations between cavitation erosion resistance and material properties requires not only the tensile strength to be taken into account but also further macroscopic characteristics such as surface hardness, endurance strength, work-hardening capability and corrosion resistance, these being in conformity with the considerations of Pighini et al. /8/. Moreover, it will be necessary as well to distinguish what type of laboratory device is in question, and/or between cavitation under laboratory and operating conditions etc.

Table 6

Designation of material	R_m (MPa)	$MVLR_{max}$ ($x10^{-3}mm^3.min^{-1}$) Rotating-disk device	Vibratory device
ČSN 42 2650	min 500	32,3	
E-B 410	1400-1500	4,1	11,8
E-B 472	700-780	10,8	6,8
E-B 417	500-580	4,8	16,6

a) b)

Fig. 3 Impeller blade a) after one-year operation (fundamental material)

b) after five-year operation (stainless steel overlay by electrode E-B 410)

From the energy point of view it is necessary for the achievement of a convenient correlation parameter stating the cavitation erosion resistance of material to apply the method of determination of energy exerted on plastic deformation, initiation of cracks and their propagation, and/or phase transformations etc.

6. CONCLUSION

From the laboratory test results conclusions can be drawn that the relative resistance to cavitation erosion of the respective stainless steels is altering in dependence upon cavitation intensity and a change of order of the individual steels with a different structure type occurs.

Furthermore, due to cavitation intensity under laboratory conditions the material resistance dependence upon the mechanical properties of material including parameter UR is changing. Some results from the investigations of cavitation erosion under operating conditions outline that the tensile strength of material and hence the parameter UR are not decisive for the material resistance assessment.

The initial mechanical properties are confirmed not to be in a good correlation with the resistance to cavitation erosion which is attributed to the mechanical properties change of the material surface layer during cavitation erosion.

REFERENCES

/1/ HAMMITT, F.G.: Impact and Cavitation Erosion and Material Mechanical Properties, Univ. Mich., Ann Arbor, Michigan, Rep. UMICH-03371-1-T, 1969.

/2/ HOBBS, J.M.: Experience with a 20 kc Cavitation Erosion test, Erosion by Cavitation or Impingement, ASTM STP 408, 1967, 159-176.

/3/ HAMMITT, F.G. et al.: A Statistically Verified Model for Correlating Volume Loss Due to Cavitation or Liquid Impingement, Characterization and Determination of Erosion Resistance, ASTM STP 474, 1970, 288-311.

/4/ SYAMALA RAO, B.C. et al.: Cavitation Erosion Studies with Venturi and Rotating Disk in Water. Trans. ASME, Jr. of Basic Engineering, September 1970, 563-579.

/5/ TICHLER, J.W. et al.: Resistance Against Cavitation Erosion of 14 Chromium Steels, Trans. ASME, Jr. of Lubrication Technology, April 1970, 220-227.

/6/ KOUTNÝ, A.: Cavitation Erosion Resistance of Materials in Laboratory and Operating Conditions, Proc. of the 5th Conference on Fluid Machinery, Budapest, 1975.

/7/ KOUTNÝ, A., ŠPERLÍN, M.: Unpublished Research, SIGMA Research Institute, Olomouc, 1979.

/8/ PIGHINI, U. et al.: A New Parameter for a Rapid Evaluation of Metal Resistance to Cavitation Attack, Proc. of the 6th Conf. on Fluid Machinery, Budapest, 1979.

/9/ Material Resistance Determination Against Cavitation Erosion by Ultrasonic Vibratory Apparatus, Czechoslovak State Standard, Designation ČSN 01 5082, 1977.

/10/ Standard Method of Vibratory Cavitation Erosion Test. ASTM Standards, Designation G32-72, 1972.

NOTATION

A_5	elongation
C_0, C_1	constants
E	modulus of elasticity in tension
HV	Vickers hardness
MDPR	mean depth of penetration rate (= volume loss rate/ exp. area)
MVLR	mean volume loss rate
r_{xy}	correlation coefficient
R	tensile strength
R 0,2	0,2 proof stress
UR	ultimate resilience
v	peripheral velocity at the centers of the cavitation inducer holes

KOUTNÝ Alois, Eng. Grad.
SIGMA Research Institute
772 23 Olomouc, Czechoslovakia

DETERMINATION OF PRESSURE LOSS OF DUST-AIR FLOWING IN A PIPE, WITH A VIEW ON EXPANSION

dr. László Kovács - dr. László Pápai - dr. Sándor Váradi

1./ INTRODUCTION

Specific energy consumption of pneumatic transport is generally improved in the range of high ratios. Dense-flow transport is spoken of in the range $\mu = 25...150$ mixing ratios.

Determination of pressure loss in the pipeline is fundamental to design.

Great many publications on theoretical and experimental research work are available for the determination of pressure loss of thin-flow ($\mu < 25$) pneumatic transport.

Complexity of the physical process in the dense-flow pipeline during transport is responsible for the scarcity of relevant publications.

A design relationship for the computation of pressure loss obtained by the authors on the mathematical-physical model will be presented. The calculated pressure losses are in fair agreement with measured values.

2./ DENSE-FLOW PNEUMAIC TRANSPORT IN LONG PIPELINES. PRESSURE LOSS DETERMINATION

Pipeline in Fig. 1 contains material in transitional state. Namely, a part of the material glides along the pipe wall, the other part proceeds with impacts against the pipe wall and the gliding material surface.

Assuming steady state in a dense flow horizontal pipeline pressure loss (dp) acting on an elementary section /regarded as control volume chosen for analysis/ may be decomposed in to two parts. One part (dp_o) is gas friction against the pipe wall, the other part (dp_m) is accessory pressure loss due to the material flow.

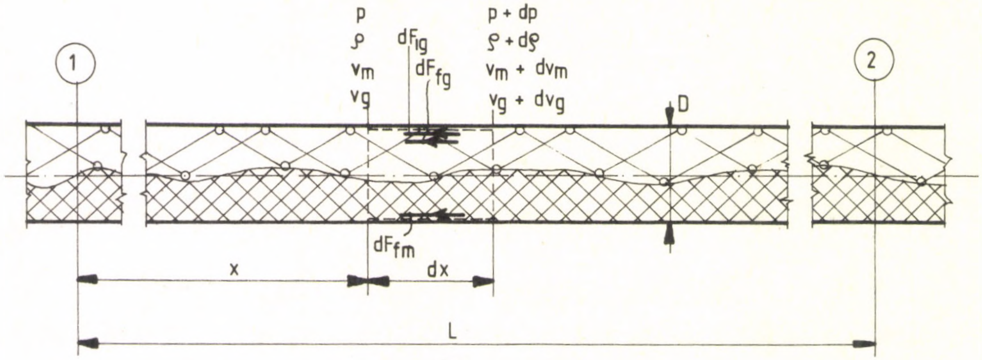

FIG.1

Formulated:

$$- dp = dp_o + dp_m \qquad /1/$$

Gas friction against the pipe wall is expressed by:

$$dp_o = \lambda \frac{\rho_g}{2D} v_g^2 dx \qquad /2/$$

This equation does not contain the contraction of cross section due to the material, and omits the pressure loss needed to accelerate the gas flow.

Accessory pressure loss due to material flow has, according to Pápai [1] , two parts:

$$dp_m = dp_f + dp_i \qquad /3/$$

Right-hand-side first term (dp_f) , and second term (dp_i) in /3/ represent pressure losses due to material friction, and impact against the pipe wall resp.

Following the train of thought of Pápai [1] : we can write:

$$dp_f = k_f \frac{\dot{m}_m g}{v_g A} dx \qquad /4/$$

and

$$dp_i = k_i \frac{\dot{m}_m v_g}{D A} dx \qquad /5/$$

In /4/ and /5/, pressure drops are axpressed in terms of gas velocity rather than of material velocity. Assuming the slip to be constant during transport (s = const.) ; $v_m = (1 - s)\, v_g$, which is considered as a fair approximation. Factors k_f an k_i in both pressure loss relationships contain concrete, measurable values of the constant slip depending on material, mass flow, etc.

Utilizing Eqs /2/, /3/, /4/, /5/, Eq. /1/ may be written as:

$$- dp = \lambda \frac{\rho_g}{2\,D} v_g^{\,2}\, dx + k_f \frac{\dot{m}_m\, g}{v_g\, A}\, dx + k_i \frac{\dot{m}_m\, v_g}{D\, A}\, dx \qquad /6/$$

Making use of

$$\dot{m}_g = v_g\, \rho_g\, A \qquad /7/$$

and the formula for isothermal state changes of the mass flow of transport gas

$$\frac{p}{\rho_g} = RT \qquad /8/$$

and after separating variables, Eq. /6/ will be as follows:

$$\frac{p\; dp}{\frac{RT}{A^2}\left(\frac{\lambda}{2D}\dot{m}_g^{\,2} + \frac{k_i}{D}\dot{m}_m\,\dot{m}_g\right) + k_f\,\frac{\dot{m}_m\, g}{\dot{m}_g\, RT}\; p^2} = - dx \qquad /9/$$

At the outlet of the conveying pipeline there is atmospheric pressure, hence, taking boundary conditions

$$x = x_2 = L; \qquad p = p_2 = p_A$$

into consideration, and having integrated Eq. /9/ for the pressure change along the pipe the following relation is got:

$$p = p_A \sqrt{e^{\frac{2\,(L-x)\; k_f\,\mu\, g}{RT}}\left[Fr^2\left(\frac{\lambda}{2\mu k_f} + \frac{k_i}{k_f}\right) + 1\right] - \left[Fr^2\left(\frac{\lambda}{2\mu k_f} + \frac{k_i}{k_f}\right)\right]} \qquad /10/$$

where:

$$Fr = \frac{v_{gA}}{\sqrt{g\ D}} = \frac{\dot{m}_g}{A\ \rho_{gA} \sqrt{g\ D}}$$ is Froude's number

referring to pipe-end velocities, and $\mu = \frac{\dot{m}_m}{\dot{m}_g}$ is the mixing ratio.

3./ ANALYSIS OF PRESSURE AND VELOCITY CONDITIONS

Calculated pressure and gas velocity values for fly-ash transport have been compiled in Figs. 2 - 5. Calculation data: $R = 287\ m^2/s^2K$; $T = 293\ K$; $p_A = 1$ bar /absolute/ and measured data: $\lambda = 0{,}015$; $k_f = 0{,}4$; $k_i = 0{,}001$

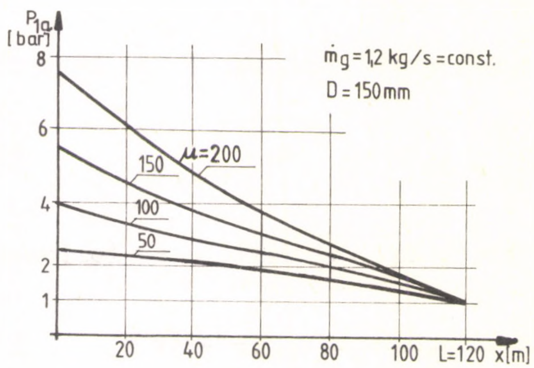

FIG. 2

Figure 2 shows relationship $p_a = f(x)$ for a pipeline of length L=120m and D=150 mm dia /with mixing ration μ as parameter/.

Initial pressure values at the inlet of the pipeline /x=0/ needed for transport for different pipe lengths L are seen in Fig. 3, with material mass flow as parameter.

Velocity values at pipeline inlet /x = 0/ for different material mass flow parameters have been also plotted in Fig.3

Figure 4 shows pressure and velocities vs. pipe length (L) at the pipe inlet /x = 0/ for a material mass flow $\dot{m}_m = 30$ kg/s = const. and for different gas mass flows.

Pressure vs. gas mass flow at the inlet of a pipe length L = 100 m /at x = 0/ have been plotted in Fig. 5, with material mass flow $\dot{m}_m$ as parameter.

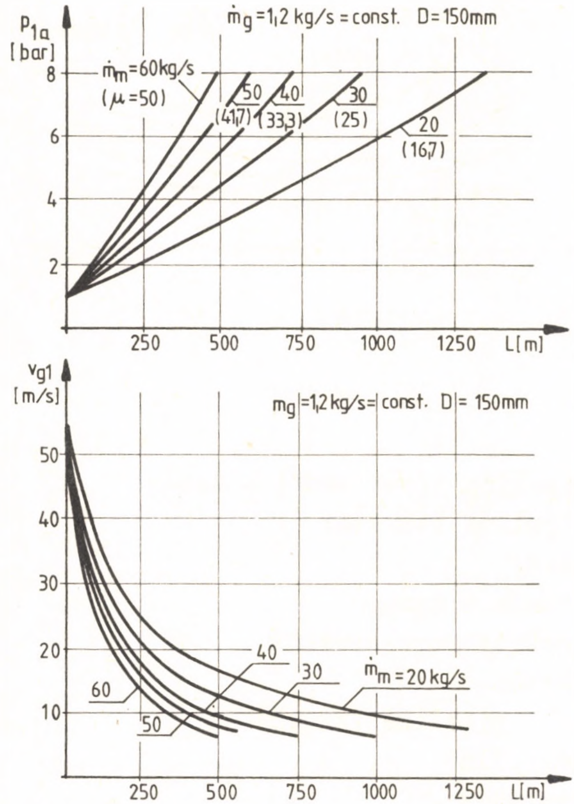

$\dot{m}_g$ = 1,2 kg/s = const. D = 150mm
P_{1a} [bar]
$\dot{m}_m$ = 60kg/s (μ = 50)
50 (41,7)
40 (33,3)
30 (25)
20 (16,7)
L [m]
v_{g1} [m/s]
m_g = 1,2 kg/s = const. D = 150mm
60
50
40
30
$\dot{m}_m$ = 20 kg/s

FIG.3

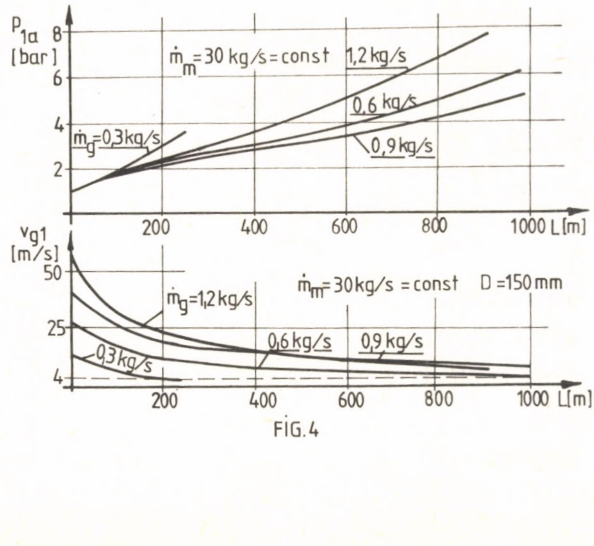

P_{1a} [bar]
$\dot{m}_m$ = 30 kg/s = const
1,2 kg/s
0,6 kg/s
0,9 kg/s
$\dot{m}_g$ = 0,3 kg/s
L [m]
v_{g1} [m/s]
$\dot{m}_g$ = 1,2 kg/s
$\dot{m}_m$ = 30 kg/s = const D = 150 mm
0,6 kg/s
0,9 kg/s
0,3 kg/s

FIG.4

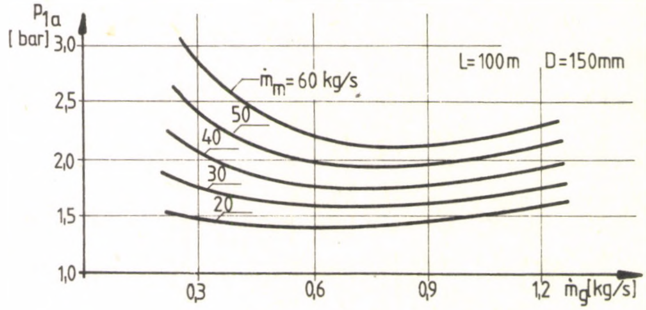

FIG. 5

LEGEND

A	m^2	pipeline cross section area
D	m	pipeline diameter
F	N	power
Fr	–	Froude's number
g	m/s^2	gravity acceleration
k	–	factor
L	m	full pipeline length
$\dot{m}$	kg/s	mass flow
p	Pa, bar	pressure
R	m^2/s^2K	gas constant
T	K	temperature
v	m/s	velocity
x	m	horizontal distance
λ	–	pipe friction coefficient
μ	–	mixing ratio
ρ	kg/m^3	density

SUBSCRIPTS

a	absolute
A	atmospheric
f	frictional
g	gas
i	impact

m material
1 pipeline inlet
2 pipeline outlet

REFERENCES

1 Pápai, L.: Pneumatic and Fluidizational Material Handling. Notebook of the Institute for Postgraduate Engineering Education, Budapest, 1975.

2 Váradi, S.: Control of a Pressure Vessel Pneumatic Transport system. Doctor's Thesis, Budapest, 1981.

3 Pápai, L.: Druckberechnung für pneumatische Dichtstromförderung. Periodica Polytechnica, Mech.Eng. Budapest, Vol. 25 /1982/, No. 1.

4 Sártory, M.: Determination of the pressure Distribution along the Pipeline in Pneumatic Transport. Scientific Students' Circle Composition, Technical University, Budapest, 1982.

Dr.-Ing. L. Kovács Ass. prof.
Dr.-Ing. L. Pápai Professor
Dr.-Ing. S. Váradi Res. Eng.
Dept. of Hydr. Mach. T.U. Budapest
P.B. 91. Hungary 1521